Phase 3A Year 2

Annual Report

July 29, 2022

DE-EE0007080

University of Utah

UTAH FORGE U.S. Department of Energy

Phase 3A Year 2 Annual Report

ENHANCED GEOTHERMAL SYSTEM TESTING AND DEVELOPMENT AT THE MILFORD, UTAH FORGE SITE

Utah FORGE

University of Utah

423 Wakara Way, ste 300

Salt Lake City, UT, 84105

Prepared for the U.S. Department of Energy
Office of Energy Efficiency and Renewable Energy
Contract DE-EE0007080

July 29**, 2022**

Table of Contents

A. OVERVIEW OF PHASE 3A ANNUAL ACTIVITIES

The ultimate objective of Utah FORGE is to demonstrate the viability of Enhanced Geothermal System (EGS) energy development. The project will create a controlled environment where EGS technologies and approaches can be developed, tested and optimized. The laboratory will function as a dedicated site for technical interaction and public education to support the widespread adoption of EGS as an energy source.

This report presents an overview of Phase 3A Year 2 activities. Year 1 activities transitioned the Utah FORGE project from site characterization and baseline monitoring to infrastructure development required for full deployment of the Utah FORGE laboratory.

The major accomplishments of the Utah FORGE team:

1. Completed construction of the main elements of the Utah FORGE field laboratory, including three additional deep wells (16A(78)-32, the injection well, 56-32 and 78B-32). Well 16A(78)-33 was drilled approximately parallel to S_{hmin} to a depth of 5938 ft before being deviated 65° from vertical. The well has a total measured depth of 10987, a true vertical depth of 8559 ft and a temperature of 428°F.
2. Awarded $49.5 M for seventeen R&D projects in five topic areas including: tools for zonal isolation, estimation of stress parameters, field scale characterization of reservoir evolution, stimulation and configuration of the wells, integrated laboratory and modeling studies. The projects will develop and test new technologies, operationally-oriented equipment, methods for reservoir stimulation, and address fundamental issues that limit commercialization of EGS development, and methods for reservoir stimulation, monitoring and testing.
3. Much of the infrastructure for the seismic monitoring network was completed. When fully deployed, the network will consist of two rings of surface and borehole geophones at 3 and 8 km, from the center of the Utah FORGE footprint, fiber optic cables in wells 78-32 and 78B-32, and deep geophone strings at reservoir depths in wells 56-32, 58-32 and 78B-32. The 3 km ring is operational, and installation of the 8 km ring was advanced, wherein seismometer stations were permitted and the postholes were drilled. Multilevel geophone strings, Nodal arrays, and additional fiber optic cables will augment the monitoring network during stimulations.
4. A plan for stimulating three stages near the toe of well 16A(78)-32 was approved. Approximately 10,000 barrels of water will be injected; 4500 barrels in the open hole section and 2500 barrels in each of two stages in the cased section of the well.
5. Completed repeat groundwater, gravity, GPS, InSAR surveys for baseline characterization of the subsurface.
6. Performed detailed mineralogic and lithologic analyses of the cores and cuttings obtained from the drill holes.
7. Prepared a preliminary design for well 16B(78)-32. This well will serve as the

production well for reservoir creation, fluid circulation and demonstration of heat extraction.

8. Increased stakeholder interactions with expansion of the Outreach and Communications. Information is available on the Utah FORGE website, social media platforms, U-tube videos, E newsletter, podcasts, and scientific forums. This outreach activities provide information suitable for the general public, students fromgrade school to graduate levels, scientists and geothermal specialists.
9. Uploaded more than 200GB of data to the Geothermal Data Repository (GDR). There were more than 27000 downloads of the data. Forty papers were published and 80 presentations were given at Technical Conferences.
10. Collected and placed in the public domain a complete suite of data, logs, cuttingsand core samples.
11. Conducted detailed fracture analysis of the Formation Microimager and UltrasonicBorehole logs and developed a refined Discrete Fracture Network (DFN).
12. Thoroughly tested drilling, logging, and seismic monitoring tools and methods at the Utah FORGE site under conditions appropriate for commercial EGS development.
13. Utah FORGE is the most thoroughly characterized of any EGS sites in the world.

During Year 2 of Phase 3, the infrastructure at the Utah FORGE site was expanded significantly. Three deep wells were successfully completed for reservoir creation, monitoring, and tool testing (Fig. 2). New pads and roads were built, the 1.2 mile (3 km) ring for seismic monitoring was completed, deep wells for deploying geophones at reservoir depth were drilled, and R&D field projects were initiated. Well 16A(78)-32 was drilled to the southeast from a pad on the west end of the Utah FORGE site. The well was drilled to a vertical depth of 5938 ft, then deviated 65° from vertical, before reaching a total measured depth of 10987 and a true vertical depth of 8559 ft. The initial demonstration reservoir will be created between well 16A(78)-32 and a parallel well, 16B(78)-32 planned for late 2022.

The two new vertical wells, 56-32 (drilled to 9145 ft) and 78B-32 (drilled to 9500 ft), and well 58-32 (total depth of 7536 ft) will be used for tool testing and seismic monitoring at near reservoir depths. All of the wells recorded similar conductive thermal gradients. Beneath the alluvium and basin bounding fault, the wells encountered Tertiary rhyolite and granitoid and Precambrian metamorphic rocks. Well 78B-32, the deepest well, has an estimated bottom hole temperature of 465°F. With the exception of a single zone in well 78-32 that took 17 barrels of mud, there were no measurable mud losses or gains during drilling. These observations support the conclusion that the permeability of the basement granitoid and metamorphic rocks is extremely low.

One-half of the funding for Utah FORGE is obligated for external, competitively bid research. Contracts for 17 R&D projects totaling $ 49.5 M were awarded under Solicitation 1. R&D topics included tool development, stress analysis, field scale characterization, well stimulation, and thermo-hydrologic-mechanical-chemical modeling. An additional $44.5 M will be awarded

under Solicitation 2 in 2023. These field and laboratory investigations are being supported by Utah FORGE infrastructure development, high resolution monitoring activities, injection testing, and numerical simulations of the reservoir evolution and well tests. Technical information on Utah FORGE is being shared with the scientific community through the Utah FORGE website, conferences and publications, field trips, and the DOE Geothermal Data Repository (GDR).

An extensive suite of geophysical and image logs was run in all wells. The image logs allowed refinement of the Discrete Fracture Network (DFN). Analysis of Diagnostic Fracture Injection Tests (DFITs) in well 16A(78)-32 and previously in well 58-32 confirmed earlier interpretations of the stress magnitudes while numerical simulations of the updated DFN have provided new insight into the three-dimensional fracture network that will form the geothermal reservoir. A plan to stimulate three zones near the toe of well 16A(78)-32, one in the 200 ft of open hole at total depth and two zones behind casing was developed. The stimulation was conducted in April 2022.

Monitoring of the seismicity surrounding the Utah FORGE site continued. No events have been detected beneath the Utah FORGE site since monitoring in the region began in 1981, supporting the conclusion the risk from induced seismicity is low. The seismic monitoring network will incorporate temporary arrays of surface seismometers, surface and borehole Distributed Acoustic Sensing (DAS) cables, and shallow borehole broadband instruments in concentric rings at 3 km (1.9 miles) and at 8 km (5 miles), ground motion sensors.

InSAR, gravity, water levels and GPS baseline monitoring occurred on a quarterly basis. Changes in gravity, water level and GPS data are interpreted to reflect temporal variations resulting from seasonal changes in precipitation. No deformation was observed in the InSARdata.

The conceptual geologic model has been updated. Of particular interest are the presence of a thick section of sheared rhyolite in well 16A(78)-32, interpreted as a dike, within the uppermost portion of the basement rocks, high grade Precambrian metamorphic rocks near the base of the deep wells and results of MTinterpretation, which reveal the resistivity structure and the distribution of impermeable basement and hot fluids down to 50 km depth.

Public outreach remains a priority of the Utah FORGE program. Information about geothermal energy is distributed to the public through the Utah FORGE website, online presentations, podcasts, videos, Twitter, Facebook and LinkedIn, and our popular e-newsletter “At the CORE”. Several new YouTube videos, podcasts, lesson plans, and STEM activities were developed despite quarantines due to the COVID-19 pandemic. Scientific data is available through numerous publications and conference proceedings (refer to the Utah FORGE website), and the Geothermal Data Repository (GDR). More than 200 GBytes of data have been uploaded to the GDR since the project was initiated.

Table A-1. *Deliverables submitted to DOE for Phase 3 Year 2.*

Task 3.1.1 – Updated PMP, including SOP appendices (subtask 3.1.1.1)and Indemnification Strategy and Process	Nov 18, 2020

Subtask 3.1.2 – Updated Environmental, Safety and Health Plan	Jul 8, 2020
Subtask 3.1.3 – Updated Sample Handling and Core Curation Plan –	Mar 27, 2020
Subtask 3.1.4 – Updated Outreach and Communication Plan	Jun 30, 2020
Addendum	Nov 19, 2020
Subtask 3.1.5 – Annual Phase 3 Topical Report(s)	Dec 31 , 2021
Task 3.2.0 – Draft of the Phase 3 annual R&D Solicitation	May 28, 2020
Subtask 3.3.1 – Updated Seismic Monitoring Plan Same as Seismic Drilling Plan (56-32)?	Sep 1, 2020
Subtask 3.3.2 – An updated Induced Seismicity Mitigation Plan (ISMP) with an updated Probabilistic Seismic Hazard Analysis (PSHA) as appendix –	Jun 25, 2021
Subtask 3.4.6 – Deep Well #1 Drilling Plan	Oct 4, 2020
Subtask 3.4.9 – FORGE Pilot Well Drilling Plan -	May 28, 2021
Subtask 3.5.1 – Modeling and Simulation Plan	Apr 3, 2020
Subtask 3.5.6 – Stimulation Test Plan – Go/No-Go below	Jan 3, 2022
Task 3.10 – Permitting and Regulatory Compliance Documents	Ongoing
Go/No-Go Decision Point #3 Pilot Well Drilling Plan – '*Drilling Program 78B-32 Utah FORGE*'	Jun 2, 2021
Go/No-Go Decision Point #4 Reservoir Testing of Deep Well #1 Plan – '*Well 16A(78)-32 StimulationOperations Plan*'	Jan 11, 2022

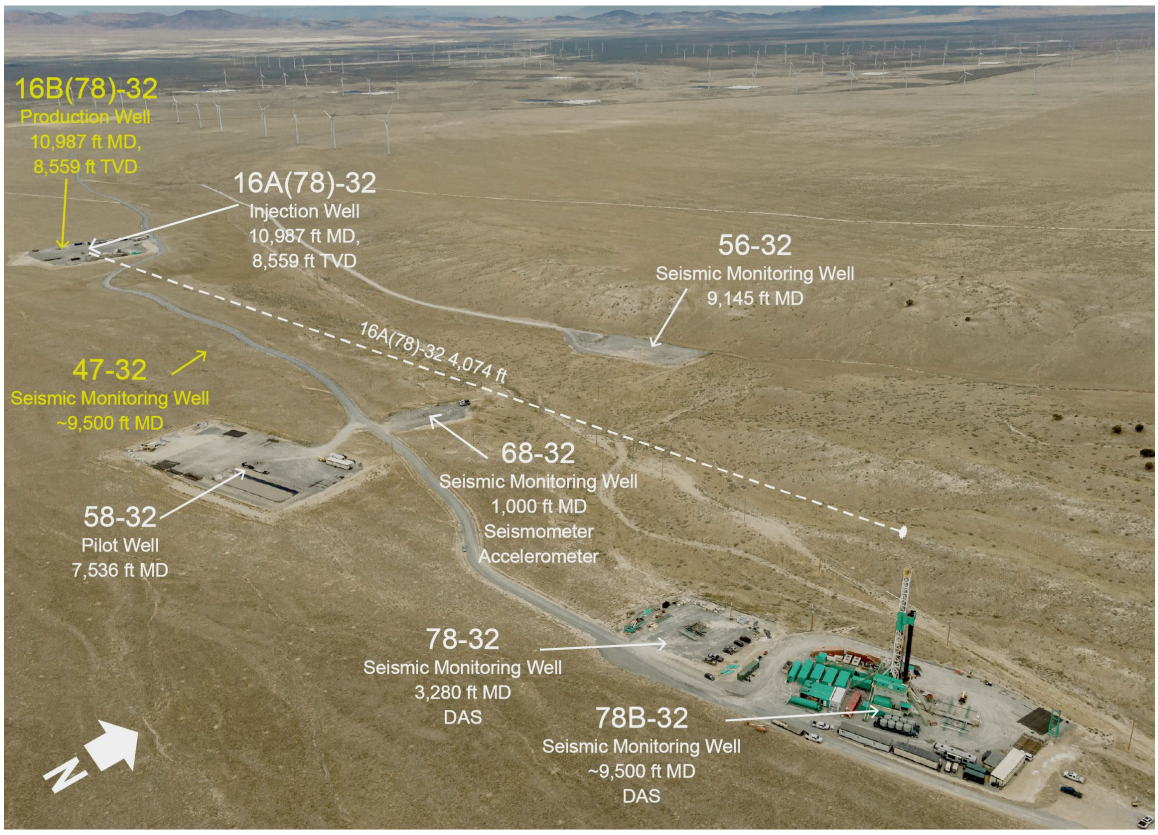

Figure A-2. *Utah FORGE infrastructure. Wells shown in white have been drilled, those in yellow are planned. The dotted line shows the trajectory of well 16A(78)-32, which will serve as one of the two wells that will be stimulated to create the Utah FORGE EGS reservoir.*

The major accomplishments of Utah FORGE include the following:

1. Established a state-of-the-art field laboratory for testing technologies and tools forcreating, monitoring, and sustaining EGS reservoirs
2. Deployed a seismic network for monitoring induced and natural seismicity, includingmonitoring the stimulation of well 16A(78)-32 and long-term circulation testing
3. Drilled and tested well 16A(78)-32, the first full-sized highly deviated EGS well at the site.
4. Drilled well 56-32 to 9145 ft north of the trajectory of well 16A(78)-32 for seismic monitoring.
5. Drilled Well of Opportunity-1 (WOO-1) to 9500 ft for testing EGS technologies andseismic monitoring.
6. Developed a comprehensive dataset of the site - all data is publicly available

throughthe GDR

7. Obtained complete suites of geophysical and image logs
8. Refined the Discrete Fracture Network (DFN), developed a methodology for selecting the most appropriate zones for stimulation, and predicted the size andshape of the fracture network that will be created during the stimulation of well16A(78)-32
9. Demonstrated successful stimulation of cased wells
10. Identified technology gaps
11. Provided core and cuttings for study
12. Awarded 17 external competitively bid R&D projects. Participated in STATdiscussions on topic selection for Solicitation 2.
13. Expanded the Outreach and Communications Program to showcase to the public,stakeholders, and the energy industry that EGS technologies and conventional geothermal energy have the potential to contribute significantly to power generation in the future.
14. Provided extensive educational and research opportunities for students at all levels.
15. Uploaded 200 GB to the GDR

B. RESULTS

B.1. SITE INFRASTRUCTURE & OPERATIONS

Infrastructure for the Utah FORGE site has been continuously upgraded to support drilling, stimulation, other site activities, and environmental and seismic monitoring. These cover earthworks, installation of power supply lines, and an upgrade to telecommunications for data transmission.

EarthWork

Earthwork projects completed (Figure B.1-1) include:

- Construction of the well 16A(78)-32 drill pad and sump
- Construction of the well 56-32 drill pad and Mag Lee Rd
- Construction of the well 78B-32 drill pad
- Deployment of geophones in BOR 3, 1, 2, 3 on the 1.2-mile (3 km monitoring ring) and construction of pads for BOR 4, 5, 6 on the 5.0-mile (8 km) ring for seismic monitoring
- Regrading of the well 16A(78)-32, 56-32 and 78B-32 pads following demobilizationof the drill rig and supporting equipment
- Improvement of FORGE Road from Antelope Point Rd to the west, through the UtahFORGE site and on to the gas compression station to the east and this was done in partnership with Beaver County and Smithfield Foods
- Trenching for power and data cables to and across drill pads
- Cleanout and relining of the well 16A(78)-32 sump prior to the 16A(78)-32stimulation
- Repair eroded western edge of the 16A(78)-32 drill pad
- Construction of a road within the well 16A(78)-32 drill pad to support traffic patternsduring stimulation activities
- Data cable trenched to continuous GPS monitoring station adjacent to the 58-32 drillpad
- Maintenance to roads and pads as needed

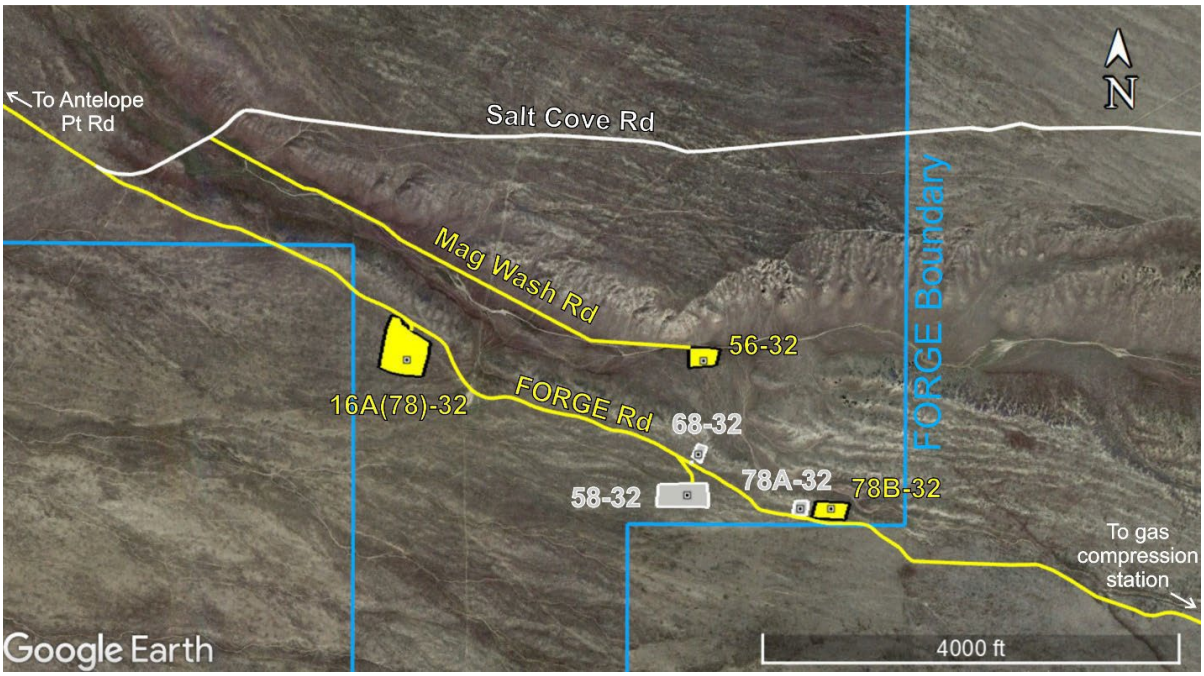

Figure B.1-1. *Earthwork completed during the reporting period is shown in yellow. This includes construction of the 16A(78)-32, 56-32 and 78B-32 drill pads. Construction of Mag Wash Rd to access the 56-32 drill pad, and the improvement of FORGE Rd, both within, and beyond the Utah FORGE footprint (blue).*

Electric Infrastructure

The electric infrastructure has been engineered to provide power for present and future needs. Spur lines were constructed by Rocky Mountain Power from the main electric distribution line to locations on the pads for wells 16A(78)-32, 58-32, 78A-32 and 56-32 (Figure B.1-2). Each spur line can provide 3-phase power for pumps as needed. Meter bases have been installed at the terminations of the spur lines.

Power has been trenched to electric distribution points on all drill pads except for 68-32 (Figure B.1-2). These electric distribution points will provide power for:

- Internet endpoints and temporary trailers for the man camp on the well 16A(78)-32drill pad (at two locations)
- Temporary trailers, seismic monitoring equipment and internet endpoints ~20 ftfrom the 56-32 and 78B-32 wellheads
- Internet distribution on the well 78A-32 drill pad

Future plans include trenching power to distribution panels near the 16A(78)-32 and 16B(78)-32 wellheads to power 125 hp injection and production pumps and potentially installing down hole and transfer pumps for a water well.

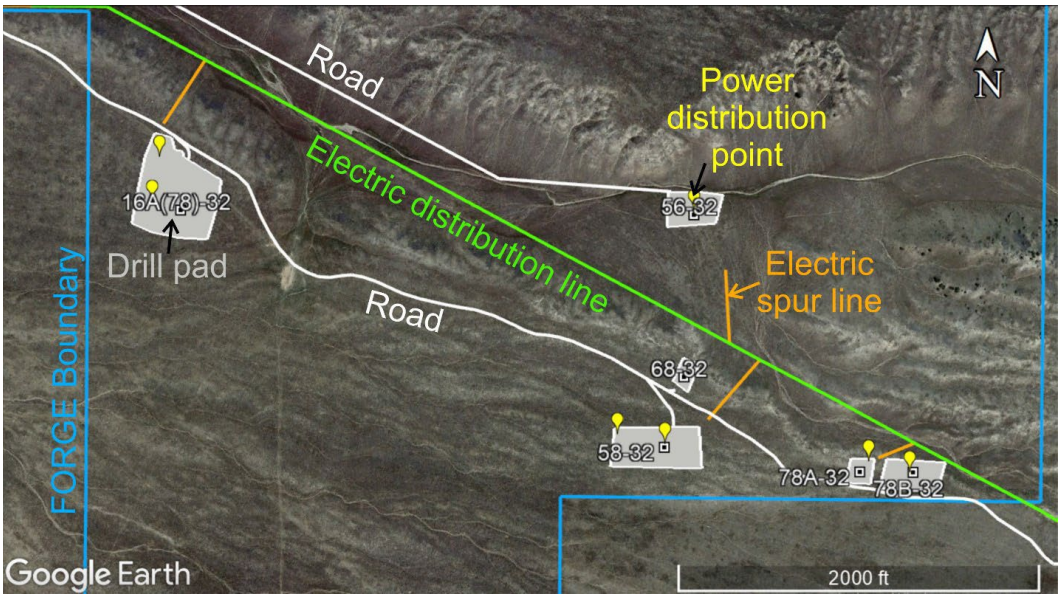

Figure B.1-2. *Electric infrastructure map for Utah FORGE. The main, overhead electric distribution line in shown in green. Electric spur lines to various points within the Utah FORGE footprint(blue) are shown in orange. Power distribution points on the drill pads (gray) are shown in yellow.*

Internet Connection/Communications

Internet services are provided free of charge by the Utah Education and Telehealth Network (UETN). Internet services are routed to the existing communications mast on the well 58-32 drill pad (Figure B.1-3) with supporting equipment located in the adjacent trailer owned by Idaho National Laboratory. To distribute signal across the entire Utah FORGE site, a directional link has been established between the existing communications mast and a newly erected 30 ft mast on the well 78A-32 drill pad. Supporting equipment is stored in a weathertight panel ~100 ft away. Trenching was required to route power the enclosure and for data cabling that runs from the enclosure to the mast. At the top of the new communications mast are three radial antennas that broadcast the signal in all directions. Endpoints have been set up at the power drops on the well 16A(78)-32, 58-32, 56-32 and 78B-32 drill pads, providing both wireless and hardwired internet access.

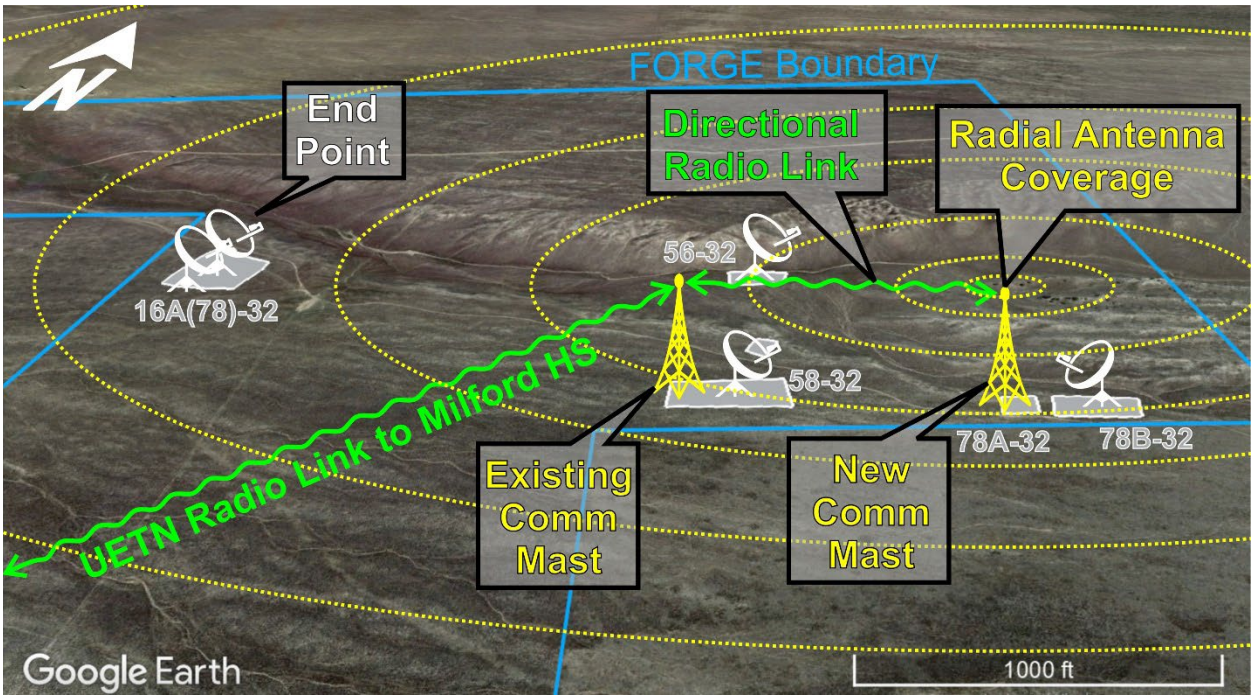

***Figure B.1-3**. Internet infrastructure at the Utah FORGE site. Internet services provided by UETN are relayed to the communications mast on the well 58-32 pad, then relayed to the communications mast on the 78A-32 pad, and finally broadcast to end user sites across the whole Utah FORGE site.*

Continuous Environmental Monitoring

Monitoring and managing the effects of EGS reservoir formation is an important objective of Utah FORGE operations. Seismic monitoring is currently the main technique for monitoring reservoir evolution, fracture growth and induced seismicity resulting from reservoir stimulation and fluid circulation. However, seismicity is not sensitive to the presence of reservoir fluids and large seismic clouds have formed with apparently little interconnectivity of fluid-filled fractures at other sites.

A variety of techniques, in addition to seismic monitoring, are being tested at Utah FORGE. These techniques, which include repeat microgravity, GPS, InSAR (Interferometric Synthetic Aperture Radar), and magnetotelluric surveys, have the potential to identify the presence and characterize the distribution of liquid within the reservoir. The application of these methods has been documented in many conventional geothermal systems. Repeat microgravity measurements provide information on mass changes induced by fluid withdrawal or injection (Allis, 2000. Hunt, 1995; Hunt et al., 2002; Portier et al. 2022; Nishijima et al., 2005; Sofyan et al., 2010). Repeat GPS, and InSAR surveys can be used to track surface deformation (Falorni et al., 2011; Hole et al., 2007; Nishijima et al., 2005). Monitoring surface deformation is important because it can have a significant impact on both on the stability and safety of above ground facilities. Because InSAR utilizes images of the Earth's surface collected from orbiting satellites,

ground installations are not required. Consequently, it is ideal for monitoring large remote sites such as Utah FORGE.

In contrast to other techniques, magnetotelluric surveys provide a measure of the electrical conductivity contrasts in the subsurface. Although commonly employed to define the clay caps over high-temperature geothermal systems, repeat magnetotelluric surveys also offer the potential to monitor transient changes in conductivity related to periods of fluid injection (Peacock et. al, 2012). G. Newman (unpub. data, 2015) and Peacock et. al (2012, 2013) provide examples of repeat magnetotelluric surveys conducted to delineate fluid flow directions during stimulation of the EGS reservoirs at Raft River, Idaho and the Cooper Basin, Australia.

As part of the overall characterization efforts, groundwater levels are being measured in wells that tap a shallow aquifer beneath the Utah FORGE site. The composition of the aquifer has also been determined. In the future, this aquifer will be used as the primary source of water for drilling, well stimulation and circulation testing within the reservoir. Knowledge of the water levels is needed to assess effects of fluid withdrawal from the aquifer. The chemical data will allow us to characterize the effects of mineral deposition and dissolution on the reservoir rocks as they are heated and cooled. In addition to monitoring water levels in the aquifer wells, water levels in the deep wells will be monitored. This information will provide hydrologic information on the reservoir.

The monitoring surveys are providing necessary baseline data on the Utah FORGE site. The data will: 1) be compared to measurements obtained during stimulation activities and circulation testing to evaluate reservoir changes and fluid distributions; and 2) allow evaluation of the resolution of the monitoring techniques.

Across the Utah FORGE site, a distributed network comprising 20 monuments are surveyed on a quarterly basis by the Utah Geological Survey using GPS methods to characterize ground deformation (Figure B.1-4). In Phase 3, eight surveys were completed and a time series summary of all the survey results is shown in Figure B.1-5. Over time, the average displacement ranges from -10 to +25 mm. Comparison with rainfall and water level data suggest the possibility of seasonal effects on the pattern of vertical movement.

Compared to the GPS monitoring, analysis of InSAR images by the University of Wisconsin team shows minimal surface deformation of <2 mm (Figure B.1-6). These analyses include data collected up to and following the stimulation of well 58-32 in 2019.

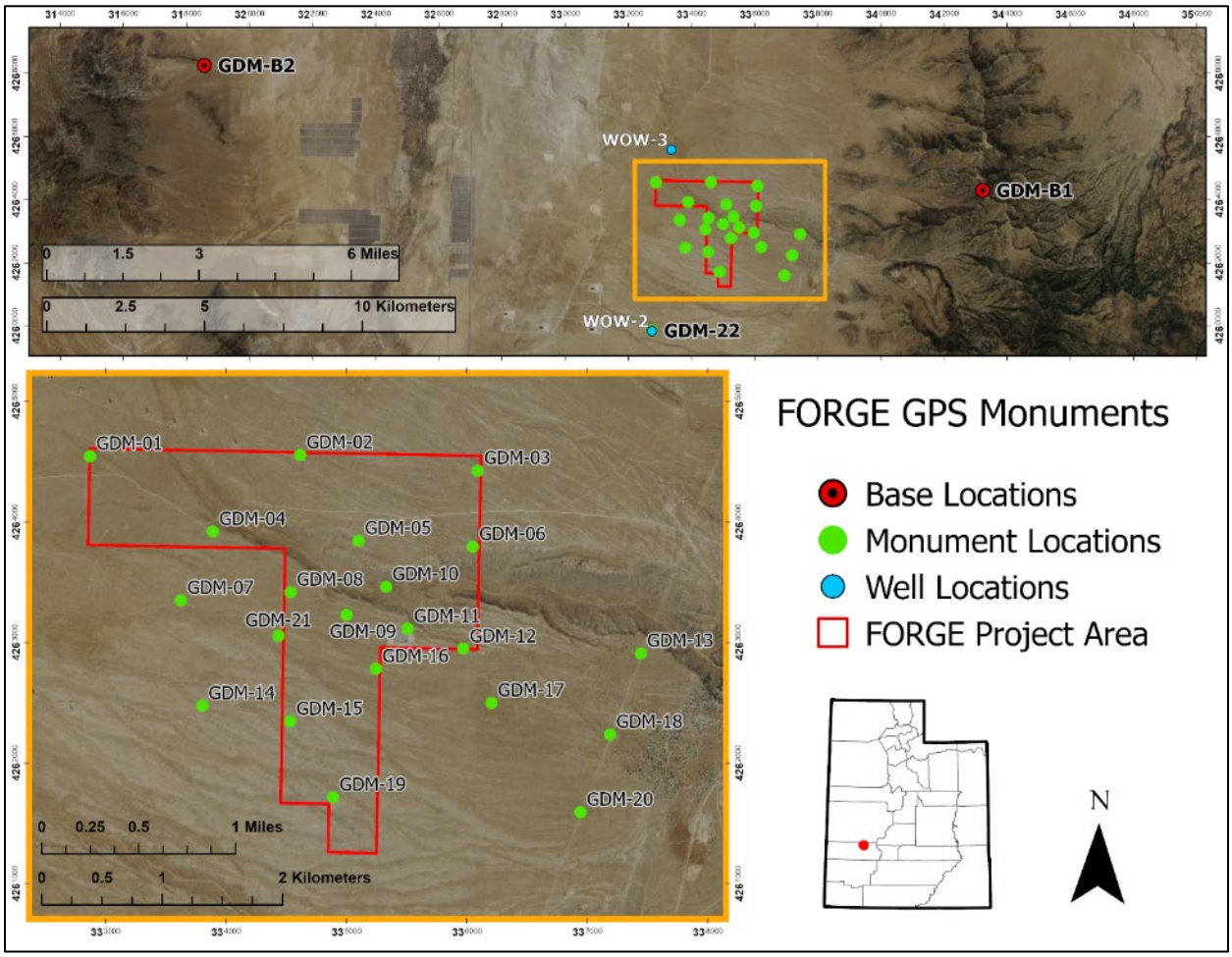

Figure B.1-4. *Location map of the Utah FORGE project area including point locations of the GPS monuments and gravity monitoring stations. WOW 2 and WOW 3 are shallow groundwater wells that are monitored for water levels.*

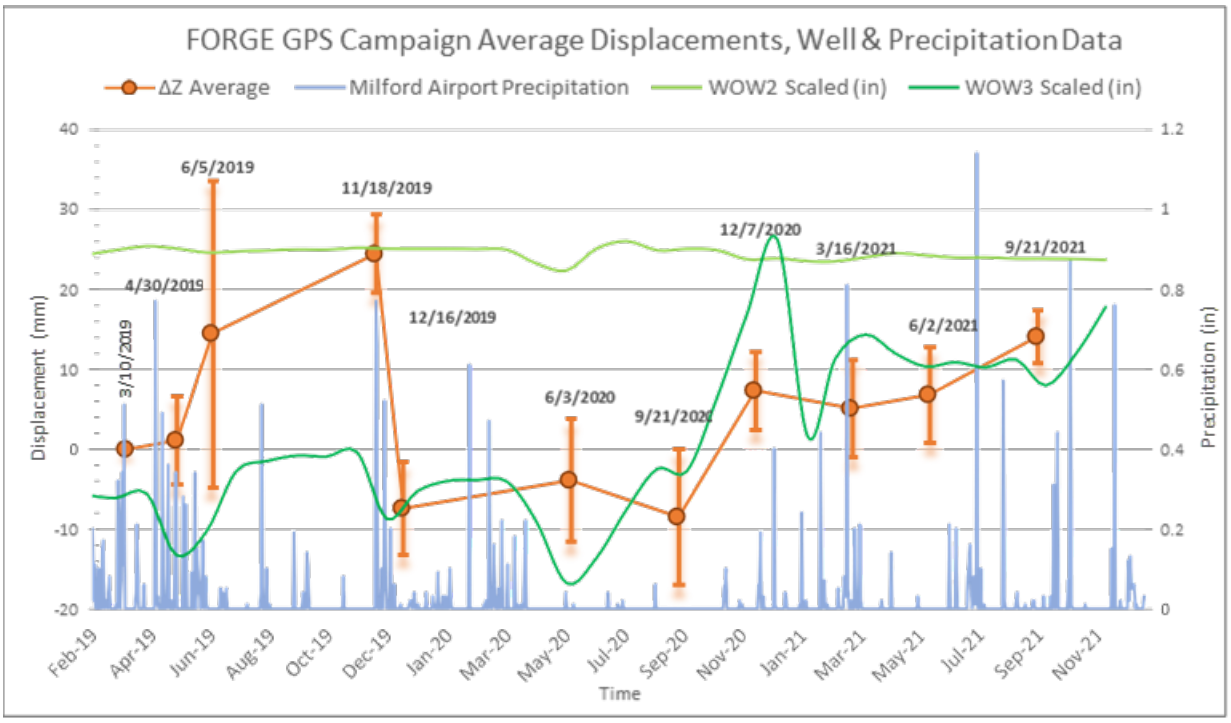

Figure B.1-5. *Time series graph showing average vertical displacements of all monuments compared to precipitation at the Milford Municipal Airport and the groundwater levels of wells WOW2 and WOW3.*

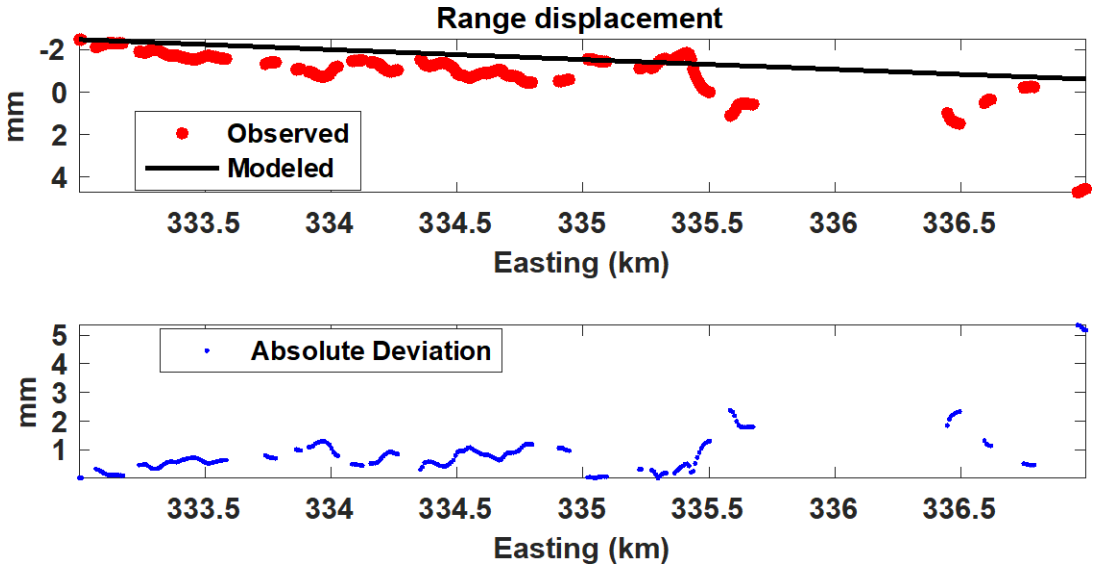

Figure B.1-6*. Profile of range change in ground deformation determined from InSAR data alonga profile striking west to east at UTM northing coordinate 4962.994 km, which runs through cross the Utah FORGE site between about 334.5 and 335.5 easting km.*

Repeat gravity surveys of the GPS monuments by the Utah Geological Survey shows time series variation of -20 to +400 uGal (Figure B.1-10), and this variation seems to correlate with the GPS data. Continued monitoring of the monuments is expected to resolve the source(s) of the time series trends.

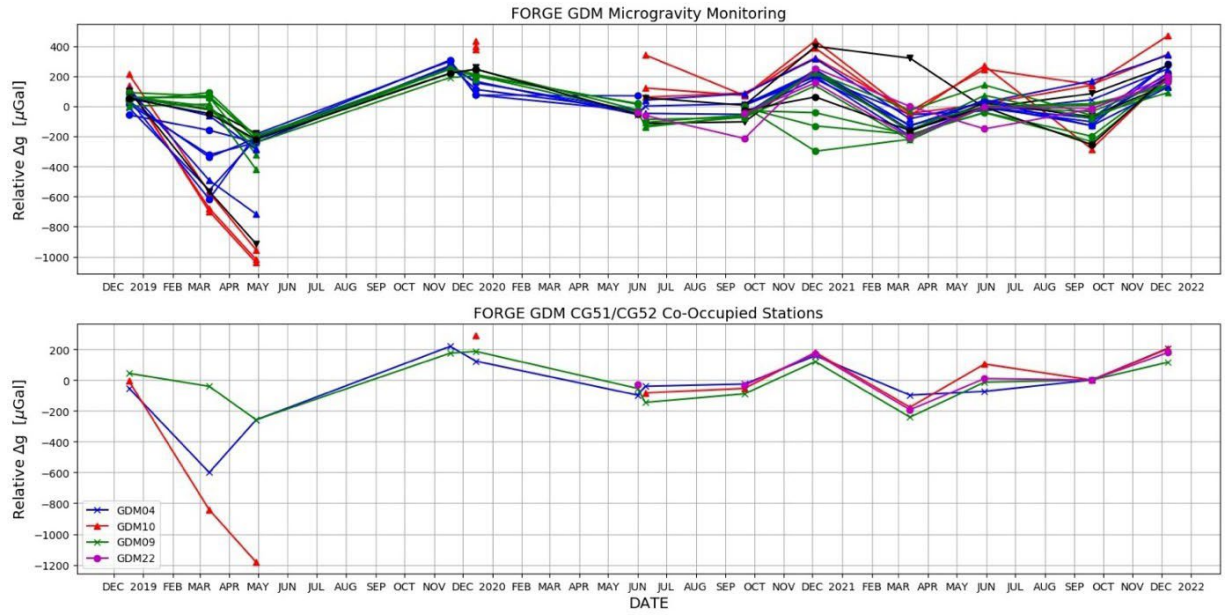

Figure B.1-7. *Plot of gravity station results from December 2018 to December 2021. Top panel shows the observed gravity changes in µGal; bottom panel shows the trends of the local field tie points (GDM10, GDM22) and daily loop base stations (GDM04, GDM09). Tie points are fixed at zero for the September 2021 campaign for display purposes only due to later campaigns having better controls. Assigned colors based on earlier groupings according to qualitative signal trends.*

Groundwater levels are monitored in two shallow wells, WOW2 and WOW3, and these are the only wells in which access for such measurements are available. WOW2 shows relatively constant water levels with a total change of less than 0.5 feet, whereas WOW3 shows much greater variability of up to 20 feet (Figure B.1-4). This difference is likely due to the confined nature of the aquifer at WOW3 and its proximity to supply wells located west and north of the Utah FORGE site that are subject to intermittent pumping.

A comprehensive geochemistry survey of groundwater compositions was completed during Phase 3. Water samples from 23 wells in total have now been acquired and analyzed (Figure B.1-8). The results show what has long been inferred and that is the predominance of a shallow hydrothermal outflow that flows down the hydraulic gradient from Roosevelt Hot Springs westward across the Utah FORGE site. The aquifer is contained within basin-fill gravels before

redirecting northward in the middle of the North Milford valley. On the periphery of theoutflow plume, saline thermal waters are diluted by mixing with distal fresh waters.

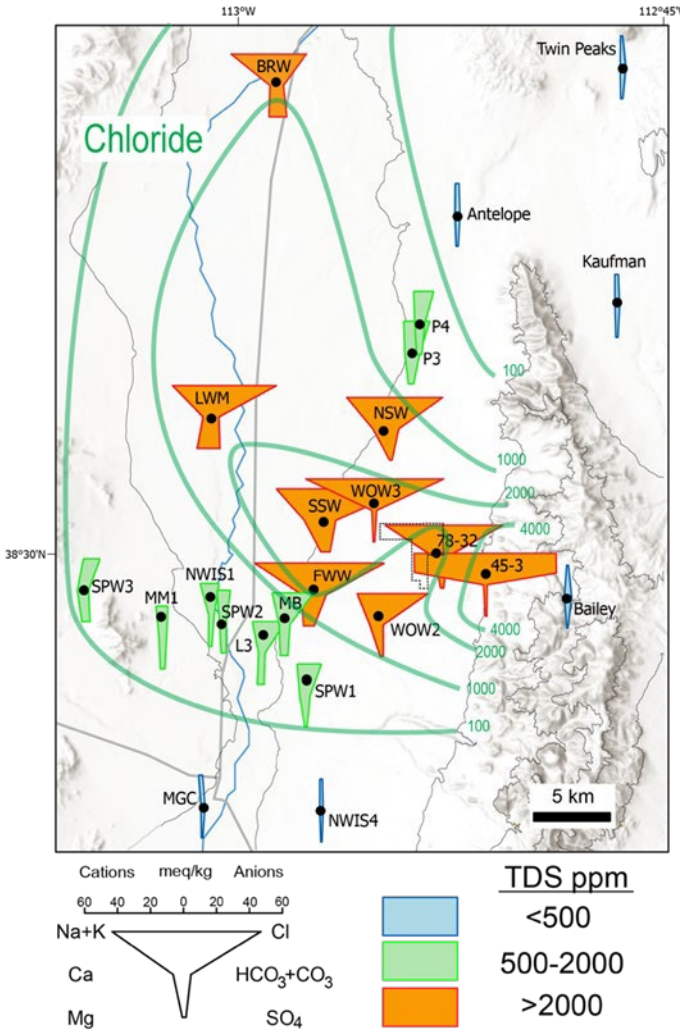

Figure B.1-8. *Geochemistry and spatial variation in groundwater compositions across the North Milford Valley and in the vicinity of Utah FORGE based on data collected between 2018 and 2021. Groundwater compositions are graphically represented as color-coded Stiff plots. Green contours reflect the gradient in chloride concentrations (mg/kg). The Utah FORGE site is delineated by the thin black line near well 78-32. The Beaver River which flows from south to north is represented by the blue line on the west side of the map. Bailey is a freshwater spring in the Mineral Mountains.*

Lastly, the high-resolution MT survey data collected in Phase 2C from 122 stations were processed in Phase 3 using 3D finite element inversion analysis. Good data quality at most sites was obtained in the period range 0.005 to 850 s, which covers the depth interval of ~200 m to

50 km (Figure B.1-9). Properties of the finite element mesh and inversion mechanics are detailed in Attachment 3 (Appendix A2).

The goal of this 2C survey has been to refine the native state model of physical properties over the FORGE and enclosing areas, verify whether dense fracture sets such as seen in the Mineral Mountains project under the FORGE area, and to identify possible heat sources for the hot dry crystalline volume. These all fall under the site characterization rubric. Subsequent work to assess possible reservoir zone changes with injection over time would utilize an additional clustered data set and a locally finer inversion mesh.

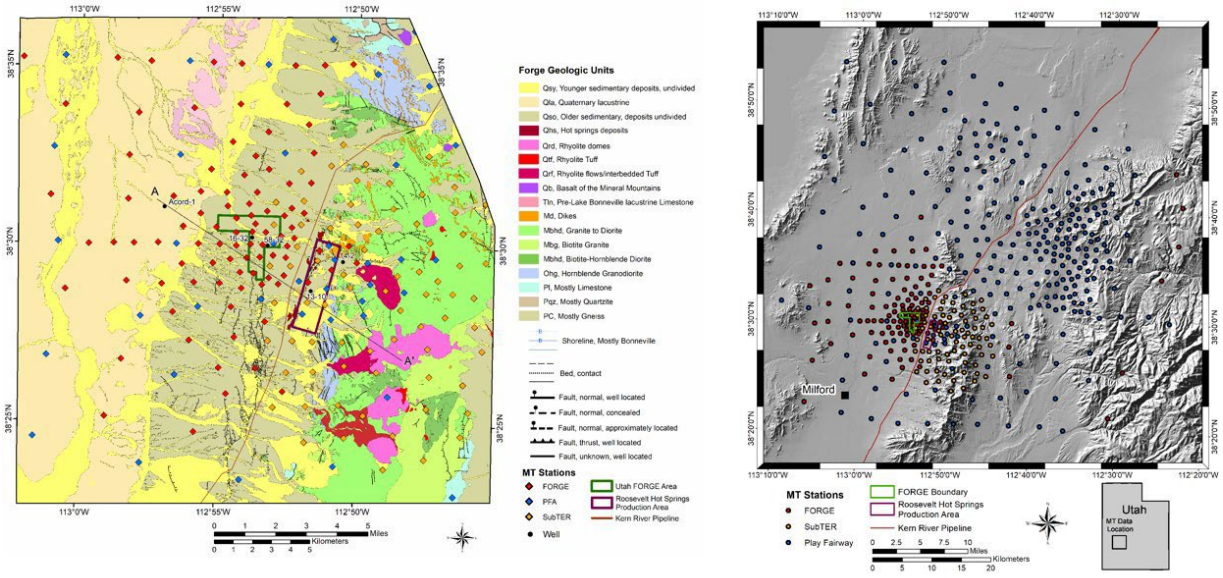

MT Surveying Over FORGE/RHS Areas
Project Scale View

MT Surveying Over FORGE/RHS Areas
Semi-Regional Scale View

Figure B.1-9. *MT site survey map of the Utah FORGE project area showing station coverage (red, FMT). Red-brown trend running NNE-SSW through the project area is the Kern River pipeline (KRP). The Utah FORGE property boundary is shown as a dark green polygon. The dark red-brown rectangle shows the approximate production area of the Roosevelt Hot Springs (RHS) geothermal system. The left view shows the detailed coverage over the Utah FORGE site, while the right view shows the total site distribution incorporated into the 3D inversion model.*

An east-west cross section through the Utah FORGE site (Figure B.1-10) outlines a shallow basin filled with conductive sediments underlain by a thick mass of highly resistive crystalline basement rock that hosts the Utah FORGE EGS reservoir. No clear pre-existing fracture sets such as are apparent in equivalent crystalline lithologies to the east in the Mineral Mountains are imaged below FORGE. A high-angle low-resistivity structure originating in the lower crust rises with a strand projecting directly into theRoosevelt Hot Springs producing area (refer to Appendix A2). We suggest this is the hydrothermal feeder zone to that resource. The model sections in Appendix A2 also imply that volumes of tight hot rock in the extensional Great Basin

province have obtained their heat from neighboring large-scale hydrothermal-magmatic systems.

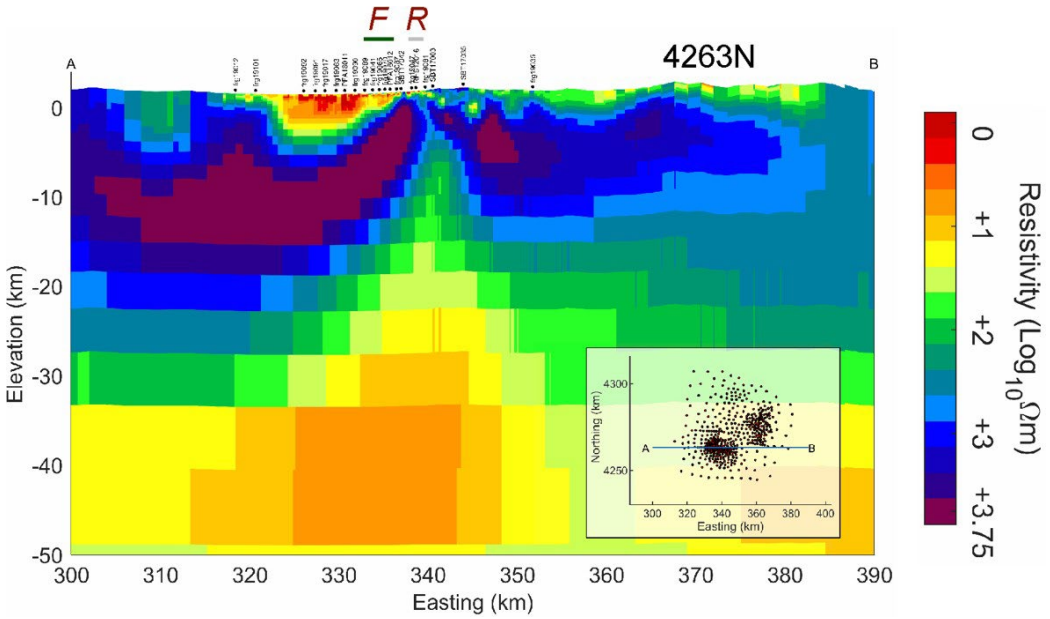

***Figure B.1-10**. E-W section view through the Utah FORGE site and the Mineral Mountains showing the interpreted resistivity structure to 50 km depth; F=Utah FORGE and R=RooseveltHot Springs.*

References

Allis, R. G. (2000). Review of subsidence at Wairakei field, New Zealand. *Geothermics*, *29*(4-5), 455-478.

Falorni, G., Morgan, J., and Eneva, M. (2011). Advanced InSAR techniques for geothermal exploration and production. GRC Transactions, 35, 1661-1666.

Hunt, T. M. (1995). Microgravity measurements at Wairakei Geothermal Field, New Zealand; a review of 30 years data (1961-1991). Proceedings World Geothermal Conference, 863-868.

Hole, J. K., Bromley, C. J., Stevens, N. F., and Wadge, G. (2007). Subsidence in the geothermal fields of the Taupo Volcanic Zone, New Zealand from 1996 to 2005 measured by InSAR. Journal of Volcanology and Geothermal Research, **166**(3-4), 125-146.

Peacock, J.R, Thiel, S., Graham, S., Heinson, G. S., and Reid, P. (2013). Case History: Time-lapse magnetotelluric monitoring of an enhanced geothermal system. Geophysics, **78**, No. 3, P. B121–B130.

Peacock, J. R., Thiel,S., Reid,P., and G. Heinson, G. (2012). Magnetotelluric monitoring of a fluid injection: Example from an enhanced geothermal system. Geophysical Research Letters, 39, L18403, doi:10.1029/2012GL053080.

Portier, N., Forster, F., Hinderer, J., Erbas, K., Jousset, P., Drouin, V., & Bernard, J. D. (2022). Hybrid microgravity monitoring of the Theistareykir geothermal reservoir (North Iceland). Pure and Applied Geophysics, 1-30.

Sofyan, Y., Daud, Y., Kamah, Y., and Ehara, S. (2010). Microgravity method to model mass balance in the Kamojang Geothermal Field. Current Applied Physics, **10**(2), S108-S112.

B.2 SEISMIC MONITORING

The two tasks for seismic monitoring—(1) Convene Expert Seismology Panel and (2) Update Induced Seismicity Monitoring Plan (ISMP)—defined in the SOPO are complete. The expert seismology panel met in November 2019. The results from that meeting and continued discussion with DOE informed the now implemented Utah FORGE seismic network plan. The updated seismic network plan, updates to site characterization, and updates in the communication plan were integrated into the updated ISMP based on the Majer et al. (2016) guidelines. The updated ISMP was accepted in June 2021. Both documents are available on the GDR.

In addition to the tasks explicitly stated in the SOPO, activities related to seismic monitoring include: outreach related talks (Table B.2-1), seismic monitoring of earthquake activity in the region surrounding Utah FORGE, the build-out of the seismic network and the design for borehole seismic monitoring, improved site characterization, analysis of data from the 2019 stimulation, and preparation for the 2022 stimulation.

Table B.2-1. *Seismic outreach talks.*

1. Geothermic DEEP Annual Meeting—Invited Speaker, Seismic Monitoring at Utah FORGE, November 2021.
2. Pivot 2021: Geothermal Reimagined—Panel member, On Solid Ground: Induced Seismicity Forecasting, Prevention and Mitigation, July 2021.
3. AAPG Pivoting 2021: Learning from other industries—Geothermal, machine learning, smart completions, Panel Member, April 2021
4. IRIS, Best Practices for Seismic Posthole Emplacement Webinar and Panel, Panel Member, January 2021
5. Seismic Monitoring at Utah FORGE, ANSS NIC Meeting, January 2021
6. Seismic Monitoring at Utah FORGE, Utah Seismic Safety Commission, October 2020

7. Seismic Monitoring at Utah FORGE, Beaver County Commissioners and Milford Public Outreach, September 2020

Seismic Monitoring

Dedicated seismic monitoring of the Utah FORGE site using both the regional and local Utah FORGE seismic networks has been ongoing since Phase 2A. Earthquake locations, event waveforms, and continuous waveforms are available at http://quake.utah.edu/forge-map. Raw seismic data are available at the IRIS DMC and seismic events are also available via the USGS Comcat catalog. For this reporting period October 1, 2020 through March 9, 2022, 408 earthquakes (M -0.97 to 2.85) have been located (Figure B.2-1 and Figure B.2-2). Primary sources of earthquakes are located under the Mineral Mountains to the east of the Utah FORGE site near the Blundell power plant and further east in a known earthquake swarm region (Mesimeri et al., 2021; Zandt et al., 1982). The seismicity close to the Blundell power plant tends to be shallow, and we hypothesize it is a byproduct of production activities. We have recorded three additional clusters of earthquakes. The first cluster is located near station FOR6. These events are ongoing throughout the project time period but are small in magnitude and occur at very low rates. The other two clusters represent isolated sequences. The first located near station FOR1 is a swarm (no clear mainshock). 125 events with magnitudes between 0.53 and 3.53 (note that the M 3.53 occurred south of the normal Utah FORGE reporting region) define this sequence. The events appear to define a structure dipping to the west and the focal mechanisms indicate normal faulting on a mostly north-south plane. A more complete analysis of this swarm is ongoing and will be presented at the 2022 Annual Seismological Society of America Meeting (Whidden et al., 2022). The cluster in the southeast corner of the map is a recent (November 26 – December 26, 2022) potential swarm sequence. Thirty events with magnitudes between 0.07 and 2.85 define this sequence. Notably, outside of the 2019 stimulation period no earthquakes have been recorded within the Utah FORGE footprint.

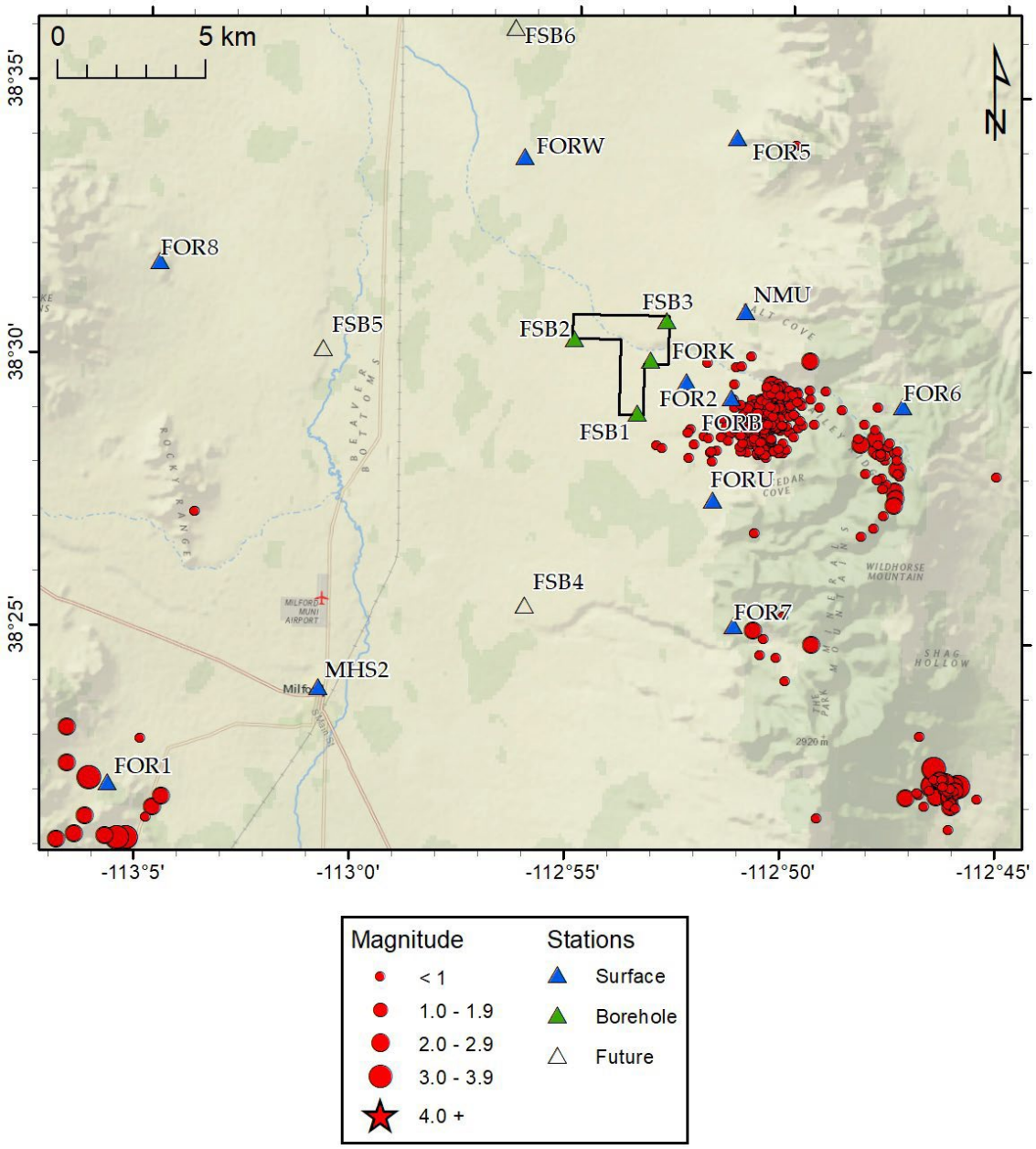

Figure B.2-1. *Seismicity in proximity of the Utah FORGE site for the time period October 1, 2020 through March 9, 2022 recorded as part of the Utah FORGE project.*

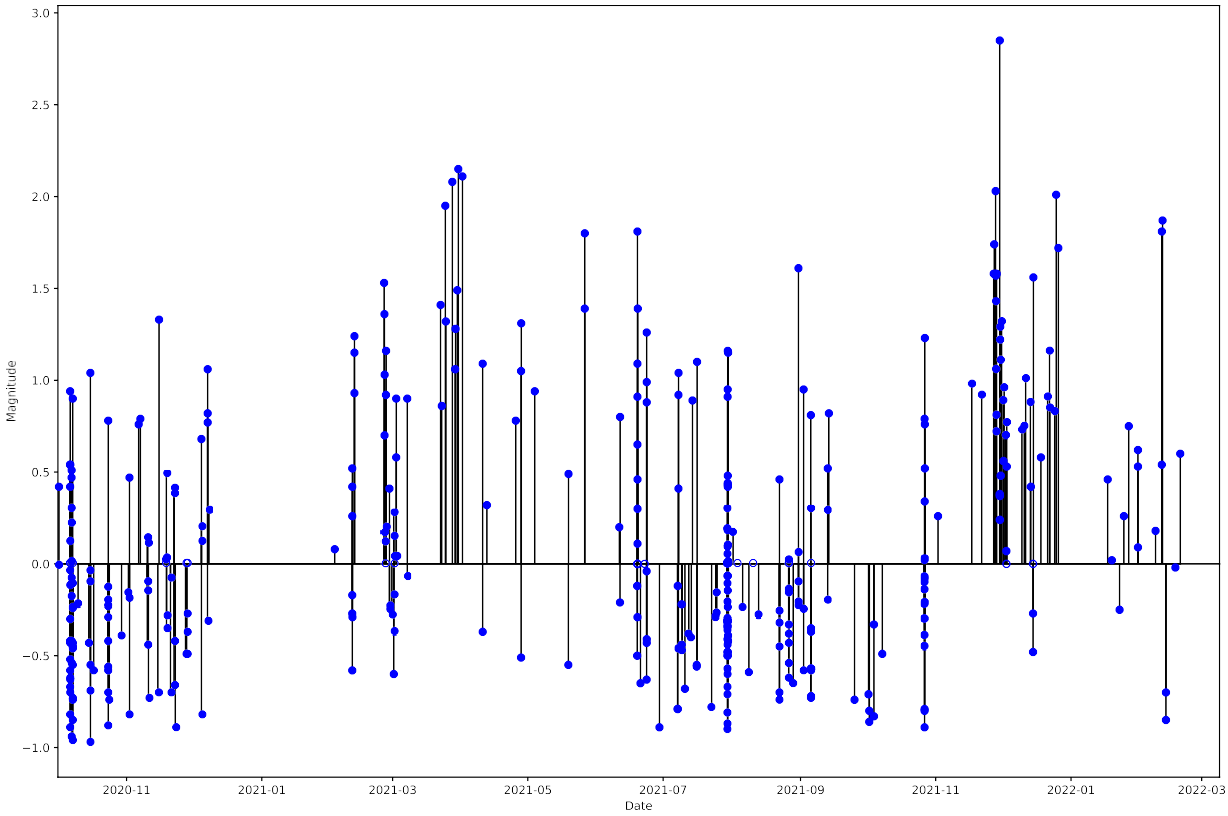

Figure B.2-2. *Magnitude time histories for seismicity located in proximity to the Utah FORGE site (Figure 3.3.0-1) recorded as part of the Utah FORGE project. Open circles indicate events for which a magnitude was not able to be calculated. Time period the same as Figure 3.3.0-1.*

Seismic Network

The goal for the seismic network is (1) to monitor sub-magnitude zero events to understand the development of the EGS geothermal reservoir and (2) to monitor the larger seismicity to inform the understanding of seismic hazard and risk in the immediate area and to inform a traffic light system during operations. EGS reservoir monitoring at Utah FORGE is accomplished using seismic instrumentation of deep boreholes and local monitoring at Utah FORGE is accomplished using a mix of surface and shallow borehole instrumentation with both broadband and accelerometer sensors. The development of each network is presented below. During the reporting period, details of the seismic monitoring have or will be presented at GRC (Rutledge, et al., 2021), ARMA (Rutledge et al., 2022) and SSA (Pankow et al., 2022).

Deep Borehole Monitoring

Downhole seismic monitoring activities to date in Phase 3A have been comprised of planning, quantitative modeling, and contracting for two stages of deep sensor emplacement. These sensors are to go into the three deep vertical wells 58-32, 56-32 and 78B-32 (Figure B.2-3). The first of these activities is associated with the stimulation experiment to take place nominally

over 10 days at three stages near the toe of injector well 16A(78)-32 in mid-April, 2022. The borehole sensors are to be eight-level (8L), three component (3C) digital geophone strings manufactured by Avalon Sciences Ltd (ASL) (Geochain model) with levels separated by 100 feet. These sensors incorporate active solid-state cooling to keep internal temperatures to within 165C when the external temperatures may reach 210C. Two of the Geochains will be operated by subcontractor Schlumberger Inc in wells 58-32 and 56-32, while the third will be operated by the maker Avalon at well 78B-32 under supervision of Dr. Ben Dyer of Geo Energie Suisse (GES), with which Utah FORGE has formalized a cooperative research arrangement.

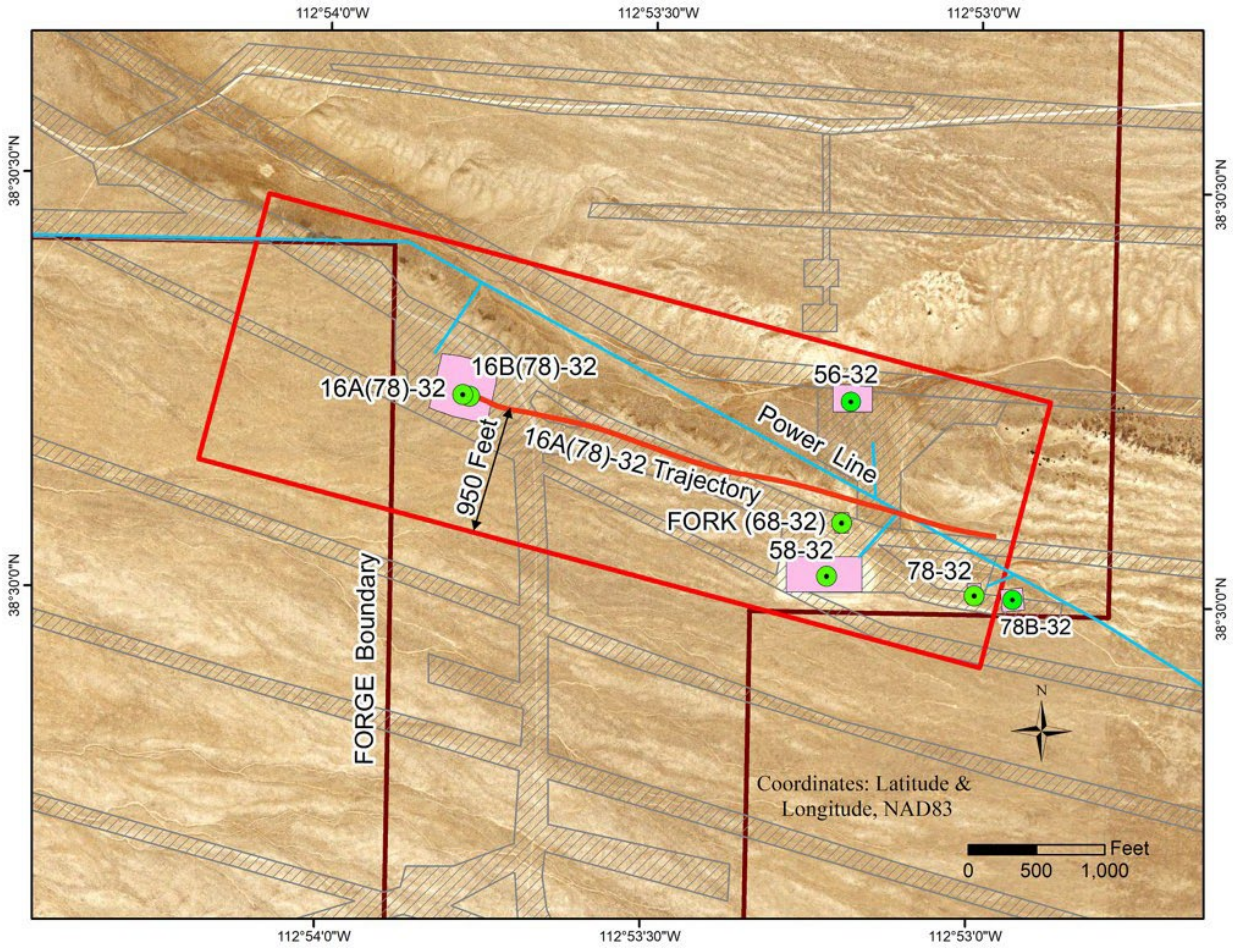

Figure B.2-3. *Plan view of Utah FORGE deep wells. The trajectory of the 16A(78)-32 is shownred. Herein, we refer to 16A(78)-32 as 16A. Wells 58-32, 56-32 and 78B-32 are three existingdeep seismic monitor wells at total depths (TDs) of 7536, 9004 and 9500 feet, respectively.*

Rigorous computer simulation of location accuracy and minimum magnitude of detection using downhole 3C strings was undertaken by Dyer to demonstrate the large gains possible in detectability by having a deeper well in the general 78-32 area, and to optimize location of 78B-

32 in that vicinity. The modeling is described by Rutledge et al (2021, 2022) and illustrated in Figure B.2-4 for trial string bottom depths of 5000 ft and 7500 ft. For the latter depth, location accuracies within 50 ft may be achieved for a length approaching 2500 ft along the tangent of 16A from its toe, while for the former the uncertainties may rise to 100 feet. This underscores that having sensors deployed as deep as possible while still in a safe temperature range is of significant advantage for monitoring. Protocols have been worked out to allow essentially real-time sharing of the seismicity time series at all three wells by both Schlumberger and GES for independent analyses of event locations and magnitudes.

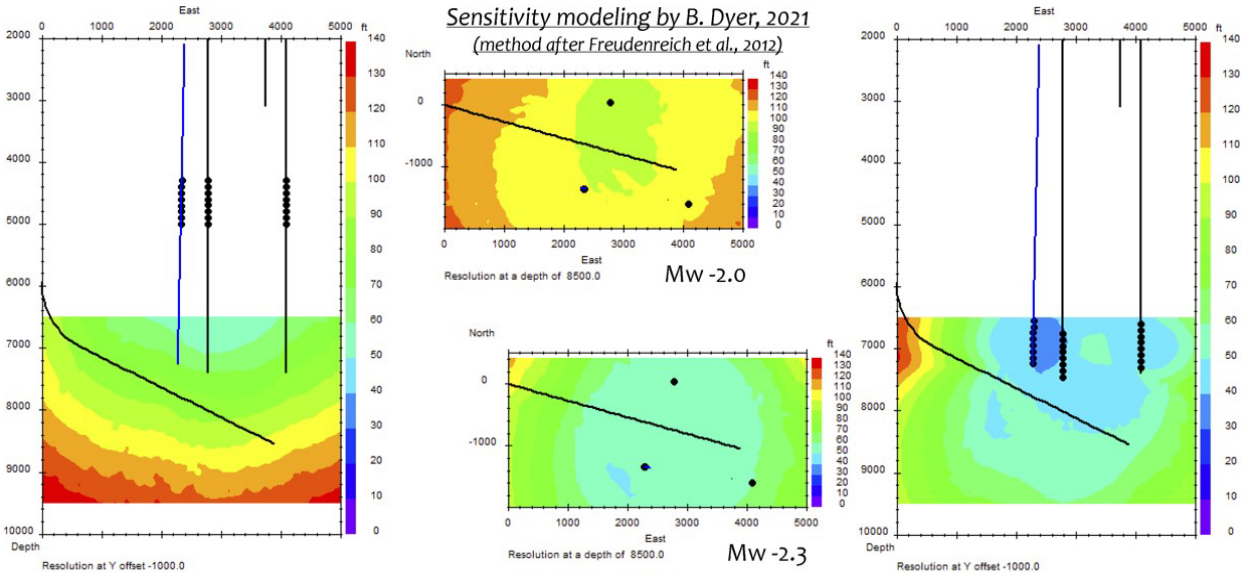

Figure B.2-4. *Results of sensitivity simulation for microseismic event location and magnitude estimation for eight-level, 3C string sensors down vertical wells 56-32, 58-32 and 78B-32. Results for string bottom depths at 5000 ft are to left and upper middle, while results for string bottom depth at 7500 ft are to right and lower middle.*

A check shot just before injection experimentation commences will be fired for string orientation, with backup by a vibroseis truck of Schlumberger on site. At the same time as the deep three-well string deployments, GES (Dyer) will deploy the Avalon BOSS three level fiber-optic 3C mini-chain for performance testing in the relatively shallow well 78-32. This tool currently is rated to 200C (higher is possible) and contains no downhole electronics.

Seismic events are anticipated to continue after injection stimulation and the accompanying main string monitoring described above. Monitoring that activity is expected to expand the

known domain of brittle failure and clarify preferred deformation directions, especially in light of the mix of Miocene plutonic and Proterozoic metamorphic rocks. To carry this out, we plan to deploy pairs of high-temperature, gained analog 3C sensors down each of the three monitoring wells for up to three years (ASL model PSS-53 rated to 500 F (260 C) for 500 hrs, or

>1 year at 210C) (Figure B.2-5). Similar modeling by Dyer indicates that event sensitivity should be comparable to that of the 8L strings, albeit with reduced sensor redundancy. The analog sensor deployment is to be carried out by Schlumberger with supervision by Avalon also as part of their overall contract. If placed at 7500 feet depth, the lower sensor of each pair may experience a temperature of close to 200C (Figure B.2-5). A dedicated subcontract was issued at the end of this quarter for ISTI Inc and its subcontractor ASIR Inc to incorporate digitizing hardware onto the long-term monitoring wire lines, and to record, process and deliver the seismic data to Utah FORGE for further analysis and presentation to the public.

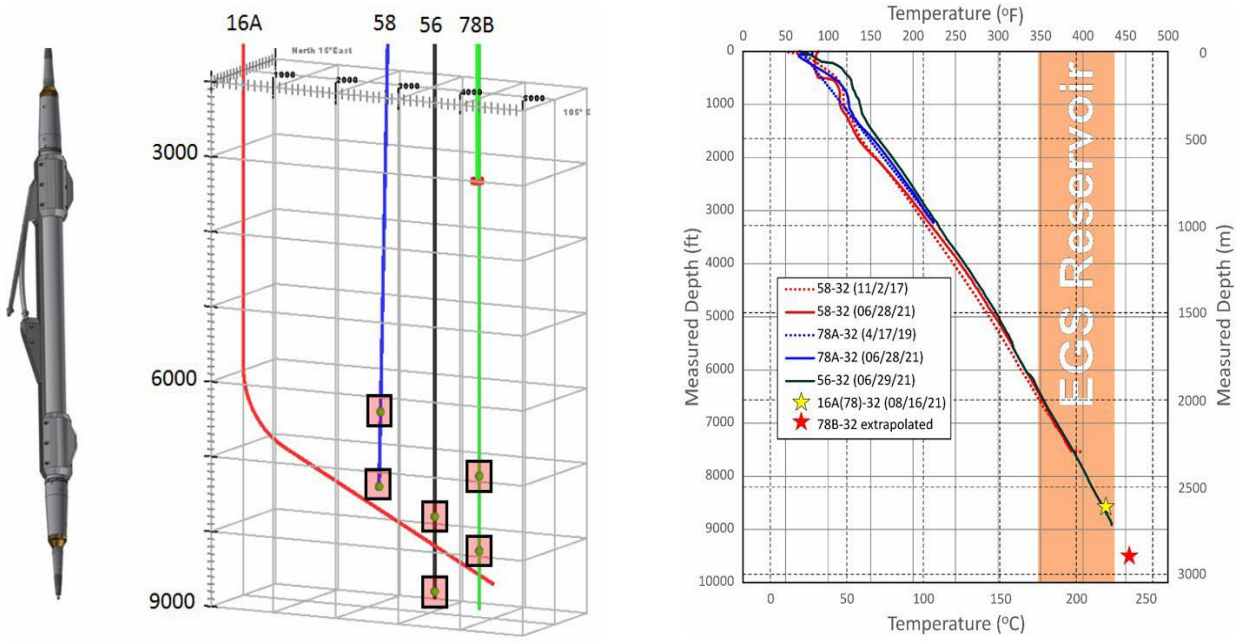

Figure B.2-5. *Left two panels: Diagrammatic view of Avalon PSS-53 analog geophone to be deployed in pairs separated by 1000 ft down each of the three deep monitoring wells. Picture from Rutledge et al (2021). Right: Thermal profiles of deep wells at the Utah FORGE project. Note these all are referenced to depth of zero, whereas elevation of well pad 78B-32 is ~50m higher than that of 58-32, which in turn is essentially equal to that of 56-32.*

Local Monitoring

The initial Utah FORGE seismic network consisted of five surface broadband stations. Four were located close to the Utah FORGE site and the fifth south of Milford. The station south of Milford was designed to close an azimuthal gap in monitoring of the Utah FORGE region. There were

also three strong-motion stations integrated into the network, and a ~300 m borehole was instrumented in 2019, station FORK. During the reporting period, the network was upgraded to reflect the developed seismic monitoring plan and ISMP. The basis of the seismic monitoring plan was to have a subset of stations at a distance of ~3 km for depth control and a second set of stations at ~8 km for epicentral control. Specific upgrades during the reporting period include relocating the strong-motion station at Milford High School due to construction issues, decommissioning surface stations FOR3 and FOR4, installing broadband surface stations FOR5, FOR6, FOR7 and FOR8, and installing broadband and accelerometer seismic instrumentation in three shallow (~30 m) boreholes, FSB1, FSB2, and FSB3. The current seismic network is shown in Figure B.2-1 and recording parameters in Table B.2-2.

***Table B.2-2**. Description of local seismic monitoring stations.*

Type	SEED Name	Depth	Datalogger	Sensor	Sampling Rate
Shallow borehole	UU. FORK.EH[Z,1,2] UU. FORK.GH[Z,1,2] UU. FORK.EN[Z,1,2] UU. FORK.GN[Z,1,2]	~305 m (~1000')	Obsidian	OMNI-2400 (short-period) Silicon Audio (accelerometer)	200 sps 1000 sps 200 sps 1000 sps
Shallow borehole	UU.FSB[1,2,3].HH[z,1,2] UU.FSB[1,2,3].EN[z,1,2] UU.FSB[1,2,3].DN[z,1,2]	~30 m (~100')	Centaur	Trillium Cascadia (broadband) Titan (acceleromoter)	200 sps 200 sps 500 sps
Rock Site	UU.FOR[1,5,6,7,8].HH[Z,E,N]	Surface	Centaur	Trillium 120, 120[Q,P]A, or Horizon (broadband)	200 sps
Soil Site	UU.FOR2.HH[Z,E,N]	Surface	Centaur	Trillium 120PA (broadband)	200 sps
Rock Site	UU.FORU.HH[Z,E,N]	Surface	Reftek RT-130	Guralp-40T (broadband)	200 sps
Strong-motion	UU.[FORB, FORW].EN[Z,E,N]	In-building, Surface	Basalt Obsidian	Episensor	200 sps
Strong-motion	UU.MHS2.EN[Z,E,N]	In-building	Etna 2	Episensor	100 sps

Photographs of the new surface stations are shown in Figure B.2-6). Due to permitting issues, there are three additional shallow boreholes in the 8 km ring yet to be installed, FSB4, FSB5, and FSB6 (shown as open symbols on the map).

A.

B.

C.

Figure B.2-6. *Photos of new rock sites (A) FOR6, (B) FOR7, and (C) FOR8.*

Site Characterization

Continued improvements to site characterization is an important aspect of seismic monitoring. During the reporting period improved site characterization took two forms: (1) improving details of the seismic velocity model and (2) in-depth analysis of seismicity clusters.

Shear Wave Velocity Model

During the reporting period, we generated a shallow shear wave velocity model local to the Utah FORGE area and in a synergistic study (non-FORGE funded project) a crustal shear wave velocity model for the larger central Utah geothermal region. The shallow shear wave model (Zhang and Pankow, 2021) utilized the nodal array deployed in 2016 and spatial autocorrelation (SPAC) to generate 61 1D velocity models encompassing the local Utah FORGE footprint. The 1D models were stitched together to form a quasi-3D model. The models are relatively high resolution to depths approaching 2 km and readily map the sediment bedrock interface throughout the region (Figure B.2-7). The model also provides layering detail within the overriding sedimentary basin. This model was used in the probabilistic seismic hazard analysis to get site specific values for the average shear wave velocity in the upper 30 m and the depths corresponding to 1.0 and 2.5 km/s velocities. These are parameters that are used in estimating ground motion from prediction equations. This shear wave model is also being used to refine the shallow velocity structure for seismic location and synthetic waveform generation.

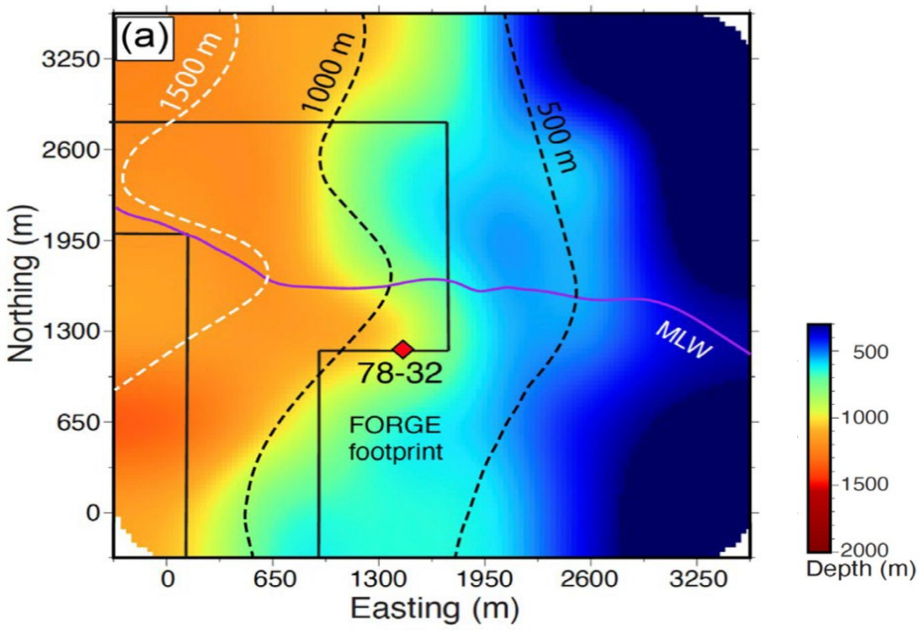

Figure B.2-7. *Shear wave velocity model from Zhang and Pankow (2021) showing the depth to bedrock compared to depths estimated fromthe seismic reflection survey (dashed lines; Miller et al., 2019).*

In the second study, ambient noise seismic beamforming tomography and ellipticity were used to develop a crustal scale shear wave velocity model to depths of ~15 km for the larger region surrounding Utah FORGE (Wells et al., submitted). Figure B.2-8 shows an east-west cross-section near the Utah FORGE footprint. A key result of this study is a low velocity shear wave layer beginning at depths around 10 km with the regionally lowest velocity regions coinciding with high surface heat flow and geothermal areas. Once peer reviewed this model will be integrated into the local velocity model used for earthquake locations.

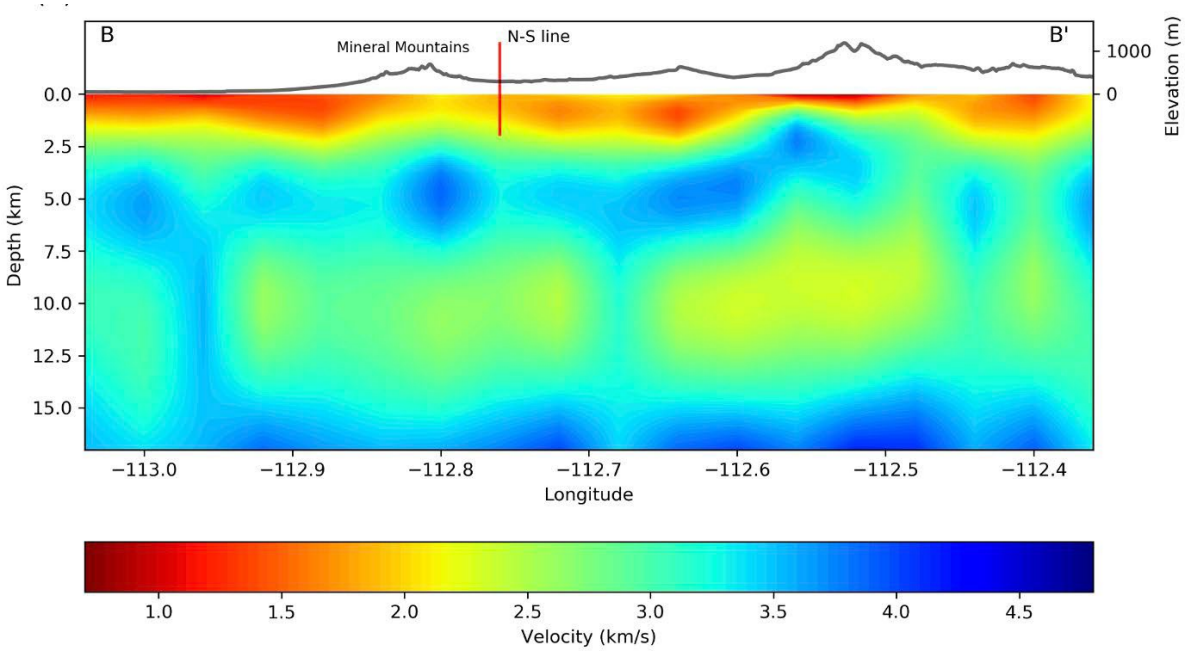

Figure B.2-8. *An east-west shear wave cross-section located close to the Utah FORGE site from Wells et al. (2022). A notable feature of this model is the low velocity feature beginning at depths around 7.5 km.*

Seismic Cluster Analysis

Two tectonic seismic source areas were further analyzed during the project period. The first study took a closer look at the swarm zone region originally identified by Zandt et al. (1982). In the Zandt study, it was concluded that the region east of the Blundell power plant was a swarmgenic region. However, with the regional seismic monitoring, outside of the swarm that Zandt recorded in the 1980s, there were no significant bursts of seismicity. However, it was not clear if this was a seismic detection issue or a process of the seismic zone. To address this question, Mesimeri et al. (2021) used 75 template events and a matched-filter methodology to build a catalog of over 1000 earthquakes located in the identified source zone. This study found that the seismicity is spatially concentrated in a < 2 km long east-west striking zone. Additionally, they found 15 distinct periods of elevated seismicity (small swarms). Analysis of the best recorded sequence indicates a complex mechanism of both fluid migration and aseismic processes.

In the second study, the swarm of earthquakes occurring between March 19 and May 5, 2021 near station FOR1 (Figure B.2-1) was analyzed. The 125 catalog events in the swarm were used as templates in a matched-filter analysis, and over 1000 earthquakes were detected in addition to the 125 catalog events. We will relocate templates and a subset of the detections using a double difference method, and then evaluate diffusion patterns related to the swarm. Moment tensors of the largest five swarm events show a consistent near-N striking fault plane, and catalog locations suggest a fault plane dipping to the west. Analysis is ongoing with final results to be presented at SSA.

Analysis of 2019 Stimulation

The immediate analysis of seismicity related to the 2019 stimulation was primarily provided by Schlumberger (SLB; analysis of the geophone string) and Silixa (analysis of the DAS data). The local network detected only a few of these small microseismic events. The most complete catalog (434 events) was generated by SLB using the downhole geophones. However, their monitoring was limited to the time period of stimulation and consisted of routine processing. In further analysis, we are working to improve the SLB locations using refined picks and integrating picks from station FORK and the nodal array that was deployed at the time and are using enhanced detection algorithms to better utilize the nodal array and the 300 m instrumented borehole, FORK. We also recently started to look at focal mechanisms for some of the larger events. While no results are currently available, an abstract was submitted for the 2022 GRC meeting (Bradshaw et al., 2022).

Improving the SLB locations from the 2019 stimulation

Efforts were made to reprocess the Schlumberger events detected during the three phases of pumping. This included 1) picking the data, 2) trying to improve the hodogram data, and incorporating the arrival time data from a handful of stronger events detected on FORK 68-32 and the surface Nodal network.

We took the Schlumberger (SLB) continuous SEGY waveform data and converted to SAC format. Using SLB's event times we cut the SAC into 5-second event records and rotated them to P, Sh, Sv components based on SLB's original locations. P and Sh arrival times were picked from the rotated waveforms. We computed hodograms (particle motion trajectories) to compute azimuths from receivers to source and attempted to use the Sh phases to see if we could further improve the relative azimuths. Because the S phases often have greater signal-to-noise ratios than P arrivals, using the Sh hodograms can work well to obtain azimuth to source if Sh and Sv phase arrivals are adequately separated at the receivers. Using the Sh phases with these data did not show improvement over the P-data hodograms.

There were 12 events from the SLB catalog that were detected at the borehole receiver in 68-32. Of these twelve events, six were detected on multiple stations of the surface Nodal array. In relocating the SLB with new picks we computed P and Sh station corrections for the downhole data by fixing the phase-2 events at the perf-2 locations and computing the mean residuals travel time residuals. This allowed the correct depth placement of all the microseismic events.

After synchronizing the FORK 68-32 picks with the downhole picks we relocated with the FORK picks and the geophone string together. Figure B.2-9 shows the improvements in locations with the addition of the FORK picks. Next, we will try locating the subset of six events with the picks obtained from the Nodal array as well.

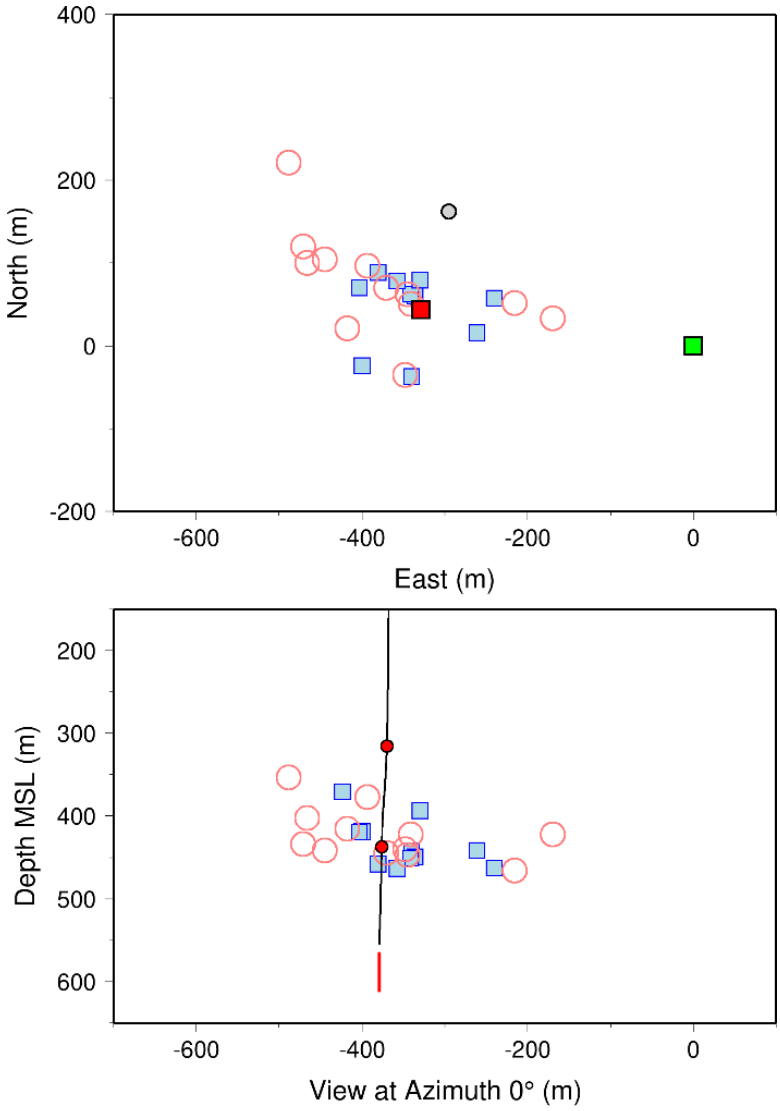

Figure B.2-9. *One-well versus two-well source locations in plane and depth views for twelve events detected in common on the FORK 68-32 and the SLB geophone string. The red circles are the initial locations determined with the SLB string alone. The blue squares are the re-locations with the addition of the FORK 68-32 picks, showing tighter locations near the phase 2 injection point (deeper red circle in depth view). The SLB string is in the 78-32 well shown as green square. The treatment well is the red square and the FORK well is the small gray circle in the map view. The red interval at the toe of the treatment well marks the uncased, open-hole interval.*

Seismic Event Detection

For the detection work, we first developed a new detection algorithm for array processing the nodal data using the frequency domain and then used back projection to get locations (Mesimeri et al., 2021). For a two-hour period, coincident in time with the SLB catalog, we detected and located 6 events with magnitudes from -1.8 to -0.5 (magnitudes calculated by SLB) compared to the SLB catalog for the same time period that contained 61 events with magnitudes between -1.9 and -0.5. Notably, the array used in this analysis was limited to 70 seismic stations located at 500 to 2500 m distant. We find this approach promising, with the limited array we were able to detect and locate 10% of the catalog to almost the same magnitude detection levels as the geophone string. We will continue to build on this method for future stimulations. Events detected on the nodes using this approach were visually inspected and P- and S- arrival times determined for integration in the improved location analysis.

The second detection analysis focused on seismic station FORK (300 m borehole). The goal of this analysis was to determine a detection threshold for station FORK, look at the continuous time window during the stimulation experiment (not just during stimulation phases), and to determine a robust b-value for the induced seismicity. The results of this work were presented by an undergraduate intern at the 2022 Stanford Geothermal Workshop (Dzubay et al., 2022). Using matched-filters, resulted in 111 seismic events not in the SLB catalog with many of these events occurring during and after the stimulation phases (Figure B.2-10). The minimum magnitude detected was an M -1.8 and one of the largest detected events occurred ~20 days after the end of the stimulation. With the enhanced catalog, a new b-value calculation was performed. However, a more robust estimate of 1.61 was determined using the new b-positive approach (van der Elst, 2021).

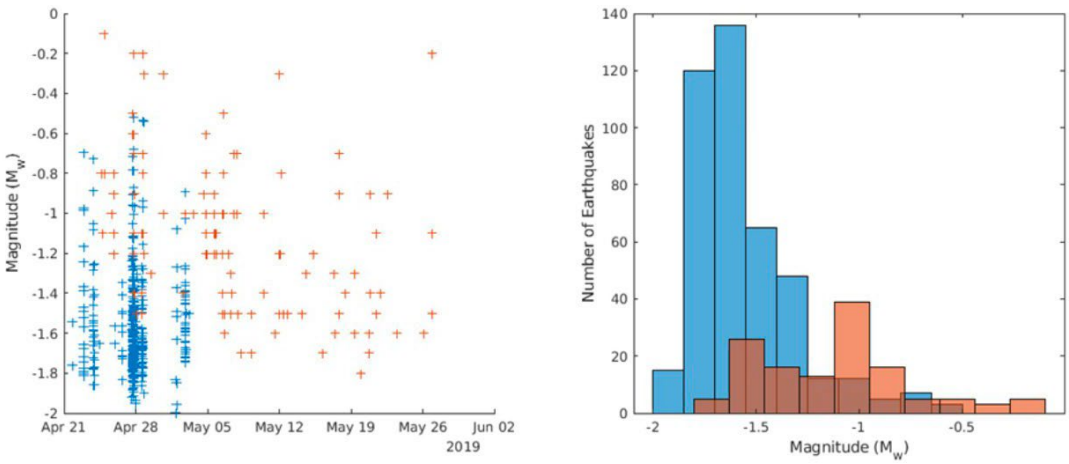

Figure B.2-10. *Matched filter detection results determined at station FORK (orange) compared to the SLB catalog (blue). (Figure from Dzubay et al., 2022)*

Preparation for 2022 Stimulation

A great deal of effort has been expended preparing for the 2022 stimulation. This work falls into two general categories: (1) field experiments and (2) data analysis.

Field Work

For the 2022 stimulation, Utah FORGE will deploy 13 patches of 16 geophones spaced 30 m apart (Figure B.2-11). The design is to enhance the signal in each of the patches using stacking. This design was suggested by Nidhal Belayouni from Baker Hughes.

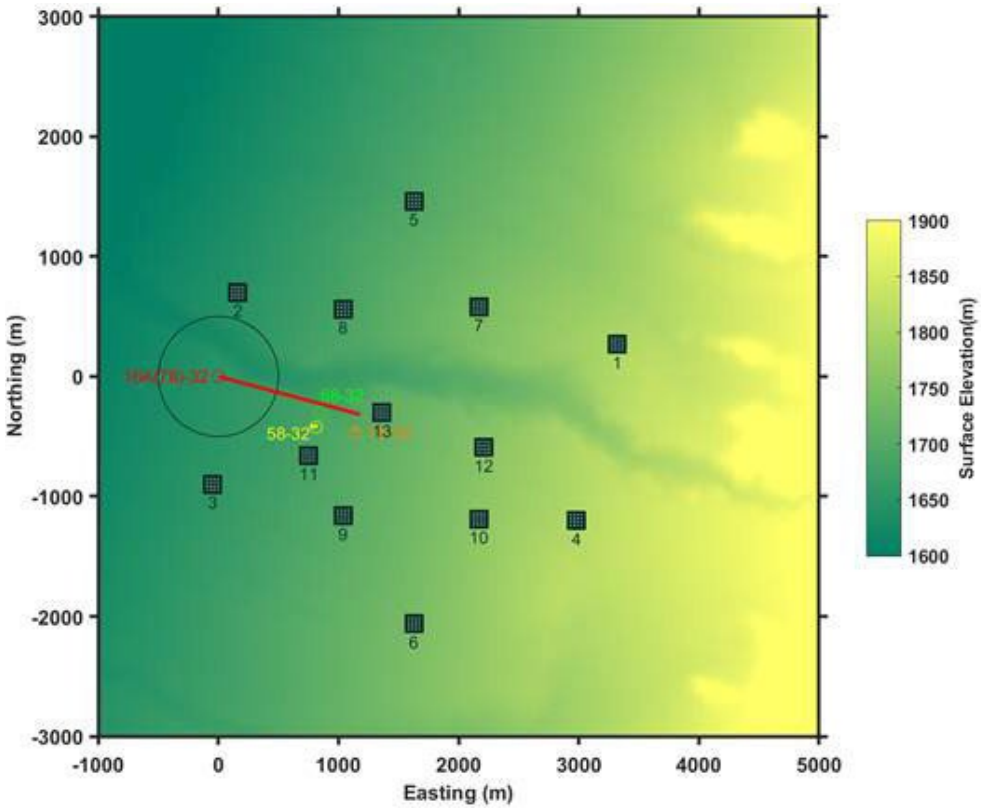

***Figure B.2-11**. Proposed Nodal geophone array for 2022 Stimulation. Each patch consists of 16 geophones spaced 30 m apart.*

Data Analysis

Regarding the data analysis, UUSS has integrated the data streams from the new stations into the AQMS Quake Monitoring Software, has updated the seismic triggering subnets, and has implemented station corrections for calculating local magnitudes using the new stations. Automatic alarms for M ≥ 2.0 will be sent to the duty seismologist for review and if the magnitudes are confirmed SMS messages will be sent to the Utah FORGE contact list. Automatic

alarms for M ≥ 3.0 will be sent to both duty seismologists and the Utah FORGE contacts. For M ≥ 2.5 earthquakes, a ShakeMap will be automatically generated and those on the Utah FORGE contact list will receive an email. In addition, to the routine processing and alarming, configuration files have been generated to run hypoDD daily to refine the seismic locations and code is being developed to track b-positive in near-real-time. Post-stimulation processing projects are also being developed. These will include source analysis and matched-filter studies, as well as the planned processing from the geophone experiment.

Discussion

Continued seismic monitoring of the region reinforced previous reporting—the region immediate to Utah FORGE is characterized by low rates and small magnitude earthquakes primarily located to the east under the Mineral Mountains. Bursts of seismicity tend to occur in swarms that may be related to fluids and possibly aseismic deformation. B-positive calculations for the 2019 stimulation are greater than one, as is typical for an induced sequence. Based on the monitoring re-enforcing the previous analyses there are no updates to the seismic potential of the site. It should still be considered a region of low to moderate seismic hazard.

Both a local and crustal shear wave velocity model have been generated for the Utah FORGE site and the results of the local model were integrated into the probabilistic seismic hazard analysis in the ISMP. The refined models are also being used to update the models used for seismic event location.

A key test of the ISMP will be the 2022 stimulation. The results from this stimulation will beused to update mitigation strategies in a revised ISMP.

As a result of these lessons, we will rely on the analysis of deep borehole geophone data from three wells to characterize seismicity associated with reservoir development. Fiber optic tools will be tested and monitored, but real-time monitoring will focus on the geophone strings. The nodal experiment has been designed using patches to further leverage array processing for detection and location of the microseismicity. We will implement a near-real-time b-positive estimator and will also use matched-filters with the shallow borehole data to improve the transition from reservoir to local seismic monitoring.

Future Efforts

We have partnered with experts in seismology to design the Utah FORGE seismic monitoring network and for developing plans for monitoring the 2022 stimulation. To the extent possible, lessons learned from the 2019 stimulation have been folded into the 2022 planning. The mid-April 2022 stimulation will be a good test of both what we learned from 2019 and the expectations of the experts. As such, one of the first activities following the stimulation will be a workshop for all those involved in the seismic monitoring to share results and help to develop a lessons-learned report. This report will inform plans for potential changes and augmentations to seismic monitoring at Utah FORGE. In addition to the workshop, the ISMP will be updated

with the new information. An important aspect of the seismic monitoring will be continued seismic catalog building and adherence to the Traffic Light System, since experience shows that the larger induced events tend to occur after injection phases.

References

Bradshaw, P., G. Petersen, and K. Pankow (2022). Characterizing the induced microseismicity ofthe 2019 Utah FORGE well stimulation, *GRC transactions, **46**, in preparation.*

Dzubay, A., M. Mesimeri, K. M. Whidden, D. Wells, and K. Pankow (2022). Developing a comprehensive seismic catalog using a matched-filter detector during a 2019 stimulation atUtah FORGE: *Proceedings, 47th Workshop on Geothermal Reservoir Engineering*, Stanford University, CA February 7- 9, 8 p.

Majer, E., Nelson, J., Robertson-Tait, A., Savy, J., & Wong, I. (2016). Best practices for addressing induced seismicity associated with enhanced geothermal systems (EGS), Topical report, Lawrence Berkeley National Laboratory, prepared at the direction of the Dept. Of Energy Geothermal Technologies Program, April 8, 115 pp.

Mesimeri, M., K. L. Pankow, B. Baker, and J. M. Hale (2021). Episodic earthquake swarms in the Mineral Mountains, Utah driven by the Roosevelt hydrothermal system, *J. Geophys. Res.: Solid Earth*, 126, e2021JB021659. https://doi.org/10.1029/2021JB021659.

Mesimeri, M., K. Pankow, and J. Rutledge (2021). A frequency-domain-based algorithm for detecting microseismicity using dense surface seismic arrays, *Bull. Seism. Soc. Am.*, **111**, 1-11,doi: 10.1785/0120210062.

Miller, J., Allis, R., and Hardwick, C. (2019). Interpretation of seismic reflection surveys near the FORGE enhanced geothermal systems site, Utah, in Allis, R., and Moore, J.N., editors, Geothermal characteristics of the Roosevelt Hot Springs system and adjacent FORGE EGS site, Milford, Utah: Utah Geological Survey Miscellaneous Publication, 169-H, 13 pp.

Pankow, K., J. Rutledge, B. Dyer, P. Bradshaw, A. Dzubay, J. M. Hale, G. Petersen, J. Rusho, P. Wannamaker, K. Whidden, J. Moore (2022). Local seismic monitoring of a stimulation at the Utah Frontier Observatory for Research in Geothermal Energy site, 2022 Annual SeismologicalSociety of America Meeting, Bellevue, WA, April 10-23, 2022.

Rutledge, J**.,** K. Pankow, B. Dyer, P. Wannamaker, P. Meier, F. Bethmann, and J. Moore (2021). Seismic monitoring at the Utah FORGE EGS site*, GRC Transactions, **45**,* 13 pp.

Rutledge, J., B. Dyer, P. Wannamaker, K. Pankow, F. Bethmann, P. Meier, and J. Moore (2022). Downhole microseismic monitoring of injection stimulations at the Utah FORGE EGS site, *56th U.S. Rock Mechanics/Geomechanics Symposium, in press.*

Van der Elst, N. J., B-positive : A Robust Estimator of Aftershock Magnitude Distribution in Transiently Incomplete Catalogs. Journal of Geophysical Research: Solid Earth, 126(2), (2021).

Wells, D., F. C. Lin, K. Pankow, B. Baker, and J. Bartley (2022). Combining dense seismic arrays and broadband data to image the subsurface velocity structure in geothermally active south- central Utah, J. Geophys. Res: Solid Earth, submitted.

Whidden, K., M. Mesimeri, and K. Pankow (2022). The 2021 Milford, UT earthquake sequence, 2022 Annual Seismological Society of America Meeting, Bellevue, WA, April 10-23, 2022.

Zandt, G., McPherson, L., Schaff, S., & Olsen, S. (1982). Seismic baseline and induction studies: Roosevelt Hot Springs, Utah and Raft River, Idaho. Topical report No. DOE/ID/01821-T1.

University of Utah Research Inst., Earth Science Lab, Salt Lake City (USA) 63 pp.

Zhang, H. and K. L. Pankow (2021). High-resolution Bayesian spatial auto-correlation (SPAC) pseudo-3D Vs model of Utah FORGE site with a dense geophone array, *Geophys. Res. Int*, https://doi.org/10.1093/gji/ggab049

B.3 UTAH FORGE MODELING

Introduction

Modeling and simulation will play a critical role at the site and needs to be considered as a general scientific discovery tool to elucidate behavior of enhanced geothermal systems and as a deterministic (or stochastic) tool to plan and predict specific activities.

The Utah FORGE site is located in a broad zone of elevated heat flow inside the southeast margin of the Great Basin. The regional stratigraphy is made of folded and imbricated Paleozoic-Mesozoic strata that has been overprinted by widespread Basin and Range style extension and eruption of Tertiary-recent mafic-felsic magmatic centers. Near the Utah FORGE site, Paleozoic-Mesozoic strata are absent, and consequently the stratigraphy is divided into two broadly defined units, comprising crystalline plutonic rocks that form the basement and younger overlying bedded alluvium and volcanic deposits that fill the basin. The processing of a 3D seismic reflection highlights the westward-dipping surface that separates these two units, which forms the basement contact.

Multiphysics reservoir models have been developed to simulate the coupled thermo-hydro-mechanical responses in the subsurface to Utah FORGE reservoir creation and operation activities. The numerical reservoir models are based on the reference geologic model discussed above and will be used as a tool to better understand the physics of the reservoir-creation process and to elucidate the behavior of the system. Numerical implementation of the conceptual model has been made with both commercial software packages and open-source numerical packages to enable greater collaboration among the team (and the geologic community) and to drive understanding of the system using state of the art tools. The modeling and simulation team used these models to preliminarily evaluate drilling directions and injection pressures to both stimulate existing fractures and generate new ones for potential Utah FORGE operational wells.

Continuum-based modeling codes are by far the most prevalent in geothermal reservoir engineering. Solution schemes based on finite-difference, finite-element, or finite-volume methods all represent the subsurface as a generalized representative elementary volume, at various grid scales, to simulate and predict behavior. In densely fractured formations, it is common to use a discrete fracture network (DFN) as a starting point to develop upscaling relationships in the development of continuum models. For Utah FORGE, the project team has established a reference DFN using FracMan and a reference native state model using the FALCON code.

This section of the report will summarize the modeling and simulation activities undertaken in Year 2 of Phase 3A. In many sections, the descriptions will come directly from papers published by the modeling team.

Reference Phase 2C Native State Reservoir Model

As presented in Attachment 1, a reference THM reservoir model was developed at the end of Phase 2C. This model served as the basis for the initial modeling in Phase 3A. Geologic characterization activities combined with historical information culminated in a conceptual model of the site, which is dominated by thermal conduction in a large granitoid body with a top surface that dips generally to the west. The granitoid reservoir is overlain by younger sedimentary materials that host a non-potable groundwater resource. A reference earth model was constructed based on the geologic conceptual model that will be used to assess all future changes in geologic understanding at the site.

A detailed native-state Thermal-Hydraulic-Mechanical model of the region of the site where stimulation and operations are expected to occur was created based upon the reference earth model. The modeled boundary conditions were mapped directly from geologic, geographic, and hydrogeologic conditions measured at the site, and were modified along with select reservoir properties to come to a calibrated steady-state solution. A reference set of reservoir flow, heat transport, DFN, and mechanical properties was developed from the calibration exercise, and used by the team for follow-on modeling to ensure comparability of results. Considerable care and attention were placed in developing the framework of the native-state numerical model.

The geologic structure developed in the earth model was mapped onto a uniform 50m grid, on a domain that is generally centered around well 58-32 and the region where Phase 3A activities are envisioned to take place. The numerical representation of the earth model comprised two general geologic units, sedimentary/alluvial deposits and the underlying granitoid basement.

Hydrologic and mechanical properties of the sedimentary deposits were considered to be spatially uniform and based off of data collected as part of Utah FORGE characterization. This unit, however, is not part of the reservoir, so the native-state modeling efforts did not focus on this unit. The complete top of the model domain was set to be in the sediments for convenience in setting to top-boundary conditions (body forces). The granitoid that makes up the planned EGS reservoir was assigned a heterogeneous and anisotropic permeability field based upon the reference DFN developed for the site. The porosity was also based on the

upscaled DFN, while other reservoir properties (such as density and thermal conductivity) were assigned uniform values.

For the stress model, we incorporated detailed surface topography and relief of the granitoid contact, as these can cause perturbations in the stress field at depth. The native- state model shows small perturbations in Sh_{min} that generally follow the granitoid-alluvium contact, and in some areas several hundred meters into the granitoid materials. Calibration of the native-state model consisted of adjusting the grain density and porosity of the sediments and the density of the granitoid to match those measured in well 58-32. The thermal conductivity of both the sediments and granitoid were slightly modified from initial estimates, as was the maximum temperature at the base of the earth model. Reservoir permeability was taken from upscaling the reference DFN, and went unchanged in the native-state model. Only the top boundary pressure was modified to ensure it matched measured values at well 58-32.

Estimation of Fracture Size for the Utah FORGE Discrete Fracture Network Model

As presented in Attachment 2, a detailed evaluation of the fracture networks at the Utah FORGE site has been completed. The Utah FORGE geothermal reservoir is sited in deep granitoid bedrock near the town of Milford, Utah. A Discrete Fracture Network (DFN) model has been created to explicitly represent the natural fracture population in the reservoir (Finnila et al., 2019). In the DFN, fractures are modeled as planar and roughly circular, having a range of orientations, local intensity, and sizes consistent with what has been observed from both image log data from a vertical well 58-32, and measurements from outcrops in the nearby mountains (Figure B.3-1). Previous to this work, fracture sizes were estimated from the Salt Cove outcrop trace data. The fracture traces from the Salt Cove outcrop data set have lengths between 3 and 282 m and can be fit with either a lognormal distribution or a truncated power law distribution, also known as a Pareto distribution. Trace lengths are converted to fracture radius using the FracMan software package (Golder Associates, 2020) which uses the method from Zhang et. al. (2002). Given the Utah FORGE reservoir location in an intrusive igneous formation, fractures are assumed to be roughly circular and are modeled in the DFN as regular hexagons. Fracture size is therefore specified using a fracture radius. While the lognormal distribution provides a much better fit to the trace length data compared with the power law distribution, this is often the case when the underlying distribution is in fact a power law distribution which has some measurement bias leading to under-sampling of the smaller size range.

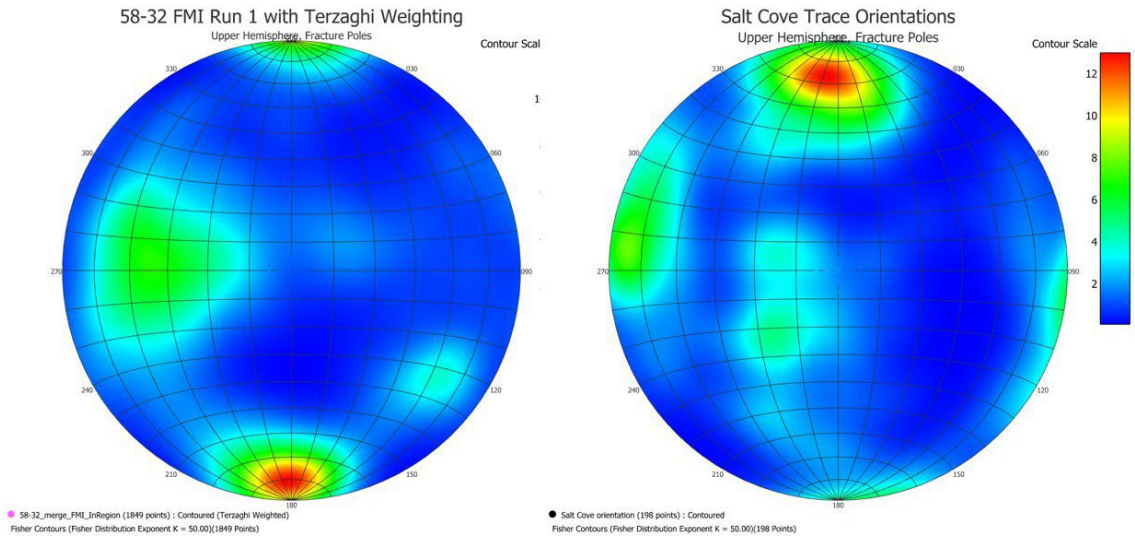

***Figure B.3-1**. Upper hemisphere stereonets showing the natural fracture orientations from well 58-32 (left) and the fractures mapped from the Salt Cove outcrop in the Mineral Mountains (right).*

Although both distributions can match the trace length data for large fractures having a radius in the 20 to 50 m range, the two distributions differ significantly in the smaller fracture size range. Determination of the correct parameterization for the fracture size is critical for correctly adjusting the fracture intensity in the DFN based on different choices for minimum fracture size. Once a DFN is fully specified, subsets are often created by filtering the model using a minimum fracture size. These subsets of the Utah FORGE DFN are used as initial conditions for researchers simulating processes such as well hydraulic stimulation, local stress evolution, flow pathway analysis, and thermal breakthrough in proposed injection and production well configurations. The fracture intensity of the model subsets will vary based on the fracture size parametrization. For the Utah FORGE DFN, the fracture intensity is based on the intensity measured in the Formation MicroImager (FMI) log, which may be including fractures with a radius as small as half a meter. A DFN subset using a minimum fracture size of 10 m would need to reduce the fracture intensity much more for a power law size distribution compared with a lognormal distribution.

We examined the fracture size information present in the FMI log from the pilot well at the Utah FORGE site in order to better constrain the fracture size population of the DFN. There are four outcrops with trace mapping data available from the nearby mountains in the same rock unit as the Utah FORGE reservoir. Trace lengths between 40 and 100 m show a range of slopes ranging from -3.7 for Pinnacle Pass to -2.0 for Baily Spring South. This results in estimated D values for the Pareto distribution between 3.0 and 4.7. The question arises as to whether we could match the FMI intersection data using different values of D. As was previously done, 100 realizations of the DFN were generated for each of five different D values, and fracture-borehole intersection statistics were again collected and compared with those found in the FMI

data. For this purpose, the D values ranged from 2.3 to 3.5. Larger values for D were not modeled as the number of small fractures becomes unwieldly high as the value of D increases and the trend was clear using the lower values. The results are d summarized in Table B.3-1. By adjusting the value of x_0, it is possible to get reasonable matches with all these values of D. The value of x_0 ranges between 0.29 m and 0.54 m, steadily increasing as the value of D increases. Both the low- and high-end values seem possible. While the forward modeling seems to rule out the lognormal size distribution found from the outcrop data and supports having a Pareto distribution, it has not demonstrated a unique parameter selection for D and x_0.

From this description of the fracture sets in the Mineral Mountain range, we would expect the E-W subvertical set to be generally longer than the other two sets. This, indeed, appears to be the case for the traces mapped at the Salt Cove outcrop. With the E-W set fractures commonly bounding the other two sets, we might expect a power law size scaling for that set but not the other two. This needs to be investigated further before the updated fracture size parameterization is finalized for the updated DFN.

Table B.3-1. *Forward modeling estimates for x_0 using a range of D values in the Pareto distribution.*

D	x_0 Pads 1-4 [m]	x_0 Pads 8 [m]	Delta [m]	Mean x_0
2.3	0.29	0.42	0.13	0.36
2.6	0.37	0.55	0.18	0.46
2.9	0.44	0.67	0.23	0.56
3.2	0.49	0.76	0.26	0.63
3.5	0.54	0.84	0.30	0.69

While the outcrop trace data for fractures having a radius between 20 – 50 m match both lognormal and power law distributions, the FMI log data which appear to sample fractures having a median radius of 1.4 m are consistent only with the power law distribution found. Although the FMI log data could also be fit with a lognormal distribution, the mean value needed would be much smaller than that found for the lognormal distribution matching the outcrop data.

Knowing the fracture size distribution for those fractures sampled by the FMI log allows fracture intensity truncation factors to be calculated for DFN models having different minimum fracture sizes. The Pareto distribution used to describe the power law relationship has two parameters: the shape which is found from the outcrop trace length data (power law exponent), and the scale which is found from the minimum fracture radius sampled by the data. While the minimum fracture size identified in the FMI log is hard to determine, it can be

estimated from the forward modeling results. A Pareto fracture size distribution having a power law exponent of 3.2 and a minimum fracture radius of 0.63 m is consistent with both the log data which samples small fracture sizes and the outcrop data sampling large fracture sizes. The fracture intensity, as measured in the FMI log as the number of fractures per unit length (P_{10}) and then converted to the total fracture area per unit volume (P_{32}) by accounting for the geometry between the borehole and fracture orientation, then requires a truncation factor of

0.57 for DFN models using a minimum radius of 1 m, or 0.035 for those using a minimum radius of 10 m.

Numerical Simulation of Injection Tests into Well 58-32

As presented in Attachment 3, a detailed numerical evaluation of the injection tests conducted in well 58-32 were completed. In 2017, well 58-32 was drilled vertically to a depth of 7536 ft to characterize subsurface temperatures, lithologies and permeabilities. In 2017, a series of injection tests were conducted in the uncased barefoot section of the well from 7375 to 7525 ft measured depth (MD), denoted as Zone 1. In 2019, a second series of tests were conducted in Zone 1 and in the cased and perforated portions of the well at depths of 6964 – 6974 ft MD, and 6565 – 6575 ft MD, respectively (Zone 2 and Zone 3). Up to nine test cycles were conducted in each zone. Descriptions of the injection activities and in-situ stresses and permeability interpretations from these pump-in/shut-in or pump-in/flowback tests are well documented in Xing et al. (2020a) and Xing et al. (2020b). Two tests, Cycle 4 and 5 were conducted in the

lower-cased section of the well (Zone 2), where the formation contains abundant pre-existing fractures critically oriented for slip. These two injection cycles were selected for back analysis and history pressure matching. Injection pressure histories during both cycles show a monotonously increasing trend, and the pressures in the second test (Cycle 5) are consistently greater than those during the first test (Cycle 4). The purpose of the back analysis was to understand the mechanisms resulting in the trends observed from the field data, validate the numerical model by qualitatively reproducing the data trends, and calibrate the model with respect to unknown and uncertain input parameters by improving the quantitative match between numerical results and the field data.

The back analysis was conducted using *XSite*, a numerical software for simulation of hydraulic fracturing in naturally fractured reservoirs. The code can simulate propagation and interaction of multiple hydraulic fractures and pre-existing joints. Hydraulic fractures propagate through a combination of predominantly tensile fracturing through intact rock at the fracture tip and opening and slip of pre-existing fractures.

In this analysis, the data from Cycles 4 and 5 from Zone 2 in well 58-32 are used. Figure B.3-2 shows the injection pressures from two models, one assuming non-dilatant pre-existing DFN fractures and the other with dilatant fractures characterized by a 2° dilation angle, compared with the pressure history recorded during Cycle 4. The initial pressure peak (i.e., the breakdown pressure), probably resulting from fracture initiation, is not captured in the model results because the model did not have sufficient resolution and used a small startup joint through the

perforation cluster to represent the already initiated hydraulic fractures. Both models qualitatively match the general increasing trend in the injection pressure history. However, the case with assumed non-dilatant joints seems to be a better match of the magnitude of the injection pressure increase during Cycle 4. The pressure increase in the model with dilatant joints is smaller because joint dilatancy results in greater fracture aperture and permeability.

However, the model with dilatant fractures better matched pressures after shut-in as shown in Figure B.3-3. Therefore, this model was used for simulation of both Cycles 4 and 5.

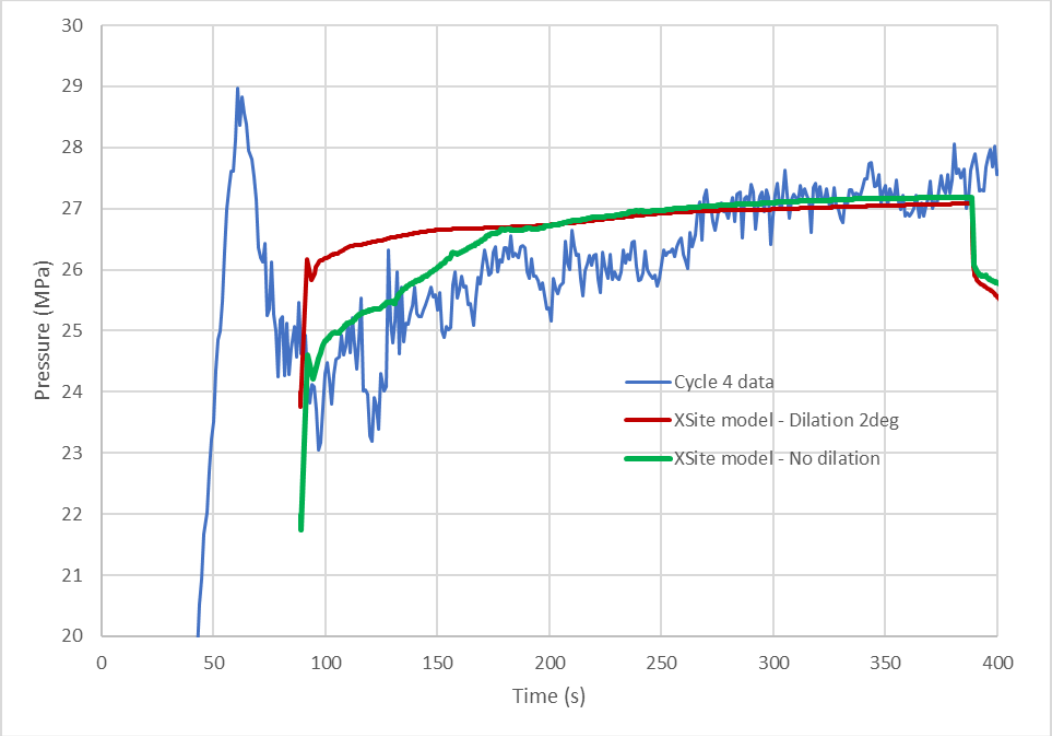

Figure B.3-2. *Cycle 4: Pressure history matching during injection.*

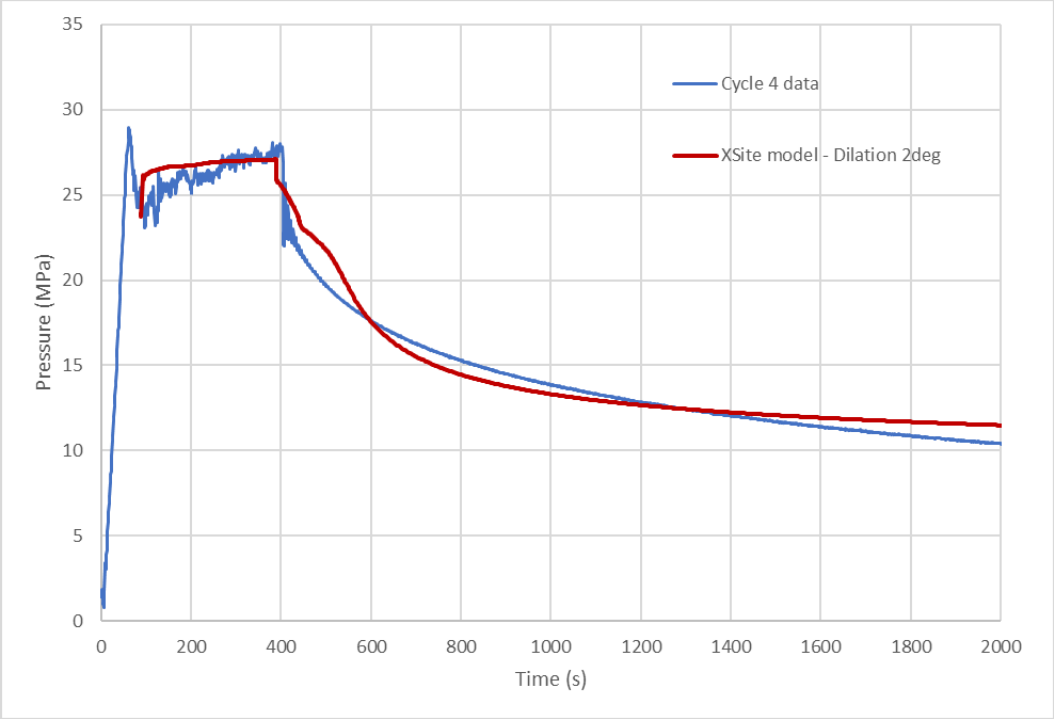

Figure B.3-3. *Cycle 4: Pressure history matching during injection and initial shut-in.*

For the model with dilatant fractures (2° dilation angle), the contours of net pressure (the pressure in excess of the minimum principal stress) and the fracture apertures at the end of Cycle 4 injection, and the end of injection of Cycle 5 indicate that the formation response to injection is dominated by the fluid flow and pressure dissipation in the DFN and, in particular, the pre-existing fracture from the critically oriented set close to the perforation cluster. The hydraulic fracture is arrested by the pre-existing fracture and does not propagate a large distance from the perforation cluster, which is consistent with results from the small-scale model. Examination of apertures illustrates the localization of deformation along the closest DFN fracture from the critically oriented set. The indicators of slip predicted by the models confirm that slip and fracture dilation (along the closest fracture from the critically oriented set) are the leading causes for localization of deformation and increase in aperture.

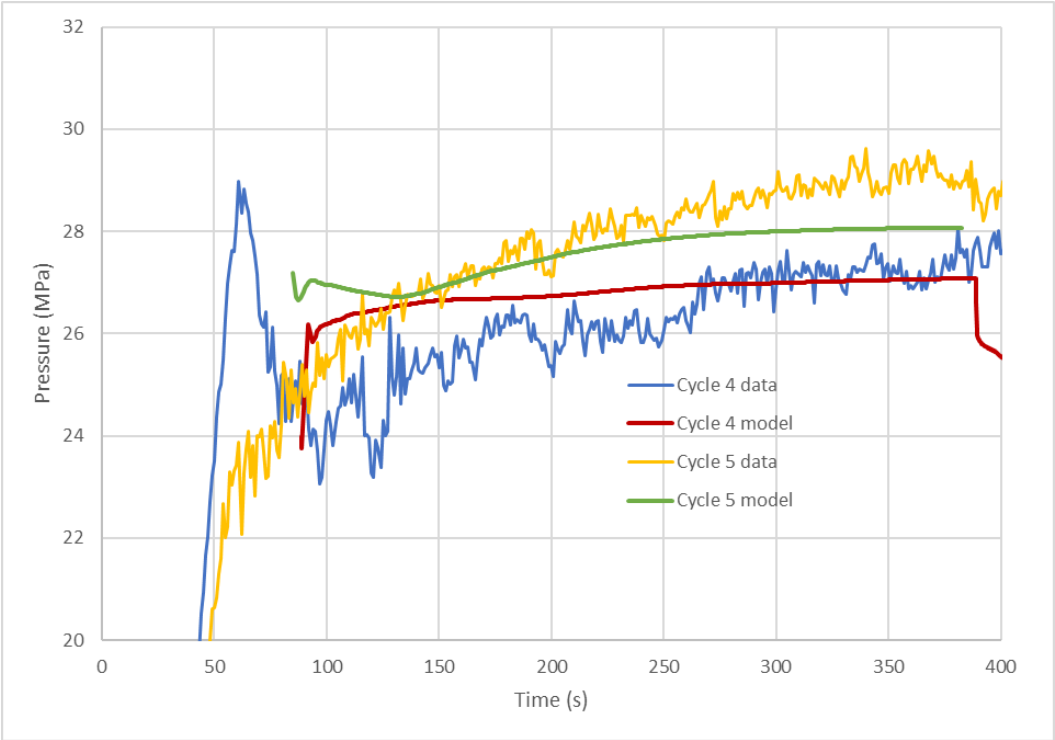

Figure B.3-4. *Cycles 4 and 5: Pressure (surface pressure) history matching during injection.*

The recorded data and simulated (for the case with a 2° dilation angle for the DFN) pressures from Cycles 4 and 5, are compared in Figure B.3-4. The model results match the important data trends. The injection pressure generally increases with time in both cycles. Also, the injection pressures during Cycle 5 are continuously greater than during Cycle 4. The increased injection pressure in Cycle 5 in the numerical model is due to the change in the minimum principal stress relative to the initial far-field state in the model. Before Cycle 4 there is no stress change except for relatively localized perturbations around the pre-existing fractures. The contours before Cycle 5 exhibited an irreversible increase in the confining stress in the volume of the rock mass around the injection cluster even after dissipation of injection-reduced fluid pressures. The increase is caused by irreversible (slip related) deformation of the DFN resulting from an increase in the fluid pressure during injection.

Slippage on the fractures from the critically oriented set results in irreversible deformation and increased minimum principal stress after dissipation of the fluid pressure following 20 hours of leakoff during shut-in. This effect is more pronounced if fractures are dilatant. However, there is an increase in the normal stress in the direction of the initial minimum principal stress even when fracture slip is not associated with dilatancy. Thus, the subsequent injection test (Cycle 5) experienced greater “confining stress”, resulting in increased injection pressures.

Revisions to the Discrete Fracture Network Model

As presented in Attachment 4, the reference discrete fracture network was updated to include newly collected data. The DFN is used to characterize the natural fractures present in the reservoir. Subsets of the model are used as initial conditions for researchers simulating processes such as well hydraulic stimulation, local stress evolution, flow pathway analysis, and thermal breakthrough in the proposed injection and production well configurations. Image logs from the vertical pilot well, 58-32, along with outcrop data from the nearby Mineral Mountains provided the data used to construct the original DFN model in 2019. Two new wells have been drilled in the past year: a highly deviated injection well, 16A(78)-32, and another deep vertical well, 56-32. Data collected from these wells have been analyzed to further constrain fracture orientations and intensity (Table B.3-2, Figure B.3-5). Estimates for fracture sizes have been adjusted based on forward modeling work performed on fracture penetration statistics collected from the image log data. Mechanical and hydraulic fracture apertures have been estimated for both pre- and post-stimulation states based on pressure history matching of injection well tests and measured values from electrical resistivity logs.

The updated DFN model and three realizations of the model were uploaded to the Geothermal Data Repository (GDR) for public access. Each realization includes planar fractures representing both the known location and orientation of fractures identified from the well logs as well as stochastic fracture sets that do not intersect the wells. Individual fracture properties include center coordinates, orientation, fracture size represented both as a radius and as a six-sided polygon, mechanical aperture, hydraulic aperture, permeability, and compressibility. Fracture properties are calibrated so that the upscaled DFN is consistent with measured bulk rock porosity and permeability. The fracture sets are applicable in, but not limited to well hydraulic stimulation, local stress evolution, flow pathway analysis, and thermal breakthrough in proposed injection and production well configurations. The DFN is also upscaled to provide continuum modelers 3D properties such as fracture porosity, directional permeability and sigma factor.

Table B.3-2: *Mean orientations of four fracture sets.*

Mean Trend	Mean Plunge	Mean Strike	Mean Dip	Fisher Concentration	Description
88.5	46	178.5	44	15	South striking moderately dipping west
1.5	13.5	91.5	76.5	30	East striking steeply dipping south
131	5	221	85	30	SSW striking vertical
260	17	350	73	10	North striking steeply dipping east

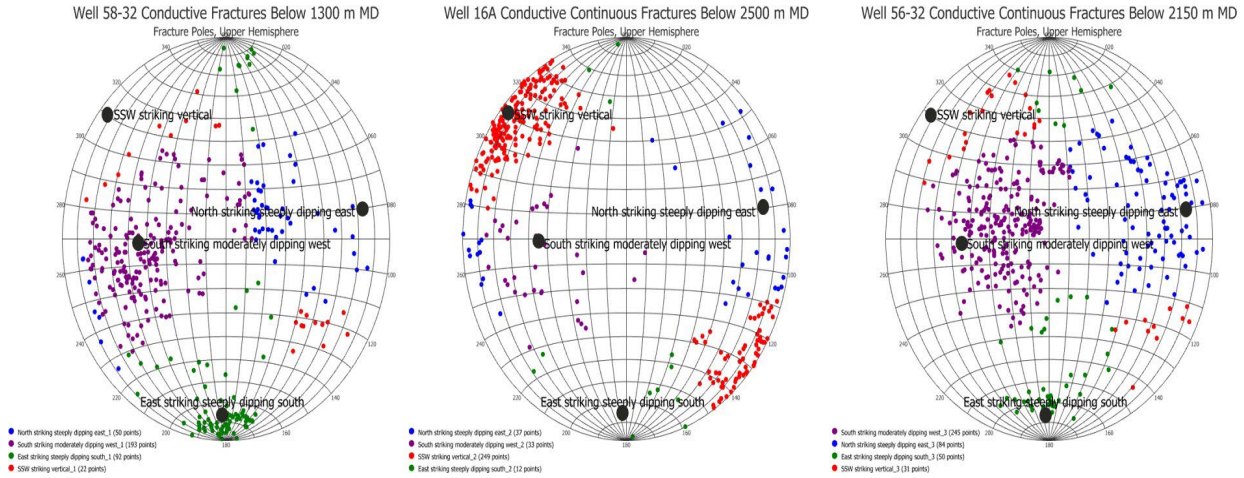

Figure B.3-5. *Fracture orientations from FMI data in the deepest portion of the reservoir. Fracture poles are plotted in upper hemisphere stereonets with the color indicating assignment to the nearest mean fracture set pole.*

Stochastic fracture sets generated based on these mean set orientations can use the full range of orientations found by using a Fisher distribution with the concentration parameters shown, or they can be “simplified” in order to prevent small angle intersections by only using the mean orientation values. These simplified DFN sets can be more easily meshed when used as input for other modeling software.

In order to assist continuum modeling, the DFN is also upscaled to provide bulk rock values for such parameters as porosity, directional permeability, and sigma factor. The properties can be averaged over varying length scales as needed. These properties can be transferred to other simulators using grid file formats or point data having associated mean property values (Figure B.3-6).

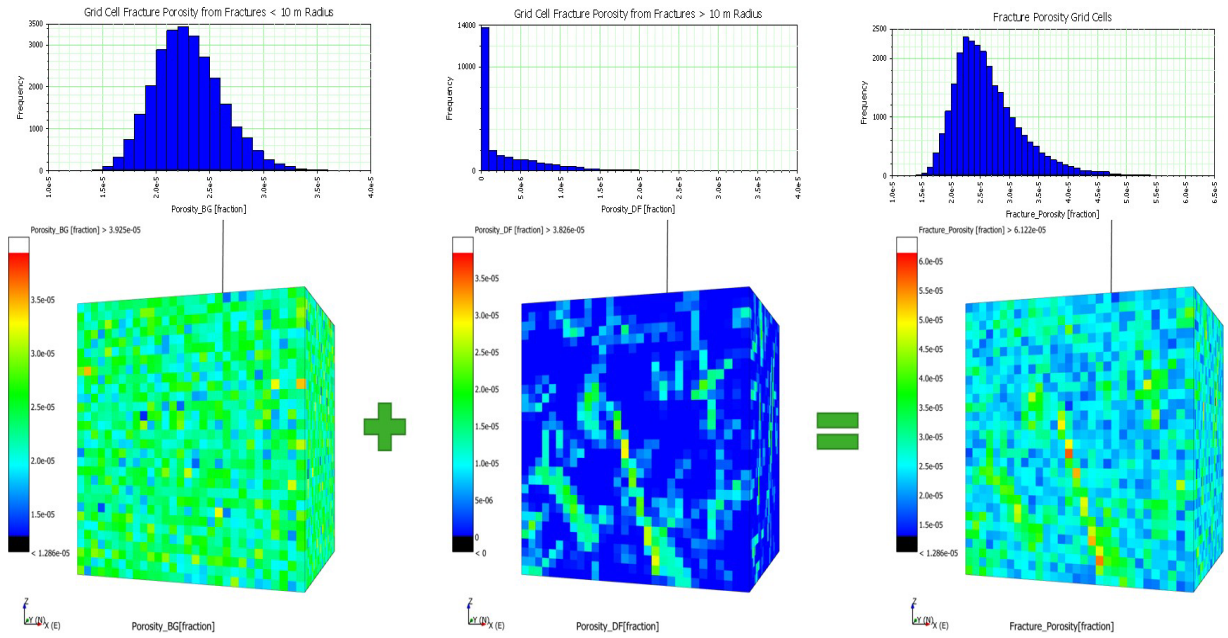

Figure B.3-6. *Upscaled porosity values for well 58-32 Zone 2 DFN.*

In addition to providing the three DFN realizations consisting of individual fractures, a more general description of the fracture sets was developed. These summary set orientations, intensities, and size parameterizations can be used to generate additional, compatible DFN representations of the Utah FORGE reservoir.

Numerical Simulation of Hydraulic Fracturing Stimulation in Well 16A(78)-32

As presented in Attachments 5 and 6, a detailed numerical evaluation of stimulation options for well 16A(78)-32 was completed. Production well 16B(78)-32 will be drilled with a trajectory designed to intersect the microseismic cloud produced during creation of the hydraulic fractures near the toe of well 16A(78)-32. A key consideration is the geometry of these “near-toe” fractures in the injection well and the need to ensure effective hydraulic communication between the two wells.

We used a fully coupled hydro-mechanical modeling software, XSite (Itasca, 2020), to history match the legacy pressure data from pilot well 58-32 and develop an acceptable representation of the properties and discontinuities of the reservoir and the morphologies of the hydraulic fractures (see previous section). The numerical analyses from the pressure history matching for well 58-32 showed that the specifics of the 3D DFN are key to understanding injection pressure performance. The location, size, and properties of the natural fractures significantly affect the injection pressure. The numerical investigation enhanced the understanding of the Utah FORGE reservoir and shed light on what might be called self-shadowing, where one injection cycle impacts the injection performance of a subsequent stage pumped at the exact same physical location.

The numerical model, calibrated by pressure history matching of injections in well 58-32, validates the existing geologic model at that location and constrains the in-situ stresses. With the refined understanding of the Utah FORGE reservoir based on the calibrated numerical model, preliminary designs for the connecting hydraulic fracturing treatments are proposed and analyzed for well 16A(78)-32 in this study. Parametric evaluations include DFN dilatancy, fluid type, and pumping rate. Both slickwater and crosslinked treating fluids (with a large cooldown pad) are considered. The analysis focused on a preliminary simulation of potential stimulation in well 16A(78)-32.

In this study, two different DFN realizations (denoted as DFN1 and DFN2) were investigated (Figure B.3-7). Each set has more than 2000 natural fractures. The DFN model was created using preliminary information, which might change as a result of detailed study and interpretation of the FMI logs from well 16A(78)-32. Discrete fractures with a radius of 50 m to 150 m are provided in the full model region while fractures with a radius of 10 m to 50 m are present in a smaller 250 m cube region in the middle. Fractures with a radius less than 10 m (0.63 m to 10 m), as well as those in the 10 m to 50 m range outside the central 250 m cube, are accounted for with upscaled properties. The DFN close to the injection point is shown in Figure B.3-7.

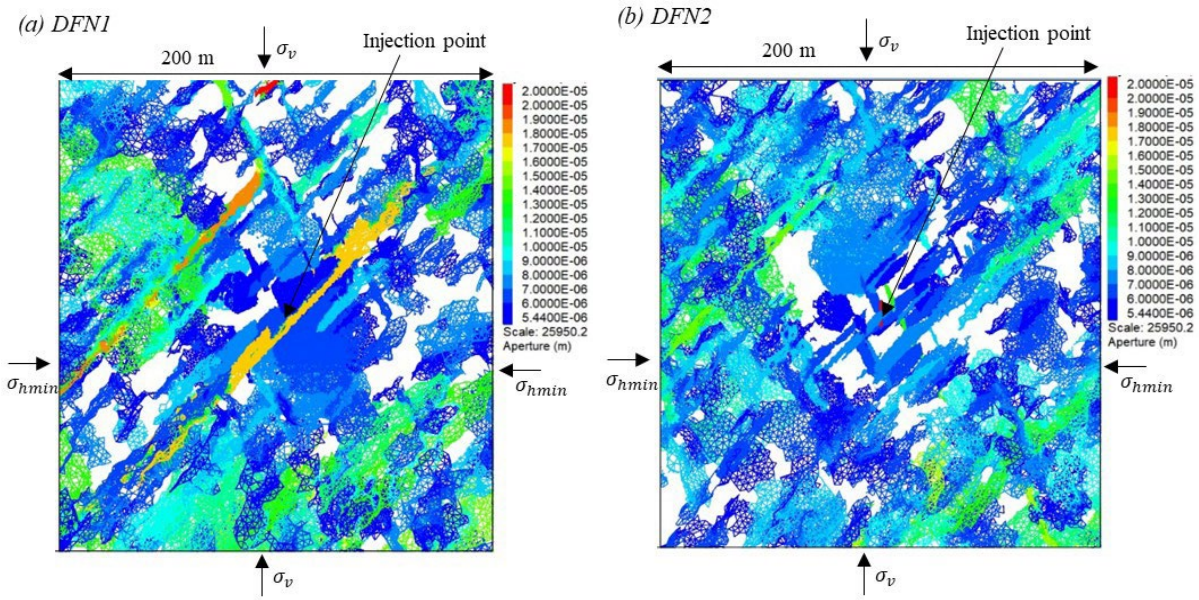

Figure B.3-7. *Description of different DFN sets around injection point and their initial apertures.*

In the simulations, it was assumed that the DFN natural fractures are frictional, with a 37° friction angle, zero cohesion, and zero tensile strength. The initial fracture apertures are correlated with fracture sizes. The initial apertures range between 5 and 20 μm.

A series of simulations for well 16A(78)-32 have been conducted (Table B.3-3). For the natural fracture networks considered, the formation response to injection was dominated by the DFN,

especially the large natural fracture closest to the cluster. Of course, this proximity to a large natural fracture will vary with position along the wellbore. For the base model, the pumping rate is 20 bpm, pumping time is 15 minutes, fluid viscosity is 2 cP, and DFN realization DFN1 is considered. In the base model, the resulting net fluid pressure is 11.8 MPa, the maximum fracture aperture is 0.01 m, the maximum length of the fracture failure in shear is 78 m, and that of failure in tension is 63 m. For most of the DFN, the failure mode is a mixture of tension and shear. The elevated net pressure remains a concern. Openhole DFIT testing in well 16A(78)-32 was substantially lower.

Table B.3-3. *Summary of the simulation results.*

Case	Height (m) of aperture > 0.2 mm	Area (m^2) of aperture > 0.2 mm	Height (m) of slip	Slip area (m^2)	Height (m) of open fracture	Open fracture area (m^2)	Lateral extent (m)
Case 1: 20 bpm, 600 bbl, 2 cP, no dilation, weak DFN	235	3.18E+05	93	9700	73	5730	130
Case 2: 20 bpm, 600 bbl, 2 cP, 2° dilation, weak DFN	235	3.00E+05	93	9441	73	4123	134
Case 3: 40 bpm, 600 bbl, 2 cP, no dilation, weak DFN	193	2.87E+05	92	19356	73	9134	125
Case 4: 10 bpm, 600 bbl, 2 cP, no dilation, weak DFN	280	3.53E+05	75	4329	50	2529	131
Case 5: 20 bpm, 600 bbl, 2 cP, no dilation, strong DFN	110	1.26E+05	108	3999	108	8844	33
Case 6: 20 bpm, 600 bbl, 20 cP, no dilation, weak DFN	121	1.32E+05	93	30137	82	23897	88

The net fluid pressure for the case with DFN2 is 3.7 MPa lower than DFN1 because the normal stress acting on the closest-to-cluster natural fracture is lower. The net pressure has a similar trend for both DFN sets. In either case, the elevated net pressure suggests refinement is still required in the DFN or natural fracture properties. For the cases with a 2° dilation angle for the DFN, the net fluid pressures are lower than those without dilatancy because natural fracture permeability increased due to aperture increasing during slip. Generally, the cases with DFN dilatancy resulted in a smaller area of DFN failing in tension (DFN1 and DFN2) but approximately the same slipping area compared to those simulations without dilatancy.

Increasing the pumping rate from 20 bpm to 40 bpm resulted in a slightly higher (1 MPa higher) net fluid pressure and an increase in the area of DFN failure in shear and tension.

The model has been calibrated by pressure history matching the injection tests in pilot well 58-32. The calibration helps to constrain the material properties and initial stress conditions. The lessons learned from the pressure history matching include:

(i) the formation response to the injection is dominated by the fluid flow and pressuredissipation in the DFN;

(ii) increasing pressure trends are due to fluid diversion into the DFN as localized leakoffand deformation of the DFN;

(iii) previous injection affects the subsequent injection pressure cycles due to theirreversible deformation.

The simulations allow prediction of the formation response to injection in well 16A(78)-32 for the current interpretation of the DFN (Figure B.3-8). In all the cases, the formation response is dominated by the DFN, and failure is the combination of fracture opening and natural fracture slipping. For the base model, the pumping rate is 20 bpm, the pumping time is 30 minutes, and the fluid viscosity is 2 cP. The resulting net treatment pressure is 7.5 MPa, the height of stimulated fractures above the injection point, defined by induced aperture greater than 0.2 mm, is 235 m, the lateral extent is 130 m, and the height of stimulated fractures defined by open fractures is 73 m.

For the cases with a 2° dilation angle for the natural fractures, the net fluid pressures are lower than those without dilatancy. Increasing the pumping rate from 20 bpm to 40 bpm resulted in a larger area of open and slipping fractures while decreasing the pumping rate from 20 bpm to 10 bpm resulted in a smaller area of open and slipping fractures. For the case with a “stronger” DFN (10 MPa cohesion), the area of slipping fractures is smaller but the area of open fractures is larger. Increasing fluid viscosity from 2 cP to 20 cP resulted in a much higher injection pressure and hence larger area of slipping and open fractures.

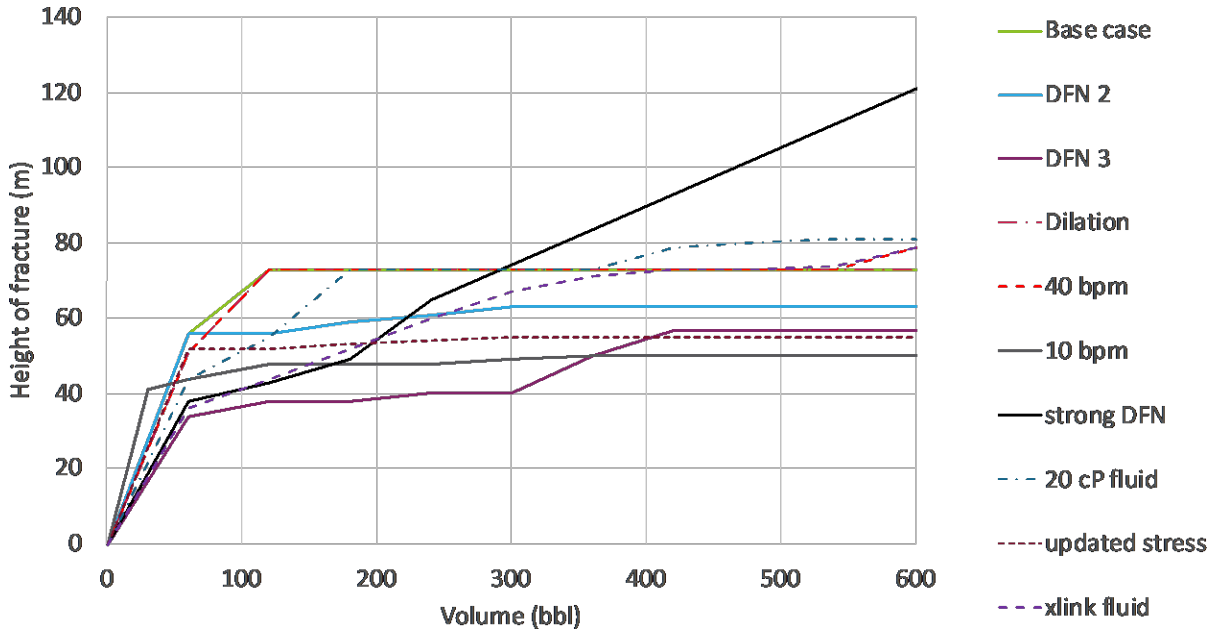

Figure B.3-8. *Summary of the results – Hydraulic Fracture Height*

Analytical Model for Fluid Flow Distribution

Enhanced geothermal system (EGS) is often envisioned to consist of at least two wells spaced sufficiently apart and connected by fractures that serve as flow paths. All the flow paths mustbe utilized efficiently to ensure the system is operated at its highest potential. However, building an efficient and sustainable EGS is a complicated process as the fluid always choosesthe path of least resistance, which can lead to uneven flow distribution among the fracture zones. As presented in Attachment 7, a reduced order analytical model was developed to examine potential doublet well completion options.

This effort focused on several critical parameters related to well designs, which can potentially allow for optimized flow distribution. An analytical model is developed based on Kirchhoff's law to calculate the flow distribution in any doublet EGS. Wellbore perforations in the completed wellbores and the fractures are simulated as resistance while the fluid is simulated as a current analog. The model solves the pressure at each node, analogous to voltage, using pipe flow equations and Darcy's law. The model then calculates the flow rate for the next step by solving the set of equations implicitly. This process is continued until convergence is achieved.

Three different doublets EGS designs (parallel, anti-parallel and non-parallel, see Figure B.3-9) were simulated using the model, and a detailed sensitivity study was performed. The results for all the cases were compared using the pressure head loss and deviation from ideal flow (equal) distribution in the fractures. It was observed that the anti-parallel and non-parallel designs performed the best, both leading to better flow distribution and having lower pressure losses.

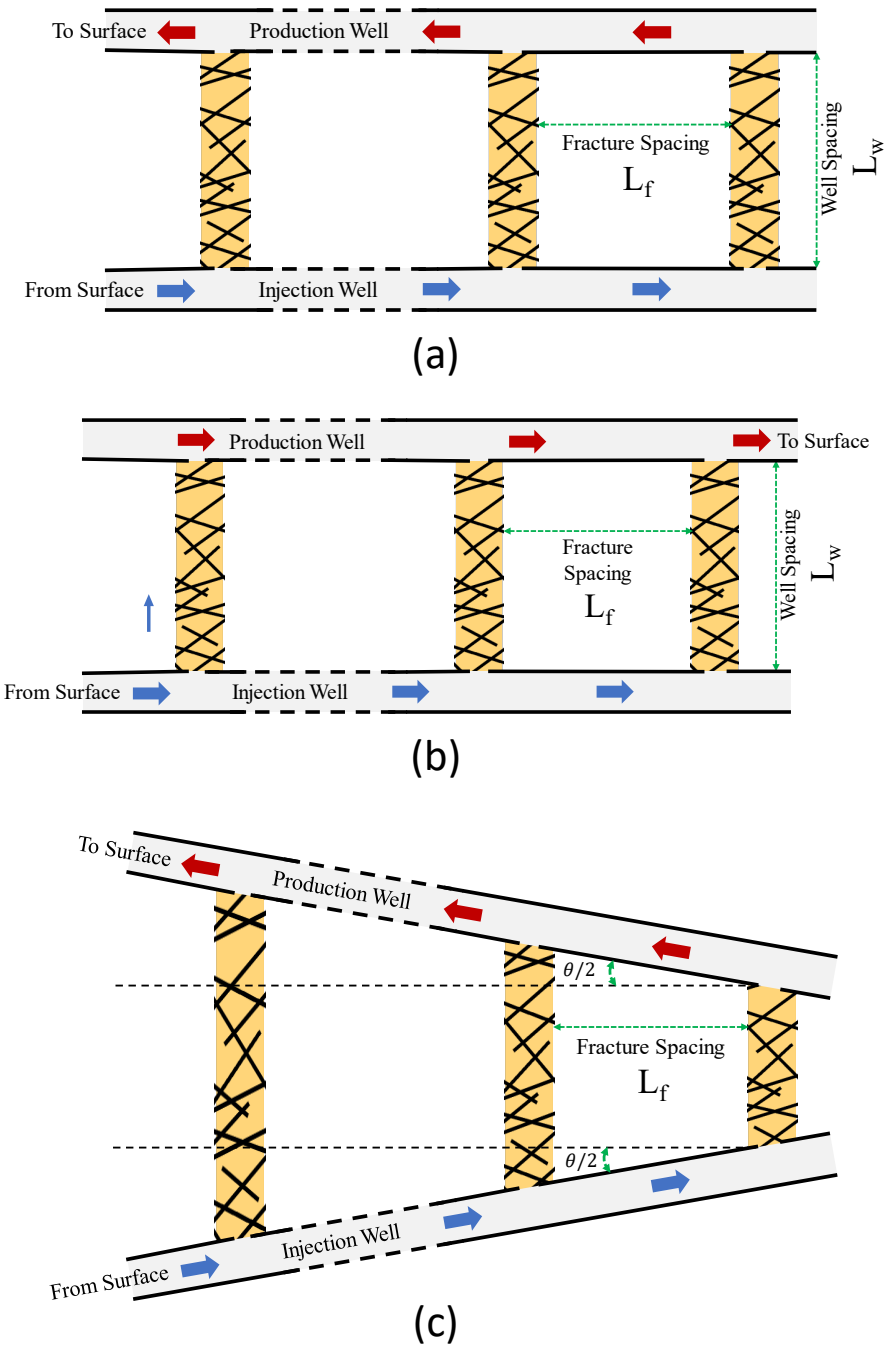

Figure B.3-9. *Schematic of different doublet well designs drilled in the xy-plane (elevation view) and passing through multiple fracture zones: (a) Parallel well doublet system, (b) Anti-parallel well doublet system, (c) Non-parallel well doublet system.*

The flow in either an injection or production wellbore can be described primarily by the Poiseuille flow equations, while the flow in the fractures can be approximated using Darcy's

law. These two sets of equations can be solved iteratively using a node-loop method to determine the fluid distribution in multiple fractures that make up an EGS. This problem is similar to flow distribution in a network of pipes laid around a city block to distribute water to households. Some of the complexity of the problem arises due to the dependence on friction factor, Reynolds' number, and surface roughness in the pipe flow. Due to this, it is necessary to solve the equations iteratively to arrive at a converged solution. This is analogous to current distribution in a circuit consisting of multiple branches and resistors. The maximum current passes through the path of least resistance, leading to uneven current distribution in the system. Solving for current distribution in a circuit is relatively simple since the resistance of a resistor is not a strong function of the current flowing through it. However, unlike resistors, the friction factor used for predicting turbulent flow in a pipe or fracture is susceptible to the flow rate of the fluid.

For a multiple-fractured EGS with identical fracture conductivities, an anti-parallel design leads to a more uniform flow distribution compared to the other two designs. The counter flow in the production and injection well has symmetry about the central fracture (the fracture that is an equal distance from the heel and toe fractures), improving the flow distribution. Another advantage of using an anti-parallel well system is the reversibility in the flow direction.

Changing the flow direction in the system would allow even heat extraction from the reservoir, thus increasing the overall efficiency.

The non-parallel design also gives better flow distribution with lower pressure drop. The system performance is optimized when the deviation of the wells is tailored to the reservoir and operational conditions. Any changes to the fracture zone permeability or the flow rate would lead to a skewed flow distribution. However, this sensitivity toward the flow rate could be used as an additional control variable to optimize the flow distribution throughout the lifecycle of the EGS, which is not feasible in the other two designs.

The parallel well EGS performed the poorest of all. The improvement in the flow distribution solely relies on creating a limited entry scenario (i.e., smaller diameter perforations near the heel of the injection well) at the fracture wellbore interface through smaller-diameter perforations, leading to increased pumping costs.

The results of our studies indicate that the anti-parallel and non-parallel designs performed the best. In a parallel well design, the improvement in the flow distribution solely depends on creating a limited/restricted entry situation. Whereas, in the anti-parallel well design, the counter-flow direction of the wellbore facilitates a better flow distribution. In case of non-parallel design, the different length of fractures leads to better flow distribution.

A Mixed Fracture-Matrix Model for Evaluating Well Orientation and Completion Options

Numerical Method Development

As discussed above, orientation and completion for well pairs that have been subjected to multi-zonal stimulation play a critical role in the long-term performance of an Enhanced

Geothermal Reservoir. Here we develop a methodology to rapidly and efficiently numerically simulate mixed fracture-matrix flow systems for evaluation of well design and completion options. An example evaluation based on a small fracture network representative of Utah FORGE well 16(A and B)-78(32) is used to numerically validate the model and prepare for a full stimulated DFN evaluation. Attachment 8 contains full details of the theory and numerical implementation.

Predictive simulations involving fractured porous media requires an accurate representation of the DFN and its role in physical phenomena related to flow and transport. Predictive simulations using computational methods like the finite element method require the geometry to be discretized into elements of a mesh. Ideally, all the DFN's complex geometric features must be captured by the mesh. Creating a 3D mesh containing a 2D or 3D representation of the DFN is difficult. For this reason, we developed a modeling methodology in which the fractured porous media is decomposed into two separate domains – one representing the DFN network and the other containing the surrounding porous matrix – and loosely couple these two domains by exchanging heat energy (Figure B.3-10). This simplifies our workflow by allowing us to produce a mesh of the matrix material completely independent from the mesh of the DFN.

Although the main goal of this loose coupling strategy is to simplify the meshing process, we also expect decreases in computational costs for the following reasons.

(1) This simplification in the mesh reduces the number of volumetric elements in the matrixmaterial leading to a smaller computational cost.

(2) The computational cost is further reduced by separating the "faster" physics of porousflow in the fracture network from the "slower" diffusion in the matrix, allowing us to use different timestep sizes on each domain.

(3) The separation of fast and slow physics also leads to a better conditioned linear system,further reducing the computational overhead.

On the other hand, the loose coupling breaks the unconditional stability of a fully-implicit, fully-coupled solve.

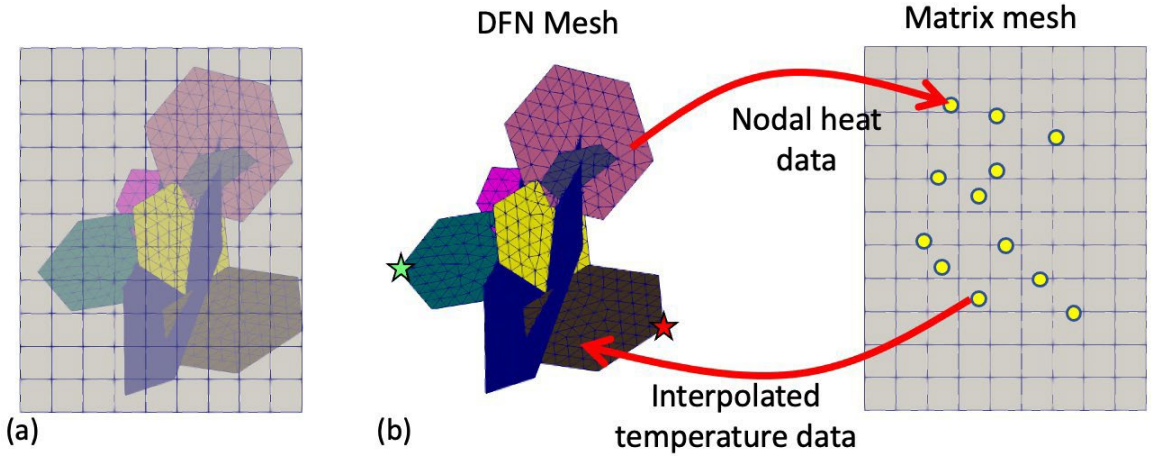

Figure B.3-10. *(a) The 2D DFN sits within the volumetric domain of the 3D porous matrix, but the meshes do not conform. (b) Illustrates the separate computational domains and the loose coupling. The green and red stars indicate the injection and production points of the example, below.*

Figure B.3-11 shows the temperature at the production bore. It is clear that the matrix provides substantial heat-energy to the injectate. However, as time proceeds, the cold injectate cools the surrounding matrix, leading to cooler production temperatures. These figures show how the results depend on the matrix and fracture mesh sizes. Keep in mind, the "20 m, 9.2 m" case is not expected to be accurate for time-scales less than about 500 days.

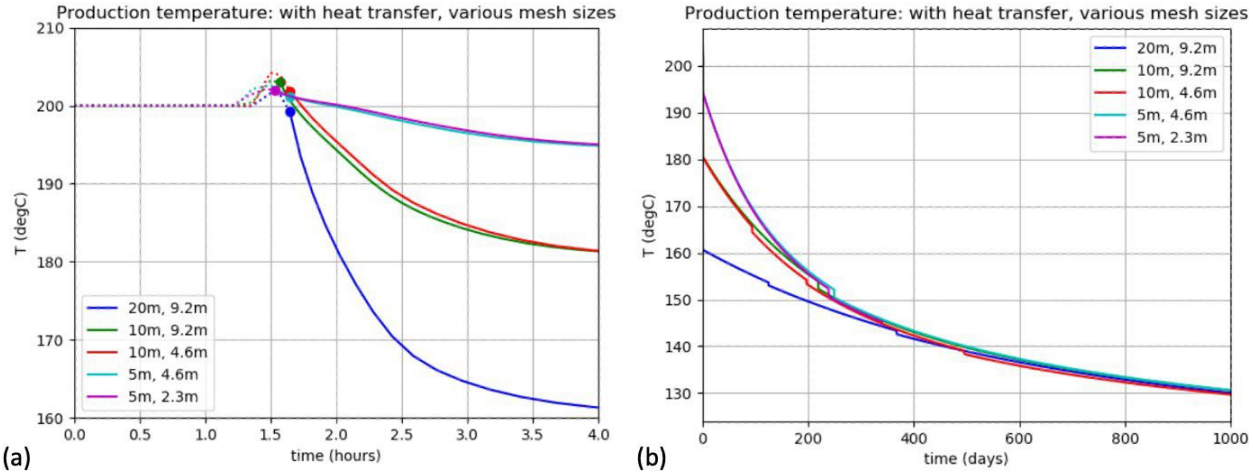

Figure B.3-11. *(a) Short term and (b) long term well production temperatures for the loosely coupled DFN-Matrix simulations. The first number in the legend is the mesh element size, while the second is the fracture element size.*

Stochastic Optimization of DFN Energy Output with Parallel Subset Simulation

The DFN models must have injection and production locations for extracting heat output from the geothermal system. The coordinates of the production locations can significantly impact the energy output from the system. Owing to the computational complexity of the DFN models, it is infeasible to run these models numerous times by naively randomizing the production location in order to optimize the energy output. Therefore, we are using a stochastic optimization algorithm termed parallel subset simulation (PSS) to efficiently optimize the energy output with complex DFN models. Figure B.3-12 presents a schematic of the PSS algorithm, wherein, the different subsets indicate the levels of optimization. In level 1, the algorithm performs a regular Monte Carlo to explore the parameter space. Then, from levels 2 and higher, the algorithm initiates numerous Markov chains to explore the space in an efficient fashion to optimize the quantity of interest. Since these Markov chains are independent, they can be run on

independent sets of processors in parallel. Coupled with an intelligent space exploration via Markov chains, parallel computing can lead to computational efficiencies when conducting stochastic optimization.

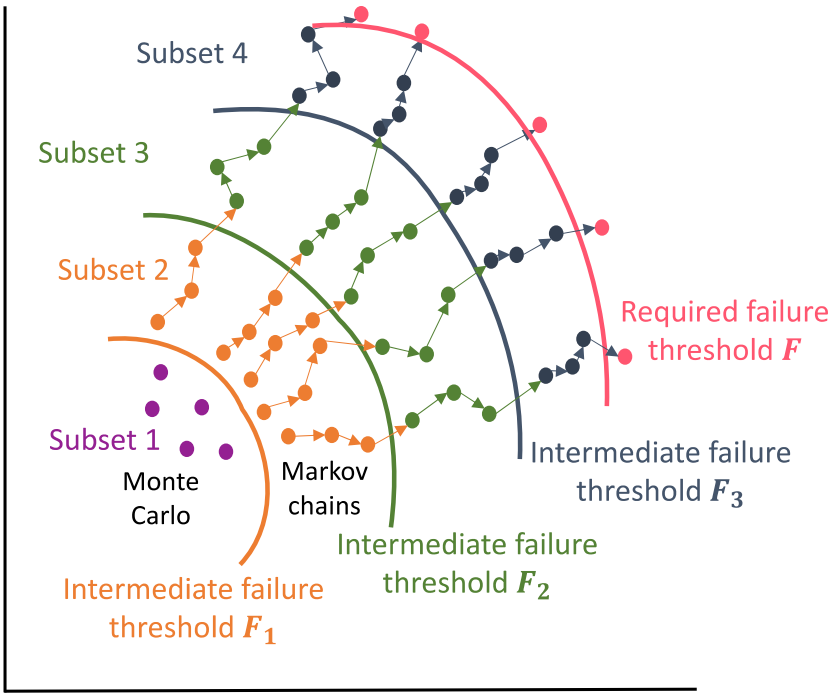

***Figure B.3-12**. Schematic of the parallel subset simulation (PSS) algorithm for efficiently exploring the space leveraging massively parallel computing.*

Figure B.3-13(a) presents a test study on using the PSS algorithm with a simple DFN model. Two levels of optimization were conducted. In level 1, the sampled points are uniformly distributed. In level 2, the algorithm only picks those points that have a high energy output value. As a work in progress, we are scaling the PSS algorithm to a more complex DFN model presented in Figure B.3-13(b). In here, the red dots represent a uniform sampling in level 1 of PSS. For higher levels of PSS, it is expected that the sampled production locations are concentrated in regions with a high energy output. Ensuring that fractures in the DFN model are connected is important for an effective optimization.

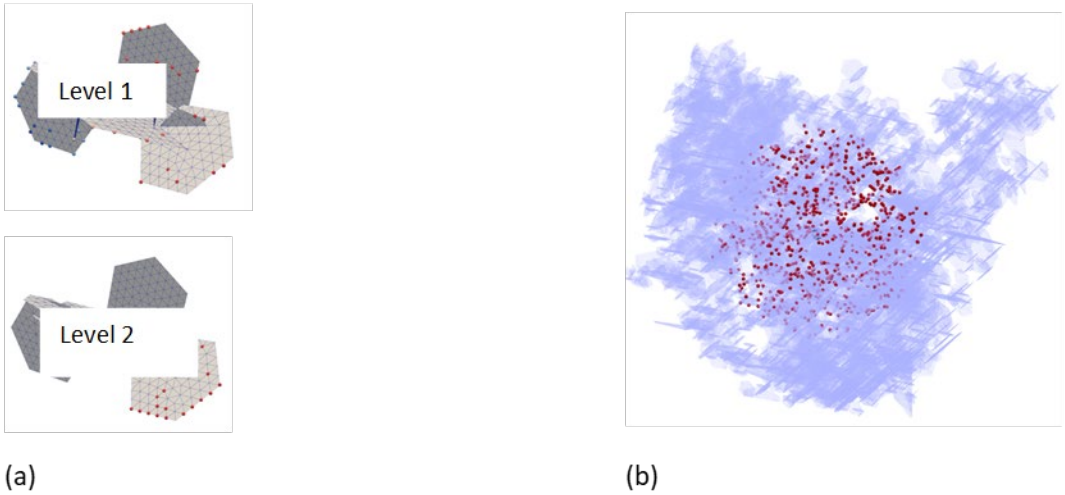

Figure B.3-13. *(a) Testing the PSS algorithm on a simple DFN model with two levels of optimization. Blue dots indicate low output and red dots indicate high output. (b) Scaling of the PSS algorithm to a more complicated DFN model.*

Simplified Simulation Scheme to Reduce Computational Needs

The optimal location for well pairs placed in a discrete fracture network is determined in this work. The input location for the well in the DFN is fixed, shown by the blue sphere in Figure B.3-14. The production point, shown by the red sphere, is randomly placed using Monte Carlo and adaptive sampling methods described above.

In order to further speed up the thousands of needs simulations, the network is modeled using a two-component fluid using the Darcy flow equations in the MOOSE porous flow module.

Tracer fluid is injected and the mass fraction of tracer material recorded at the test and production point are plotted in Figure B.3-15. After a short time delay, the tracer material passes the test point and the mass fraction of tracer material goes to 1. At the production location, tracer and fracture fluid are being withdrawn at the same time, resulting in a more gradual increase in the mass fraction of tracer material, shown by the blue line in Figure B.3-15. Once optimal regions are identified, thermal hydraulic simulations with coupling between the fracture network and matrix will be performed. The example shown in Figure B.3-14 only contains a small portion of the overall fracture network.

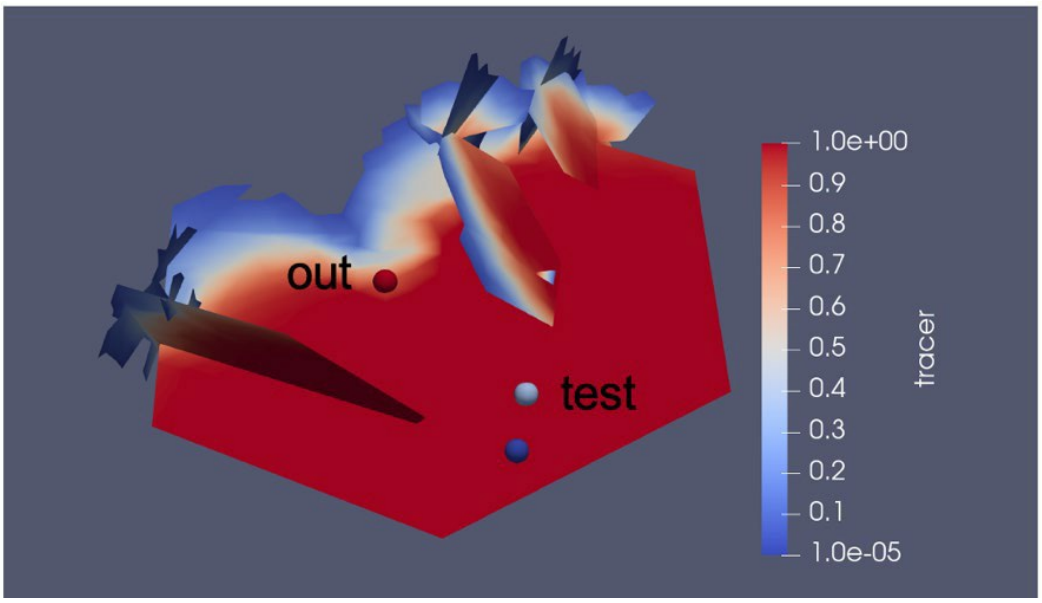

Figure B.3-14. *Pressurized DFN containing two components colored by the mass fraction of injected fluid (tracer). The blue sphere is the injection point, the red point is the production point. The light blue point is a test point for sampling.*

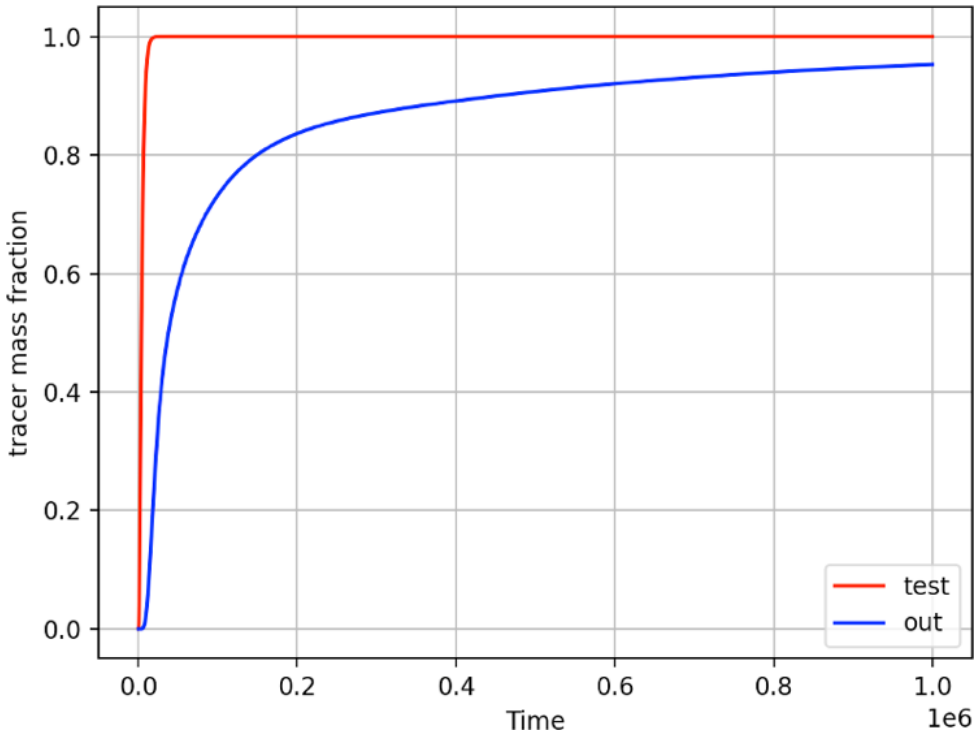

Figure B.3-15. *Mass fraction of injected fluid (tracer) at the production point (blue line) and test point (red line) shown in Figure B.3-14.*

These methods will be full developed as Phase 3 progresses and be used to inform the location and completion options for well 16B.

Phase 3 Native State Model Revision

A numerical implementation of the conceptual and earth models has been developed of the Utah FORGE reservoir and surrounding area to estimate the spatial distribution of native state pressure, temperature, and stress conditions.

The primary goal of this effort was threefold.

1. Incorporate detailed 3D parameter distributions and complex boundary conditionsidentified from characterizing the site.
2. Better understand the spatial distribution of stress and how it may influence reservoirstimulation.
3. Establish a reference (or baseline) set of parameter and property distributions that can be used among the team (and modeling community at large) to ensure consistency andcomparability of simulation results.

The data and results included here are from the reference models completed in March 2022.

Model Dimensions

The Phase 3A numerical model domain sized to enclose a volume of the reservoir intersected by wells 56-32, 58-32, 16A, 78B-32, and 78-32 and a significant subsurface volume below the Utah FORGE site. The model domain of 4.0 km x 4.0 km x 4.2 km is located approximately between depths of 4000 to 4200 m below the land surface. A nonuniform mesh spacing of average 40 m was used, with a total of 0.24 million tetrahedron elements. Figure B.3-16 shows the model geometries, the upper sedimentary layer (red), the lower granitoid layer mesh. This image also presents the global coordinate system where Z-axis is along vertical direction and X-axis is along the minimum horizontal direction.

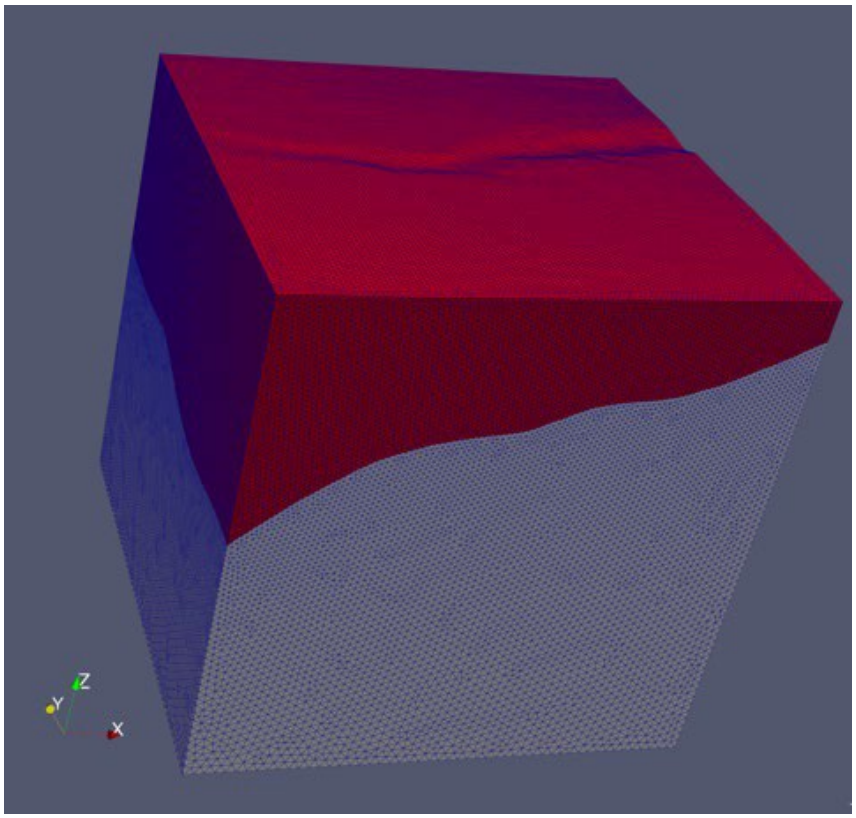

Figure B.3-16. *The model geometries, the upper sedimentary layer (red), the lower granitoid layer mesh.*

Boundary and Initial Conditions

Both native static and transient models are based on complex coupled pore fluid flow, thermal, and solid field equations. The setup on appropriate boundary conditions for each field equation are critical to solving such a complex multiphysics problem. Boundary conditions for native static model were based on results obtained and compiled during Phase 3A, which relied on both new data collection and information obtained from field tests and the literature.

Specifically, based on field well tests, the direction of the maximum principal stress has been evaluated not along the vertical direction. This complicates stress field boundary conditions as the traction in shear component besides of the normal traction should be included in the model.

(a) Boundary conditions for the fluid flow field equation:

1. Prescribed zero pore pressure on the top surface;
2. Prescribed pore pressure on the bottom surface;
3. No flow boundary conditions for all side surfaces.

(b) Boundary conditions for the thermal field equation:

1. Prescribed temperature on the top surface;
2. Prescribed and varied temperature input on the bottom surface.
3. No heat flux boundary conditions for all side surfaces.

(c) Boundary conditions for the stress field equation:

1. Displacement along horizontal X-direction at the two side surfaces perpendicular to X-axis are constrained;
2. Displacements along horizontal Y-direction at the side surface perpendicular to and cross over the negative Y-axis is constrained;
3. Displacement along vertical Z-direction at the bottom surface is constrained;
4. Atmosphere pressure is applied on the top surface for the normal traction;
5. Prescribed both normal traction and shear traction along vertical (Z-axis) directionon the side surface perpendicular to and cross over the positive Y-axis;
6. Body force due to gravity is applied.

By applying these boundary conditions and gravity (body force), the solution from native static model provides initial conditions including pore pressure, temperature, and stress for further transient analysis where fluids are injected through wellbores.

Figure B.3-17 presents boundary conditions for coupled three field equations. A more detailed displacement and traction boundary conditions for the stress field are plotted in 2D in the image.

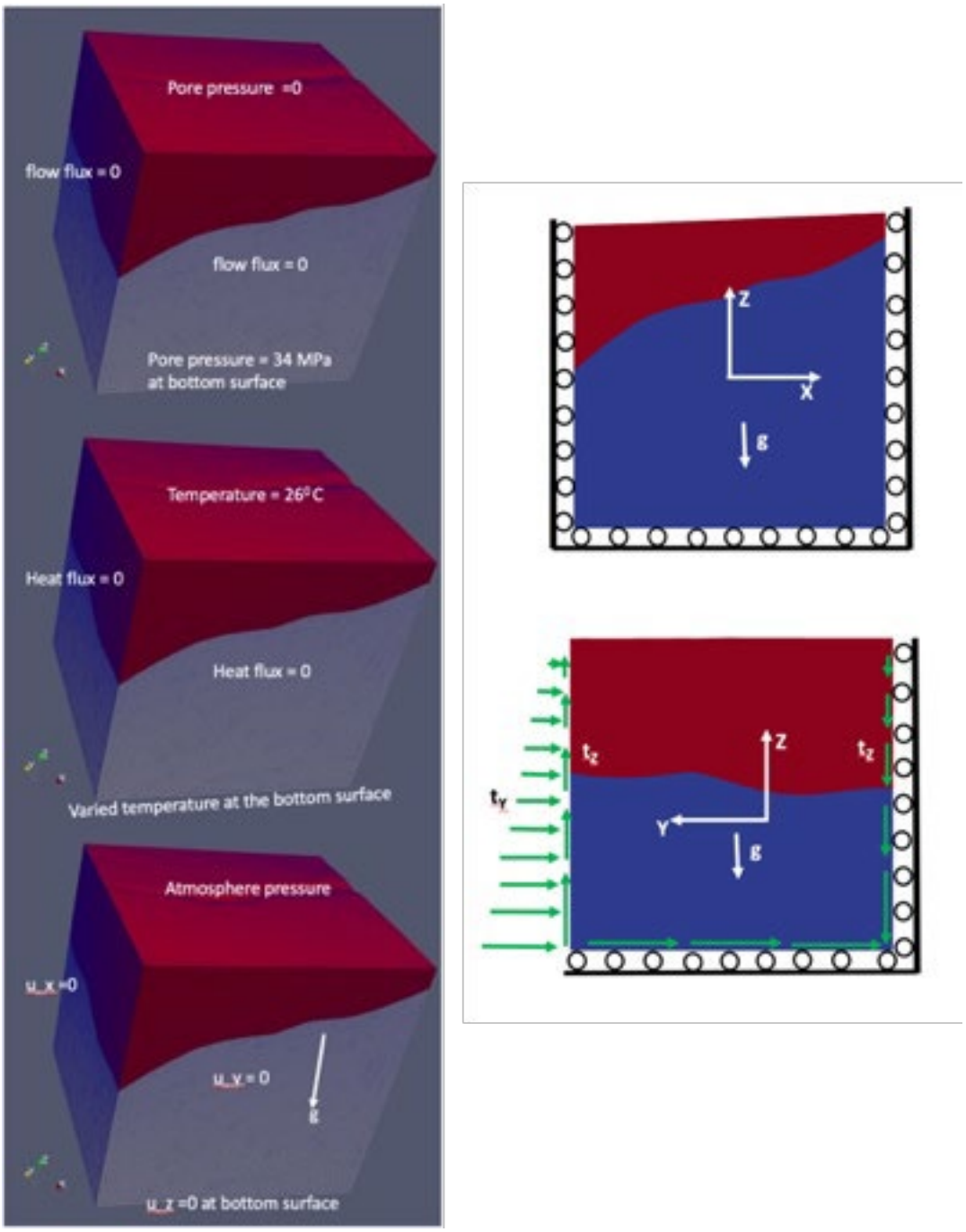

Figure B.3-17. *Boundary conditions for coupled three field equations(left). A detailed displacement and traction boundary conditions for the stress field are also shown (right).*

Reservoir Model Properties

Initial reservoir properties used in the native state model were taken directly from characterization data when possible. In many cases, a range of possible values were available,

and the mean or median was used, with the values being adjusted within the measured range during model calibration. In all cases, uniform reservoir properties are used within the alluvium. For the granitoid, heterogeneous property distributions are applied where appropriate and data are available. Table B.3-4 summarizes the property values used. These are the "reference" values for the current state of Utah FORGE.

Table B.3-4. *Summary of the parameter values used in the native state model.*

Parameter	Units		Source/Comment
Compressibility	1/kPA	2.52E-12	Upscaled DFN
K_{ii}	m2	1.00E-18	Core and reservoir testing
K_{jj}	m2	1.00E-18	Core and reservoir testing
K_{kk}	m2	1.00E-18	Core and reservoir testing
Porosity	—	1.00E-03	Core and cuttings analysis
Rock grain density	kg/m3	2750	Core and cuttings analysis, model calibration
Specific heat capacity	J/kg K	790	
Grain thermal conductivity	W/m K	3.05	Thermal conductivity data analysis
Young's Modulus	Pa	6.50E+10	Core analysis
Drained Poisson's Ratio	—	0.3	Core analysis
Biot coef	—	0.47	Injection test analysis
Thermal expansion coef	—	6.00E-06	

Native State Model Results

The images to the left from the top to the bottom present contoured results for the pore pressure for the fluid flow field, temperature for the thermal field, the vertical effective normal stress in the Z-direction, the horizontal effective normal stress in the X-direction, the horizontal effective stress in the Y-direction, the shear stress in Y-Z plane along vertical direction, the mean stress (hydrostatic pressure), and von Mises stress for the solid field obtained from the native steady state model. All predicted field variables in the contours exhibit a linear distribution over the vertical direction where the minimum is on the top surface and the maximum is on the bottom surface. However, it also shows that all these pressure, temperature, and stresses exhibit appreciable variations along the horizontal direction.

Furthermore, due to the applied shear traction besides the normal pressure traction boundary condition for the solid field, the stress shows a more significant variation across the interface between the sediment and granitoid. The shear stress level is roughly 10% of the vertical normal stress.

The above native steady state model results are based on a series of calibrations that adjust some parameters to make the predicted field variables closely match the field measurements along wellbores. For example, the far field bottom temperature is slightly raised and the predicted distribution of temperature matches the temperature recorded from well logging. Importantly, it is evaluated from field fracture tests that the maximum principal stress is not exactly along the vertical direction but slightly rotates about either the maximum horizontal stress axis or the minimum horizontal stress axis. However, it is undetermined that this rotation is about which axis. By running various models with different boundary conditions, it is suggested that such a rotation is around the minimum horizontal stress axis.

Figures B.3-19 and B.3-20 show the comparisons between the measured pore pressure, and temperature, field stresses and the model predicted pore pressure, and temperature, field stresses from the native static model for wells 56-32, 58-32, 16A, and 78B-32.

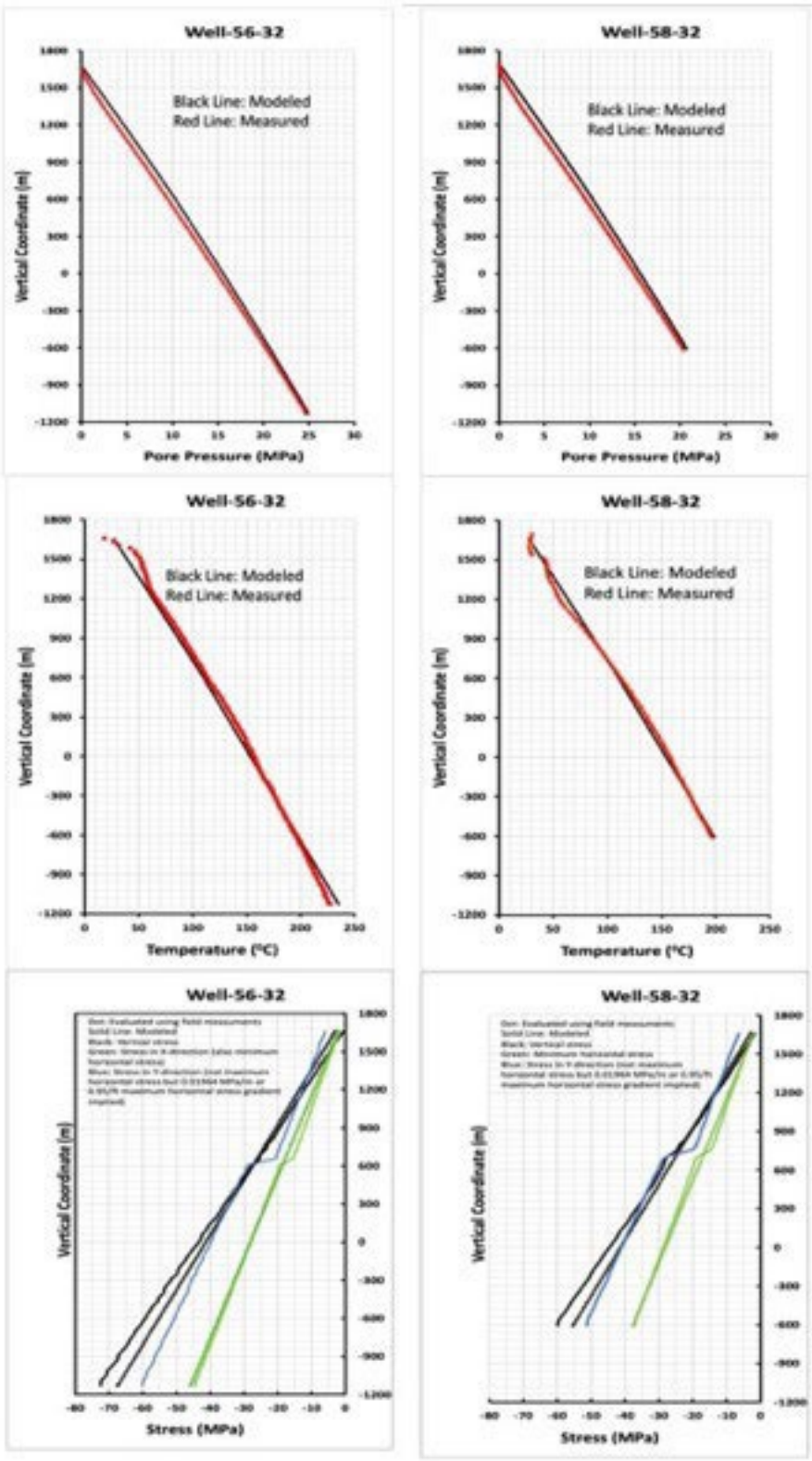

Figure B.3-19. *Native state model results for wells 56-32 and 58-32.*

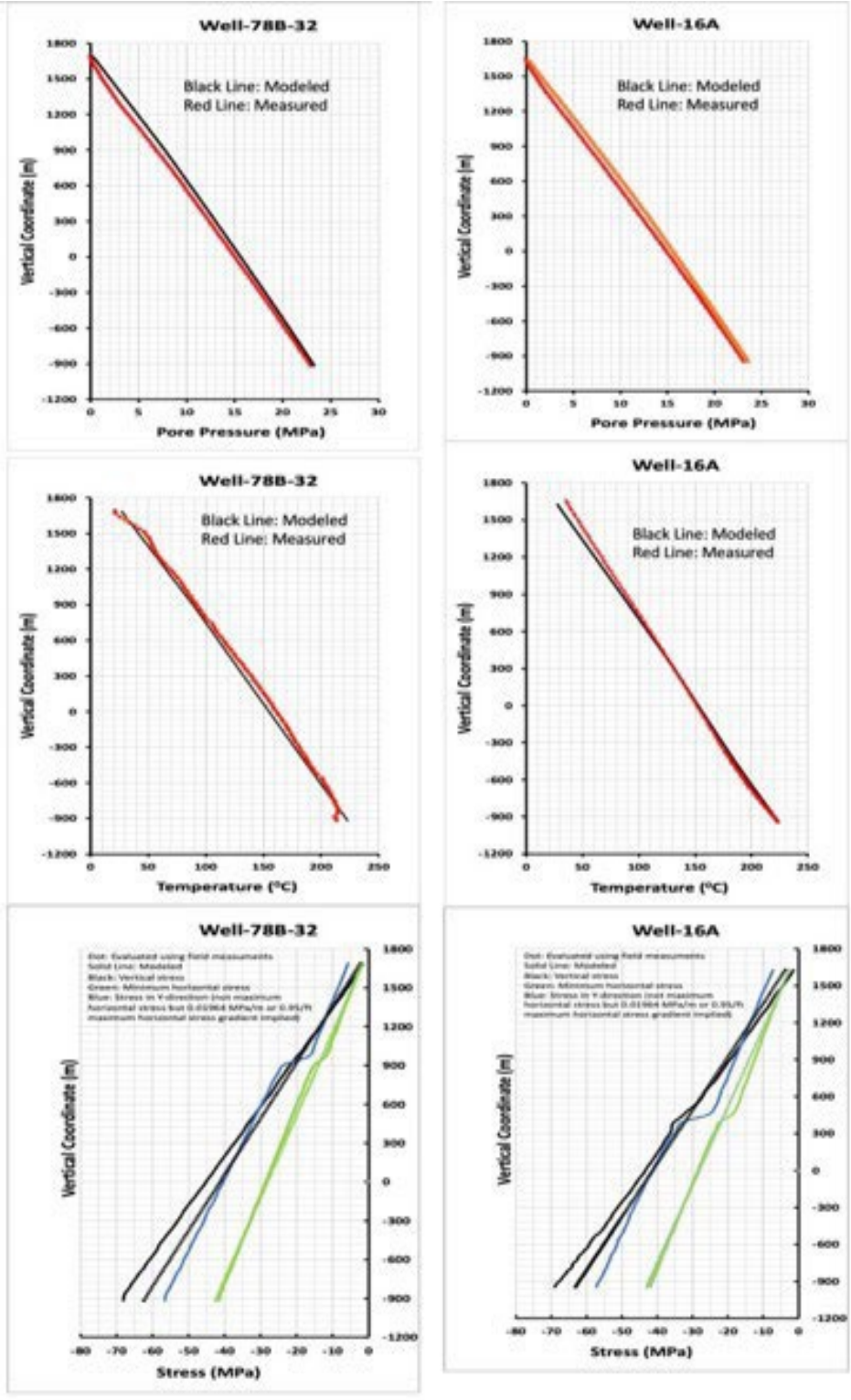

Figure B.3-20. *Native state model results for wells 78B-32 and 16A(78)-32.*

B.4 EXTERNAL R&D

External R&D comprises a portfolio of 17 projects that covers 5 topic areas having a total value of $53.03 million (Tables B.4-1, B.4-2). The awardees were selected through a competitive process involving responses to the Utah FORGE Solicitation 2020-1, which was published in April 2020. Full proposals were received from 63 applicants, and these were rigorously reviewed in a step wise manner. The prescreening of applications was undertaken by TARMaC (a committee composed of Utah FORGE and DOE-GTO representatives). Formal reviews were obtained from external referees, and follow up recommendations for funding were made by STAT. The final funding recommendations were made by the R&D Steering Committee (also composed of Utah FORGE and DOE-GTO representatives). DOE announced the selectees for contract negotiation in February 2021 and by October 2021, 14 of the 17 contracts were signed and underway. One contract was signed in December 2021. The last 2 contracts were finalized by the end of February, 2022.

***Table B.4-1**. Utah FORGE Solicitation 2020-1 R&D Topic Areas.*

Topic 1—*Enable strategic permeability enhancement and control, via the development of an integrated zonal isolation and flow control system, operational at temperatures in excess of 225°C, in both cased and open-hole wellbores.*
Topic 2—*Analyze stresses in the reservoir rocks to design and execute additional in situ stress measurements to support informed and effective stimulations in the Utah FORGE team's field campaign.*
Topic 3—*Develop a suite of advanced, complementary characterization methods and processing techniques to supplement existing data on the Utah FORGE site and further the community's understanding of the development and evolution of fracture systems.*
Topic 4—*Develop and test innovative stimulation techniques and methods in available portions of this Utah FORGE well, pair these results with in-depth analysis and recommendations on the orientation and/or completion style of the long reach well (yet to be drilled) to best access the created fracture network.*
Topic 5—*Integrate experiments and/or in situ measurements of rock and reservoir properties in concert with THMC modeling to determine fracture behavior, permeability evolution, and heat transfer over time at Utah FORGE and develop an improved understanding of which properties are most critical for the development of EGS.*

Table B.4-2. *R&D Award Prime Recipients & Project Titles.*

Topic-ID	Title	Recipient	Period	DOE cost	Total Value
1-2551	Development of Multi-Stage Fracturing System and Wellbore Tractor	Colorado School of Mines	10/1/2021-9/30/2024	$4,604,667	$5,342,323
1-2410	Development of a Smart Completion & Stimulation Solution	Welltec	10/1/2021-9/30/2024	$3,887,574	$4,385,707
1-2409	Zonal Isolation Solution for Geothermal Wells	PetroQuip	10/1/2021-9/30/2024	$2,813,596	$3,516,995
2-2439	A Multi-Component Approach to Characterizing In-Situ Stress	Battelle	10/1/2021-9/30/2024	$2,994,436	$2,994,436
2-2446	Closing the loop between in situ stress complexity and near-wellbore fracture complexity	Lawrence Livermore National Lab	3/1/2022-2/28/2025	$1,599,616	$1,599,616
2-2404	Application of Advanced Techniques for Determination of Reservoir-Scale Stress State	Univ. Oklahoma	10/1/2021-9/30/2024	$1,164,581	$1,164,581
3-2418	Wellbore fracture imaging using inflow detection measurements	Stanford Univ.	10/1/2021-9/30/2024	$2,250,623	$2,250,623
3-2535	Joint electromagnetic/seismic/InSAR imaging	Lawrence Berkeley National Lab	12/1/2021-9/30/2024	$2,171,421	$2,258,910
3-2417	Fiber-optic geophysical monitoring of reservoir evolution at Utah FORGE	Rice Univ.	10/1/2021-9/30/2024	$4,411,914	$$4,921,540
3-2514	A Strain Sensing Array to Characterize Deformation at Utah FORGE	Clemson Univ.	10/1/2021-9/30/2024	$3,972,453	$3,972,453

4-2492	Design and implementation of innovative stimulation treatments to maximize energy recovery efficiency	Univ. Texas Austin	10/1/2021-9/30/2024	$3,636,311	$3,673,811
4-2541	Optimization and validation of a plug-and-perf stimulation treatment design at Utah FORGE	Fervo	10/1/2021-9/30/2023	$6,231,329	$7,822,007
5-2419	Seismicity-permeability relationships probed via nonlinear acoustic imaging- of fractures in shear	Penn State Univ.	10/1/2021-9/30/2024	$1,504,415	$1,504,415
5-2615	Experimental determination and modeling-informed analysis of thermo-poromechanical response of fractured rock	Univ. Oklahoma	10/1/2021-9/30/2024	$1,130,229	$1,130,229
5-2565	Evolution of permeability and strength recovery of shear fractures under hydrothermal conditions	US Geological Survey	10/1/2021-9/30/2024	$1,848,564	$1,848,564
5-2428	Coupled investigation of fracture permeability impact on reservoir stress and seismic slip behavior	Lawrence Livermore National Lab	3/1/2022-2/28/2025	$2,350,000	$2,366,291
5-2557	Role of fluid and temperature in fracture mechanics and coupled THMC processes	Purdue Univ.	10/1/2021-9/30/2024	$2,282,941	$2,282,941

Project by Project Summaries of Objectives and Activities

1-2551 Colorado School of Mines: Development of Multi-Stage Fracturing System and Wellbore Tractor to Enable Zonal Isolation During Stimulation and EGS Operations in Horizontal Wellbores

Objectives: Develop, test and conduct field trials for 1) sliding casing frac sleeves and 2) a tractor with flow meter survey capability, to control and manage fluid flow in deviated wells for EGS development.

Activities: Tool development, testing & field deployment.

1-2410 Welltec: Development of a Smart Completion & Stimulation Solution

Objectives: Develop an isolation system comprising an annular barrier and flow valve capable of withstanding geothermal downhole conditions in Utah FORGE wells.

Activities: Lab experiments; data analysis; tool development, testing & field deployment.

1-2409 PetroQuip: Zonal Isolation Solution for Geothermal Wells

Objectives: Design and build two retrievable tools, a locking bridge plug and a open-hole packer, that perform for extended periods of up to 12 months at EGS geothermal reservoir conditions, and impervious to proppant-bearing stimulation fluids.

Activities: Tool development, testing & field deployment.

2-2439 Battelle: A Multi-Component Approach to Characterizing In-Situ Stress at the Utah FORGE EGS Site: Laboratory, Modeling and Field Measurement

Objectives: Characterize the stresses in the EGS reservoir based on: 1) the relationship between applied stresses and ultrasonic wave velocities (from Triaxial [polyaxial] stress ultrasonic velocity [TUV] rock physics experiments) and sonic well-log data for the well(s), enabled by machine learning methods; 2) measurement of stresses at multiple depths in Utah FORGE 16B(78)-32 wellbore with a downhole tool; 3) development and application of numerical modeling to estimate far-field (reservoir) stress that is distinct from nearfield stress determined in 1 and 2.

Activities: Lab experiments; data analysis; measurements of stress in up to 10 discrete intervals downhole in well 16B(78)-32 using a subcontracted off the shelf tool. Note, downhole tool deployment requires long open hole interval that may compete with needs to case the deviated leg.

2-2446 Lawrence Livermore National Laboratory: Closing the loop between in situ stress complexity and near-wellbore fracture complexity

Objectives: High-fidelity estimations of in-situ reservoir stress based on minifrac and DFIT tests combined with experimental and modeling results. Laboratory experiments will be used to measure rock properties, and both validate and improve numerical model results. The numerical models will simulate fracture initiation and propagation under various conditions.

Activities: Lab experiments; numerical modeling; Utah FORGE data analysis.

2-2404 University of Oklahoma: Application of Advanced Techniques for Determination of Reservoir-Scale Stress State

Objectives: Develop a technology for determination of the in-situ stress state in the reservoir at Utah FORGE via application and integration of alternative wellbore methods and a reservoir-scale methods in conjunction with DFIT and flowback data. Improve estimates of the near-wellbore and the reservoir-scale in-situ stress tensor. The methods include anelastic strain recovery (ASR), fracture mechanics analysis of drilling induced cracks, novel interpretation of induced seismicity focal mechanisms.

Activities: Lab experiments; data analysis; deployment of ASR tool on surface and acquisition of newly recovered drill core to determine transient changes in in-situ stress.

3-2418 Stanford University: Wellbore fracture imaging using inflow detection measurements

Objectives: Make measurements in the Utah FORGE wells, using a refurbished downhole tool with a specific ion probe that detects Cl, for before and after fracturing experiments, detecting flowing fractures and estimating inflow magnitudes in real time.

Activities: Recondition downhole tool; deploy tool in well 16 after stimulation to detect fracture control inflows.

3-2535 Lawrence Berkeley National Laboratory: Joint electromagnetic/seismic/InSAR imaging of spatial-temporal fracture growth and estimation of physical fracture properties during EGS resource development

Objectives: Estimate spatio-temporal fracture growth and fracture properties during the enhanced geothermal system (EGS) experiment at the Utah FORGE site, using electromagnetic, seismic and InSAR data in a novel joint inversion scheme that includes coupled THMC parameter estimation.

Activities: Recondition VEMP downhole tool; obtain/compile before and after geophysical data (EM, induced seismicity, geodetic-strain); joint inversion modeling of geophysical data.

3-2417 Rice University: Fiber-optic geophysical monitoring of reservoir evolution at UtahFORGE

Objectives: Map conductive fractures that contribute to circulation in an EGS reservoir by development and deployment of a state-of-the-art distributed fiber optic monitoring system, utilizing Distributed Acoustic, Distributed Temperature, and Distributed Stress Sensing.

(DAS/DTS/DSS) combined with periodic hydraulic tests and an array of automated surface seismic sources to constrain multiple phases of fracture evolution induced by stimulation.

Activities: (a) design and install an integrated fiber-optic sensing system for the Utah FORGE site, (b) execute multi-physics field monitoring experiments including the approaches described above (microseismic, time lapse VSP, hydraulic testing), and (c) analyze data and integrate into a THM model.

3-2514 Clemson University: A Strain Sensing Array to Characterize Deformation at Utah FORGE

Objectives: Demonstrate that strains can be measured and interpreted during EGS reservoir stimulations, using strain meter network deployed in shallow boreholes and one deep well.

Activities: Build and deploy strain meters, monitor stimulations, analyze field data.

4-2492 University of Texas-Austin: Design and implementation of innovative stimulation treatments to maximize energy recovery efficiency

Objectives: Use 3-D geomechanical, compositional and coupled reservoir-fracturing simulators to compare three different well completion/stimulation strategies: (i) Plug and perforate (PnP) completion with limited entry uniform or geometric perf design, (ii) Plug and perforate (PnP) with limited entry tapered perf design, and (iii) a single point entry completion with sliding-sleeves. These will be used to: (1) place fractures uniformly in a horizontal well (improve cluster efficiency) to ensure a uniform distribution of flow into the fractures; (2) maximize the surface area of the created fracture network; (3) ensure connectivity of the fractures from the injector to the producer; (4) ensure fracture size is optimized not to exceed well spacing.

Activities: Analyze Utah FORGE field data to design and implement stimulation in well 16B(78)-32, instrument well 16B with fiber optic cable.

4-2541 Fervo: Optimization and validation of a plug-and-perf stimulation treatment design at Utah FORGE

Objectives: Design and run stimulation at Blue Mountain and use results to advise best stimulation design at Utah FORGE

Activities: Plan and implement EGS reservoir stimulation at Blue Mountain.

5-2419 Penn State University: Seismicity-permeability relationships probed via nonlinear acoustic imaging- of fractures in shear.

Objectives: (1) Explore active and passive acoustic signatures of seismic and aseismic evolution of permeability for fractures in shear, (2) Link this to key features of the pre-existing stress state (proximity to failure) as a precursor to, and a key predictor of, moment magnitude of prospective triggered seismicity, and (3) upscale these indexes to reservoir scale as diagnostics

and tools to drive successful reservoir stimulation, production and management. The nonlinear acoustic characterizations of (1) permeability evolution and (2) antecedent stress state for triggered seismicity will be completed in the laboratory and (3) upscaled against field observations using nested micromechanical models.

Activities: Lab experiments; data analysis.

5-2615 University of Oklahoma: Experimental determination and modeling-informed analysis ofthermo-poromechanical response of fractured rock

Objectives: Combine 3D thermo-poromechanical modeling with rock mechanics experimental results to demonstrate the role of thermo-poroelastic effects in reservoir development.

Activities: Lab experiments; data analysis.

5-2565 US Geological Survey: Evolution of permeability and strength recovery of shear fracturesunder hydrothermal conditions

Objectives: 1) An enhanced understanding of the mechanisms controlling fracture property evolution and the conditions at which different processes are active, and 2) improved models for predicting fracture evolution at hydrothermal conditions.

Activities: Lab experiments; data analysis.

5-2428 Lawrence Livermore National Laboratory: Coupled investigation of fracture permeability impact on reservoir stress and seismic slip behavior

Objectives: Develop, apply and validate a holistic thermal, hydrologic, mechanical, and chemical (THMC) workflow that includes evaluation of induced seismic slip in EGS reservoirs. Integrate experimental and modelling approaches to reduce parameter uncertainty and better predict and mitigate seismic hazard.

Activities: Lab experiments; data analysis.

5-2557 Purdue University: Role of fluid and temperature in fracture mechanics and coupled THMC processes for enhanced geothermal systems.

Objectives: Develop and validate a macroscopic model of local deformation/frictional behavior, seismic/aseismic behavior, chemical reactions, and determine the adequacy of classic Coulomb failure vs. rate-and-state friction in response to hydrothermally induced perturbations.

Integrate experimental data and modeling results to: 1) design the reservoir to achieve optimal heat recovery; 2) quantify coupled THMC processes that govern fracture evolution.

Activities: Lab experiments; data analysis.

R&D Management

All projects are carefully monitored using conventional reporting tools, including quarterly and annual reports, and Go/No Go stage gates. Projects within each Topic are managed by Topic Leads (a team comprising one to two Utah FORGE representatives and two DOE-GTO representatives). The R&D Co-Leads (a team of two from Utah FORGE) oversee the Topic Leads, and they report to the Utah FORGE Principal Investigator and the Utah FORGE Business Manager who have executive decision-making authority on behalf of the University of Utah.

As of March 31, 2022, only the first project quarter (October 1-December, 31, 2021) reports had been submitted and evaluated. Health Indicators for 15 out of 17 projects were finalized February, 2022 after consultation with all the Topic and R&D Leads. Two of the projects had not yet commenced as of December 31, 2021 hence they were excluded from the review. All the projects were judged to have a green health indicator in reference to scope, schedule and expenditure, except for one in which a noncompliant report was submitted; after the project Principal Investigator was notified and advised of deficiencies, a satisfactory report was received.

In addition, one Go/No Go Stage Gate was approved for project 4-2541 (Fervo) after a thorough review of submitted documents by the Topic Leads.

For 2022, the Annual meeting is provisionally scheduled for August 15, in advance of which a short annual report will have been submitted along with a slide deck that is to be presented by each Project Principal Investigator. These materials will be peer reviewed by external referees as well as the Topic and R&D Leads to make recommendations to the Utah FORGE Business Manager regarding project continuance, which will be finalized before September 30, 2022. For projects that did not start in October, 2021, separate annual reporting dates will be scheduled.

B.5 OUTREACH & COMMUNICATIONS

Outreach and Communication activities were expanded during Phase 3 Years 2, extendinginto the no-cost extension period. Our efforts realized exponential and measurable success during this period, as illustrated in Table B.5-1.The Outreach and Communication team welcomed the addition of a new intern from the University of Utah College of Architecture and Planning to work on graphics, animations and other images. She replaced the previous intern in this position.

Because of the limitations of face-to-face meetings imposed by COVID 19, the outreach program made extensive use of electronic media, including the Utah FORGE website. Although in-person meetings have increased during, electronic media remained a primary means of communication.

Website

We utilized the website to provide updates about the progress of the Utah FORGE project, while offering resources and information to increase overall geothermal and EGS literacy. This included creating five new web pages (Modeling and Simulation Forum, Solicitation, Sample Curation, Education, Data Dashboard and Seismic Monitoring), and developing seven new web features (Did You Know, Share a Scientific Paper, Partner Spotlight, Lectures/Podcasts, Word of the Week, Animations, Informational Timeline). The education page was redesigned based on feedback from educational experts, and now includes four lesson plans for teachers. Additionally, based on a user survey, a website redesign was begun.

The website has gained considerable traction during the reporting period, with nearly 75,000-page views during Year 2, an increase of nearly more than double from the previous period. The homepage and top viewed pages all realized significant growth.

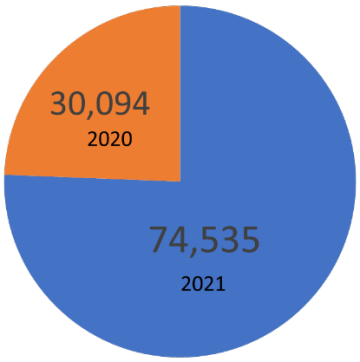

***Figure B.5-1**. All page views 2020 compared to 2021.*

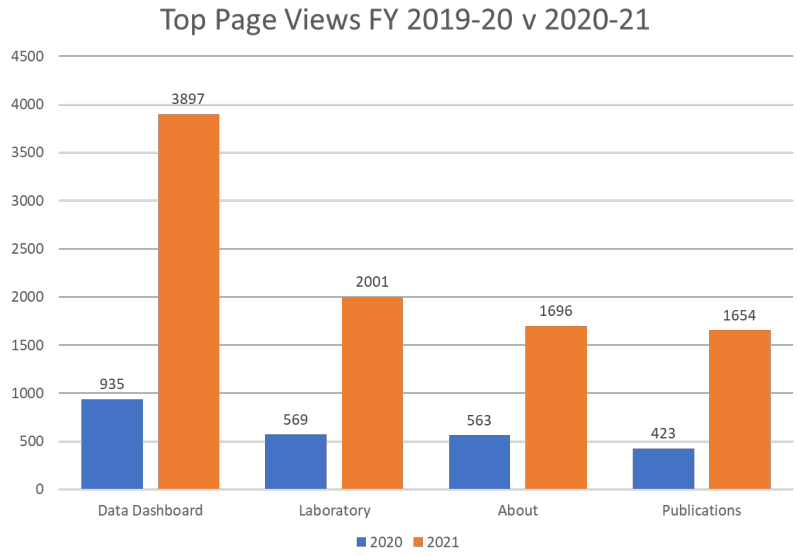

***Figure B.5-2.** Top page views 2020 compared to 2021.*

In only one area did was growth not realized. Not surprisingly, it was with the Solicitation page, which was launched in April 2020 to coincide with the release of the FOA. During first Fiscal Year, there were 8,220 visits to the Solicitation page. During the second Fiscal Yea, a total of 3,707 visits occurred.

Social Media

During the first Fiscal Year, there were 133 social media announcements posted on Utah FORGE's social media platforms: Facebook (60), Twitter (57) and LinkedIn (16), with a total of 384 followers across all three platforms (151 on Facebook, 184 Twitter, 49 LinkedIn). Over the course of Phase 3 Year 2, the number of social media posts nearly quadrupled with 517 posts across the three platforms: Facebook (201), Twitter (207) and LinkedIn (109). The number of followers also increased significantly to 1681 (Facebook 235, Twitter 432, and LinkedIn 1014). Additionally, impressions on LinkedIn grew from 1285 to 114,126.

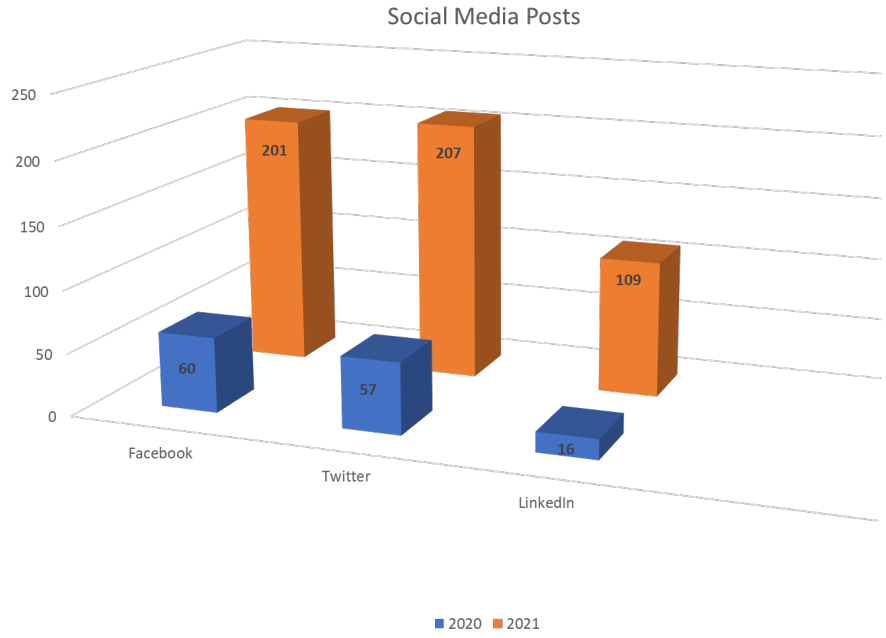

Figure B.5-3. *Growth in Social Media Posts*

E-Mail Distribution Subscribers

The Outreach and Communication team also instituted and cultivated a subscription list during the reporting period. The list is used to email information, announcements and the quarterly e-newsletter "*At the Core*" directly to subscribers. The total number of subscribers grew from 276 in the first year to 533 currently, and the number of emails increased from 27 to 62.

Furthermore, according to Campaign Monitor, successful email marketing campaigns result in open rates of 15-25%; Utah FORGE's open enjoys a lifetime average of 49%.

Media Relations Outreach

Coverage of the Utah FORGE project was highlighted in the general mainstream media and in geothermal and other energy industry outlets. The media kit was updated to include Frequently Asked Questions, information defining the scope and purpose of the project, easily understood background information on EGS, and several images.

During this time, journalists were proactively pitched news and story ideas, resulting in an increase of media stories from 20 to 65 plan year over plan year. Media stories were run in general consumer publications such as *The Deseret News*, two national-level outlets (*Forbes Magazine* and *USA Today*,) and on radio and television. Stories also appeared in *Utah Business Magazine*, *University of Utah Magazine* (the U's alumni magazine),the Beaver County Journal and the Milford City newsletter.

Story topics included the deep deviated well, collaboration between the Utah FORGE project and other areas within the University of Utah, the potential of EGS, and opinion pieces about geothermal energy.

Although it is impossible to calculate how many people were reached through media relations efforts, we can quantify that *USA Today* has a combined print and online circulation of 7 million readers, *Forbes* circulation is over 650,000, KUER (NPR affiliate in Utah) enjoys a listenership of over 300,000, and *University of Utah Magazine* has a circulation of approximately 560,000.

Scientific Outreach

Research findings were presented at scientific conferences throughout the reporting period. Over 60 posters and papers were presented at a variety of conferences, seminars, and webinars. Two E-posters, and a short video were submitted to the Geothermal Resources Council meeting. Four manuscripts were also submitted to journals for publication. A virtual presentation was made in the American Rock Mechanics Association (ARMA) Endless Summer Series. Dr. Joseph Moore participated in the ICDP workshop held at Cornell University. Other presentations were made atthe Utah Seismic Commission, the Geothermal Rising Annual Meeting and Expo, the Stanford Geothermal Workshop, the Annual Meeting of the Seismological Society of America, ARMA's 55th US Rock Mechanics / Geomechanics Symposium, the Unconventional Resources Technology Conference (URTeC), IRIS webinar series, the Geothermal-DHC webinar series, the Society of Economic Geologists McGill Student Chapter Lecture Series, the Annual Meeting of Seismological Society of America, the MIT Earth Resource Library's Friday Information Seminar Hour, PIVOT 2021, the American Association of Petroleum Geologists (AAPG) Annual Conference and Exposition, the World Geothermal Congress, E3 Student Conference, AIChE, and the American Geophysical Union (AGU) Fall Meeting.

Field Trips

COVID-19 continued to limit field trips to the project site during the reporting period. However, Utah FORGE personnel were able to conduct six field trips for 30 individuals. Among those attending the field trips were the Lt. Governor of Utah; the Energy Advisor to Utah Governor Spencer Cox; the Executive Director of the Public Lands Policy Coordinating Office; the

Executive Director of the Department of Natural Resources; Beaver County Commissioners; Milford City Councilmembers; the Director of Beaver County Emergency Services; and the Chief of Staff to the Lt. Governor. Former *The New York Times* science writer, Justin Gillis, who is currently working on a book about the climate crisis visited the site. Additionally, 16 students plus three instructors participating in the National Science Foundation-funded Research Experience for Undergraduates (REU) / Research Experience in Utah for Sustainable Materials Engineering (ReUSE) at the University of Utah's Materials Science and Engineering Department toured the site. The students were from a variety of universities such as Carnegie Melon, University of California Berkeley, Wellesley, and University of California Los Angeles.

Webinars, Videos and Podcasts

Webinars and videos continued to be an important communication tool for the Utah FORGE Outreach and Communication team. During the reporting period, a total of eleven webinars were produced, recorded and promoted, including a webinar intended for grade school students. The webinars have had over 9,000 combined views.

Two podcasts in the initial series *FORGEing Ahead with Geothermal Energy* were written, recorded and released. The last of these podcasts featured Beaver County Commission Chair Mark Whitney. The podcasts were listened to over 250 times, with the entire three podcast series heard more than 400 times.

A short video was submitted to the Geothermal Resources Council meeting, and Seequent released a video showcasing Leapfrog's modeling capabilities featuring the Utah FORGE project. Additionally, Utah FORGE produced four videos and four shorter videos. These videos were viewed over 4,200 times.

Please refer to table B.5-1 for a full list.

Modeling and Simulation Forums

A total of thirteen Modeling and Simulation Forums were hosted.

Tools for Visualizing Data

Tools for visualizing Utah FORGE data have been developed and updated. A tool to examine Utah FORGE Stimulation Data is posted on the dedicated Utah FORGE Geothermal Data Repository archive page hosted by NREL. The interactive geologic map based in ArcGIS was updated with new features. Additionally, the Utah FORGE map was upgraded to include information on the individual stations.

Brochures and Printed Materials

The Utah FORGE Frequently Asked Questions (FAQ) sheets and an overview brochure were revised and updated. Kiosk panels describing geothermal energy and Utah FORGE were installed on Antelope Point Road near the Utah FORGE site.

With the addition of two interns from the University of Utah College of Fine Arts and the Department of Communication, the media kit was updated and posted on the website. A poster

about the project was also created and placed in a display case in Caboose Park in Milford, Utah. Three new banner posters for use at conferences and other events where Utah FORGE has a booth presence were also created.

Surveys

Two surveys were created and distributed by Utah FORGE. The first was to obtain website user feedback and input. Based on respondents' comments, the education page and the outreach page of the website were updated to allow for easier access to information. The second survey gained insights from newsletter readers. In response, highlighted scientific papers and information about upcoming Utah FORGE activities were added to the quarterly newsletter.

A survey focused on the general public's understanding of geothermal energy and EGS was also conducted in cooperation with the University of Utah Department of Communication. The survey is discussed below.

Outreach to Elected and Other Officials

Elected officials and regulators were briefed about Utah FORGE through testimony presented by Dr. Joseph Moore to the U.S. House of Representatives Science, Space and Technology Committee. Meetings with County and City officials, presentations to U.S. Congress members and their support staffs, individual Utah state legislators, the Utah Legislature's Natural Resources, Agriculture and Environment Interim Committee, members of the American Legislative Exchange Council (ALEC), Utah Lt. Governor Deidre Henderson, and the President of the Utah state Senate were also held. Well over 100 stakeholders have participated in virtual and face-to-face meetings during the reporting period, including U.S. Congressmen Chris Stewart, Dan Newhouse, and Markwayne Mulling.

K-12 Education

Prior to COVID-19 restrictions, STEM modules were presented and shared at ten events, including scheduled school visits, open houses, and STEM events. A prototype of a new STEM module showing how convection works using a thermochromatic display was developed. A team of undergraduate students from the University of Utah's Department of Chemical Engineering achieved an outstanding result at the November 2019 National American Institute of Chemical Engineers (AIChE) Competition, proudly taking 2nd place in the K-12 STEM Outreach Competition for a Peltier engine module. In order to develop a program of K-12 education, an undergraduate intern a from the University of Utah College of Education began to draft a high school lesson plan on geothermal energy and other renewables.

This initial work was expanded on by Tamara Young, a Ph.D. candidate in the same program. Four lesson plans were developed: "*Exploring Different Renewable Resources Across the U.S.*", "*Design, Build, and Refine a Device that Works without Given Constraints to Convert One Form of Energy to Another Form of Energy*", "*Plan and Conduct an Investigation to Provide Evidence that the Transfer of Thermal Energy When Two Components of Different Temperature are Combined within a Closed System Results in a More Uniform Energy Distribution Among the Components in the System (Second Law of Thermodynamics)*", and *"Design a Method to Change*

the Rate of Heat Transfer Accommodations". To ensure equal access for students of different learning abilities, Special Education (SPED) requirements were also incorporated into the lesson plans. Teachers can download the plans from the Utah FORGE website's education section. Moreover, our graphics intern designed a cohesive package for the lesson plans that will be proactively provided to science teacher leads across the state.

Limited student activities continued throughout the pandemic. Indeed, STEM Fest 2020 was held virtually, however information about Utah FORGE was included on the STEM Fest website for students to access. With the limitations on in-person meetings, attention turned to teachers. Tamara Young attended the "30 Demos in 60 Minutes" session at the American Association of Physics Teachers (AAPT) Summer Meeting and demonstrated a module created by Dr. Tony Butterfield and his students from the University of Utah Department of Chemical Engineering to some 60 teachers from around the country.

Also, an advanced undergraduate level capstone class in the Department of Communications, University of Utah, with 15 students, was initiated in the fall 2020 semester under the instruction of Professor Sara K. Yeo, to develop public survey data of lay opinion, awareness, and knowledge of geothermal energy. The survey was distributed through a third-party surveying software (Qualtrics). It consisted of a sample size of over 1,000 respondents in 10 western states. Dr. Yeo was joined by Dr. Meaghan McKasy of the Utah Valley University Department of Communication in analyzing the data.

As pandemic restrictions slowly eased, more in-person activities became possible. Through a partnership with Enel, a pilot geothermal song parody contest was launched in Mr. Zac Taylor's 7^{th}-9^{th} grade science class at Milford High School. Students were tasked with creating lyrics using pre-determined geothermal terms, sung to an existing song tune. As part of the program, Utah FORGE Communication and Outreach team members presented information about the project to the students during a field trip to the Cove Fort geothermal plant. The trip was attended by 37 students and 4 adults.

Community Relations

Throughout the reporting period, Utah FORGE engaged business groups and the community at large. Dr. Joseph Moore presented at the Energy Technology and Innovation Outlook breakout session during the Governor's Economic and Energy Summit. He also presented information about Utah FORGE, geothermal energy, and Enhanced Geothermal Systems to representatives from the Vernal (Utah) Chamber of Commerce and Uintah County Economic Development.

Members of the Outreach and Communication team also apprised the Director of Environmental and Public Affairs at Smithfield Foods of upcoming activities.

Moreover, Dr. Joseph Moore provided an overview of geothermal energy and the Utah FORGE project to members of the Citizens' Climate Lobby – Utah Valley Chapter. Additionally, members of the Utah FORGE Outreach and Communication team staffed a booth during the annual Beaver County Fair in Minersville, Utah, providing information, answering questions, listening to concerns and comments, and interacting with the fair attendees. Overall, about 350 people visited the booth. Finally, to ensure the residents of Beaver County have access to

information about the project and seismicity, computers were delivered and installed in the Beaver City and Minersville libraries. The computers allow users to monitory real-time seismicity and visit Utah FORGE's seismic webpage, which includes resources about seismic activity.

Milestones

Eleven milestones were achieved during the reporting period, four lesson plans written and published; three university-level lectures / technical webinars on geothermal resources; the development and distribution of a geothermal literacy survey; the development and distribution of a newsletter reader survey; the recording and production of a general geothermal webinar intended for grade school students; an analysis and summary of the newsletter survey; the appointment of an undergraduate student from the College of Fine Arts (University of Utah); and the developmentof a virtual site tour.

Table B.5-1: *Full list of communication products with links*

Full Videos	6	1. Forging New Geothermal Technologies Part One; 2. FORGE: Exploring Utah's Potential for Enhanced Geothermal Systems Part Two; 3. Unearthing the Utah FORGE Site's Data; 4. FORGEing into the Future; 5. Energy Success Stories Discovering; 6. Drilling into the Geothermal Future
Short Videos / Video Clips	4	1. Short Visit to the Utah FORGE Area; 2. Flyover Infrastructure at the Utah FORGE Site; 3. Utah FORGE gearing Up to Drill a Seismic Monitoring Well; 4. Utah FORGE Drill Site Overview – Well 16A(78)-32
Modeling and Simulation Forum	15	Modeling and Simulation Forum Page
Webinars	11	1. Informational Webinar – Utah FORGE Solicitations 2020-1 2. Utah FORGE Geoscientific Overview 3. Geothermal Energy in the 21st Century: Conventional Resources 4. Updated: Geothermal Energy in the 21st Century: Unconventional EGS Resources 5. Status of Utah FORGE Operations and Future Plans 6. Geothermal Energy and the Heath Beneath Our Feet 7. Update to the Utah FORGE Geoscientific Overview 8. Virtual Geological Tour of the Utah FORGE Area 9. Utah FORGE Orientation Webinar for R&D Performers 10. Utah FORGE R&D Orientation Webinar and Q&A Session One 11. Utah FORGE R&D Orientation Webinar and Q&A Session Two
Animations	3	1. Making of an Enhanced Geothermal Reservoir 2. Geothermal Flash Plant 3. Geothermal Binary Cycle Plant
Podcasts	32	1. What is an Enhanced Geothermal System? 2. Interview with Beaver County Commissioner Mark Whitney
Lesson Plans	4	1. Exploring Different Renewable Resources Across the U.S. (Student Handouts)

		2. Building a Device that Converts Energy from One Form of Energy to Another to Solve a Problem (Student Handouts) 3. Plan and Conduct an Investigation to Provide Evidence that the Transfer of Thermal Energy When Two Components of Different Temperature are Combined within a Closed System Results in a More Uniform Energy Distribution Among the Components in the System (Second Law of Thermodynamics) (Student Handouts) 4. Design a Method to Change the Rate of Heat Transfer Accommodations (Student Handouts)
Media	65	1. Oct. 20, 2020, *The Salt Lake Tribune*, Geothermal could help make Utah's 2. climate compact a reality 2. Oct. 21, 2020, Vox, Geothermal energy is poised for a big breakout 3. Oct. 30, 2020, *The Deseret News*, Why there's global significance at a geothermal project in Beaver County 4. Oct. 30, 2020, *The Deseret News*, Why there's global significance at a geothermal project in Beaver County 5. Nov. 2, 2020, *Drilling Contractor*, Utah FORGE begins drilling of highly deviated geothermal well 6. Nov. 3, 2020, *GeoDrilling International*, Utah FORGE drills first of two deep wells 7. Nov. 18, 2020, *Beaver County Journal*, Utah FORGE Drills First of Two Deep Wells 8. Nov. 27, 2020, *St. George News*, Forging the path for renewable energy in Utah: Drilling begins on geothermal well near Milford 9. Dec. 11, 2020, *Forbes Magazine*, Does Geothermal Energy Have a Future Under the Biden Administration? 10. Dec. 13, 2020, Think GeoEnergy, As part of wider clean energy efforts, geothermal has important role to play for U.S. 11. Jan. 7, 2021, @TheU, FORGEing a new partnership 12. Jan. 30, 2021, Think GeoEnergy, With first well drilled, what are the next steps for the Utah FORGE project? 13. Feb. 2, 2021, *Think GeoEnergy*, With first well drilled, what are the next steps for the Utah FORGE project? 14. Feb. 3, 2021, *Renewable Energy Magazine*, Utah FORGE successfully completes drilling of first deviated deep well 15. Feb. 3, 2021, *Beaver County Journal*, Utah FORGE Completes First Well 16. Feb. 3, 2021, *Journal of Petroleum Technology*, Utah FORGE Drills First Deviated Deep Well 17. Feb 8, 2021, *GeoDrilling International*, Utah FORGE completes drilling of first deviated deep well 18. Feb. 24, 2021, *Mirage News*, Utah FORGE Chooses 17 project selectees to begin negotiations 19. Feb. 24, 2021 @TheU, Utah FORGE Chooses 17 project selectees to begin negotiations 20. Feb. 24, 2021, *Think GeoEnergy*, Utah FORGE selects 17 groups for up to $46m in DOE funding. 21. Feb. 24, 2021, *Power Magazine*, DOE Awards $46 Million for Geothermal Projects 22. Feb. 24, 2021, Science News Net, Utah FORGE Chooses 17 Selectees to Begin Negotiations 23. Feb. 24, 2021, 15 Minute News, Utah FORGE chooses 17 selectees to begin negotiations

		24. Feb. 25, 2021, CleanTechnica, U.S. Department Of Energy Awards $46 Million For Geothermal Initiative Projects With Potential To Power Millions Of U.S. Homes 25. Feb. 25, 2021, Rigzone, DOE Awarding up to $46MM for Geothermal Projects 26. Feb. 26, 2021, *Daily Energy Insider*, Department of Energy awards $46M to 17 domestic geothermal initiative projects 27. Feb. 26, 2021, *Energy Live News*, Geothermal energy projects in the US receive $46m boost. 28. March 2, 2021, *Think GeoEnergy,* Utah FORGE selects 17 groups for up to $46m in DOE funding 29. March 2, 2021, Silixa News, Silixa LLC's joint proposal for Fiber-Optic Geophysical Monitoring of Reservoir Evolution at the FORGE Milford Site, led by Rice University, selected to enter final negotiations for award by the FORGE Utah team 30. April 2021, AAPG *The Explorer*, Utah FORGE Applies Unconventional Resource Methods for Geothermal Research 31. April 17, 2021, SLTrib.com, Shanelle Loren: It is time to unleash the potential of geothermal energy 32. April 29, 2021, AAPG *The Explorer*, Explorer Live 33. May 3, 2021, *Power Magazine*, Groundswell of Support Heats Geothermal Innovation 34. Summer 2021 *U Magazine*, Heat Beneath Our Feet 35. June, 5 2021, U Magazine e-newsletter, Heat Beneath Our Feet 36. June 30, 2021, *The Beaver County Journal*, Utah FORGE Update 37. July, 1, 2021, *The Journal of Petroleum Technology*, Utah FORGE Spuds New EGS Well 38. July 6, 2021, KUER, Project in Rural Utah Aims to Tap into the 'Inexhaustible' Geothermal Energy Below Our Fee 39. July 11, 2021, Associated Press, Project in Rural Utah aims to tap into geothermal energy 40. July 12, 2021, *USA Today*, News From Around Our 50 States: Utah 41. July 15, 2021, ABC4, Project in Rural Utah aims to tap into geothermal energy 42. August 18, 2021, *Drilling Contractor*, Physics-based approach improves drilling of FORGE geothermal well by identifying mitigating limiters 43. August 23, 2021, *Think GeoEnergy*, Drilling deep at Utah FORGE project requires developing the right tools for the job, such as strong drill bits 44. September 13, 2021, *Survey Notes*, Energy News: Geothermal in Utah and he USA: Is a Sleeping Energy Giant Awakening 45. September 23, 2021, *The Salt Lake Tribune* Online, Opinion – Joseph Moore: Time for Utah to tap the energy that lies beneath our feet" 46. September 24, 2021, Public News Service, Geothermal Has a Role in Utah's Clean-Energy Plan 47. Oct. 18, 2021, *Think GeoEnergy* – Video, Utah FORGE reports success on drilling of first deep deviated well 48. Oct. 27, 2021, T*he Deseret News*, Opinion: Utah Lawmakers should focus on boosting clean energy 49. Nov. 1, 2021, *AAPG The Explorer*, Casting Sunlight on the Deep Heat Sources with Magnetotelluric Geophysical Imaging 50. Nov. 19, 2021, *Utah Business*, Milford, Utah could become the world's next geothermal hub 51. Nov. 23, 2021, *The Beaver County Journal*, Commission Conner

		52. Nov. 24, 2021, *Ramblers*, Did You Know? Some Neat Facts About Ramblers / Green Energy 53. Dec. 29, 2021, *The Beaver County Journal*, County Commission Gets Updates on FORGE Project CAFO Map 54. Dec. 30, 2021, *Daily Energy Insider*, Energy & Geoscience Institute Partners with NETL in Pursuit of Enhanced Geothermal Systems 55. Dec. 31, 2021, *Opera News*, Energy & Geoscience Institute Partners with NETL in Pursuit of Enhanced Geothermal Systems 56. Jan. 24, 2022, *GeoDrilling International*¸ NETL project partner to advance new enhanced geothermal system technologies 57. Jan. 26, 2022, MarketScreener, Zero-emission energy: Not all wind and solar 58. Feb. 23, 2022 KSL, University of Utah strikes advanced research agreement with Idaho National Laboratory 59. Feb. 24, 2022, *The University of Utah Engineering News*, U of U/ INL Announce Research Partnership 60. Mar. 21, 2022, *The Daily Utah Chronicle*, Utah FORGE Continues Groundbreaking Research 61. March 25, 2022, PBS Newshour, Is Geothermal Energy a Viable Alternative to Fossil Fuels 62. March 30, 2022, *The Beaver County Journal,* Commission Corner

Table B.5-2: *List of presentations and lectures*

Presentations and Lectures			
Oct. 2, 2020	Graduate Seminar at the University of Pittsburgh	Dr. John McLennan and Dr. Pengju Xing	Closure stress diagnosis at the FORGE site
Oct. 21, 2020	Geothermal Rising Annual Meeting and Expo	Dr. Pengju Xing	Interpretation of In-Situ Stresses at the Utah FORGE Site using Pressure and Temperature Signatures
Oct. 21, 2020	Geothermal Rising Annual Meeting and Expo	Dr. Joseph Moore	The Utah Frontier Observatory for Research in Geothermal Energy (FORGE): A Laboratory for Characterizing, Creating and Sustaining Enhanced Geothermal Systems
Oct. 29, 2020	Utah Seismic Safety Commission meeting	Dr. Kristine Pankow	Discussion about Monitoring for Potential Induced Seismicity from the Utah Frontier Observatory for Research in Geothermal Energy (FORGE) Project
Nov. 4, 2020	ARMA-DGS-SEG International Geomechanics Symposium	Dr. John McLennan	Drilling, Reservoir Characterization, and Fracturing at the Utah FORGE Site
Nov. 12, 2020	CouFrac 2020	Dr. John McLennan	Historical Perspective, *Upcoming* Activities, Modeling and Simulation at Utah FORGE
Nov. 25-27, 2020	NZ Geothermal Workshop	Dr. Stuart Simmons	Overview of the Geoscientific Understanding of the EGS Utah FORGE Site, Utah, USA
Jan. 28,	IRIS webinar on the Best	Dr. Kristine Pankow	A short presentation on the Utah

2021	Practices for Seismic Posthole Emplacement		FORGE postholes
Feb. 3, 2021	Texas A&M Participants	Dr. John McLennan, Duane Winkler and Leroy Swearingen	An interactive virtual presentation on FORGE Well 16A(78)-32:EOWR and Lessons Learned
Feb 16, 2021,	Stanford Geothermal Workshop	Dr. Pengju Xing, et al	Numerical Simulation of Injection Tests at Utah FORGE Site
Mar. 4, 2022	Utah Science Teachers' Association	Tamara Young	Presentation on energy transfer
Mar. 22, 2021	Geothermal-DHC Webinar	Dr. Joseph Moore	The Utah Frontier Observatory for Research in Geothermal Energy (FORGE) – an International Laboratory for EGS Research
Mar. 31, 2021	Society of Economic Geologists (SEG) McGill Student Chapter Lecture Series	Dr. Stuart Simmons	Geothermal Resources in the 21st Century
Apr. 14, 2021	SPE Hydraulic Fracturing Community's Technical Section	Dr. John McLennan	Advancements in the Geothermal Industry Attributed to Oilfield Technologies
Apr. 14, 2021	Duke University's Civil & Environmental Engineering	Dr. Robert Podgorney	The Frontier Observatory for Research in Geothermal Energy, a Field Laboratory for Demonstrating, Testing, and Validating Enhanced Geothermal Systems
Apr. 15, 2021	The Sustainable Energy Class as part of Penn State University's Cameo Lecture Series	Dr. Joseph Moore	EGS and the Utah Frontier Observatory for Geothermal Research (FORGE)
Apr. 21, 2021	Annual Meeting of Seismological Society of America	Dr. Hao Zhang	High-Resolution Bayesian Spatial Auto-Correlation (Spac) Pseudo-3D vs Model of Utah Forge Site with a Dense Geophone Array
Apr. 29, 2021	EGU General Assembly	Dr. Maria Mesimeri	Episodic earthquake swarms in the Mineral Mountains, Utah driven by the Roosevelt hydrothermal system
June 23, 2021	ARMA's 55th US Rock Mechanics/Geomechanics Symposium	Dr. Pengju Xing	Numerical Simulation of Hydraulic Fracturing Simulations of the Enhanced Geothermal System Well at the Utah FORGE Site
June 25, 2021	ARMA's 55th US Rock Mechanics/Geomechanics Symposium	Dr. Aleta Finnela	Estimation of Fracture Size for a Discrete Fracture Network Model of the Utah FORGE Geothermal Reservoir Using Forward Modeling of Fracture-Borehole Intersections.
July 16, 2021	MIT Earth Resource Library's Friday Informal Seminar Hour (FISH)	Dr. Joseph Moore	Utah Frontier Observatory for Research in Geothermal Energy (FORGE)
July 20, 2021	PIVOT 2021	Dr. John McLennan	Forging Ahead: A Deep Dive on the U.S. Department of Energy FORGE Initiative

July 22, 2022	PIVOT 2021	Dr. Kristine Pan	On Solid Ground: Induced Seismicity Forecasting, Prevention and Mitigation
July 27, 2021	The Utah Energy Tour breakout session of the American Legislative Exchange Council (ALEC) Annual Conference	Dr. Ben Barker and Christopher Katis	Overview of Utah FORGE
Aug. 4, 2021	The American Association of Physics Teachers (AAPT) Summer Meeting	Tamara Young	Energy Transformation with Utah FORGE: Keys to Sustainable Energy Solutions
Sept. 15, 2021	Society of Petroleum Engineers, Salt Lake City Section	Dr. Joseph Moore	Creating Enhanced Geothermal System Reservoirs: The Utah Frontier Observatory for Research in Geothermal Energy
Oct. 5, 2021	Geothermal Rising Conference	Dr. Joseph Moore	Current Activities at the Utah Frontier Observatory for Research in Geothermal Energy (FORGE): A Laboratory for Characterizing, Creating and Sustaining Enhanced Geothermal Systems
Oct. 5, 2021	Geothermal Rising Conference	Dr. Pengju Xing	Numerical Investigation of Stimulation of the Injection Well at Utah FORGE site
Oct. 5, 2021	Geothermal Rising Conference	Dr. Pengju Xing	In-Situ Stresses and Permeability Measurements from Testing in Injection Well 16A(78)-32 at Utah FORGE Site
Oct. 5, 2021	Geothermal Rising Conference	James Rutledge	Seismic Monitoring at the Utah FORGE EGS Site
Oct. 5, 2021	Geothermal Rising Conference	Dr. Aleta Finnila	Revisions to the Discrete Fracture Network Model at Utah FORGE site
Oct. 30, 2021	World Geothermal Congress	Dr. Joseph Moore	The Utah Frontier Observatory for Research in Geothermal Energy (FORGE): A Laboratory for Characterizing, Creating and Sustaining Enhanced Geothermal Systems
Nov. 9, 2021	E3 Student Conference	Dr. Joseph Moore	Geothermal Applications for the FORGE Project
Nov. 15	AIChE Great Salt Lake Local Section Meeting and the University of Utah Chemical Engineering Graduate Seminar	Dr. Joseph Moore	Creating Enhanced Geothermal System Reservoirs
Nov. 17	Energy & Geoscience Institute Advisory Board	Dr. Joseph Moore	The Utah Frontier Observatory for Research in Geothermal Energy (FORGE) – a National Laboratory for EGS Research
Dec. 14, 2021	American Geophysical Union (AGU) Fall Meeting	Dr. Joseph Moore	Applications of Geophysics to Enhanced Geothermal System Development: The Utah FORGE Experience
Jan. 10,	Utah Geological Association	Dr. Joseph Moore	An Overview of the Utah FORGE

2022			Project
Jan. 26, 2022	International Union of Geological Science (IUGS) Energy Transition Series	Dr. Joseph Moore	An Overview of the Utah FORGE Project
Feb. 7-9, 2022	Stanford Geothermal Workshop	Alex Dzubay	Developing a Comprehensive Seismic Catalog Using a Matched Filter Detector During a 2019 Stimulation at Utah FORGE
Feb. 7-9, 2022	Stanford Geothermal Workshop	Dr. Sang Lee and Dr. Ahmad Ghassemi	Numerical Stimulation of Fluid Circulation in Hydraulically Fractured Utah FORGE Wells
Feb. 7-9, 2022	Stanford Geothermal Workshop	Dr. Abraham Samuel	Improvement in Rate of Penetration in FORGE Drilling Through Real Time MSE Analysis and Improved PDC Technology
Mar. 20, 2022	University of Montana Spring Break Trip	Dr. Joseph Moore	An Overview of the Utah FORGE Project

Table B.5-3: *List of publications.*

1.	*Developing a comprehensive seismic catalog using a matched-filter detector during a 2019 stimulation at Utah FORGE*, Alex Dzubay, Maria Mesimeri, Katherine M. Whidden, Daniel Wells, Kris Pankow, Stanford Geothermal Conference. *Link*
2.	*Numerical Simulation of Fluid Circulation in Hydraulically Fractured Utah FORGE Wells,* Sang H. Lee, Ahmad Ghassemi, Stanford Geothermal Conference. *Link*
3.	*In-situ Stresses and Fractures Inferred from Image Logs at Utah FORGE*, Pengju Xing, Andy Wray, Edgar Ignacio Velez Artega, Aleta Finnila, Joseph Moore, Clay Jones, Erik Borchardt, John McLennan, Stanford Geothermal Conference. *Link*
4.	*Episodic earthquake swarms in the Mineral Mountains, Utah driven by the Roosevelt hydrothermal system*, Mesimeri, M., K. L. Pankow, B. Baker, and J. M. Hale (2021b) in *J. Geophys. Res.: Solid Earth*, 126, e2021JB021659. *Link*
5.	*A frequency-domain-based algorithm for detecting microseismicity using dense surface seismic arrays*, Mesimeri, M., K. Pankow, and J. Rutledge (2021c) in *Bull. Seism. Soc. Am.*, *Link*
6.	*Unusual seismic signals in the Sevier Desert, Utah possibly related to the Black Rock volcanic field*, Mesimeri, M., K. L. Pankow, W. D. Barnhart, K. M. Whidden, and J. M. Hale (2021d) in *Geophys. Res. Lett*, *Link*
7.	*Minimum in-situ stress measurement using temperature signatures, Geothermics*, 98, Xing, Pengju, Joseph Moore, J. McLennan.
8.	*In-Situ Stresses and Permeability Measurements from Testings in Injection Well 16A(78)-32 at Utah FORGE Site*, Geothermal Rising Conference, Xing, P., D. Winkler, L. Swearingen, J. Moore, J. McLennan.
9.	*Numerical Investigation of Stimulation from the Injection Well at Utah FORGE Site*, Geothermal Rising Conference, Xing, P., B. Damjanac, Z. Radakovic-Guzina, A. Finnila, R. Podgorney, J. Moore, J. McLennan.
10.	*In-Situ Stress Measurements at the Utah Frontier Observatory for Research in Geothermal Energy (FORGE) Site, Energies.*

C. LESSONS LEARNED

DRILLING

The following is taken verbatim from Sugiura et al. (2021), and it summarizes the lessonslearned from drilling the 16A(78)32 injection well from 4,552 ft to10,955 ft MD.

- Mud coolers allow the bottom hole assembly (BHA) temperatures to remain below 230°F (110°C) at the toe of the well, where the granite formation temperature at thetoe is expected to exceed 442°F (228°C).
- The BHA cooling enabled standard oil and gas drilling tools to be used toeconomically drill a geothermal well.
- Standard oil and gas drilling optimization techniques, such as drilling parameter roadmapping, real-time surface mechanical specific energy (MSE) surveillance, drill-bit forensics, bit/BHA design changes, etc. can be applied to incrementally improve rateof penetrations (ROP) and footage for subsequent runs.

Drilling the Vertical Section of the Well

- Motor-assist mechanical vertical drilling tools were used to keep the wellinclinations below 2°.
- PDC drill bits are viable in hard-rock applications.
- 13-mm cutters worked better in granite than 16-mm cutters.
- V-shaped, shearing cutters worked best (rather than ridged diamond cutters orconical shaped cutters).

Drilling the Curved Section of the Well

- Torque-control (depth of cut-DOC-limiter) elements were not needed past 43° ofinclination (after BHA 22) to build angle to landing point.
- 0.24 rev/gal motor (curve & lateral) outperformed 0.15 rev/gal motor (vertical)
- Bent-housing motor (0.24 rev/gal) assemblies outperformed motor-assist (0.15rev/gal) vertical-drilling tool

Drilling the Tangent Section of the Well

- Friction reduction tools in a long tangent section improve the weight transfer, ROPand tool face control
- Double-stabilized steerable motors were used to improve the neutral BHA tendency.
- Torque-control (DOC limiter) elements are not needed to mitigate cutting structuredamage.
- Higher back rakes and increased chamfer lengths (BHA 39) improved

durabilitywithout loss of ROP.

The following is excerpted and paraphrased from Dupriest and Noynaert, 2022, based on theexperience of drilling 16A(78)32, 56-32 and 78B-32.

Surface Hole

- ROP can be very rapid. Cuttings transport and handling can be difficult. Possiblesolutions are viscosification of mud and/or putting cuttings directly in the sump.

Intermediate Hole in the Alluvium

- Find higher speed motors capable of 15,000 to 18,000 ft-lbf or a vertical RSS BHAcould be designed for higher weight transfer, higher WOB, and enable 165 rpm.
- Implement standard practices for zeroing motor differential
- Ensure motor torque factor (ft-lbf/psi) and motor speed factor (rev/gal) in the EDRare changed with each motor run.

Intermediate Hole in the Granite

- Test using a high spurt mud with 100 bbl of water -this led to increased penetrationin well 78B-32. Lost circulation is not a concern in these wells. There may be some sensitivity in the alluvium farther up hole and this should be confirmed by testing.
- Redesign or select a vertical steering system with a lower intrinsic whirl.
- Re-evaluate the required amount of penetration into granite for casing point - proposed is about 400 ft. The intermediate string has conventionally been set about600 ft below the transitional granite contact. There is inferred to be more complicated lithology and some fracturing above this. However, reducing the distance should be considered.
- Consider a stabilized 1° bent motor
- Specify a higher speed motor (around 0.242 rev/gal), still capable of 13-15k ft-lbftorque.

Production Hole in the Granite

- Use high spurt loss mud or water. Before drilling, determine the effectiveness of centrifuges versus dilution in removing submicron fines and maintaining a high 5-second spurt measurement.
- Use baseline MSE to surveillance to determine if brittle comminution is occurring as will be indicated if the MSE is nominally equal to the confined compressive strength.
- Conduct RPM step tests in 10 rpm increments. MSE or lateral downhole

vibrationmeasurement identifies resonant string speeds to avoid. Approach this limit. Thisshould be done after every trip, even if the BHA is not changed.

- Similarly, conduct WOB step tests. Increment the WOB in 5000 lbf increments from a reasonable baseline. Stop increasing when MSE and other data show dysfunction.Do not exceed the bit vendor's structural limit (i.e., 60-75,000 lbf).
- Display the bit torque trace available in the EDR continuously. Note that thisrequires a motor or downhole torque sub).
- Following procedures prescribed by Watson et al., 2022 (SPE 208707) photographically archive and recognize bit damage and its root cause.
- Bit damage should be recognized by monotonic deviations from a downhole MSE baseline. Autopsy all bits and comprehend mitigate damaging events. If there is "nosmoking gun" consider trials on the next bit run to determine and possibly rectify.
- At Utah FORGE collect downhole vibrational data – especially HFTO. Prescribe limitson all vibrations. Shock levels have been high. Vibrations only limited WOB/RPM when drilling with the vertical steering tools.
- Anticipate hole roughness. In scientific wells such as these acquire and visualizeborehole profiles to mitigate reduced weight transfer.
- Implement comprehensive training programs before drilling and frequently assessand diagnose performance during drilling.

References

Sugiura, J., Lopez, R., Borjas, F., Jones, S., McLennan, J., Winkler, D., Stevenson, M., and Self, J., 2021, Oil and gas optimization technologies applied successfully to unconventional geothermalwell drilling. Society of Petroleum Engineers 2021 Annual Technical Conference, 21-23 September, 2021, SPE-205965-MS, 33 p.

Dupriest, F. and Noynaert, S., 2022, Drilling practices and workflows for geothermal operations. IADC/SPE International Drilling Conference and Exhibition, 8-10 March, 2022, SPE-208798-MS, 42 p.

SEISMIC MONITORING

Five specific lessons learned during the 2019 stimulation have helped to inform and prepare for the 2022 stimulation.

1. Geophone strings are more sensitive than DAS for detecting microseismicity. Therewas an order of magnitude more events in the SLB catalog compared to

the Silixa catalog

2. Using matched-filters the 300 m borehole had a detection threshold down to M -1.8 with a magnitude of completeness down to M -0.9 even with the anthropogenic noiselocated at the top of the well during the stimulation
3. Array processing of the Nodal geophones detected events down to M -1.8 using only70 stations located at distances from 500 to 2500 m.
4. Seismicity was continuous during the 2019 stimulation and lasted for at least onemonth following the end of pumping.
5. b-positive provides a more robust estimate of the magnitude frequency relationship ofthe 2019 microseismic events than the more traditional Gutenberg-Richter b-value

OUTREACH AND COMMUNICATIONS

Ensuring public awareness and increasing geothermal literacy within Beaver County and Utah continues to be an essential part of the Utah FORGE Outreach and Communication Program. Despite limited face-to-face contact because of the pandemic, during the reporting period significant and innovative expansion of Utah FORGE Outreach and Communication activities was realized. Additionally, engagement to new and larger groups of stakeholders was implemented.

Both virtual and in-person presentations at scientific conferences around the world, along with publications in conference proceedings and journals keep the scientific community informed. The supporting data are available to everyone on the Geothermal Data Repository.

Expansion of these efforts during this reporting period allowed for several important best practices and lessons to be learned.

1. Outreach and communication activities require a dedicated team of professional communicators. Additionally, the team should grow to include those in different areasof expertise to complement the team. The Utah FORGE team includes a full-time communications specialist and student interns with backgrounds in communications, art/graphics, and K-12 education.
2. E-newsletters, videos, lectures, webinars, podcasts and other electronic media are effective means of providing educational and informational material to the public, particularly during periods when in-person contact is limited. However, they also servean important role in establishing a compendium of information for scientists, educators and other stakeholders to draw on for information.
3. Continual upgrading and improvement of the website (www.utahFORGE.com) is imperative to driving traffic to the site. To accomplish this, the team added and

updated interactive tools and maps, links to technical publications, videos and the Geothermal Data Repository, news on Utah FORGE activities and team members, a new seismic monitoring page, Additionally, in response to comments provided in the previous year's website survey, the education page was improved by separating the resources for teachers and those for student, adding new resources (such as "fun facts" and informational videos for students, and lesson plans for teachers), and initiating a redesign of the page for easier navigation.

4. Creating new and innovative engagement vehicles fosters community participation and helps to guide messaging. For example, a webinar intended for grade school students, and a pilot geothermal parody song contest for middle schoolers were developed. Additionally, user surveys allowed for direct feedback from visitors to thewebsite and readers of the quarterly newsletter. Local stakeholder understanding and familiarity of the Utah FORGE project has increased due to increased engagement with county, city andstate representatives. Moreover, attendance at the County Fair and other events affords stakeholders the opportunity to ask questions and present any concerns they have directly to representatives from the project, facilitating open dialogue. This support is reflected in comments made at public meetings and interactions in table C-1.

***Table C-1**. Comments received from elected officials and public*

Comments made from elected officials and the public between October 1, 2021 and March 31, 2022.	
	– "Thank you for your continued commitment to keeping the money being spent staying here in the community with local businesses," Commission Chair Mark Whitney.
	– "This is exciting. It just keeps getting more exciting," Commission Chair Mark Whitney.
	– "The potential extension to 2030 is exciting," Commissioner Tammy Pearson.
	– "In regard to the infrastructure bill, we're working on trying to get transmission lines to serve Utah. Most of the clean energy that's produced here goes out of state. We want to serve Utah, especially with Salt Lake County and other counties wanting their energy to come from renewable sources by 2030. We're working to get a transmission line headed North out of the Milford Valley to the rest of the state," Commission Chair Mark Whitney.
	– "Our new Utah state Representative, Carl Albrecht, is sponsoring legislation to help secure the power grid so Utah doesn't experience an event like occurred in Texas," Commissioner Tammy Pearson. o Dr. Moore added that the road maintenance agreement with Beaver County has been signed and provided a brief timeline of payment schedules.
	Dr. Moore added that the road maintenance agreement with Beaver County has been signed and provided a brief timeline of payment schedules.
	– "Thanks for the presentation, we always appreciate the updates," Commissioner Wade Hollingshead.
	– "I wanted to add that Utah FORGE had a really fun booth at the fair. The kids loved it!" Commission Secretary Stephanie Laws.
	– "We really appreciate the updates; thanks for coming," Mayor Nolan Davis.

	– "We also appreciate that you keep Robert Pyles (Beaver County Administrator and Economic Development Director) up-to-date; we meet with him monthly, and he also provides updates to us about what you're doing," Mayor Nolan Davis.
	– "The lesson plans are really working well and are well written." Zac Taylor
	– "The kids are really excited about the contest." Zac Taylor
	– "I'm really looking forward to having speakers in the class and to the field trip." Zac Taylor
	– "I have a smaller class of high schoolers; I'd like to take them to the site during stimulation if possible." Zac Taylor
	– "This is exciting. I can't wait to see the rig," Commission Chair Mark Whitney.
	– "I've always said that this project would put Beaver County on the map," Commission Chair Mark Whitney.
	– "Thank you for going above and beyond in your outreach and engagement to the community. Not just with the quarterly meetings here but getting out and engaging with the community at large," Commissioner Tammy Pearson.
	– "We appreciate everything you've done and the updates; and we really appreciate you getting the younger generation involved and giving them an idea of what's going on. We appreciate that a lot," Mayor Nolan Davis.
The following comments were made by visitors to the Utah FORGE booth at the Beaver County Fair in August 2021:	
	– I follow Utah FORGE on my Facebook page.
	– I read about the project in the newspaper.
	– This is fascinating. (Made by a child)
	– This is really interesting.
	– This is so cool. (Made by a child)
	– I think this is neat. (Made by a child)
	– I follow you guys in the newspaper.
	– Good luck!
	– I hope you're successful.
	– Very interesting.
	– Thank you so much for coming, we really appreciate you being here.

5. Discussing a visitor center with local stakeholders, revealed no support for a conventional physical building, so virtual options needed to be explored. Understanding the scope of the planned visitor center helped manage potential vendor expectations, allowing them to better determine possible budgets and plans. Postponed during the no-cost extension, further refinement of the scope for the

virtual visitor center was completed in the Phase 3B year 1, with requests for a proposal and cost estimates sought from three vendors.

6. Favorable viewer comments and growing audiences suggest regular social media postings are having positive results, while increasing public awareness of geothermal energy. Additionally, resharing and/or commenting on others' relevant posts increasesUtah FORGE's exposure. Finally, limiting the frequency of posts to avoid oversaturation prevents loss of followers.

7. Collaboration with other departments within the University of Utah, Beaver County, and others in the geothermal industry community opens new avenues for engagement. This cooperation led to a poster in a display case in a local park, industry and general interest interviews and articles in the media and the Utah FORGE e-newsletter *At the Core*. Additionally, a "Capstone" class in the Department of Communication at the University of Utah was concluded in the first quarter of Phase 3A Year 2. The 15 undergraduates developed a survey to gauge the public's knowledge of geothermal energy, which was distributed in the winter 2021. A second professor from the Utah Valley University Department of Communication joined the efforts in an analyzing the results , and is currently finalizing her findings for publication.

8. Regular internal updates from the Outreach and Communication team to other teamson the Utah FORGE and partners at the DOE have proved invaluable. Along with others knowing about current engagements, these updates allow for others on the project to make suggestions, offer ideas and provide alerts about their own activities that may be spur new outreach opportunities.

CONCLUSIONS & FORWARD PLAN

Utah FORGE is a unique, publicly funded field-scale laboratory dedicated to developing the tools and technologies required for commercialization of EGS development. Critical issues that must be addressed include development of a fracture network capable of efficient heat extraction over long periods of time without significant temperature declines, economic flow rates, and mitigation of detrimental induced seismicity (>M2 events).

In Year 2 of Phase 3A, Utah FORGE activities focused on expanding the field laboratory, completing the seismic network, conducting high-resolution geophysical and geochemical monitoring, and modeling the effects of future stimulations and fluid circulation on the reservoir. Three deep wells were completed, and plans and vendor contracts for stimulation of well 16A(78)-32, the injection well, were put in place. Planning for drilling well 16B(78)-32 was initiated.

The major accomplishments of the Utah FORGE team:

1. Completed construction of the main elements of the Utah FORGE field laboratory, including three additional deep wells (16A(78)-32, the injection well, 56-32 and 78B-32) (Table D-1). Well 16A(78)-33 was drilled approximately parallel to Shmin to a depth of 5938 ft before being deviated 65° from vertical. The well has a total measured depth of 10987, a true vertical depth of 8559 ft and a temperature of 428 °F.
2. Awarded $49.5 M for seventeen R&D projects in five topic areas including: tools for zonal isolation, estimation of stress parameters, field scale characterization of reservoir evolution, stimulation and configuration of the wells, integrated laboratory and modeling studies. The projects will develop and test new technologies, operationally-oriented equipment, methods for reservoir stimulation, and address fundamental issues that limit commercialization of EGS development, and methods for reservoir stimulation, monitoring and testing.
3. Much of the infrastructure for the seismic monitoring network was completed. When fully deployed, the network will consist of two rings of surface and borehole geophones at 3 and 8 km, from the center of the Utah FORGE footprint, fiber optic cables in wells 78-32 and 78B-32, and deep geophone strings at reservoir depths in wells 56-32, 58-32 and 78B-32. The 3 km ring is operational, and installation of the 8 km ring was advanced, wherein seismometer stations were permitted and the postholes were drilled. Multilevel geophone strings, Nodal arrays, and additional fiber optic cables will augment the monitoring network during stimulations.
4. A plan for stimulating three stages near the toe of well 16A(78)-32 was approved. Approximately 10,000 barrels of water will be injected; 4500 barrels in the open holesection and 2500 barrels in each of two stages in the cased section of the well.
5. Completed repeat groundwater, gravity, GPS, InSAR surveys for baseline characterization of the subsurface.
6. Performed detailed mineralogic and lithologic analyses of the cores and cuttings obtained from the drill holes.

7. Prepared a preliminary design for well 16B(78)-32. This well will serve as the production well for reservoir creation, fluid circulation and demonstration of heat extraction.
8. Increased stakeholder interactions with expansion of the Outreach and Communications. Information is available on the Utah FORGE website, social media platforms, YouTube videos, E newsletter, podcasts, and scientific forums. This outreach activities provide information suitable for the general public, students fromgrade school to graduate levels, scientists and geothermal specialists.
9. Uploaded more than 200GB of data to the Geothermal Data Repository (GDR). There were more than 27000 downloads of the data. Forty papers were published and 80 presentations were given at Technical Conferences.
10. Collected and placed in the public domain a complete suite of data, logs, cuttingsand core samples.
11. Conducted detailed fracture analysis of the Formation Microimager and Ultrasonic Borehole logs and developed a refined Discrete Fracture Network (DFN).
12. Thoroughly tested drilling, logging, and seismic monitoring tools and methods at the Utah FORGE site under conditions appropriate for commercial EGS development.
13. Utah FORGE is the most thoroughly documented of any EGS sites in the world.

Table D-1. *Summary of well data.*

Well	Latitude	Longitude	Ground level (ft)	Kelly Bushing Height (ft)	Measured Depth (ft) from GL	True Vertical Depth (ft)	Max Recorded Temperature (°F)	Core Interval 1 (ft MD)	Core Interval 2 (ft MD)
58-32	38.50051644	-112.8870119	5527.5	21.5	7,536	7,528	386.0	6,800 - 6810.25	7,440 - 7,452.15
68-32	38.50157333	-112.8866409	5530.4	5.7	1,000				
78-32	38.50016375	-112.8832204	5583.7	5.7	3,280		223.8		
16A(78)-32	38.50402147	-112.8963897	5413.5	30.4	10,987	8,559	426.8 [428.7]	5,473 - 5,892	10,955 - 10,987
56-32	38.50402364	-112.8864923	5451.6	30.4	9,145	9,138	435.1		
78B-32	38.50010313	-112.8822486	5595.9	30.4	9,500	9,497	426.8 [463.5]	6,700 - 6,740	8,500 - 8,540

[] = Extrapolated to TD

Table D-2. *Impacts of Key Accomplishments in Phase 3A, Year 2: A High-Level Overview.*

Key Accomplishments	Impact
Drilling and Infrastructure	
Completed drilling of well 16A(78)-32	Serves as injection well of injection - production pair for reservoir creation and long-term circulation. First highly deviated (65°), long reach, large diameter (7 inch) well drilled specifically for geothermal purposes.
Constructed pads for wells 56-32 and 78B-32	Required for drilling deep vertical wells.
Drilled wells 56-32 and 78B-32	Supports drilling, monitoring and tool testing programs. Allows: 1) data collection and tool testing at reservoir depths; and 2) seismic monitoring during stimulations and long-term circulation testing.
Utilized PDC bits and applied MSE calculations	Demonstrated application of MSE for optimizing drilling parameters and Rates of Penetration (ROP) in real time. Reduced ROP by 50%, significantly reducing drilling costs.
Completed and awarded bids to contractors for stimulation at the toe of well 16A(78)-32	Supports Proof of Concept for stimulating low permeability granite within cased wells at industrial flow rates
Completed critical infrastructure for seismic monitoring network	Allows detection of induced seismic events, facilitates location of these events and mitigates hazards. This information is essential for managing stimulations and fluid circulation
Permitting completed and boreholes drilled for seismic monitoring locations BOR-4, 5, 6 on the 5-mile (8 km) ring	Provides monitoring capability to detect fractures resulting from Utah FORGE operations at distance from the wells during drilling and initial testing of 16A(78)-32. These are shallow deployments for permanent monitoring that are part of the overall seismic monitoring network.
Tested tools for drilling and stimulation under reservoir conditions	Limitations of these tools and techniques has been documented and made publicly available.
Completed electric distribution lines	Allows connecting electric power to the drill pads and facilities for Phase 3 operations and R&D activities
Seismic Evaluations and Planning	

Continued microseismic monitoring	Demonstrates low natural seismicity at the Utah FORGE site and low risk of seismic hazards
Reservoir Characterization	
Fracture analysis of Formation Microimager and Ultrasonic Borehole logs	Confirms stress orientations and allows refinement of the Discrete Fracture Network (DFN)
Repeat gravity, GPS, water levels, InSAR surveys	Provides baseline data for monitoring density changes in subsurface. No surface deformation or changes in water levels that can be correlated with site activities.
Refined conceptual model	Provides basis for reference numerical model.
Collected extensive suite of data, logs, cuttings and core samples.	Provides basic data for detailed analysis of the geological, geochemical, geophysical, and stress characteristics of the reservoir. These geoscientific investigations have confirmed the conceptual geologic model that informs the earth model. This model is essential for planning the drilling and stimulation program.
Numerical Simulations	
Refined DFN	Provides basis for numerical modeling of fracture behavior including ability to initiate, extend, dilate and/or reactivate fractures behind casing. Allows history matching of previous injection data.
Refined reference numerical reservoir model	Informs drilling and stimulation programs in Phase 3, indicating anticipated temperature, pressure and stress values, according to acquired logging and other geophysical information.
Refined dynamic reservoir modeling	Allows improved probability for predicting the geometry of the of the interconnected fracture network formed during reservoir evolution.
Management and Outreach Activities	
Awarded 17 projects proposed under Solicitation 1	Addresses R&D needs defined by the STAT.
Outreach and communications activities	Engages stakeholders including general public, students, the scientific community, legislators, regulators, educators, and local stakeholders.

PHASE 3 YEAR 3 PLANNED ACHIEVEMENTS

Year 3 of Phase 3 will focus on reservoir creation and circulation of fluids between the production and injection wells. The major achievements planned for Phase 3, Year 3 include:

1. Plan, drill, complete, and stimulate well 16B(78)-32. Well 16B(78)-32 will be geosteered into the microseismic cloud enveloping the fractures created by the stimulation at the toe of well 16A(78)-32.
2. Perform a short circulation test after drilling to ascertain connectivity between the injection and production wells before additional stimulations are conducted in thetwo wells to create the reservoir.
3. Issue Solicitation 2, review submitted proposals and make awards. Continuetechnical and financial management of Solicitation 1 projects.
4. Complete deployment of the seismic monitoring network, including installation of instruments in three boreholes on the 5 mile (8 km) monitoring ring and strings of dual analog geophones in wells 56-32, 58-32 and 78B-32 to reservoir depths. Augment the network with surface instruments and multilevel geophone strings during well stimulations.
5. Monitor the evolution of the reservoir utilizing the continuous seismic record and high-resolution geophysical surveys
6. Drill Well of Opportunity -2 (well 47-2) for tool testing and seismic monitoring.
7. Continue to advance drilling improvements through development of modified bitsand application MSE during drilling.
8. Organize and consolidate well and field data submitted to the Geothermal Data Repository (GDR) for easy access.
9. Encourage industry and R&D performers to develop and test different stimulation techniques. Potential techniques could include the use of proppant, cold water injection, propellant, abrasive slotting and novel approaches such as CO_2 activated proppant.
10. Expand the Outreach and Communication program by fostering a greater understanding of geothermal energy and EGS across a broad range of audiences, including the general public, the scientific community, students, legislators, regulators, educators, and local stakeholders. Continue engaging these audiences through our website, social media platforms, emails, e-newsletter, community relations, scientific conferences, YouTube videos, webinars, podcasts, and presentations.
11. Augment existing outreach activities with the construction of a virtual visitor center.

VISION

Meeting the US DOE's goal of 60,000 MWe by 2050 requires multiple, large scale EGS development. No other approach, including the development of conventional geothermal resources, offers the potential to reach this goal. Since the late 1970s, there have been more than a dozen attempts worldwide to create EGS reservoirs by hydraulically fracturing hot rocks. While there have been important learnings, no commercial scale reservoir has been created.

Utah FORGE is on the verge of demonstrating the necessary technology for the first time. No similar field laboratory exists elsewhere in the world.

The primary objectives of Utah FORGE are to: 1) create a fractured volume with sufficient permeability to extract heat from hot rock for long periods of time; 2) achieve economic flow rates (>40 l/s) without significant reservoir cooling; 3) mitigate detrimental induced seismicity; and 4) demonstrate commercial viability of EGS.

Existing oil and gas tools were expected to be suitable for use in the hot, abrasive reservoir rocks at the Utah FORGE site. This has not been the case, and tool failure has been a persistent problem. Because tools must be replaced when they fail, failed tools lead to unnecessary downtime while tripping in and out of the hole to replace them. Tools capable of withstanding temperatures exceeding 420 ^{o}F, especially zonal isolation tools (e.g., packers, bridge plugs, sliding sleeves) are, in our opinion, the number one priority for creating EGS reservoirs.

Few logging and monitoring tools have been designed to work at Utah FORGE reservoir temperatures. Image and geophysical logs are essential for characterizing and analyzing fracture distributions, stress orientations, and rock properties, monitoring reservoir changes, determining the effectiveness of the cement bond, and measuring temperature. Utah FORGE has attempted to collect complete suites of image (FMI and UBI) and geophysical logs from each well drilled. Because of the high temperatures and lack of permeability, the wells heat up quickly after being cooled, even for long periods of time. This rapid temperature build-up has precluded the collection of image logs in some wells (e.g. 78B-32 from 8500 to 9500 ft), even when using Schlumberger's Through the Bit (TTB) logging tools, which allow for cooling while running in the hole.

The current generation of seismic monitoring tools is similarly temperature limited. Temperatures and casing depths in the three deep vertical wells will constrain placement of the geophones to approximately 7500 to 8500 ft, no deeper than the true vertical depth of the toe of well 16A(78)-32. Geophones will require replacement approximately every 6 months.

Meeting the objectives of Utah FORGE, the DOE and achieving commercialization of EGS will require: 1) developing new completion methodologies; 2) developing high temperature zonal isolation and drilling tools; and 3) managing the stress field to control permeability and induced seismicity. Utah FORGE is actively engaged with the R&D and commercial tool communities to meet these objectives and develop a roadmap toward commercialization through its external, competitively awarded R&D program and operational activities

The Gantt Chart in Figure D-1 illustrates the succession of field operations that will be undertaken at the Utah FORGE site beginning in Phase 3B and extending through September 2024. In Phase 3B well 16B-(78)-32 will be drilled to initiate reservoir creation. Well 16B(78)-32 will provide the first opportunity to demonstrate the application of tools and techniques developed under Solicitation 1. Short and long-term injection tests will establish connectivity between the injection well 16A(78)-32 and the production well 16B(78)-32, which will be separated by a relatively short distance. Fiber optic cables deployed by UT Austin and University of Texas at Rice in the annulus of the 7-inch production casing will allow us to assess their application in monitoring fluid flow behind casing, locate zones of high permeability and improve subsurface characterization of the reservoir rocks. The stimulation program for connecting well 16A(78)-32 and 16B(78)-32 will incorporate field and modeling results from Fervo and UT Austin, and the application of shallow strainmeters deployed by Clemson University in a geothermal environment.

Once connectivity is demonstrated, the size of the stimulated rock volume and the circulation times will be increased. In Phase 4, a third deviated well 16C(78)-32 will be drilled based on detailed analysis of all data acquired, including that resulting from the stimulation, flow testing, and seismic monitoring of wells 16A(78)-32 and 16B(78)-32. No additional deep wells suitable for multi-well flow tests can be drilled within the proposed budgets.

Although the 2019 DOE road mapping report, GeoVision, did not identify drilling tools and technologies as a funding priority for EGS development, Utah FORGE drilling and stimulation results demonstrate that improvements are necessary. These improvements are especially important for controlling fluid flow and the wellbore shape, smoothness, and deviation.

Improvements in five areas are particularly relevant: 1) reducing vibrations at the bit through improvements in bottom hole assembly designs and vibration measurement; 2) high temperature Rotary Steerable Systems (RSS) and fixed angle mud motors for controlling well deviations; 3) bit designs that support longer performance and faster drilling while preserving well bore smoothness; and 4) improved recovery of material from cored intervals. Substantial progress has been achieved in bit designs by working closely with the bit designers. However, because of the large hole diameters required for geothermal production compared to oil and gas wells, and the relatively small geothermal market, it is unlikely the manufacturers of wellbore completion and production tools (e.g., packers) will take on the challenge of redesigning the required tools without significant financial incentives from DOE or Utah FORGE.

The first generation of new tools essential for managing fluid flow in EGS reservoirs are being developed by Welltec and Petroquip (packers), and the Colorado School of Mines (sliding sleeves/tractors). Although these tools may not be available prior to drilling and completion of well 16B(78)-32, they will be available for use in well 16C(78)-32 in FY 2025-6, as will other new tools resulting from Solicitation 2 and 3.

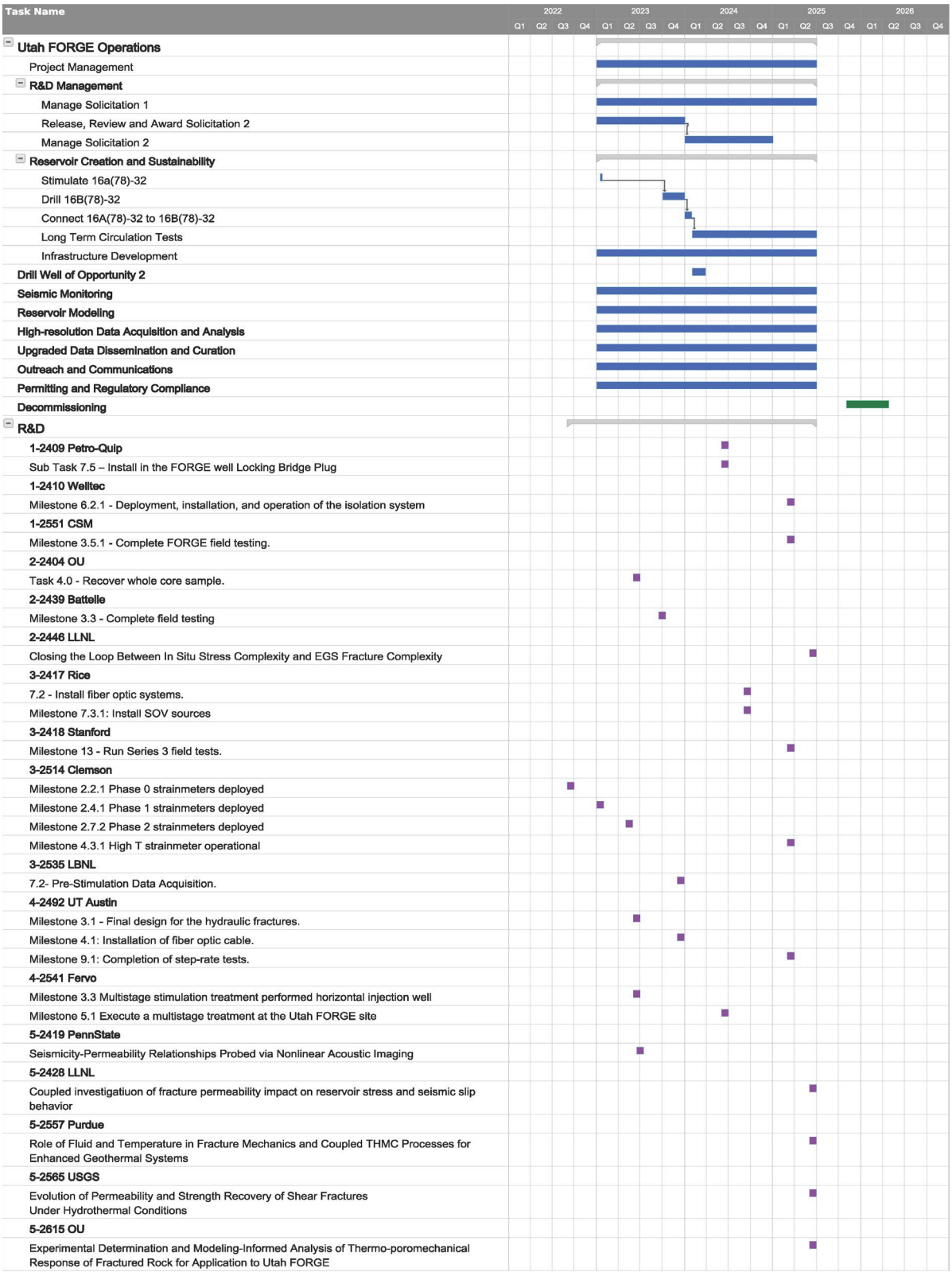

Figure D-1. *Gantt chart of Utah FORGE Operations integrated with R&D activities*

Six wells will be available throughout the project life for testing tools, geophones, and new technologies under reservoir conditions These include: wells 56-32, (cased to TD of 9200 ft), 58-32 (uncased from 7500-TD at 7536 ft) 78B-32 (uncased from 8500-9500 ft), and future Wells of Opportunity – 2 and – 3 and Monitoring Well – 1. The new wells will provide opportunities for post stimulation reservoir characterization; seismic monitoring; core collection; in-situ stress and other measurements; chemical monitoring techniques; and tool testing (e.g., flow control tools, and drilling tools such as bits and motors).

Our vision for Utah FORGE is not limited to technical accomplishments. Outreach and Communication activities will continue to expand as the project evolves. The Virtual Visitor Center will provide access to information about the project, geothermal energy and EGS to unlimited audiences. Our outreach activities will be broadened to include underrepresented communities, such as those in rural and remote areas, communities of color, the Native Tribes, the LGBTQ+ community, those for whom English is not a first language, and girls and women in STEM programs.

APPENDICES

Phase 3A Year 2 Annual Report

Enhanced Geothermal System Testing and Development at the Milford, Utah FORGE Site

Appendix A1: Infrastructure Assessment

Phase 3A Year 2 Annual Report

Enhanced Geothermal System Testing and Development at the Milford, Utah FORGE Site

Utah FORGE
University of Utah
423 Wakara Way, ste 300
Salt Lake City, UT, 84105

Prepared for the U.S. Department of Energy

Office of Energy Efficiency and Renewable Energy

Contract DE-EE0007080

April 30, 2022

A1. FORGE INFRASTRUCURE ASSESSMENT

This section considers the infrastructure and budget required to support Utah FORGE operations and R&D activities in Phase 3B. Anticipated expenditures for infrastructure development in Phase 3B are included in the following sections. These budgets reflect estimated costs in the DOE approved Phase 3B budget.

WELL 16B(78)-32

Well 16B(78)-32 will serve as the production well for the Utah FORGE field laboratory. It will be drilled approximately parallel and above well 16A(78)-32 on the same pad. The design and trajectory of the well will be based on stimulation results from the toe of well 16A(78)-32, R&D requests, and operational requirements (e.g., deployment of optic fibers , core, open hole measurements, through the bit logging). Utah FORGE will work closely with the STAT, DOE, R&D project teams, and drilling and stimulation experts to design the well, determine its trajectory, prepare the drilling plan and identify tools that require long lead times to procure. A budget of $13,200,000 is available for drilling, supervision and experts.

WELL OF OPPORTUNITY-2 (WOO-2)

Well of Opportunity - 2 (WOO-2) is anticipated to be drilled in mid-2023. The purpose of this well is to provide opportunities for testing EGS technologies and for seismic monitoring. Meetings will be convened with the STAT, DOE and Utah FORGE to discuss well design requirements and review possible well locations. It is anticipated drill pad construction, biological surveys, and connection to the electrical power line will be required.

A total of $ 13,000,000 was budgeted by the DOE for drilling WOO-1 (renamed 78B-32) and WOO-2. Currently $ 6,200,000 remains for drilling and decommissioning WOO–2 and decommissioning WOO-1.

SEISMIC MONITORING NETWORK

Continuous real time monitoring of low magnitude induced and natural seismicity is essential. Full deployment of the seismic monitoring network will be completed in early Phase 3B (Fig. A1-1). Wells 58-32, 68-32 and 78B-32 comprise the central portion of the network. Multilevel geophone strings of self-cooling geophones will be deployed in these wells during the stimulation of well 16A(78)-78. Each of these strings will be replaced with two analog geophones after the stimulation for long-term monitoring. FSB-1,-2 and-3, located on the 1.9 mile (3 km) ring were instrumented with broadbands seismometers in Phase 3A. FSB-4, -5 and -6 were drilled and will be instrumented in early Phase 3B.

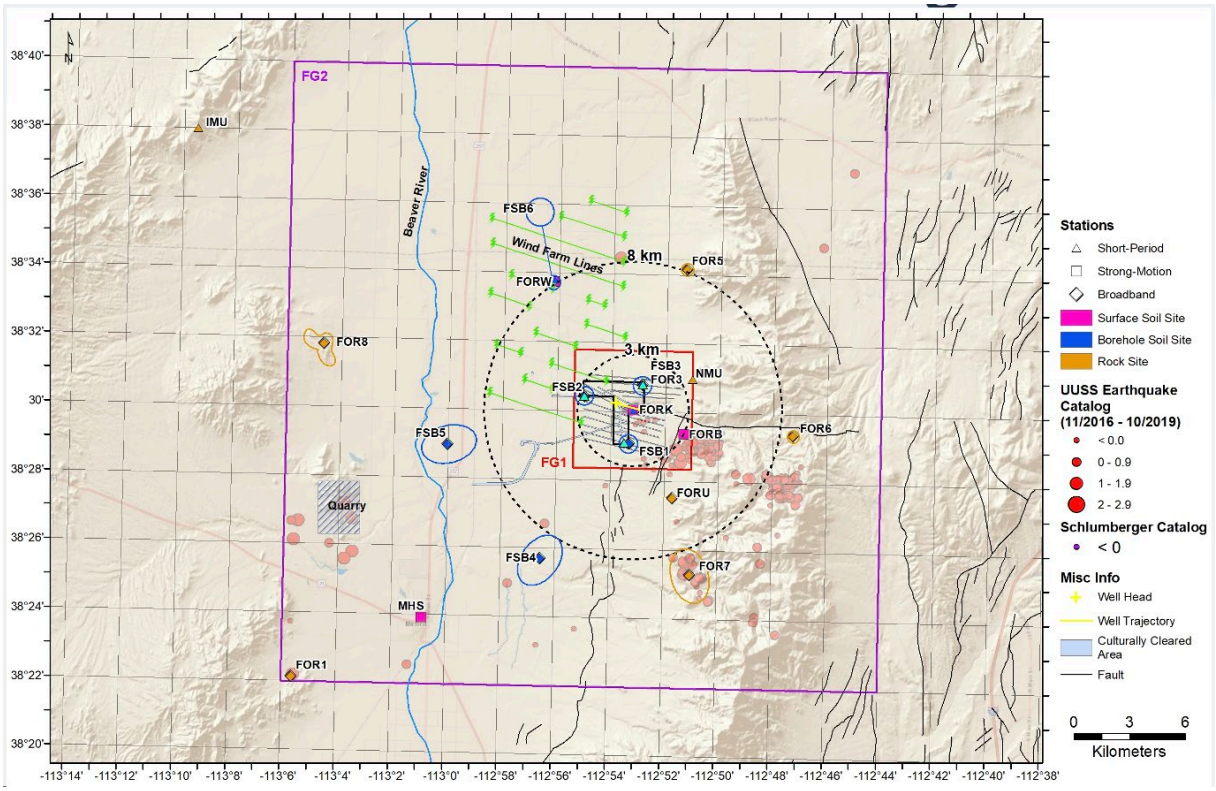

***Figure A1-1**. Final seismic network. Full deployment of the network will be completed early in Phase 3B with the installation of broadband instruments in FSB -4,-5, and -6 on the 5 miles (8 km) ring. The trajectory of 16A(78)-32 passes between monitoring wells 56-32 on the north and 58-32 and 78B-32 on the south. Strings of dual analog geophones will replace multilevel strings deployed in these wells during the stimulation of well 16A(78)-32. Symbols: triangle = short period instrument; square = strong motion sensor; diamond = broadband instrument. Locations of proposed shallow boreholes are shown in blue and rock stations in gold.*

ELECTRICAL REQUIREMENTS

Electric power is available at all of the pads (Fig. A1-2). The electric lines have been engineered to provide power for present and future needs, including housing, large (125 hp) pumps for circulation testing and water wells, seismic monitoring, and communications. Additional spur lines may be required in the future for WOO-2 and any monitoring wells that are drilled. $30,000 has been budgeted to cover the cost of electrical use during Phase 3B.

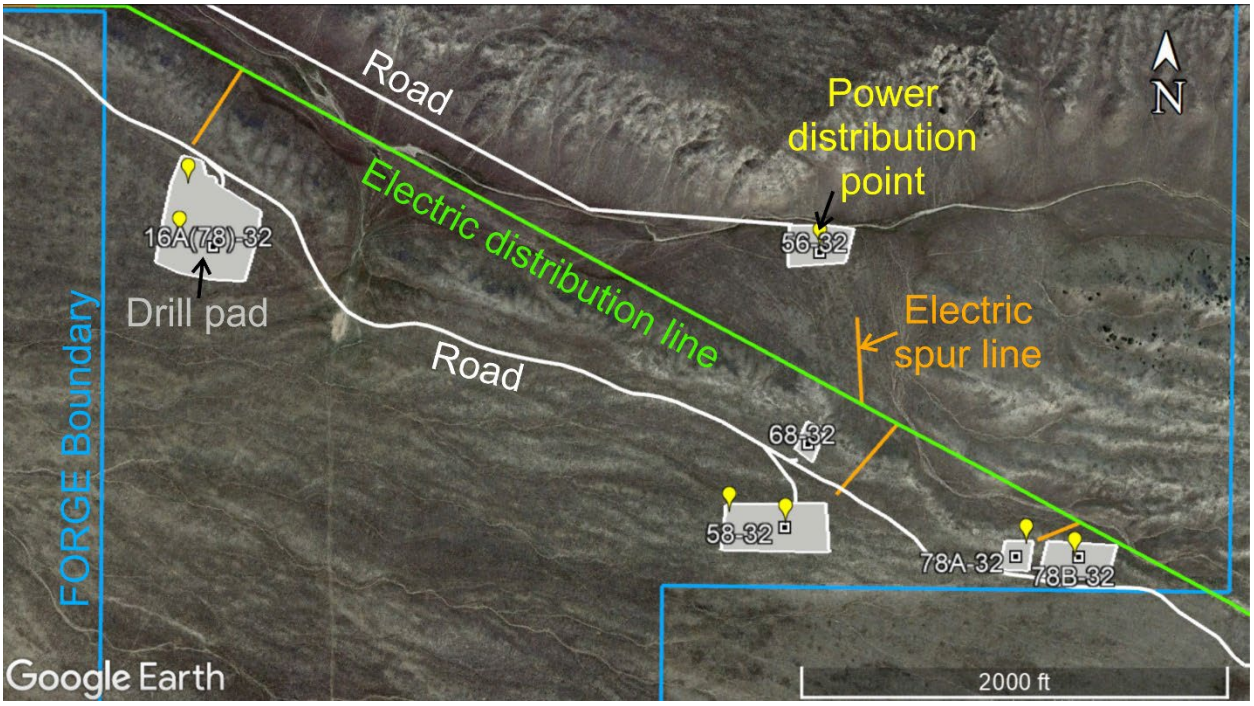

Figure A1-2. *Electric infrastructure map for Utah FORGE. The main, overhead electric distribution line in shown in green. Electric spur lines to various points within the Utah FORGE footprint (blue) are shown in orange. Power distribution points on the drill pads (gray) are shown in yellow.*

ROAD MAINTENANCE AND CONSTRUCTION

All of the well pads drill pads are accessible by roads. During Phase 3B, Utah FORGE will continue to provide routine site maintenance. The majority of the work will consist of road grading, snow clearing and pad maintenance.

Utah FORGE has agreed to provide a one-time contribution of $150,000 to Beaver County to help pay for recently completed road improvements. We have budgeted $75,000 in Phase 3B Year 1 for the remainder of this contribution.

CULTURAL SURVEYS

The existing culturally cleared (Fig A1-3)areas provide flexibility for the operational and R&D activities that will be conducted during Phase 3B. The locations of future activities, including the drilling of wells 16A(78)-32, WOO – 2, the water supply well and the strainmeter boreholes required by Clemson University (Fig A1-4) can be drilled on locations that are culturally cleared. Sites for Surface Orbital Vibrators (SOV) required by Rice University and large-scale surveys may

necessitate new or expanded cultural clearances. Depending on the time of year, biological clearances may be required on culturally cleared land prior to conducing site activities. Utah FORGE will assist the R&D performers in obtaining the necessary clearances.

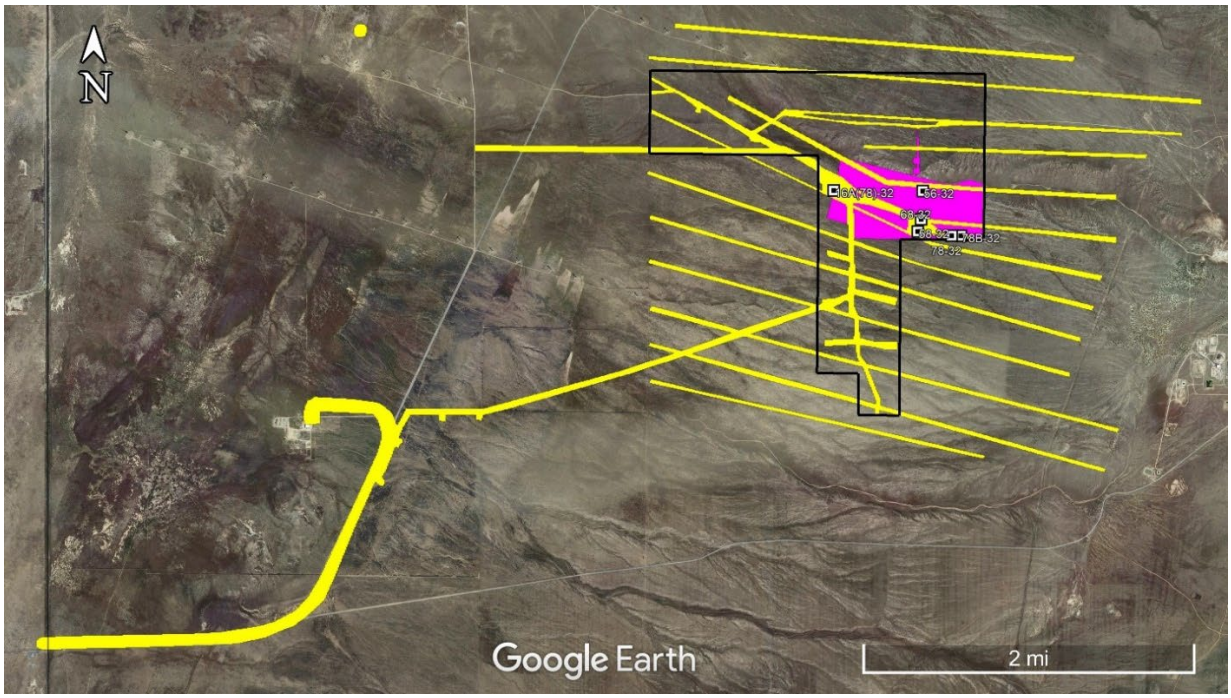

***FigureA1-3**. Areas that have been culturally cleared within the Utah FORGE footprint during the reporting period are shown in magenta. Previously cleared land is shown in yellow.*

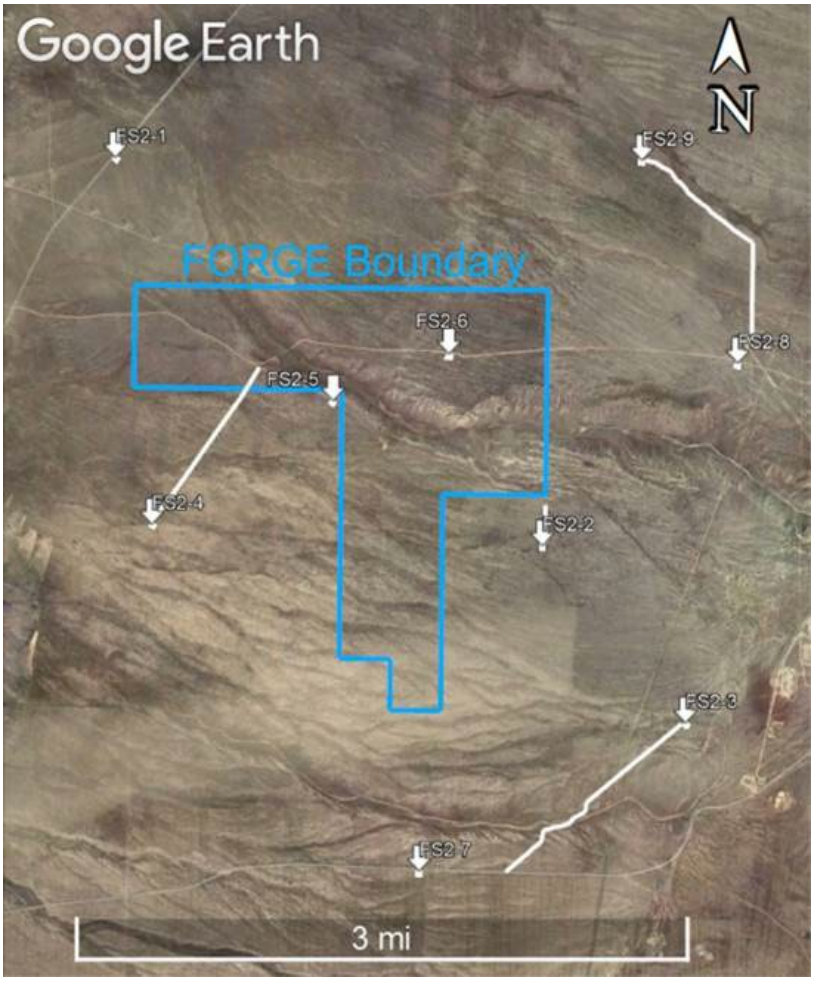

Figure A1-4. *Clemson University strainmeter sites. The drill sites are shown as small white squares at the arrow tips; two track access roads to the drill pads are shown as white lines. The pad locations and roads have been culturally cleared. Biological clearances by Clemson University are pending.*

FUTURE WATER NEEDS

At least one water well will be required for future drilling, stimulation and circulation testing. Water rights for 250 acre-ft per year (81 million gallons/year) of non-consumptive use (Water Right 71-5429) and 50 acre-ft per year (16 million gallons/year) for consumptive use (Water Right 71-5430) have been acquired by the project. An additional 200 acre-ft of water has been offered by Smithfield Foods under a lease arrangement. Water can also be purchased from Milford. Water from Milford was used for drilling and testing wells 16A(78)-32 and 56-32, and will be purchased for the well 16A(78)-32 stimulation.

Testing of well 78-32 indicated that the aquifer could produce 200 gpm, a volume considered sufficient for circulation testing. We have evaluated several options for water storage. The most feasible is to use the existing sumps on the well 58-32 and 16A(78)-32 pads. Water produced near well 78-32 and stored in the well 58-32 sump could be gravity fed to well 16A(78)-32 for injection. $345,000 has been budgeted for the drilling of the water well.

All electric drops have been oversized to accommodate both a 105 hp water well pump and a 75 hp booster pump, giving flexibility in the placement of a future groundwater well.

COMMUNICATION SYSTEM

A microwave radio link to bring high-speed internet to the Utah FORGE site has been installed by Utah Education and Telehealth Network (UETN). Internet connections were adequate for the well 16A(78)-32 stimulation but upgrading the antennas and radios could improve the communication system. We are currently exploring these options. We expect the cost to upgrade the communication system will be less than $10,000.

PROJECT OFFICE

Several attempts have been made to procure a permanent project office, but all have resulted in higher than anticipated costs. In addition to the structure itself, costs for maintenance, furnishings, external supporting systems and security were considered. Maintenance includes frequent cleaning, delivery of potable water, removal of sewage and/or household waste. Furnishings would be required to outfit a conference room, kitchenette, offices and communal work areas.

Few of the R&D projects will require on-site visits and most of these will occur during periods of drilling and stimulation. Mobile offices will be made available at these times to accommodate the R&D teams. Because of their portability, mobile offices can also be procured at other times if needed. These offices will be equipped with appropriate furnishings, built in work space, sufficient space and outlets for computers and other electronic equipment, restrooms, microwave/sink/refrigerator and internet access. Mobile offices can be obtained in a variety of sizes and configurations, with or without separate private office space, and can be connected to create space for several independent groups

Preliminary figures from Civeo suggest that these units could be deployed on site for up to 5 two months periods.

R&D SUPPORT

Several of the R&D projects will require significant support for testing tools and stimulation technologies. On-site facilities during these periods could include drill rigs, cranes/boom trucks, storage facilities, a Project Office and oversight by the Site Safety Manager and the Drill Site Manager. Additional personnel may be required, depending on the activities to ensure they are conducted in a safe manner, will not cause damage to the infrastructure and wells, and are in accordance with permitted activities. Every attempt will be made to schedule R&D activities at times when costs can be minimized. However, we will work closely with the R&D teams to ensure their projects are completed in a timely manner. $500,000 has been budgeted per year in Phase 3B to support these R&D projects, but the actual costs are expected to many times this amount as new tools and technologies and readied for testing.

DECOMMISSIONING

The site must be decommissioned, or transferred to a third party, at the conclusion of the project. The current project end date is July, 26, 2025. Decommissioning requires returning all pads to grade level, plugging and abandoning the wells, and reseeding. All equipment and site facilities must be removed, unless transferred to the land owner, Utah School and Institutional Trust Lands Administration (SITLA). We currently have budgeted/encumbered $3,000,000 for restoration and abandonment through Phase 3B.

Appendix A2: Update on Site Data Uploaded to the GDR Data Archive

Phase 3A Year 2 Annual Report

Enhanced Geothermal System Testing and Development at the Milford, Utah FORGE Site

Utah FORGE
University of Utah
423 Wakara Way, ste 300
Salt Lake City, UT, 84105

Prepared for the U.S. Department of Energy

Office of Energy Efficiency and Renewable Energy

Contract DE-EE0007080

April 30, 2022

A2. DATA SHARING

Work during Phase 3A has produced a tremendous amount of data as well as reports. All of data and reports as of April 2022 has been uploaded to the Geothermal Data Repository and is available for downloading. These data include the following:

(1) High-Resolution DAS microseismic data from Well 78-32 (two separate submissions 11/13/2019 & 04/01/2020):
https://gdr.openei.org/submissions/1185 and https://gdr.openei.org/submissions/1207

127,676 files

(2) Utah FORGE: Phase 2C topical report (added 12/09/2019):
https://gdr.openei.org/submissions/1187

34 files

(3) Data for 3-D model development - lithology, temperature, pressure, and stress (added 03/13/2020): https://gdr.openei.org/submissions/1205

12 files

(4) Utah FORGE well 16A(78)-32 planned trajectory coordinates and depths (added 03/24/2020): https://gdr.openei.org/submissions/1208

1 file

(5) 2019 ARMA Slide presentation (added 03/24/2020):
https://gdr.openei.org/submissions/1209

1 file

(6) 58-32 Injection and packer performance, April 2019 (added 03/25/2020):
https://gdr.openei.org/submissions/1210

1 File

(7) Utah FORGE seismic activity: April 2019 (added 04/24/2020):
https://gdr.openei.org/submissions/1215

1 file

(8) Report: numerical modeling of microearthquake monitoring
at the Utah FORGE Site, LANL (added 06/08/2020):

https://gdr.openei.org/submissions/1187

1 file

(9) Utah FORGE Well 16(78)-32 planned trajectory (added 04/29/2020):
https://gdr.openei.org/submissions/1216

1 file

(10) Discrete fracture network (DFN) data (added 06/24/2020):
https://gdr.openei.org/submissions/1222

154 files

(11) InSAR Study results: report and data (added 09/29/2020):
https://gdr.openei.org/submissions/1251

279 files

(12) Ground water monitoring data from wells WOW-2 and WOW-3 (added 09/30/2020):
https://gdr.openei.org/submissions/1252

1 file

(13) Microgravity data through time (added 10/7/2020):
https://gdr.openei.org/submissions/1256

1 file.

(14) Magnetotelluric (MT) data (added 10/7/2020):
https://gdr.openei.org/submissions/1255

3 files.

(15) Utah FORGE updated Phase 2C well location coordinates (added 12/7/2020):
GDR: Utah FORGE Updated Phase 2C Well Location Coordinates (openei.org)

9 files.

(16) Utah FORGE seismograph stations link (added 1/26/2021):
GDR: Utah FORGE Seismograph Station Information and Data (openei.org)

1 link

(17) Well 16A(78)-32 Drilling Data: daily reports, drilling data @ 10 second intervals, drilling data @ 1 second intervals, standard survey report, summary of daily operations, survey data, and rig photos.
(added 3/1/2021 by NREL):
https://gdr.openei.org/submissions/1283

116 Files

(18) Well 16A(78)-32 Logs: mud logs, Sanvean Technologies logs, and Schlumberger logs These include (1) through bit FMI, (2) through bit sonic, (3) time lapse casing integrity, (4) CBL and gamma, (5) mud temperature and gamma, (6) array induction and gamma, (7) array induction, spectral density, dual spaced neutron/gamma ray, (8) spectral GR and temperature, (9) HID, (10) temperature, (11) ultrasonic imager/casing integrity/gamma ray-CCL, and (12) ultrasonic borehole imager logs. (added 3/10/2021):
GDR: Utah FORGE Well 16A(78)-32 Logs (openei.org)

122 files.

(19) Well 56-32 Drilling Data, bit data, BHA data, mud motor data, well logs, Pason data, daily reports, days vs depth, and daily mud logs. Schlumberger Logs: FMI, shear anisotropy analysis, memory, sonic, array induction/spectral density/dual spaced neutron/gamma ray/caliper, spectral GR/temperature, Gardner density correlation, caliper, and well survey data (added 4/7/2021):
GDR: Utah FORGE Well 56-32 Drilling Data and Logs (openei.org)

180 files

(20) 1-D seismic velocity models: Kristine Pankow, University of Utah Seismic Stations (added 3/18/2021):
GDR: Utah FORGE Seismic Velocity Models, February 2021 (openei.org)

64 files

(21) Summary of drilling activities for well 16A(78)-32 (added 3/21/2021):
GDR: Utah FORGE Well 16A(78)-32: Summary of Drilling Activities (openei.org)

1 file

(22) Text file containing the results of a final Schlumberger FMI log run from 7390' to 7527' in well 58-32, originally known at well MU-ESW1. (added 4/4/2021)
https://gdr.openei.org/submissions/1299

1 file

(23) Simplified DFN files and short report for well 16A(78)-32. (added 6/2/2021):
GDR: Utah FORGE Well 16A(78)-32 Simplified Discrete Fracture Network Data (openei.org)

25 files

(24) Utah Geological Survey interactive geoscience map. (added 6/10/2021):
GDR: Utah FORGE UGS Interactive Geoscience Map (openei.org)

1 link

(25) Induced seismicity mitigation plan revision and addendum. (added 6/29/2021):
GDR: Utah FORGE Induced Seismicity Mitigation Plan (openei.org)
2 files

(26) Utah FORGE Seismic stations and wells GPS survey data (UGS), 2021 (added 7/7/2021):
GDR: Utah FORGE Seismic Stations and Wells GPS Survey Data, 2021 (openei.org)
1 file

(27) Well 58-32 Schlumberger sonic waveform data (added 7/7/2021):
GDR: Utah FORGE: Logs and Data from Deep Well 58-32 (MU-ESW1) (openei.org)
4 files

(28) 2020-2021 Geothermal energy/EGS knowledge survey and results (added 7/20/2021):
GDR: Utah FORGE 2020 Geothermal Energy/EGS Survey and Results (openei.org)
2 files

(29) XRD data from well 16A(78)-32 (added 7/29/2021):
GDR: Utah FORGE Well 16A(78)-32 X-ray Diffraction Data (openei.org)
2 files

(30) Updated well temperature and pressure logs for wells 58-32, 56-32, and 78-32 (added 8/6/2021):
GDR | Successfully Submitted Utah FORGE Wells Updated Temperature/Pressure Logs (6/2021) (openei.org)
8 files

(31) Updated Utah FORGE composite raw gravity dataset covering the period from December 2018 to June 2021 (added 8/9/2021):
GDR | Successfully Submitted Utah FORGE Composite Raw Gravity Data 2021 (openei.org)
3 files

(32) Well 16A(78)-32 core photos (added 8/11/2021):
GDR: Utah FORGE Well 16A(78)-32 Core Photos (openei.org)
30 files

(33) Schlumberger Logs for well 78B-32 from the following tools:

1. QAIT - Slim Hostile Array Induction Tools
2. QSLT - Slim Xtreme Sonic Logging Tool
3. QCNT - Slim Hot Compensated Neutron Tool
4. QTGC - SlimXtreme Telemetry and Gamma Ray
5. HLDS - Hostile Litho-Density Sonde Tool
6. QCNT - Slim Hot Compensated Neutron Tool
7. QAIT - Slim Hostile Array Induction Tool
8. USIT - Ultrasonic Imager Tool
9. PPC - Powered Positioning Caliper Tool
10. GPIT - General Purpose Inclinometry Tool
11. FMI - Fullbore Formation Microimager
12. UBI - Ultrasonic Borehole Imager

(added (8/23/2021):
GDR: Utah FORGE Well 78B-32 Daily Drilling Reports and Logs (openei.org)
68 files

(34) Schlumberger concrete bond log (CBL) for 16A(78)-32, which also included gamma and mud temperature logs (added 9/7/2021):
GDR: Utah FORGE: Well 16A(78)-32 Logs (openei.org)
3 files

(35) Schlumberger concrete bond log (CBL) for 56-32, which also included gamma and mud temperature logs (added 9/7/2021):
GDR: Utah FORGE: Well 56-32 Drilling Data and Logs (openei.org)
2 files

(36) Utah FORGE groundwater data from well WOW2 and WOW3 updated by the Utah Geological Survey on 10/5/2021 (added 10/12/2021):
GDR: Utah FORGE Groundwater Levels: Updated 2021 (openei.org)
2 files

(37) Utah FORGE microgravity data composite updated on October 1, 2021 by the Utah Geological Survey (added 10/14/2021):
GDR: Utah FORGE Microgravity Composite Data: Updated 10/2021. (openei.org)
3 files

(38) North Milford Valley Groundwater Geochemistry (added 10/18/2021):
GDR: Utah FORGE: North Milford Groundwater Geochemistry 2021 (openei.org)

10 files

(39) Well 78B-32 core photos, but wet and dry (added 10/22/2021):
GDR: Utah FORGE Well 78B-32 Core Photos: Wet and Dry in Boxes (openei.org)
42 files

(40) Well 78B-32 Schlumberger 7-inch casing cement bond log data (added 10/29/2021):
GDR: Utah FORGE Well 78B-32 Daily Drilling Reports and Logs (openei.org)
5 files
(41) Well 78B-32 1 and 10 second Pason drilling data (added 12/6/2021):
GDR: Utah FORGE Well 78B-32 Daily Drilling Reports and Logs (openei.org)
3 files

(42) Well 56-32 1 and 10 second Pason drilling data (added 12/6/2021):
GDR: Utah FORGE: Well 56-32 Drilling Data and Logs (openei.org)
2 files

(43) Well 78B-32 directional survey (added 12/14/2021):
GDR: Utah FORGE Well 78B-32 Daily Drilling Reports and Logs (openei.org)
2 files

(44) Updated (model 17) MT model cell center data (added 12/6/2021):
GDR: Utah FORGE: Phase 3 Magnetotelluric (MT) Data (openei.org)
3 files

(45) Updated GPS survey coordinates for wells, well pads, and seismic stations completed in December, 2021 by the Utah Geological Survey (added 12/6/2021):
GDR: Utah FORGE Updated Well, Well Pad, and Seismic Station GPS Coordinates December, 2021 (openei.org)
1 file

(46) 1-D seismic velocity models coordinate data (latitude and longitude): Kristine Pankow, University of Utah Seismic Stations (added 12/17/2021):
GDR: Utah FORGE Seismic Velocity Models, February 2021 (openei.org)
1 file

(47) Sanvean Technology data for Well 78B-32. This included information such as Gyro performance, shock, vibration, and temperature (added 12/20/2021):
GDR: Utah FORGE Well 78B-32 Daily Drilling Reports and Logs (openei.org)
14 Files

(48) The Geothermal Resources Group “End of Well Report” for well 78B-32 (added 12/20/2021):

GDR: Utah FORGE Well 78B-32 Daily Drilling Reports and Logs (openei.org)
1 File

(49) X-ray diffraction results for 69 samples taken from well 56-32 from depths between 3050 and 9130 feet (added 12/21/2021):
GDR: Utah FORGE: Well 56-32 Drilling Data and Logs (openei.org)
1 file

(50) Final mud log from well 16A(78)-32 from Horizon Well Logging, Inc. (added 12/23/2021):
GDR: Utah FORGE: Well 16A(78)-32 Drilling Data (openei.org)
1 file

(51) Well 16A(78)-32 DFN Permeability Tensor Supplement -- Golder Associates Inc. (added 01/05/2022):
GDR: Utah FORGE Well 16A(78)-32 Simplified Discrete Fracture Network Data (openei.org)
7 files

(52) Well 58-32 one-foot interval drilling data (01/13.2022):
GDR: Utah FORGE: Logs and Data from Deep Well 58-32 (MU-ESW1) (openei.org)
1 file

(53) MT model 17 cell corner data (added on 02/21/2022):
GDR: Utah FORGE: Phase 3 Magnetotelluric (MT) Data (openei.org)
2 files

(54) Reinterpreted FMI data from well 56-32 (added on 02/21/2022):
GDR: Utah FORGE: Well 56-32 Drilling Data and Logs (openei.org)
5 files

(55) Schlumberger processed anisotropy log data for well 16A(78)-32 (added 3/7/2022).
GDR: Utah FORGE: Well 16A(78)-32 Logs (openei.org)
6 files

(56) Woolsey Land Surveying, as located, Longitude and Latitude coordinates for shallow seismic well locations including FSB4, FSB5, and FSB6 (added 3/8/2022).
GDR: Utah FORGE FSB4, FSB5, & FSB6 Shallow Seismic Well Locations (openei.org)
1 file

(57) Utah FORGE water table levels for wells WOW2 and WOW3 updated on 3/16/2022 by the Utah Geological Survey (added 3/16/2022).
GDR: Utah FORGE Groundwater Levels: Updated March 2022 (openei.org)
1 file

Phase 3A work produced a total of 128,923 files and 2 external data links which are all publicly available.

Supporting reports to the Phase 3A Yr2 Annual Report are attached as Attachments App-A2-Attachment 1 through -6.

Appendix A3: Updated Permitting Inventory

Phase 3A Year 2 Annual Report

Enhanced Geothermal System Testing and Development at the Milford, Utah FORGE Site

Utah FORGE
University of Utah
423 Wakara Way, ste 300
Salt Lake City, UT, 84105

Prepared for the U.S. Department of Energy

Office of Energy Efficiency and Renewable Energy

Contract DE-EE0007080

April 30, 2022

A3. PERMITTING & CULTURAL CLEARANCES

Cultural and biological surveys have been conducted both within and outside of the Utah FORGE footprint. Within the Utah FORGE footprint, additional areas have been cleared to support operations (Figure A3-1).

Outside of the Utah FORGE footprint, locations for three shallow seismic monitoring wells (FSB4, FSB5 and FSB6) have been permitted on State of Utah School and Institutional Trust Lands Administration (SITLA) property. Utah FORGE entered into a lease agreement with SITLA for three 2.5-acre leases (Figure A3-2). Prior to preparing the drill pads, biological and cultural surveys were performed by SWCA environmental consultants and approval was issued by the Utah State Historical Preservation Office (SHPO).

Utah FORGE has worked collaboratively with R&D recipient Lawrence Murdoch of Clemson University to locate and permit nine parcels of Bureau of Land Management (BLM) property outside of the Utah FORGE footprint and one location on SITLA property within the Utah FORGE footprint for the installation of a network of shallow boreholes to house strain meters (Figure A3-3). These locations include areas to host the drill pads and roads to access the drill pads (when not adjacent to an existing road). Utah FORGE has filed paperwork with the BLM, on Clemson University's behalf, to begin the permitting process, and contracted SWCA environmental consultants to conduct cultural surveys. Contracting biological surveys and finalizing permitting will be the responsibility of Clemson University.

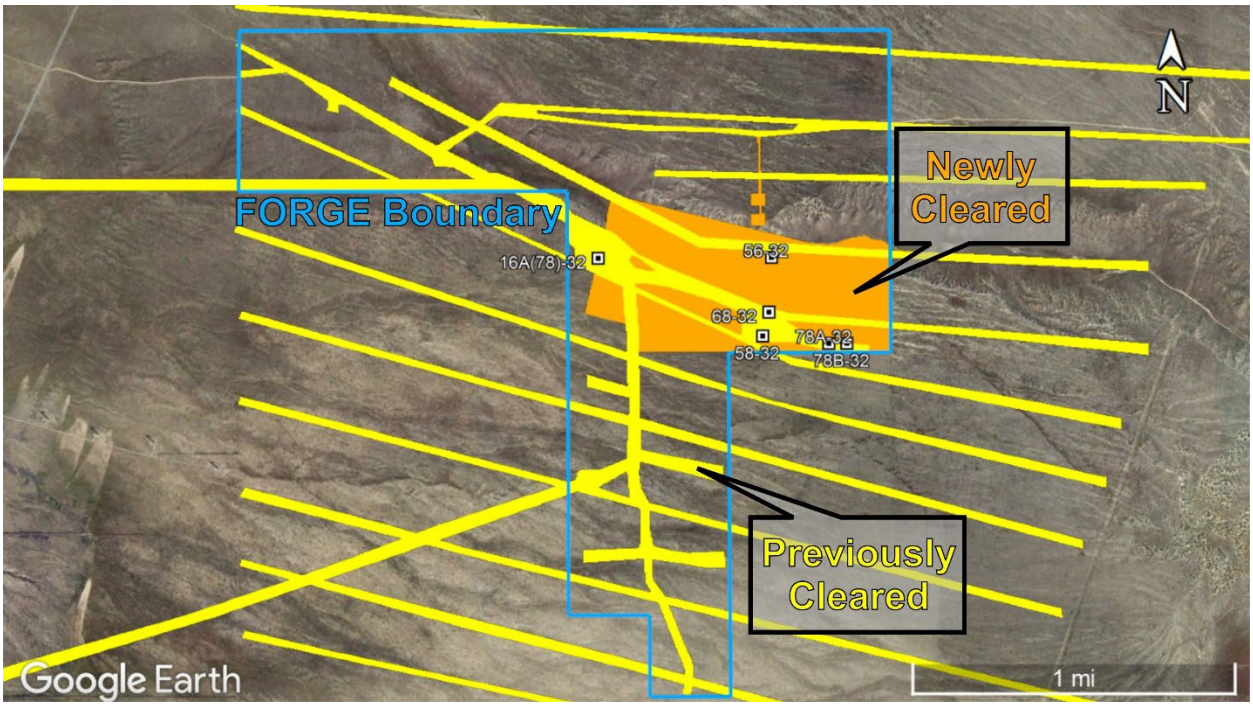

***Figure A3-1**. Areas that have been culturally cleared within the Utah FORGE footprint during the reporting period are shown in orange. Previously cleared land is shown in yellow.*

FigureA3-2. *Locations of the 2.5-acre sites that have been permitted for shallow seismic wells FSB4, FSB5 and FSB 6 on SITLA property leased by Utah FORGE. The Utah FORGE footprint is shown in blue.*

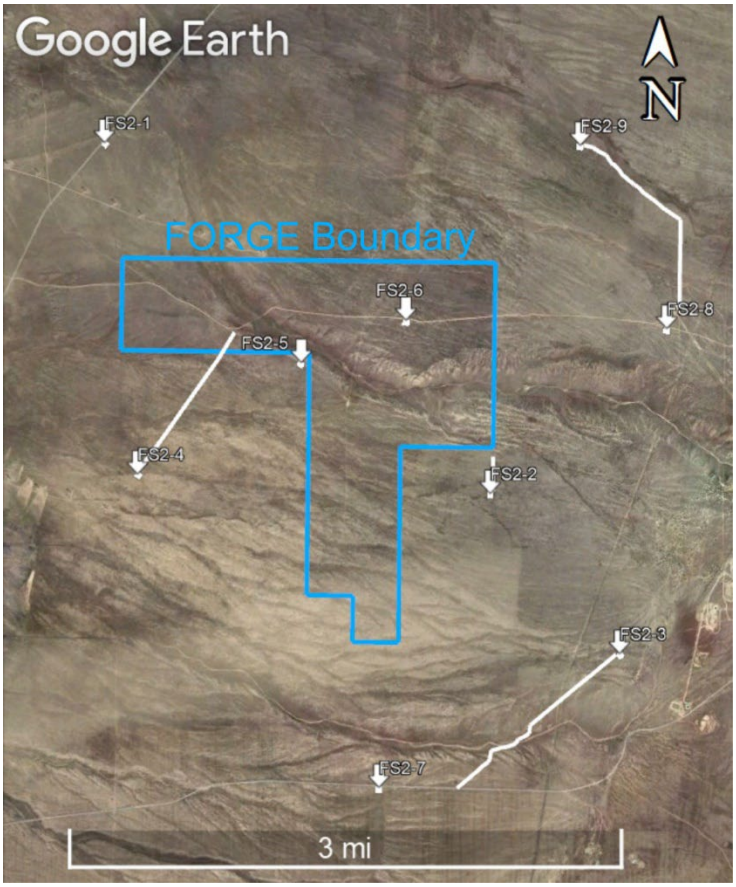

Figure A3-3. Areas over which cultural surveys have been conducted (white lines) to support installation of boreholes strain meters (white arrows).

Attachment 1

Phase 3A Year 2 Annual Report – Appendix A2

Enhanced Geothermal System Testing and Development at the Milford, Utah FORGE Site

Utah FORGE
University of Utah
423 Wakara Way, ste 300
Salt Lake City, UT, 84105

Prepared for the U.S. Department of Energy

Office of Energy Efficiency and Renewable Energy

Contract DE-EE0007080

April 30, 2022

Attachment 1

Phase 3A Year 2 Annual Report – Appendix A2

Enhanced Geothermal System Testing and Development at theMilford, Utah FORGE Site

Utah FORGE
University of Utah
423 Wakara Way, ste 300
Salt Lake City, UT, 84105

Prepared for the U.S. Department of Energy
Office of Energy Efficiency and Renewable Energy
Contract DE-EE0007080
April 30, 2022
Revision 1 July 18, 2022

Reservoir Geology & Mineralogy

Introduction

During the reporting period three deep wells have been drilled at the Utah FORGE site, 16A(78)-32 to 10,987 ft measured depth (MD), 56-32 to 9,145 ft MD and 78B-32 to 9,500 ft MD. Multiple sets of cuttings samples were collected at 10 ft intervals during drilling, providing a semi-continuous record of the lithologies intersected by these wells. Coring operations in 16A(78)-32 and 78B-32 recovered 74 ft and 54.75 ft, respectively. Examination of the cuttings and core retrieved while drilling these wells informs the conceptual geologic model (Figure 1) and ground truths other data sets.

Cuttings

Coupled X-ray diffraction (XRD) and thin section petrography analyses have been conducted on cuttings samples at 100 ft nominal spacing in the basement lithologies. Additional samples have been selected in areas of interest identified in well logs. XRD analyses of the cuttings has been used to classify the plutonic rocks via the ternary IUGS classification scheme (Le Maitre et al., 1989) by normalizing quartz (Q), alkali/K-feldspar (A), and plagioclase feldspar (P) abundances to 100%. These three phases, the most common in the earth's crust, comprise on average 86 wt% of the basement rocks intersected by 16A(78)-32, 81 wt% of the basement rocks in 56-32 and 89 wt% of the basement rocks in 78B-32. The majority of the samples fall in the lower, right-hand portion of the IUGS ternary diagram (Figure.2), and they are relatively plagioclase-rich and quartz and K-feldspar-poor. The most common granitoid lithologies are diorite, monzodiorite, monzonite, quartz monzonite, quartz monzodiorite, granite and granodiorite, with a few samples plotting in the quartz-rich granitoids, tonalite and quartz diorite fields.

Metamorphic rocks encountered in the lower parts of wells 16A(78)-32, 56-32 and 78B-32 have also been plotted on the IUGS diagrams for comparison to the intrusive lithologies. A summary of data from the Acord 1 well through to wells in Roosevelt Hot Springs are compared to the Utah FORGE data in Figure 3.

Thin sections have been made of the same sample for which XRD analyses were conducted. Cuttings from 16A(78)-32, 56-32 and 78B-32 wells drilled with polycrystalline diamond (PDC) drill bits produce much finer-grained cuttings (generally less than 1 mm) than those from earlier wells (58-32 and 78A-32) drilled at Utah FORGE in which tricone bits were used. The small grain size of the cuttings obscures larger scale rock textures and fabrics. However, distinctive textures, minerals and mineral relationships provide essential information on deformation, alteration, open-space filling mineralization and rock type.

Thin section petrography shows episodes of brittle and ductile deformation, with late brittle overprinting on to earlier-formed ductile deformation. Brittle deformation is most often manifest as shearing resulting in grain size reduction by mechanical failure, increasing proportions of open-space filling mineralization (veins), and alteration of primary phases.

Ductile deformation also commonly results in a grain size reduction by dynamic recrystallization without fracturing the rock but producing foliation.

One of the more distinctive occurrences encountered is that of dolomite rhombs in very fine-grained silica. This distinct texture has been observed in reservoir rocks in 16A(78)-32, 56-32 and 78B-32. These are interpreted as veins that may have formed from incursion of shallow groundwater in the Milford Valley that is saturated with respect to these phases.

Core

Prior to any subsampling of the core. Pictures were acquired to document the textures of the core. Thin sections and XRD analyses have been conducted on core samples to characterize rock textures/fabrics.

Figures 4 and 5 give a summary of coring operations and pictures of the recovered core in well 16A(78)-and 78B-32, respectively. In total 128.75 ft of core has been recovered from these two wells. An additional 22.4 ft was recovered from the pilot well 58-32, for a total of 151.2 ft of core from the Utah FORGE site.

A total of 30.3 ft of core from 16A(78)-32 and 78B-32 have been distributed to external R&D recipients at the University of Pittsburg, the US Geological Survey, the University of Oklahoma, Penn State University and Lawrence Livermore National Laboratory for lab testing. Samples have also been requested by, and allocated to Benedikt Ahrens (Fraunhofer IEG, Bochum, Germany). In addition to core samples, boulders collected from the Mineral Mountains east of the Utah FORGE site where lithologies similar to those in the reservoir are exposed on the surface, have been sent to external R&D recipients at the University of Pittsburg and Penn State University.

Additional core samples from 16A(78)-32 and 58-32 were sent by Utah FORGE to Metarock Laboratories to document thermal expansion and compressional velocity at various pressuresto better understand properties of the reservoir rock.

Two core samples from the pilot well 58-32 were dated via U-Pb geochronology of zircons by graduate student Kyle Krajewski at the University of North Carolina at Chapel Hill (Drew Colman supervisor). A diorite dike from well 58-32 in a core sample from 7,443 ft yielded a weighted mean age of 12.06 ± 0.14 Ma, showing that it is younger than the granitic host rock which was dated at 21.975 ± 0.022 Ma. Analyses of Mineral Mountains Batholith outcrop samples led to the conclusion that the ages of the granitoid increase (25-12 Ma) from the NW to SE and that cooling ages (16-9 Ma, biotite Ar-Ar) decrease across the same transect.

Lessons Learned

A mix of lithologies have been intersected by drilling beneath the Utah FORGE site, including granitoid and gneiss. As they resemble rock types occurring in the Mineral Mountains, it is clear that the crystalline basement that hosts the Utah FORGE EGS reservoir is part of a laterally extensive complex of rocks which form the basement units on the east side of the north Milford

valley.

Reference

Le Maitre, R.W., Dudek, P., Keller, A., Lameyre, J., Le Bas, J., Sabine, M.J., Schmid, P.A., Sorensen, R., Streckeisen, H., Woolley, A., and Zanettin, A.R., 1989, A classification of igneous rocks and glossary of terms—Recommendations of the International Union of Geological Sciences, Sub commission on the Systematics of Igneous Rocks: International Union of Geological Sciences. Blackwell Science, Oxford, p. 236.

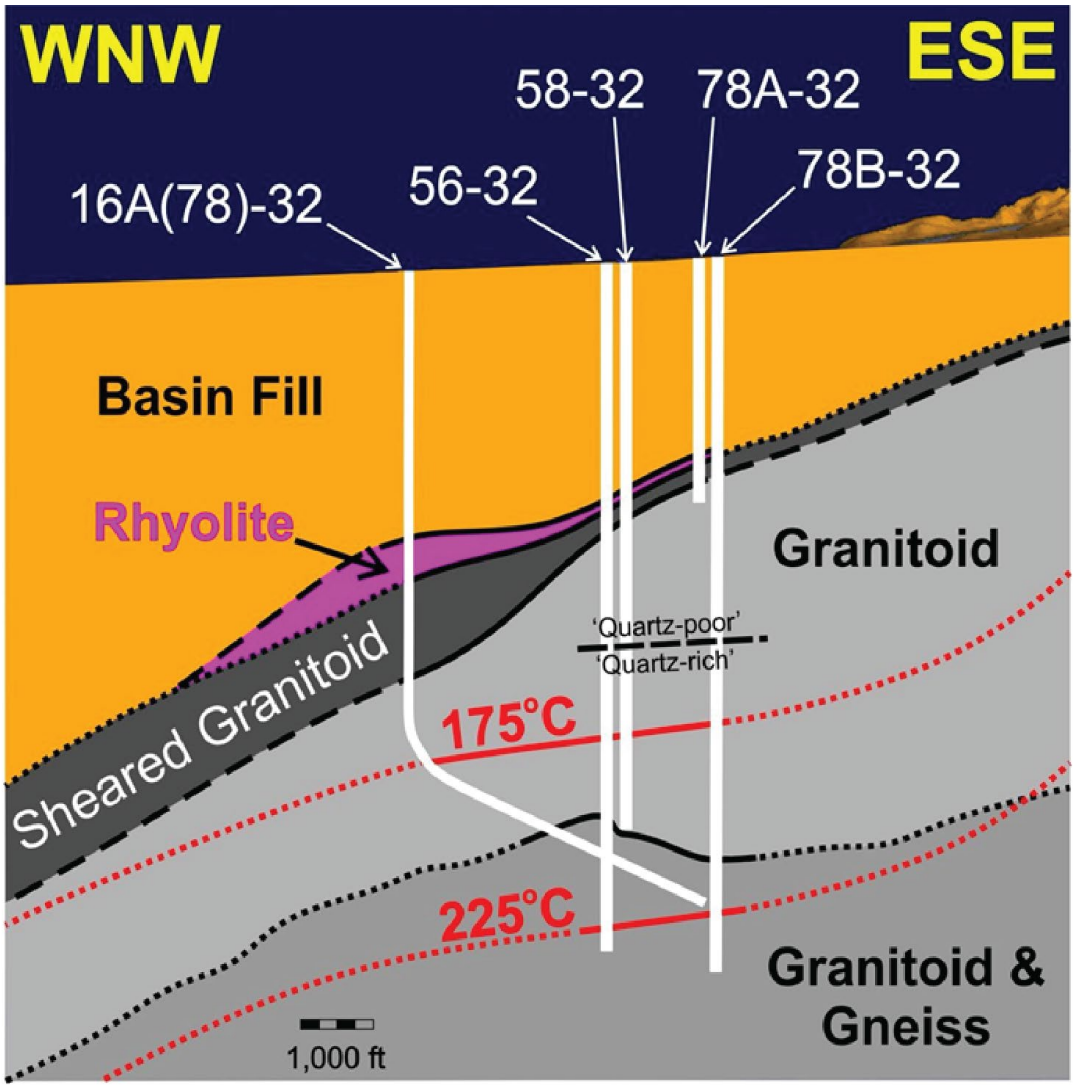

Figure 1. *Cross-section of the Utah FORGE EGS reservoir based on XRD analyses and petrologic thin section examination of cuttings and core.*

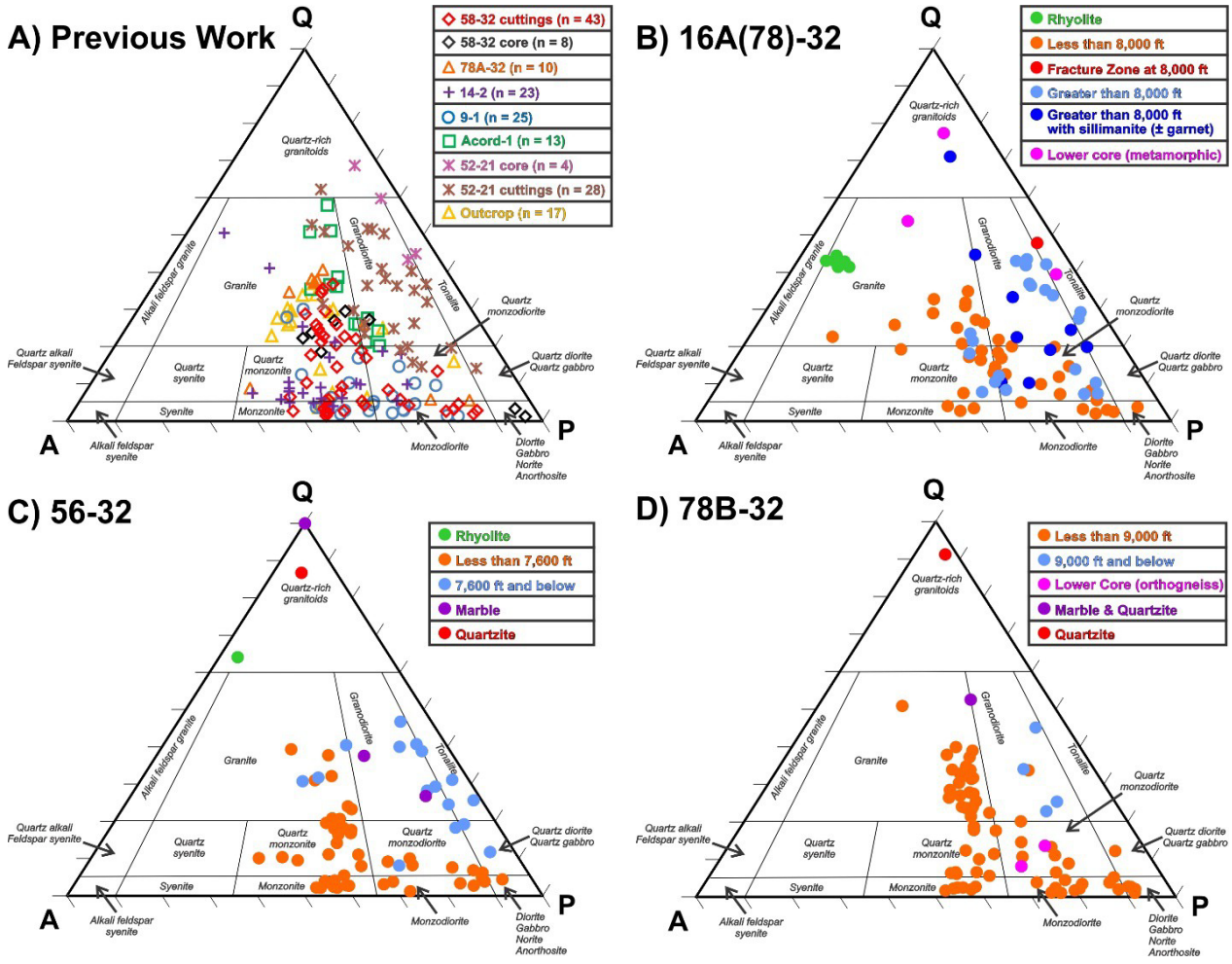

Figure 2. *XRD data from the basement rocks encountered in boreholes drilled within and adjacent to the Utah FORGE site. The data are normalized to 100 weight percent quartz (Q), alkali/K-feldspar (A), and plagioclase (P) and plotted on the IUGS classification diagram for plutonic rocks (Le Maitre et al., 1989). A) XRD data from wells drilled prior to the reporting period from within and adjacent to the Utah FORGE site. B) XRD data from basement rocks encountered in well 16A(78)-32 with samples differentiated by sample type, rock type, mineralogy and depth as shown in the legend. C) XRD data from basement rocks encountered in well 56-32 with samples differentiated by rock type and depth as shown in the legend. D) XRD data from basement rocks encountered in well 78B-32 with samples differentiated by sample type, rock type and depth as shown in the legend.*

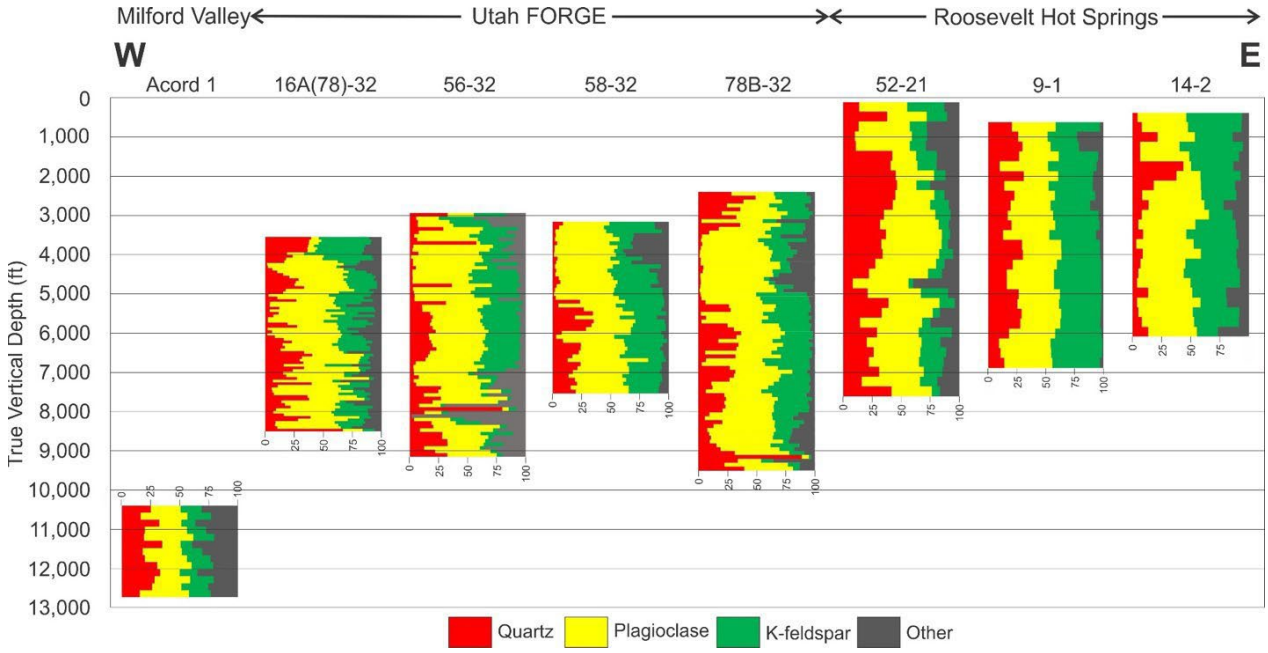

Figure 3. *Bulk XRD results of cuttings samples of the Mineral Mountains batholith divided into abundances of quartz, plagioclase feldspar, K-feldspar (alkali feldspar), and other (in weight percent of sample) plotted at measured depth for all wells with the exception of deviated well 16A(78)-32 which is plotted vs true vertical depth. The figure represents a rough east to west transect from wells in or around the Roosevelt Hot Spring geothermal system (14-2, 9-1 and 52-21) in the east, into the FORGE project (78B-32, 58-32, 56-32 and 16A(78)-32) and out into the Milford Valley to the west (Acord 1).*

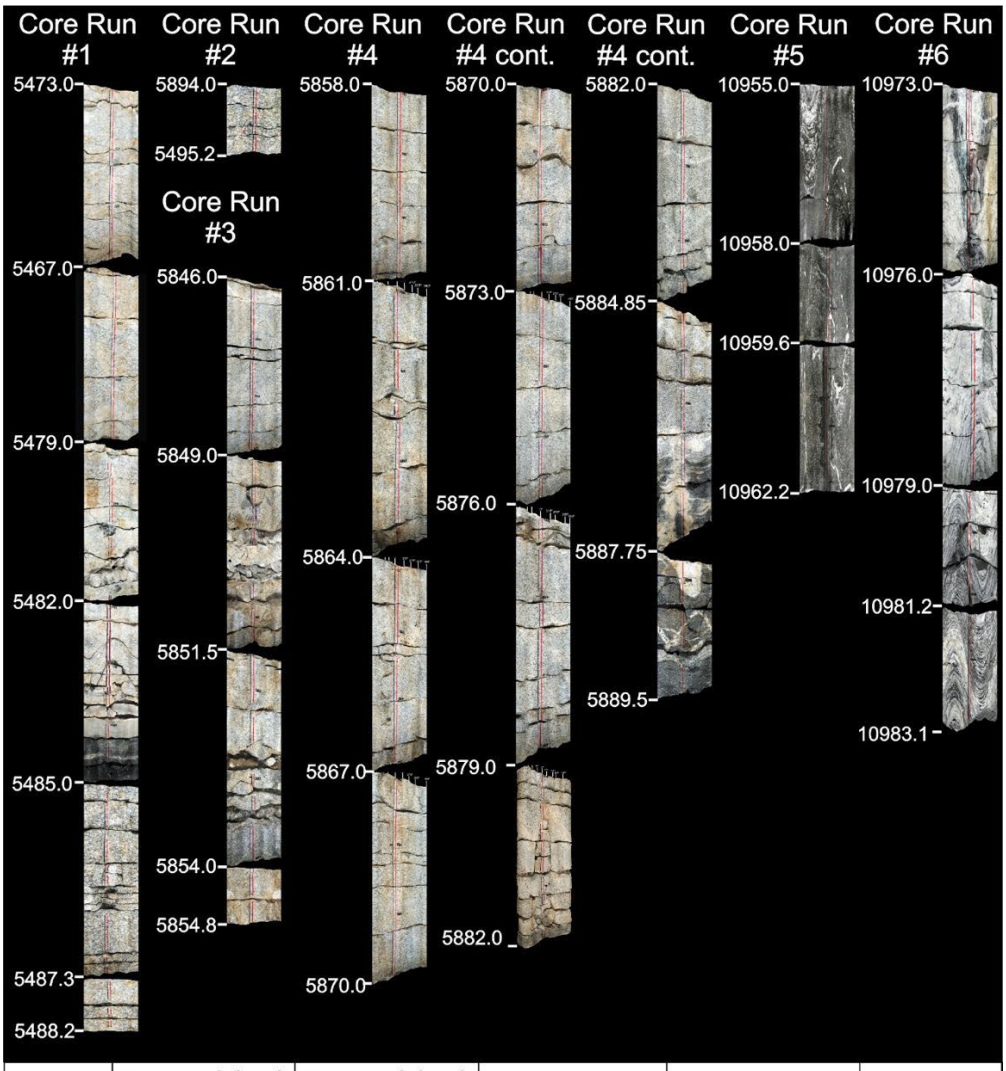

Core run	Measured depth top (ft)	Measured depth bottom (ft)	Cored lengthl (ft)	Core recovery (ft)	Recovery (%)
1	5,473	5,494	21	15.2	72%
2	5,494	5,505	11	1.2	11%
3	5,846	5,856	10	8.8	88%
4	5,858	5,892	34	31.5	93%
5	10,955	10,971	16	7.2	45%
6	10,973	10,987	14	10.1	72%
		Totals	**106**	**74.0**	**70%**

Figure.4. *Images of core recovered from Utah FORGE well 16A(78)-32 (top) divided by core run and marked with measured depths. These images are 360° views of the cylindrical core's exterior, a product of the Utah Geologic Survey. A summary each core run is given at the bottom of the figure.*

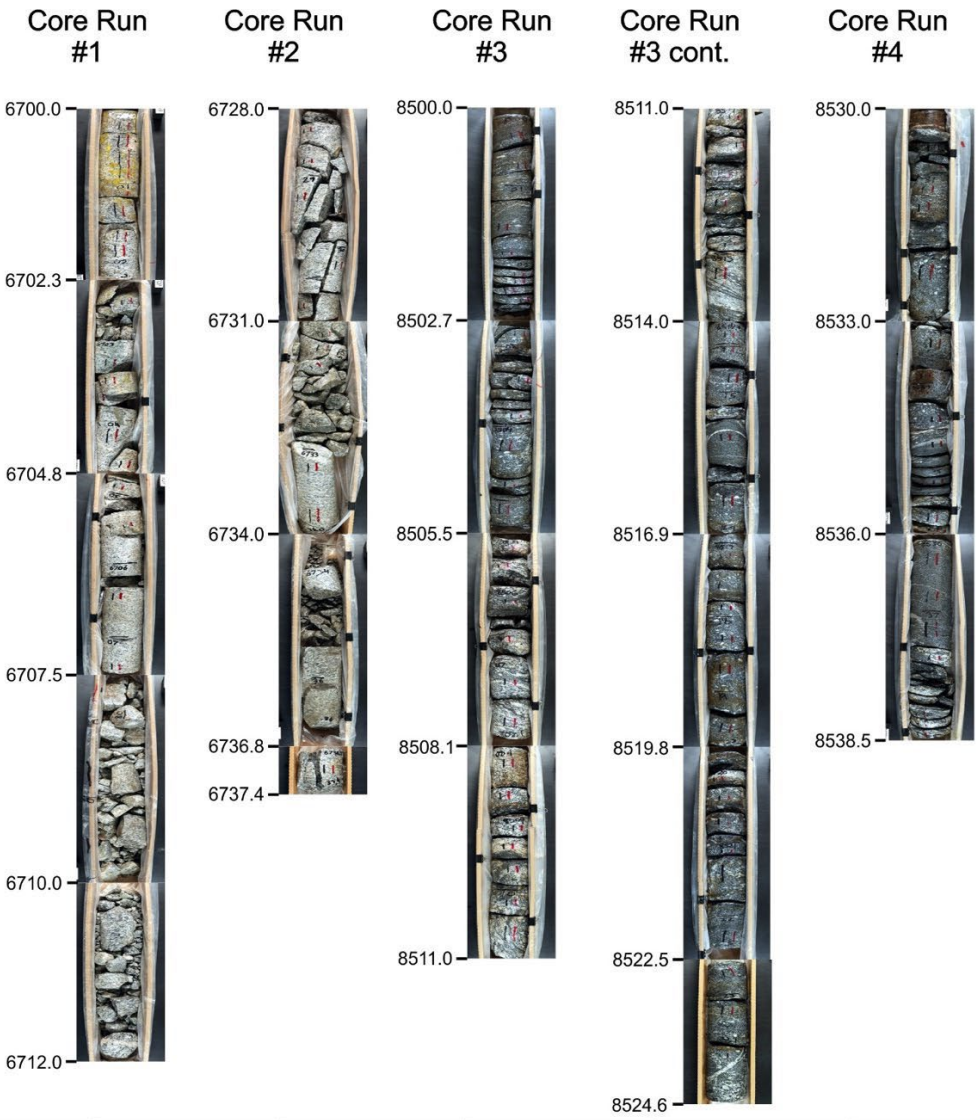

Core run	Measured depth top (ft)	Measured depth bottom (ft)	Cored length (ft)	Core recovery (ft)	Recovery (%)
1	6,700	6,728	28	12.0	43%
2	6,728	6,740	12	9.4	78%
3	8,500	8,530	30	24.9	83%
4	8,530	8,540	10	8.5	85%
		Totals	**80**	**54.8**	**68%**

Figure 5. *Images of core recovered from Utah FORGE well 78B-32 (top) divided by core run and marked with measured depths. These images show the highly fractured core in boxes that have been expanded (widened) to better show rock textures. A summary each core run is given at the bottom of the figure.*

Attachment 2

Phase 3A Year 2 Annual Report – Appendix A2

Enhanced Geothermal System Testing and Development at the Milford, Utah FORGE Site

Utah FORGE
University of Utah
423 Wakara Way, ste 300
Salt Lake City, UT, 84105

Prepared for the U.S. Department of Energy

Office of Energy Efficiency and Renewable Energy

Contract DE-EE0007080

April 30, 2022

Water Chemistry and Hydrology

Since the beginning of the Utah FORGE project, groundwater chemistry data have been compiled and augmented with new data to characterize the nature and possible origins of shallow fluids and to identify potential sources of water required for the Utah FORGE project operations. In Phase 3, twelve new groundwater samples were collected and analyzed. Groundwater data are now available from 23 sites that were sampled in the period 2018-2021 across the North Milford Valley and in the vicinity of Utah FORGE https://gdr.openei.org/submissions/1139.

Figure 1 shows the samples sites and the spatial variation in groundwater compositions. Orange-filled Stiff plots and chloride concentration contours demarcate a plume of saline water (>2000 TDS) that originates from the Roosevelt Hot Springs hydrothermal system as represented by well 45-3, which has the highest chloride concentration (>4000 mg/kg Cl). The upper reaches of the plume flows in a westerly direction down hydraulic gradient turning northward as the center of the North Milford Valley is approached. The hot water cools as it flows laterally through shallow aquifers hosted by basin fill alluvium that overlies the granitic basement rock. It was intersected and sampled during the drilling of well 78-32 located in the eastern part of the Utah FORGE site, and groundwater from BRW appears to be the most distal representative of the outflow plume. The high TDS concentrations of these groundwaters has long been known, and as a result, this water is non-potable and unsuitable for stock tanks or human consumption. On the northern and southern fringes of the plume, groundwaters are more dilute (500-2000 TDS; 100-1000 mg/kg Cl, green-filled Stiff plots) representing a gradation in composition likely caused by mixing and interaction with regional fresh groundwaters (<500 TDS; <100 mg/kg Cl, blue-filled Stiff plots) found in wells on the periphery of the survey area.

Water levels at WOW2 and WOW3 have been recorded continuously since February 2019 (Figure 2; https://gdr.openei.org/submissions/1371). These are the only wells in which access for such measurements are available, and the results are adjusted for barometric change using data from a logger located at the WOW3 site. WOW2 shows relatively continuous water levels and total change of less than 0.5 feet, whereas WOW3 shows much greater variability of up to 20 feet. This variability is likely due to the confined nature of the aquifer at WOW3 and its proximity to supply wells located west and north of the Utah FORGE site that are subject to intermittent pumping.

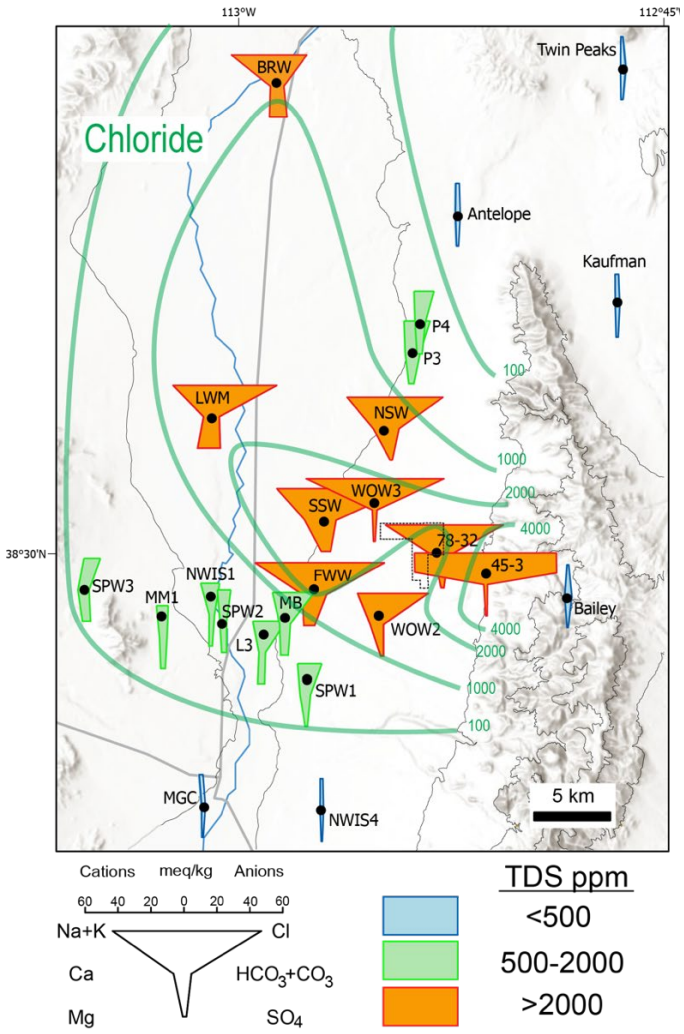

Figure 1. *Geochemistry and spatial variation in groundwater compositions across the North Milford Valley and the vicinity of Utah FORGE based on data collected in the period 2018-2021. Groundwater compositions are graphically represented as color-coded Stiff plots, and the green contours reflect the gradient in chloride concentrations (mg/kg). The Utah FORGE site is delineated by the thin black line near well 78-32. The Beaver River which flows from south to north is represented by the blue line on the west side of the map. Bailey is a freshwater spring in the Mineral Mountains.*

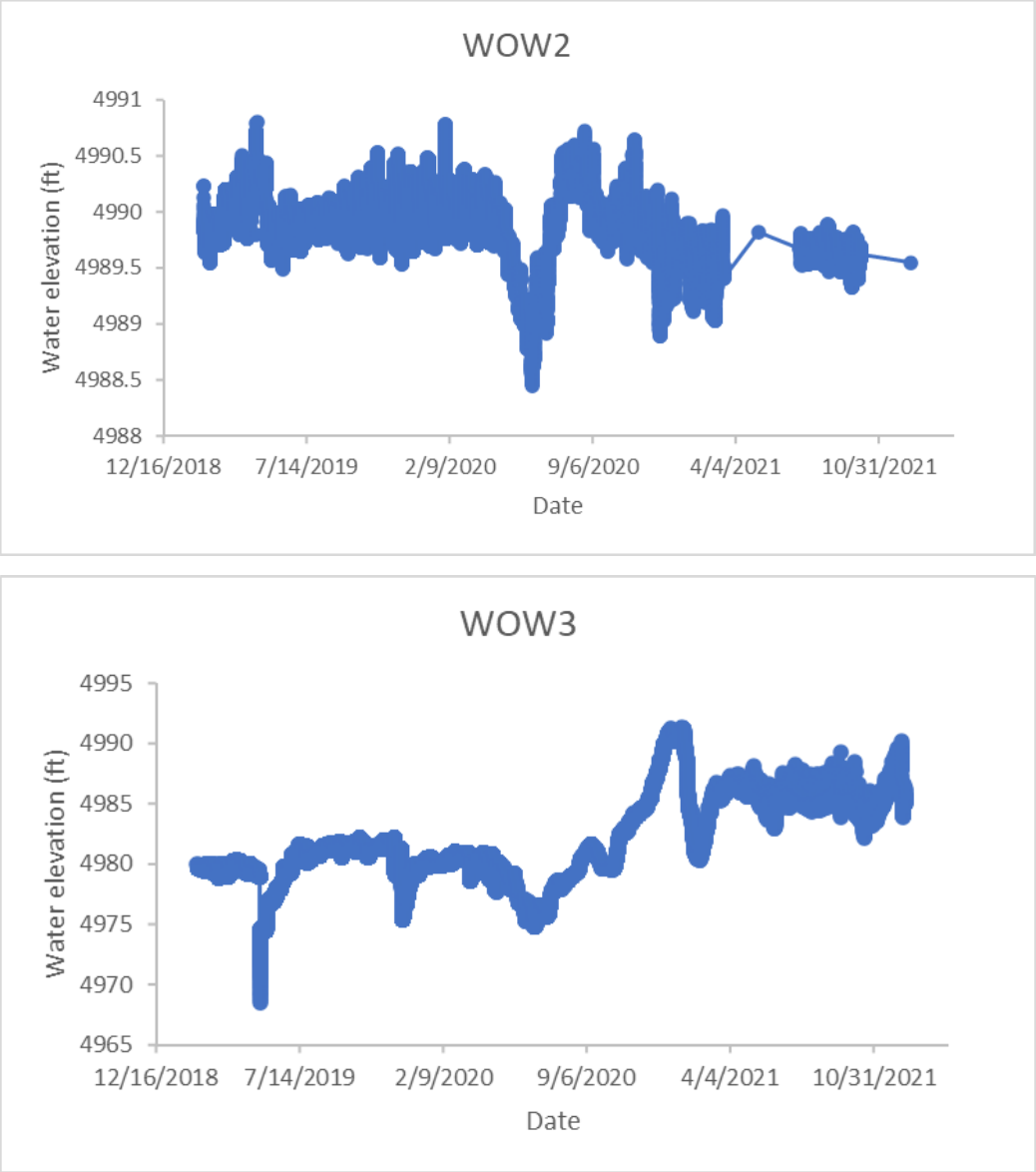

Figure 2. *Continuous water levels for the WOW2 and WOW3 monitoring sites. Water level fluctuations likely result from disturbances caused well pumping and/or infrastructure development near these sites.*

An accompanying survey of helium isotope compositions in groundwaters reveals a large mantle He anomaly (R/Ra>2) covering an area ~25x25 km^2, which incorporates the upflow zone of the Roosevelt Hot Springs hydrothermal system (Figure 3). The enormity of the anomaly which extends across the variation in groundwater compositions shown in Figure 1, suggests the existence of multiple pathways for deep sourced helium to transect the crust. Some clues about the nature of these pathways are interpreted from the gradients in the $^{4}He/^{20}Ne$ ratio, wherein higher values are believed to represent the noble gas composition at mid-crustal levels (>10 km below the surface); by contrast, low $^{4}He/^{20}Ne$ values reflect inmixing of atmospheric helium. The contouring of values suggests that underlying conduits have an east-northeast

trend. More importantly, the size of the mantle He anomaly suggests the potential area of geothermal resource is much larger than what has been determined so far from heat flow assessments alone. This is the subject of ongoing analysis.

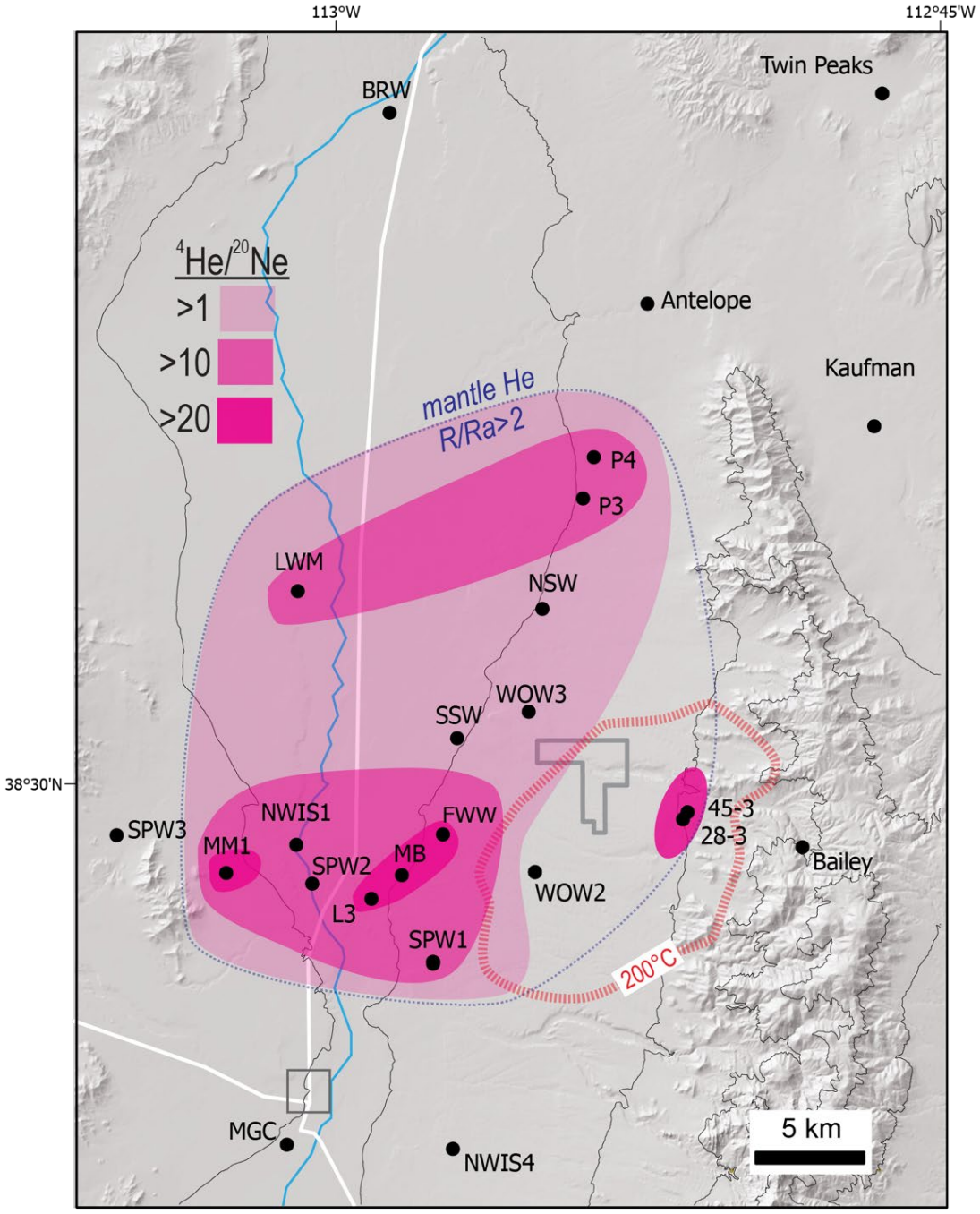

Figure 3. *Map showing the extent of the North Milford valley mantle helium anomaly and the internal variation in $^4He/^{20}Ne$ ratios. The 200°C contour at 3 km depth is shown for reference.*

Lessons Learned

Groundwater compositions in the vicinity of Utah FORGE are controlled by outflow of hydrothermal fluids from Roosevelt Hot Springs. This outflow extends into the center of the North Milford valley and then flows northward down the hydraulic gradient. Water level changes in two continuously monitored wells show the variable and localized effects of pumping, which are unrelated to drilling and stimulation activities at Utah FORGE. The detection of an extensive mantle helium anomaly based on helium isotope ratios suggests the existence of a geothermal resource that is much larger than that predicted from heat flow studies alone.

Attachment 3

Phase 3A Year 2 Annual Report – Appendix A2

Enhanced Geothermal System Testing and Development at the Milford, Utah FORGE Site

Utah FORGE
University of Utah
423 Wakara Way, ste 300
Salt Lake City, UT, 84105

Prepared for the U.S. Department of Energy

Office of Energy Efficiency and Renewable Energy

Contract DE-EE0007080

April 30, 2022

Attachment 3

Phase 3A Year 2 Annual Report – Appendix A2

Enhanced Geothermal System Testing and Development at theMilford, Utah FORGE Site

Utah FORGE University of Utah

423 Wakara Way, ste 300

Salt Lake City, UT, 84105

Prepared for the U.S. Department of Energy

Office of Energy Efficiency and Renewable Energy

Contract DE-EE0007080

April 30, 2022

Annual Research Performance Progress Report

Subtask 3.7.1. High Resolution Magnetotelluric (MT) Survey

In the first two years of Phase 3 of Utah FORGE, quantitative 3D analysis of 122 tensor MT stations acquired in Phase 2C was undertaken (Figure 3.7.1-1). The results are intended to: 1), Delineate the densities of faults and fractures in crystalline basement rocks so that they can be compared to independent data acquired from drilling, geologic field mapping, seismic reflection and gravity surveys, and to properties in the Mineral Range; 2), Illuminate potential heat sources for the Utah FORGE area and perhaps adjacent Roosevelt Hot Springs (RHS); and 3), Derive baseline 3D resistivity structure for possible MT monitoring of temporal changes in resistivity structure following well stimulation. Most of what is discussed below is described in Wannamaker et al (2021). The acquired Utah FORGE MT data set from contractor Quantec Geoscience Inc. was merged with the broader MT set in the region including the adjacent SubTER and Play Fairway Analysis responses for a total of 470 sites. Use of an ultra-remote MT reference in western Nevada helped improve midband data quality in places where cultural and geothermal field noise was strong. Most soundings were given ~15 hours of recording that ran over-night. Good data quality at most sites was obtained in the period range 0.005 to 850 s, which covers the depth interval ~200 m to 50 km.

Analysis centers on use of our 3D finite element (FE) algorithm described by Kordy et al (2016a,b) supported by prior DOE/GTO contract DE-EE002750 to Wannamaker. It has been used in various Play Fairway Analysis (PFA) and related studies (e.g., Wannamaker et al., 2019). A finite element mesh for inversion imaging was constructed which accommodates the MT data in the region (Figure 3.7.1-2). The mesh consists of 162 (x=north) by 166 (y=east) by 60 (z=down) cells with 15 layers of air. Project area elevations for the finite element mesh nodes are from the SRTM resource and the outmost FE surface elevations are fixed to a regional average of 1500 m. The mesh is deformed vertically to mimic the topography at the air-earth interface. It also is deformed in the E-W direction such that the FE cells representing the Kern River pipeline passing between the Utah FORGE project area andthe Roosevelt Hot Springs can mimic its path with minimal deviation through the broader Utah FORGE area. In addition, to be precise, the mesh x-axis is oriented N020 so that the pipeline aligns directly up the page in the vicinity of FORGE and RHS.

The smallest cell widths in the center of the MT data coverage are 200 m, except across the Kern River pipeline (see below), while the thinnest cells at the surface are 30 m growing by 15% per element with depth. Element thicknesses in the reservoir zone at depths of ~2.5 km are ~300 m; for any subsequent temporal modeling of resistivity associated with reservoir injection, a new mesh will be defined which is more local and with finer element discretization. Apart from a two-element rim around the mesh edge and the fixed air resistivity, all elements are inversion parameters for a total of 1126224. Air is assigned a fixed resistivity at 10^{18} Ωm, while the earth starting resistivity is 40 Ωm. The inversion period range is 0.0133 to 500 s. Error floors are applied to the real and imaginary parts of the complex impedance elements Zij of 5%(|Zxy-Zyx|/2) and to the tipper elements of 0.04 at each frequency. The inversion is parallelized to run on a linux workstation with 36 cores and 1.5 TB RAM and takes about three weeks. Numerous test runs were done to fine tune stabilization.

The Kern River pipeline is represented by a 4x4 line of elements each 12.5 m wide for a total pipeline width of 50 m. In this fashion, the pipeline is narrowed and does not require any side-stepping to represent pipe meanders along its path as is necessary with finite difference modeling codes; the finite element flexibility should be much more favorable for accurate current flow. The finite element approach also allows a higher contrast between pipe and earth host, and reduces the effect of finite cell width. The pipeline is buried in the mesh at a nominal depth of 50 m and inverted MT stations do not lie closer than 500 m to the pipe. We examined several starting guesses for pipeline resistivity. Published property accounts suggest an equivalent resistivity of 0.0182 ohm-m within the 50 m wide pipe representation to preserve conductivity-area product of the 0.5” thick, 42” diameter carbon steel pipe. Aeromagneticsurveying centered on the Mineral Mountains to the east in the SubTER project indicated that the pipe had negligible magnetic permeability. However, inversion experience over time suggests that the pipe acted as though discontinuous in its electrical conduction along its length, with electrical interruptions at kinks in its orientation. These variations only appear to affect earth structure within 1-2 km of the pipe in the several inversion runs we tried. This matter is undergoing further investigation.

A model fitting the data well using the low starting pipe resistivity is shown in Figures 3.7.1-3 through 3.7.1-7. A final nRMS misfit in the impedance data of 1.28 is achieved from a starting value of 21.8 for the preferred resistivity model shown here. To start, the crystalline lithology below the Utah FORGE project area is of very high resistivity, on the order of 10,000 ohm-m. That is consistent with very low porosity and the absence of significant fracturing. On the other hand, strong N-S low-resistivity lineaments are visible in the central Mineral Mountains in the upper few km in analogous lithology (Figures 3.7.1-5 and 3.7.1-6). These curious features correlate with N-S steep preferred fracture patterns with movement mapped in the Mineral Mountains (Bartley, 2019) under the Utah FORGE project. In the deeper plan view at 3.6 km (Figure 3.7.1-3), the conductive lineaments correspond closely with the locus of seismic swarm events discussed by Mesimeri et al (2021), the typical interpretation of which involves deep fluid upwelling and diffusion. These and other features are discussed in more detail in Wannamaker et al (2021).

At greater depths (Figure 3.7.1-4), a conductive body under the main Quaternary rhyolite flows may be related to that igneous event, mostly likely remnant fractured and fluidized rock. Significant low resistivity bodies also are seen below the northern Cove Fort-Dog Valley areas to the northeast, below Twin Peaks to the northwest, and below northern Milford Valley to the west. These all are locations of enhanced ^{3}He in water samples recovered from deep water wells or springs (S. Simmons, 2021, pers. comm.). Below 12km, the Mineral Mountains body begins to merge with the Cove Fort transverse zone to the east (Rowley et al., 2013) (Figure 3.7.1-4). This effect increases with depth. These features too are discussed in more detail in Wannamaker et al (2021).

Further structural and thermal insights from the MT model are apparent in E-W section views across the Mineral Mountains. In Figure 3.7.1-5 through the Roosevelt Hot Springs and Mineral Mountains, a high-angle low-resistivity structure originating in the lower crust rises with a strand projecting directly into the Roosevelt Hot Springs producing area (Allis et al., 2019). The added aperture to the west by including the Utah FORGE MT data was crucial in resolving this deeper structure to a better extent than is possible for either data set individually. Such structures have been correlated with crustal scale permeability and magmatic input at other geothermal systems such as Dixie Valley and McGinness Hills (Wannamaker et al., 2019). In the southerly cross section of Figure 3.7.1-5, the low resistivity structure in the upper 5 km shows more complexity, with a sharp lateral bend coincident with the centroid of the seismic swarm of Mesimeri et al (2021). Diverse structural intersections associated with periodic fluid release are suggestive of fault valve phenomena (Sibson, 2014), with the fluid source being a mixture of deep magmatic and circulating meteoric waters (Wannamaker et al., 2021).

Additional section views are shown in Figure 3.7.1-6. A section near the north end of the Mineral Mountains north of Pinnacle Pass shows the prior deep conductor veering eastward and merging with the Cove Fort transverse zone. A concentrated shallowing of low resistivity now underlies the Cove Fort geothermal area and presumably represents and upwelling of fluids and heat. A N-S section through Milford Valley shows the northern Milford Valley conductor of Figure 3.7.1-6 which dips northward and may represent an auxiliary source of heat on the west side of theUtah FORGE system. Its presence also is consistent with elevated ^{3}He anomalies in well ground waters beneath central Milford Valley (R/Ra of order 2) that do not appear to correlate with major element water chemistry and thus cannot merely reflect outflow from the Roosevelt Hot Springs (S. Simmons, S. Kirby, pers. comm.). Finally, a N-S section down the central Mineral Mountains shows the Moho-level conductorupwelling as seen in Figure 3.7.1-4b below the northern rhyolite domes which them veers eastward toward Cove Fort. A pronounced, steeply north-dipping conductor connects from the Twin Peaks Quaternary rhyolite center to the lower crust and is taken to represent the pathway of magmas upward to eruption.

An interpretive portrayal of magmatic and eruptive processes that may pertain to the Mineral Mountains and the FORGE/RHS area is shown in Figure 3.7.1-7. It is a slightly deeper view through the swarm area to demonstrate that the lower crustal low-resistivity magma underplating zone is limited in depth extent. This geometry compares favorably to that generated in computer continuum modeling by Schubert et al (2013) where progressive buildup of basaltic magma at Moho levels generates rhyolite above through differentiation and hybridization, induces overpressures, and leads to eruption of rhyolite potentially to the surface in time frames of only a few thousand years. The process may be periodic if upper mantle basalt replenishment is continuous.

Toward the close of this project period, the extensive MT data set taken over the Sevier basin to the north

of the Mineral Mountains and Utah FORGE was integrated with the data described herein and a sufficiently large finite element inversion mesh defined to contain the total data set (Figure 3.7.1-8). An inversion run was started in the last week of December, 2021, and is expected to run for approximately one month on our 1.5 TB large-RAM workstation. Additional test runs are expected to be necessary. We expect the magmatic geothermal structure to differ significantly under the northern region as the upper one-third of the crust is dominated by Paleozoic sediments and the lower crust has not been intruded by mid-Cenozoic plutonic rocks. A preliminary inversion model of just the Sevier Basin area appears in Wannamaker et al (2013).

Wannamaker presented 3D inversion analysis and thermal implications of the joint Utah FORGE-SubTER-PFA MT data sets in the area in person at the 2021 annual meeting of the GRC in San Diego,October 5, 2021 (Wannamaker et al., 2021).

References:

Allis, R., M. Gwynn, C. Hardwick, W. Hurlbut, S. M. Kirby and J. N. Moore, Thermal characteristics of the Roosevelt Hot Springs system, with focus on the FORGE EGS site, Milford, Utah, in Allis, R., and J. N. Moore, eds, Geothermal characteristics of the Roosevelt Hot Springs and adjacent FORGE EGS site, Milford, Utah, Utah Geological Survey Miscellaneous Publication, 169-D, 22 pp., 2019.

Bartley, J. M., Joint patterns in the Mineral Mountains intrusive complex and their roles in subsequent deformation and magmatism, in Allis, R., and J. N. Moore, eds, Geothermal characteristics of the Roosevelt Hot Springs and adjacent FORGE EGS site, Milford, Utah, Utah Geological Survey Miscellaneous Publication, 169-C, 13 pp., 2019.

Kordy, M. A., P. E. Wannamaker, V. Maris, E. Cherkaev, and G. J. Hill, Three-dimensional magnetotelluric inversion using deformed hexahedral edge finite elements and direct solvers parallelized on SMP computers, Part I: forward problem and parameter jacobians: Geophysical Journal International, 204, 74-93, 2016a.

Kordy, M. A., P. E. Wannamaker, V. Maris, E. Cherkaev, and G. J. Hill, Three-dimensional magnetotelluric inversion using deformed hexahedral edge finite elements and direct solvers parallelized on SMP computers, Part II: direct data-space inverse solution: Geophysical JournalInternational, 204, 94-110, 2016b.

Mesimeri, M., K. L. Pankow, B. Baker, and J. M. Hale, Episodic earthquake swarms in the Mineral Mountains, Utah driven by the Roosevelt hydrothermal system: Journal of Geophysical Research:126, e2021JB021659, https://doi.org/10.1029/2021JB021659, 15 pp., 2021.

Moore, J., S. Simmons, J. McLennan, K. Pankow, P. Xing, C. Jones, A. Finnela, P. Wannamaker and R. Podgorney, Current Activities at the Utah Frontier Observatory for Research in Geothermal Energy (FORGE): A Laboratory for Characterizing, Creating and Sustaining Enhanced Geothermal Systems: Geothermal Resources Council Transactions, 45, 12 pp. 2021.

Nielson, D. L., Evans, S.H., and Sibbett, B.S., Magmatic, structural, and hydrothermal evolution of the Mineral Mountains intrusive complex, Utah: Geological Society of America Bulletin, 97, 765-777, 1986.

Rowley, P. D., E. F. Rutledge, D. J. Maxwell, G. L. Dixon, and C. A. Wallace, Geology of the Sulphurdale geothermal-resource area, Beaver and Millard counties, Utah: Utah Geological Survey, Open-File Report, 609, 33 pp., 2013.

Schubert, M., Driesner, T., Gerya, T. V., and Ulmer, P., Mafic injection as a trigger for felsic magmatism: A numerical study: Geochemistry, Geophysics, Geosystems, v. 14, p. 1910–1928, doi:10.1002/ggge.20124, 2013.

Sibson, R. H., Earthquake rupturing in fluid-overpressured crust: How common?: Pure and Applied Geophysics, v. 171, p. 2867–2885, 2014.

Wannamaker, P. E., V. Maris, and C. Hardwick, Basin and rift structure of the central Black Rock Desert, Utah, and initial thermal implications, from 3D magnetotellurics: Geothermal Resources Council Transactions, 37, 41-44, 2013.

Wannamaker, P. E., J. E. Faulds, B. M. Kennedy, V. Maris, D. L. Siler, C. Ulrich, and J. N. Moore, Integrating magnetotellurics, soil gas geochemistry and structural analysis to identify hidden, high enthalpy, extensional geothermal systems: Proc. 43rd Workshop Geothermal Reservoir Engineering, Stanford University, Stanford, CA, SGP-TR-214, 19 pp., 2019.

Wannamaker, P., V. Maris, K. Mendoza and J. Moore, Deep heat and fluid sources for the Roosevelt Hot

Springs hydrothermal system and potential heat for the Utah FORGE EGS from 3D FORGE and SubTER magnetotelluric coverage: Geothermal Resources Council Transactions, 45, 17 pp., 2021.

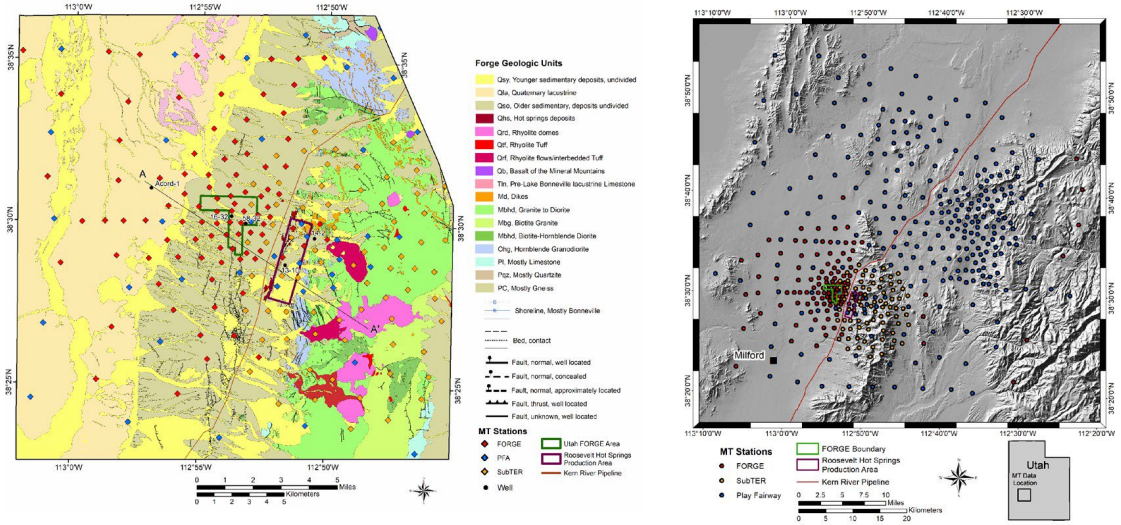

MT Surveying Over FORGE/RHS Areas
Project Scale View

MT Surveying Over FORGE/RHS Areas
Semi-Regional Scale View

Figure 3.7.1-1. MT site survey map of the Utah-FORGE project area showing prior other (blue, OMT) and new station coverage (red, FMT). Red-brown trend running NNE-SSW through the project area is the Kern River pipeline (KRP). Utah FORGE property boundary is shown as dark green polygon Dark red-brown rectangle shows approximate production area of the Roosevelt Hot Springs (RHS) geothermal system. Left view is detailed coverage over Utah FORGE, while right view shows total site distribution going into the 3D inversion model.

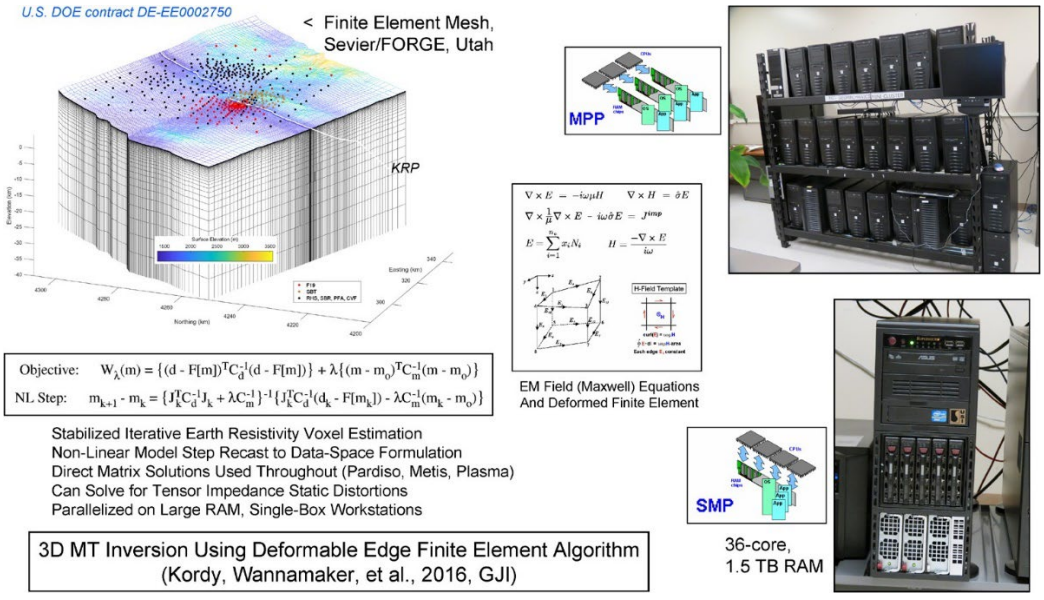

Figure 3.7.1-2. Finite element mesh representation of earth resistivity model for the combined FORGE-SubTER-PFA MT data set (red, orange, black). This file is input to our 3D non-linear inversion algorithm (Kordy et al., 2016a,b). Horizontal units are NAD84 UTM Zone 12S. Principles of the finite element forward and inversion formulation, plus schematics and phots of Shared Memory Processing (SMP) architecture compared to conventional Massively Parallel Processing (MPP) architecture.

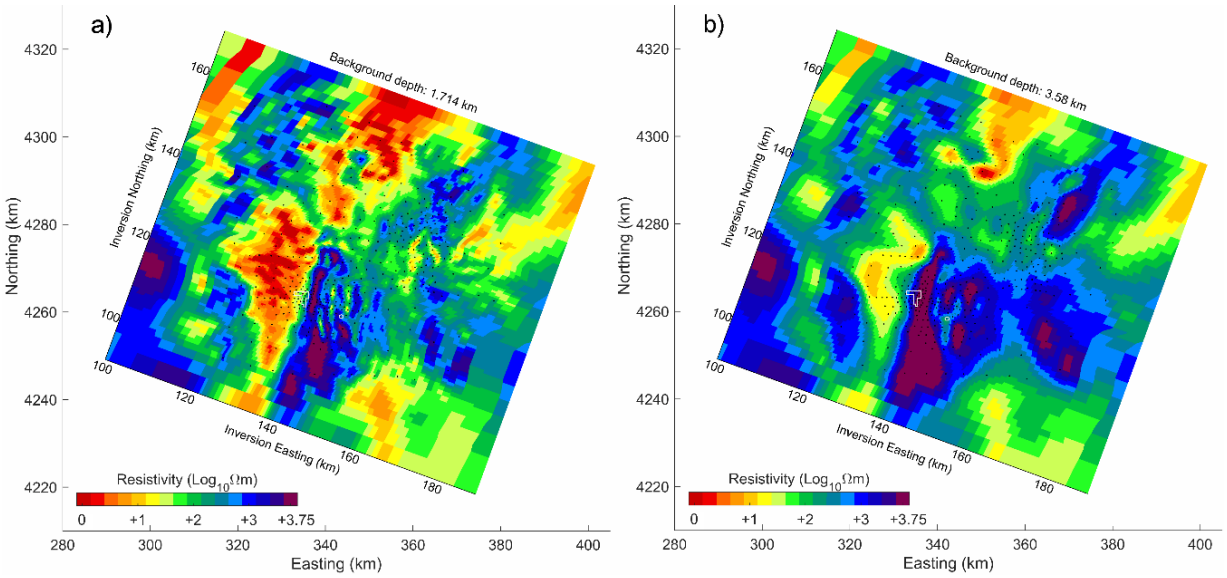

Figure 3.7.1-3. Plan views at two relatively shallow elevation slices through the SubTER-FORGE-PFA MT data set. North is up. Large tabular conductors in upper 2 km in the west-central and north-central areas are Milford Valley and Sevier Basin sediments. Note low-resistivity lineations in the central Mineral Mountains trending north-south. Small white oval near 340.2E 4260N denotes location of seismic swarm discussed by Mesimeri et al (2021).

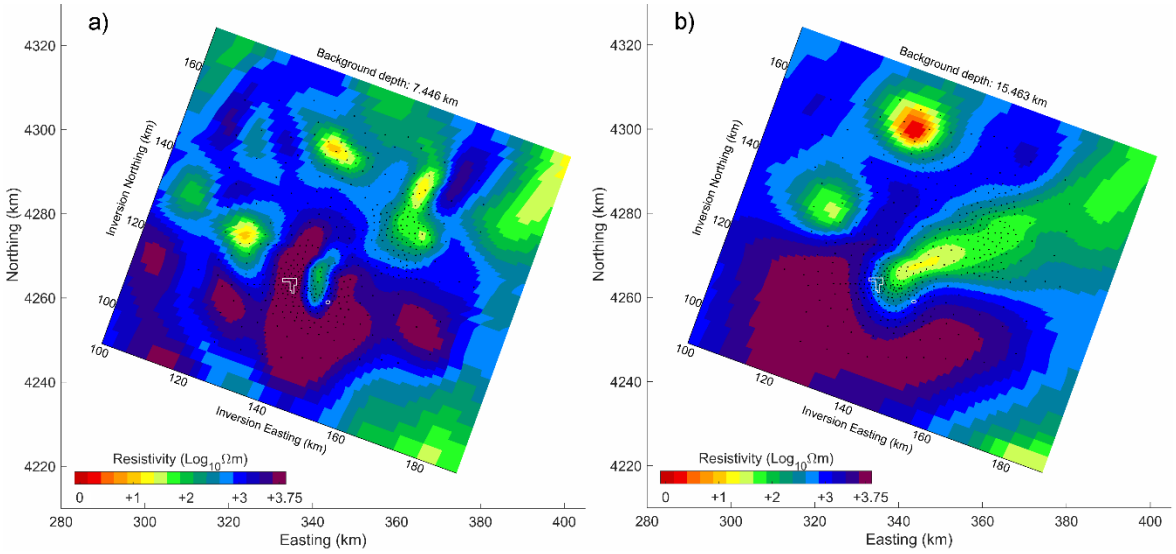

Figure 3.7.1-4. Plan views at two deeper elevation slices through the MT data set. North is up. Left view reveals possible low resistivity body below Mineral Mountains Quaternary rhyolite flows, below the northern Cove Fort-Dog Valley areas to the northeast, below Twin Peaks to the northwest, and below northern Milford Valley to the west. At yet deeper levels (b), the Mineral Mountains conductor merges with an ENE trend through the Cove Fort system.

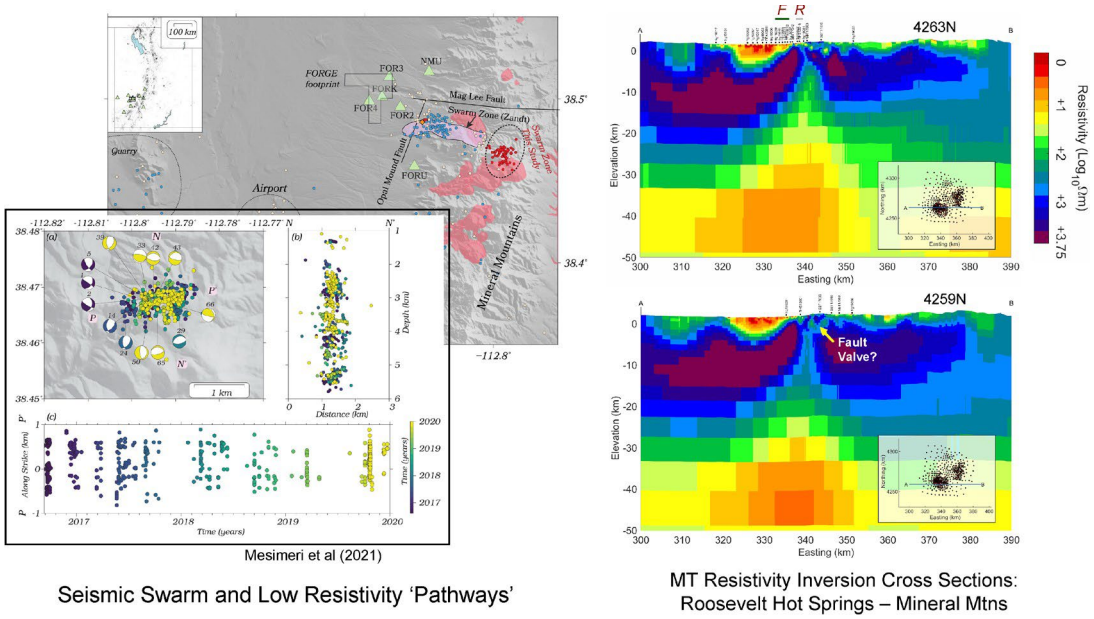

Figure 3.7.1-5. Left: Seismic swarms recorded and discussed by Mesimeri et al (2021) under the Mineral Mountains ESE of FORGE (F) and Roosevelt Hot Springs (R). Right: Two E-W section views through FORGE-SubTER model across the Utah FORGE property, Roosevelt Hot Springs (RHS) and central Mineral Mountains. UTM northing location printed to upper right. Possible fault valve resistivity structure is located coincident with the centroid of the seismic swarm.

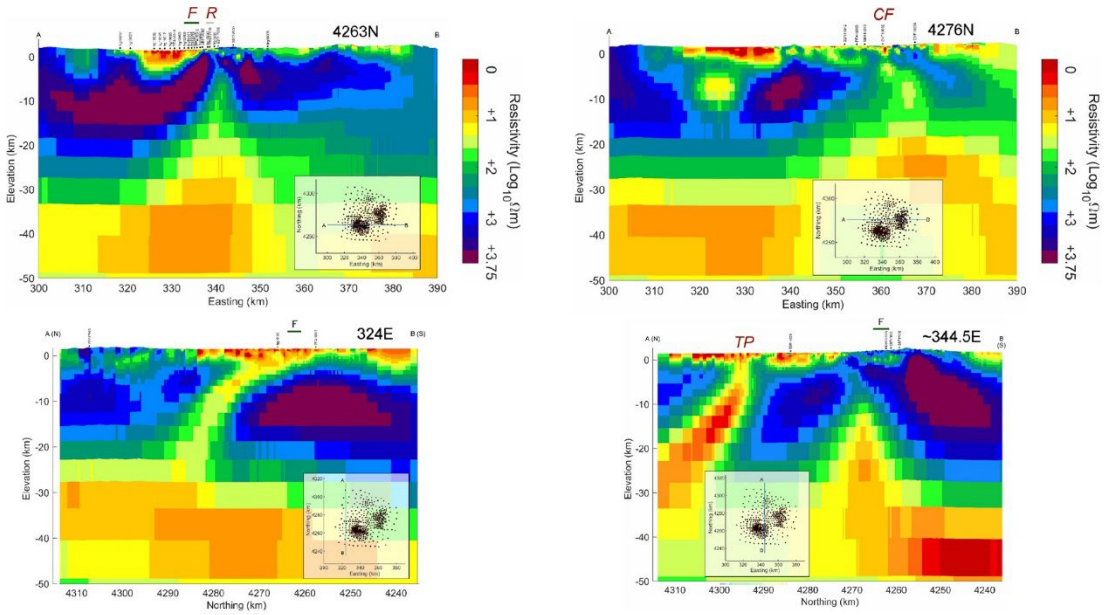

Figure 3.7.1-6. E-W (top) and N-S (bottom) section views through FORGE-SubTER model. CF is Cove Fort and TP is Twin Peaks.

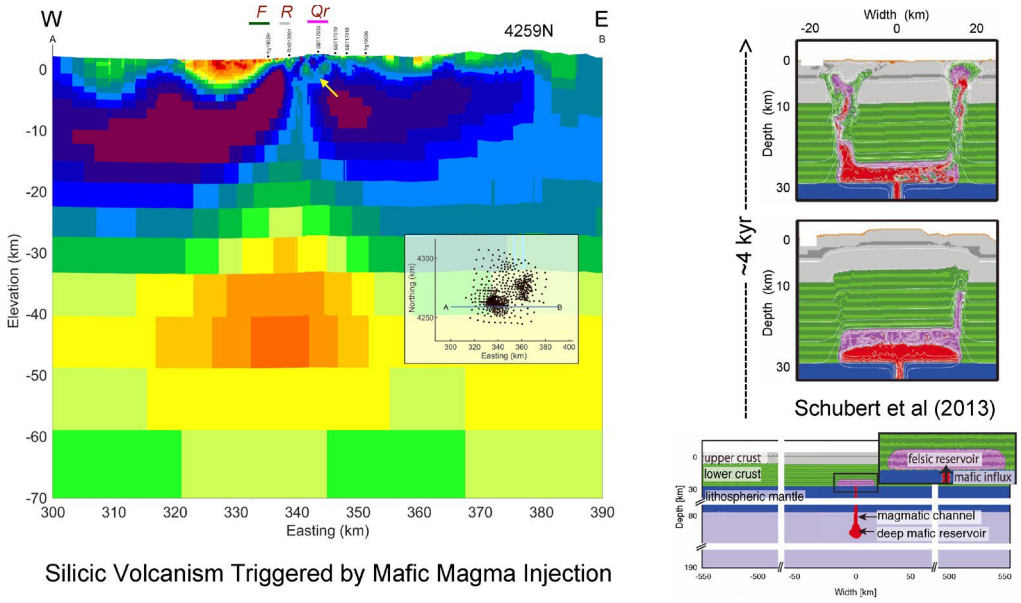

Figure 3.7.1-7. Left: Slightly deeper E-W section view through FORGE-SubTER model along the latitudeof the seismic swarms (yellow arrow). Qr denotes N-S axis of Quaternary rhyolite domes. Right: section views through continuum computer simulation model of Schubert et al (2013) showing evolution of rhyolites formed in response to continuous basaltic undeplating.

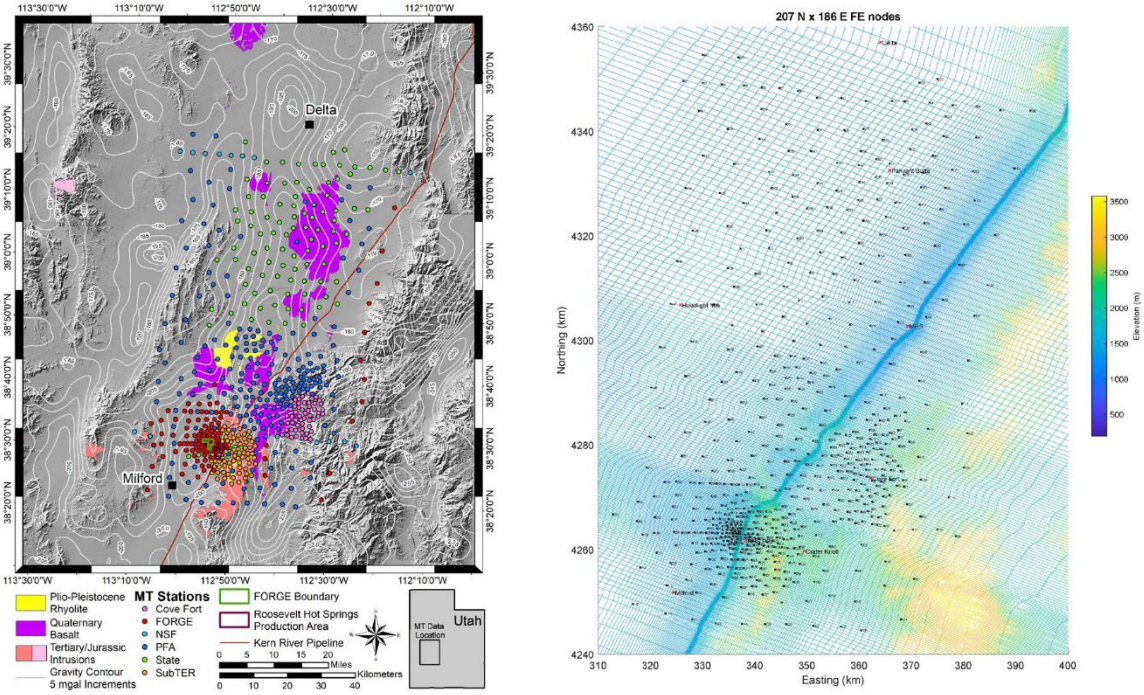

Figure 3.7.1-8. Left: Total MT site distribution currently undergoing inversion analysis. Right: Surface viewof finite element mesh for total MT data set.

Attachment 4

Phase 3A Year 2 Annual Report – Appendix A2

Enhanced Geothermal System Testing and Development at the Milford, Utah FORGE Site

Utah FORGE
University of Utah
423 Wakara Way, ste 300
Salt Lake City, UT, 84105

Prepared for the U.S. Department of Energy

Office of Energy Efficiency and Renewable Energy

Contract DE-EE0007080

April 30, 2022

Progress Report to FORGE

For ENERGY & GEOSCIENCE INSTITUTE (EGI) AT UNIVERSITY OF UTAH

QuarterlyReportTask3_7_3_20211011.docx

Annual Report October 1st, 2019 through March 31st, 2022

Kurt L. Feigl and Sam Batzli

1. *Department of Geoscience, University of Wisconsin-Madison, U.S.A.*

Submitted March 2022

*Address for correspondence
Kurt Feigl
Department of Geoscience
University of Wisconsin-Madison
1215 West Dayton Street
Madison, WI; 53706 USA
feigl@wisc.edu
Tel. +1 608 262-0176; Fax. +1 608 262-0693

SUBTASK 3.7.3 – CONDUCT INSAR ANALYSIS (FEIGL & BATZLI)

This subtask aims to quantify deformation at the Utah FORGE site using Interferometric Synthetic Aperture Radar (InSAR). During this reporting period, we have analyzed the SAR data from early January 2019 (20190131) through December 2021 (20211222). This data set consists of SAR images acquired by TerraSAR-X and TanDEM-X satellite missions operated by the German Space Agency (DLR). DLR charges a fee of 200 EUR for one scene as the cost of fulfilling user requests (COFUR) under the "general science" category. The images acquired on individual dates are listed in Table 1.

As described previously [*Reinisch et al.*, 2018; *Reinisch et al.*, 2020], the InSAR data products are registered ("geo-coded") to a digital elevation model (DEM) in cartographic (Universal Transverse Mercator Zone 12) coordinates to within ~10 m. We have produced geo-coded interferograms for pairs of SAR images that correlate successfully. To produce the interferograms, we analyze the SAR data at UW-Madison using the GMT5SAR suite of open-source software [*Sandwell et al.*, 2011].

We have calculated many different interferometric pairs. We have focused on the stimulation experiment in April 2019, when approximately ~60 cubic meters were injected into Well 58-32 at a depth of approximately ~1350 m (Table 1). An interferometric pair spanning this experiment appears in Figure 1 in terms of wrapped phase. For comparison, two other interferometric pairs, spanning different time intervals, are shown in Figure 2 and Figure 3.

In these individual pairs, we do not observe any deformation that is obviously associated with the deep well 58–32 (black triangle). No deformation larger than several millimeters is expected. The crenulated patterns are probably the result of atmospheric effects that are partially correlated with topography. The wide-scale patterns are probably the result of unmodeled orbital effects in the satellite trajectories. The gray pixels show locations where the radar phase decorrelated between the two different acquisition dates.

To interpret the deformation field, we perform inverse modeling using the General Inversion of Phase Technique (GIPhT [*Feigl and Thurber*, 2009]). We apply this approach to the interferometric pair spanning the time interval from February 22, 2019 to May 10, 2019 to estimate the parameters in a model [*Okada*, 1985]. This model assumes a dislocation buried in a half space with uniform elastic properties. Since the volume injected during the stimulation experiment in March 2019 is small, less than 60 cubic meters, the expected deformation would form a small bowl of subsidence (increasing range) that deviated from a straight line by considerably less than 1 mm (Figure 5).

The results of the inverse modeling appear in Figure 4, which shows the deformation fields in terms of the (wrapped) phase change from InSAR data. The estimated values of the parameters that best fit the InSAR data are listed in Table 2. The estimated tensile opening is not significantly different from zero with 95% confidence. The

volume change estimated from the InSAR data alone is approximately 23 cubic meters. Assuming a shear modulus of 30 GPa, we calculate an equivalent moment of 7 x 10^{11} N.m, corresponding to a moment magnitude $M_w < 1.9$.

The estimated value of the nuisance parameter accounting for an eastward phase gradient, however, is significantly different from zero with 95% confidence. Such a gradient can be interpreted as unmodeled orbital effects. Similarly, the nuisance parameter accounting for an upward phase gradient is marginally different from zero. This gradient can be interpreted as unmodeled tropospheric and/or topographic effects. Such effects probably also account for the red streak to the north of the deep well in the map of observed phase change (panels a and e in Figure 4)

To improve the precision of the deformation measurement, we have formed a stack of 104 interferometric pairs, as listed in the file named **TSX_T30_forge_pairs2019_2021.xlsx.** For each pixel in the stack, we calculate a time series of pair-wise measurements of unwrapped range change in meters. An example time series for one pixel appears in Figure 6. Next, we calculate the mean rate of range change and its standard error for each pixel in the stack with at least 50 good pair-wise measurements.

Figure 3 shows the mean rate of range change in map view. Figure 4 shows the standard error of the mean rate of range change. Figure 5 shows the mean rate for those pixels that have rates that are significantly different from zero with 95% confidence. To make this plot, we calculate the so-called "Z-score" as the mean rate normalized by its standard error. Using the standard error of the estimated rates, we can test the null hypothesis of no deformation. Using a Student's T-test, if the null hypothesis fails to be rejected with 95% confidence, then the mean rate is not shown in Figure 5.

Regarding the area within 300 m of deep well 58-32 in the stack of radar images spanning from January 2019 through December 2021, we do not see any deformation with a mean rate of range increase (downward motion) greater than 3 mm/year. Accordingly, we infer that any processes at work below ground are not causing measurable deformation at the Earth's surface.

The geocoded data products have been delivered to the prime contractor in a CSV file format that can be imported into LeapFrog. These files have been uploaded into the shared data repository at the following URL:

https://foundry.openei.org/29/insar?resources[]=5225261

The data products are also archived at UW-Madison.

In summary, the InSAR data collected through 2021 do not show any measurable deformation in the area immediately surrounding the deep well 15-32. This result is not surprising since the stimulation experiment in March 2019 injected a small volume at a depth of more than 1000 m. Although the stimulation experiment planned for April 2022 will produce more deformation at the earth's surface, it may still be too small to measure by InSAR. A seismic event with magnitude M ~ 4, however, would likely produce measurable deformation, depending on depth and focal mechanism.

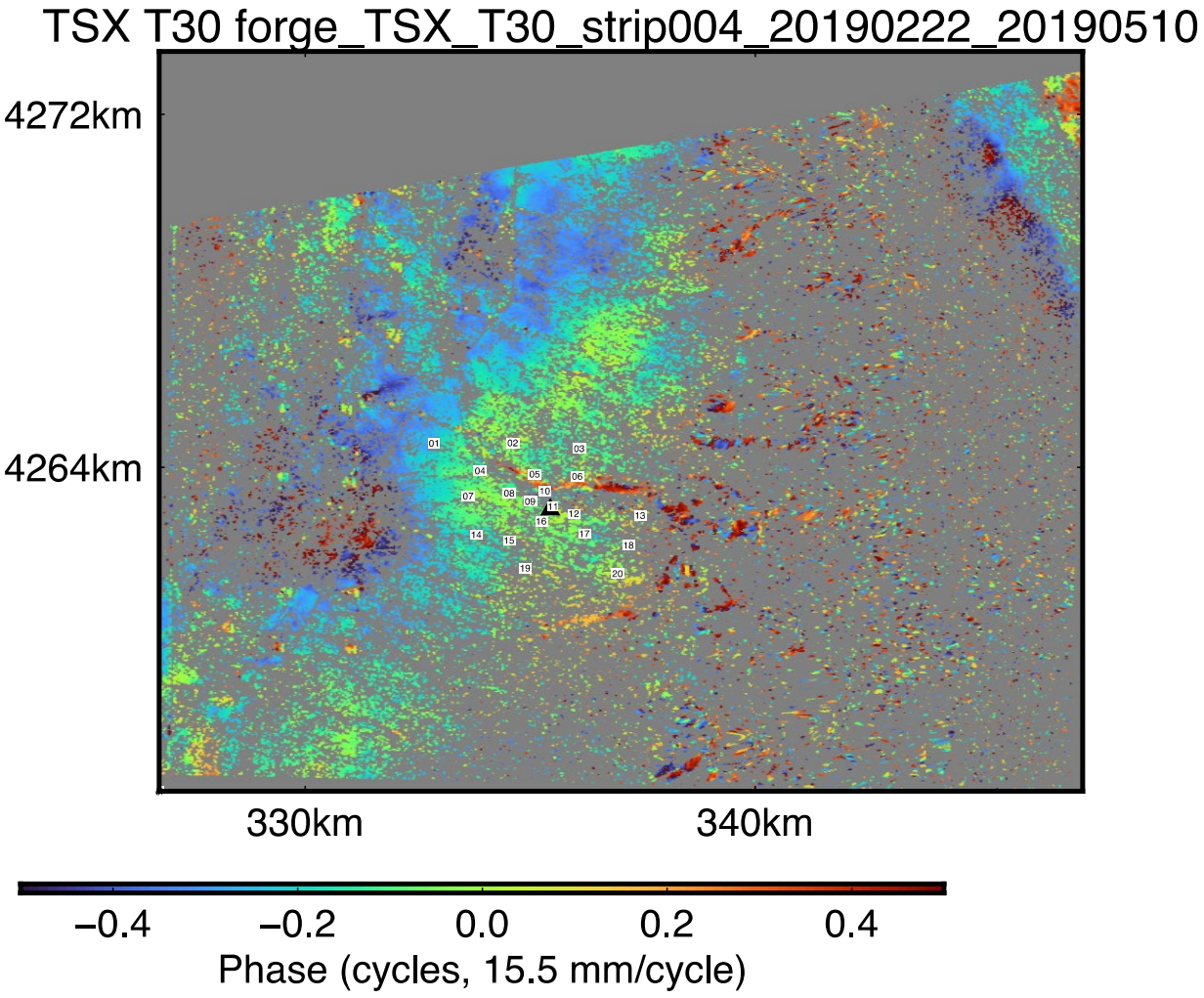

Figure 1. Map of deformation during the time interval from February 22, 2019 to May 10, 2019 (77 days apart) as measured by interferometric synthetic radar (InSAR). The white squares represent GPS reference stations ("GDM-NN_060519"). Perpendicular component of orbital separation ("Bperp") is 21.6 meters. The interferogram shows wrapped phase, after masking and filtering. Black triangle represents "Utah FORGE Deep Well 58-32".

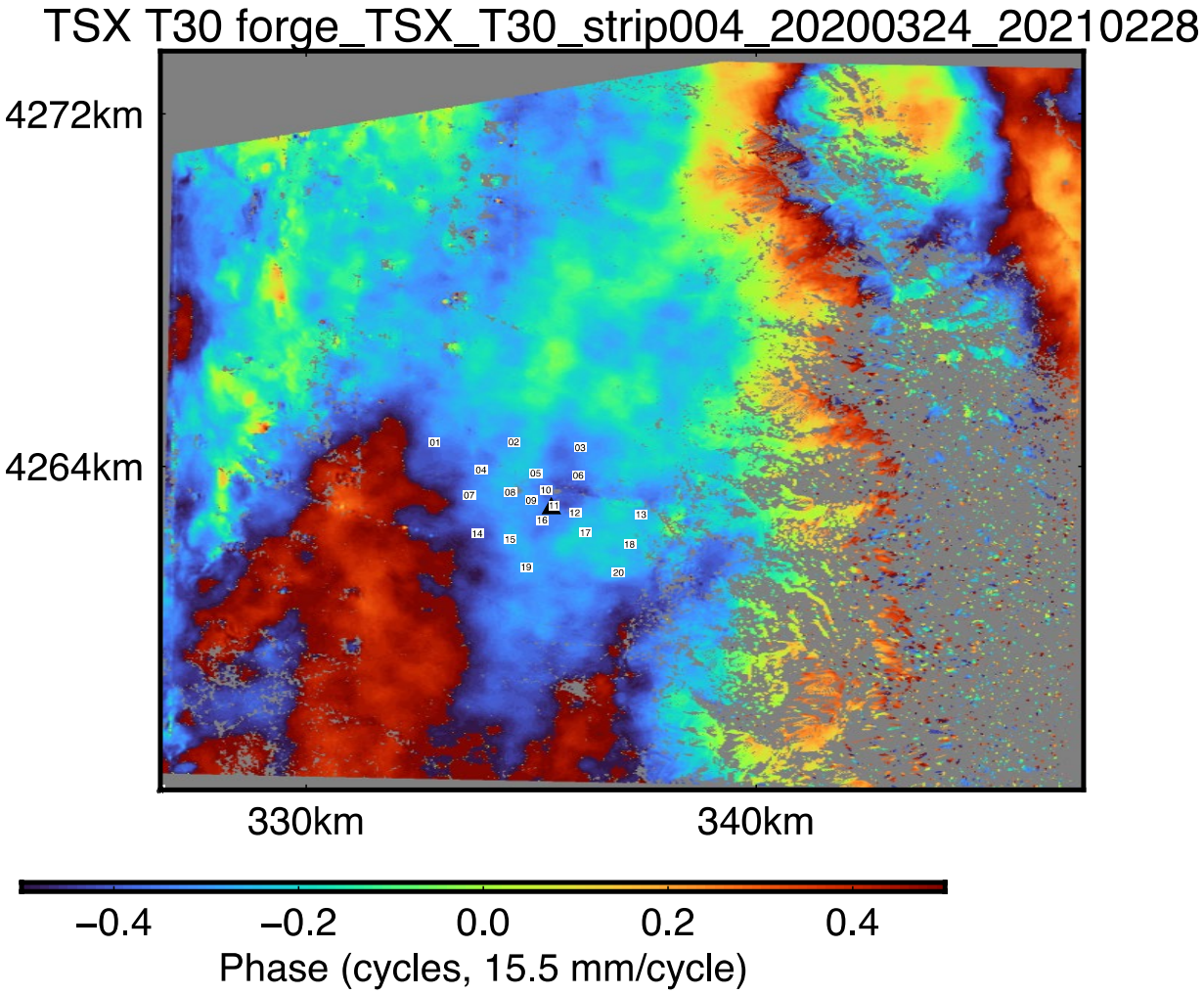

Figure 2. Example of a filtered and masked wrapped phase interferogram representing the pair of March 24, 2020 with February 28, 2021 (341 days apart). The white squares represent GPS reference stations ("GDM-NN_060519"). Perpendicular component of orbital separation ("Bperp") is 90.1 meters. Black triangle represents "Utah FORGE Deep Well 58-32".

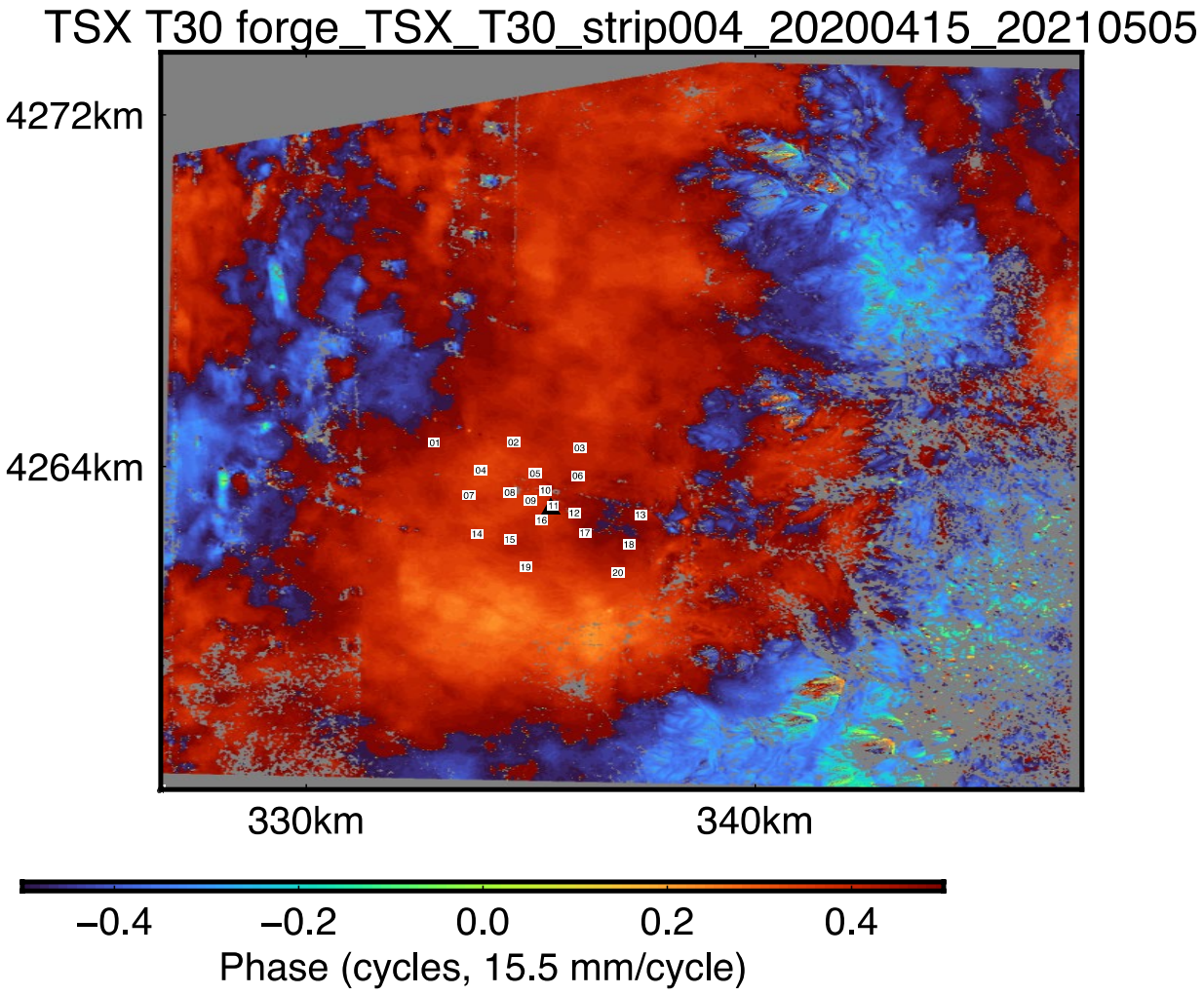

Figure 3. Map of deformation during the time interval from April 15, 2020 with May 5, 2021 (385 days apart). The white squares represent GPS reference stations ("GDM-NN_060519"). Perpendicular component of orbital separation ("Bperp") is -20.4 meters. Black triangle represents "Utah FORGE Deep Well 58-32".

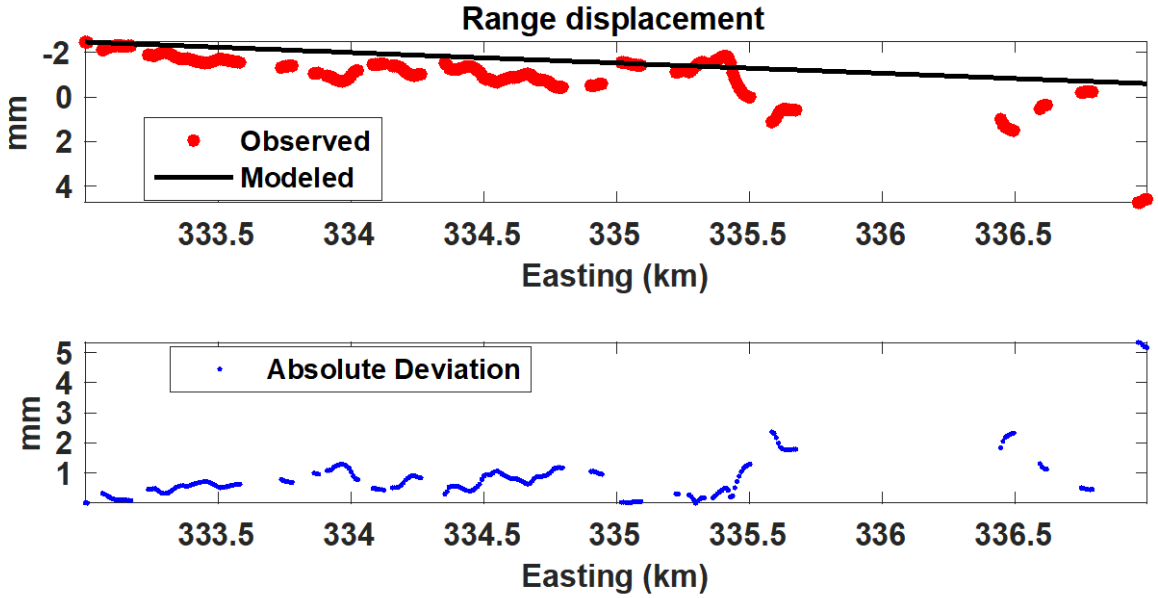

Figure 4. Profile of range change along a profile striking from west to east at UTM northing coordinate 4962.994 km.

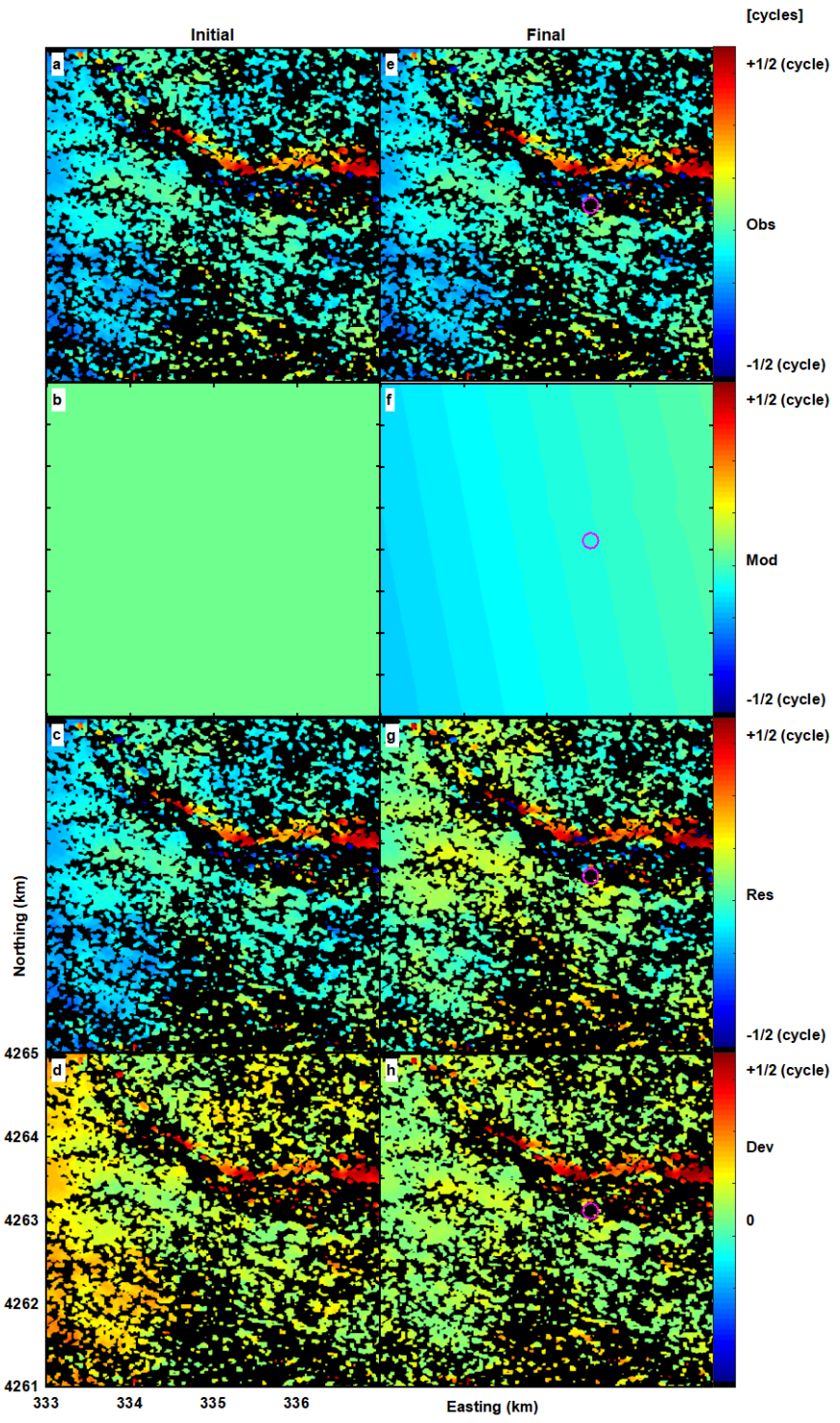

Figure 5. Deformation fields in terms of the (wrapped) phase change from InSAR data spanning 2019/02/22 through 2019/05/10 showing:

(a, e) observed phase change acquired by the TerraSAR-X satellite in track 30 without accounting for atmospheric effects;

(b, f) modeled rate of range change;

(c, g) residual between observed and modeled;

and (d, h) absolute value of residuals.

Left column, including panels a, b, c, and d, shows initial estimate of model parameters.

Right column, including panels e, f, g, and h, shows final estimate of model parameters.

One cyclically colored fringe indicates 15.5 mm of change in range. Warm colors indicate positive (increasing) phase changes that correspond to motion away from the satellite.

Coordinates are easting and northing [km] in Universal Transverse Mercator (UTM) projection zone 11N, WGS84. This is GIPhT solution 20220308_211509.

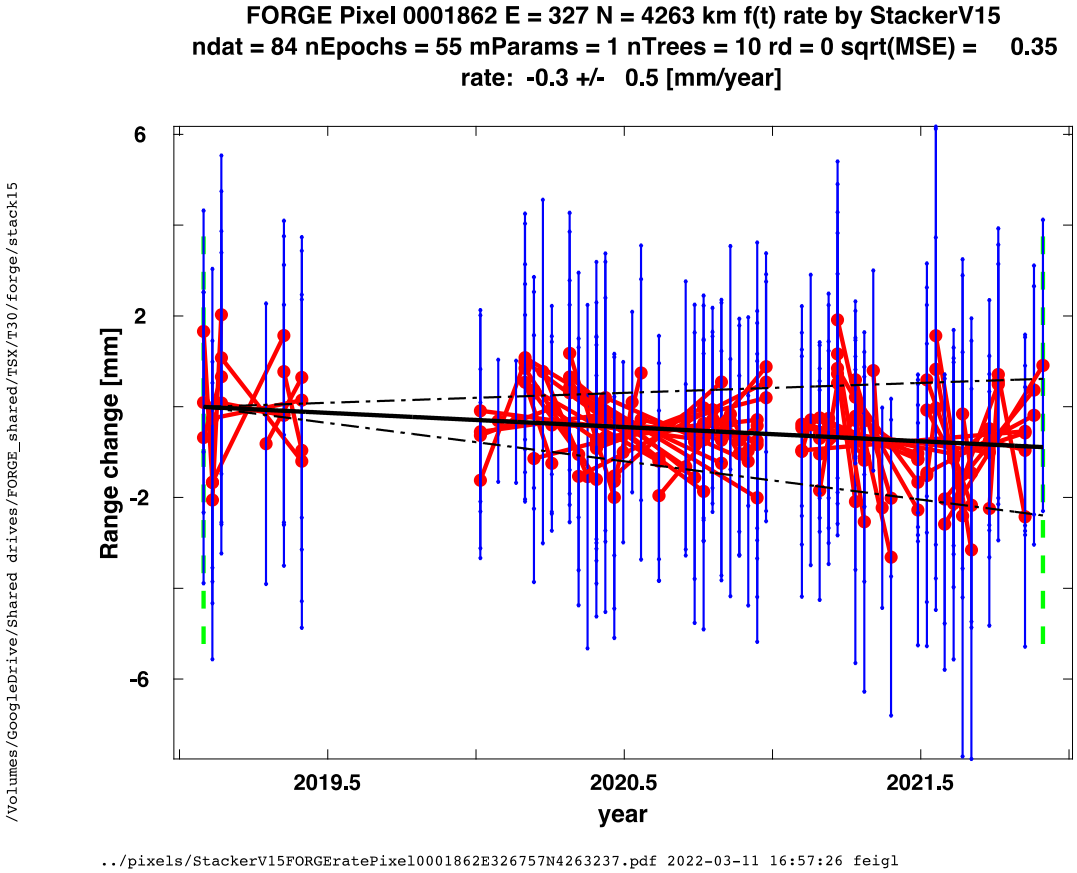

Figure 6. InSAR range change as a function of time for a pixel located at UTM (Easting, Northing) = (327, 4263) km in a stack of 104 interferometric pairs spanning the time interval from 20190131 to 20211108. Black lines show the modeled range change estimated by temporal adjustment [Reinisch et al., 2016]. Dashed black lines show 68% confidence intervals. Red segments indicate measurements of observed range change derived from individual geodetic pairs. For each pair, the range change at the mid-point of each time interval is plotted to fall on the modeled curve and the vertical blue bars denote 1σ measurement uncertainty after scaling by the square root of the variance scale factor. Dashed green lines indicate the beginning and end of the time interval.

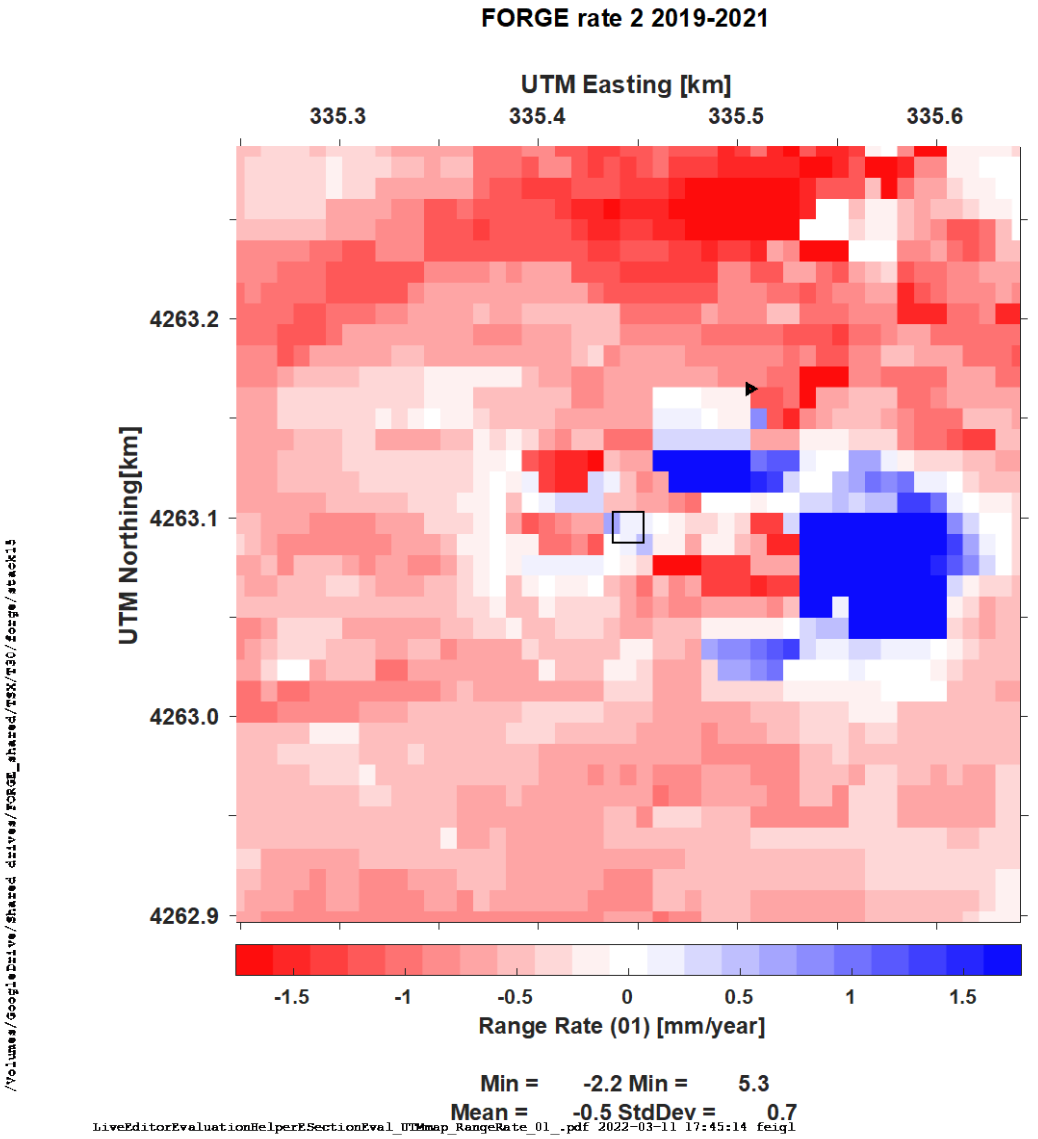

Figure 7. Mean rate of range change in mm/year for the stack of 104 interferograms spanning the time interval from 20190131 to 20211108. Coordinates are UTM (zone 12) easting and northing in km. The small black square delimits the location of deep well 58-32. Black triangle denotes the GPS station named "GDM-10_060519".

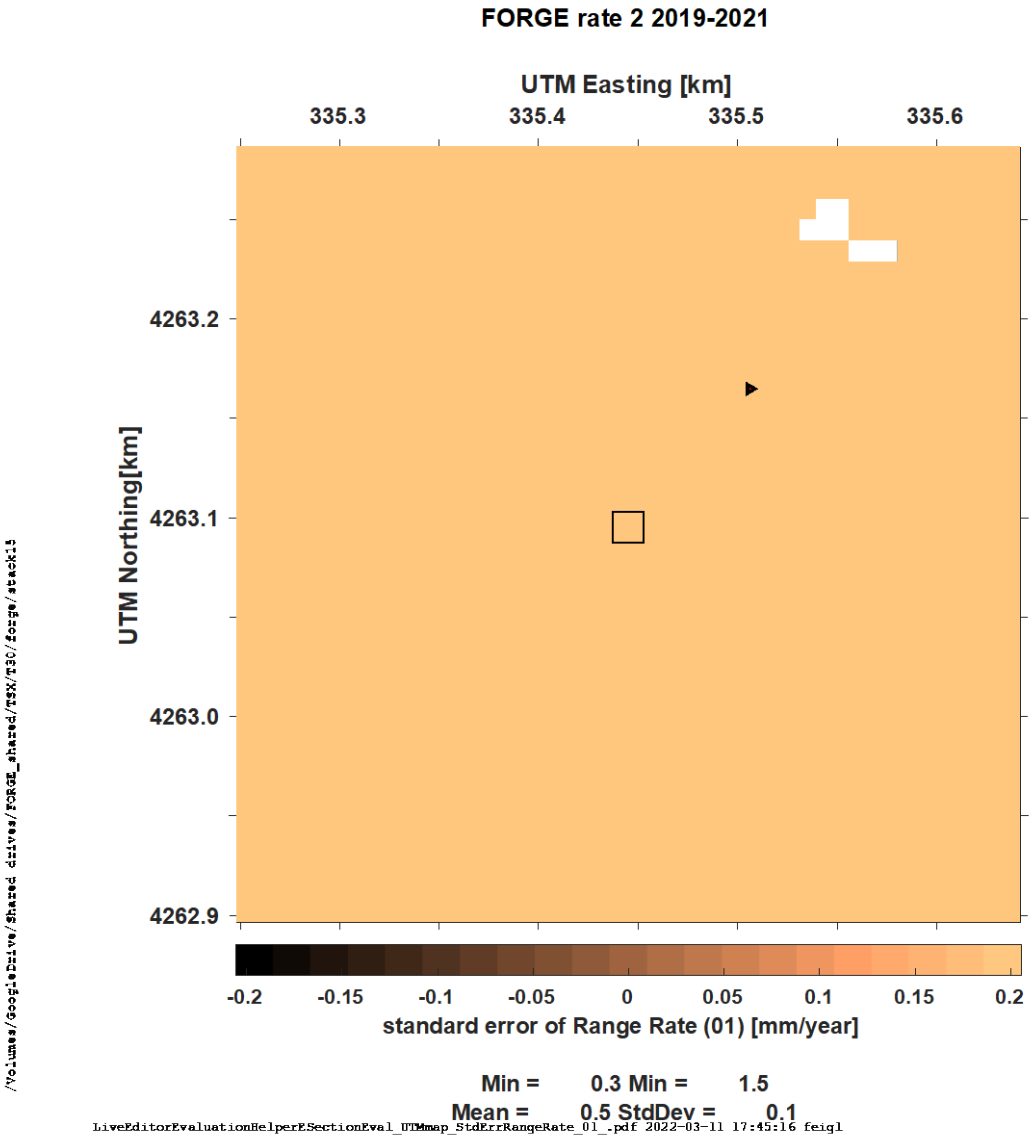

Figure 8. Standard error of mean rate of range change in mm/year for stack of interferograms. Plotting conventions as in previous figure.

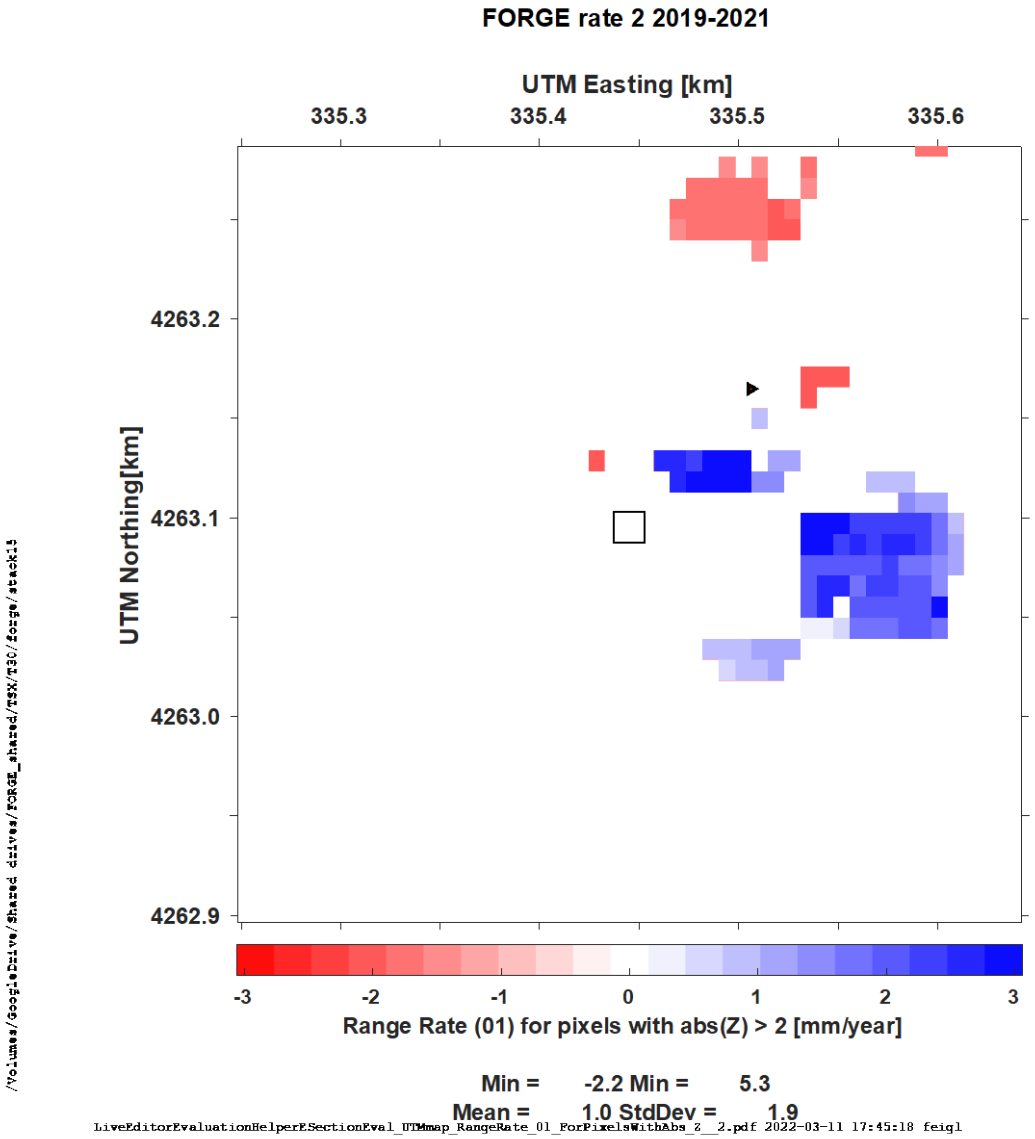

Figure 9. Mean rate of range change in mm/year for stack of interferograms, showing only pixels with rates that are significantly different from zero with 95% confidence. Increasing range denotes motion away from the satellite, e.g., downward motion or subsidence. spanning the time interval from 20190131 to 20211108. Coordinates are UTM (zone 12) easting and northing in km. The small black square delimits the location of deep well 58-32. Black triangle denotes the GPS station named "GDM-10_060519".

Table 1 Injection start and stop times with total injected volume including flowback (email from Phil Wannamaker January 07, 2022). A characteristic depth of ~1350m might be apt.

Zone	Start time (MDT)		End time (MDT)		Total injected volume (bbl)	Total injected volume (m^3)	Flowback volume (bbl)	Flowback volume (m^3)	Maximum event magnitude
Zone 1	21-Apr-19	10:20:00	24-Apr-19	11:14:00	421.5	67.0	86.7	13.8	-0.697
Zone 2	25-Apr-19	17:38:50	28-Apr-19	12:44:50	558	88.7	225.6	35.9	-0.519
Zone 3	1-May-19	9:00:30	1-May-19	18:46:30	488	77.6	70	11.1	-0.89

Table 2. Model parameters estimated from InSAR pair spanning injection experiment in March 2019.

```
Cost  of null  model   = 0.1159361 [cycles] for   4145 observations in inverted data set
Cost  of initl model   = 0.1158048 [cycles] for   4145 observations in inverted data set
Cost  of final model   = 0.0683752 [cycles] for   4145 observations in inverted data set
Cost  improvement      = 0.0474296 [cycles] for   4145 observations in inverted data set
Critical value of cost = 0.0690694 [cycles] for   4145 observations in inverted data set
```

I		Name	P0(pre-fit)	P1(post-fit)	Adjust.	Sigma[3]	Signif	Bound
F#	1	time_fn_@_epoch_001_in_years____	2019.1414	2019.1414	0.0000	NaN	NaN	0.0000
F#	2	time_fn_@_epoch_002_in_years____	2019.3522	2019.3522	0.0000	NaN	NaN	0.0000
F#	3	E_grad__@_epoch_001_dimless_____	0.00e+00	0.00e+00	0.00e+00	NaN	NaN	0.00e+00
E#	**4**	**E_grad__@_epoch_002_dimless_____**	**0.00e+00**	**5.08e-07**	**5.08e-07**	**1.25e-07**	**4.1**	**1.00e-06**
F#	5	N_grad__@_epoch_001_dimless_____	0.00e+00	0.00e+00	0.00e+00	NaN	NaN	0.00e+00
E#	6	N_grad__@_epoch_002_dimless_____	0.00e+00	7.98e-08	7.98e-08	1.56e-07	0.51	1.00e-06
F#	7	U_grad__@_epoch_001_dimless_____	0.00e+00	0.00e+00	0.00e+00	NaN	NaN	0.00e+00
E#	**8**	**U_grad__@_epoch_002_dimless_____**	**0.00e+00**	**-9.38e-07**	**-9.38e-07**	**9.69e-07**	**0.97**	**1.00e-06**
E#	31	Okada1_Length_in_m_____________	10.0000	13.6807	3.6807	9.6875	0.38	10.0000
E#	32	Okada1_Width_in_m______________	10.0000	10.6254	0.6254	9.6875	0.06	10.0000
E#	33	Okada1_Centroid_Depth_in_m_____	1350.0000	1287.3359	-62.6641	96.8750	0.65	100.0000
E#	34	Okada1_Dip_in_deg______________	0.0000	7.5996	7.5996	9.6875	0.78	10.0000
E#	35	Okada1_Strike_CW_from_N_in_deg__	10.0000	9.2131	-0.7869	9.6875	0.08	10.0000
E#	36	Okada1_Centroid_Easting_in_m____	335451.0	335523.3	72.4	96.9	0.75	100.0
E#	37	Okada1_Centroid_Northing_in_m___	4263037.9	4263109.9	72.0	96.9	0.74	100.0
F#	38	Okada1_Coplanar_slip_in_m_______	0.00e+00	0.00e+00	0.00e+00	NaN	NaN	0.00e+00
E#	39	Okada1_Rake_in_deg_CCW_________	-90.0000	-87.4322	2.5678	9.6875	0.27	10.0000
E#	**40**	**Okada1_Tensile_Opening_in_m_____**	**0.6000**	**0.1557**	**-0.4443**	**0.5813**	**0.76**	**0.6000**
F#	61	Poisson_Ratio_dimless__________	0.2500	0.2500	0.0000	NaN	NaN	0.0000
F#	62	Shear_Modulus_in_Pa____________	3.00e+10	3.00e+10	0.00e+00	NaN	NaN	0.00e+00
D#	95	Derived_Okada1_potency_in_m3____	60.0000	22.6395	-37.3605	NaN	NaN	NaN
D#	96	Derived_Okada1_moment_in_Nm_____	1.80e+12	6.79e+11	-1.12e+12	NaN	NaN	NaN
D#	97	Derived_Okada1_Mw_______________	2.1402	1.8580	-0.2822	NaN	NaN	NaN

Table 3. List of SAR acquisitions from TerraSAR-X and TanDEM-X radar satellite missions showing date (YearMonthDate) and orbit number. The status flags are defined as follows: "D" represents a scene that has been delivered. "C" denotes a cancelled scene acquisition, usually for technical reasons at the source. "P" denotes a scene that is planned for acquisition in the future. All of these acquisitions follow Track 30 in an ascending orbital pass that crosses the equatorial plane from south to north.
Included in file named table3.txt *https://foundry.openei.org/29/insar/report2022?resources[]=5225262*

```
$ grep forge /s12/insar/TSX/TSX_OrderList.txt | cut -c 1-78 | sort -un
#date     site   sat  track  swath       frame  orbit ascdes   status  source
20161108  forge  TDX  T30    strip_004   nan    35404  A       D       dlrdlr

20181115  forge  TDX  T30    strip_004R  nan    46593  A       D       dlrdlr

20190131  forge  TSX  T30    strip_004R  nan    47762  A       D       dlrdlr
20190211  forge  TSX  T30    strip_004R  nan    47929  A       D       dlrdlr
20190222  forge  TSX  T30    strip_004R  nan    48096  A       D       dlrdlr
20190418  forge  TSX  T30    strip_004R  nan    48931  A       D       dlrdlr
20190510  forge  TSX  T30    strip_004R  nan    49265  A       D       dlrdlr
20190601  forge  TSX  T30    strip_004R  nan    49599  A       D       dlrdlr
20190623  forge  TSX  T30    strip_004R  nan    nan    A       C       dlrdlr
20190715  forge  TSX  T30    strip_004R  nan    nan    A       C       dlrdlr

20200107  forge  TSX  T30    strip_004R  nan    52939  A       D       dlrdlr
20200129  forge  TSX  T30    strip_004R  nan    53273  A       D       dlrdlr
20200220  forge  TSX  T30    strip_004R  nan    53607  A       D       dlrdlr
20200302  forge  TSX  T30    strip_004R  nan    53774  A       D       dlrdlr
20200313  forge  TSX  T30    strip_004R  nan    53941  A       D       dlrdlr
20200324  forge  TSX  T30    strip_004R  nan    54108  A       D       dlrdlr
20200404  forge  TSX  T30    strip_004R  nan    54275  A       D       dlrdlr
20200415  forge  TSX  T30    strip_004R  nan    54442  A       D       dlrdlr
20200426  forge  TSX  T30    strip_004R  nan    54609  A       D       dlrdlr
20200507  forge  TSX  T30    strip_004R  nan    54776  A       D       dlrdlr
20200518  forge  TSX  T30    strip_004R  nan    54943  A       D       dlrdlr
20200529  forge  TSX  T30    strip_004R  nan    55110  A       D       dlrdlr
20200609  forge  TSX  T30    strip_004R  nan    55277  A       D       dlrdlr
20200620  forge  TSX  T30    strip_004R  nan    55444  A       D       dlrdlr
20200701  forge  TSX  T30    strip_004R  nan    55611  A       D       dlrdlr
20200712  forge  TSX  T30    strip_004R  nan    55778  A       D       dlrdlr
20200723  forge  TSX  T30    strip_004R  nan    55945  A       D       dlrdlr
20200803  forge  TSX  T30    strip_004R  nan    56112  A       D       dlrdlr
20200814  forge  TSX  T30    strip_004R  nan    56279  A       D       dlrdlr
20200825  forge  TSX  T30    strip_004R  nan    56446  A       D       dlrdlr
20200905  forge  TSX  T30    strip_004R  nan    56613  A       D       dlrdlr
20200916  forge  TSX  T30    strip_004R  nan    56780  A       D       dlrdlr
20200927  forge  TSX  T30    strip_004R  nan    56947  A       D       dlrdlr
20201008  forge  TSX  T30    strip_004R  nan    57114  A       D       dlrdlr
20201019  forge  TSX  T30    strip_004R  nan    57281  A       D       dlrdlr
20201030  forge  TSX  T30    strip_004R  nan    57448  A       D       dlrdlr
20201110  forge  TSX  T30    strip_004R  nan    57615  A       D       dlrdlr
20201121  forge  TSX  T30    strip_004R  nan    57782  A       D       dlrdlr
20201202  forge  TSX  T30    strip_004R  nan    57949  A       D       dlrdlr
20201213  forge  TSX  T30    strip_004R  nan    58116  A       D       dlrdlr
20201224  forge  TSX  T30    strip_004R  nan    58283  A       D       dlrdlr
```

#date	site	sat	track	swath	frame	orbit	ascdes	status	source
20210104	forge	TSX	T30	strip_004R	nan	58450	A	D	dlrdlr
20210115	forge	TSX	T30	strip_004R	nan	58617	A	D	dlrdlr
20210126	forge	TSX	T30	strip_004R	nan	58784	A	D	dlrdlr
20210206	forge	TSX	T30	strip_004R	nan	58951	A	D	dlrdlr
20210217	forge	TSX	T30	strip_004R	nan	59118	A	D	dlrdlr
20210228	forge	TSX	T30	strip_004R	nan	59285	A	D	dlrdlr
20210311	forge	TSX	T30	strip_004R	nan	59452	A	D	dlrdlr
20210322	forge	TSX	T30	strip_004R	nan	59619	A	D	dlrdlr
20210402	forge	TSX	T30	strip_004R	nan		A	C	dlrdlr
20210413	forge	TSX	T30	strip_004R	nan	59953	A	D	dlrdlr
20210424	forge	TSX	T30	strip_004R	nan	60120	A	D	dlrdlr
20210505	forge	TSX	T30	strip_004R	nan	60287	A	D	dlrdlr
20210516	forge	TSX	T30	strip_004R	nan	60454	A	D	dlrdlr
20210527	forge	TSX	T30	strip_004R	nan	60621	A	D	dlrdlr
20210607	forge	TSX	T30	strip_004R	nan		A	P	dlrdlr
20210618	forge	TSX	T30	strip_004R	nan		A	P	dlrdlr
20210629	forge	TSX	T30	strip_004R	nan	61122	A	D	dlrdlr
20210710	forge	TSX	T30	strip_004R	nan	61289	A	D	dlrdlr
20210721	forge	TSX	T30	strip_004R	nan	61456	A	D	dlrdlr
20210801	forge	TSX	T30	strip_004R	nan	61623	A	D	dlrdlr
20210812	forge	TSX	T30	strip_004R	nan	61790	A	D	dlrdlr
20210823	forge	TSX	T30	strip_004R	nan	61957	A	D	dlrdlr
20210903	forge	TSX	T30	strip_004R	nan	62124	A	D	dlrdlr
20210914	forge	TSX	T30	strip_004R	nan		A	C	
20210925	forge	TSX	T30	strip_004R	nan	62458	A	D	dlrdlr
20211006	forge	TSX	T30	strip_004R	nan	62625	A	D	dlrdlr
20211017	forge	TSX	T30	strip_004R	nan		A	C	dlrdlr
20211028	forge	TSX	T30	strip_004R	nan		A	C	dlrdlr
20211108	forge	TSX	T30	strip_004R	nan	63126	A	D	dlrdlr
20211119	forge	TSX	T30	strip_004R	nan	63293	A	D	dlrdlr
20211130	forge	TSX	T30	strip_004R	nan	63460	A	D	dlrdlr
20211211	forge	TSX	T30	strip_004R	nan	80357	A	D	dlrdlr
20211222	forge	TSX	T30	strip_004R	nan	80524	A	D	dlrdlr

#date	site	sat	track	swath	frame	orbit	ascdes	status	source
20220102	forge	TSX	T30	strip_004R	nan	80691	A	D	dlrdlr
20220113	forge	TSX	T30	strip_004R	nan		A	C	dlrdlr
20220124	forge	TSX	T30	strip_004R	nan	81025	A	D	dlrdlr
20220204	forge	TSX	T30	strip_004R	nan	81192	A	D	dlrdlr
20220215	forge	TSX	T30	strip_004R	nan	81359	A	D	dlrdlr
20220226	forge	TSX	T30	strip_004R	nan	64796	A	D	dlrdlr
20220309	forge	TSX	T30	strip_004R	nan		A	P	dlrdlr
20220320	forge	TSX	T30	strip_004R	nan		A	P	dlrdlr
20220331	forge	TSX	T30	strip_004R	nan		A	P	dlrdlr
20220411	forge	TSX	T30	strop_004R	nan		A	P	dlrdlr
20220422	forge	TSX	T30	strop_004R	nan		A	P	dlrdlr
20220503	forge	TSX	T30	strop_004R	nan		A	P	dlrdlr
20220514	forge	TSX	T30	strop_004R	nan		A	P	dlrdlr
20220525	forge	TSX	T30	strop_004R	nan		A	P	dlrdlr
20220605	forge	TSX	T30	strop_004R	nan		A	P	dlrdlr
20220616	forge	TSX	T30	strop_004R	nan		A	P	dlrdlr
20220627	forge	TSX	T30	strop_004R	nan		A	P	dlrdlr

Acknowledgments:

Interferograms were created using GMT-SAR processing software [*Sandwell et al.*, 2011]. Several figures were created using the Generic Mapping Tools [*Wessel et al.*, 2013]. We gratefully acknowledge support from the Weeks family to the Department of Geoscience at the University of Wisconsin-Madison. Synthetic Aperture Radar data from the TerraSAR-X and the TanDEM-X satellite missions operated by the German Space Agency (DLR) were used under the terms and conditions of Research Project RES1236.

Software is available publicly on GitHub for the General Inversion of Phase Technique (GIPhT) [*Feigl et al.*, 2019], the PoroTomo project [*Reinisch and Feigl*, 2018], and the UW Madison HTCondor InSAR Workflow [*Reinisch et al.*, 2018a].

References

Feigl, K. L., and C. H. Thurber (2009), A method for modelling radar interferograms without phase unwrapping: application to the M 5 Fawnskin, California earthquake of 1992 December 4, *Geophysical Journal International, 176*, 491-504. http://dx.doi.org/10.1111/j.1365-246X.2008.03881.x

Okada, Y. (1985), Surface deformation due to shear and tensile faults in a half-space, *Bulletin of the Seismological Society of America, 75*, 1135-1154. http://www.bssaonline.org/content/75/4/1135.abstract

Reinisch, E. C., M. Cardiff, and K. L. Feigl (2016), Graph theory for analyzing pair-wise data: application to geophysical model parameters estimated from interferometric synthetic aperture radar data at Okmok volcano, Alaska, *Journal of Geodesy*, 1-16. http://dx.doi.org/10.1007/s00190-016-0934-5

Reinisch, E. C., M. Cardiff, and K. L. Feigl (2018), Characterizing Volumetric Strain at Brady Hot Springs, Nevada, USA Using Geodetic Data, Numerical Models, and Prior Information, *Geophysical Journal International*, 1501–1513. http://dx.doi.org/10.1093/gji/ggy347

Reinisch, E. C., M. Cardiff, C. Kreemer, J. Akerley, and K. L. Feigl (2020), Time-series Analysis of Volume Change at Brady Hot Springs, Nevada, USA using Geodetic Data from 2003 – 2018, *Journal of Geophysical Research: Solid Earth, n/a*, e2019JB017816. http://dx.doi.org/10.1029/2019jb017816

Sandwell, D., R. Mellors, X. Tong, M. Wei, and P. Wessel (2011), Open radar interferometry software for mapping surface deformation, *Eos, Transactions American Geophysical Union, 92*, 234-234. http://topex.ucsd.edu/gmtsar

Attachment 5

Phase 3A Year 2 Annual Report – Appendix A2

Enhanced Geothermal System Testing and Development at the Milford, Utah FORGE Site

Utah FORGE
University of Utah
423 Wakara Way, ste 300
Salt Lake City, UT, 84105

Prepared for the U.S. Department of Energy

Office of Energy Efficiency and Renewable Energy

Contract DE-EE0007080

April 30, 2022

Utah FORGE GPS Ground Deformation Monitoring Summary Phase 3A Subtask 3.7.5

By: Ben Erickson

Overview

The Utah Geological Survey actively monitored the potential ground deformation related to activities performed during Phase 3, October 1, 2019, to September 30, 2021, by the subsurface field lab at the Utah FORGE site near the city of Milford in Beaver County, Utah (Figure 1). The ground deformation monitoring, subtask 3.7.5, relies on precise point monitoring at geophysical stations with the use of Global Network Satellite Systems (GNSS), including the United States operated Global Positioning System (GPS) satellite constellation. Monitoring entails the recording of signals transmitted by multiple satellite constellations to calculate positions then determine ground movement by comparative analysis through time.

GPS ground deformation monitoring began prior to phase 3 where geophysical monitoring stations were installed. The monitoring stations consisted of a rod driven several feet into the ground with protective surface coverings to provide minimal environmental disturbances. A total of twenty monitoring stations were installed at the Utah FORGE site and two far field, bedrock anchored base points were established. Additionally, four monitoring campaign measurements were performed as an initial baseline. The baseline measurements took place from December 2018 to June 2019. The initial measurement timeframe provided methodology to be established but was not sufficient for understanding the potential seasonal variations of the site. Winter to spring comparisons showed up to a 5 cm of uplift to the area. Through environmental evaluations, the displacement was caused by transient groundwater movement induced by melting snowpack infiltrating into the subsurface, a seasonal variation.

A determination was made to use the second campaign, identified as Initial B measured in March 2019, to compare future measurement. Initial B is the primary reference point comparison in processing and ground deformations are linked to the measurement. Comparisons are also made from campaign to campaign to provide insight of changes between measurements.

Phase 3 GPS monitoring began November 2019 with a subsequent measurement in December 2019. Comparative analysis of these measurements showed ground deflation to the level of measurements taken in March 2019, providing evidence of seasonal influences in the area. Measurements throughout phase 3 has shown similar, but not as extensive as the 2019 spring displacement, seasonal impacts of the area. A total of eight GPS measuring campaigns were performed in phase 3, measured on a quarterly interval.

In addition to the quarterly measurements, two additional geophysical monitoring stations were installed and two proposed continuous GPS stations. Of the geophysical stations, one is a replacement to a station impacted by a built-up drilling pad and the other station is near a groundwater monitoring well.

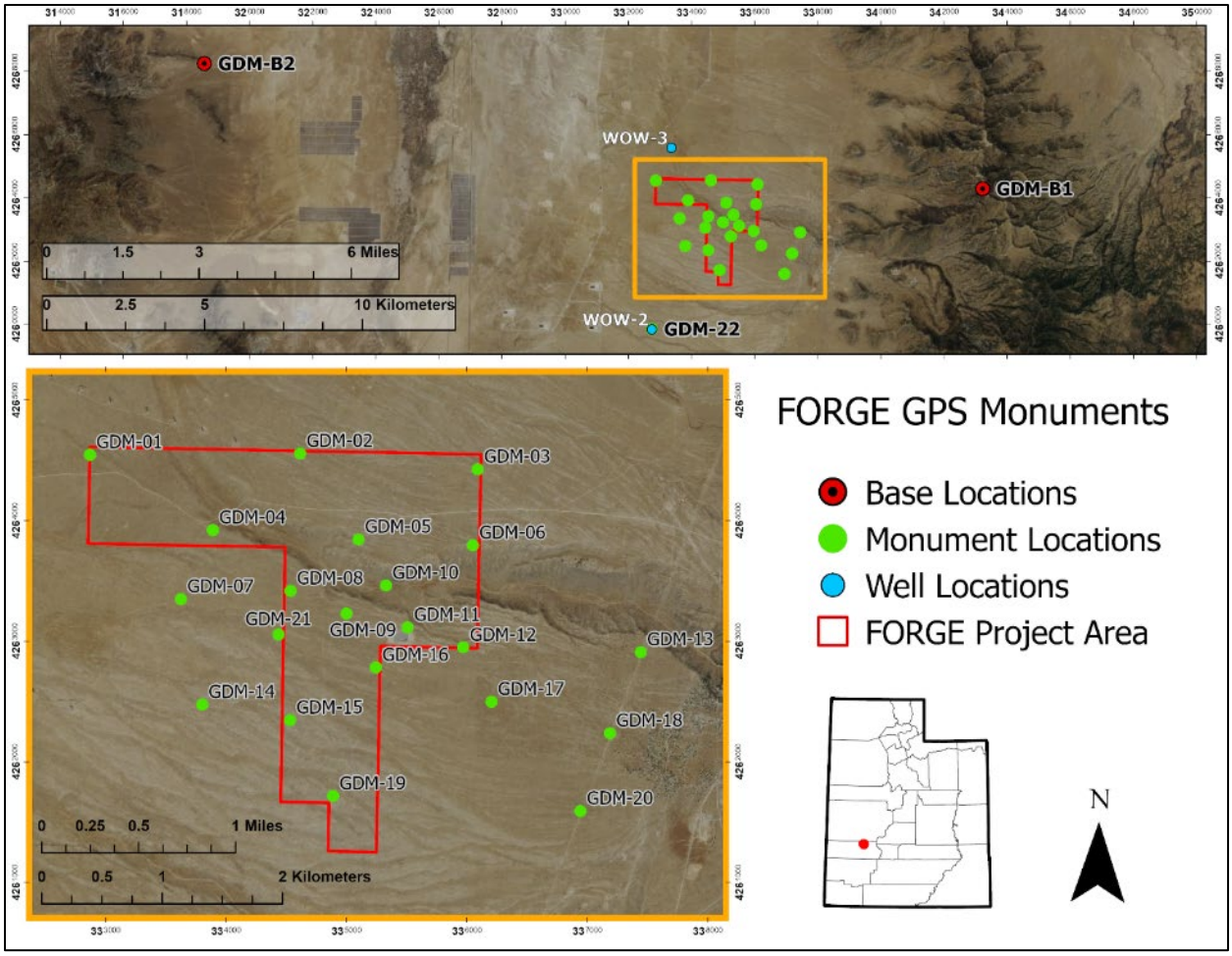

Figure 1: Location map of the Utah FORGE project area including point locations of the geophysical monitoring stations and groundwater monitoring wells.

Results

Monitoring Campaign 3

Campaign 3 was performed on November 18, 2019, using ATV and truck transport between ground deformation monument (GDM) stations. Stations GDM-B1, GDM-B2, GDM-01, GDM-02, and GDM-07 were started the night prior to the rest of the campaigns. Another overnight occupation was planned for three additional stations, but due to significant inclement weather, the overnight occupation was not performed. During Station GDM-B1 equipment retrieval, it was discovered that the power supply cable connection became detached and the receiver recorded under five hours of data as a result. No other significant issues occurred during this occupation.

The results of Monitoring Campaign 3 are summarized in Figure 2. When comparing to the Initial Monitoring Campaign B, in March, there is an overall inflation throughout the Utah FORGE site. The site shows an average vertical inflation of 24.5 mm, with a maximum of 31.6 mm and a minimum 14.9 mm, all exceeding the calculated GNSS errors for both occupations. Due to lack of long-term, seasonal data for the area, including groundwater levels and the nearby Blundell Geothermal Plant production and injection wells influence, and that no Utah FORGE project well testing occurred during the time period prior to Campaign 3, we theorize the ground inflation is related to natural effects in the area, such as from groundwater changes. However, as further occupations add to the dataset of ground monitoring data, seasonal and other natural effects should be more discernable in developing a more accurate conclusion related to the ground deformation observed in the GNSS data. The Monitoring Campaign Initial B to 3 horizontal vectors show a general movement trend to the east/southeast. The Monitoring Campaigns 2 to 3 (Figure 3) show horizontal vectors in a general movement trend to the southwest with a magnitude less than between the Initial B campaign to Campaign 3.

Surface interpolation was performed on the vertical displacement values between the measurements. Colors grading to dark red highlight the areas of positive change or inflation of the area. Colors grading to dark blue highlight areas of negative change or deflation of the area. Displacement graphs were also added to accommodate the updated map scale. The graphs plot the measured displacement for each GDM station and the distribution of XY, and Z changes. These graphs include the maximum GPS error range determined through the calculations between the two campaigns.

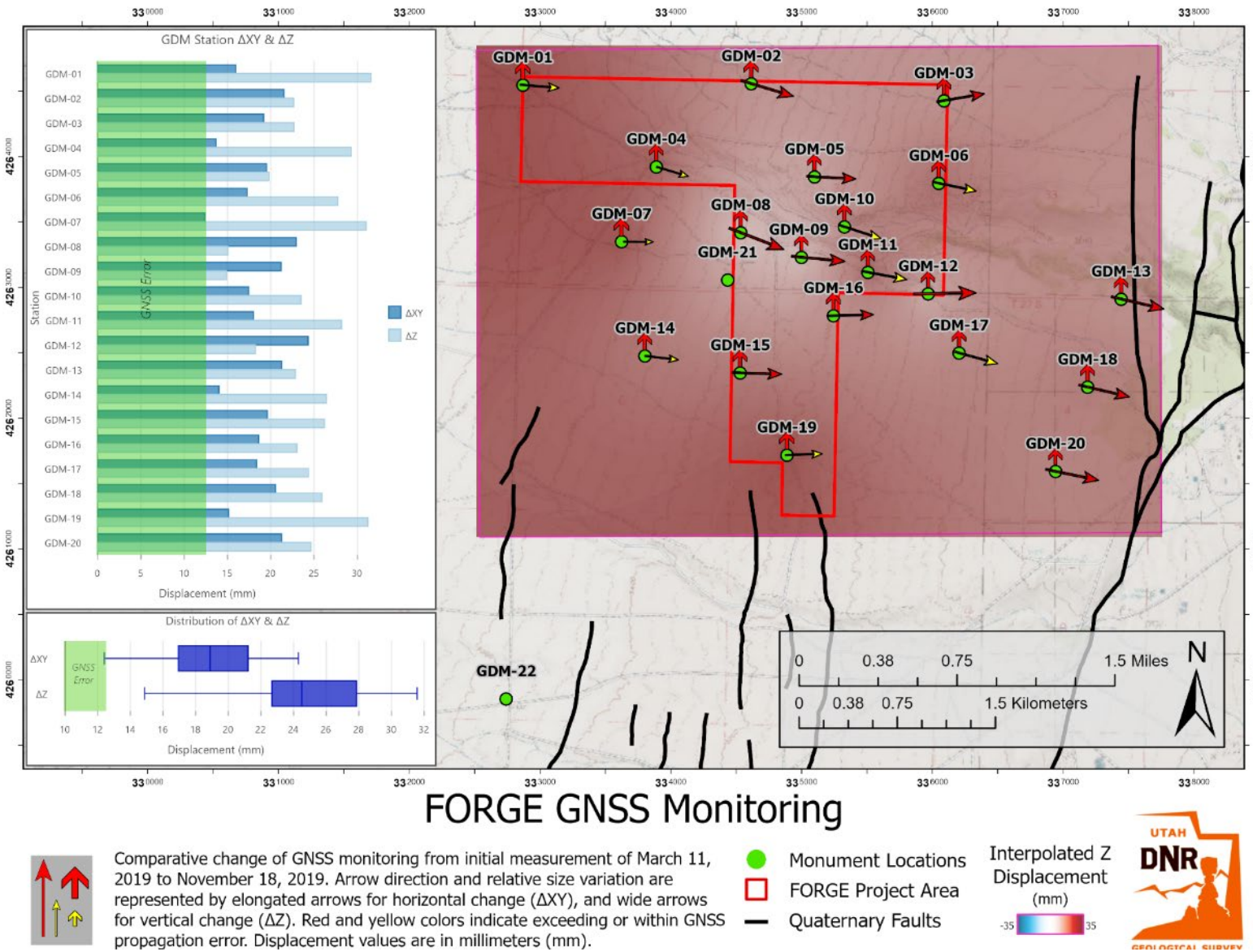

Figure 2: Vector map and displacement interpolation of monument movements measured between Monitoring Campaigns Initial B and 3. Displacement surface interpolation range is ±35 mm, located to lower right of figure.

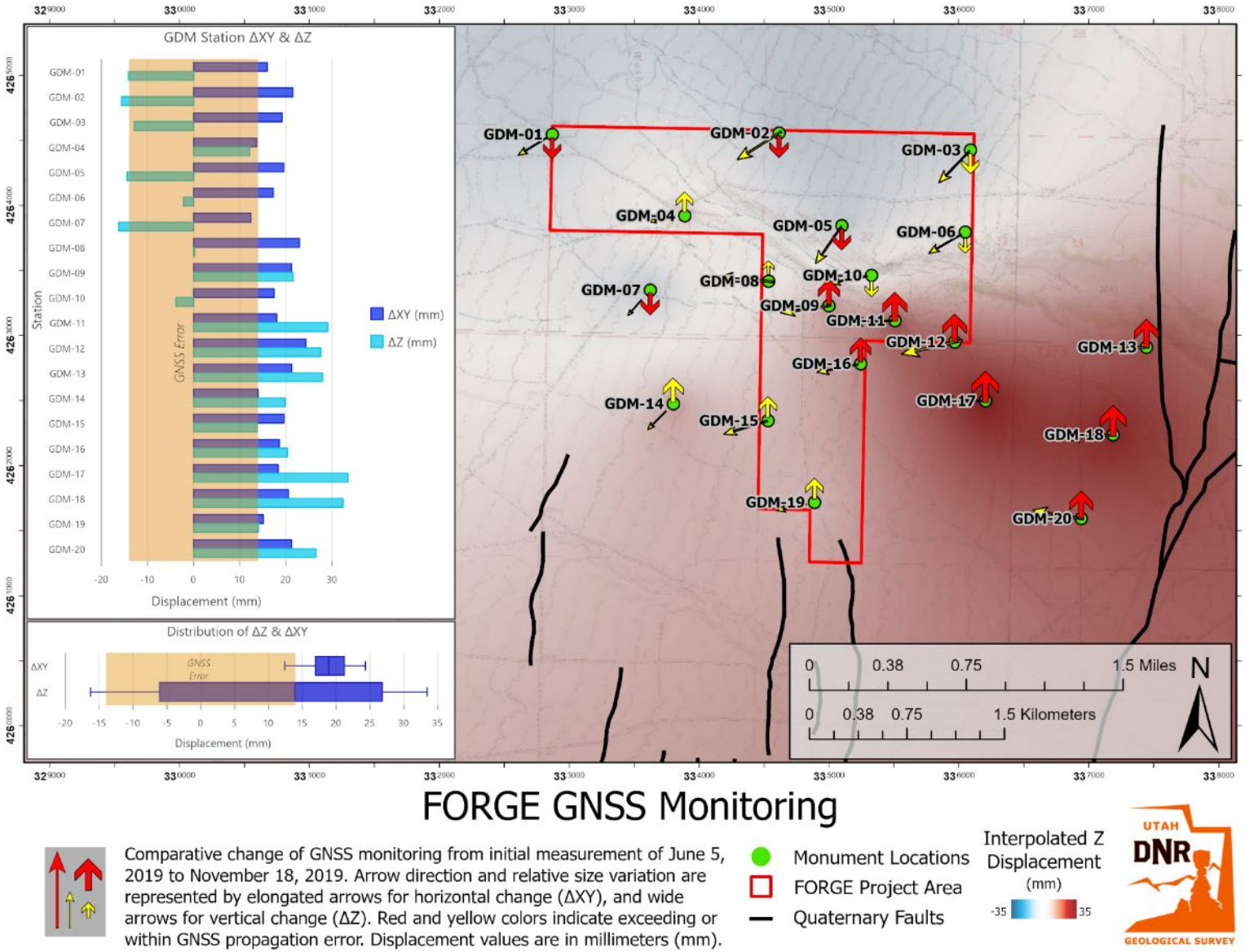

Figure 3: Vector map and displacement interpolation of monument movements measured between Monitoring Campaigns 2 and 3. Displacement surface interpolation range is ±35 mm.

Monitoring Campaign 4

Monitoring Campaign 4was performed on December 16, 2019, using ATV and truck transport between monitoring stations. There was snow on the ground at station GDM-B1 and was not accessible by truck, 3-foot-high snow drifts prevented access. However, the lightweight ATV was nimble enough to traverse the snow and was used to setup and take down station GDM-B1. As was done for Monitoring Campaign 3, stations GDM-B1, GDM-B2, GDM-01, GDM-02, and GDM-07 were started the night prior to the rest of the campaign. Additionally, stations GDM-04, GDM-11, and GDM-18 were started at the end of the campaign and allowed to record throughout the night. Stations GDM-01 and GDM-04 had a battery issue and only recorded 10 hours, acquiring additional batteries is being considered. No other significant issues occurred during this occupation.

The results of Monitoring Campaign 4 when comparing to the Initial Monitoring Campaign B in March 2019 (Figure 4) show an overall reduction or ground deflation throughout the Utah FORGE site. Unlike Monitoring Campaign 3, the site shows an average vertical deflation of -7.4 mm, with a maximum of -16.7 mm, and a minimum inflation 2.9 mm. The resulting reversal to what was observed in Monitoring Campaign 3, provides further evidence of the dynamic behavior of the area. The time of year further suggests the influence of groundwater in the area, as it appears groundwater transience is lowest in the winter months. However, without a measurable groundwater monitoring well in the area, we can only rely on what is observed in similar basins and assume similar mechanisms are at work. A study where groundwater deformation was recorded using GPS measurements within a basin over the course of a year showed similar horizontal and vertical change as the groundwater deformed the ground surface throughout the year.

Comparison to Campaign 3 (Figure 5), shows significant deflation to the area. The fast deformation over a month suggests a rapid groundwater withdrawal to the area and further suggests a seasonal influence. Additional measurements can provide the required insight needed to better understand the influences of environmental impacts on the site.

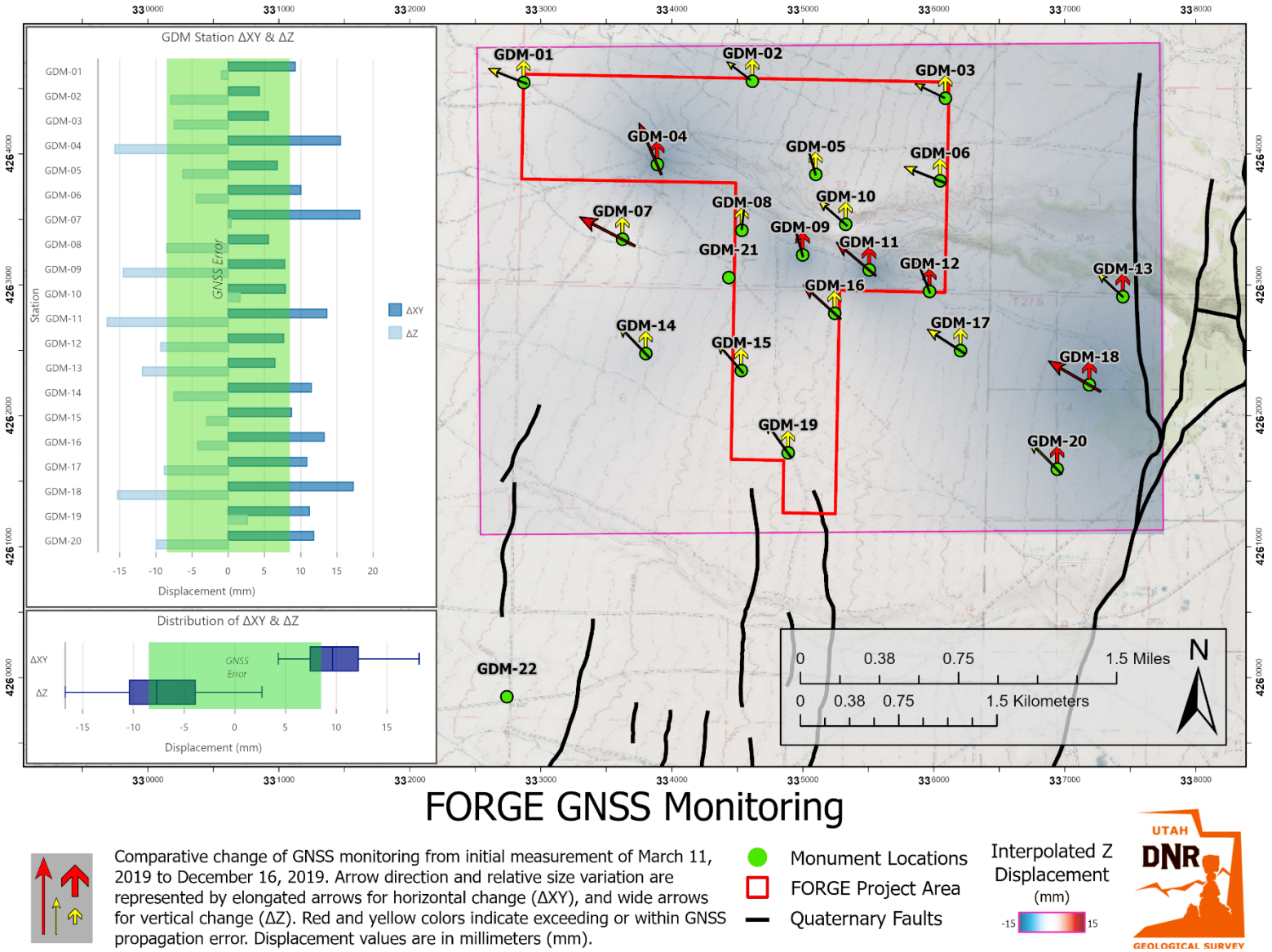

Figure 4: Vector map and displacement interpolation of monument movements measured between Monitoring Campaigns Initial B and 4. Displacement surface interpolation range is ±35 mm.

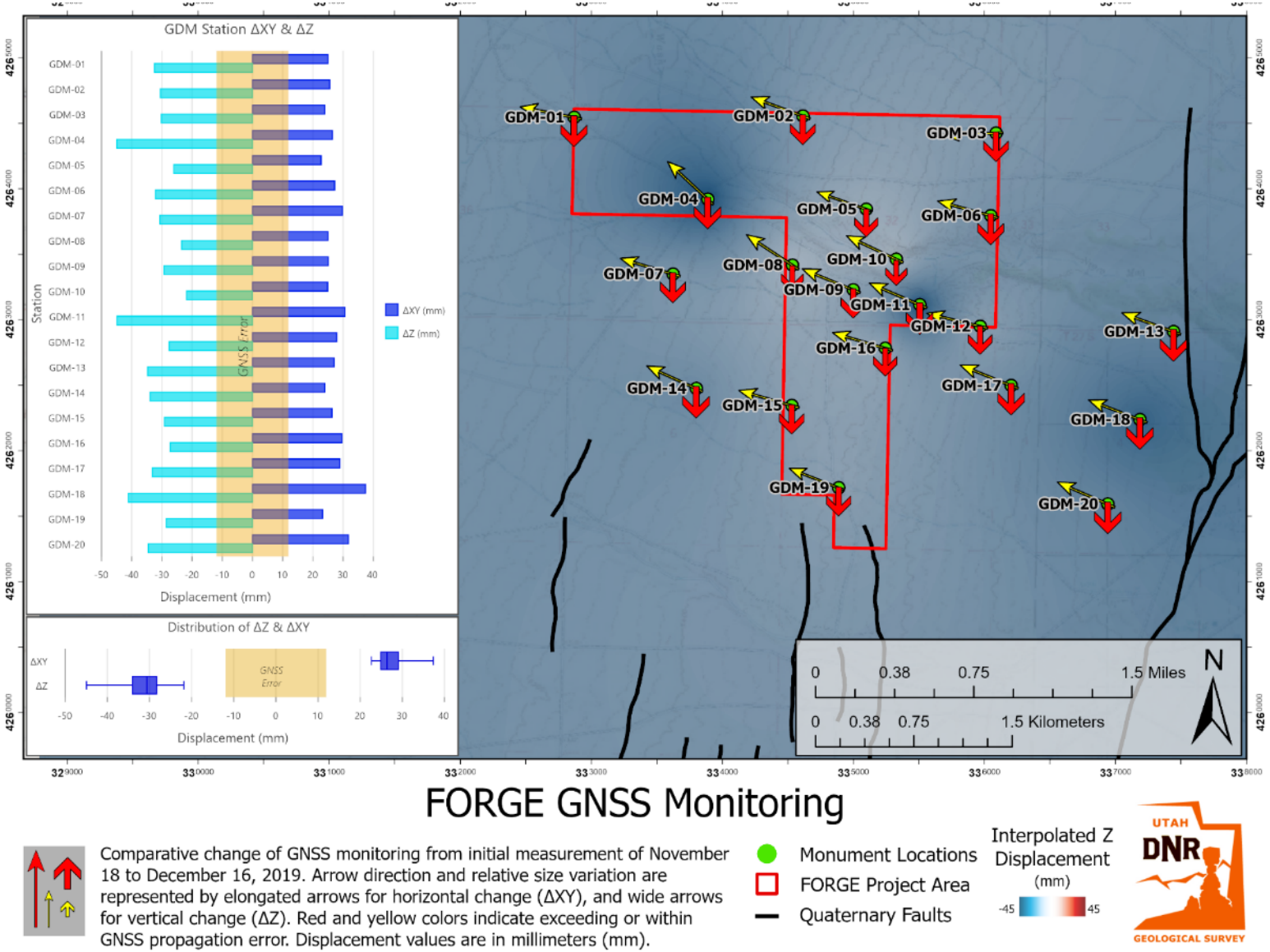

Figure 5: Vector map and displacement interpolation of monument movements measured between Monitoring Campaigns 3 and 4. Displacement surface interpolation range is ±45 mm.

Monitoring Campaign 5

In spring of 2020, a new pad was installed in the proximity of GDM-08. During Campaign 5 on June 2, a review of station GDM-08 was performed and was found to be intact; however, concerns were raised over the effect of the proximity of the adjacent new drill pad on the gravity measurements. A new monument was installed in similar fashion as the 20 previous installations, with a three-person crew, using the same methods implemented previously. An additional new monument was installed near regional water well WOW2, on the southern end of the Utah FORGE Project area, approximately 2.8 km southwest of GDM-19, near the Blundell Geothermal access road using the same installation methods (Figure 1). Monitoring Campaign 5, starting June 1, 2020, was performed using ATV and truck transport between monitoring stations.

As was performed for previous monitoring campaigns, stations GDM-B1, GDM-B2, GDM-04, GDM-08, and GDM-09 were started the night prior to the rest of the campaign. Station GDM-08 had battery issues and only recorded 1.5 hours. Additionally, stations GDM-11, GDM-12, and GDM-21 were started at the end of the campaign and allowed to record through the night. When comparing to the Initial Monitoring Campaign B in March 2019 (Figure 6), there is little change, unlike Campaign 2 of June 2019, occupied at the same time of year, where an inflation was detected on the western end of the study area. The largest change is a deflation at GDM-12 of 15.0 mm with the overall trend of negative values in the area. GDM-01 shows the highest inflation value of 10.6 mm, but the overall area shows little ground deformation to within estimated uncertainties of 5-6 mm. The lack of a heavy snow year likely contributed to the lack of inflation, as seen in spring of 2019.

Figure 7 below shows the results of Campaigns 5 compared to Campaign 6, where there are relatively minor changes to the area between campaigns.

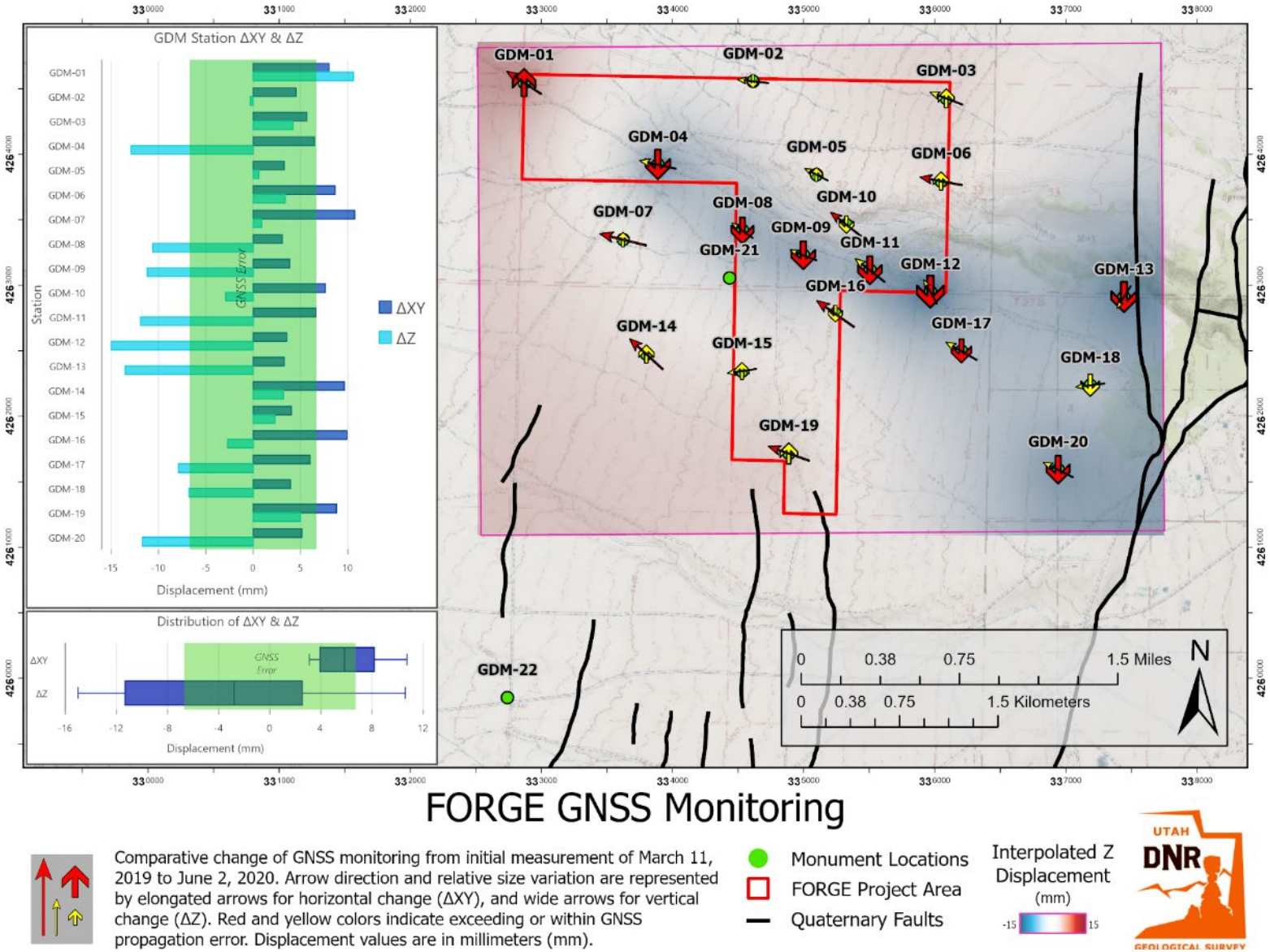

Figure 6: Vector map and displacement interpolation of monument movements measured between Monitoring Campaigns Initial B and 5. Displacement surface interpolation range is ±35 mm.

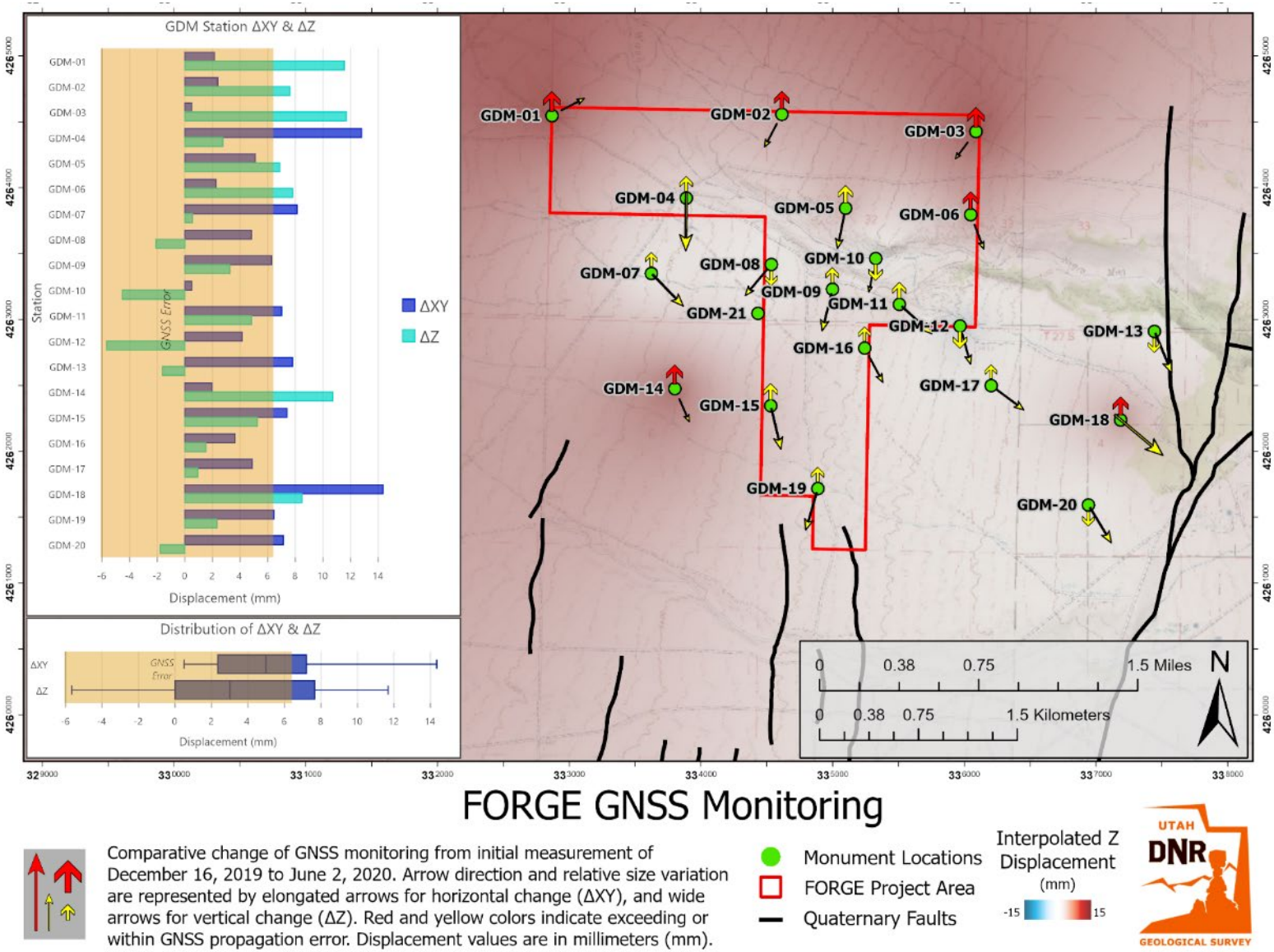

Figure 7: Vector map and displacement interpolation of monument movements measured between Monitoring Campaigns 4 and 5. Displacement surface interpolation range is ±15 mm.

Monitoring Campaign 6

In September 2020 monitoring Campaign 6 was performed with an ATV and a truck, similar to earlier campaigns. GDM-B2 was set up and configured first, followed by GDM-B1. After the two bases were started there was enough time in the day to begin measuring other monuments. GDM-22, GDM-18, GDM-13, GDM-12, GDM-09, and GDM-04 were completed where GDM-20, GDM-11, and GDM-01 were left overnight for their measurements. The remaining monuments were measured the following day with sporadic rain hampering the campaign in the late afternoon. GDM-03, GDM-10, and GDM-08 were left for overnight measurements. No issues were encountered when retrieving GDM-B1 and GDM-B2.

The results of Campaign 6 compared to March 2019 (Figure 8), shows an overall negative displacement in the area. There is larger downward trend along Mag Lee Wash south ridge with GDM-04 measuring the highest negative displacement, with GDM-09, GDM-12, and GDM-13 forming a trend along the south ridge.

Comparing the deformation between Campaigns 5 and 6 (Figure 9) show similar results as compared to the initial campaign, but the more negative values are measured north of Mag Lee Wash with an inflation in the southeast of the area.

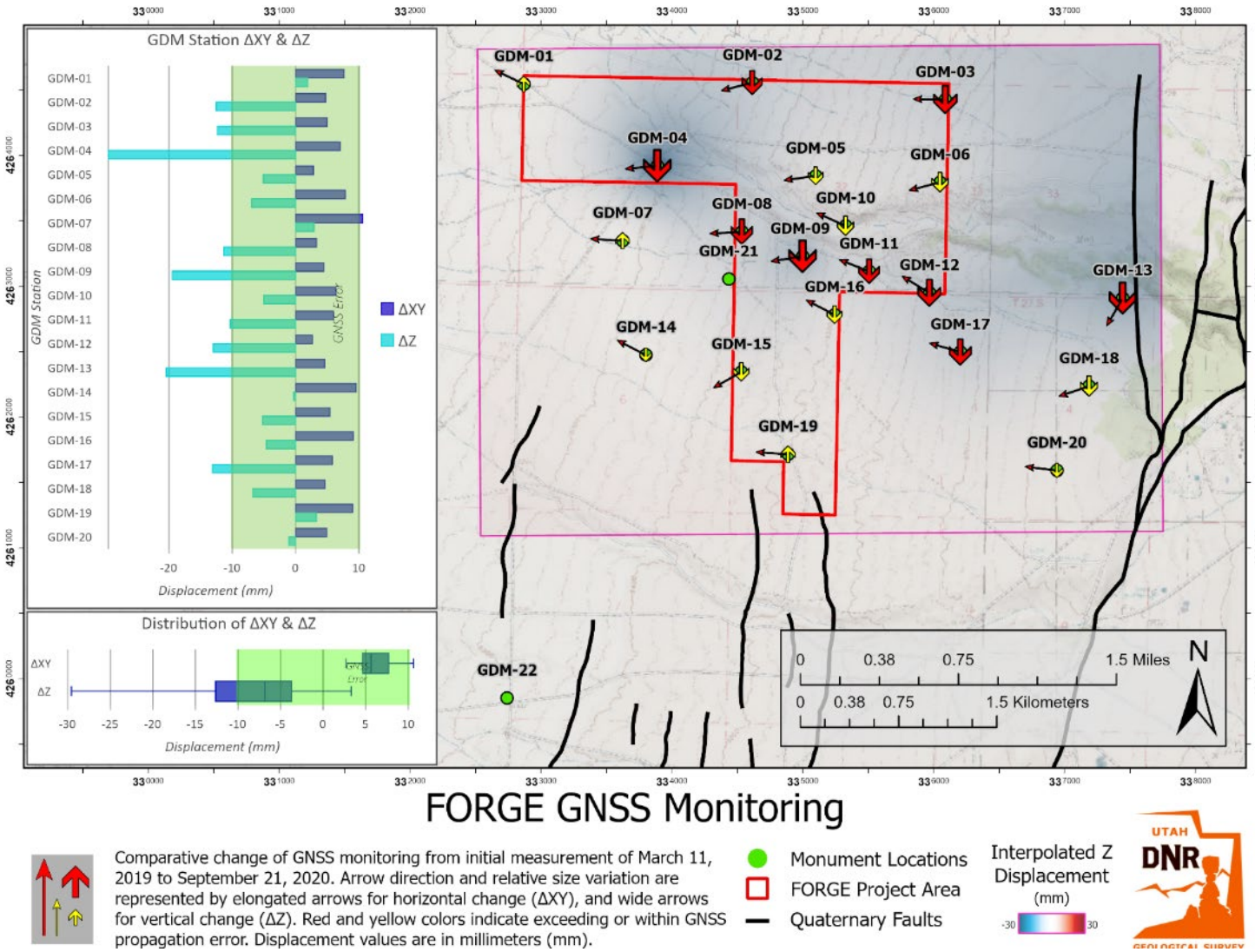

Figure 8: Vector map and displacement interpolation of monument movements measured between Monitoring Campaigns Initial B and 6. Displacement surface interpolation range is ±35 mm.

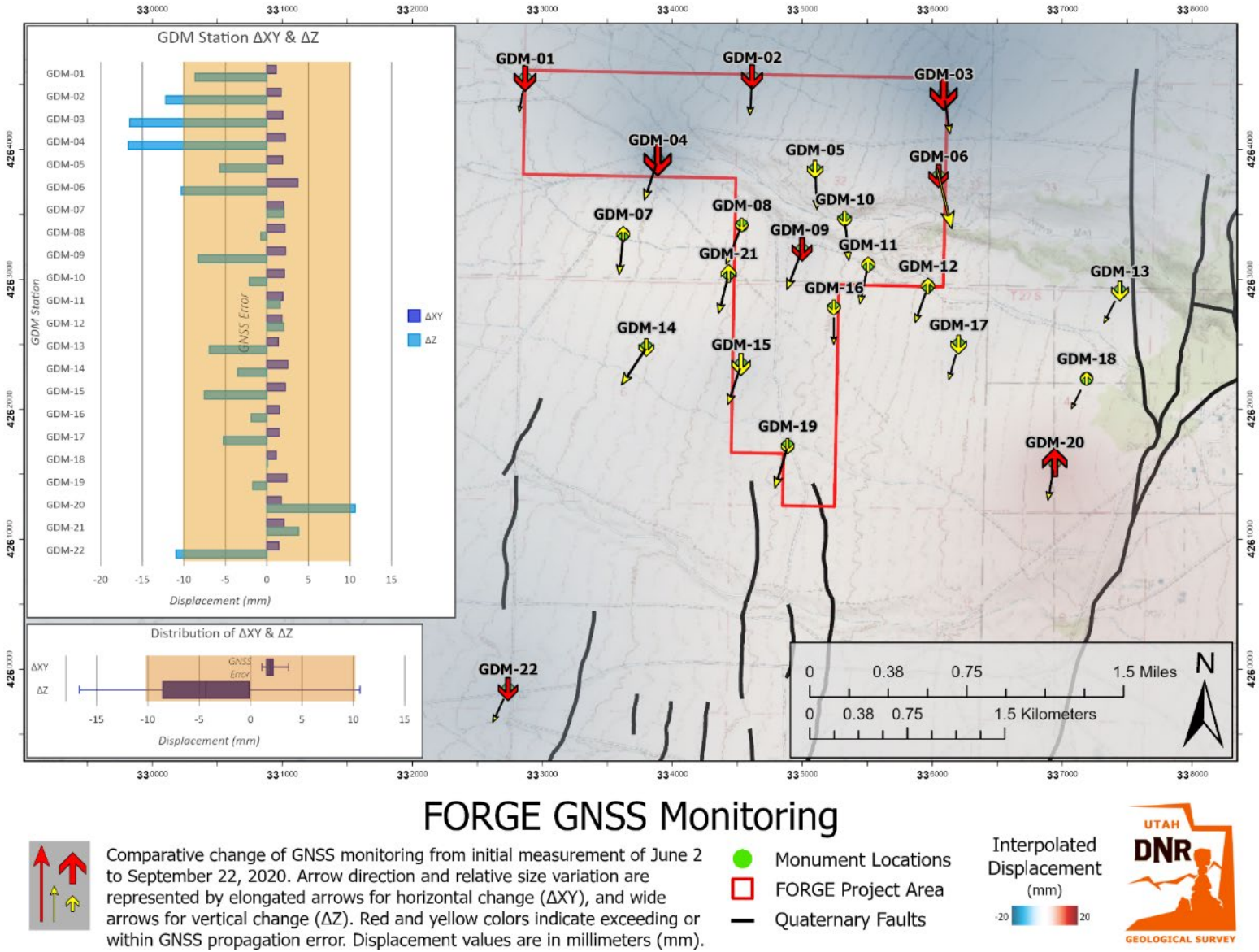

Figure 9: Vector map and displacement interpolation of monument movements measured between Monitoring Campaigns 5 and 6. Displacement surface interpolation range is ±20 m

Monitoring Campaign 7

Monitoring Campaign 7 was performed on December 7, using ATV and truck transport between monitoring stations. The installation process for continuous GPS stations were started through augering a total of four holes, two holes per station. The GPS antenna mount was installed in a similar manner as the other geophysical stations, with a wide augered hole three-feet deep and twelve-inches wide. A three-quarter-inch aluminum rod was driven to a minimum depth of thirty feet with a greased isolating, protective sleeve placed around the rod. A six-inch diameter PVC pipe was placed with sand around the rod, extended eight inches above the surface for further stability and protection against the environmental impacts of flowing water and snow accumulation. In addition to the augered hole for the antenna rod, an additional hole was augered to anchor a metal mounting pole for the protective cabinet housing the GPS receiver and solar power supply. Additional installation steps were taken on subsequent monitoring campaigns.

The results of Monitoring Campaign 7 are summarized in Figures 10 and 11. When comparing to the Initial Monitoring Campaign B in March 2019, Figure 10, shows an overall minor inflation throughout the Utah FORGE site. The site shows an average vertical inflation of 7.4 mm, with a maximum displacement of 18.9 mm. The majority of measurements are within the GNSS errors for both occupations. Comparing Campaign 6, September 22, 2020, and Campaign 7 in Figure 11, there was a greater inflation trend to the Utah FORGE site from September to December 2020. The inflation suggests there was seasonal shallow groundwater influence driving the displacement, primarily in the Mag Lee Wash area.

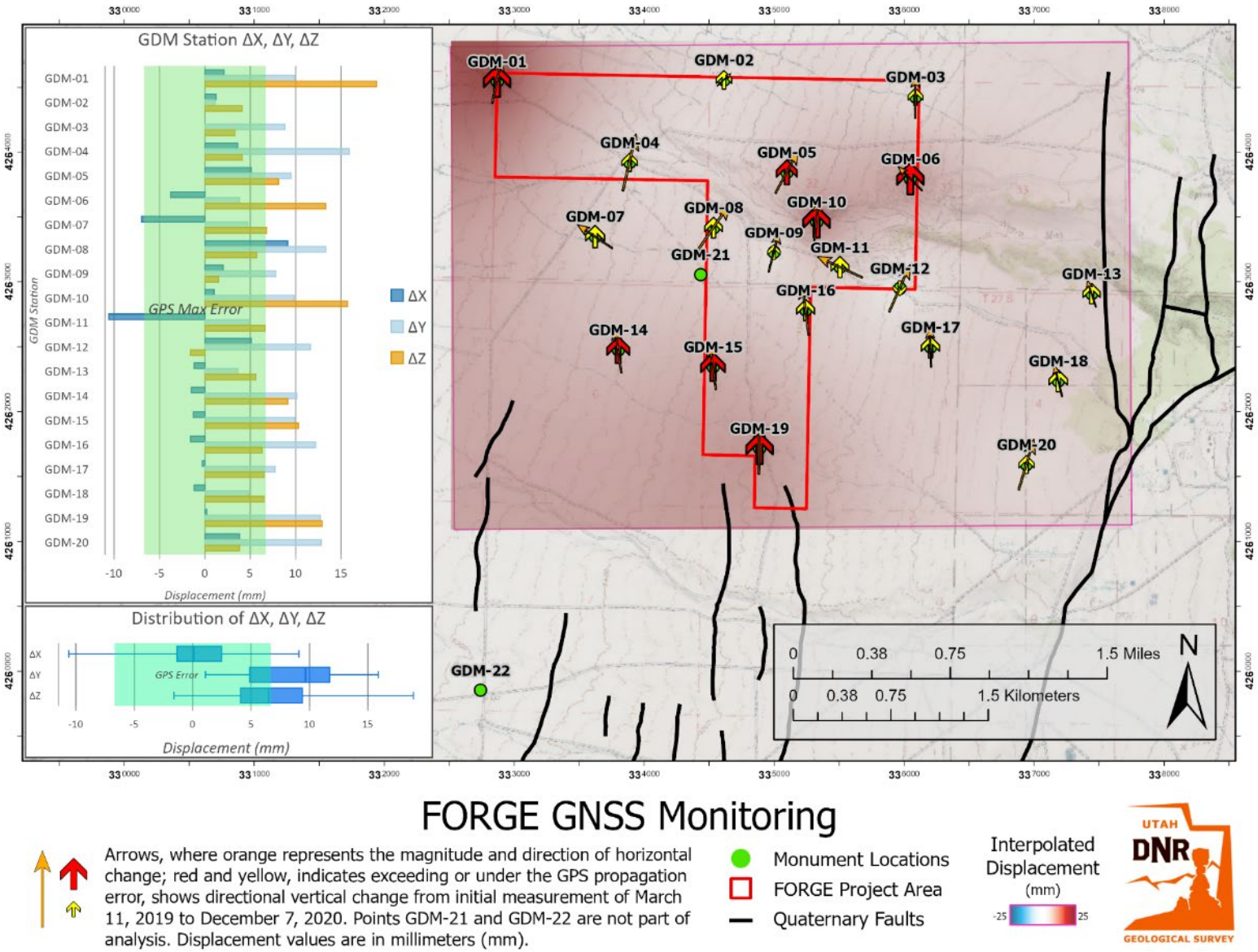

Figure 10: Vector map and displacement interpolation of monument movements measured between Monitoring Campaigns Initial B and 7. Displacement surface interpolation range is ±25 mm, located to lower right of figure.

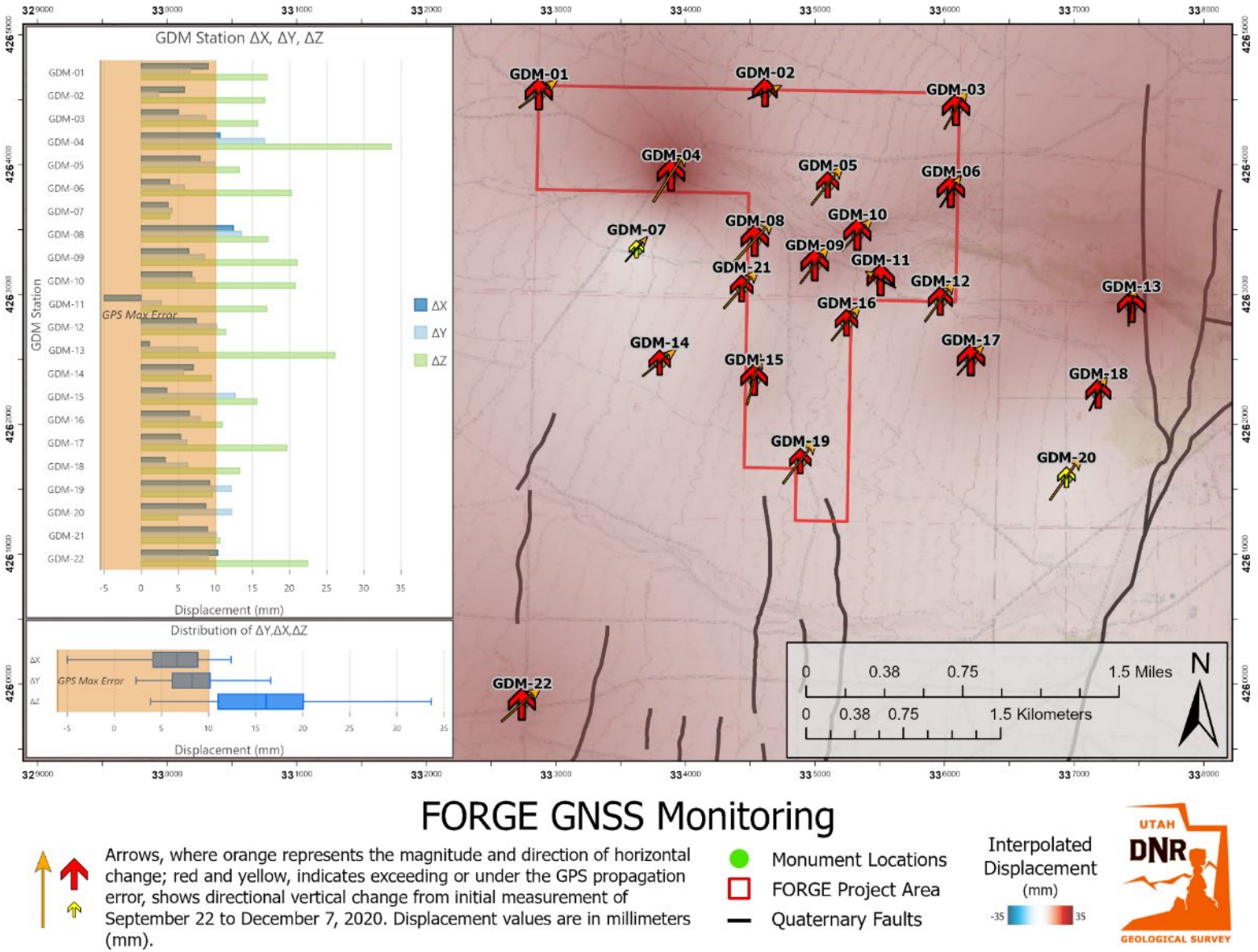

Figure 11: Vector map and displacement interpolation of monument movements measured between Monitoring Campaigns 6 and 7. Displacement surface interpolation range is ±35 mm.

Monitoring Campaign 8

Monitoring Campaign 8 was performed on March 6, 2021, using ATV and truck transport between monitoring stations. There was snow on the ground at station GDM-B1 making access not possible by truck due to unexpected high snowpack. Measurements from GDM-B1 were not performed. The majority of the hardware for the continuous GPS stations were installed, at the base of the western embankment of pad 58-32 (Figure 12) and the other continuous station near the northern seismic monitoring station FSB3.

Figure 12: Continuous GPS station, GDM-C1. Installation is west of pad 58-32 embankment.

The comparative results (Figure 13) show minimal upward displacement from the initial measurement of March 2019. The maximum measured displacement was near GDM-01, with a value of 21.6 mm, with an outlier at GDM-08 showing a deflation of -6.5 mm. Figure 14 shows an overall deflation since Monitoring Campaign 7, December 2020. GPS stations GDM-08 and GDM-10 show high negative displacement over time and may be reflective of the new infrastructures of pad 16A(78)-32, and road to pad 56-32, through adding mass near the respective stations.

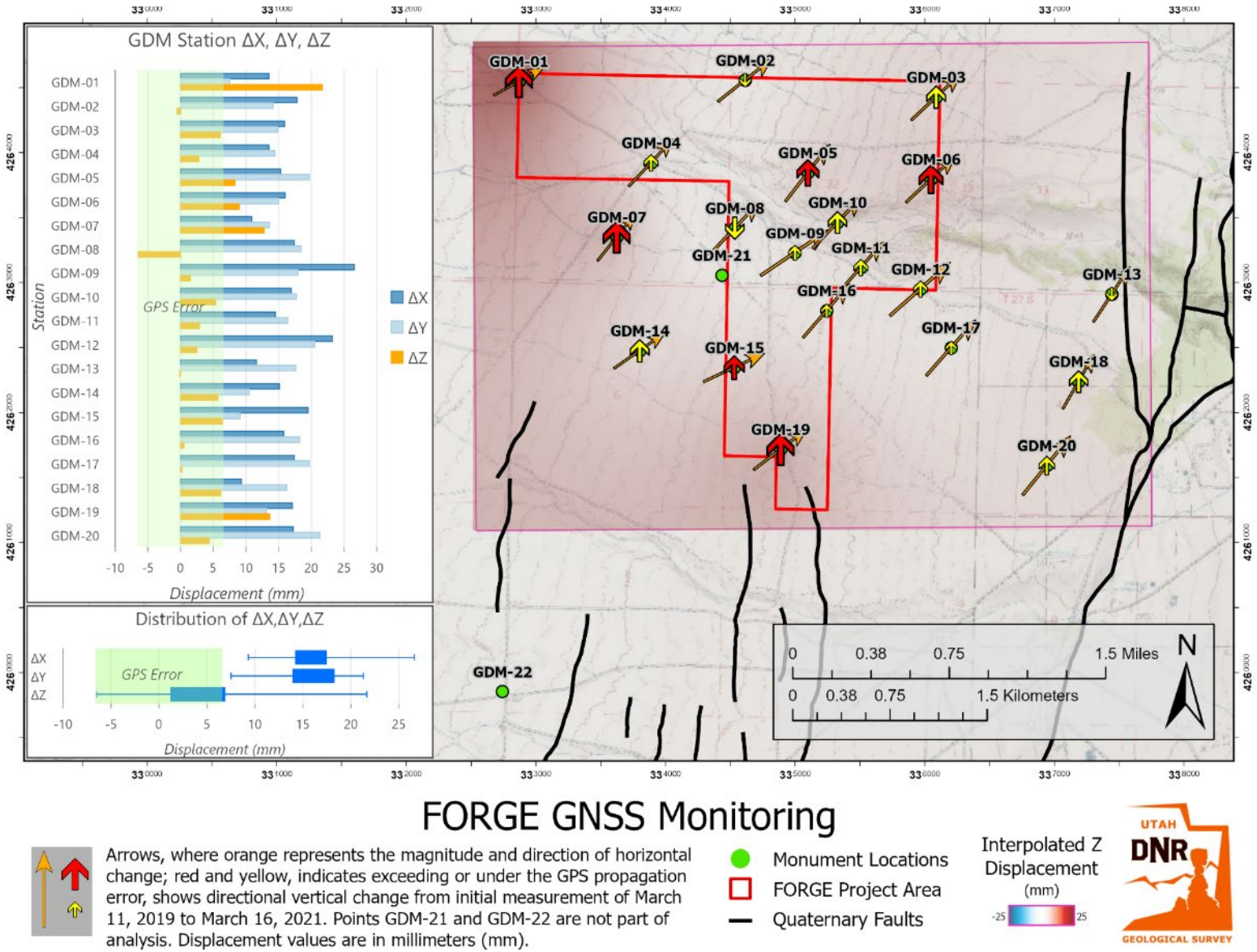

Figure 13: Vector map and displacement interpolation of monument movements measured between Monitoring Campaigns Initial B and 8. Displacement surface interpolation range is ±25 mm.

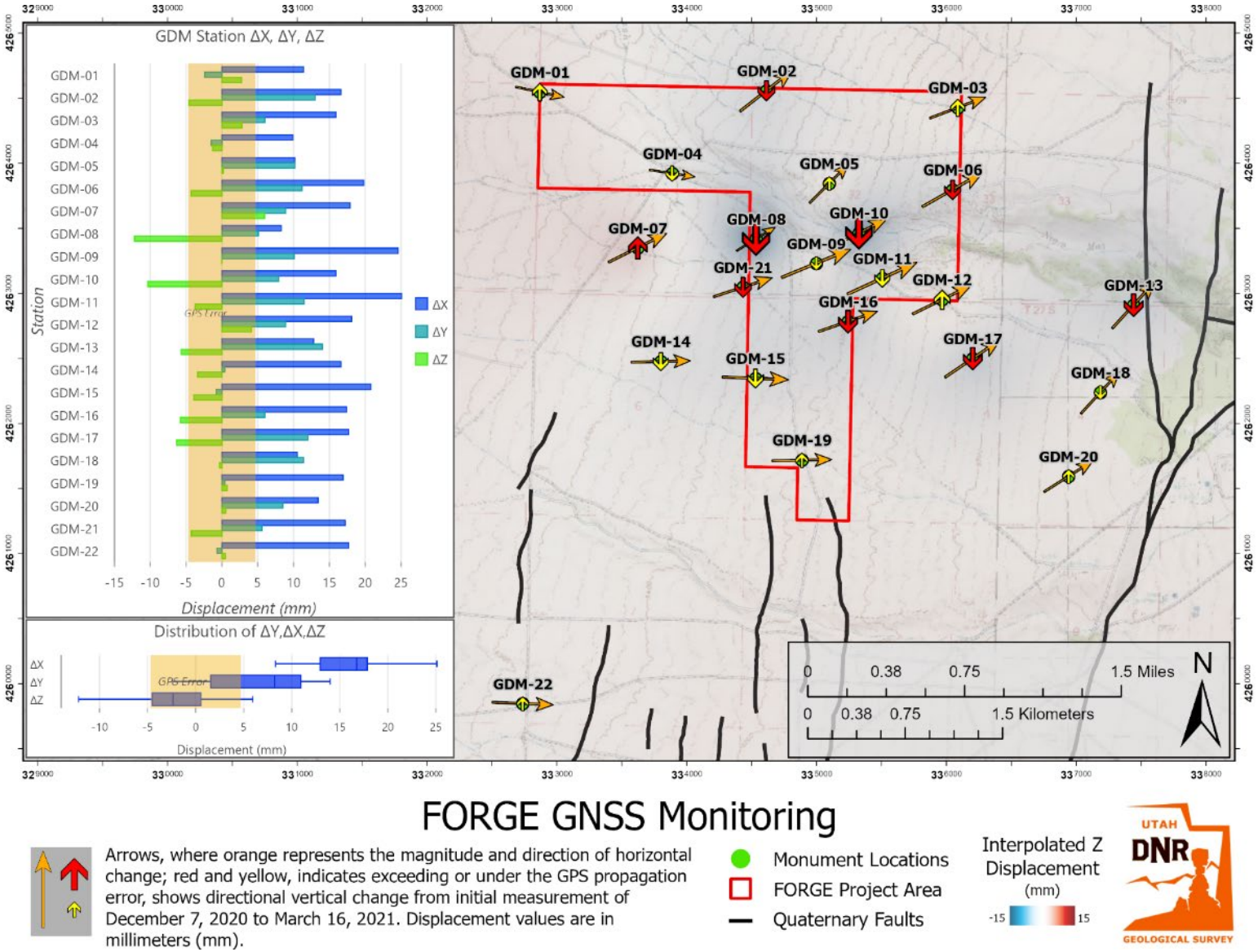

Figure 14: Vector map and displacement interpolation of monument movements measured between Monitoring Campaigns 7 and 8. Displacement surface interpolation range is ±15 mm.

Monitoring Campaign 9

Leading up to and during Monitoring Campaign 9 we contributed the upcoming update to the National Spatial Reference System (NSRS), preparing for the NSRS modernization in 2022. We performed several GNSS occupations on priority Natural Geodesic Survey (NGS) benchmarks following the GPS on benchmarks campaign outlined by the NGS. We identified 25 benchmarks near the Utah FORGE site for occupation. From the list of 25, we were able to confirm and measure 11 benchmarks for the 2022 update. The goal of the NSRS is to use this data to enable conversions from current vertical datums to the North American-Pacific Geopotential Datum of 2022 (NAPGD2022). Further information about the update is available from the NGS GPS contribution website, https://geodesy.noaa.gov/GPSonBM/. This new datum will provide higher quality results in future measurements, a benefit to the Utah FORGE ground deformation monitoring. Figure 15 is a location map of the measured benchmarks and nearby Continuous Operating Reference Stations (CORS). Table 1 is the occupation results and statistics of the measurement processing associated with the CORS data. Additional measurements can be done to further contribute to the update.

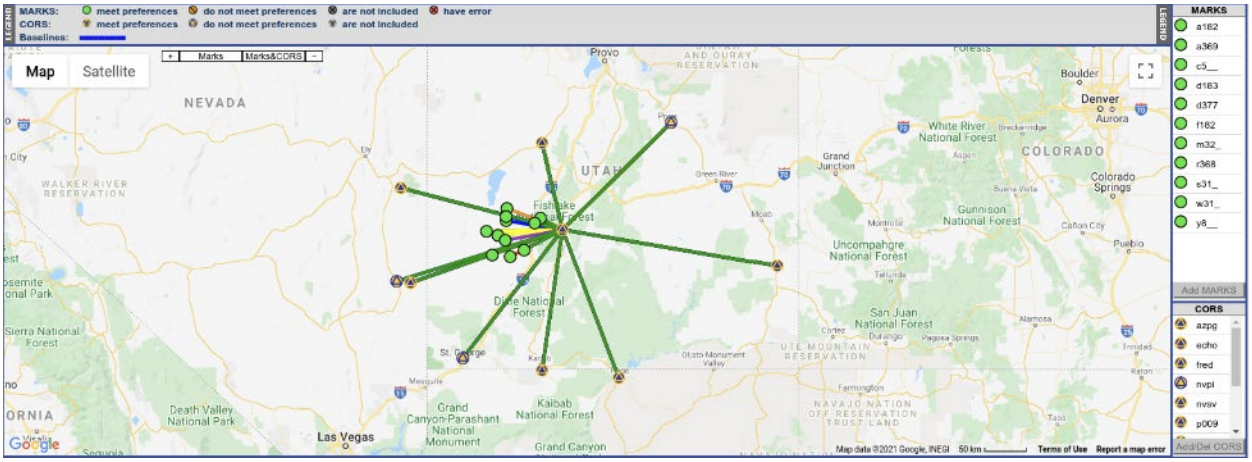

Figure 15: Vector map of NGS benchmarks and CORS locations near the Utah FORGE site. Green points are measured benchmarks and the circled triangle points are CORS near the Utah FORGE site. The multicolor connective lines indicate time-related baselines to a specified CORS anchor, for precision location processing

Monitoring Campaign 9, performed June 2, 2021, base station GDM-B1 was measured by one of two newly acquired Septentrio GNSS receivers, model PolaRx5e. The second unit was not ready for use for this campaign and GDM-B2 was not measured. When processing the data, GDM-B1 results showed a high displacement, much higher than previous measurements. Further investing is required to determine the cause of the error; the collected data was not used in processing. Using CORS date to supplement the missing base stations, the results showed within normal displacements (Figure 16). The comparative results show minimal vertical displacements from the initial measurement of March 2019; an overall trend of horizontal displacement to the northeast is shown, which has been consistent when comparing previous campaigns. The maximum measured displacement was near GDM-01, with a value of 17.9 mm; an overall minor deflation is detected throughout the study area. Comparing campaign 8 and 9 (Figure 17) shows

an overall deflation and the horizontal displacement was consistent in direction but decreased since last monitoring campaign 8, March 2021.

MARKS	Solution & Statistics									MARKS
	occupations count	occupations used	solutions count	Obs Used	Obs Used(%)	AMB Fixed(%)	North P2P(cm)	East P2P(cm)	Up P2P(cm)	
a182	2	2	2	7856	89.8	98.9	0.1	0.7	1.4	a182
a369	2	2	2	16471	89.9	97.2	0.0	0.3	1.0	a369
c5__	1	1	1	3790	91.9	95.1	–	–	–	c5__
d183	2	2	2	19271	90.3	96.9	0.2	0.6	0.2	d183
d377	2	2	2	17535	88.6	98.1	0.2	0.1	0.8	d377
f182	1	1	1	4068	92.3	94.2	–	–	–	f182
m32_	2	2	2	8165	94.0	93.7	0.4	0.3	2.3	m32_
r368	2	2	2	8400	91.7	95.3	0.1	0.2	2.5	r368
s31_	2	2	2	11337	82.4	95.1	0.4	0.4	2.5	s31_
w31_	2	2	2	12705	91.3	99.4	1.6	0.4	0.1	w31_
y8__	1	1	1	9869	90.9	100.0	–	–	–	y8__
azpg	6	6	9	142555	92.6	92.0	0.84	1.46	1.87	azpg
echo	7	6	9	154428	92.1	97.5	1	0.95	1.7	echo
fred	4	3	5	63253	92.7	98.0	0.63	0.81	1.97	fred
nvpi	2	2	3	42539	90.9	86.9	1	0.5	1.98	nvpi
nvsv	7	6	9	149499	92.2	92.0	0.92	0.69	2.94	nvsv
p009	7	6	9	1199340	91.8	94.8	0.09	0.17	0.02	p009
p012	6	6	9	150557	90.5	97.6	0.72	0.95	2.68	p012
p105	6	6	9	154073	92.1	97.6	0.59	0.74	2.28	p105
puc2	6	6	8	98701	91.3	93.7	0.66	0.94	1.79	puc2
sgu1	7	6	9	124268	93.2	90.7	0.74	0.74	1.89	sgu1

Table 1: Results of the benchmark solutions when processed with the surrounding CORS data. Marks in red are benchmarks measured near the Utah FORGE site. Majority of benchmarks were occupied two times; each occupation was measured for over 4 hours.

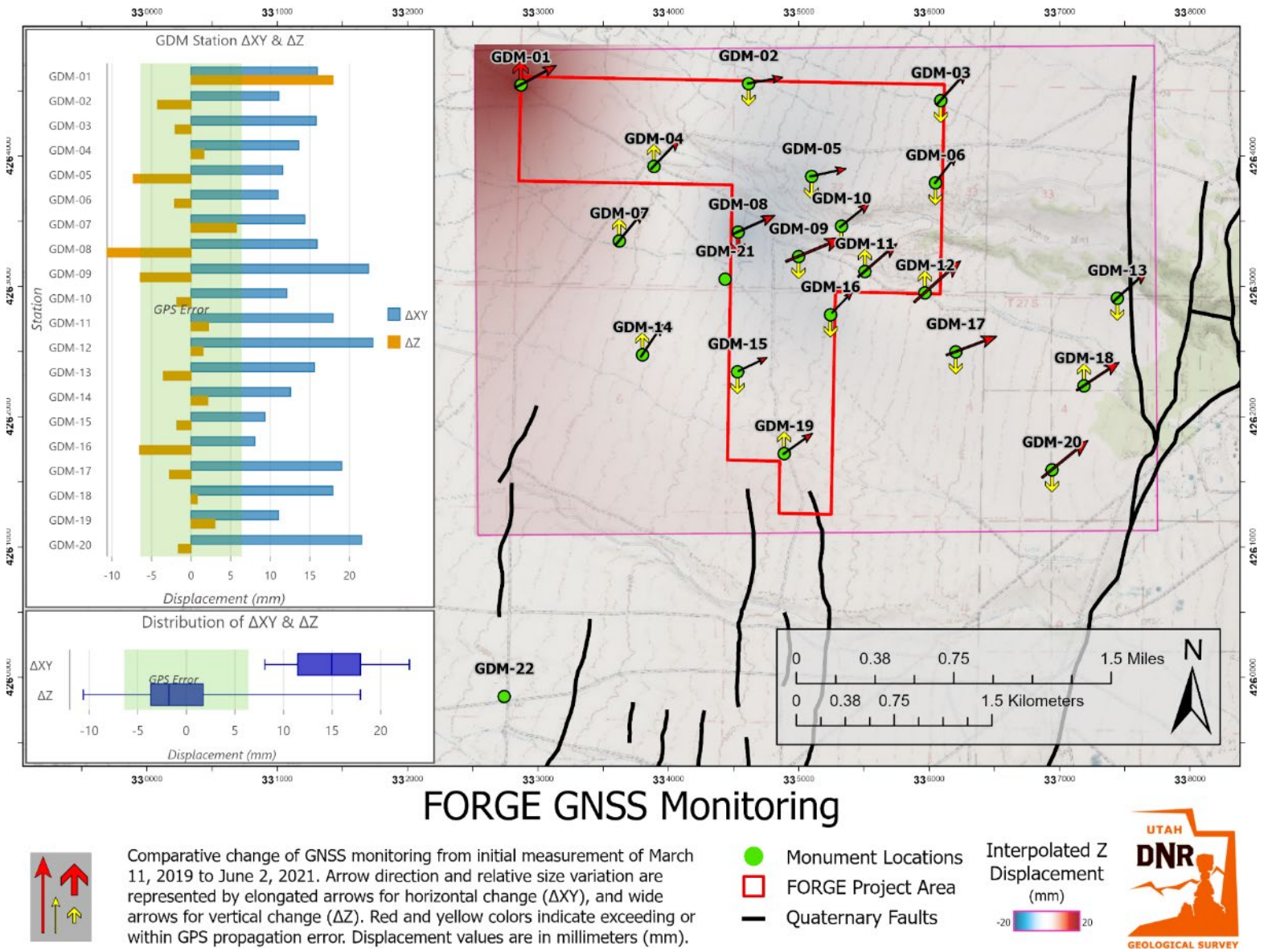

Figure 16: Vector map and vertical displacement interpolation of monument movements measured between Monitoring Campaigns Initial B and 9. Displacement surface interpolation range is ±20 mm.

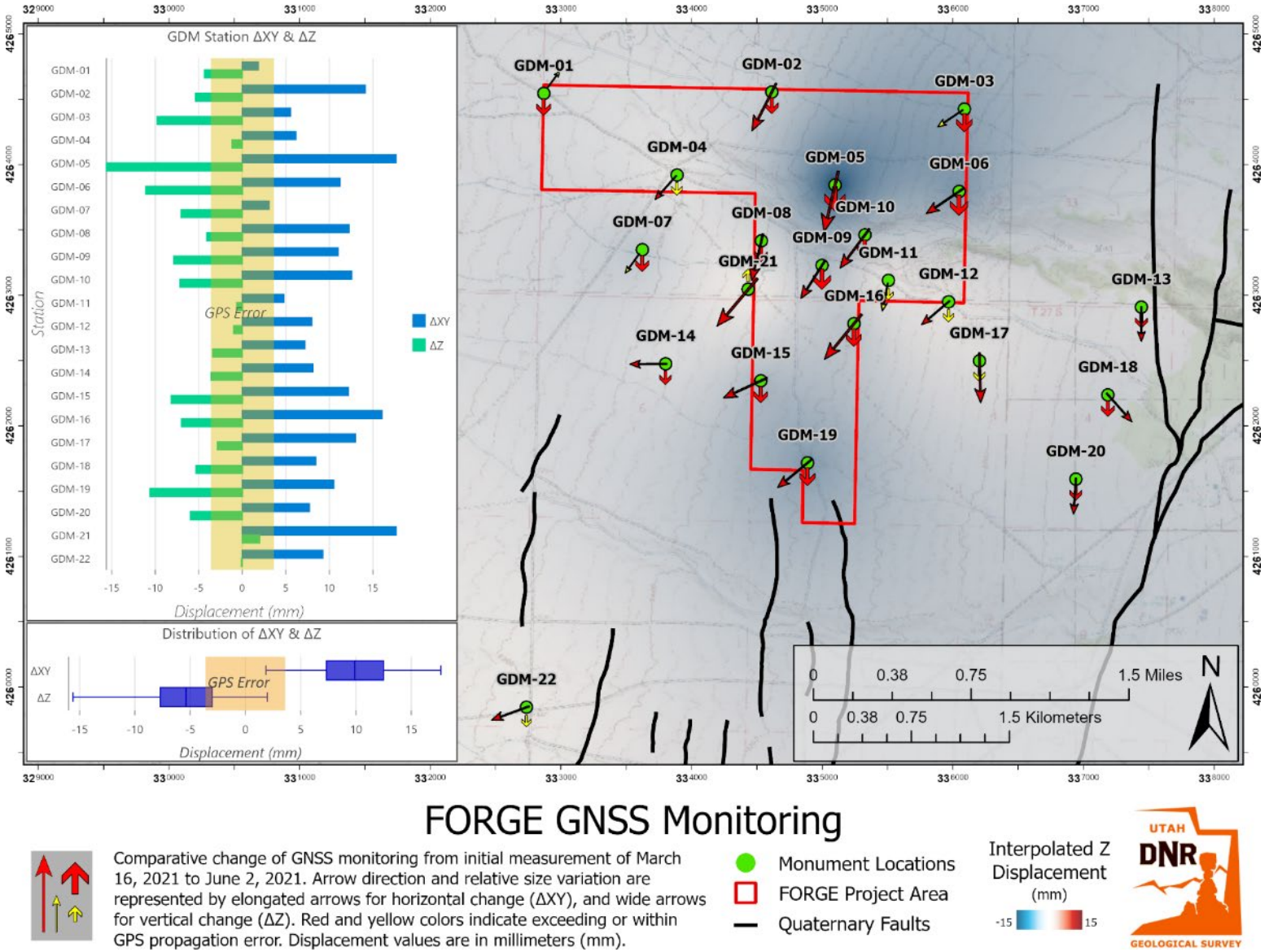

Figure 17: Vector map and vertical displacement interpolation of monument movements measured between Monitoring Campaigns 8 and 9. Displacement surface interpolation range is ±15 mm.

Monitoring Campaign 10

For Monitoring Campaign 10, performed September 20, 2021, base stations GDM-B1 and GDM-B2 were measured by the Septentrio GNSS receivers, model PolaRx5e and external antennas. Additionally, three newly acquired Septentrio Altus NR3 units were used in the measurements of the monuments, totaling nine units to perform the campaign. During the campaign assistance was provide in the installation of the wireless internet infrastructure. The completion of the wireless infrastructure will facilitate the final requirements for the continuous GNSS receivers on site. A trench was excavated, and data line laid to the continuous GPS receiver near well 58-32. Unfortunately, the RJ45 connecting ends were not installed preventing online access for the receiver.

When processing the campaign data, results showed a high displacement, much higher than previous measurements for GDM-B1 and GDM-B2, similar to last campaign. It was determined the processing software was not providing the proper antenna calibration information for accurate processing. A support ticket was submitted requesting the correct antenna file to be included in the software. As was performed last campaign, using data from nearby CORS bases allowed proper processing of the data and results are within normal measurements.

The comparative results (Figure 18) show an inflation of vertical displacements from the initial measurement of March 2019; an overall trend of horizontal displacement to the northeast, as has been typical with past campaigns. The maximum measured displacement was near GDM-01, with a value of 20.8 mm, with an overall inflation detected throughout the study area. Additionally, Figure 19 shows an overall inflation, and the horizontal displacement was more random in direction since last monitoring campaign, June 2021. A similar trend of early fall inflation was seen in 2019. The area is expected to have a deflation in the winter months, as seen in in follow-up measurements in 2020. These results appear to show a seasonal trend most likely cause by near-surface groundwater fluctuations.

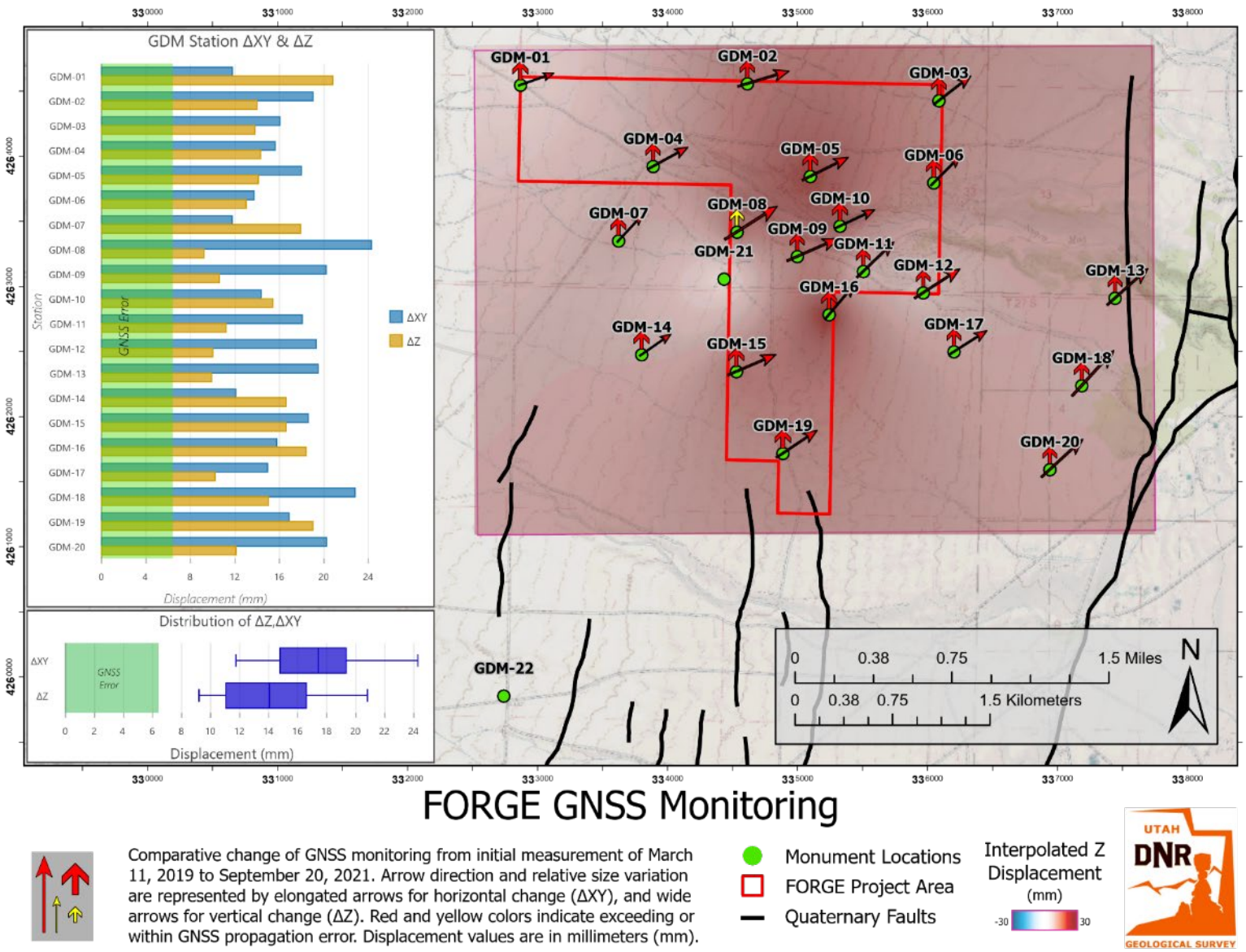

Figure 18: Vector map and vertical displacement interpolation of monument movements measured between Monitoring Campaigns Initial B and 10. Displacement surface interpolation range is ±30 mm.

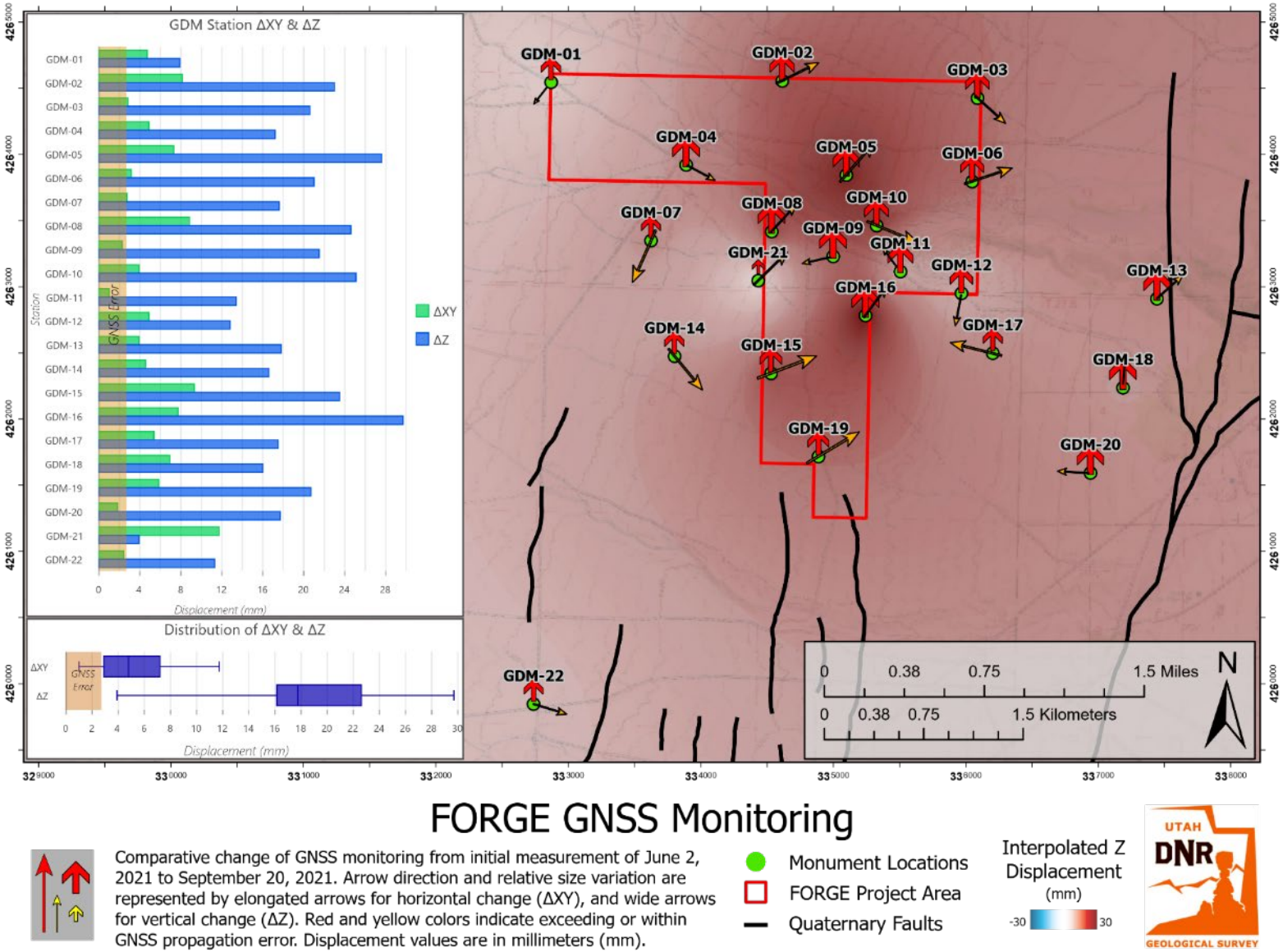

Figure 19: Vector map and vertical displacement interpolation of monument movements measured between Monitoring Campaigns 9 and 10. Displacement surface interpolation range is ±30 mm.

Overall Results

The results of all campaigns from Initial B to Campaign 10 are summerized in Figure 20. The results represented in the graph are the overall average diplacement when compared to Initial B. The error bars for each campaign is the standard deviation to the average of the displacement. Also included are nearby water influences from the Milford Airport, approximately 9 miles (14 km) to the south east of the Utah FORGE site. The precipitation data provides potential near surface water influences at the stations. The well data provide insight to the established groundwater table levels and the potential influence they can have on the stations.

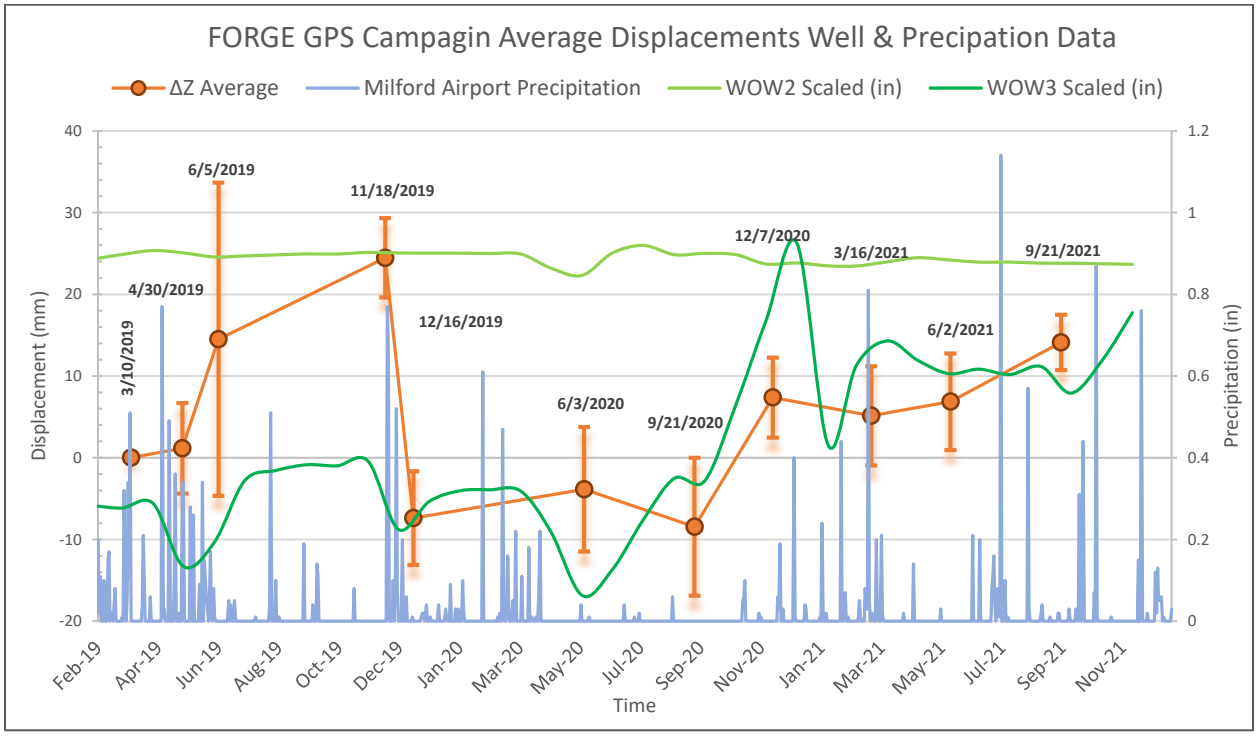

Figure 20: Graph comparing the precipitation at the Milford Municipal Airport and the groundwater levels of wells WOW2 and WOW3 to the displacement average change from the March 2019 Initial B campaign.

Similarly, to Figure 20, Figure 21 shows the potential influence of the SNOTEL site located at the nearby Merchant Valley station, approximately 20 miles (32 km) to the southeast of the Utah FORGE site. The SNOTEL station reports, among other measurements, the snow water equivalent at the station. The snow water equivalent provides anticipated water runoff in the area that will cause groundwater influences. Although it is challenging to determine direct influence by these water measurements, trends can develop over time and can provide a better understanding of the influential impacts of surface to subsurface water.

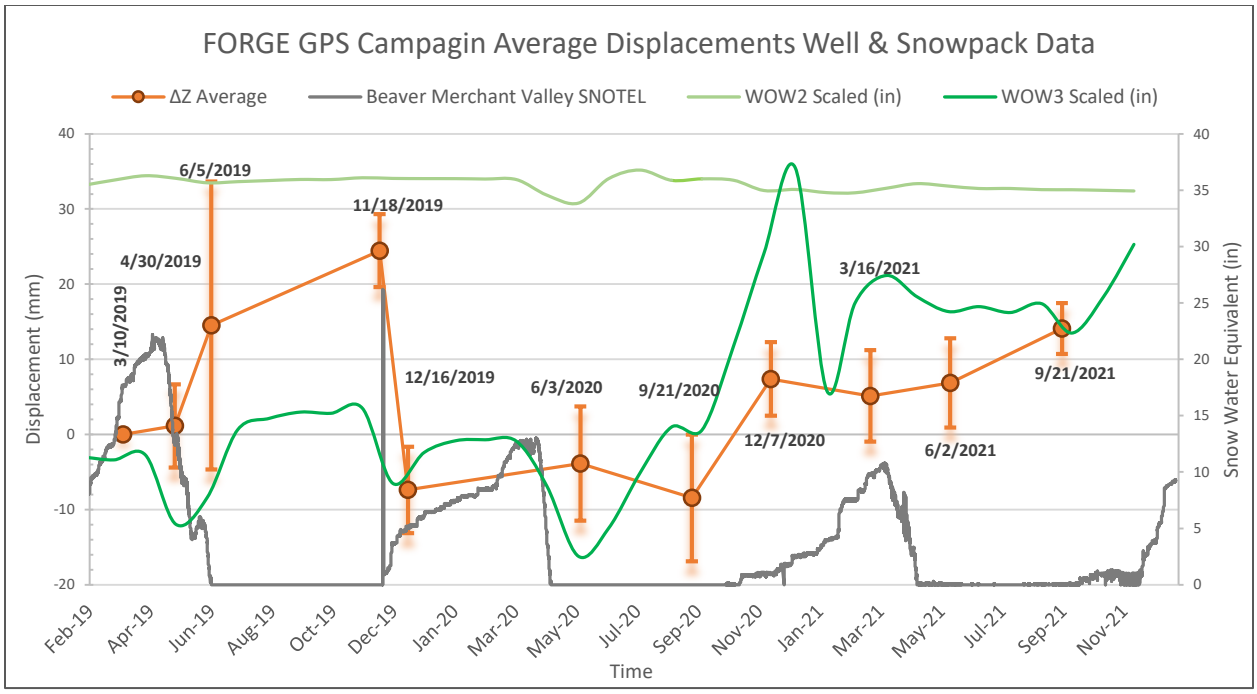

Figure 21: Graph comparing the snow water equivalent as measured at the Beaver Merchant Valley SNOTEL and the groundwater levels of wells WOW2 and WOW3 to the displacement average change from the March 2019 Initial B campaign.

Lessons Learned

Over the course of eight GPS campaign measurements, adjustments in measuring and processing methodology needed to be addressed to better understand the results of the measurements. The adjustments included measuring for longer durations, ensuring the results were within a high resolution for comparison. This includes measuring confidence through propagation error calculations to provide a higher level of assurance that ground deformation is taking place.

Seasonal impacts will be detected in the GPS measurements. Understanding the trends of the season and the potential influences they bring, will provide a more accurate detection of artificial influences. Increasing our awareness and measuring the seasonal data allows for better results and understanding of surficial ground deformations.

Conclusions

The GPS ground deformation monitoring has been maturing in the results and measurement confidence over the course of Phase 3. With the addition of new GNSS receivers and with the installation of the continuous GPS stations, results and measurements will continue to mature and provide high quality data. The measuring campaigns will continue to take place at a quarterly interval with additional measurements when needed. The first of the two continuous GPS stations will shortly be coming online to provide daily positions to the Utah FORGE location, allowing near real-time measurements to the site. The results of the GPS monitoring have provided a better understanding of the surficial dynamics and will continue to be an essential tool for the future of Utah FORGE investigating actives.

Attachment 6

Phase 3A Year 2 Annual Report – Appendix A2

Enhanced Geothermal System Testing and Development at the Milford, Utah FORGE Site

Utah FORGE
University of Utah
423 Wakara Way, ste 300
Salt Lake City, UT, 84105

Prepared for the U.S. Department of Energy

Office of Energy Efficiency and Renewable Energy

Contract DE-EE0007080

April 30, 2022

Annual Research Performance Progress Report:

Subtask 3.7.4. 4D Gravity Survey

Overview

Following the SOPO for the first two years of Phase 3, Utah FORGE is to conduct repeat measurements at a series of GPS stations over the Utah FORGE area plus two survey base monument stations established in Phase 2C to determine if ground motion has occurred as a result of ground water drawdown or downhole stimulation. This is to be done by completing campaign gravity loops of the Utah FORGE stations on all geophysical deformation (GPS) monuments four times in 2021. We were to reprocess previously measured microgravity data with an improved routine and combine with local hydrological data.

Results

Four complete microgravity campaigns consisting of four trips to the Utah FORGE site comprise this period's tasking. A total of 22 stations were successfully occupied each trip, locations shown in Figure 3.7.4-1. Preliminary data analysis shows coherency in trends of certain groups of stations (see Figures 3.7.4.-2 through 3.7.4-4). Gravity changes to be expected due solely to elevation changes are calculated using the free air correction (-0.3086 mGal/m or -3 µGal/cm). Anticipated microgravity changes due to GPS-measured vertical differences for the Utah FORGE area (centimeter scale) are on the order of 10 µGal. Real gravity signals due to subsurface mass changes in basin settings are typically on the order 50-200 µGal. Preliminary data processing shows changes at stations in the field exceeding 200 µGal which are suspected of noisy station occupation suffering from transit effects on the sensor due to rough inter-station ATV transport. These data points are subject to a higher level of discrimination until they are investigated further and determined to be real signals. Currently, calculated gravity effects due to elevation changes as detected by GPS are below the noise level of even the quieter stations within the Utah FORGE microgravity dataset (10-15 µGal).

Implementation of a modified dense-network microgravity survey routine is assisting with the mitigation and quantification of short-term, non-linear drift that is unique to each gravimeter's sensor as well as the unwanted transit effects. The dense-network routine places focus on smaller, more frequent station loops. For example, stations A through E that were previously done by two loops in a day (A-B-C-D-E-A-B-C-D-E-A) are rearranged into smaller loops (i.e., A-B-C-B-A-C-D-E-D-E-A). This method is more robust and allows for better bracketing of non-linear senor drift which directly affects the stations inside of a loop. Another benefit of the dense network is that measurements can be stopped at any time (for bad weather, etc.) and resumed later without needing to repeat the full prior loop. Current processing results show measurement uncertainties vary by station occupation and field campaign. They can be as low as 10 µGal for some of the quietist sites and as high as 100 µGal for noisier measurements. Mean standard deviation values per field campaign are typically below 50 µGal, however, a handful do have residuals on the order of 150 µGal. This is attributed to the noisy station measurements, particularly those that require ATV transport as the bumpy ride necessitates more time for the gravimeter sensor to recover once immobilized. Currently the noisy stations are kept in the suite of microgravity data until it is certain the data are unrecoverable. It should be noted that these are typically non-issues with regional gravity surveys due to the difference in the required precision of said measurements (mGal vs. µGal).

Microgravity signals shown are currently referenced to a far-field station located at the Milford Valley Memorial Hospital gravity base station (MGB). It is likely that a significant component of the coherent signal in the local tie points is due to changes at the far-field base. Careful investigation of nearby water wells and other hydrological data will help shed light on the amplitude of the MGB signal in order to differentiate from local microgravity signals in the Utah FORGE area.

Lessons Learned

Changes in micro gravity due to elevation changes of the scale resolved by campaign GPS measurements (centimeter scale) are small (10-15 μGal) compared to typical basin scale mass changes due to hydrological variations (of order 100 μGal). Issues of sensor drift, some of which may be related to transport, require particular care in microgravity surveying beyond that of normal regional gravity surveys.

Conclusions and Plans

We plan to repeat loops of gravity station measurements on all monuments 4 times annually to continue the monitoring campaign. The addition of continuous GPS stations will assist in further analyzing gravity data to better understand its relationship with ground deformation and subsurface mass changes. Loops of gravity station measurements on all monuments in Spring 2022 will be repeated to continue the monitoring campaign. We will complete the careful data scrutiny and analysis of the revised post-processing methodology. We will incorporate groundwater level data, meteorological data, and regional NASA Gravity Recovery and Climate Experiment (GRACE) data. These datasets will assist in quantifying expected changes in the regional and local field and separating real gravity signals from instrumental noise.

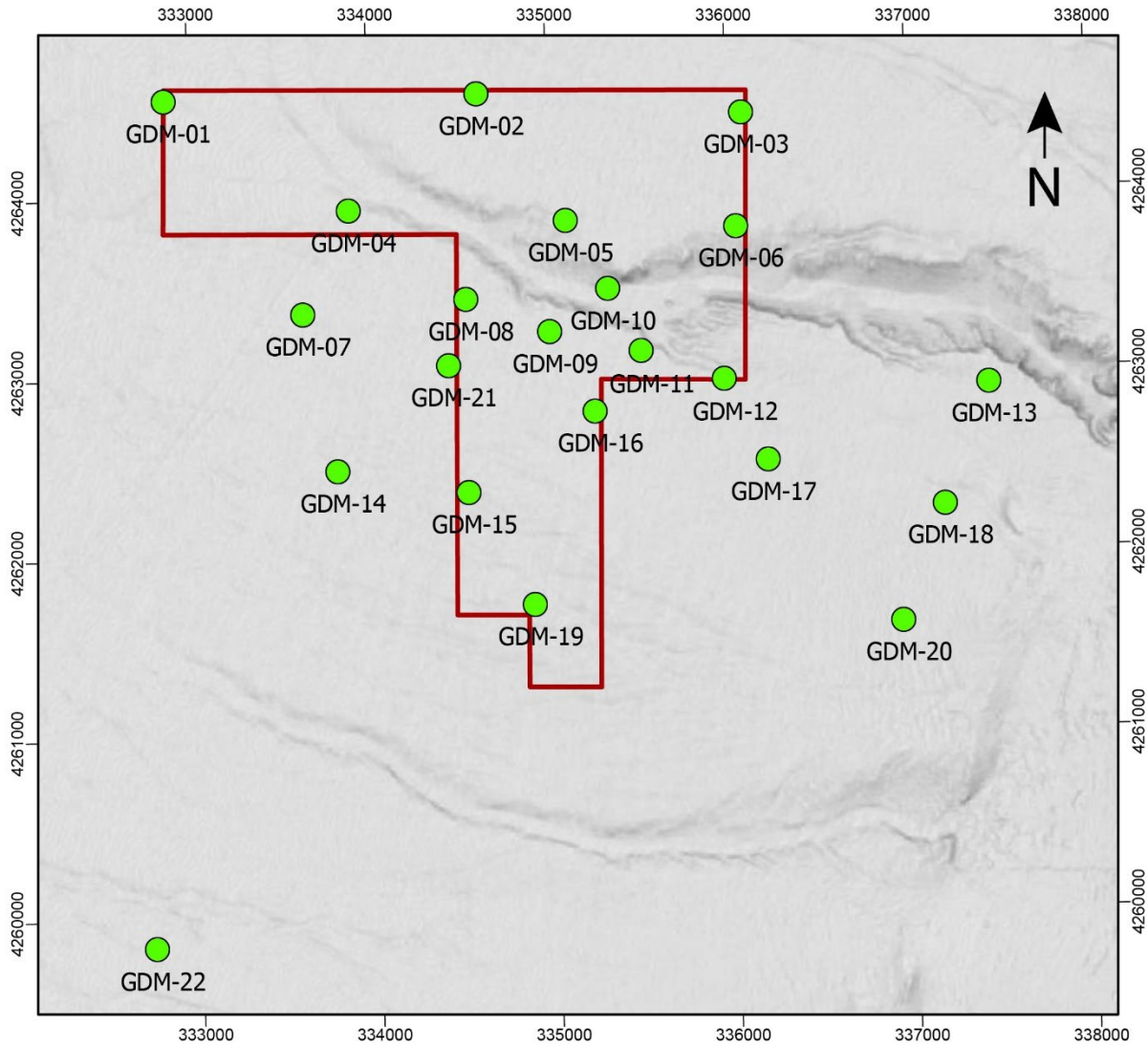

Figure 3.7.4-1. Map of Utah FORGE 4D gravity station locations for 2022.

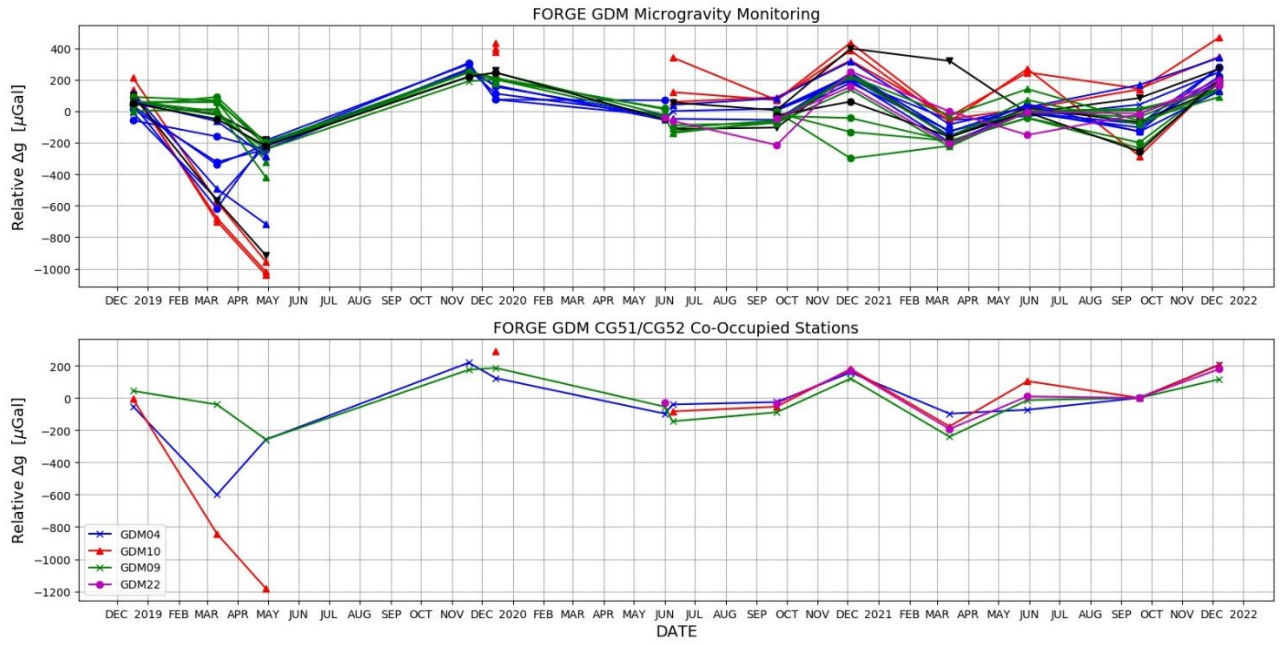

Figure 3.7.4-2. Plot of Utah FORGE 4D gravity station trends from December 2018 to December 2021. Top panel shows the observed gravity changes in μGal, bottom panel shows the trends of the local field tie points (GDM10, GDM22) and daily loop base stations (GDM04, GDM09). Tie points are fixed at zero for the September 2021 campaign for display purposes only due to later campaigns having better controls. Assigned colors based on earlier groupings according to qualitative signal trends.

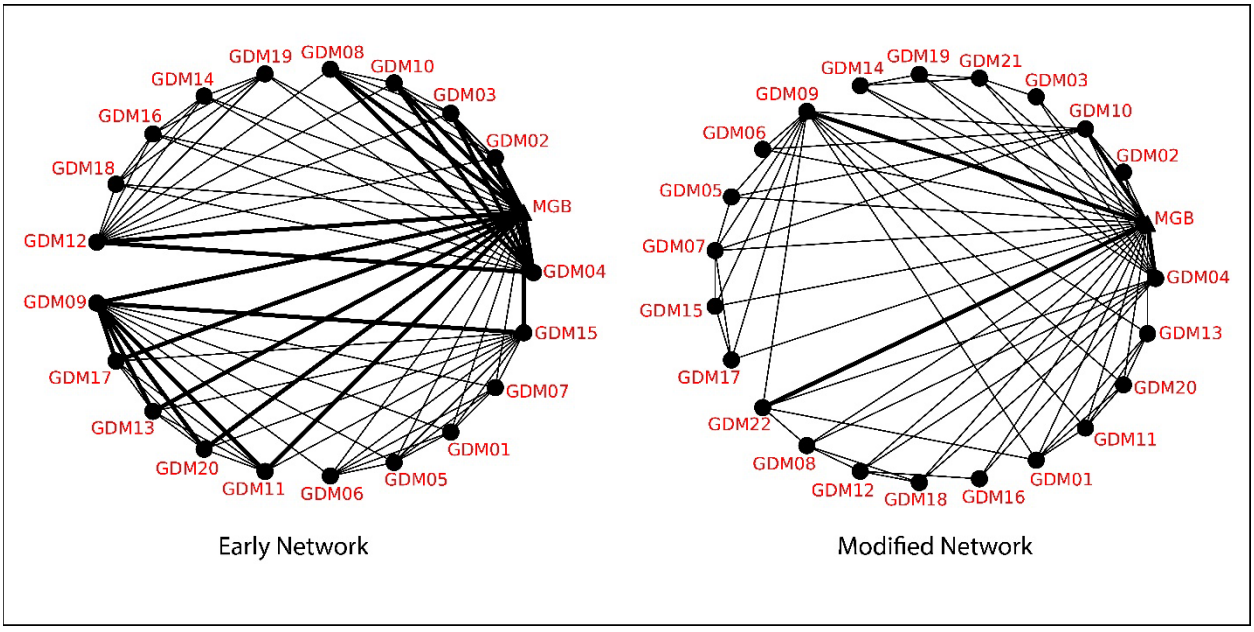

Figure 3.7.4-3. Schematic of the microgravity station network. Left-hand plot shows the early gravity station repeat occupation network, right-hand plot shows the modified gravity station repeat occupation network which includes more station overlap between the two gravimeters (CG51, CG52) used at the Utah FORGE field site.

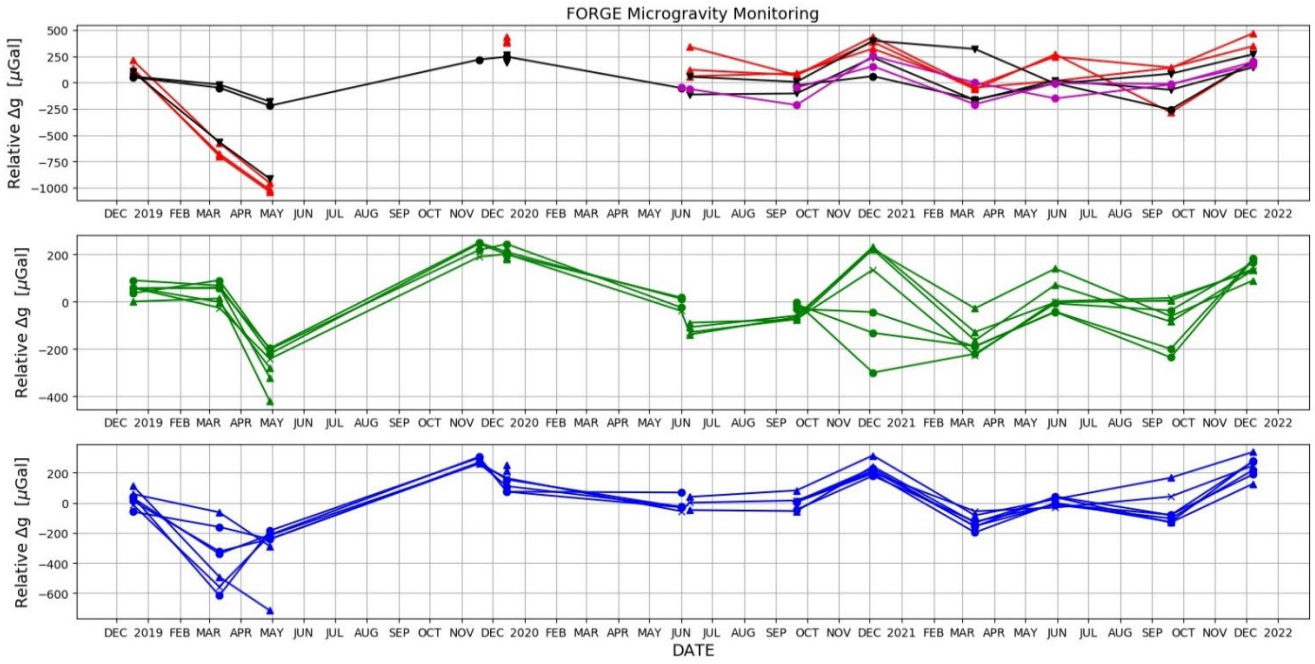

Figure 3.7.4-3. Plot of Utah FORGE 4D gravity station trends from December 2018 December 2021 shown in 3 panels based on early groupings. The more recent data is thought to have higher confidence in measurement of relative gravity values.

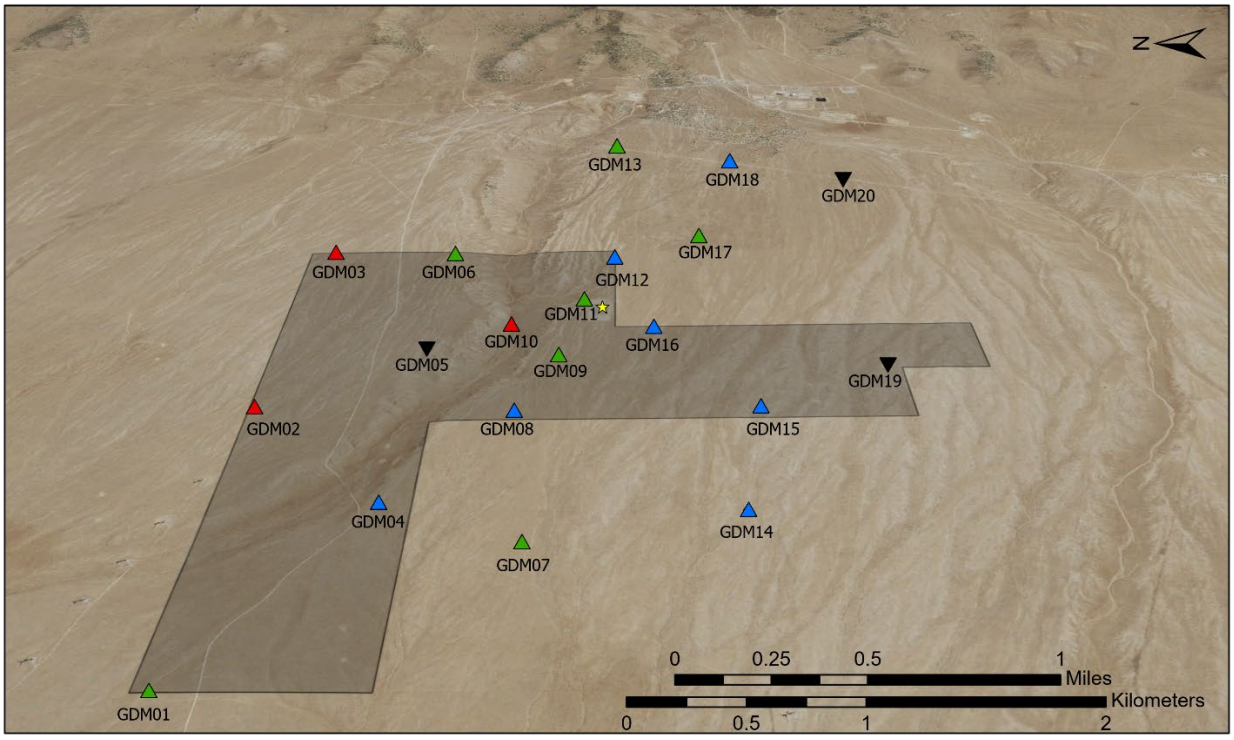

Figure 3.7.4-4. Map of Utah FORGE 4D gravity stations. Symbology coloring based on preliminary groupings using signal trends (see Figures 3.7.4-2 and 3.7.4-3). GDM-21, GDM-22 not shown.

Attachments 1-8 Section B3 Results: Utah FORGE Modeling

Phase 3A Year 2 Annual Report – Appendix A2

Enhanced Geothermal System Testing and Development at the Milford, Utah FORGE Site

Utah FORGE
University of Utah
423 Wakara Way, ste 300
Salt Lake City, UT, 84105

Prepared for the U.S. Department of Energy

Office of Energy Efficiency and Renewable Energy

Contract DE-EE0007080

April 30, 2022

MDPI

Article

A Reference Thermal-Hydrologic-Mechanical Native State Model of the Utah FORGE Enhanced Geothermal Site

Robert Podgorney [1]*, Aleta Finnila [2], Stuart Simmons [3], John McLennan[4]

[1] Idaho National Laboratory; robert.podgorney@inl.gov
[2] Golder Associates Inc.; Aleta_Finnila@golder.com
[3] EGI, University of Utah; Department of Chemical Engineering; ssimmons@egi.utah.edu
[4] EGI, University of Utah; Department of Chemical Engineering; jmclennan@egi.utah.edu
* Correspondence: robert.podgorney@inl.gov; Tel.: 208-526-1524

Abstract: The Frontier Observatory for Research in Geothermal Energy (FORGE) site is a multi-year initiative funded by the U.S. Department of Energy for enhanced geothermal system research and development. The site is located on the margin of the Great Basin near the town of Milford, Utah. Work has so far resulted in the compilation of a large amount of subsurface data which have been used to improve the geologic understanding of the site. Based on the compiled data, a three-dimensional geologic model describing the structure, composition, permeability, and temperature at the Utah FORGE site was developed. A deep exploratory well (Well 58-32) and numerous tests conducted therein provides information on reservoir rock type, temperature, stress, permeability, etc.

Modeling and simulation will play a critical role at the site and needs to be considered as a general scientific discovery tool to elucidate behavior of enhanced geothermal systems and as a deterministic (or stochastic) tool to plan and predict specific activities. This paper will present the development of a reference native state model, and calibration of the model to the reservoir pressure, temperature, and stress measured in Well 58-32.

Keywords: Enhanced geothermal systems; native state; FORGE; FALCON

Citation: Podgorney, R.; Finnila, A.; Simmons, S.; McLennan, J. A Reference Thermal-Hydrologic-Mechanical Native State Model of the Utah FORGE Enhanced Geothermal Site. *Energies* **2021**, *1*, 0. https://doi.org/

Received:
Accepted:
Published:

1. Introduction

Drilling into hot crystalline basement rocks and extracting heat through an artificially engineered reservoir is a concept that dates back many decades [1,2]. First described as a hot dry rock (HDR) system and originated at the Los Alamos National Laboratory (LANL) in the 1970s [3], it became clear in early projects that rather than creating new hydraulic fractures, the existing natural fractures provided the flow paths, and their transmissibility was improved by stimulation [4–6]. This has lead to the use of the term Enhanced (or Engineered) Geothermal Systems (EGS).

The development of EGS has the potential to dramatically increase the deployment of geothermal resources in the US and around the world [7–9]. EGS resources are far more abundant and widespread than conventional geothermal systems, but require advances in drilling, characterization, monitoring, and reservoir creation technologies to enable EGS resources to be commercially viable.

The U.S. Department of Energy's Geothermal Technologies Office (GTO) has launched a series of research initiatives to accelerate the development of EGS technologies. The Frontier Observatory for Research in Geothermal Energy (FORGE) is one such initiative. The FORGE site is located inside the southeast margin of the Great Basin near the town of Milford, Utah (Figure 1 and Figure 2). The FORGE initiative consisted of three phases, which can be generally described as initial site selection (Phase 1), site characterization and down-selection (Phase 2), and site establishment and operations (Phase 3). The work and results discussed in this paper are inclusive of all Phase 1 and Phase 2 efforts at the Utah FORGE site.

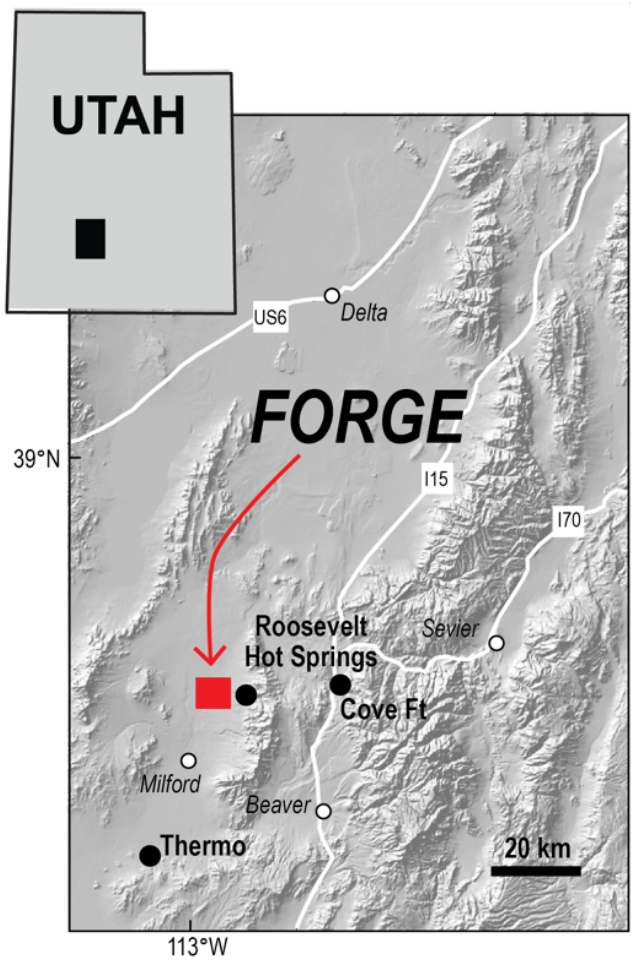

Figure 1. Location of FORGE Site near Milford, Utah, USA.

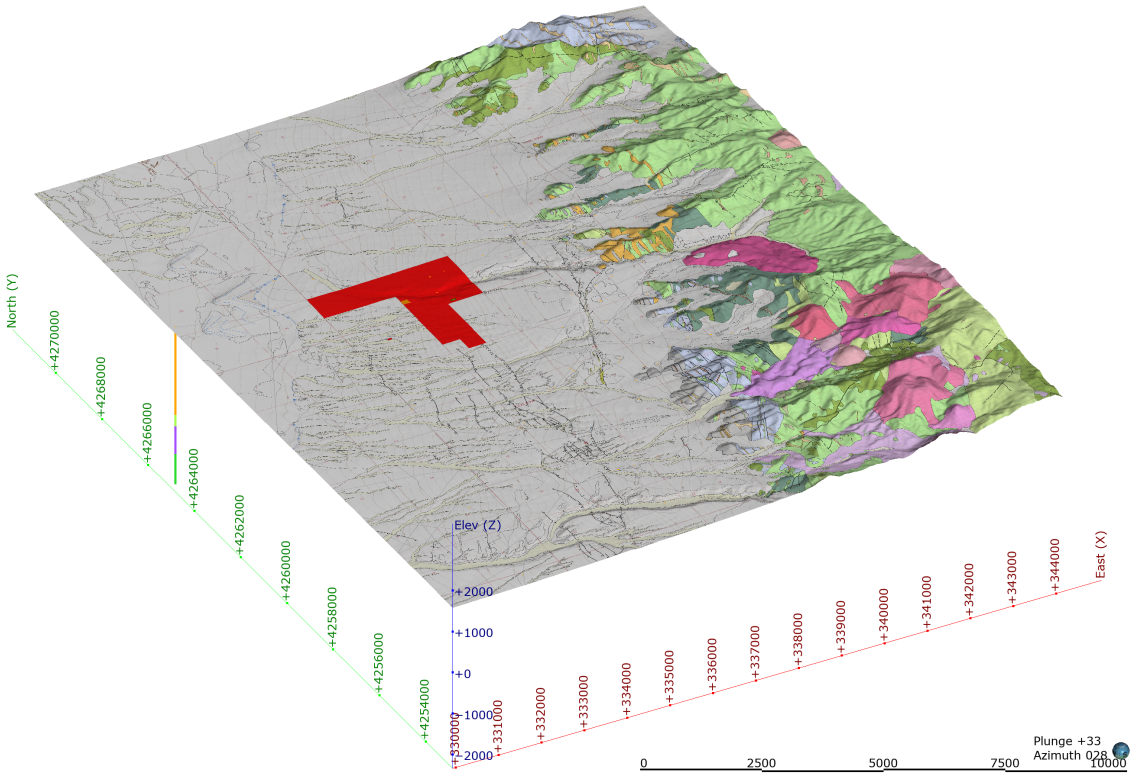

Figure 2. Location map of the Utah FORGE Site (red highlighted area) earth model domain, with an oblique view showing the topography and the updated geologic map [10]. Scalebar at bottom right is 10 km, with axes units in UTM (meters), Zone 12N, NAD83, and NAVD88. Major geologic units shown are green colors for undifferentiated granite, reddish/purple for rhyolite, and gray for alluvial sediments.

The work through the end of Phase 2 at the Utah FORGE site resulted in the compilation of a large amount of new and legacy data within and surrounding the project site, incorporating information for Roosevelt Hot Springs, the central segment of the Mineral Mountains, and most of the north Milford valley. Results from the deep subsurface characterization were used to further improve the geologic understanding of the site. Site characterization is described in detail in the Utah FORGE Phase 2 report [11]. Based on the compiled data, a three-dimensional (3D) geologic model describing the structure, composition, permeability, and temperature at the Utah FORGE site was developed [11,12].

1.1. Overview of the Geologic Model

The Utah FORGE site is located in a broad zone of elevated heat flow inside the southeast margin of the Great Basin. The regional stratigraphy is made of folded and imbricated Paleozoic-Mesozoic strata that has been overprinted by widespread Basin and Range style extension and eruption of Tertiary-recent mafic-felsic magmatic centers [10,13,14]. Near the Utah FORGE site, Paleozoic-Mesozoic strata are absent, and consequently the stratigraphy is divided into two broadly defined units, comprising crystalline plutonic rocks that form the basement and younger overlying bedded alluvium and volcanic deposits that fill the basin. The processing of a 3D seismic reflection highlights the westward-dipping surface that separates these two units, which forms the basement contact.

The basement rocks are made of granitoids, which were emplaced between 26 and 8 Ma [14]. They represent products of magmatic processes, which most recently resulted in the eruption of young rhyolite centers (0.5–0.8 Ma) in the Mineral Mountains [15]. The granitoid plutons intruded tightly folded Pre-cambrian gneiss (1720 Ma), but only rafts of this older lithology are preserved, as seen in the western foothills of the Mineral Mountains.

The basin fill consists of a layered sequence of sedimentary and volcanic deposits (>3000 m thick), which range from Tertiary to recent in age. The strata from youngest to oldest consist of calcareous lacustrine siltstones and sandstones, volcaniclastic sandstones and gravels, tuffaceous deposits, and localized flows of andesitic lavas. On the surface, the youngest deposits in the vicinity of Well Acord 1 are composed of fine sediments and reworked alluvium that were deposited in Lake Bonneville, whose shoreline is marked by wave-cut escarpments and westward-extending point bars. To the east, including the area surrounding the FORGE site, late Pleistocene alluvial fans are mainly composed of pea-sized gruss and scattered fragments of obsidian, derived from the Mineral Mountains. Across the Opal Mound fault, around the area of Roosevelt Hot Springs, the alluvium deposits are older, more than 0.8 Ma, as constrained by dates on overlying flows of rhyolite [15]. The oldest alluvium likely dates back several million years, and it is restricted to a few isolated exposures [10,16].

As part of the FORGE Phase 2 activities, the Utah FORGE team developed a comprehensive earth model of the Milford Site and surrounding area. The key outcome from the earth modeling, in addition to incorporating the geologic, geophysical, geochemical data, etc., was the establishment of a "reference" earth model for use by numerical modelers to ensure consistent geologic structural features and reservoir parameters could be used in numerical simulations. All the data used to create the reference earth model are also available on the National Geothermal Data System [17–21] and the Utah FORGE website. Note that all earth modeling data uses SI units in UTM, Zone 12N, NAD83, and NAVD88 referenced coordinates.

1.2. Modeling and Simulation Overview

Multiphysics reservoir models have been developed to simulate the coupled thermo-hydro-mechanical responses in the subsurface to FORGE reservoir creation and operation activities. The numerical reservoir models are based on the reference geologic model

discussed above and will be used as a tool to better understand the physics of the reservoir-creation process and to elucidate the behavior of the system. Numerical implementation of the conceptual model has been made with both commercial software packages and open-source numerical packages to enable greater collaboration among the team (and the geologic community) and to drive understanding of the system using state of the art tools. The modeling and simulation team used these models to preliminarily evaluate drilling directions and injection pressures to both stimulate existing fractures and generate new ones for potential FORGE operational wells.

Continuum-based modeling codes are by far the most prevalent in geothermal reservoir engineering. Solution schemes based on finite-difference, finite-element, or finite-volume methods all represent the subsurface as a generalized representative elementary volume, at various grid scales, to simulate and predict behavior. In densely fractured formations, it is common to use a discrete fracture network (DFN) as a starting point to develop upscaling relationships in the development of continuum models. For Utah FORGE, the project team has established a reference DFN using FracMan [22] and a reference native state model using the FALCON code [23,24].

1.2.1. FRACMAN

Golder's FracMan® code is commercially available DFN software and can be used to fully capture the anisotropy and connectivity of the fracture system. The rock mass fracture system can be explicitly modeled by building 3D net-works of both deterministically mapped larger structures and stochastically generated smaller fractures. Models can be calibrated against well log information, outcrops, well test data, and seismic data to ensure a good match between field data and the model. Once developed, these models can be used for critical rock mechanics analyses and fluid-flow modeling. Multiple stochastic realizations can be generated for uncertainty management through Monte Carlo simulation and analysis. The DFN model can also be converted into equivalent grid properties, including fracture rock mass properties and directional stiffness through an upscaling process.

1.2.2. FALCON

FALCON (Fracturing And Liquid CONvection [23,25] is a multipurpose subsurface simulator for coupled thermal-hydraulic-mechanical-chemical (THMC) problems and has been used for the study of geothermal reservoir dynamics, groundwater flow and transport, carbon sequestration, etc. The code built using Idaho National Laboratory's (INL) Multiphysics Object-Oriented Simulation Environment (MOOSE) framework [26,27]. The architecture that FALCON inherits from MOOSE has a plug-and-play modular design structure based on representing each piece of the residual term in a weak form of the governing partial differential equations (PDEs) as a "kernel." Kernels may be coupled together to achieve different application goals and are solved using a finite element scheme. The basic architecture of the code allows convenient coupling of different processes. FALCON has been rigorously validated through a number of benchmark problems and made available as an open-source toolkit [24]. While it is beyond the scope of this manuscript to discuss the governing equations in great detail (see references cited above, or the MOOSE documentation page for full details), the discussion that follows provides a summary of the governing equations.

Mass Conservation.Mass conservation for fluid species κ is described by the continuity equation

$$0 = \frac{\partial M^\kappa}{\partial t} + M^\kappa \nabla \cdot \mathbf{v}_s + \nabla \cdot \mathbf{F}^\kappa + \Lambda M^\kappa - \phi I\text{chem} - q^\kappa \,. \tag{1}$$

Here M is the mass of fluid per bulk volume (measured in kg m^{-3}), $\mathbf{v}_s$ is the velocity of the porous solid skeleton (measured in m s^{-1}), $\mathbf{F}$ is the flux (a vector, measured kg s^{-1} m^{-2}), Λ is a radioactive decay rate, ϕIchem represents chemical precipitation or dissolution and q is a source (measured in kg m^{-3} s^{-1}). The coupling to the solid

mechanics is via the $M\nabla \cdot \mathbf{v}_s$ term, as well as via changes in porosity and permeability. Coupling to heat flow and chemical reactions is via the equations of state used within the terms of Equation 1, as well as the source term q^κ.The species are parameterised by $\kappa = 1, \ldots$.

Mass Density.The mass of species κ per volume of rock is written as a sum over all phases present in the system:

$$M^\kappa = \phi \sum_\beta S_\beta \rho_\beta \chi_\beta^\kappa (1-\phi) C^\kappa \tag{2}$$

The solid's porosity is ϕ. S_β is the saturation of phase β (solid, liquid, gas, NAPL). ρ_β is the density of phase β. χ_β^κ is the mass fraction of component κ present in phase β. The final term represents fluid absorption into the porous-rock skeleton: C^κ is the mass of absorbed species per volume of solid rock-grain material. The density ρ_β is typically a function of pressure and temperature, but may also depend on mass fraction of individual components, as described by the equation of state used.

Flux. The flux is a sum of advective flux and diffusive-and-dispersive flux:

$$\mathbf{F}^\kappa = \sum_\beta \chi_\beta^\kappa \mathbf{F}_\beta^{\text{advective}} + \mathbf{F}^\kappa_{\text{diffusion+dispersion}} \tag{3}$$

Advective flux is governed by Darcy's law. Each phase is assumed to obey Darcy's law. Each phase has its own density, ρ_β, relative permeability $k_{\text{r},\beta}$, viscosity μ_β, and pressure P_β. These may all be nonlinear functions of the independent variables. With them, we can form the advective Darcy flux:

$$\mathbf{F}\beta^{\text{advective}} = \rho_\beta \mathbf{v}_\beta = -\rho_\beta \frac{k, k_{\text{r},\beta}}{\mu_\beta} (\nabla P_\beta - \rho_\beta \mathbf{g}) \tag{4}$$

In this equation $\mathbf{v}_\beta$ is the Darcy velocity (volume flux, measured in m.s^{-1}) in phase β. It is used below in the diffusive-and-dispersion flux too. The absolute permeability is denoted by k and it is a tensor. The relative permeability of phase β is denoted by $k_{\text{r},\beta}$. It is always a function of the saturation(s), but with Klinkenberg effects, it may also be a function of the gas pressure. Relative permeability can also be hysteretic, so that it depends on the history of saturation.

Heat Transport. Energy conservation for heat is described by the continuity equation

$$0 = \frac{\partial \mathcal{E}}{\partial t} + \mathcal{E}\nabla \cdot \mathbf{v}s + \nabla \cdot \mathbf{F}^T - \nu(1-\phi)\sigma^{\text{eff}}ij \frac{\partial}{\partial t} \epsilon_{ij}^{\text{plastic}} q^T \tag{5}$$

Here $\mathcal{E}$ is the heat energy per unit volume in the rock-fluid system, $\mathbf{v}_s$ is velocity of the porous solid skeleton, $\mathbf{F}^T$ is the heat flux, ν describes the ratio of plastic-deformation energy that gets transferred to heat energy, $\sigma^{\text{eff}}ij$ is the effective stress (see Equation 7), $\epsilon_{ij}^{\text{plastic}}$ is the plastic strain, and q^T is a heat source.

The coupling to the solid mechanics is via the $\mathcal{E}\nabla \cdot \mathbf{v}_s$ term, the $\nu(1-\phi)\sigma^{\text{eff}}ij \frac{\partial}{\partial t} \epsilon_{ij}^{\text{plastic}}$ term, as well as via changes in porosity and permeability. Coupling to the fluid flow and chemical reactions is via the equations of state used within the terms of Equation 5, as well as the source term q^T.

Here it is assumed the liquids and solid are in local thermal equilibrium i.e. there is a single local temperature in all phases. If this doesn't hold, one is also normally in the high-flow regime where the flow is non-Darcy as well.

The heat flux is a sum of heat conduction and convection with the fluid:

$$\mathbf{F}^T = -\lambda \nabla T + \sum_\beta h_\beta \mathbf{F}\beta \,. \tag{6}$$

Here λ is the tensorial thermal conductivity of the rock-fluid system, which is a function of the thermal conductivities of rock and fluid phases. The specific enthalpy of phase β is denoted by $h\beta$, and $\mathbf{F}_\beta$ is the advective Darcy flux.

Mechanics. Most of the solid mechanics used by the FALCON is provided by the MOOSE Tensor Mechanics module, which was developed from the pure mechanics perspective. This section provides a brief overview, concentrating on the aspects that differ from pure solid mechanics.

The total stress tensor is denoted by σ^{tot}. An externally applied mechanical force will create a nonzero σ^{tot}, and conversely, resolving σ^{tot} into forces yields the forces on nodes in the finite-element mesh.

The effective stress tensor is denoted by σ^{eff}. It is defined by

$$\sigma^{\text{eff}}ij = \sigma^{\text{tot}}ij + \alpha_B \delta_{ij} P_f \, . \tag{7}$$

where P_f is a measure of pore pressure. In single-phase, fully-saturated situations it is traditional to use $P_f = P_\beta$. α_B is the Biot coefficient. This obeys $0 \leq \alpha_B \leq 1$.

The formulation in FALCON assumes that the elastic constitutive law reads

$$\sigma^{\text{eff}}_{ij} = E_{ijkl}(\epsilon^{\text{elastic}}_{kl} - \delta kl \alpha_T T) \, , \tag{8}$$

with α_T being the thermal expansion coefficient of the drained porous skeleton, and $\epsilon_{kl} = (\nabla_k u_l + \nabla_l u_k)/2$ being the usual total strain tensor (u is the deformation of the porous solid), which can be split into the elastic and plastic parts, $\epsilon = \epsilon^{\text{elastic}} + \epsilon^{\text{plastic}}$, and E_{ijkl} being the elasticity tensor (the "drained" version).

The conservation of momentum is

$$\rho_{\text{mat}} \frac{\partial v^j_s}{\partial t} = \nabla_i \sigma^{\text{tot}}_{ij} + \rho_{\text{mat}} b_j = \nabla_i \sigma^{\text{eff}}_{ij} - \alpha_B \nabla_j P_f + \rho_{\text{mat}} b_j \, , \tag{9}$$

where $\mathbf{v}_s = \partial \mathbf{u}/\partial t$ is the velocity of the solid skeleton, ρ_{mat} is the mass-density of the material (this is the undrained density: $\rho_{\text{mat}} = (1-\phi)\rho^R + \phi \sum_\beta S_\beta \rho_\beta$), and b_j are the components of the external force density (for example, the gravitational acceleration).

2. Native State Modeling

A numerical implementation of the conceptual and earth models was developed of the FORGE reservoir and surrounding area to estimate the spatial distribution of native-state pressure, temperature, and stress conditions. The primary goal of this effort was threefold.

- Incorporate detailed 3D parameter distributions and complex boundary conditions identified from characterizing the site;
- Better understand the spatial distribution of stress and how it may influence reservoir stimulation;
- Establish a reference (or baseline) set of parameters and property distributions that can be used among the modeling community to ensure consistency and comparability of simulation results.

As discussed in the following subsections, the native-state model is based on relevant site data and uses very complex boundary and initial conditions to represent the earth model as realistically as possible. The initial reservoir parameters and boundary conditions were modified as needed during calibration of the native-state model. The native state model will updated at regular intervals, corresponding to advances in site characterization and data availability with annual revisions expected.

2.1. Model Location and Dimensions

The Phase 2 FORGE numerical model domain was sized to accommodate the geothermal reservoir intersected by the site pilot well, Well 58-32, and envisioned future

injection and production wells along with their predicted stimulation volumes created during FORGE Phase 3. A region box 2.5 km × 2.5 km × 2.75 km, located approximately between depths of 400 m to 3200 m below the surface (see Figure 3). The mesh was aligned with the principal stress direction (N25E) estimated from borehole breakout and drilling induced fracturing analysis in Well 58-32 [11]. A uniform mesh spacing of 50 m was used, which resulted in a total of 137,500 grid cells.

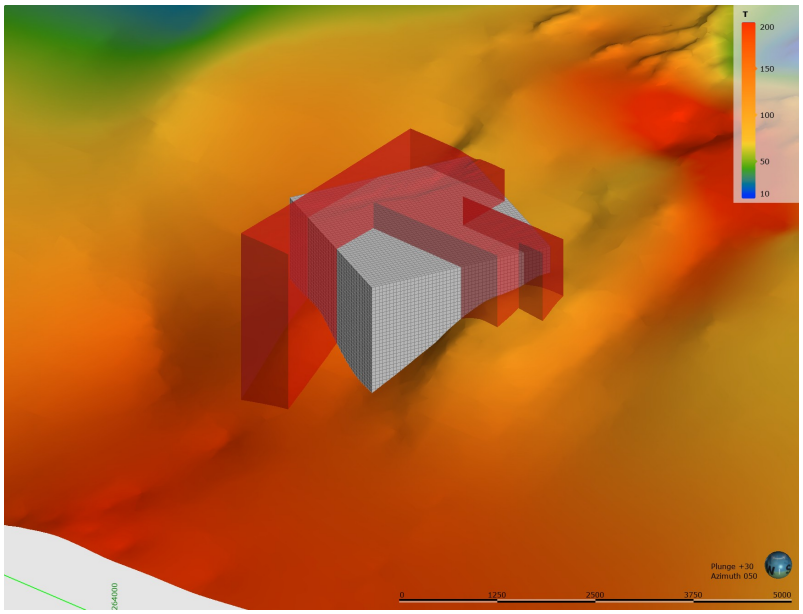

Figure 3. Native-state model domain (gray box) shown in relation to the full extents of the FORGE Site (red shape) within the earth model domain. Surface shown is the top of the granitoid with the estimated temperature draped over the surface.

The lithology was divided into the two broadly defined units from the conceptual model, consisting of granitic basement rocks (granitoid) and the overlying basin fill sedimentary deposits (Figures 3 and 4). The depth to the top of the model domain was chosen so that the entire top of the model was located within the alluvium materials. This was chosen for several reasons:

1. To avoid lateral groundwater flow in the near surface sediments originating from the east side of the Opal Mound Structure (the southeast side of the model domain). Little data area available regarding the near surface flow system, but given the near surface temperature distributions significant lateral flow is likely. This area is of little interest to the present study.
2. To avoid the unsaturated portions of the near surface sediments. As we are simulating the system in a fully-coupled thermal-hydrologic-mechanical numerical framework, including the unsaturated zone has practical, and significant, implications for the computational burden and applicability of the equations of state at negative (capillary) pressures. None of these issues are insurmountable, but the at the present time the effort required to overcome them can't be justified for an area of the site that is not of interest to the present study.
3. To facilitate establishment of the stress boundary condition on the top model surface and aid in the calibration of the vertical stress in the model. The use of the Leapfrog Geothermal earth modeling package [28] (see below) allowed for summation of the saturated and unsaturated sediment column above the model domain and applying this as a overburden load on the top of the model domain. This enabled the evaluation of the grain density of the overlying sediments required for model calibration.

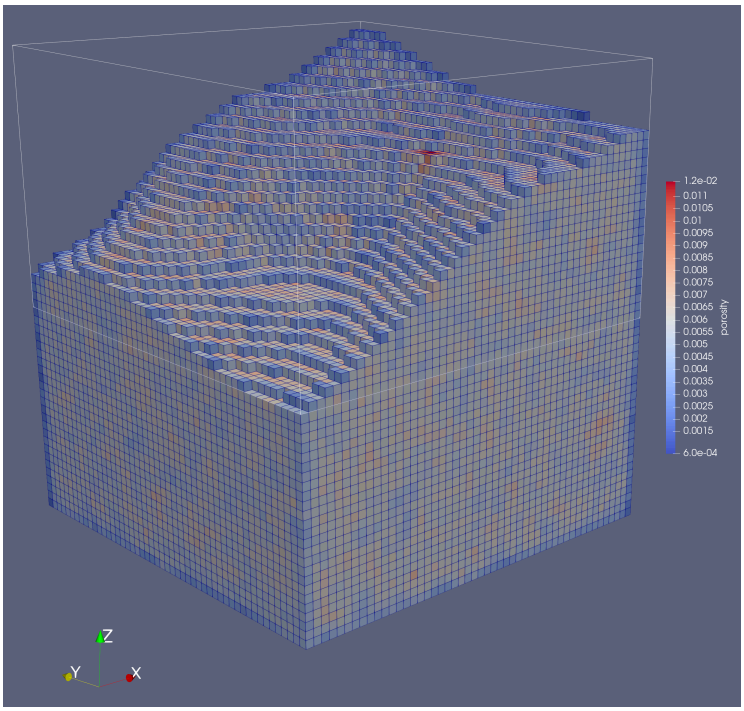

Figure 4. Numerical model domain of the granitoid shown with grid cells, looking from the southwest toward the northeast. Granitoid coloring is based on porosity determined from upscaling the DFN. Dimensions are 2.5 km × 2.5 km in the horizontal directions and 2.75 km in the vertical direction.

The model domain was constructed in geologic modeling software package LeapFrog Geothermal [28]. A commercial earth modeling package was chosen so that property distribution estimates from the FORGE characterization and historical studies could be easily extrapolated onto the numerical grid. The resultant numerical domain and mesh used the same reference Universal Transverse Mercator (UTM) coordinate system which allowed for importing of numerical results back into the earth model for display, comparison, and archiving.

2.2. Reference Discrete Fracture Network

The FORGE reference DFN model was constructed using FracMan software [22]. The DFN incorporates measured surface and well log site data to create planar fractures that communicate as a single hydrological and mechanical system. The reference DFN consists of a deterministic set of fractures intersecting Well 58-32 where fracture locations and orientations are known, plus a stochastic set of fractures away from well control. The stochastic fracture-set orientations and intensity are based on fracture data from Well 58-32 while fracture sizes were based on nearby trace length data collected in the Mineral Mountains. Multiple realizations can be generated to show a range of possible reservoir natural fracture set populations. Some highlights of the DFN parameterization are discussed in the following section (more details can be found in [29]).

Fracture orientations are based on Formation Micro Scanner (FMI) log interpretation of Well 58-32 [11]. Measured orientations have been weighted using the Terzaghi correction factor [30] using a maximum value of seven. This weighting factor is used to account for the bias introduced by sampling inclined or vertical fractures from a vertical well. Figure 5 shows contour plots of the fracture pole orientations on upper hemisphere stereonets both with and without the Terzaghi weighting. This weighting only affects the apparent concentrations of the fracture poles on contour plots and does not change the locations of the poles which represent the measured fracture orientations. The fractures in the DFN were generated by randomly selecting values from the Terzaghi weighted

population and so mirror the measured values quite well. Three sets have been identified for use by other researchers with mean orientations and intensities listed in Table 1.

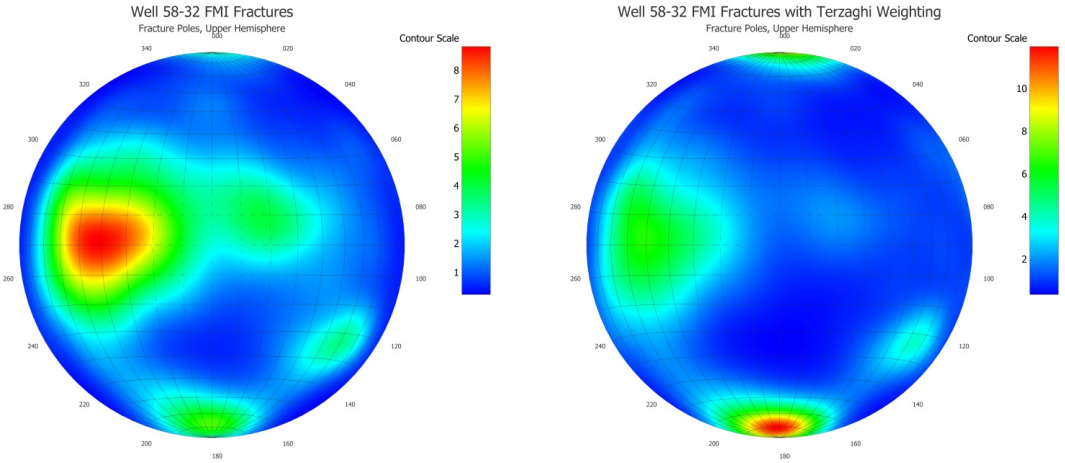

Figure 5. Contour plots of 58-32 FMI fracture poles in upper hemisphere, equal area stereonets showing the relative intensities before bias correction (left), and after applying Terzaghi weighting (right).

Table 1. Fracture set orientations and intensity from Well 58-32 FMI data. Intensity data is based on the Terzaghi weighted distribution. P_{32} is defined as the total fracture area per unit volume.

	Units	EW Vertical	NS Inclined Dipping West	NE Steeply Dipping SE
Set Intensity	P_{32} (m^{-1})	0.78	1.41	0.31
	Percent	31	56	12
Mean Set Orientation	Strike (deg)	96	185	215
	Dip (deg)	80 S	48 W	64 SE

Fracture intensity in the FORGE reservoir DFN is also based on the FMI log interpretation of Well 58-32. The lineal fracture intensity, P_{10}, is defined as the number of fractures per unit of length [31,32]. On a Cumulative Fracture Intensity (CFI) plot, the slope of the line shows the inverse of the P_{10} value, so higher slopes correspond to lower fracture intensities. The CFI plot for 58-32 (Figure 6) shows that there are two distinct regions of fracture intensity: (1) a shallower region extending from the top of the granitoid to a measured depth in the well of approximately 1300 m having higher lineal fracture intensity and (2) a deeper region extending to the bottom of the well having a lower lineal fracture intensity. This corresponds to the transition from the monzodiorite to the monzonite lithology where the bulk porosity also drops correspondingly. As the FORGE site is primarily investigating the potential for exploitation at deeper, hotter zones, the choice was made to use a single fracture intensity value corresponding to the deeper zone where the P_{10} is 1.18 m^{-1}.

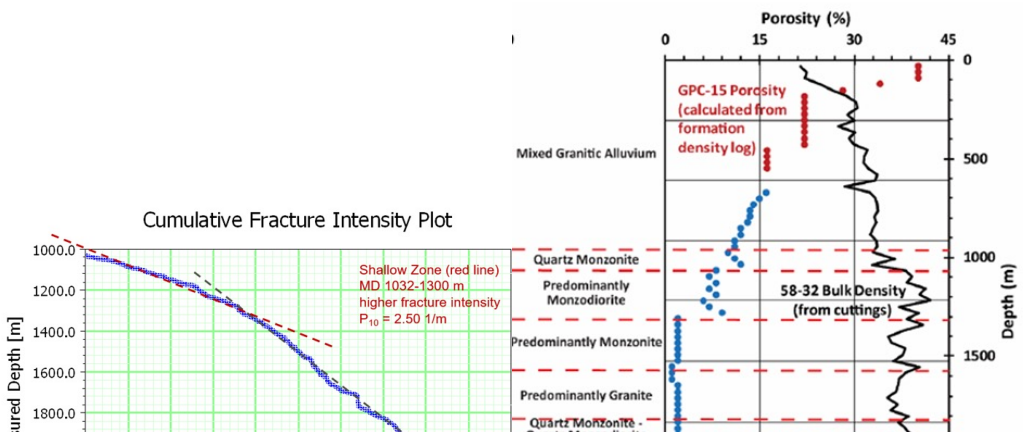

The P_{10} intensity measure will vary as a function of the relative angle between the fracture set orientations and the trajectory of the well where the measurement is made. Another fracture intensity measure, the volumetric fracture intensity, P_{32}, is defined as the fracture area per unit of volume. This intensity measure can be derived from the P_{10} once the fracture orientations of the population are determined and is independent of the original method of collecting the intensity data. Because P_{32} can be reported independently from the well and fracture set orientations, it is better suited to represent both the relative and total fracture set intensities. Table 1 provides the P_{32} values of the three fracture sets.

Fracture size was estimated using trace-length data from the nearby outcrops in the Mineral Mountains [34] that are comprised of the same geologic unit that is present in the FORGE reservoir. The trace-length data fit log-normal distributions with an average mean and standard deviation of 57.0 m and 50.4 m respectively. Measured values fitting a log-normal distribution often represent data sets that are actually present in a power law distribution. Power law distributions that are truncated at both the low and high ends of the range appear as log-normal. Therefore, the trace data was also fit to a power law distribution, as shown in Figure 7. DFNs were created for the FORGE work using both the log-normal distribution and a power law distribution with parameter D equal to 2.6 (negative trace length slope + 1). Depending on the use of the DFN, minimum and maximum size cutoffs were also used during fracture generation. For the reservoir scale model, a minimum fracture radius size of 10 m was used while for well-scale DFNs, a minimum size of 1 m was used. The maximum size of fracture radius was 150 m. Fracture shapes were assumed to be roughly circular and are represented as six-sided polygons.

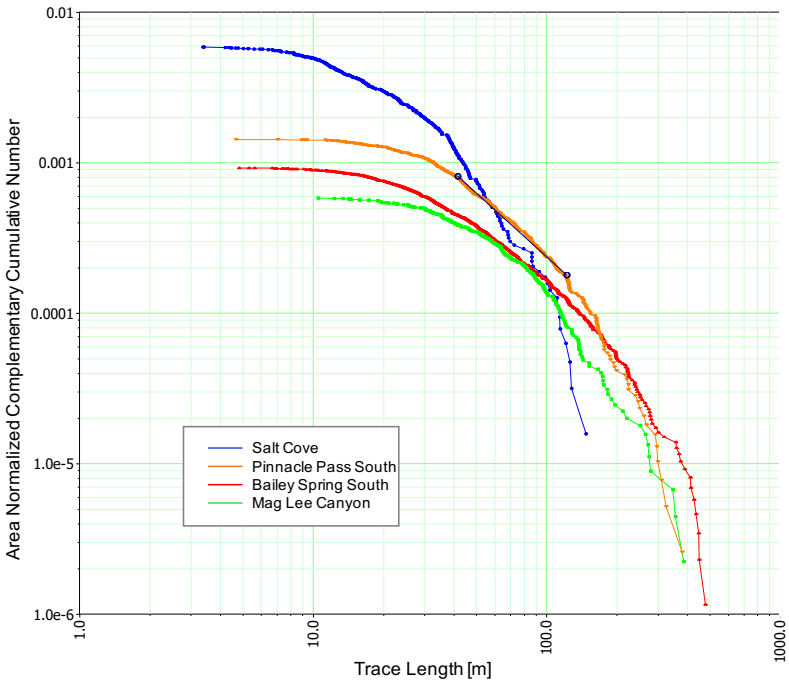

Figure 7. Power law fit to outcrop trace length data. The slopes of the straight-line segments on this log-log plot of the area normalized complementary cumulative number vs the trace lengths range from -1.3 to -1.9.

2.3. Rock and Fluid Properties

Rock and reservoir fluid properties used for the simulations were based on a combination of site characterization results and values from literature. Because the focus of the research and the majority of the characterization data are from the granitoid reservoir, the majority of the modeling efforts are also focused on the granitoid. As

discussed in the following sections, stochastic property distributions were used where justified, otherwise single parameter values were used.

2.3.1. Hydrologic Properties

Mean bulk porosity of the granitoid reservoir was 1–2% at reservoir depths based on the Well 58-32 neutron porosity log while core sample porosity measurements were 0.5% [11,33,35,36]. Bulk porosity is composed of both matrix porosity and fracture porosity with the fracture porosity component, ϕ_F, estimated from upscaling the DFN:

$$\phi_F = \frac{\sum A_F e}{V_C} \tag{10}$$

Where A_F, the fracture area in a grid cell, and e, the fracture aperture, get multiplied together for each fracture in a grid cell and summed while V_C is the grid cell volume. Apertures are assumed to be linearly related to the square root of the fracture radius, R:

$$e = a\sqrt{R} \tag{11}$$

The linear coefficient, a, was found through a calibration process so that the mean upscaled fracture porosity was approximately 0.5%. Additional porosity may come from the rock matrix.

The average rock in-situ permeability of the granitoid is estimated to be 4.7x10^{-17} m^2 from well testing performed in Phase 2B [17]. In a similar workflow as was utilized to estimate fracture apertures, a relationship between fracture permeability k_F, and aperture is assumed:

$$k_F = be^{1.5} \tag{12}$$

The linear coefficient, b, is determined by requiring that the upscaled fracture permeability match the measured granitoid permeability. Once upscaled to continuum values, the average directional fracture permeabilities in cell coordinate directions for the granitoid were 6.5×10^{-17} m^2, 6.5×10^{-17} m^2, and 7.0×10^{-17} m^2, respectively. A histogram of the upscaled fracture vertical permeability is shown in Figure 8. Table 2 summarizes the granitoid permeability and porosity.

Permeability and porosity for the sedimentary materials were estimated from aquifer tests conducted at the FORGE site [37], analysis of cuttings collected during the drilling of Well 58-32 [11,33,36], and geophysical well logs collected in Well 58-32 [11,33,36]. As the sedimentary materials were not the focus of this modeling study, single values were used to represent the permeability and porosity, as summarized in Table 3.

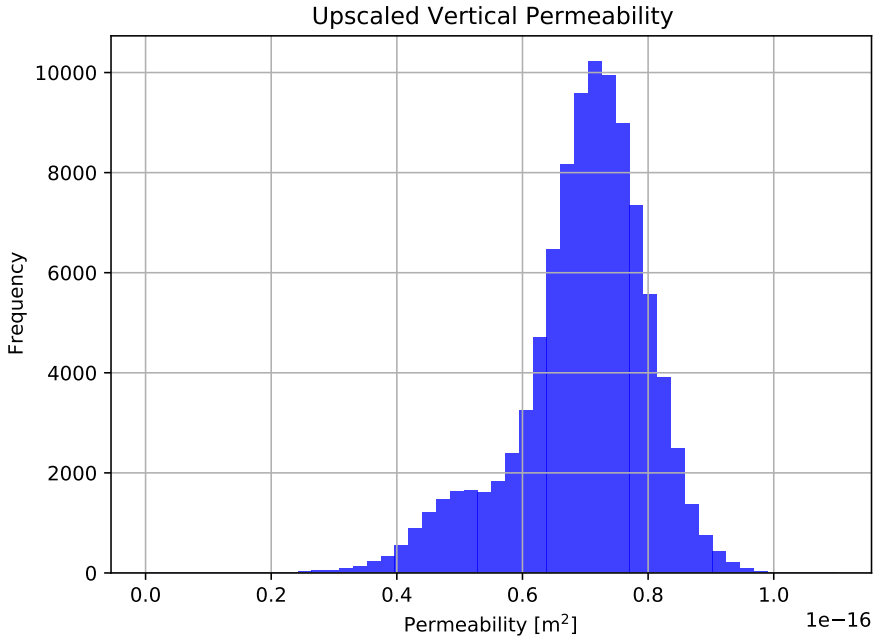

Figure 8. Upscaled vertical permeability values for the forge reference DFN model generated using a log-normal fracture size distribution.

2.3.2. Thermal Properties

Thermal properties of the grantoid reservoir and overlying sediments were studied in detail using rock core and cuttings obtained during the drilling of Well 58-32 [11,33, 36,38]. Measurements of specific heat capacity and thermal conductivity were made at nominally 33 m (100 ft) intervals along the length of Well 58-32. As we only have data from one well, spatial distributions of these parameters within each unit was not attempted nor justified at the present time, therefore single values for specific heat capacity and thermal conductivity were used for the granitoid and sedimentary materials. Tables 2 and 3 summarize the values used.

For long-term operational modeling of the FORGE reservoir, temperature dependent thermal expansion coefficients will be critical and will require site specific measurements. For the current, steady-state modeling efforts, temperature invariant uniform thermal expansion coefficients obtained from the literature [39,40] were used for the granitoid and sedimentary units, as summarized on Tables 2 and 3.

2.3.3. Mechanical Properties

Mechanical properties of the granitoid reservoir rocks were determined from laboratory analysis of core plugs from Well 58-32, geophysical logs, and values reported in the literature [11,41]. Young's modulus and Poisson's ratio were determined from laboratory testing on the two core sections and also measured from well logs. Horizontal and vertical plugs were taken from four different zones in the two cores and tested. Different hydraulic confining pressures were applied to these samples to simulate different stress regimes (near the wellbore where stresses can be elevated because of stress concentrations and away from the wellbore where the stresses are consistent with the measured stresses). The confining pressures ranged from zero (unconfined compression) to 51.7 MPa (7500 psi) [11]. This covers the full range of effective stresses that would be experienced in this reservoir.

Compressional and shear wave travel times from the Dipole Sonic Imager (DSI) and bulk density from the triple combo logging suite (gamma ray, neutron and density porosity and resistivity) were also used to calculate dynamic elastic properties. Mechanical properties inferred from the logging operations were corrected using the laboratory

measurements [11]. The Biot coefficient of the granitoid was taken from the literature [41]. Granitoid mechanical properties are summarized in Table 2.

Mechanical properties Young's Modulus, Poisson's Ratio, and Biot coefficient of the sedimentary materials were taken from the literature [42–44] and are summarized on Table 3.

2.3.4. Fluid Properties

FALCON uses the MOOSE Fluid Properties module to estimate the fluid density, viscosity, and thermal conductivity. In the native state simulations, a pure water formulation was used. Detailed geochemical modeling and laboratory analysis will be used as inputs for future FORGE reservoir modeling efforts.

The water implementation in Fluid Properties is the International Association for the Properties of Water and Steam (IAPWS) Industrial Formulation 1997 for the Thermodynamic Properties of Water and Steam [45]. This formulation calculates properties of water and steam using pressure and temperature as inputs. The IAPWS-IF97 formulation is split into five different regions in the phase diagram. All five regions are implemented in the Fluid Properties module. To avoid iteration in region 3 of the IAPWS-IF97 formulation, the backwards equations from [46] are implemented.

Viscosity is calculated using the IAPWS 2008 formulation [47]. Note that the critical enhancement has not been implemented. Thermal conductivity is calculated using the IAPWS 1985 formulation [48]. Although there is a newer formulation available [49], it is significantly more complicated, so has not been implemented yet. Dissolution of a dilute gas into water is calculated using Henry's law [50]. The Fluid Properties implemented in FALCON are valid for the follow temperature and pressure ranges:

- $273.15\,K \leq T \leq 1073.15\,K$, for $P \leq 100\,MPa$
- $1073.15\,K \leq T \leq 2273.15\,K$, for $P \leq 50\,MPa$

Table 2. Properties for the granitoid reservoir used in the native state simulation. Values based on field and laboratory measurements and model calibration.

Parameter	Units	Min	Max	Source
Permeability$_{ii}$	m^2	6.9e-18	1.2e-16	Upscaled DFN[29,51] Core-Reservoir testing[11]
Permeability$_{jj}$	m^2	4.5e-18	1.5e-16	Upscaled DFN[29,51] Core-Reservoir testing[11]
Permeability$_{kk}$	m^2	6.2e-18	1.1e-16	Upscaled DFN[29,51] Core-Reservoir testing[11]
Porosity	–	1.0e-07	1.2e-02	Upscaled DFN[29,51] Core-Reservoir testing[11]
Specific Heat Capacity	J kg^{-1} K^{-1}	7.90e+02		Cuttings analysis[38] Literature[52] Model calibration
Grain Thermal Conductivity	W m^{-1} K^{-1}	3.05		Cuttings analysis[38] Model calibration
Thermal Expansion Coefficient	K^{-1}	6.00e-06		Literature[39]
Rock Grain Density	kg m^{-3}	2.75e+03		Core-cuttings analysis[11] Model calibration
Young's Modulus	Pa	6.2e+10		Core testing[11]
Poisson's Ratio	–	0.30		Core testing[11]
Biot Coefficient	–	0.60		Literature[41]

Table 3. Properties for the sedimentary overburden used in the native state simulation. Values based on field and laboratory measurements and model calibration.

Parameter	Units	Value	Source
Permeability	m^2	1.7e-14	Aquifer testing[11]
Porosity	–	1.2e-01	Aquifer testing[11] Model calibration
Specific Heat Capacity	J kg^{-1} K^{-1}	8.30e+02	Literature[52]
Grain Thermal Conductivity	W m^{-1} K^{-1}	2.0	Cuttings analysis[38] Model calibration
Thermal Expansion Coefficient	K^{-1}	2.00e-06	Literature[40]
Rock Grain Density	kg m^{-3}	2.50e+03	Cuttings analysis[11] Model calibration
Young's Modulus	Pa	3.0e+10	Literature[42]
Poisson's Ratio	–	0.30	Literature[43]
Biot Coefficient	–	0.60	Literature[44]

2.4. Boundary Conditions

Boundary conditions for pressure, temperature, and stress were based on site characterization results [11]. Due to the complex nature of the distributions of pressure, temperature, and stress, all boundary conditions in the native state model have varying degrees of spatial variability, which were implemented using Dirichlet conditions. Specific boundary conditions and the values used will be discussed in detail in the following sections.

2.4.1. Temperature

Temperatures in the model region were predicted to be between 60 °C and 250 °C based on measurements in Well 58-32 and numerous temperature gradient wells in the vicinity of the FORGE site [38], which resulted in a complex, 3D thermal structure in the vicinity of the FORGE site. The complex temperature distribution is due to the interaction of thermal fluids moving through the upper sediments around a portion of the Opal Mound Fault and conduction from what is taken to be an irregularly shaped thermal regime at depth.

The 3D interpolation of the temperature data, developed in LeapFrog, was mapped onto the numerical model grid as assigned to all sides of the model domain as a Dirichlet boundary condition, as shown in Figure 9. The values for the top surface of the model domain ranged from approximately 55 °C to over 90 °C. Allis et al. [38] originally set a maximum temperature of 250 °C in their predictions as they had no way to justify using higher values. As was done for the top temperature boundary, the 3D interpolation of the temperature data was mapped onto the numerical model grid and assigned to the bottom of the model domain. As part of the model calibration exercise, the temperatures Allis et al. used for portions of the base of the earth model domain had to be raised to allow the modeled temperature to match the November 2018 logging data. The bottom temperature values ranged from approximately 220 °C to nearly 270 °C (see Figure 9). This temperature is largely controlled by conduction from the heat source originating/hosting the hydrothermal system to the east.

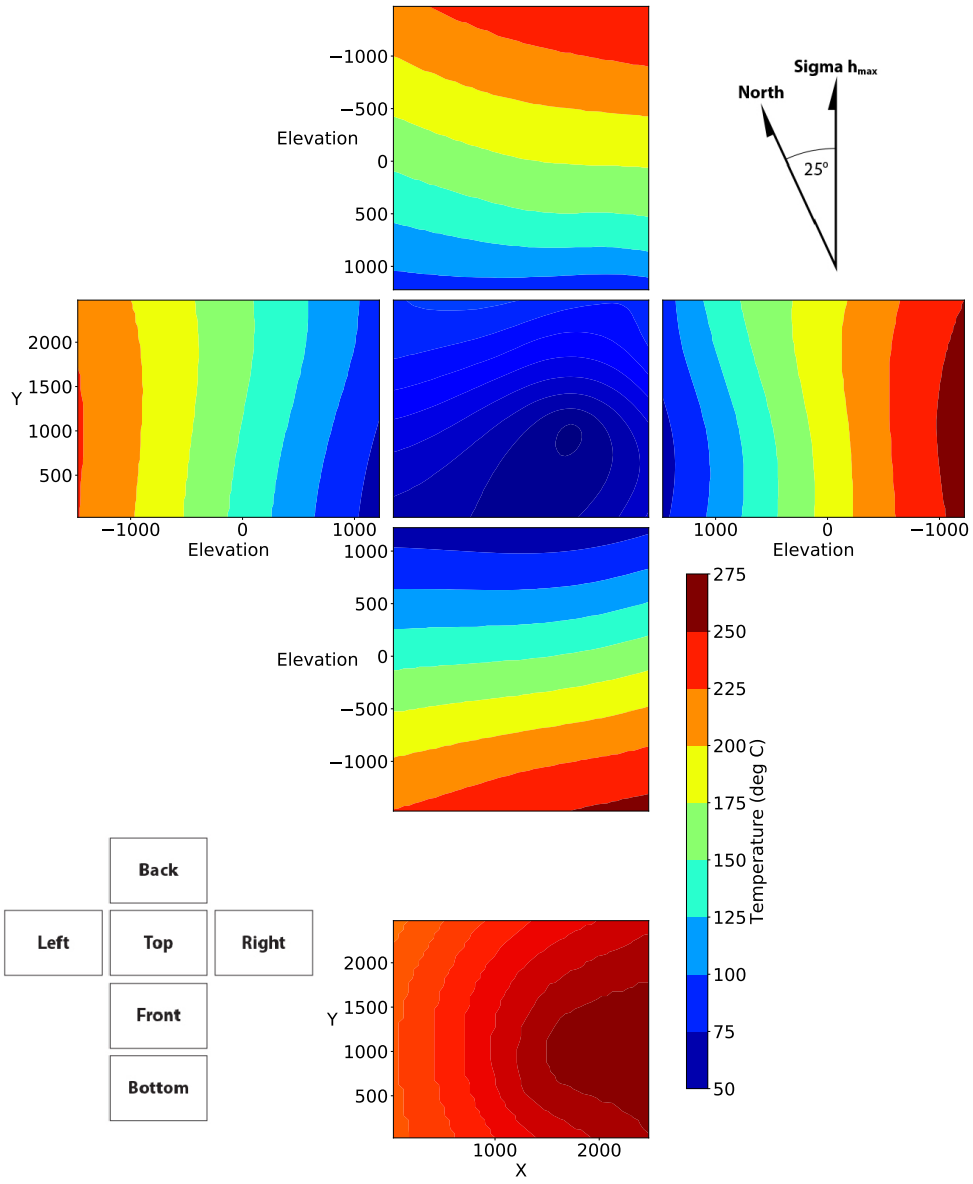

Figure 9. Temperature boundary conditions.

2.4.2. Pressure

The top surface of the model domain (see Figure 4) was assigned a Dirichlet condition for pressure. The pressure values were estimated by calculating the height of the water column between the top of the model domain and the water table [11]. The water table in the vicinity of the FORGE site slopes in a generally westward direction, resulting in the pressure gradient across the top of the model domain. The water column height was uniformly adjusted as part of the calibration process, until the modeled pressure matched the values obtained from the pressure measurements in Well 58-32 collected in November 2018. Figure 10 shows the pressure applied to the top of the model domain.

All other boundaries of the model domain were assumed to be impermeable. While this assumption may not be perfectly valid for the upper sedimentary sections, the model domain was chosen in order to omit as much of the sedimentary section as possible to

avoid having to consider lateral flow originating from the outflow around the terminus of the Opal Mound Fault. The extremely low permeability of the granitoid justifies a no-flow condition (see Table 2).

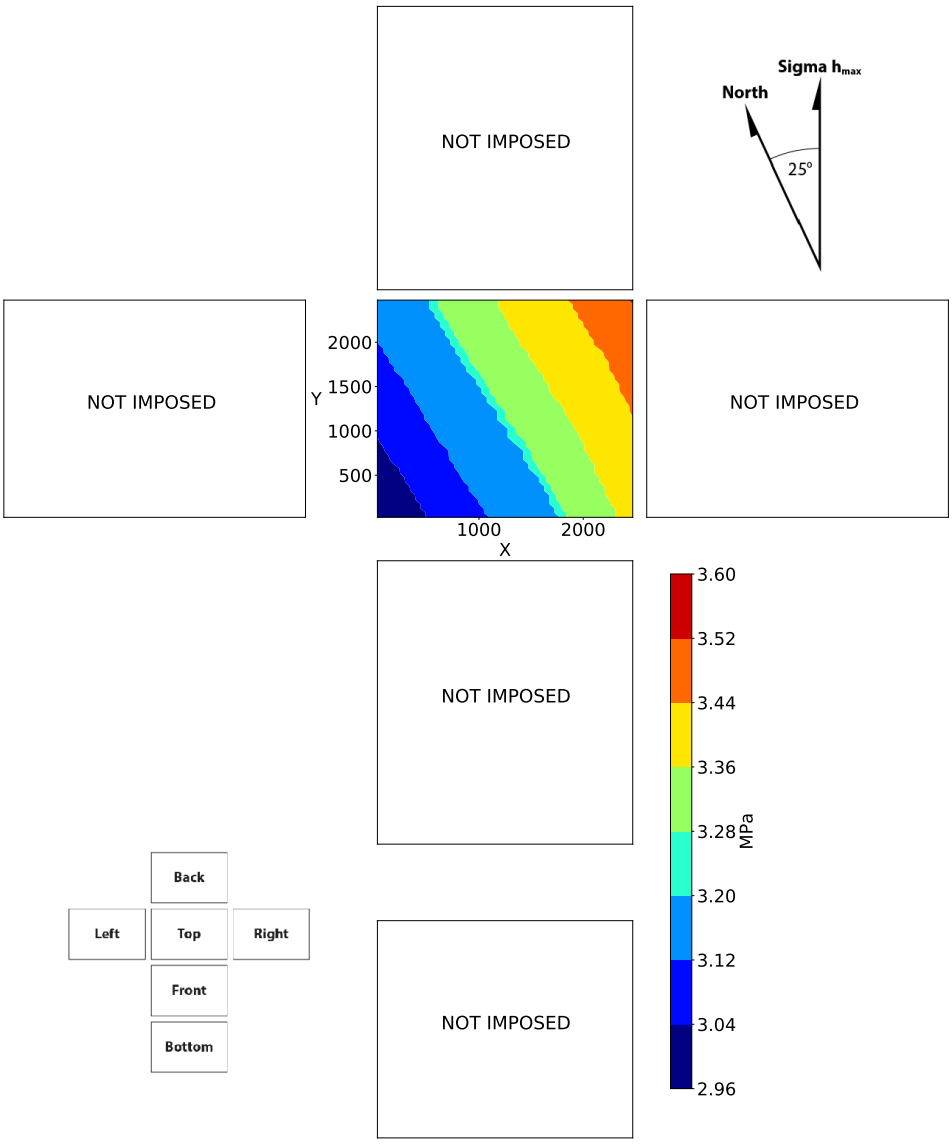

Figure 10. Pressure boundary conditions.

2.4.3. Stress

The boundary condition for total vertical stress is perhaps one of the most important for FORGE, as it will have a direct influence on predicted stress gradients at the site. Therefore, a significant amount of effort was used to develop this condition. Values for all stress components were estimated using results from stress testing in Well 58-32 from Phase 2B [51], pore-pressure information (from the pressure boundary condition discussed above), density of the sedimentary materials overlying the granite, and the land-surface topography at the site. Note that any mention of stress refers to the total stress.

A Dirichlet condition for stress (as a total body force) was applied to the top of the model domain. Included in the vertical stress boundary condition is topographic expression of land surface features (such as the Mag Lee Wash that runs through the

site) and the saturated thickness of groundwater, resulting in a range of 8.0 to 11.2 MPa being applied (see Figure 11). The bottom surface of the modeled domain was set to zero displacement in the vertical direction and a roller condition in the horizontal directions.

A gradient of 0.014 MPa/m (0.62 psi/ft) was applied to the east side of the model domain (S_h direction), while the left/west was fixed at zero displacement. Values ranged from approximately 8 MPa to over 45 MPa. A S_H gradient of 0.0174 MPa/m (0.77 psi/ft) was applied to the back side of the model domain, while the front was fixed at zero displacement. Values ranged from approximately 11 MPa to nearly 55 MPa. Figure 11 shows the stress values used on the boundaries.

These boundary conditions were chosen so that the model could honor the available data and so that the simulation results could be used to provide stress distributions on the model edges that can be used for transient simulations of injection/production at the site.

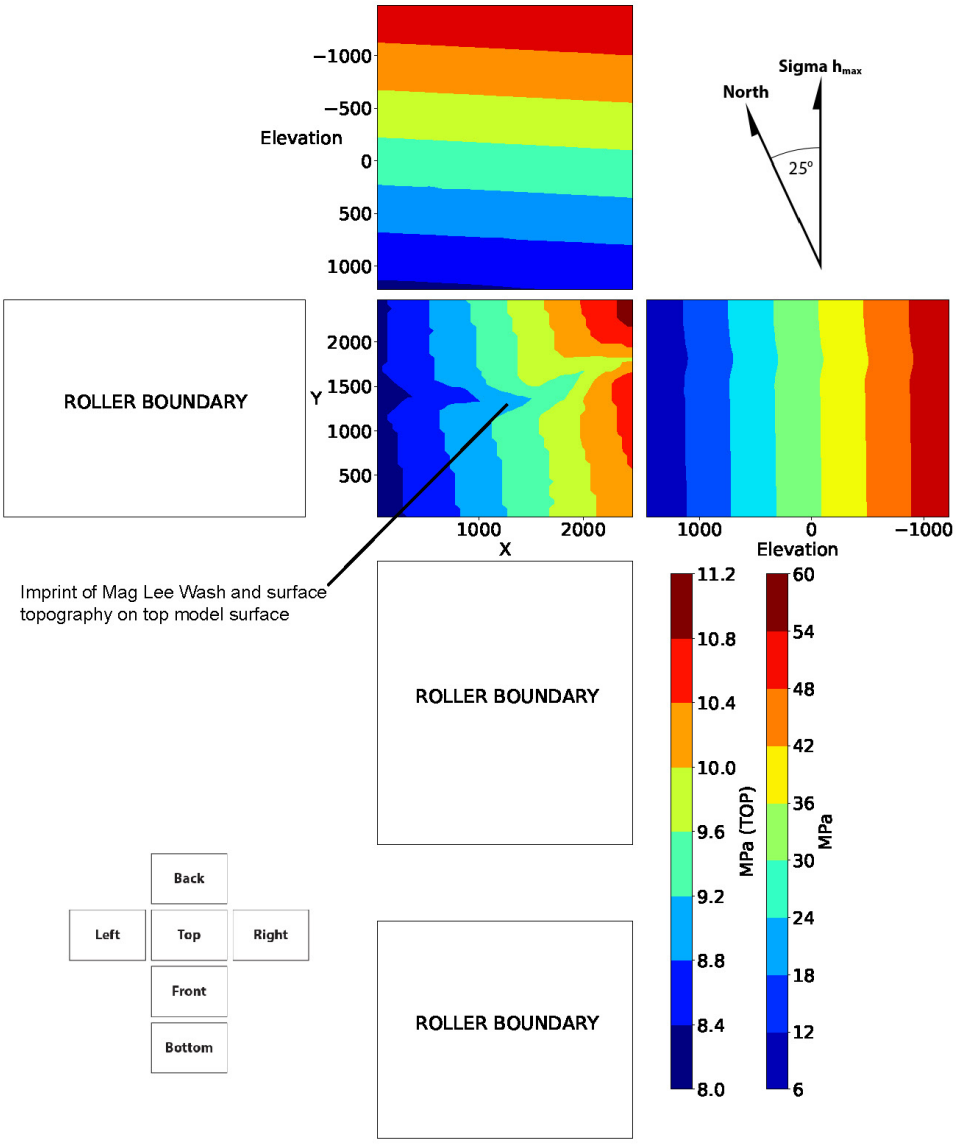

Figure 11. Stress boundary conditions as the total stress. Note the influence of the site topography imprinted on the top surface of the model domain.

2.5. Initial Conditions

Initial pressure, temperature, and stress conditions used for the native-state model were based on estimates in the earth model and assigned to the numerical model cells in a similar fashion used to assign the boundary conditions. Values for pressure were estimated based on the top boundary condition and interpolated downward as a function of depth. Temperature was directly interpolated from the earth model to the numerical model cells. In FALCON, stress is a derived quantity based on calculations of the displacement of the rock matrix. As such, it is difficult to assign apriori. A value of zero displacement was assigned as an initial condition, letting the model iterate a few extra times to come to a converged solution.

Initial reservoir properties used in the native-state model were taken directly from characterization data. In many cases, a range of possible values were available, and the mean or median was used, with the values having been adjusted within the measured range during model calibration. In all cases, uniform reservoir properties were used within the alluvium. For the granite, heterogeneous property distributions were used where appropriate and data were available. Tables 2 and 3 summarize the property values used. These are the "reference" values for the native state of FORGE at the end of Phase 2.

3. Results

The model calibration process consisted of first initializing the model with initial and boundary condition values for pressure, temperature and stress obtained from the earth model and comparing the simulated values with those obtained from measurements and logging in Well 58-32. In order to calibrate the pressure, the height of the water table was uniformly adjusted up and down until the modeled pressure distribution match the logged values from Well 58-32.

In order to calibrate the modeled temperature field, several adjustments had to be made. These involved manually varying the thermal conductivity of both the granitoid and sedimentary units. In order to obtain a match with field measurements, the temperatures at the bottom of the earth model had to be reinterpreted (raised from 250 ^{o}C to 270 ^{o}C) for portions of the inferred heat source underlying the site. This change required the entire thermal structure at the site to be re-estimated followed by regenerating the model initial and boundary conditions. This process was repeated iteratively until an acceptable match was obtained between the simulated temperature field and the measured values in Well 58-32.

Figure 12 presents the modeled pressure, temperature, and stress along the trajectory of Well 58-32 with the data from pressure-temperature logging collected in November 2018. As seen on Figure 12, the simulated pressure and temperature match the field-measured data quite well. The pressure distribution is largely linear along the length of Well 58-32 within the model domain and shows little to no differentiation between the overlying sediments and granitoid reservoir. The modeled temperature distribution also matches the field-measured data quite well and shows a break in slope at the sediment-granitoid contact. Input and mesh files for the native state simulations can be found in the Geothermal Data Repository[53].

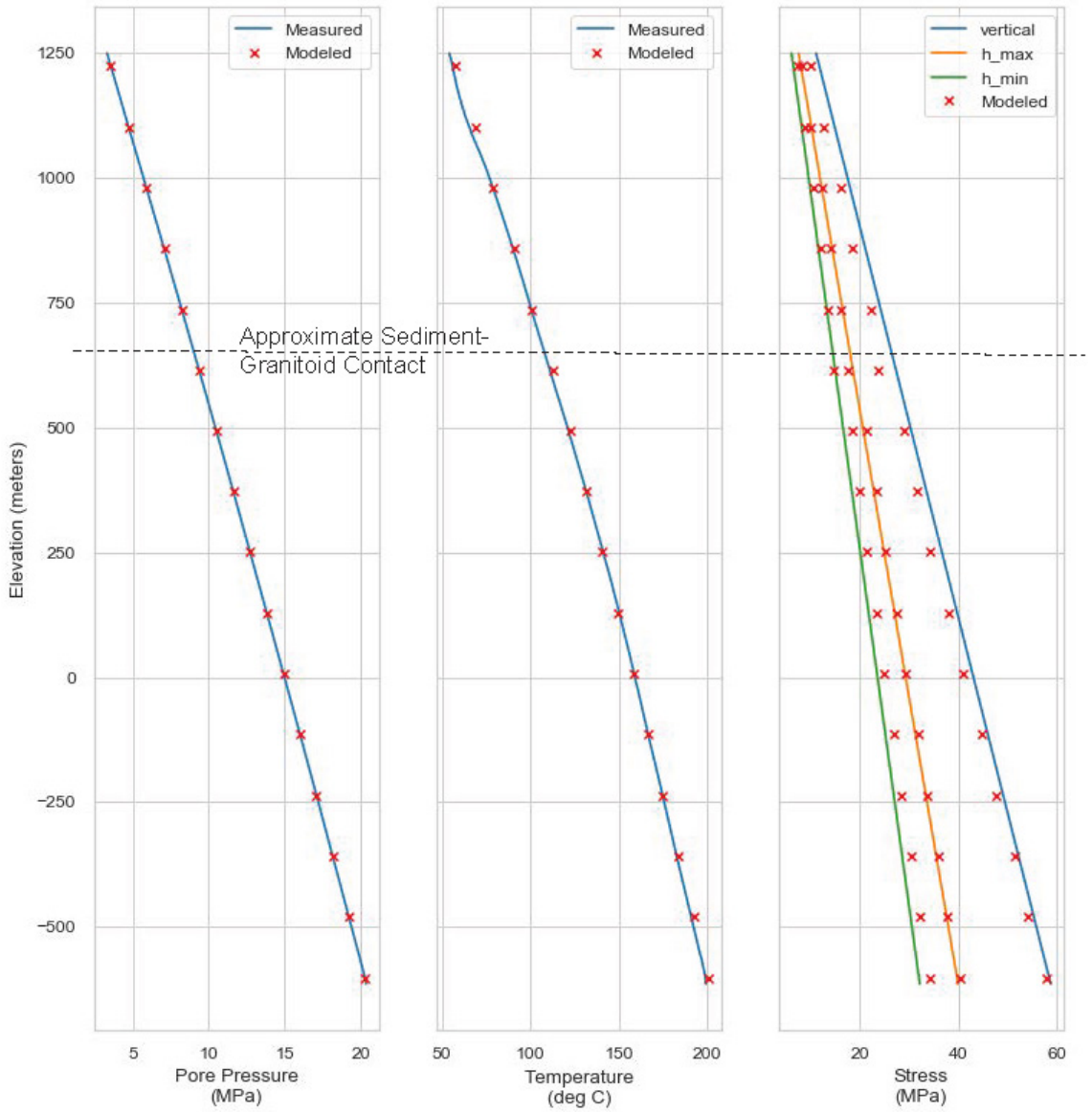

Figure 12. Native state model results compared with pressure-temperature log collected in November 2018. Stress plots are from estimates from Phase 2B testing in the open hole portion of Well 58-32. Note that the granitiod-sediment contact is at an approximate elevation of 720 meters.

The stress-gradient data from Phase 2 were collected in the toe of Well 58-32. On Figure 12, the gradient estimate is plotted over the entire length of Well 58-32, along with the modeled native-state stress. The vertical stress was calibrated by adjusting the sediment density and porosity, as well as the density of the granitoid, within the range of measured values, until the modeled vertical stress matched the field measurements at the toe of Well 58-32. The simulated minimum and maximum horizontal stresses were slightly overestimated, but were within the range of measured values.

Figures 13 and 14 show this simulated native-state pressure and stress on the edges of the model domain. Temperature results are not plotted as Dirichlet conditions were assigned on all sides of the domain. The pressure results for the bottom of the model domain show significant variation, largely due to the significant differences in the thermal regime (see Figure 9). As shown on Figure 9, the temperature assigned to the bottom of the model domain ranged from approximately 220 °C to 270 °C, resulting in fluid density differences of over 70 kg/m^3.

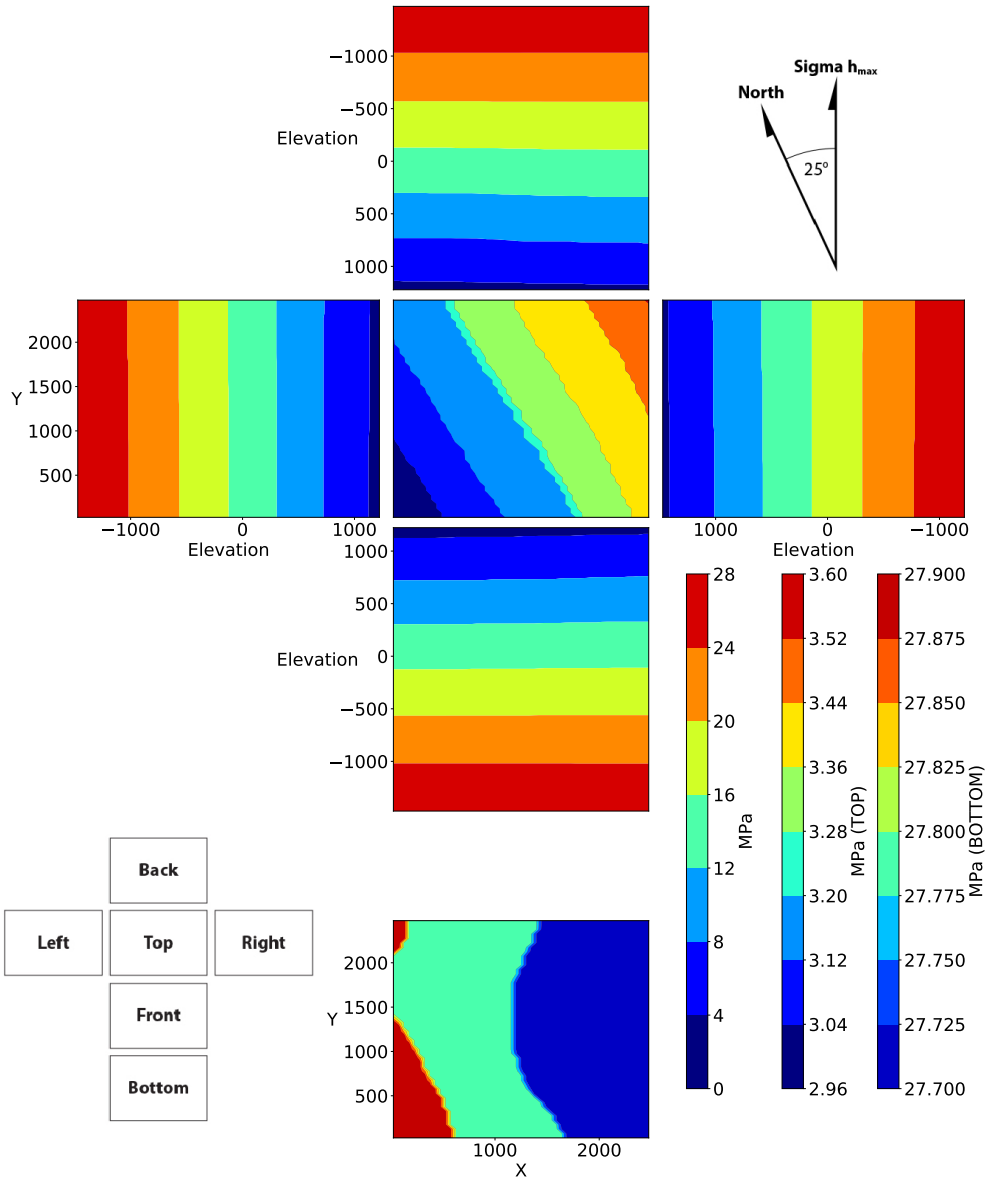

Figure 13. Native-state pressure distribution.

Topographic effects resulted in significant variation in vertical stress, as shown on Figure 14. The general westward slope of the land surface (i.e., thicker overburden on the eastern side the of model domain) resulted in an approximate 3 MPa difference in the stress applied to the top boundary. Superimposed on the westward slope of the ground surface was the topographic expression of the Mag Lee Wash. The effects of both the slope and wash are reflected in the predicted vertical stress on the bottom surface of the model.

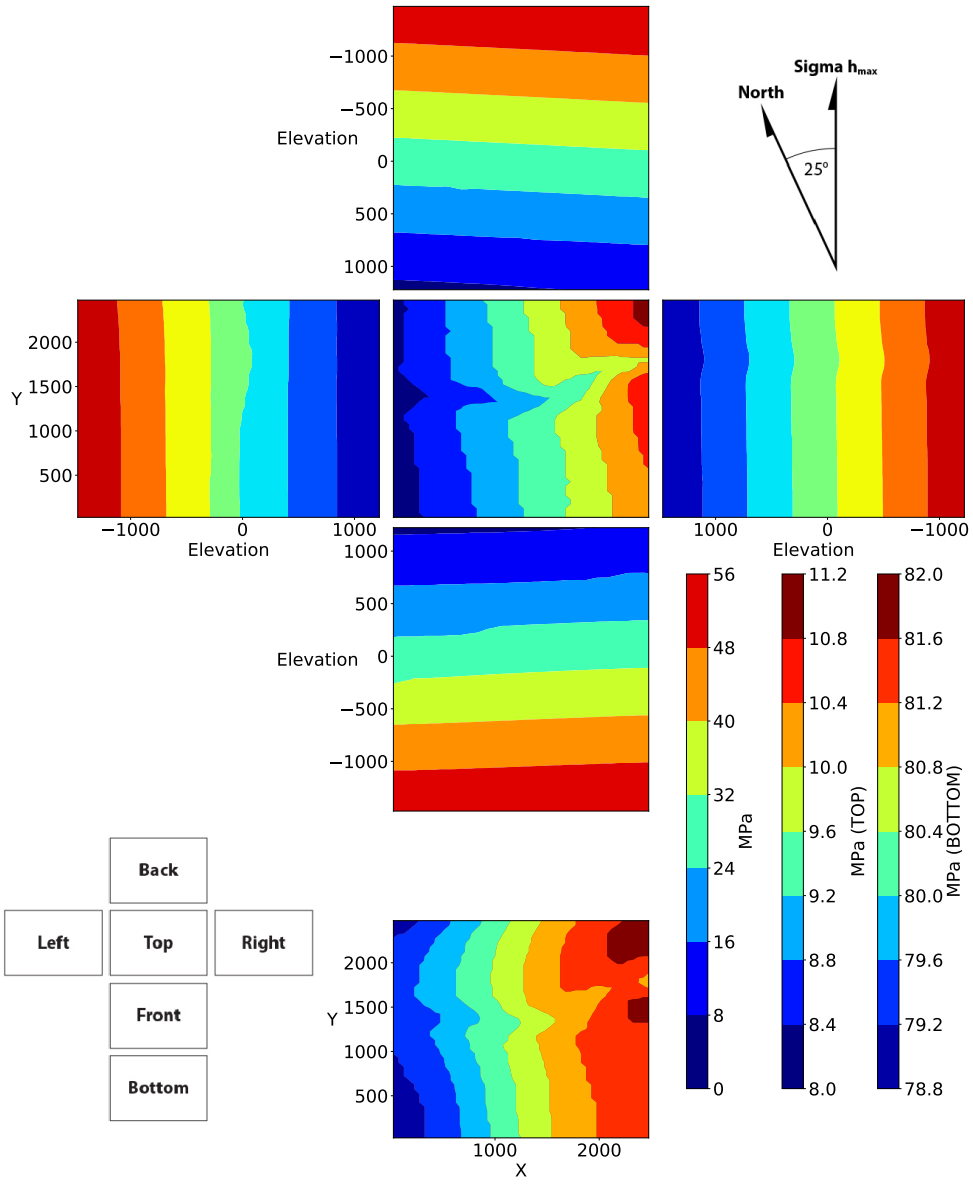

Figure 14. Native-state stress distribution.

As part of the planning for future injection and production wells at the FORGE site, a number of potential trajectories were evaluated as part of the Phase 2 activities. A full discussion of the well evaluation procedure is beyond the scope of this paper. Here, we focus on providing information on the final selected well trajectory. Figure 15 shows the final selected well trajectory (Well 16A-78(32)) along with an outline of the FORGE site. The well will be located near the center of the FORGE site, with a planned trajectory that travels along an azimuth of N15E, plunging 65 degrees from the vertical. The predicted pressure, temperature, and stress along the planned path of Well 16A-78(32) are shown in Figure 16.

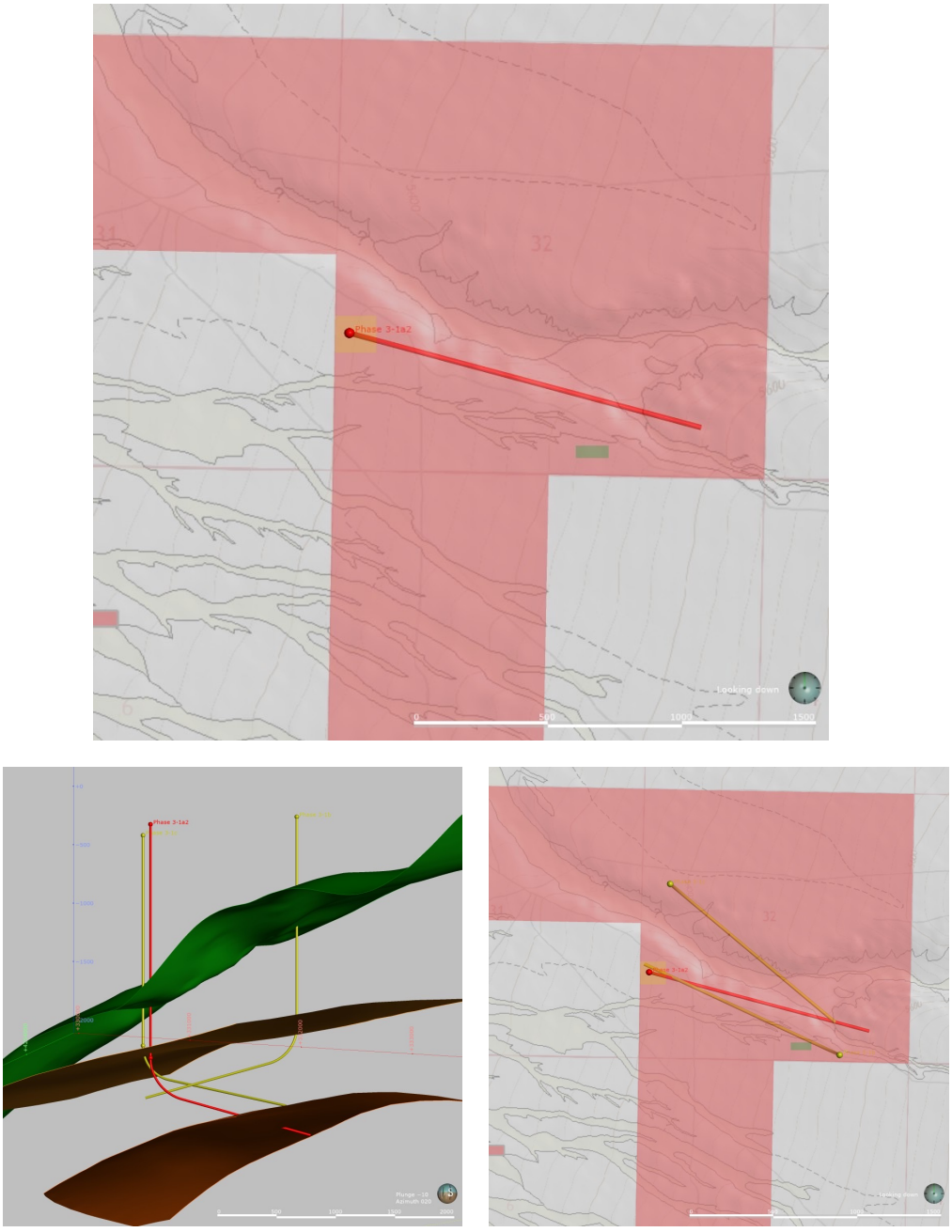

Figure 15. Map view of the FORGE site (red shaded area) showing the proposed trajectory for the first Phase 3 well (top), oblique cross-section view that shows the top of the granite surface(green); 175 ^{o}C and 225 ^{o}C isosurfaces, and several previously evaluated trajectories (bottom-left); and a map view showing several previously evaluated trajectories (yellow lines) and the recommended trajectory (red line) (bottom-right). Scale bar on top figure represents 1,500 meters.

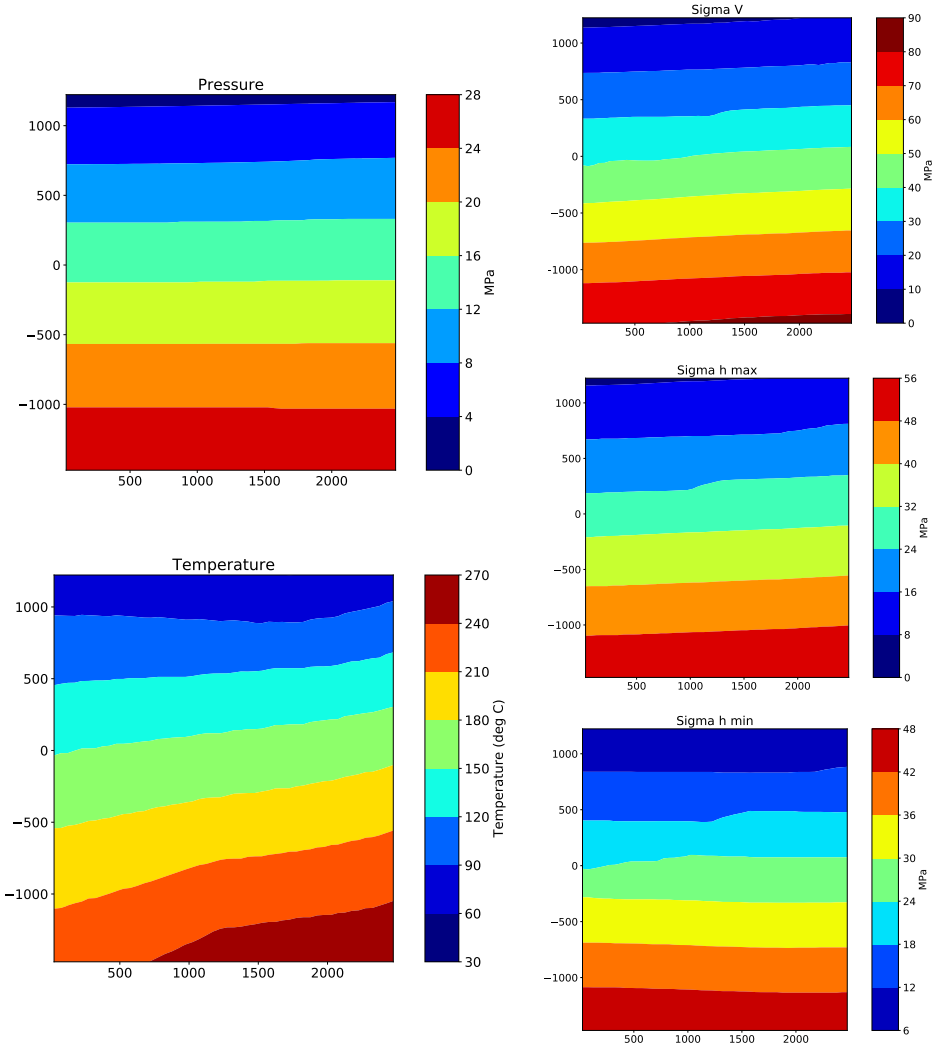

Figure 16. Predicted pressure, temperature, and stress along the planned trajectory for Well 16a-78(32).

4. Summary and Conclusions

Geologic characterization activities combined with historical information culminated in a conceptual model of the site which is dominated by thermal conduction in a large granitoid body with a top surface that dips generally to the west. The granitoid reservoir is overlain by younger sedimentary materials that host a non-potable groundwater re-source. A reference earth model was constructed based on the geologic conceptual model that will be used to assess all future changes in geologic understanding at the site.

A detailed native-state Thermal-Hydraulic-Mechanical model of the region where stimulation and operations are expected to occur was created based, upon the reference earth model. The modeled boundary conditions were mapped directly from geologic, geographic, and hydrogeologic conditions measured at the site, and were modified along with select reservoir properties to come to a calibrated steady-state solution. A reference set of reservoir flow, heat transport, DFN, and mechanical properties were developed from the calibration exercise, and used by the team for follow-on modeling to ensure comparability of results. Considerable care and attention were placed in developing the framework of the native-state numerical model. The geologic structure developed in the earth model was mapped onto a uniform 50 m grid, on a domain that is generally centered around Well 58-32 and the region where Phase 3 activities are envisioned to

take place. The numerical representation of the earth model comprised two general geologic units, sedimentary/alluvial materials that overlie a granitoid basement.

Hydrologic and mechanical properties of the sedimentary materials were considered to be spatially uniform and based on data collected as part of FORGE characterization or from the literature. This unit, however, is not part of the reservoir, so the native-state modeling efforts did not focus on this unit. The complete top of the model domain was set to be in the sediments for convenience in setting to top-boundary conditions (body forces). The granitoid materials that make up the planned EGS reservoir were assigned a heterogeneous and anisotropic permeability field based upon the reference DFN developed for the site. The porosity was also based on the upscaled DFN, while other reservoir properties (such as density and thermal conductivity) were assigned uniform values.

For the stress model, we incorporated detailed surface topography and relief of granite contact, as these can cause perturbations in the stress field at depth. The native-state model shows small perturbations in Shmin that generally follow the granite-alluvium contact, and in some areas several hundred meters into the granitoid materials. Calibration of the native-state model consisted of adjusting the grain density and porosity of the sediments and the density of the granitoid in order to match the field estimated measured in Well 58-32. The thermal conductivity of both the sediments and granitoid were slightly modified from initial estimates, as was the maximum temperature at the base of the earth model. Reservoir permeability was taken from upscaling the reference DFN, and went unchanged in the native-state model. Only the top boundary pressure was modified to ensure it matched measured values at Well 58-32.

Author Contributions: Geologic conceptual models and frameworks, S. Simmons; Fracture analysis and discrete fracture networks, A. Finnila; Core characterization and stress estimate, J. Mclennan; Native state modeling, R. Podgorney.

Funding: This research was funded by the US Department of Energy with additional support from Utah School and Institutional Trust Lands Administration, Beaver County, the Utah Governor's Office of Energy Development.

Data Availability Statement: The data used to create the FORGE native state model are available on a number of on-line sources, primarily the Utah FORGE Modeling and Simulation website. The FORGE website links to the Geothermal Data Repository which maintains the data in perpetuity.

Acknowledgments: This research made use of the resources of the High Performance Computing Center at Idaho National Laboratory, which is supported by the Office of Nuclear Energy of the U.S. Department of Energy and the Nuclear Science User Facilities under Contract No. DE-AC07-05ID14517.

The earth model output for this paper was generated using Leapfrog Geothermal Software. Copyright Seequent Limited. Leapfrog, Seequent and all other Seequent Limited product or service names are registered trademarks or trademarks of Seequent Limited.

Collaboration with the entire Utah FORGE team is greatly appreciated, as were the helpful discussions with Andy Wilkins at the Commonwealth Scientific and Industrial Research Organization.

Conflicts of Interest: The authors declare no conflict of interest

References

1. Batchelor, A.S. The Creation of Hot Dry Rock Systems by Combined Explosive and Hydraulic Fracturing. Proceedings of the International Conference on Geothermal Energy; , 1982; pp. 321–342.
2. Cornet, F.H. Experimental Investigations of Forced Fluid Flow through a Granite Rock Mass. Proceedings of 4th International Seminar on the Results of EC Geothermal Energy Demonstration; , 1989; pp. 189–204.
3. Smith, M.C.; Aamodt, R.L.; Potter, R.M.; Brown, D.W. Manmade Geothermal Reservoirs. Technical Report LA-UR-75-953, Los Alamos National Laboratory, New Mexico, USA, 1975.
4. Tester, J.W.; Brown, D.W.; Potter, R.M. Hot Dry Rock Geothermal Energy – A New Energy Agenda for the 21st Century. Technical Report LA-11514-MS, Los Alamos National Laboratory, New Mexico, USA, 1989.
5. Duchane, D. Hot Dry Rock: A Realistic Energy Option. *Bulletin of the Geothermal Resources Council* **1990**, *19*, 83–88.

6. Duchane, D.; Brown, D. Hot Dry Rock (HDR) Geothermal Energy Research and Development at Fenton Hill, New Mexico. *Geothermal Heat Center Bulletin* **2002**.
7. Augustine, C. Update to enhanced geothermal system resource potential estimate. Geothermal Resources Council Transactions, 2016, Vol. 40, pp. 673–677.
8. Tester, J.; Anderson, B.; Batchelor, A.; Blackwell, D.; DiPippo, R.; Drake, E.; Garnish, J.; Livesay, B.; Moore, M.; Nichols, K.; Petty, S.; Toksoz, M.; Veatch, R. The Future of Geothermal Energy: Impact of Enhanced Geothermal Systems (EGS) on the United States in the 21st Century. Technical Report INL/EXT-06-11746, Idaho National Laboratory, 2006.
9. of Energy, U.D. GeoVision: Harnessing the Heat Beneath Our Feet. Technical report, US Department of Energy, 2019.
10. Kirby, S.M. Revised mapping of bedrock geology adjoining the Utah FORGE site. In *Geothermal characteristics of the Roosevelt Hot Springs system and adjacent FORGE EGS site, Milford, Utah: Utah Geological Survey Miscellaneous Publication 169*; R., A.; Moore, J., Eds.; Utah Geological Survey, 2019; p. 6. doi:https://doi.org/10.34191/MP-169-A.
11. Moore, J.; Allis, R.; Simmons, S.; Nash, G.; McLennan, J.; Forbes, B.; Jones, C.; Pankow, K.; Hardwick, C.; Gwynn, M.; Podgorney, R. Utah FORGE: Final Phase 2B Topical Report. Technical report, DOE Geothermal Data Repository; Energy and Geoscience Institute at the University of Utah, 2018. this report is from the end of Phase 2B–it has lots individual pieces, John's 58-32 core testing.
12. Podgorney, R.; Finnila, A.; McLennan, J.; Ghassemi, A.; Huang, H.; Forbes, B.; Elliot, J. A framework for modeling and simulation of the Utah FORGE site. Proceedings, 44th workshop on geothermal reservoir engineering, Stanford University; , 2019.
13. Nielson, D.L.; Evans, S.H.; Sibbett, B.S. Magmatic structural, and hydrothermal evolution of the Mineral Mountains intrusive complex, Utah. *Geological Society of America Bulletin* **1986**, *97*, 765–777.
14. Coleman, D.S.; Walker, J.D.; Bartley, J.M.; Hodges, K.V. Thermochronologic evidence of footwall deformation during extensional core complex development, Mineral Mountains, Utah. *The Geologic Transition, High Plateaus to Great Basin-A symposium and field guide, AAPG Pacific Section Guidebook* **2001**, *78*, 155–168.
15. Lipman, P.; Rowley, P.; Mehnert, H.; Evans, S.; Nash, B.; Brown, F. Pleistocene rhyolite of the Mineral Mountains, Utah–Geothermal and archaeological significance. *U.S. Geological Survey Journal of Research* **1978**, *6*, 133–147.
16. Knudsen, T.; Kleber, E.; Hiscock, A.; Kirby, S. Quaternary geology of the Utah FORGE site and vicinity, Millard and Beaver Counties, Utah. Technical Report Miscellaneous Publication 169-B, Utah Geological Survey, 2019.
17. Podgorney, R.; McLennan, J. Utah FORGE: Well 58-32 Injection Test Data. Technical report, DOE Geothermal Data Repository; Idaho National Laboratory, 2018.
18. Podgorney, R.; Allis, R. Utah FORGE: Roosevelt Hot Springs Analytical Well-Based Temperature Model Data. Technical report, DOE Geothermal Data Repository; Idaho National Laboratory, 2018.
19. Podgorney, R.; McLennan, J.; Moore, J.; Simmons, S.; Wannamaker, P.; Allis, R.; Jones, C. Utah FORGE: Well Data for Student Competition. Technical report, DOE Geothermal Data Repository; Idaho National Laboratory, 2018.
20. Podgorney, R.; McLennan, J.; Simmons, S.; Moore, J.; Allis, R.; Hill, J.; Hartwick, C. Utah FORGE: Maps and GIS Data from the Earth Model. Technical report, DOE Geothermal Data Repository; Idaho National Laboratory, 2018.
21. Podgorney, R. Utah FORGE: Earth Model Mesh Data for Selected Surfaces. Technical report, DOE Geothermal Data Repository; Idaho National Laboratory, 2018.
22. Golder Associates. FracMan Reservoir Edition version 7.8 Discrete Fracture Network Simulator. Technical report, Golder Associates, 2019.
23. Podgorney, R.; Huang, H.; Lu, C.; Gaston, D.; Permann, C.; Guo, L.; Andrs, D. Falcon: a Physics-based and Massively Parallel and Fully-Coupled, Finite Element Model for Simultaneously Solving Multiphase Fluid Flow, Heat Transport, and Rock Deformation for Geothermal Reservoir Simulation. Technical Report INL/EXT-11e23351, Idaho National Laboratory, 2014.
24. Xia, Y.; Podgorney, R.; Huang, H. Assessment of a hybrid continuous/discontinuous Galerkin finite element code for geothermal reservoir simulations. *Rock Mechanics and Rock Engineering* **2016**. doi:https://doi.org/10.1007/s00603-016-0951-y.
25. Xia, Y.; Podgorney, R. Falcon: Finite Element Geothermal Reservoir Simulation Code.
26. Gaston, D.; Guo, L.; Hansen, G.; Huang, H.; Johnson, R.; Knoll, D.; Newman, C.; Park, H.K.; Podgorney, R.; Tonks, M.; Williamson, R. Parallel Algorithms and Software for Nuclear, Energy, and Environmental Applications Part I: Multiphysics Algorithms. *Communications in Computational Physics* **2012**, *12*, 807–833.
27. Gaston, D.; Guo, L.; Hansen, G.; Huang, H.; Johnson, R.; Knoll, D.; Newman, C.; Park, H.K.; Podgorney, R.; Tonks, M.; Williamson, R. Parallel Algorithms and Software for Nuclear, Energy, and Environmental Applications Part II: Multiphysics Software. *Communications in Computational Physics* **2012**, *12*, 834–865.
28. Seequent. User manual for Leapfrog Geothermal. *Version 5* **2020**.
29. Finnila, A.; Forbes, B.; Podgorney, R. Building and Utilizing a Discrete Fracture Network Model of the FORGE Utah Site. Proceedings of the 44th Workshop on Geothermal Reservoir Engineering, Stanford University, Stanford, CA, USA, 2019, pp. 11–13.
30. Terzaghi, R. Sources of error in joint surveys. *Geotechnique* **1965**, *15*, 287–304. doi:https://doi.org/10.1680/geot.1965.15.3.287.
31. Dershowitz, W.S.; Herda, H.H. Interpretation of fracture spacing and intensity. Proceedings; 33rd U.S. Symposium on Rock Mechanics: Santa Fe, NM, 1992.
32. Dershowitz, W.; Ambrose, R.; Lim, D.; Cottrell, M. Hydraulic Fracture and Natural Fracture Simulation for Improved Shale Gas Development. Annual Conference and Exhibition Houston; American Association of Petroleum Geologists: Houston, TX, 2011.

33. Gwynn, M.; Allis, R.; Hardwick, C.; Jones, C.; Nielsen, P.; Hurlbut, W. Compilation of Rock Properties from Well 58-32, Milford, Utah FORGE Site, FORGE Utah. Technical report, Energy and Geoscience Institute at the University of Utah, 2018.
34. Bartley, J.M. Joint patterns in the mineral mountains intrusive complex and their roles in subsequent deformation and magmatism. In *Geothermal characteristics of the Roosevelt Hot Springs system and adjacent FORGE EGS site, Milford, Utah. Utah Geological Survey Miscellaneous Publication 169*; Allis, R.; Moore, J., Eds.; Utah Geological Survey, 2019; p. 11. doi:https://doi.org/10.34191/MP-169-C.
35. Moore, J. Utah FORGE: Phase 2C Topical Report. Technical report, DOE Geothermal Data Repository; Energy and Geoscience Institute at the University of Utah, 2019. this report is from the end of Phase 2c–it has the M and S report that forms the basis of the paper, doi:10.15121/1578287.
36. Gwynn, M.; Allis, R.; Hardwick, C.; Jones, C.; Nielsen, P.; Hurlbut, W. Compilation of Rock Properties from FORGE Well 58-32, Milford, Utah. In *Geothermal characteristics of the Roosevelt Hot Springs system and adjacent FORGE EGS site, Milford, Utah: Utah Geological Survey Miscellaneous Publication 169*; R., A.; Moore, J., Eds.; Utah Geological Survey, 2019; p. 38. doi:https://doi.org/10.34191/MP-169-L.
37. Kirby, S.M.; Simmons, S.; Inkenbrandt, P.; Smith, S. Groundwater Hydrogeology and Geochemistry of the Utah FORGE Site and Vicinity. In *Geothermal characteristics of the Roosevelt Hot Springs system and adjacent FORGE EGS site, Milford, Utah: Utah Geological Survey Miscellaneous Publication 169*; R., A.; Moore, J., Eds.; Utah Geological Survey, 2019; p. 23. doi:https://doi.org/10.34191/MP-169-E.
38. Allis, R.; Gwynn, M.; Hardwick, C.; Kirby, S.; Moore, J. Thermal characteristics of the Roosevelt Hot Springs system, with focus on the FORGE EGS site. In *Geothermal characteristics of the Roosevelt Hot Springs system and adjacent FORGE EGS site, Milford, Utah. Utah Geological Survey Miscellaneous Publication 169*; Allis, R.; Moore, J., Eds.; Utah Geological Survey, 2019; p. 24. doi:https://doi.org/10.34191/MP-169-D.
39. Heard, H.C.; Page, L. Elastic moduli, thermal expansion, and inferred permeability of two granites to 350°C and 55 megapascals. *Journal of Geophysical Research: Solid Earth* **1982**, *87*, 9340–9348, [https://agupubs.onlinelibrary.wiley.com/doi/pdf/10.1029/JB087iB11p09340] doi:https://doi.org/10.1029/JB087iB11p09340.
40. Feng, Z.j.; Qiao, M.m.; Dong, F.k.; Yang, D.; Zhao, P. Thermal Expansion of Triaxially Stressed Mudstone at Elevated Temperatures up to 400°C. *Advances in Materials Science and Engineering* **2020**, *2020*, 8140739. doi:10.1155/2020/8140739.
41. Selvadurai, A. On the Poroelastic Biot Coefficient for a Granitic Rock. *Geosciences* **2021**, *11*. doi:10.3390/geosciences11050219.
42. Małkowski, P.; Łukasz Ostrowski. The Methodology for the Young Modulus Derivation for Rocks and Its Value. *Procedia Engineering* **2017**, *191*, 134–141. ISRM European Rock Mechanics Symposium EUROCK 2017, doi:https://doi.org/10.1016/j.proeng.2017.05.164.
43. Sharma, H.; Dukes, M.; Olsen, D. Field Measurements of Dynamic Moduli and Poisson's Ratios of Refuse and Underlying Soils at a Landfill Site. In *Geotechnics of Waste Fills—Theory and Practice*; Landva, A.; Knowles, G., Eds.; ASTM International, 1990; pp. 57–70. doi:https://doi.org/10.1520/STP25299S.
44. Detournay, E.; Cheng, A. Fundamentals of Poroelasticity. In *Analysis and Design Methods*; Fairhurst, C., Ed.; Pergamon: Oxford, 1993; pp. 113–171. doi:https://doi.org/10.1016/B978-0-08-040615-2.50011-3.
45. Wagner, W.; Cooper, J.R.; Dittmann, A.; Kijima, J.; Kretzschmar, H.J.; Kruse, A.; Mareš, R.; Oguchi, K.; Sato, H.; Stö̈cker, I.; Šifner, O.; Takaishi, Y.; Tanishita, I.; Trü̈benbach, J.; Willkommen, T. The IAPWS Industrial Formulation 1997 for the Thermodynamic Properties of Water and Steam . *Journal of Engineering for Gas Turbines and Power* **2000**, *122*, 150–184, [https://asmedigitalcollection.asme.org/gasturbinespower/article-pdf/122/1/150/5548474/150_1.pdf]. doi:10.1115/1.483186.
46. IAPWS. Revised Supplementary Release on Backward Equations for Specific Volume as a Function of Pressure and Temperature v(p,T) for Region 3 of the IAPWS Industrial Formulation 1997 for the Thermodynamic Properties of Water and Steam. Technical report, IAPWS, 2014.
47. IAPWS. Release on the IAPWS Formulation 2008 for the Viscosity of Ordinary Water Substance. Technical report, IAPWS, 2008.
48. IAPWS. Revised Release on the IAPWS Formulation 1985 for the Thermal Conductivity of Ordinary Water Substance. Technical report, IAPWS, 1985.
49. IAPWS. Release on the IAPWS Formulation 2011 for the Thermal Conductivity of Ordinary Water Substance. Technical report, IAPWS, 2011.
50. IAPWS. Guidelines on the Henry's constant and vapour liquid distribution constant for gases in H_2O and D_2O at high temperatures. Technical report, IAPWS, 2004.
51. Forbes, B.; Moore, J.N.; Finnila, A.; Podgorney, R.; Nadimi, S.; McLennan, J.D. Natural fracture characterization at the Utah FORGE EGS test site—discrete natural fracture network, stress field, and critical stress analysis. In *Geothermal characteristics of the Roosevelt Hot Springs system and adjacent FORGE EGS site, Milford, Utah. Utah Geological Survey Miscellaneous Publication 169*; Allis, R.; Moore, J., Eds.; Utah Geological Survey, 2019; p. 11. doi:https://doi.org/10.34191/MP-169-N.
52. Tipler, P. *Physics for Scientists and Engineers, 4th Edition*; Freeman: Texas, 1999.
53. Podgorney, R. Utah FORGE Phase 2 Native State FALCON model files, 2019.

DFNE 21–2329

Estimation of fracture size for a Discrete Fracture Network model of the Utah FORGE geothermal reservoir using forward modeling of fracture-borehole intersections

Finnila, A.
Golder Associates, Redmond, WA, USA

ABSTRACT: The FORGE geothermal reservoir is sited in deep granitic bedrock near the town of Milford, Utah. A Discrete Fracture Network (DFN) model has been created to explicitly represent the natural fracture population using both outcrop fracture trace length data and a Fullbore Formation MicroImager (FMI) resistivity log from a vertical pilot well. Natural fractures identified in the log intersect between 1-8 of the FMI pads. The percentage which fully penetrate the pilot well borehole (8 pads) and the percentage which only penetrate 1-4 pads are tabulated. These statistics are compared with the results of forward modeling many stochastic realizations of the DFN using different size distributions. Forward modeling is possible since the fracture orientations are well specified from both log and outcrop data and the well radius and trajectory are known. While the outcrop trace data for fractures having a radius between 20 – 50 m match both lognormal and power law distributions, the FMI log data appear to sample fractures having a median radius of 1.4 m and are consistent only with the power law distribution found from the outcrop data.

1. INTRODUCTION

The FORGE geothermal reservoir is sited in deep granitic bedrock near the town of Milford, Utah. A Discrete Fracture Network (DFN) model has been created to explicitly represent the natural fracture population in the reservoir (Finnila et al., 2019). In the DFN, fractures are modeled as planar and roughly circular, having a range of orientations, local intensity, and sizes consistent with what has been observed from both image log data from a vertical pilot well, Well 58-32, and measurements from outcrops in the nearby mountains. Previous to this work, fracture sizes were estimated from the Salt Cove outcrop trace data shown in Fig. 1.

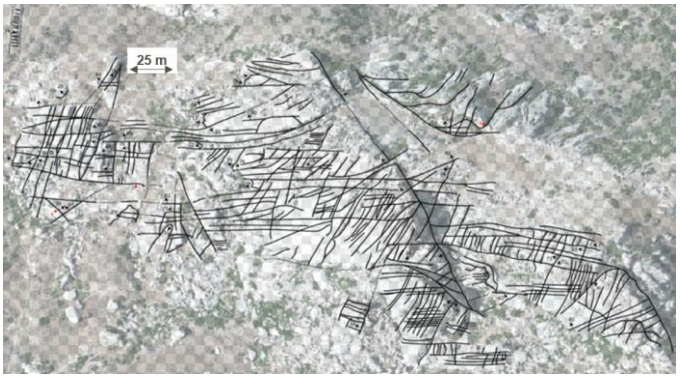

Fig. 1. Large fracture traces mapped in the Salt Cove area of the Mineral Mountains. Digitized 2D maps were created for several outcrop locations from the work of Bartley (2018) and Coleman (1991).

The fracture traces from the Salt Cove outcrop data set have lengths between 3 and 282 m and can be fit with either a lognormal distribution or a truncated power law distribution, also known as a Pareto distribution, as shown in Fig. 2. Trace lengths are converted to fracture radius using the FracMan software package (Golder Associates, 2020) which uses the method from Zhang et. al., 2002. Given the FORGE reservoir location in an intrusive igneous formation, fractures are assumed to be roughly circular and are modeled in the DFN as regular hexagons. Fracture size is therefore specified using a fracture radius. While the lognormal distribution provides a much better fit to the trace length data compared with the power law distribution, this is often the case when the underlying distribution is in fact a power law distribution which has some measurement bias leading to under-sampling of the smaller size range.

Although both distributions can match the trace length data for large fractures having a radius in the 20 to 50 m range, the two distributions differ significantly in the smaller fracture size range. Determination of the correct parameterization for the fracture size is critical for correctly adjusting the fracture intensity in the DFN based on different choices for minimum fracture size. Once a DFN is fully specified, subsets are often created by filtering the model using a minimum fracture size. These subsets of the FORGE DFN are used as initial conditions for researchers simulating processes such as well hydraulic stimulation, local stress evolution, flow

pathway analysis, and thermal breakthrough in proposed injection and production well configurations. The fracture intensity of the model subsets will vary based on the fracture size parametrization. For the FORGE DFN, the fracture intensity is based on the intensity measured in the FMI log, which may be including fractures with a radius as small as half a meter. A DFN subset using a minimum fracture size of 10 m would need to reduce the fracture intensity much more for a power law size distribution compared with a lognormal distribution.

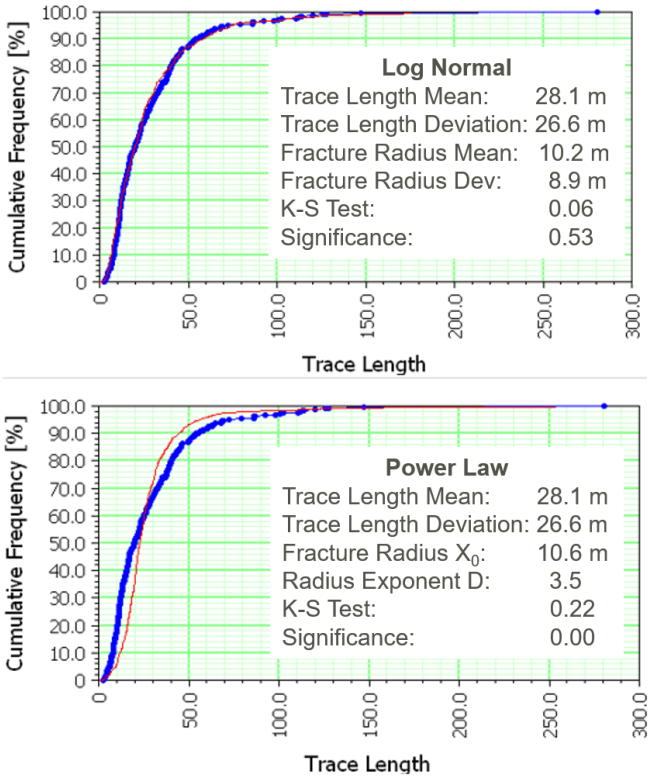

Fig. 2. Power law vs lognormal parameterization of the trace data. Blue points show trace data and red lines shows model fit.

This paper examines the fracture size information present in the High Definition Fullbore Formation MicroImager (FMI) resistivity log from the pilot well at the FORGE site in order to better constrain the fracture size population of the DFN. The pilot well, 58-32, is vertical and extends to a measured depth of 2242 m (7357 ft). The FMI log data samples a much smaller fracture size range compared with the outcrop trace lengths measured. Adjusting the fracture size parameterization in the FORGE DFN so it is consistent with both the smaller fractures sampled in the FMI, and the larger fractures measured in outcrop should improve the accuracy of the DFN model and allow for more accurate subsets to be created when adjusting the minimum fracture size.

2. ANALYSIS OF THE TRACE LENGTH DATA

The probability distribution functions for both a lognormal distribution and a Pareto distribution are shown in Equations 1 and 2. The Pareto distribution is a power law distribution which has a minimum size cutoff. The lognormal distribution is parameterized here using the mean, μ, and variance (square of the standard deviation), σ^2, of the normally distributed function; so if X is lognormally distributed, $\ln(X) \sim N(\mu, \sigma^2)$. The Pareto distribution is parameterized using the power law exponent, D, and the minimum size, x_0. In the Pareto distribution, the power law exponent (also known as the shape) is found from the outcrop trace length data. If measurement censoring is suspected, it is best to create a log-log plot of the complementary cumulative number vs trace length and use the negative value of the slope plus 1 for the exponent, D (La Pointe, 2002). The slope of the line is taken from only the linear part of the plotted data (Fig. 3). The parameter x_0 (also known as the scale) would be found from the minimum fracture radius sampled by the data set. The actual minimum size is not well known for either data set but is assumed be on the order of 10 m for the outcrop data and 1 m for the FMI log data.

$$\boldsymbol{Lognormal(\mu,\sigma^2)}: \boldsymbol{pdf(x)} = \frac{1}{x\sigma\sqrt{2\pi}} e^{-\frac{(\ln(x)-\mu)^2}{2\sigma^2}} \quad (1)$$

$$\boldsymbol{Power\ Law\ (D, x_0)}: \boldsymbol{pdf(x)} = \frac{D{x_0}^D}{x^{D+1}} \quad (2)$$

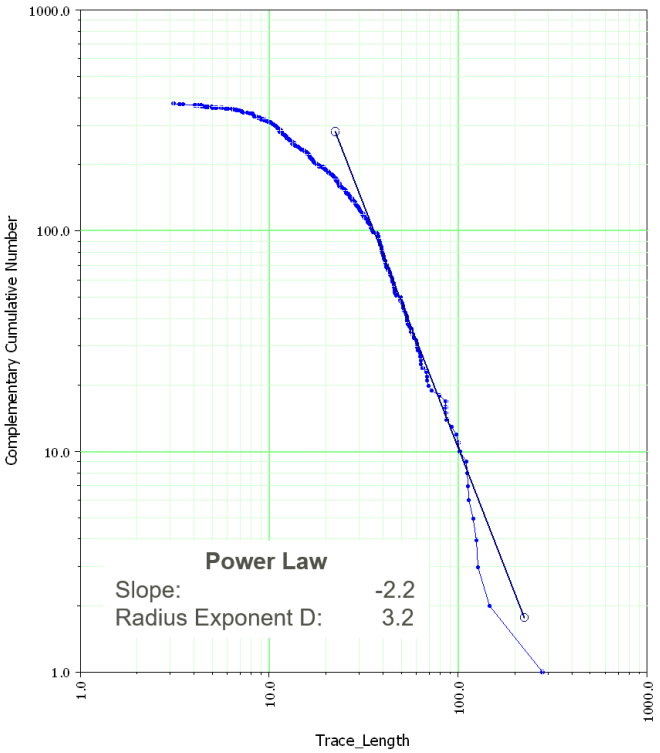

Fig. 3. Power law exponent of fracture radius using trace length data.

The power law exponent for the outcrop trace length data from Salt Cove is 3.2. This is found from the straight section of the log-log plot where trace lengths range from 40 to 100 m (Fig. 3).

In order to justify using the outcrop data to help define the fracture size distribution in the FORGE reservoir, it is important to establish that the reservoir rock is similar to the rock mapped in outcrop for the trace length data. One way to do this is compare the fracture orientations. Fig. 4 shows upper hemisphere stereonets showing the natural fracture orientations from Well 58-32 (left) and the fractures mapped from the Salt Cove outcrop in the Mineral Mountains (right). These both show an E-W striking sub-vertical set, although in Well 58-32 this set is dipping steeply to the south while in outcrop they were dipping steeply to the north. The second prominent set is also very similar in the two stereonets: a subvertical N-S striking set. The third sets are not as prominent in either stereonet. Well 58-32 shows an inclined, SSE dipping set while the outcrop data shows an inclined, west dipping set. They are considered similar enough for this analysis, however, these locations are approximately 5 miles apart and there is significant variability in the fracture populations mapped in the same unit in the Mineral mountains as discussed at the end of the paper in the Discussion section.

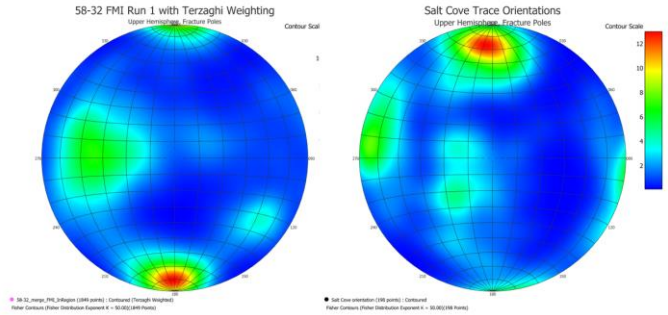

Fig. 4. Upper hemisphere stereonets showing the natural fracture orientations from Well 58-32 (left) and the fractures mapped from the Salt Cove outcrop in the Mineral Mountains (right).

3. ANALYSIS OF THE FMI LOG DATA

An FMI-HD borehole image of 58-32 was logged after drilling (Run 1 of the available FMI logs) and the interpreted pdf file, available from NGDS, 2018, was used to collect fracture-borehole statistics in the deepest 300 ft section. Note that well 58-32 was initially named MU-ESW1 which is what is listed on the pdf file. Natural fractures identified in the FMI log intersect between 1-8 of the FMI pads. The percentage which fully penetrate the pilot well borehole (imaged trace intersects all 8 pads) and the percentage which only partially penetrate (imaged trace intersects between 1-7 pads) are tabulated. For the purposes of this paper, those natural fractures shown as intersecting between 1 and 4 of the pads are combined for analysis. This group plus the one intersecting all 8 pads are used to estimate the proportions of partially penetrating and fully penetrating fractures. As will be discussed in the next section, these statistics are compared with the results of forward modeling many stochastic realizations of the DFN using different size distributions.

Fig. 5 shows a short segment of the FMI interpretation including the measured depth in feet on the far-left a panel with the static resistivity values and identified features as sinusoidal line segments in the center-left panel. The center-right panel shows the dynamically scaled resistivity where the open natural fractures (conductive, partially resistive in this image) appear as dark sinusoidal lines while the closed fractures (appear as lighter color sinusoids (resistive continuous in this image). The far-right panel shows the true dip and dip direction of natural fractures and the true dip and direction of propagation for tensile fractures.

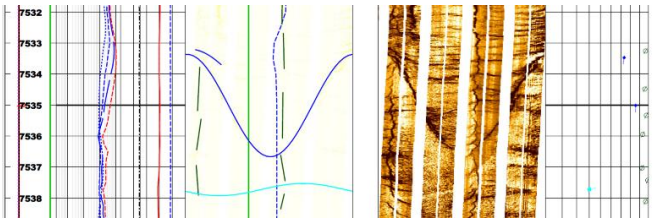

Fig. 5. HD FMI data with interpreted natural fracture intersections (dark blue sinusoid lines in center-left panel).

In the deepest 300 feet of the well, 177 fracture traces are identified with traces shown. Each of these was labeled with the number of pads it intersected. A fully penetrating fracture would show a continuous sinusoidal trace across all 8 pads while those that were only partially penetrating the borehole would intersect between 1 and 7 pads. The pads provide the contiguous vertical images in both the static and dynamic resistivity values shown in the two center panels of Fig. 5. They are grouped in four sets of two that are more closely spaced.

The pad counts for each fracture trace are shown in the histogram in Fig. 6 along with the percentage of fractures in that category. From the table included in the figure, 64% of the fractures fully penetrate the borehole. In general, larger fractures would be expected to intersect all 8 pads while smaller fractures would more often only intersect a few. The expected proportion of fractures intersecting all 8 pads depends on the size of the fractures, the size of the borehole radius, and the angle between the borehole trajectory and the fracture pole.

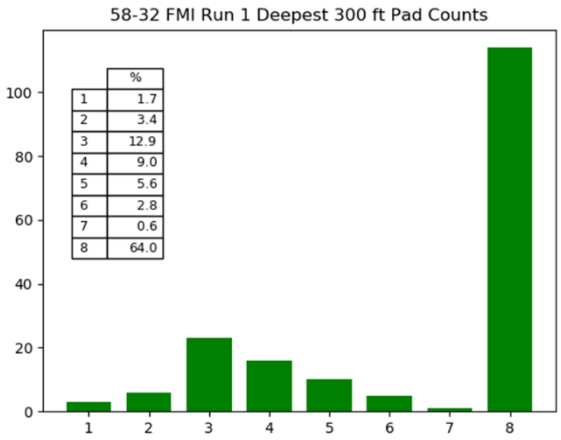

Fig. 6. Pad counts for deepest 300 ft of Well 58-32.

4. FORWARD MODELING

Forward modeling to determine the fracture size population is possible since the fracture orientations are well specified from both log and outcrop data and the well radius and trajectory are known. We can perform forward modeling to try and match the fracture pad count percentages using different fracture size parameterizations in order to determine if the lognormal or power law distributions found from the outcrop data are consistent with the FMI data. This workflow follows the methodology first described by La Pointe et al., 1993.

An eight-sided borehole having the same radius and trajectory as the bottom 300 feet of Well 58-32 is created in a FracMan model (Fig. 7). The borehole diameter of 58-32 at this depth is 8 ¾ in. so the borehole radius is 0.11 m. A DFN realization is generated using a random number seed so that a stochastic set of fractures is created. Once the fractures are generated, those that intersect the borehole are identified and their exact intersection geometry is analyzed to identify how many panels they intersect. Fig. 7 shows the intersecting traces of the fracture on the borehole and they are color coded to show how many panels they intersect. These counts are tabulated and saved as percentages for each panel count category as was done for the FMI data shown in Fig. 6.

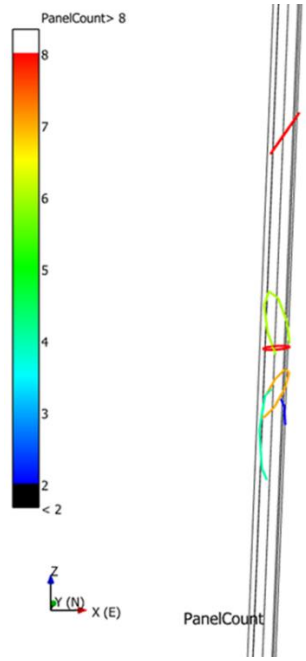

Fig. 7. Simulated borehole matching trajectory for Well 58-32 with fracture intersections shown in color.

To first get an idea of what the average size of fracture being sampled in the FMI data is, a constant fracture size was used for the forward modeling. The results of this analysis are shown in Fig. 8. Constant fracture radius values of 0.5, 1.0, 1.5, 5.0 and 10.0 m were used. One hundred realizations were generated and analyzed for each of the different fracture radius values. The box plots in Fig. 8 show the median value as an orange line in the middle of the box with whiskers on the box extending to the minimum and maximum values. The horizontal red line shows the measured value from the FMI data. The FMI data are consistent with a sampling fractures having a median value of approximately 1.4 m.

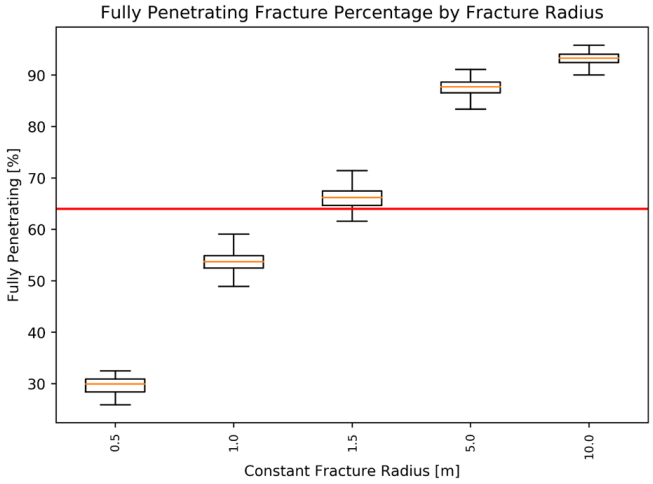

Fig. 8. Boxplots showing the percentage of fully penetrating fracture intersections as a function of DFNs composed of a single constant fracture size. Each boxplot represents 100 DFN realizations. The red horizontal line shows the value from the FMI log of Well 58-32 (deepest 300 ft).

Note from Fig. 8 that when the fracture radius is 10 m, that over 90% of the fracture-borehole intersections would be crossing all 8 pads. Recall that the lognormal fit to the Salt Cove trace length data estimated a mean fracture size of 10.2 m. This does not seem to be supported by the forward modeling results using a constant fracture radius. We can, of course, use the estimated lognormal distribution in the DFN for the forward modeling to test the hypothesis. Fig. 9 shows those results where we show the percentage of fully penetrating fractures as well as the percentage of those that only intersect between 1 and 4 pads.

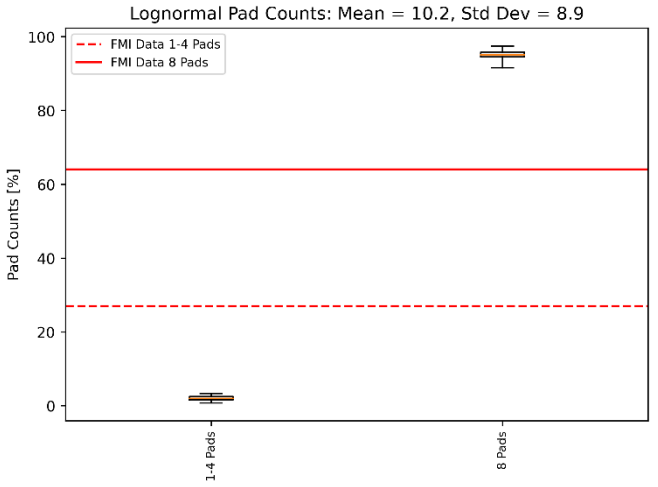

Fig. 9. Pad counts for 100 DFN realizations where the fracture sizes followed the lognormal parameterization found from the Salt Cove trace length data.

As expected, following the finding that the mean fracture radius being sample by the FMI data was only 1.4 m, the forward modeling of the lognormal distribution having a mean of 10.2 m and a standard deviation of 8.9 m shows a very poor match both for the percentage of fully penetrating fractures and for the ones only intersecting 1-4 pads. If the lognormal distribution was correct, then the expected measured percentages from the FMI data would intersect the box plots from the forward modeling results.

The next step is to evaluate if forward modeling can match the FMI data using the power law distribution found for the Salt Cove trace length data. The best estimate for the power law exponent, D, was 3.2, however, there wasn't a reasonable estimate for the minimum fracture size, x_0. While the original trace length to fracture size analysis done in FracMan gave a minimum fracture radius of 10.6 m (Fig. 2), that value is much too large now that we know that the median fracture size sampled by the FMI data is 1.4 m. We know that the minimum size must be less than 1.4 m from the forward modeling work using a constant fracture size, and we can assume that the minimum size is also constrained by the imaging resolution combined with the judgment of the log analyst, but we do not have a more precise estimate.

Additional forward modeling can address this issue by fixing the parameter D at 3.2 and then performing the forward modeling using a range of x_0 values. The value of x_0 giving the best match to the FMI pad counts is assumed to be the best estimate. Fig. 10 shows the result of searching for x_0 using both the percentage of fully penetrating fractures as well as using the percentage of partially penetrating fractures where the pad counts were between 1 and 4. Matching the pad counts of 8 yielded an x_0 value of 0.76 m while matching the pad counts of 1-4 yielded an x_0 value of 0.49 m. The best estimate for x_0 is taken as the average of these two values, equal to 0.63 m.

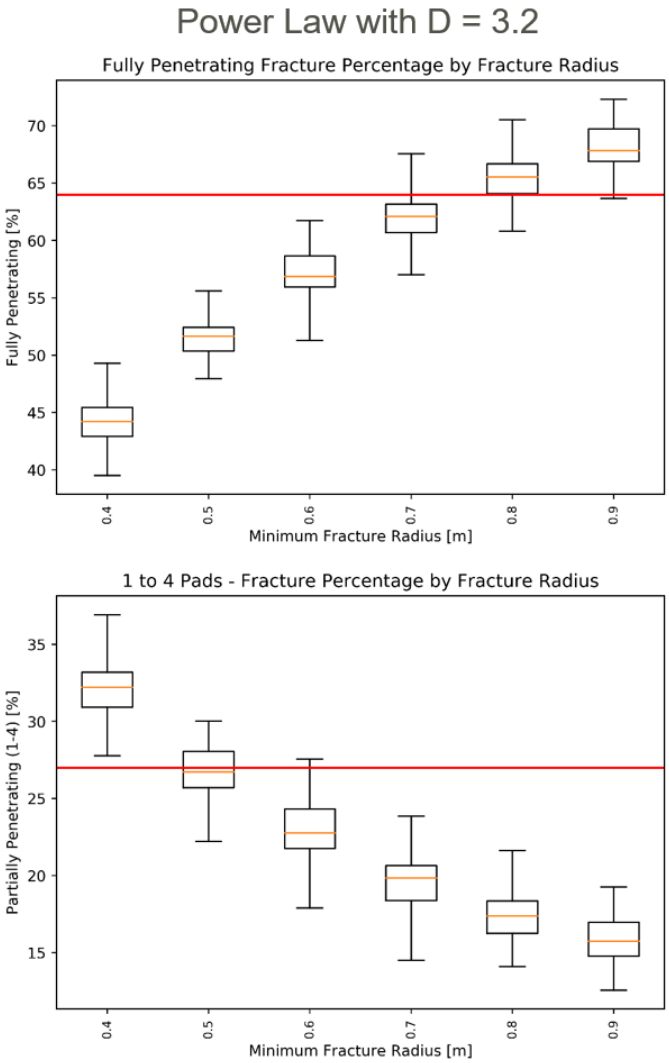

Fig. 10. Percentage of fully penetrating fractures (top) and partially penetrating fractures (bottom) from DFN realizations where the fracture sizes followed the power law size parameterization found from the Salt Cove trace data. While the power law exponent, D, is estimated from the trace data, the minimum size is not constrained so a variety of values were used.

As shown in Fig. 11, the forward modeling results using the best fit for x_0 with a Pareto distribution having a D value of 3.2 fits the FMI data, but only barely as the FMI values are only slight enclosed by the box plot whiskers. Some possible explanations for this poor match are

discussed in the following section. The power law distribution match (Fig. 11) is much better, however, than the lognormal distribution match (Fig. 9). This is true even though the outcrop trace length data fit the lognormal distribution better as can be seen from the K-S tests and significance values listed in Fig. 2.

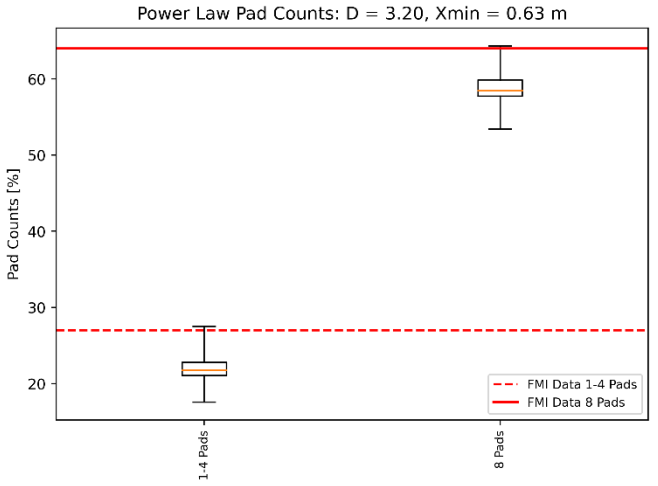

Fig. 11. Forward modeling results for power law distribution where D=3.2 and x_0=0.63m.

Given the two measurements that we have been using for the FMI data, both the percentage of fully penetrating fractures and the percentage of fractures only penetrating 1-4 pads, we could theoretically solve for both D and x_0. These would be found by minimizing the spread between the two estimates for x_0 as shown in Fig. 12. Unfortunately, as will be discussed in more detail in the next section, this does not appear to be an effective method for this particular analysis as this leads to unreasonably low values for D.

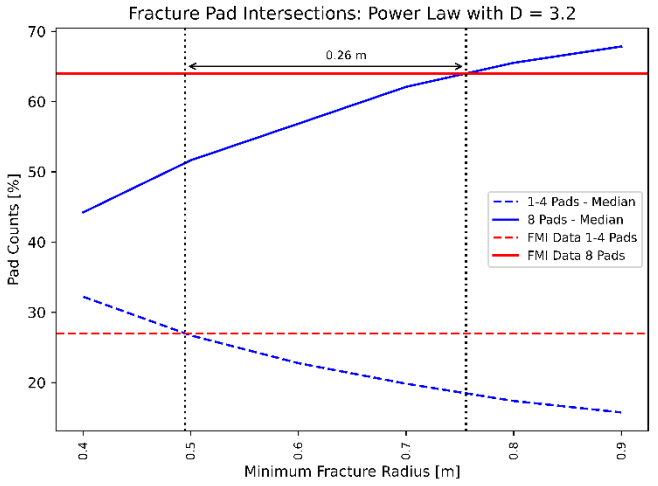

Fig. 12. Finding the minimum fracture size for the Pareto distribution by matching both the fully penetrating fracture percentage and the fracture percentage from those intersecting 1-4 pads.

5. DISCUSSION

While the Pareto distribution with D equal to 3.2 and x_0 equal to 0.63 m results in a satisfactory match of both the FMI intersection data and the trace length data measured at the Salt Cove outcrop, there are a couple of issues that warrant some discussion. The first involves the uniqueness of the solution. The second involves the assumption that there is only one size distribution present in the reservoir.

There are four outcrops with trace mapping data available from the nearby mountains in the same rock unit as the FORGE reservoir. The log-log plot of the complementary cumulative number vs trace length for all four are shown in Fig. 13. The plots are roughly linear for trace lengths between 40 and 100 m and show a range of slopes ranging from -3.7 for Pinnacle Pass to -2.0 for Baily Spring South. This results in estimated D values for the Pareto distribution between 3.0 and 4.7. The question arises as to whether we could match the FMI intersection data using different values of D. As was previously done, 100 realizations of the DFN were generated for each of five different D values, and fracture-borehole intersection statistics were again collected and compared with those found in the FMI data. For this purpose, the D values ranged from 2.3 to 3.5. Larger values for D were not modeled as the number of small fractures becomes unwieldly high as the value of D increases and the trend was clear using the lower values. The results are shown in Fig. 14 and summarized in Table 1. By adjusting the value of x_0, it is possible to get reasonable matches with all these values of D. The value of x_0 ranges between 0.29 m and 0.54 m, steadily increasing as the value of D increases. Both the low- and high-end values seem possible. So while the forward modeling seems to rule out the lognormal size distribution found from the outcrop data and supports having a Pareto distribution, it has not demonstrated a unique parameter selection for D and x_0.

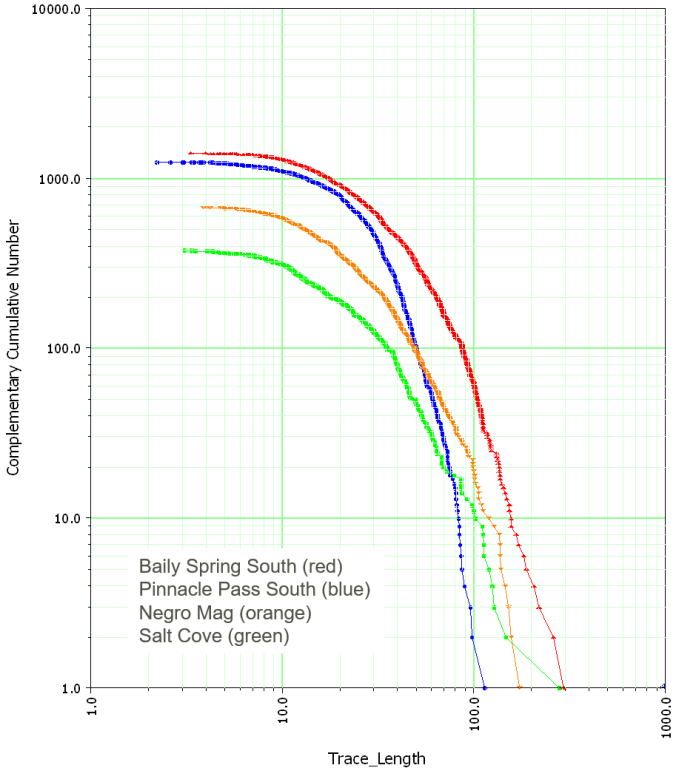

Fig. 13. Trace length data from different outcrop areas displays a range of potential power law exponents.

The second point of discussion centers around the assumption that only one size distribution is present in the natural fractures present in the FORGE reservoir. As described in Bartley, 2018, the Miocene granitic rocks in the northern half of the Mineral Mountain range all contain a similar fracture pattern. The pattern includes three fracture sets in the following general orientations: E-W to WNW-ESE striking and subvertical; NE-SW to NNE-SSW striking and steeply dipping; and gently W-dipping with strikes that vary from NW to N to NE. In some areas, two of the concentrations of poles to fractures that define the three sets merge into a girdle, but the overall pattern remains the same. In the areas which are located nearest to the FORGE area, steep E-W striking fractures form the most abundant and continuous set. The E-W fractures commonly bound the steep NE-striking and gently west-dipping fracture sets.

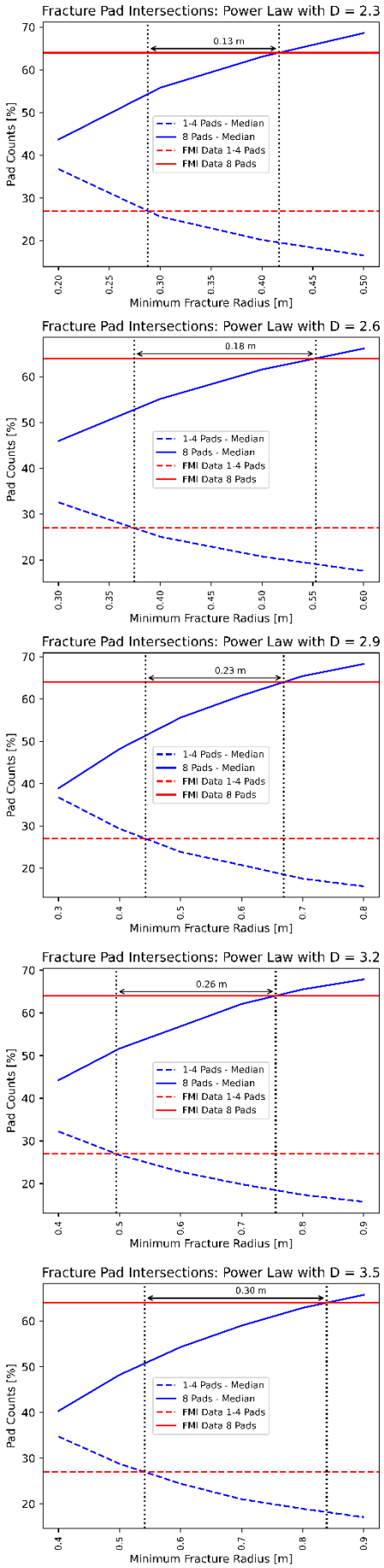

Fig. 14. Finding x_0 for various values of D.

Table 1. Forward modeling estimates for x_0 using a range of D values in the Pareto distribution.

D	x_0 Pads 1-4 [m]	x_0 Pads 8 [m]	Delta [m]	Mean x_0
2.3	0.29	0.42	0.13	0.36
2.6	0.37	0.55	0.18	0.46
2.9	0.44	0.67	0.23	0.56
3.2	0.49	0.76	0.26	0.63
3.5	0.54	0.84	0.30	0.69

From this description of the fracture sets in the Mineral Mountain range, we would expect the E-W subvertical set to be generally longer than the other two sets. This, indeed, appears to be the case for the traces mapped at the Salt Cove outcrop (Fig. 1). With the E-W set fractures commonly bounding the other two sets, we might expect a power law size scaling for that set but not the other two. This needs to be investigated further before the updated fracture size parameterization is finalized for the updated DFN.

6. SUMMARY

While the outcrop trace data for fractures having a radius between 20 – 50 m match both lognormal and power law distributions, the FMI log data which appear to sample fractures having a median radius of 1.4 m are consistent only with the power law distribution found. Although the FMI log data could also be fit with a lognormal distribution, the mean value needed would be much smaller than that found for the lognormal distribution matching the outcrop data.

Knowing the fracture size distribution for those fractures sampled by the FMI log allows fracture intensity truncation factors to be calculated for DFN models having different minimum fracture sizes. The Pareto distribution used to describe the power law relationship has two parameters: the shape which is found from the outcrop trace length data (power law exponent), and the scale which is found from the minimum fracture radius sampled by the data. While the minimum fracture size identified in the FMI log is hard to determine, it can be estimated from the forward modeling results. A Pareto fracture size distribution having a power law exponent of 3.2 and a minimum fracture radius of 0.63 m is consistent with both the log data which samples small fracture sizes and the outcrop data sampling large fracture sizes. The fracture intensity, as measured in the FMI log as the number of fractures per unit length (P_{10}) and then converted to the total fracture area per unit volume (P_{32}) by accounting for the geometry between the borehole and fracture orientation, then requires a truncation factor of 0.57 for DFN models using a minimum radius of 1 m, or 0.035 for those using a minimum radius of 10 m.

REFERENCES

1. Bartley, J.M. 2018. Characterization of fractures in the Mineral Mountains. Appendix A2 in Technical Report, Report to Department of Energy, Geothermal Technologies Office, April 2018.
2. Coleman, D.S. 1991. Geology of the Mineral Mountains batholith, Utah. Unpublished Ph.D. dissertation, University of Kansas, Lawrence, Kansas, 219 p.
3. Finnila, A., Forbes, B. and Podgorney, R. 2019. Building and Utilizing a Discrete Fracture Network Model of the FORGE Utah Site. In *Proceedings of the 44th Workshop on Geothermal Reservoir Engineering, Stanford University, Stanford, CA, USA February 11-13*.
4. Golder Associates. 2020. FracMan® Reservoir Edition, version 7.9 Discrete Fracture Network Simulator.
5. La Pointe, P.R., P.C. Wallmann, and W.S. Dershowitz. 1993. Stochastic estimation of fracture size through simulated sampling. *Int. J. Rock Mech. Sci. & Geomech. Abstr*. Vol.30, No.7: 1611-1617.
6. La Pointe, P.R. 2002. Derivation of parent fracture population statistics from trace length measurements of fractal fracture populations. *Int. J. Rock Mech. Min. Sci.* Vol. 39: 381-388.
7. NGDS. 2018. Well 58-32 PDF Logs. https://gdr.openei.org/files/1006/58-32_logs.zip. File: "University_of_Utah_MU-ESW1_FMI-HD_60in_2226-7550ft_Run1.pdf".
8. C4 Zhang, L., Einstein, H. H., and Dershowitz, W. S. 2002. *Géotechnique* 52, No. 6: 419-433.

PROCEEDINGS, 46th Workshop on Geothermal Reservoir Engineering
Stanford University, Stanford, California, February 16-18, 2021
SGP-TR-218

Numerical Simulation of Injection Tests at Utah FORGE Site

Pengju Xing[1], Branko Damjanac[2], Zorica Radakovic-Guzina[2], Aleta Finnila[3], Robert Podgorney[4], Joseph Moore[1], John McLennan[5]

1 Energy & Geoscience Institute, University of Utah, Salt Lake City, UT, USA

2 Itasca Consulting Group, Inc., Minneapolis, MN, USA

3 Golder Associates, Redmond, WA, USA

4 Idaho National Laboratory, Idaho Falls, ID, USA

5 Department of Chemical Engineering, University of Utah, Salt Lake City, UT, USA

Keywords: Numerical simulation, Pressure history matching, Hydraulic fracture, DFN, FORGE

ABSTRACT

In 2017 and 2019, injection testing was carried out in three zones in Well 58-32, drilled into granitic rock at the Frontier Observatory for Research in Geothermal Energy (FORGE) site near Milford Utah. Some of the injection tests were simulated numerically with a distinct element method (DEM) based code - XSite™, which is a fully coupled hydro-mechanical model with explicit representations of discrete fracture network (DFN). The 3D DFN contains more than 1000 natural fractures. The objective of these back analyses is to calibrate the model with respect to unknown and uncertain in situ reservoir parameters and to match the recorded pressure histories. Of particular interest are the increasing trends in the injection pressure histories and their relative magnitudes in Cycles 4 and 5, conducted in a perforated section of the cased well. The pressures measured during Cycle 5 exceeded those recorded during an identical injection stage (Cycle 4) pumped earlier in the same perforation cluster. The numerical analyses show that the interaction of the hydraulic fracture and 3D DFN, and response of DFN to fluid flow and dissipation are vital to understanding the injection pressure performance. The location, size, and properties of natural fractures significantly affect the injection pressure. The numerical study shows that the increasing pressure trends are due to fluid diversion into the DFN as localized leakoff and deformation (including slip and dilation) of the DFN. The higher pressure in Cycle 5 is mainly the result of irreversible deformation by fluid injection in the previous test (Cycle 4). The numerical investigation enhances our understanding of the FORGE reservoir. It sheds light on what might be called self-shadowing, where one injection cycle impacts the injection performance of a subsequent stage pumped at the same location.

1. INTRODUCTION

In 2017, Well 58-32 was drilled vertically to a depth of 7536 ft at the Utah Frontier Observatory for Research in Geothermal Energy (FORGE) to characterize subsurface temperatures, lithologies and permeabilities. In 2017, a series of injection tests were conducted in the uncased barefoot section of the well from 7375 to 7525 ft measured depth (MD), denoted as Zone 1. In 2019, a second series of tests were conducted in Zone 1 and in the cased and perforated portions of the well at depths of 6964 – 6974 ft MD, and 6565 – 6575 ft MD, respectively (Zone 2 and Zone 3). Up to nine test cycles were conducted in each zone. Descriptions of the injection activities and in-situ stresses and permeability interpretations from these pump-in/shut-in or pump-in/flowback tests are well documented in Xing et al (2020a) and Xing et al (2020b). Two tests, Cycle 4 and 5 were conducted in the lower cased section of the well (Zone 2), where the formation contains abundant pre-existing joints critically oriented for slip. These two injection cycles were selected for back analysis and history pressure matching. Injection pressure histories during both cycles show a monotonously increasing trend, and the pressures in the second test (Cycle 5) are consistently greater than those during the first test (Cycle 4). The purpose of the back analysis was to understand the mechanisms resulting in the trends observed from the field data, validate the numerical model by qualitatively reproducing the data trends, and calibrate the model with respect to unknown and uncertain input parameters by improving the quantitative match between numerical results and the field data.

The back analysis was conducted using *XSite* (Itasca Consulting Group, 2020), a numerical software for simulation of hydraulic fracturing in naturally fractured reservoirs. The code, which implements the synthetic rock mass (SRM) method in lattice (Damjanac et al., 2020), can simulate propagation and interaction of multiple hydraulic fractures and pre-existing joints. Hydraulic fractures propagate as a combination of predominantly tensile fracturing through intact rock at the fracture tip and opening and slip of pre-existing joints.

In this paper, the data from Cycles 4 and 5 from Zone 2 in Well 58-32 are presented first. The model input parameters are reviewed, including granitic reservoir's hydro-mechanical properties, the discrete fracture network (DFN), fluid properties, and in-situ conditions. The model results are presented and discussed, including the relevant insights learned from the back analysis.

2. INJECTION TESTS

2.1 Description

Well 58-32 was drilled to 2297 m (7536 ft) and plugged back to 2294 m (7525 ft) MD RKB (rotary kelly bushing), penetrating more than 1372 m (4500 ft) of granite. As shown in Figure 1, the well encountered low permeability crystalline rocks at a depth of 968 m (3176 ft) MD RKB and a bottom-hole temperature of 199°C (390°F).

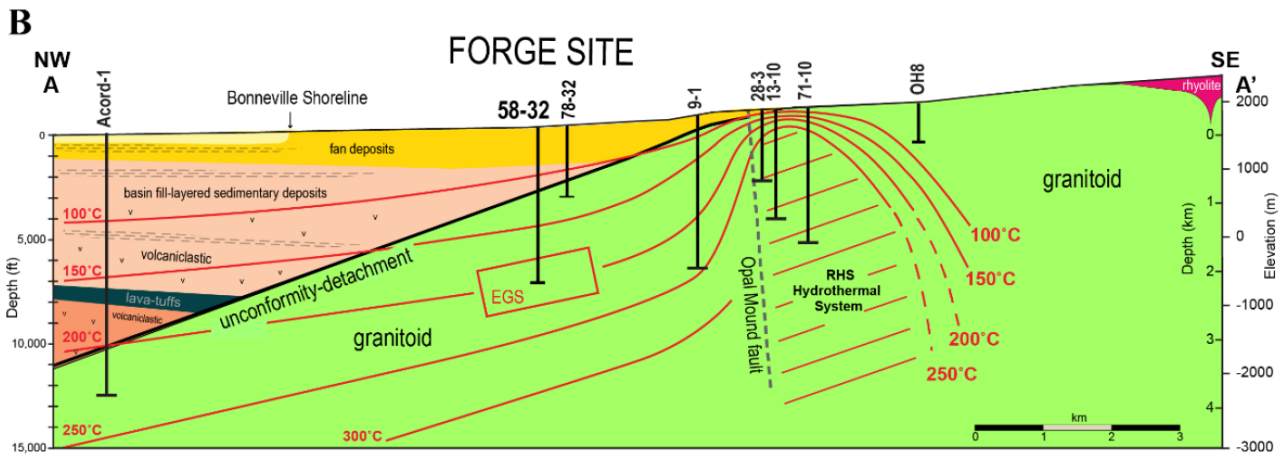

Figure 1. Northwest-southeast section through the FORGE site (adapted from Kirby et al, 2018).

In each zone, a program of up to nine injection cycles was conducted. Zone 2 was perforated over a 3.05 m (10 ft) interval from 2123 to 2126 m (6964 to 6974 ft) MD. The guns were loaded with 30-gram charges at six shots per foot and 60° phasing. Gradients were calculated using 2122 m (6961 ft) TVD (true vertical depth) RKB. This zone was picked for an injection test because it contained abundant pre-existing fractures (determined from the FMI, formation micro-imager that had been run before casing in 2017) that were estimated to be almost critically stressed and prone to shear and dilation.

During Cycle 4 for Zone 2, water was pumped for approximately six minutes at 1.32×10^{-2} m^3/s (5 bpm). The pumped volume was 5.1 m^3 (32 bbl). Subsequently, the well was shut-in for 20 hours. There was no flowback during shut-in after Cycle 4. During Cycle 5 for Zone 2, water was pumped again for six minutes at 1.32×10^{-2} m^3/s (5 bpm). The total volume of water pumped was 5.1 m^3 (32 bbl). The well was shut-in for 10 minutes after Cycle 5 pumping, during which time there was a pressure drop to 17.8 MPa (2,580 psi). Subsequently, flowback was allowed through a 1/64-inch choke after approximately 20 minutes. Next, the choke was beaned up by 1/64 inch every 5 minutes until it was fully open. The pressure drop after one hour was too small to measure, similar for flow. The total recovered water was 2.8 m^3 (17.6 bbl). After the well was shut in again, the pressure built to 0.89 MPa (130 psi). The comparison of injection parameters for Cycle 4 and 5 are summarized in Table 1.

Table 1 Injection parameters for Cycle 4 and 5, Zone 2

Parameter	Cycle 4	Cycle 5
Pumping rate	5 bpm	5 bpm
Pumping time	6 min	6 min
Pumping volume	32 bbl	32 bbl
Surface pressure at the end of injection	3700 psi	3925 psi
Shut-in time	20 hr	10 min
Flowback operation	No	Yes

The injection rate and pressure histories for Cycle 4 during pumping and the early portion of the shut-in are shown in Figure 2. Notice that, since the packer failed, a dead string (annulus between tubing and casing) was recording a slightly lower pressure than the tubing because there is no friction in that static fluid space. The pressure history exhibits an early peak corresponding to breakdown (i.e., fracture initiation from the perforations and coalescing into a vertical hydraulic fracture perpendicular to the minimum horizontal principal stress). After the pressure drop following the breakdown, the pumping pressure increases steadily.

Lack of the early peak in the pumping pressure history during Cycle 5 (shown in Figure 3) from the same perforation cluster was expected because the hydraulic fracture had already been created in Cycle 4. The pumping pressure during Cycle 5 monotonically increases for the entire duration of the pumping, as occurred during Cycle 4. Another interesting observation when the pumping pressures from Cycles 4 and 5 are compared (Figure 4) is that the pressure during Cycle 5 is greater than during Cycle 4.

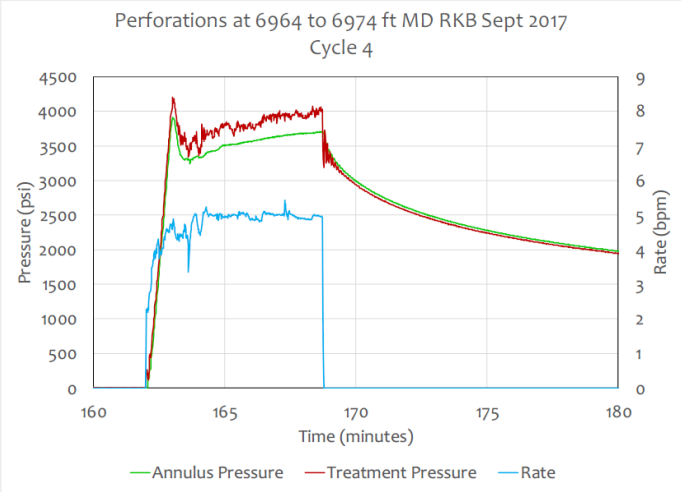

Figure 2 Injection rate and pressure histories for Zone 2, Cycle 4 showing pumping and the early portion of shut-in.

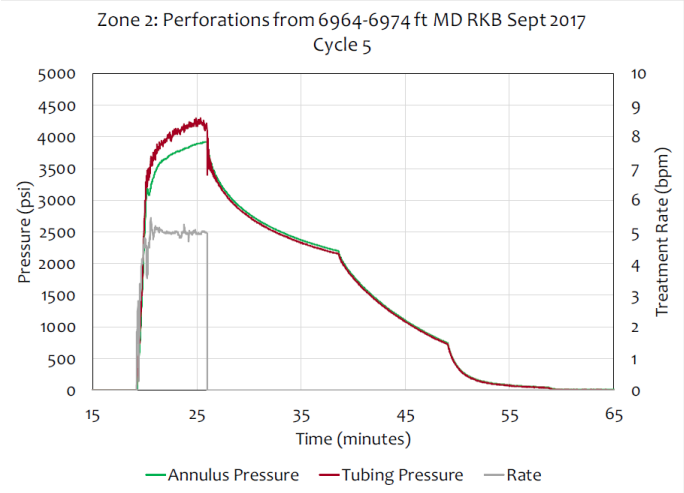

Figure 3 Injection rate and pressure histories for Zone 2, Cycle 5 showing pumping and complete shut-in and flowback.

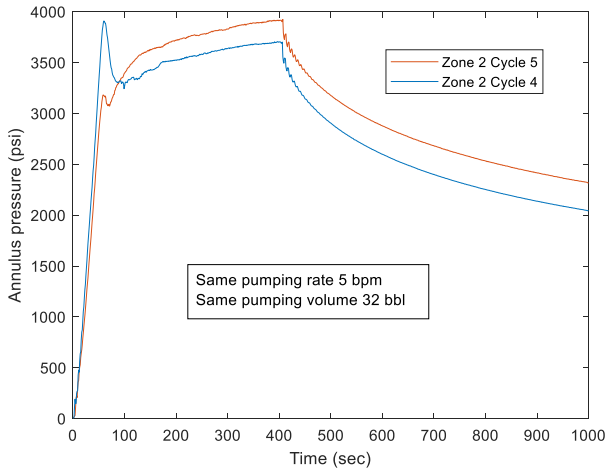

Figure 4 Comparison of pressure histories between Cycles 4 and 5 in Zone 2 during pumping and the early portion of shut-in.

2.2 Discussion

There are a couple of interesting observations from the data recorded during these two injection tests. In both tests (after breakdown in Cycle 4), the injection pressure steadily increases for the duration of the pumping. Injection into a perforation cluster in a homogeneous

continuous medium is expected to propagate a penny-shaped hydraulic fracture perpendicular to the minimum principal stress. The injection pressure in that case is also expected to decrease steadily. The increasing pumping pressure would be expected if:

- the fracture height is limited (e.g., the fracture is contained, usually by a stress barrier, within a layer of relatively small thickness);
- there is sufficient leakoff into the surrounding formation, resulting in a poro-elastic effect (due to increase in total stress); or
- the hydraulic fracture interacts with pre-existing joints, which are arresting its tip and/or diverting fluid into the fracture network (as localized leakoff).

Based on the overall geology as well as the stiffness, and permeability of the granite, determined from the tests conducted on core samples and logging, it seems that interaction of the hydraulic fracture with the DFN is the most plausible explanation for increasing pumping pressures.

Greater pumping pressures during Cycle 5 compared to Cycle 4 are a consequence of irreversible or slowly (compared to 20 hours of shut-in) evolving changes induced by fluid injection into fractures in the surrounding formation. The permeability changes resulted from pumping during Cycle 4 are associated with fracture creation and opening and slip of pre-existing fractures. With dissipation of fluid pressure, fractures that were created and opened will close. This process is certainly partially reversible. However, it might not be completely reversible because of the fracture surfaces' roughness and potential shear deformation preventing complete closure of mismatched fracture surfaces. Slip on rough fractures will result in a mostly irreversible increase in aperture (dilatancy) and permeability. However, if the increase in permeability affects subsequent pumping in the same cluster, that effect would be reduction in the injection pressure, which is opposite to the pumping data (showing increased pressures in the subsequent injection).

The other long-term transient or irreversible change caused by fluid injection is the increase in the mean stress around the injection point due to a poro-elastic effect by which the increase in pore pressure in the matrix and/or pre-existing fractures results the total stress increase. If the induced fluid (pore) pressure does not dissipate before the subsequent injection, the confining stresses will be greater, resulting in greater pressures during subsequent injection(s). However, because of small hydraulic diffusivity and a small conventionally defined Biot's coefficient for intact granite, this effect cannot be significant in the matrix during the tests at Zone 2. Although the fluid pressure is expected to dissipate into the pre-existing joints during injection, a relatively long shut-in period should be sufficient to dissipate the pore pressures. A possible exception might be if fracture closure during dissipation results in a pinching effect, leaving relatively large fluid pressures trapped around the injection point. This mechanism is not likely because the pressure history data indicate an expected dissipation of fluid pressure. Thus, the most likely mechanism that can explain an increased injection pressure during the second test (Cycle 5) is an irreversible stress change caused by irreversible deformation, specifically slip on the pre-existing DFN. Slip on pre-existing fractures, particularly if associated with dilatancy, will increase volume and hence increase in total stresses under confined conditions, requiring greater pressure to reopen the fractures. The increase of the total stresses resulted from irreversible deformation outweighed the effect of the permeability increase, thus making injection pressure higher in the subsequent cycle (Cycle 5).

The numerical model used for the back-analysis and pressure matching was setup considering the possible mechanisms. The DFN was explicitly represented in the model, and the DFN's initial apertures and permeability in the model were calibrated in this exercise. Based on hydraulic and thermal diffusivities and the relatively short duration of the injections, it was assumed that matrix leakoff and thermal effects were second-order effects on the test results. Leakoff into the DFN was explicitly represented.

3. NUMERICAL MODEL

3.1 Input Parameters

The mechanical properties of the granite, as listed in Table 2, were determined from the laboratory experiments on core samples from the well. Those properties were assigned to the entire rock formation in the model. Fluid viscosity is assumed to be 1.13×10^{-3} Pa×s (1.13 cP).

Table 2 Rock Properties

Parameter	Value
Young's modulus	50 GPa (7.25×10^{6} psi)
Poisson's ratio	0.25
Fracture toughness	1.75 MPa×$m^{1/2}$ (1600 psi×$in^{1/2}$)
Permeability	10^{-17} m^2 (10^{-2} mD)
Porosity	0.01

Four different DFN realizations shown in Figure 5 were generated with varying numbers of fractures and sizes. As shown in the upper left of Figure 5, the simplest DFN has only one steeply dipping (65°) fracture with a dip direction of N125°E (i.e., the normal at a small angle relative to the orientation of the minimum principal stress, N115°E). Within Zone 2, that fracture was explicitly mapped and is

critically oriented for slip relative to the principal stresses. However, its dimensions are uncertain. In these simulations, it was assumed that the radius of the fracture is 50 m. That fracture is included in all four DFNs. Most of the simulations discussed in this study were conducted using the model with 1992 DFN fractures (lower right of Figure 5). Some simulations were carried out with a smaller scale model with only five fractures. The purpose of the small-scale model was to investigate in more detail interactions between hydraulic fracture and natural fractures, particularly considering uncertainties in DFN strength and dilatancy.

These DFNs were simplified from the FORGE Reference DFN (Finnila et al., 2019) to allow their explicit representation in the numerical models without affecting model accuracy (and the effect of the DFN on model results), size, or execution time (i.e., the run time). The two main simplifications were:

- the minimum fracture radius is 10 m; and
- the DFN includes three fracture sets with different orientations. However, all fractures within each set have the same strike (i.e., there is no variation in fracture orientation within a single set).

In most of the simulations, it was assumed that the pre-existing fractures are frictional, with a 37° friction angle. The initial fracture apertures are correlated with fracture sizes. Selecting the variability of the initial apertures ranging between 4 and 10 μm (as shown in Figure 6) appears to yield the best pressure history matching.

The pore pressure and initial stress conditions are listed in Table 3. In the model, it was assumed that the stress and pressure variations due to in-situ gradients are not significant over the height of the domain affected by fluid injection. Therefore, the uniform stresses and pore pressures were initialized in the model.

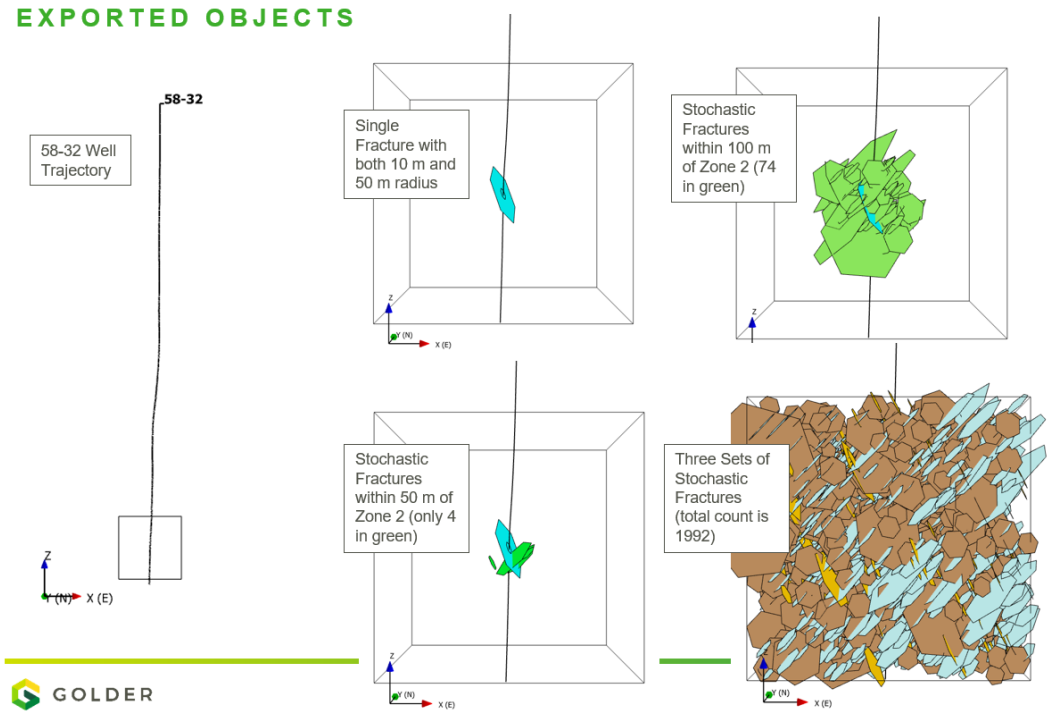

Figure 5. DFNs included in the models.

Table 3 Initial Conditions

Variable	Gradients	Magnitudes in Zone 2
Pore pressure	0.0097 MPa/m (0.43 psi/ft)	20.8 MPa (3014 psi)
Minimum horizontal stress	0.017 MPa/m (0.77 psi/ft)	37.0 MPa (5360 psi)
Maximum horizontal stress	0.0199 MPa/m (0.88 psi/ft)	42.2 MPa (6126 psi)
Vertical stress	0.0256 MPa/m (1.13 ft/ft)	54.2 MPa (7866 psi)

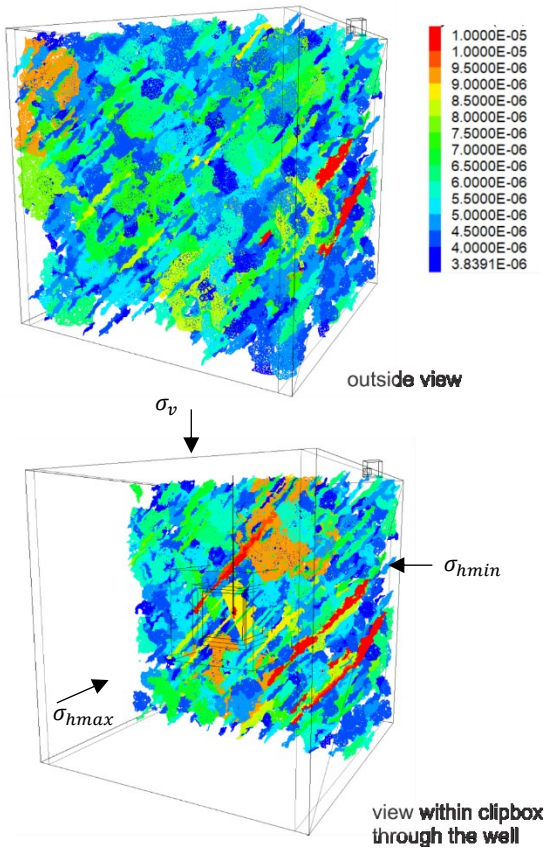

Figure 6. Initial DFN apertures (m).

3.2 Description

The large-scale model with 1992 DFN fractures has a cubic shape with an edge length of 300 m. This boundary dimension was selected so that fluid pressure and stress perturbations due to injection are relatively small at the model boundaries. These are truncation boundaries facilitating the use of a finite-size model to represent processes taking place in an infinite half-space. The outside boundaries have "rollers" in the mechanical model and are impermeable in the fluid flow model. The model is set up to simulate fracture propagation but not fracture initiation, because an attempt to capture very different time and length scales, fracture initiation and propagation, in the same model would make it excessively large and slow to execute. Therefore, the borehole and the perforations are not explicitly modeled. In the model, the hydraulic fracture starts propagation from a small start-up penny-shaped fracture perpendicular to the minimum principal stress (i.e., it is assumed that the hydraulic fracture was already initiated).

The simulation was carried out in steps. Mechanical equilibrium was achieved first for the initial stress and pore pressure conditions. Some readjustment of stresses took place as a result of the explicitly represented DFN. Subsequently, the injection tests were simulated as fully coupled hydro-mechanical processes, including Cycle 4, shut-in for 20 hours, and Cycle 5.

3.3 Parametric Study with A Small-scale Model

Before investigating the large-scale model with 1992 natural fractures, it was desirable to conduct a sensitivity study in a small-scale model. The interaction between the hydraulic fracture (HF) and the DFN was investigated in more detail using a 100 m-edge cube model (with only five fractures as shown in Figure 7) with finer resolution. This sensitivity study investigated the modes of interaction (i.e., crossing and arrest) as a function of fracture parameters, including friction angle, tensile strength, cohesion, and dilation angle.

Figure 7 through 9 depicts the effect of natural fracture (DFN) tensile strength and cohesion, friction angle, and dilatancy on HF and DFN interactions. As shown in Figure 7, when the DFN fracture is strong with high tensile strength and cohesion, the HF crosses the closest fracture from the critically oriented DFN set. On the other hand, when the DFN fracture is weak with a relatively small tensile strength and cohesion, the HF is arrested by the DFN. This suggests that the DFN tensile strength needs to be very high to promote crossing. Visual inspection of the core indicates that the natural fractures likely do not have excessive tensile strength or cohesion. In the large-scale model, the DFN tensile strength and cohesion are both defined assumed to be zero, and therefore the initiating hydraulic fracture is prone to be arrested by DFN.

The friction angle from experiment on core samples ranges between 30° and 50°. The results of bounding values of the friction angle are shown in Figure 8. In both cases, the HF is arrested by the DFN. However, in the high friction angle case, fluid pressure in the DFN is higher and the HF is shorter. The reason for this behavior is that with higher friction angles, higher pressure is required to make the DFN fail in shear. At the same time higher pressure promotes the DFN fracture opening, resulting in more fluid leaking into the DFN and forming a shorter HF.

(a)

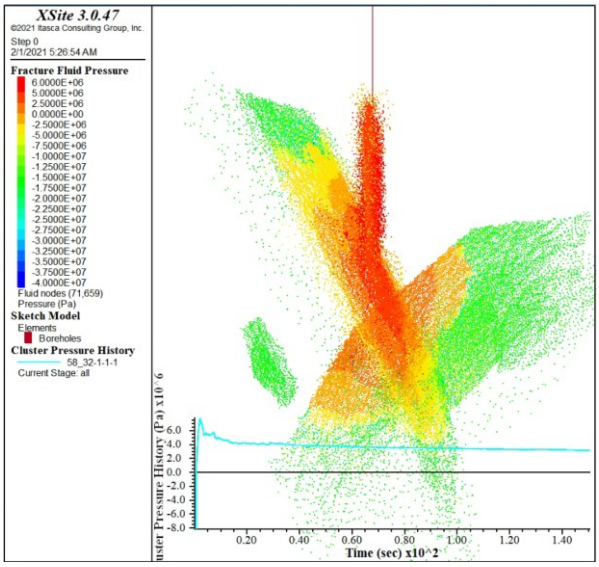

(b)

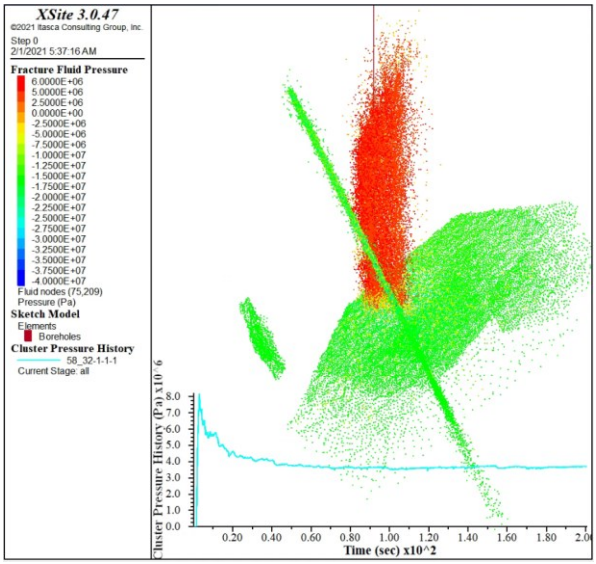

Figure 7. Effect of DFN tensile strength and cohesion on interactions of HF and DFN. (a) The HF is arrested by the DFN with a 37° friction angle, 0 MPa tensile strength, and 0 MPa cohesion. (b) The HF crosses the natural fracture with a 37° friction angle, 20 MPa tensile strength, and 20 MPa cohesion.

Figure 9 shows the effect of dilatancy on HF and DFN interactions. In Xsite, aperture increase due to dilation is given by

$$\Delta d_n = \Delta d_s \tan \phi_{dil} \tag{1}$$

where Δd_n is fracture aperture increase due to dilatancy, Δd_s is slip distance, and ϕ_{dil} is dilation angle. For the case with 2° dilation angle, the DFN fails in shear under compressive effective stress. The DFN fracture aperture increase due to the dilatancy forms a high permeability channel that increases fluid leakoff into the DFN. Also, the HF is arrested after intersecting the first DFN fracture because fluid is diverted and flow into the relatively permeable DFN fractures.

The study shows that arrest is expected for a reasonable range of strengths of DFN, e.g. relatively low tensile strength and cohesion, and a friction angle below 50°. It also appears that DFN dilatancy has a profound effect on the interactions. Even a small dilatancy causes arrest of the HF and diversion of fluid into and within the DFN.

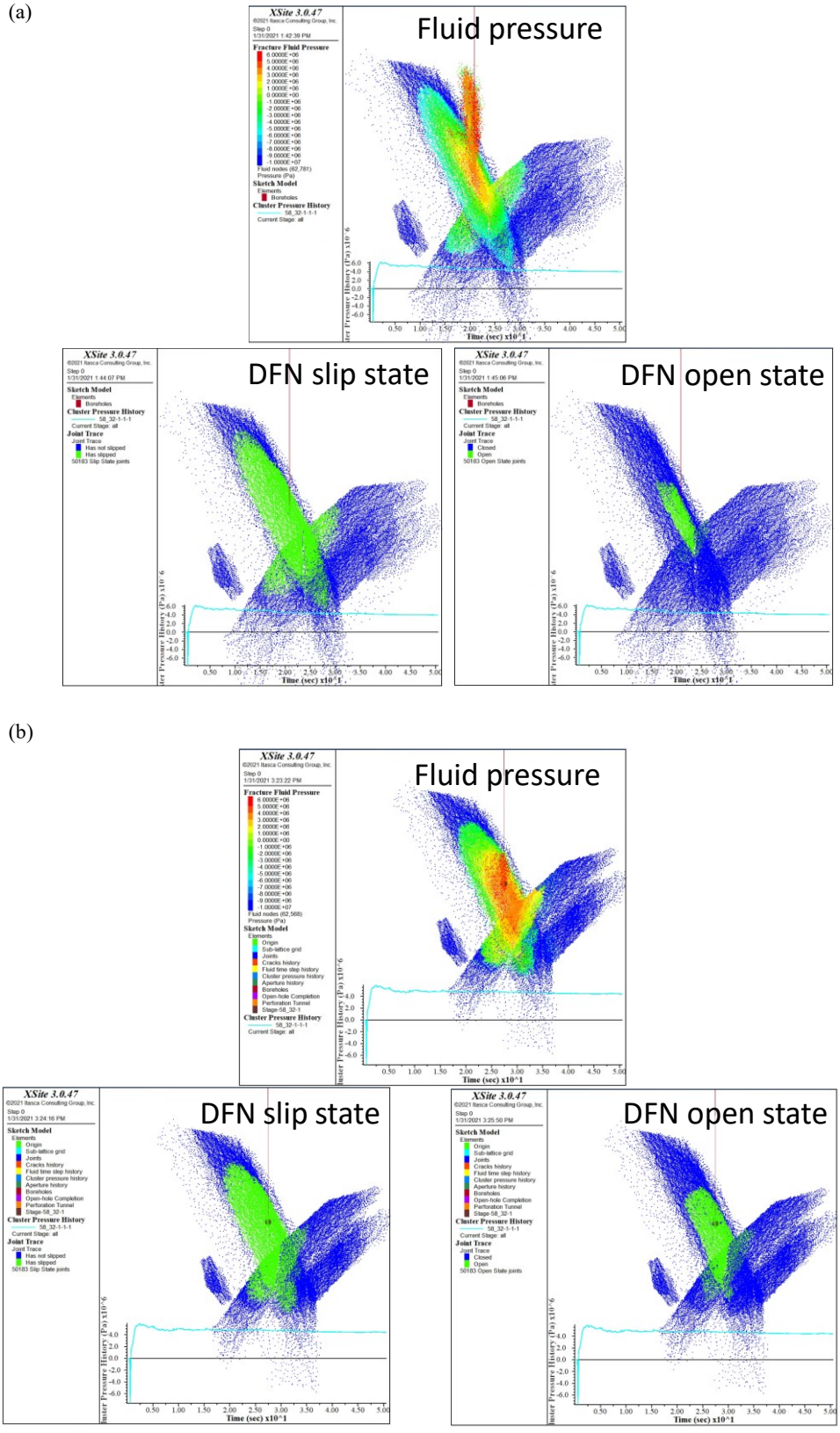

Figure 8. Effect of DFN friction angle on interactions of HF and DFN. (a) The HF is arrested by the DFN with a 30º friction angle, 0 MPa tensile strength, and 0 MPa cohesion; (b) The HF is arrested by the DFN with a 50º friction angle, 0 MPa tensile strength, and 0 MPa cohesion. A relative longer HF is created with smaller friction angle (30º) than the case with larger friction angle (50º).

(a)

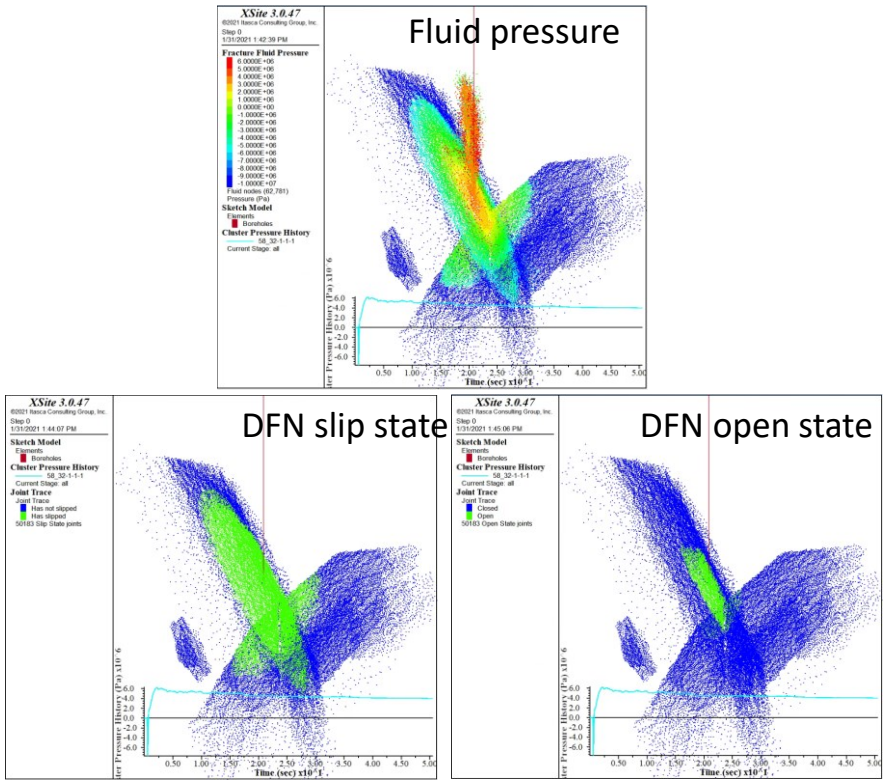

(b)

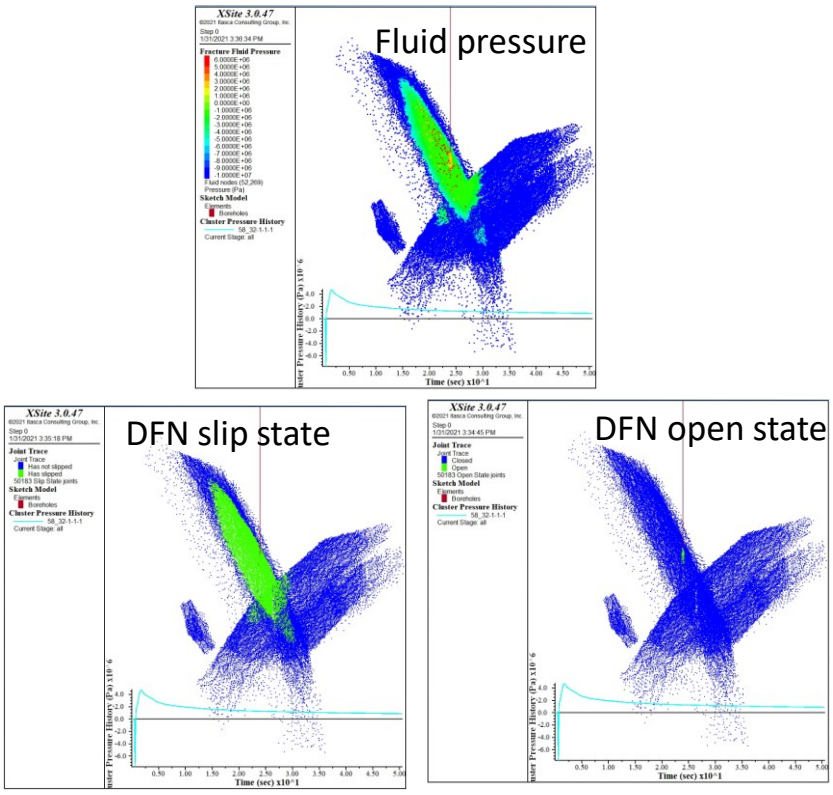

Figure 9. Effect of DFN dilation angle on interaction of HF and DFN. (a) The HF is arrested by the DFN with a 30º friction angle, 0 MPa tensile strength, 0 MPa cohesion, and no dilation; (b) The HF is arrested by the DFN with a 30º friction angle, 0 MPa tensile strength, 0 MPa cohesion, and 2º dilation angle.

3.4 Results of Large-scale Model

Figure 10 shows the injection pressures from two models, one assuming non-dilatant pre-existing DFN fractures and the other with dilatant fractures characterized by a 2° dilation angle, compared with the pressure history recorded during Cycle 4. The initial pressure peak (i.e., the breakdown pressure), probably resulting from fracture initiation, is not captured in the model results because the model did not have sufficient resolution and used a small startup joint through the perforation cluster to represent the already initiated HF. Both models qualitatively match the general increasing trend in the injection pressure history. However, the case with assumed non-dilatant joints seems to be a better match of the magnitude of the injection pressure increase during Cycle 4. The pressure increase in the model with dilatant joints is smaller because joint dilatancy results in greater fracture aperture and permeability. However, the model with dilatant fractures better matched pressures after shut-in as shown in Figure 11. Therefore, this model was used for simulation of both Cycles 4 and 5.

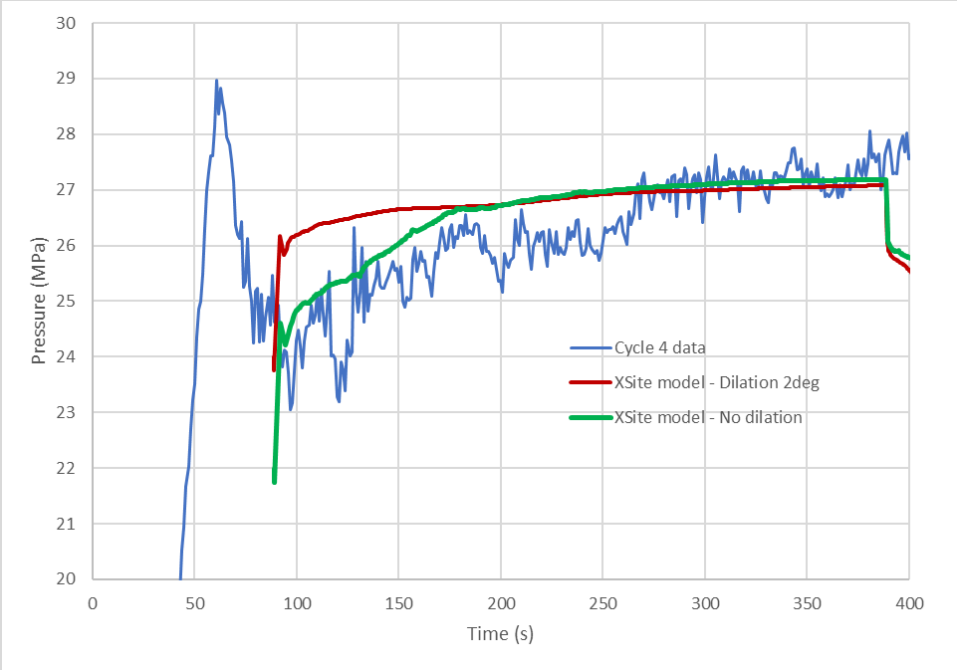

Figure 10. Cycle 4: Pressure history matching during injection.

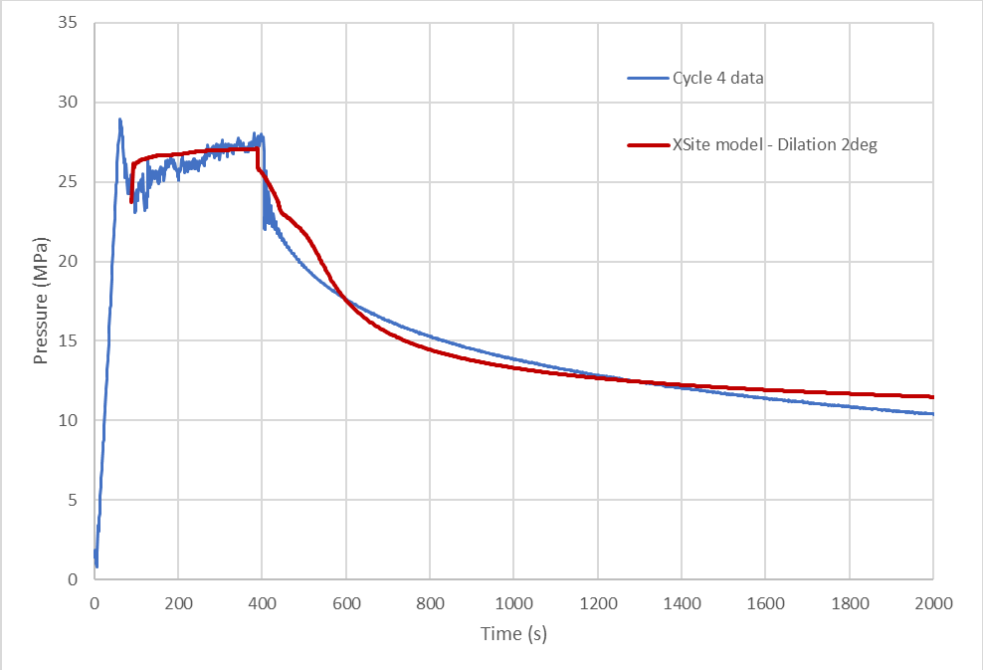

Figure 11. Cycle 4: Pressure history matching during injection and initial shut-in.

For the model with dilatant fractures (2° dilation angle), the contours of net pressure (the pressure in excess of the minimum principal stress) and the fracture apertures at the end of injection of Cycle 4, the end of the shut-in period (e.g., before Cycle 5), and the end of injection of Cycle 5 are shown in Figures 12 and 13, respectively. The results indicate that the formation response to the injection is dominated by the fluid flow and pressure dissipation in the DFN and, in particular, the pre-existing fracture from the critically oriented set close to the perforation cluster (refer to Figure 12). As shown in Figure 12, the HF is arrested by the pre-existing fracture and does not propagate a large distance from the perforation cluster, which is consistent with results from the small-scale model. The plot of aperture contours in Figure 13 illustrates the localization of deformation along the closest DFN fracture from the critically oriented set. The indicators of slip shown in Figure 14 (shown only at the end of injection of Cycle 4 because the slipping extent does not change during shut-in or Cycle 5) confirm that slip and fracture dilation (along the closest fracture from the critically oriented set) are the leading causes for localization of deformation and increase in aperture.

The recorded data and simulated (for the case with a 2° dilation angle for the DFN) pressures from Cycles 4 and 5, are compared in Figure 15. The model results match the important data trends. The injection pressure generally increases with time in both cycles. Also, the injection pressures during Cycle 5 are continuously greater than during Cycle 4. The explanation for increased injection pressure in Cycle 5 in the numerical model is illustrated in Figure 16, which, for states before Cycles 4 and 5, shows block contours (5-m edge length cells) of the change in the minimum principal stress relative to the initial far-field state. Before Cycle 4 (the top plot in Figure 16), there is no stress change except for relatively localized perturbations around the pre-existing fractures. The contours before Cycle 5 (the bottom plot in Figure 16) show an irreversible increase in the confining stress in the volume of the rock mass around the injection cluster even after dissipation of injection-reduced fluid pressures. The increase is caused by irreversible (slip related) deformation of the DFN resulting from an increase in the fluid pressure during injection.

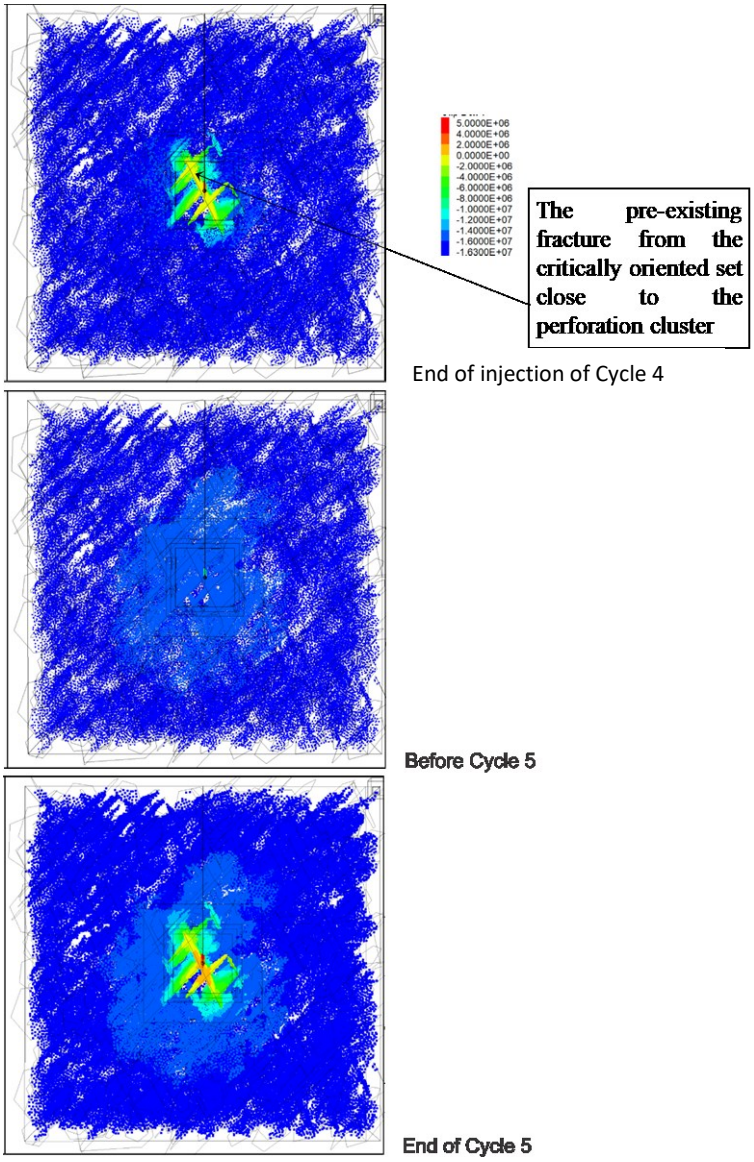

Figure 12. Fluid pressure contours (Pa) at characteristic times during injection tests in Zone 2.

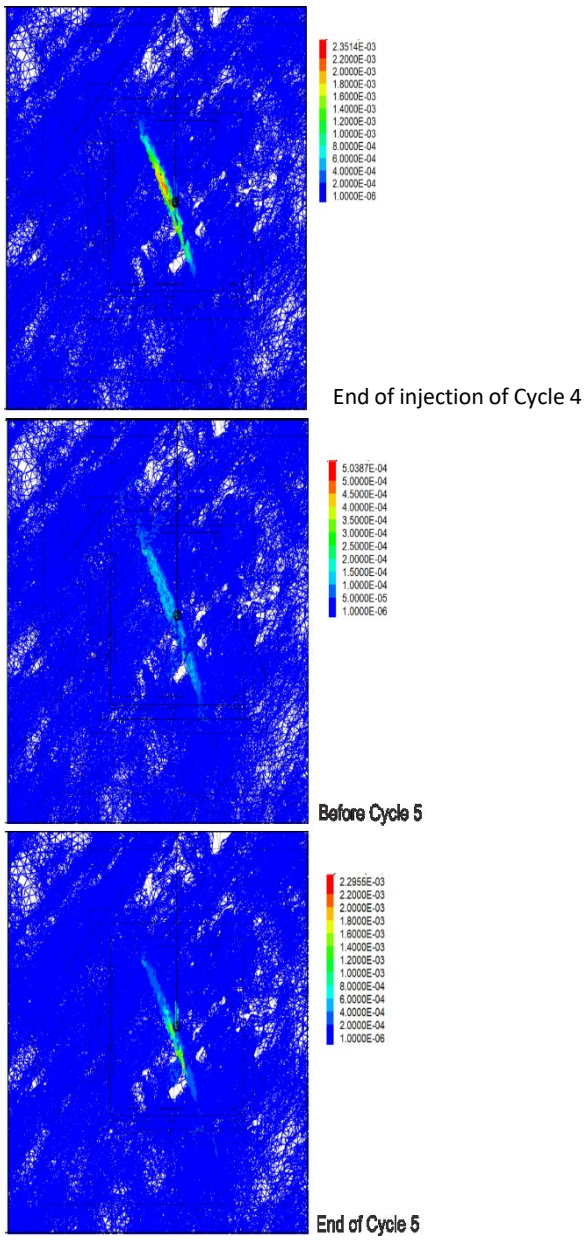

Figure 13. Fracture aperture contours (m) at characteristic times during injection tests in Zone 2.

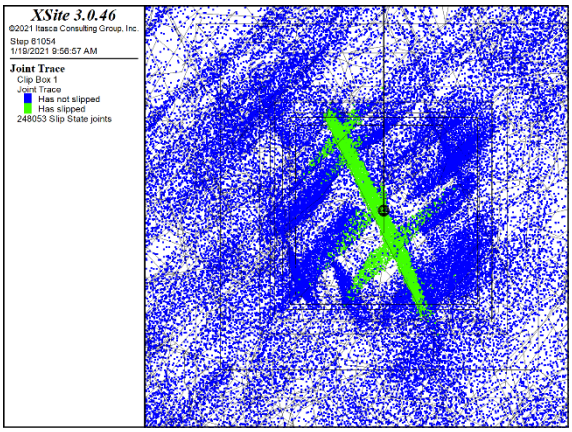

Figure 14. Indication of fracture slippage at the end of injection of Cycle 4.

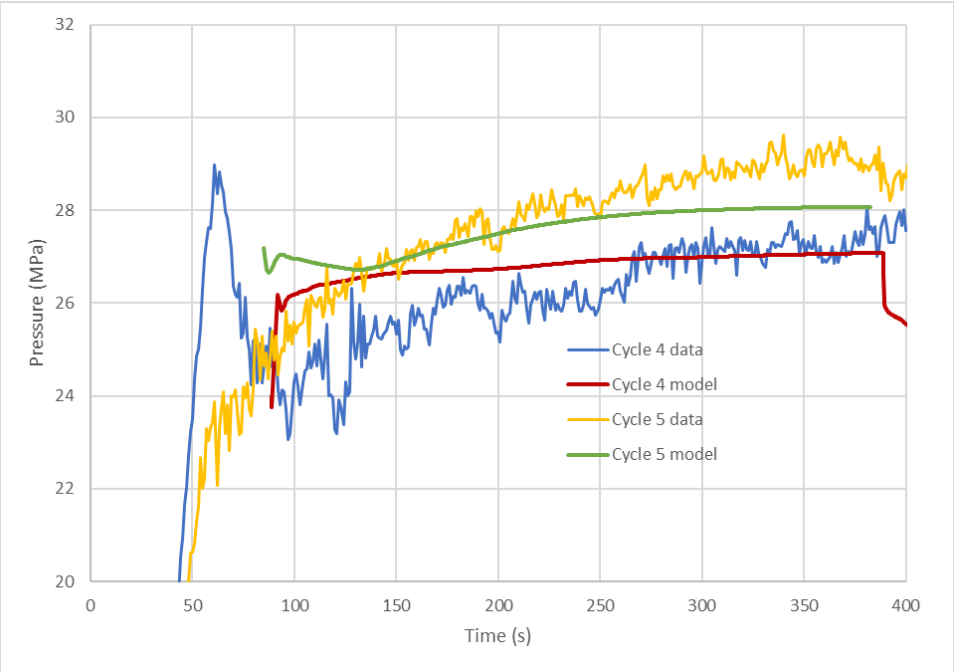

Figure 15. Cycles 4 and 5: Pressure (surface pressure) history matching during injection.

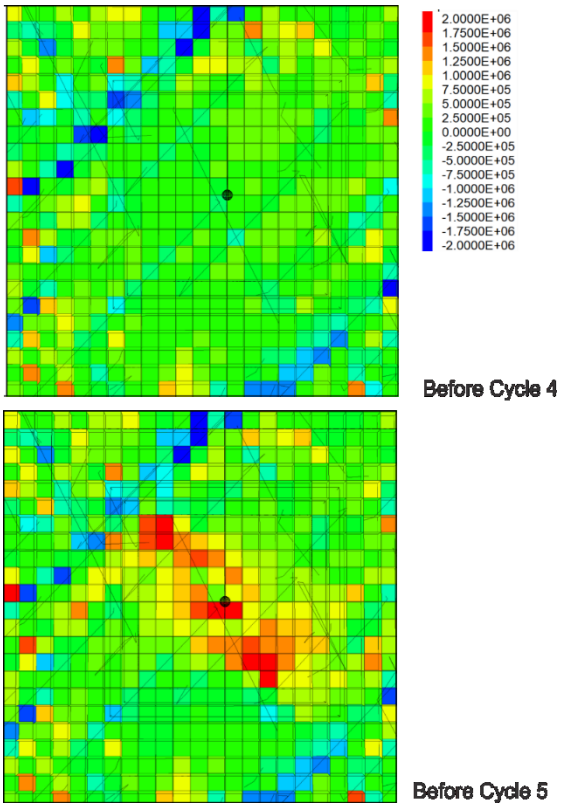

Figure 16. Contours of the change in the minimum horizontal stress (MPa) relative to the initial far-field state in the cross-section through the well, perpendicular to the maximum horizontal principal stress (refer to Figure 6).

4. CONCLUSIONS

Injection tests were conducted in perforated intervals in Well 58-32 at the FORGE site to evaluate the possibility of stimulating fractures behind casing. Clear evidence of fracture opening was observed in the lower perforated zone (Zone 2, 6964 – 6974 ft MD) during the fourth of nine injection cycles. In this study, pressures from Cycles 4 and 5 were history matched to characterize the fracture behavior.

Cycle5 was initiated after 20 hours of leakoff and shut-in. The back-analysis of Cycles 4 and 5 in Zone 2 in Well 58-32 and pressure matching indicate that the response of the formation to fluid injection is dominated by fluid flow and deformation (opening and slip) of the pre-existing fractures. The hydraulic fracture is arrested after intersecting the closest pre-existing fracture from the critically oriented set with an average dip direction of 125° and dip angle of 65°. The critical factors causing the arrest, besides the shear strength of the pre-existing fractures, are in-situ aperture and dilatant behavior, which results in a further increase in aperture (and permeability) with slip. The interaction of the relatively short hydraulic fracture with the DFN and localization of flow and deformation in the DFN cause an increase in the injection pressure.

Slippage on the fractures from the critically oriented set results in irreversible deformation and increased minimum principal stress after dissipation of the fluid pressure following 20 hours of leakoff during shut-in. This effect is more pronounced if fractures are dilatant. However, there is an increase in the normal stress in the direction of the initial minimum principal stress even when fracture slip is not associated with dilatancy. Thus, the subsequent injection test (Cycle 5) experienced greater “confining stress”, resulting in increased injection pressures.

REFERENCES

Damjanac, B., C. Detournay, and P. Cundall. (2020) "Numerical Simulation of Hydraulically Driven Fractures," in S. Baotang, O. Stephansson, & M. Rinne (Eds.), *Modelling Rock Fracturing Processes* (2nd ed., pp. 531–561). Springer, Cham. https://doi.org/https://doi.org/10.1007/978-3-030-35525-8

Finnila, A., Forbes, B., & Podgorney, R. (2019). Building and Utilizing a Discrete Fracture Network Model of the FORGE Utah Site. In *Proceedings of the 44th Workshop on Geothermal Reservoir Engineering, Stanford University, Stanford, CA, USA* (pp. 11-13).

Itasca Consulting Group, Inc. (2020) *XSite* (Version 3.0.47). Minneapolis: Itasca Consulting Group, Inc.

Kirby, S. M., Knudsen, T. R., Kleber, E., & Hiscock, A. (2018). Geologic setting of the Utah FORGE site, based on new and revised geologic mapping. *Trans. Geotherm. Resour. Counc*, *42*, 1097-1114.

Xing, P., Goncharov, A., Winkler, D., Rickard, B., Barker, B., Finnila, A., Ghassemi, A., Podgorney, R., Moore, J., and Mclennan, J. (2020a). Flowback Data Evaluation at FORGE. In *54th US Rock Mechanics/Geomechanics Symposium*. American Rock Mechanics Association.

Xing, P., McLennan, J., and Moore, J. (2020b). In-Situ Stress Measurements at the Utah Frontier Observatory for Research in Geothermal Energy (FORGE) Site. *Energies*, *13*(21), 5842.

Revisions to the Discrete Fracture Network Model at Utah FORGE Site

Aleta Finnila[1], Thomas Doe[1], Robert Podgorney[2], Branko Damjanac[3], Pengju Xing[4]

[1] Golder Associates, Redmond, WA, USA

[2] Idaho National Laboratory, Idaho Falls, ID, USA

[3] Itasca Consulting Group, Inc., Minneapolis, MN, USA

[4] Energy & Geoscience Institute, University of Utah, Salt Lake City, UT, USA

Keywords

DFN, FORGE, Milford, Utah, discrete, fracture

ABSTRACT

The Discrete Fracture Network (DFN) model for the Frontier Observatory for Research in Geothermal Energy (FORGE) site near Milford, Utah, is used to characterize the natural fractures present in the reservoir. Subsets of the model are used as initial conditions for researchers simulating processes such as well hydraulic stimulation, local stress evolution, flow pathway analysis, and thermal breakthrough in proposed injection and production well configurations. Image logs from the vertical pilot well, 58-32, along with outcrop data from the nearby Mineral Mountains provided the data used to construct the original DFN model in 2019. Two new wells have been drilled in the past year: a highly deviated injection well, 16A(78)-32, and another deep vertical well, 56-32. Data collected from these wells have been analyzed to further constrain fracture orientations and intensity. Estimates for fracture sizes have been adjusted based on forward modeling work performed on fracture penetration statistics collected from image log data. Mechanical and hydraulic fracture apertures have been estimated for both pre- and post-stimulation states based on pressure history matching of injection well tests and measured values from electrical resistivity logs.

The updated DFN model is presented, and three realizations of the model are uploaded to the U.S. Department of Energy Geothermal Data Repository (GDR) for public access. Each realization includes planar fractures representing both the known location and orientation of fractures identified from the well logs as well as stochastic fracture sets that do not intersect the wells. Individual fracture properties include center coordinates, orientation, fracture size represented both as a radius and as a six-sided polygon, mechanical aperture, hydraulic aperture, permeability, and

compressibility. Fracture properties are calibrated so that the upscaled DFN is consistent with measured bulk rock porosity and permeability.

1. Introduction

FORGE is a multi-year initiative funded by the US Department of Energy (DOE) for testing targeted EGS research and development. The site is located inside the southeast margin of the Great Basin near the town of Milford, Utah, and is described in detail in the Phase 2B Report (EGI, 2018). Current modeling work includes the development of baseline models using Earth, continuum and discrete modeling methods. One of the discrete models being developed is a reference DFN. The initial DFN developed for FORGE was described in 2019 and was based on the data available at the time, primarily data from the vertical pilot well, 58-32, and outcrop data in the nearby mountain range (Finnila et al., 2019). This paper documents the current 2021 DFN model which has been updated based on additional data from two newer wells in the reservoir, a highly deviated injection well, 16A(78)-32, and another deep vertical well, 56-32.

The updated DFN and various subsets of the DFN have been made available to researchers and the public in the GDR. These fracture sets are applicable in, but not limited to well hydraulic stimulation, local stress evolution, flow pathway analysis, and thermal breakthrough in proposed injection and production well configurations. The DFN is also upscaled to provide continuum modelers 3D properties such as fracture porosity, directional permeability and sigma factor.

2. DFN Model Construction

The FORGE reference DFN model was constructed using FracMan software (Golder Associates, 2021). A DFN model explicitly represents fractures in a rock as discrete features. Fractures are represented as planar objects oriented in 3D space with prescribed sizes, shapes, apertures, permeabilities, and compressibilities. The collection of fractures is further described by the number of fractures present and their intensity distribution. Where we know fracture location and orientation, such as at wellbore intersections identified from image log data, the fractures are created in what is termed a deterministic set. Away from measured locations, such as the bulk of the deep FORGE reservoir, fractures are created in stochastic sets where properties are assigned from statistical distributions.

The DFN description is subdivided into four sections: boundaries of the various modeling regions, the stochastic fracture set, the deterministic fracture set, and fracture property calibration.

2.1 Model Regions

There are three model regions used to generate the current DFN models available on the GDR: the largest region is a 4 km x 4 km x 4 km region spanning the full FORGE site from the surface to below the target reservoir region in the granitic bedrock, two smaller regions have been created in order to model well tests performed on Zone 2 of Well 58-32 and stimulation at the toe of well 16A(78)-32. The well-scale model for 58-32 is a cubic region having 300 m sides while the model for 16A(78)-32 is a cubic region having 1000 m sides.

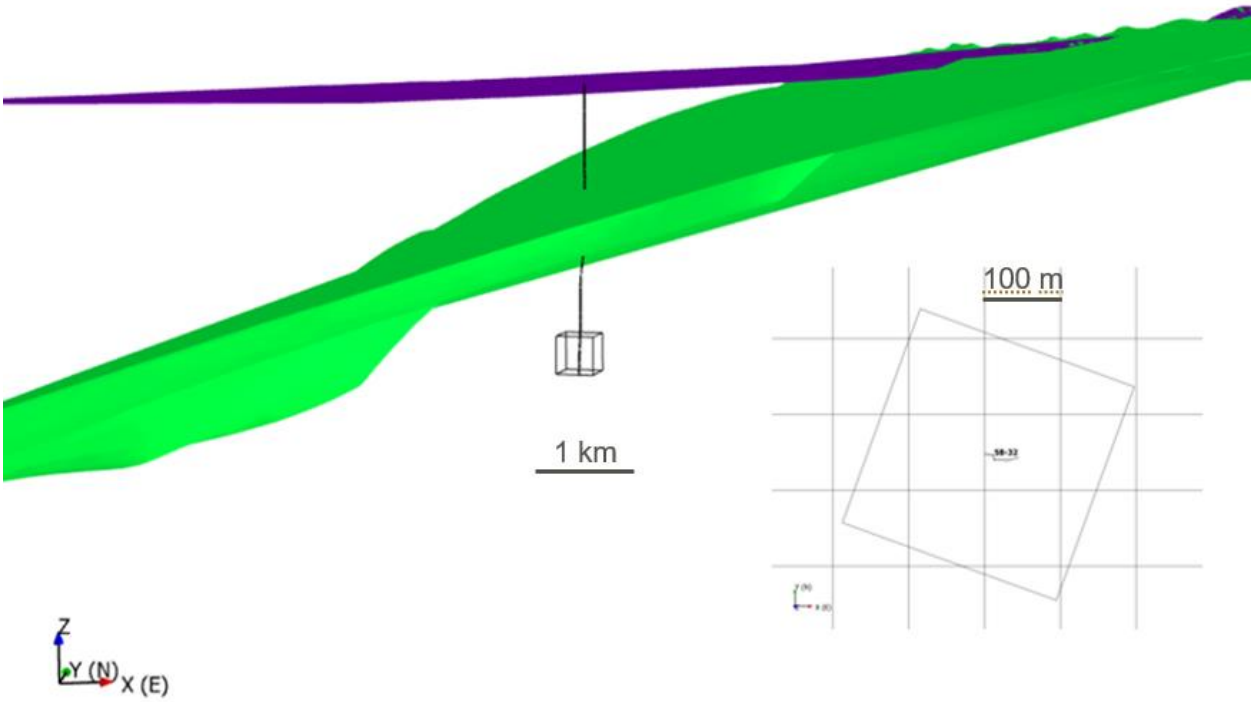

Figure 1: Region for Well 58-32 Zone 2 DFN. The purple surface is ground level while the green surface shows the top of the granitoid bedrock. Enlarged top view in 2D perspective is shown in lower right corner.

Figure 1 shows the region boundaries for the DFN for Well 58-32 Zone 2 where the region box is rotated to align with the principal stress directions with S_{Hmax} being N20E. When the DFN is provided in a local coordinate frame, the region is rotated 20 deg counterclockwise looking down to have the x and y axes aligned with the cardinal directions.

2.2 Stochastic Fracture Set

2.2.1 Fracture Orientation

Four fracture sets have been identified from the FMI data. Three were previously identified from Well 58-32 FMI data. These three were also present in the FMI data from the new vertical well, 56-32, while a new vertical SSW striking set was apparent from the deviated well 16A(78)-32 FMI data. The mean orientations of these sets are listed in Table 1 and shown as black dots on the upper hemisphere stereonets shown in Figure 2.

Table 1: Mean orientations of four fracture sets.

Mean Trend	Mean Plunge	Mean Strike	Mean Dip	Fisher Concentration	Description
88.5	46	178.5	44	15	South striking moderately dipping west
1.5	13.5	91.5	76.5	30	East striking steeply dipping south
131	5	221	85	30	SSW striking vertical
260	17	350	73	10	North striking steeply dipping east

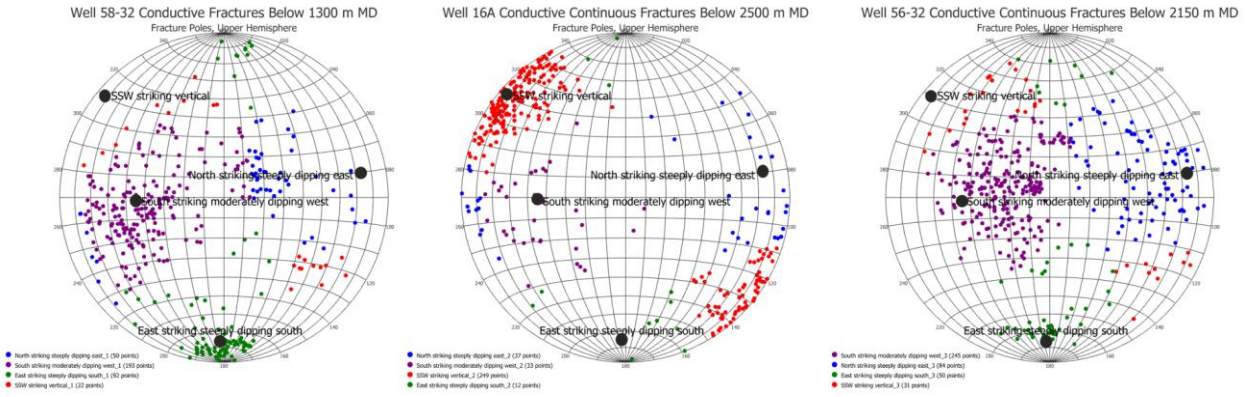

Figure 2: Fracture orientations from FMI data in the deepest portion of the reservoir. Fracture poles are plotted in upper hemisphere stereonets with the color indicating assignment to the nearest mean fracture set pole.

Stochastic fracture sets generated based on these mean set orientations can use the full range of orientations found by using a Fisher distribution with the concentration parameters shown, or they can be "simplified" in order to prevent small angle intersections by only using the mean orientation values. These simplified DFN sets can be more easily meshed when used as input for other modeling software.

2.2.2 Fracture Size and Shape

The fracture size population in the FORGE reservoir can be described by a truncated power law distribution having a power law exponent of 3.2 and a minimum fracture radius of 0.63 m (Finnila, 2021). This fracture size scaling is consistent with both the outcrop data from Salt Cove for fractures having trace lengths in the 40 to 100 m range and the much smaller fractures sampled in the FMI data for Well 58-32.

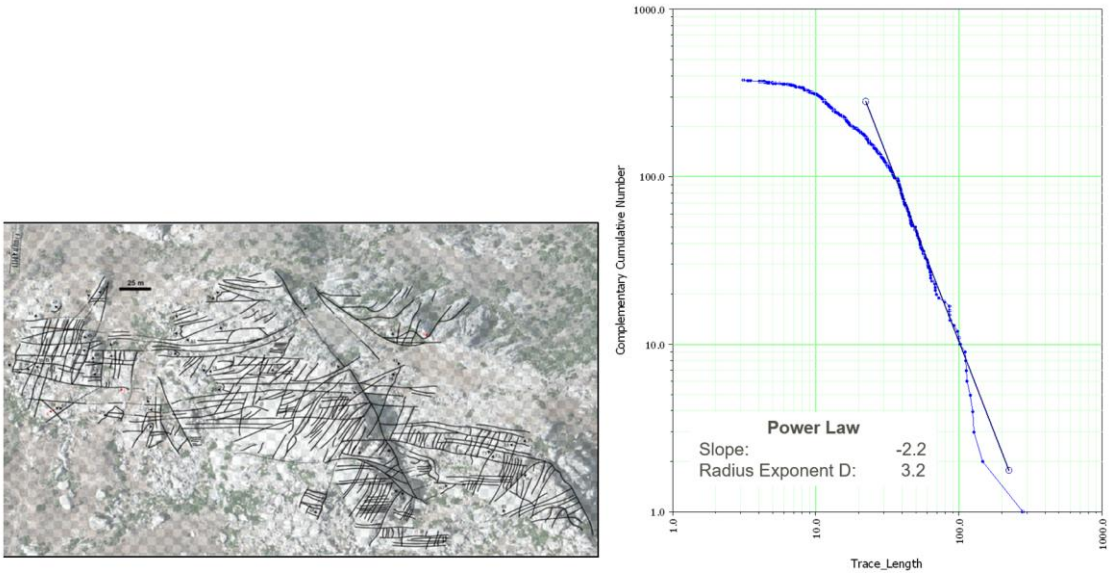

Figure 3: Power law fracture size distribution fit from outcrop trace length data.

Fracture shapes are assumed to be roughly circular and are represented in the DFN as regular hexagons for simplicity as fewer nodes are required in the model to show the extent of each fracture.

2.2.3 Fracture Intensity

Average fracture intensity was estimated in the deep reservoir by integrating the FMI data coming from 58-32, 16A(78)-32, and 56-32. Natural fractures identified in the FMI in the target reservoir depths were sorted into the four sets that were identified based on their orientations. Fracture intensities were first measured as P_{10} values, the number of fractures in the well interval divided by the interval length. This fracture intensity measurement is a function of both the well trajectory and the fracture set orientation, so needs to be converted to a P_{32} fracture intensity, fracture area divided by the volume. This fracture intensity measurement is independent of the well trajectory or fracture orientations and even sizes, so it is a better measure to use when comparing relative fracture intensities. To convert between the P_{10} and P_{32} values, a Terzaghi weight (Terzaghi, 1965) was calculated using a maximum value of 7 and the P_{32} values were then calculated as the sums of the Terzaghi weights in the interval divided by the interval length.

In Table 2Table 3, the white cells at bottom row show that the total P_{32} is quite similar between the two vertical wells, 58-32 and 56-32, while the total P_{32} is much lower in 16A(78)-32. This matches the hypothesis that the FMI for 16A(78)-32 is quite biased and only picking up fractures well-oriented to intersect the borehole. To produce average fracture intensities for the four sets, the P_{32} from the two vertical wells was averaged along with just one set from 16A(78)-32 (P_{32} values in italic text were excluded). FMI results from the vertical wells were assumed to sample all the sets reasonably well, while 16A(78)-32 was assumed to only fully sample the SSW striking vertical set. While the vertical wells would also be expected be missing intensity from any vertical sets present, 58-32 at least seems to sample the East striking steeply dipping south set reasonably well so it is unclear why it isn't picking up more of the SSW striking vertical set. Table 3 shows the final mean fracture set intensities used for the DFN in the deep reservoir region.

Table 2. Fracture set intensity by well.

	58-32		**16A(78)-32**		**56-32**	
Description	**P_{32} [1/m]**	**[%]**	**P_{32} [1/m]**	**[%]**	**P_{32} [1/m]**	**[%]**
South striking moderately dipping west	0.34	35.50%	*0.06*	10.30%	0.49	42.50%
East striking steeply dipping south	0.47	49.20%	*0.05*	8.70%	0.23	19.40%
SSW striking vertical	0.05	5.00%	0.38	68.10%	0.14	12.40%
North striking steeply dipping east	0.1	10.30%	*0.07*	13.00%	0.3	25.70%
	0.95		**0.56**		**1.16**	

Table 3: Mean deep reservoir fracture set intensity.

Description	P_{32} [1/m]	[%]
South striking moderately dipping west	0.42	36.1%
East striking steeply dipping south	0.35	30.1%
SSW striking vertical	0.19	16.6%
North striking steeply dipping east	0.20	17.2%
	1.15	**100.0%**

2.3 Deterministic Fracture Set

While a stochastic set of fractures is helpful for estimating unknown fracture populations, it is desirable for some modeling purposes to have the DFN honor the locations and orientations of fractures that have been measured in the FMI log. These are generated in a separate set referred to as the Deterministic Fracture Set. Stochastic fractures intersecting well boreholes where FMI data is available are removed so that synthetic well logs created from the trajectories of the wells will look identical to the measured ones. While this fracture set is deterministic in the sense that the general fracture locations and orientations are known to some extent, the fracture sizes, shapes and exact locations of the centers of the fractures are still randomly generated, so that different realizations of the fracture set are also possible. Figure 4 shows this workflow for the Well 58-32 Zone 2 DFN where simplified orientations were used for the four sets and the DFN only included fractures having a radius greater than 10 m.

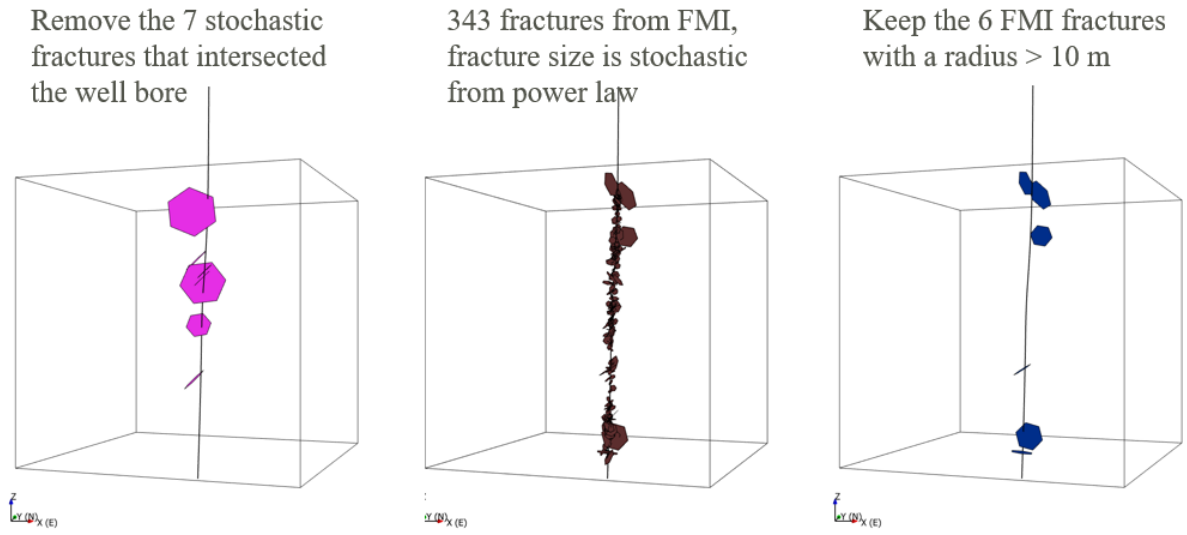

Figure 4: Creation of the deterministic fracture set for DFNs having various minimum fracture size cutoffs.

2.4 Calibration of the Model

There are some whole rock measurements available for porosity, permeability and compressibility. Once the geometrical aspects of the fractures are parameterized for the DFN such as size, shape, orientation and intensity, those properties that contribute to the whole rock properties are assigned so as to make the model consistent with these observations.

2.4.1 Fracture Aperture

Natural fracture apertures are quite complicated and can be defined in different ways. The DFNs for the FORGE site use two different ones: a mechanical aperture which contributes to the fracture porosity, and a hydraulic aperture which controls fracture hydraulic permeability. Information about the mechanical aperture comes from aperture estimates from the FMI data in Well 58-32 shown in Figure 5. Information about the hydraulic aperture comes from the well tests performed on Well 58-32 and the modeling work performed to match these tests (Xing et al., 2021). The hydraulic apertures are found to be 1-2 orders of magnitude smaller than the mechanical apertures measured from FMI (Figure 6).

In the DFN, the mechanical aperture is assigned by assuming a relation between the aperture and the fracture size. Larger fractures will have larger apertures. The bulk porosity is a combination of the fracture porosity and the matrix porosity and so is an upper bound on the fracture porosity. Lab measurements of porosity from core samples was less than 0.5% (McLennan et al., 2018). For this calibration, we assume that the aperture is linearly related to the square root of the fracture radius, R. This relation is often useful in a DFN where fractures are treated as planar features having a constant aperture.

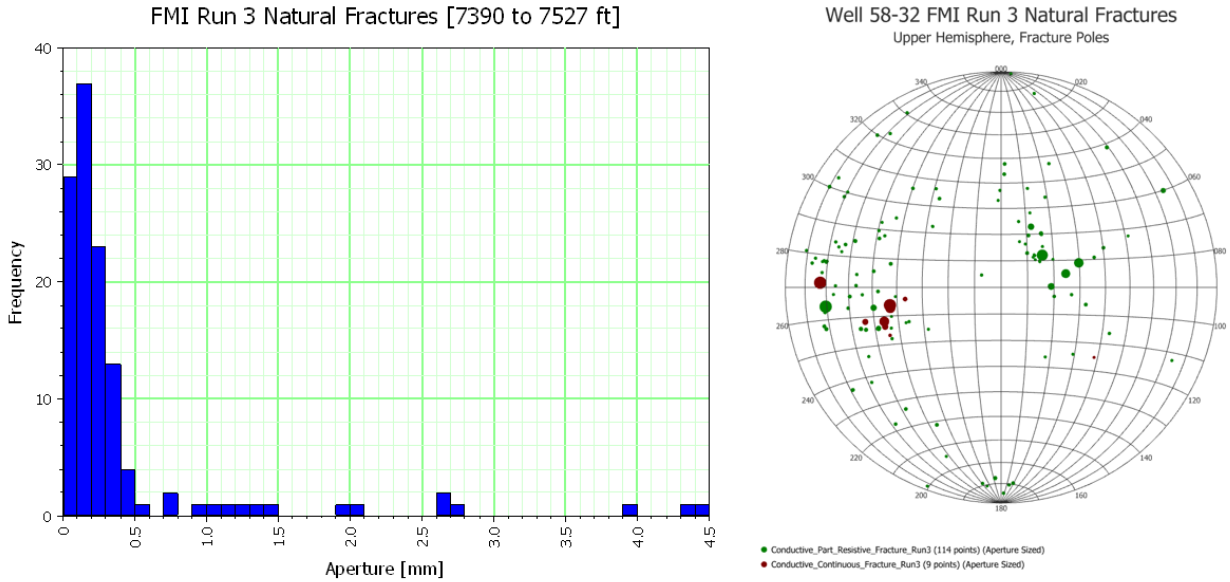

Figure 5: Mechanical apertures and fracture orientations from Well 58-32 FMI data. Upper hemisphere stereonets shows fracture orientations with the size of the dot for the fracture pole showing relative aperture sizes.

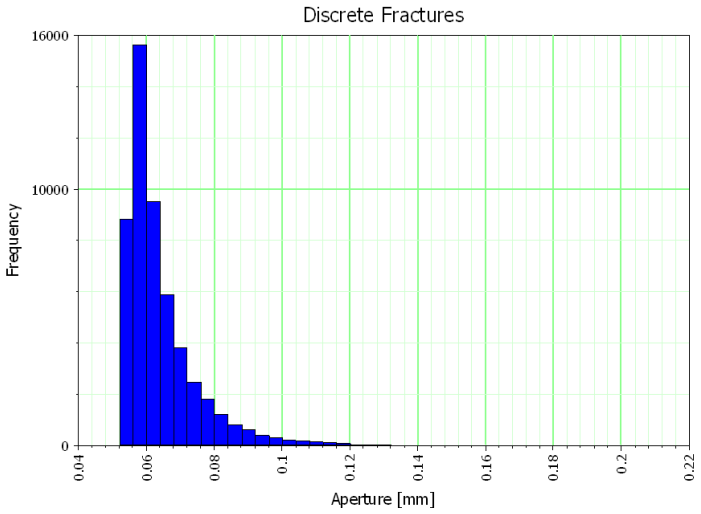

Figure 6: Hydraulic apertures assigned to Well 58-32 Zone 2 DFN.

2.4.2 Fracture Compressibility

The method for calibrating fracture compressibility remained the same as was used in the previous FORGE reference DFN and is based on measurements of Young's Modulus, E, and Poisson's Ratio, ν, in the granitoid. Rock compressibility, β, is defined as the inverse of the bulk compressibility and can be represented with these two other elastic moduli (Birch, 1961):

$$\beta = \frac{3(1-2\nu)}{E} \quad (1)$$

Using E equal to 4.5×10^{10} Pa and ν equal to 0.25 (Moore et al., 2018), the rock compressibility is 3.3×10^{-5} 1/MPa. When upscaling from a DFN, the rock compressibility is defined as:

$$\beta = \beta_F * \phi_F \quad (2)$$

where β_F is the fracture compressibility and φ_F is the fracture porosity (Golder, 2021). Since the fracture apertures have already been calculated, the fracture porosity can be determined through upscaling the DFN. Combining equations 1 and 2 then yields a mean fracture compressibility of 7.2×10^{-3} 1/MPa.

2.4.3 Fracture Permeability

The average rock in-situ permeability of the granitoid is estimated to be 4.7×10^{-17} m^2 from well testing performed in Phase 2B (McLennan et al., 2018). In a similar workflow as was utilized to estimate fracture apertures, a relationship between fracture permeability k_F, and aperture, e, is assumed:

$$k_F = be^{1.5} \quad (3)$$

Where b is a constant that needs to be empirically determined. Using a value of b equal to 3.13×10^{-15} for the fractures in the reference DFN yields permeabilities in the cell coordinate directions IJK of 4.6×10^{-17} m^2, 4.6×10^{-17} m^2, and 4.9×10^{-17} m^2 respectively.

3. DFN Subsets and Availability

The DFNs described in the paper are available on the GDR in both the global coordinates and local coordinates. The individual discrete fractures are available in different size ranges and upscaled values are provided for the smaller fractures that are not explicitly represented.

3.1 Discrete Fracture Sets

With millions of fractures potentially generated in the reference DFN for the largest modeling region, it can be useful to provide various subsets depending upon the desired purpose. Some common subsets are to filter the fractures by size to only consider the largest ones, or to perform a critical stress analysis on them and only select the ones which show high values of critical stress. In both cases, it is generally assumed that these subsets will include the most hydraulically significant fractures. Some subsets have been filtered to only include fractures that are connected to the well(s) of interest.

3.2 Upscaled DFN Properties

In order to assist continuum modeling, the DFN is also upscaled to provide bulk rock values for such parameters as porosity, directional permeability, and sigma factor. The properties can be averaged over varying length scales as needed. These properties can be transferred to other simulators using grid file formats or point data having associated mean property values. Figure 7 shows how fracture porosity from small, background fractures can be combined with upscaled large discrete fractures to provide a model suitable for continuum modelers.

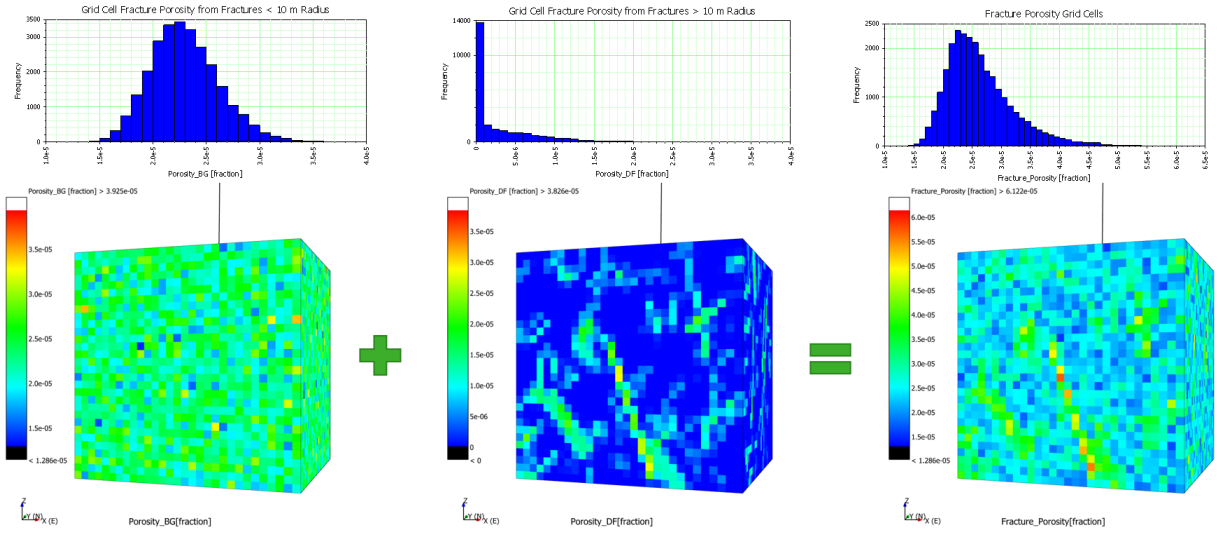

Figure 7: Upscaled porosity values for Well 58-32 Zone 2 DFN.

4. Conclusion

In addition to providing the three DFN realizations consisting of individual fractures, a more general description of the fracture sets is provided in tabular form in the paper. These summary set orientations, intensities, and size parameterizations can be used to generate additional, compatible DFN representations of the FORGE reservoir.

Acknowledgement

Funding for this work was provided by the U.S. DOE under grant DE-EE0007080 "Enhanced Geothermal System Concept Testing and Development at the Milford City, Utah FORGE Site". We thank the many stakeholders who are supporting this project, including Smithfield, Utah School and Institutional Trust Lands Administration, and Beaver County as well as the Utah Governor's Office of Energy Development.

REFERENCES

Birch, F. "Velocity of compressional waves in rocks to 10 kilobars, Part 2." *J. Geophys. Res.*, 66, (1961), 2199-2224.

Energy and Geoscience Institute at the University of Utah. "Roosevelt Hot Springs, Utah FORGE Final Topical Report 2018" [data set]. Retrieved from http://gdr.openei.org/submissions/1038, (2018).

Finnila, A., Forbes, B., and Podgorney, R. "Building and Utilizing a Discrete Fracture Network Model of the FORGE Utah Site." *Proceedings, 44th Workshop on Geothermal Reservoir Engineering*, Stanford University, Stanford, CA (2019).

Finnila, A. "Estimation of Fracture Size for a Discrete Fracture Network Model of the Utah FORGE Geothermal Reservoir using Forward Modeling of Fracture-Borehole Intersections." Paper presented at the 55th U.S. Rock Mechanics/Geomechanics Symposium, physical event cancelled, June 2021. Originally accepted for the 3rd International Discrete Fracture Network Engineering Conference. DFNE 21-2329 (2021).

Golder Associates: FracMan® Reservoir Edition, version 8.1 Discrete Fracture Network Simulator, (2021).

McLennan, J., Nadimi, S., Trang, T. and Forbes, B. "Permeability Measurements, FORGE Utah Technical Report." Report to Department of Energy, Geothermal Technologies Office, April 2018, (2018).

Moore, J., McLennan, J., Handwerger, D., Finnila, A., and Forbes, B. "Mechanical Property Measurements, FORGE Utah Technical Report." Report to Department of Energy, Geothermal Technologies Office, April 2018, (2018).

Terzaghi, R.: Sources of Error in Joint Surveys, *Géotechnique*, **15**, (1965), 287-304.

Xing, P., Damjanac, B., McLennan, J., Radakovic-Guzina, Z., Finnila, A., Podgorney, R., and Moore, J. "Numerical Simulation of Injection Tests at Utah FORGE Site." *Proceedings, 46th Workshop on Geothermal Reservoir Engineering*, Stanford University, Stanford, CA (2021).

ARMA 21–1168

Numerical Simulation of Hydraulic Fracturing Stimulation of the Enhanced Geothermal System Well at Utah FORGE Site

Xing, P.
Energy & Geoscience Institute, University of Utah, Salt Lake City, UT, USA
Damjanac, B. and Radakovic-Guzina, Z.
Itasca Consulting Group, Inc., Minneapolis, MN, USA
Finnila, A.
Golder Associates, Redmond, WA, USA
Podgorney, R.
Idaho National Laboratory, Idaho Falls, ID, USA
Moore, J.
Energy & Geoscience Institute, University of Utah, Salt Lake City, UT, USA
McLennan, J.
Department of Chemical Engineering, University of Utah, Salt Lake City, UT, USA

ABSTRACT: In January 2021, highly deviated injection well, 16A(78)-32, was drilled to a total depth 10,987 ft at the Frontier Observatory for Research in Geothermal Energy (FORGE) site near Milford, Utah. After a brief hiatus, hydraulic fracturing will be carried out near the toe. The production well, 16B(78)-32, will be drilled with a trajectory designed to intersect the microseismic cloud observed during creation of these stimulated fractures. The stimulation, which aims to connect injection and production wells, was simulated with a distinct element method (DEM) based code, *XSite*^{TM}, fully coupled hydro-mechanical model with explicit representation of the discrete fracture network (DFN). The model has been calibrated by a pressure history matching of the injection tests of the pilot well, 58-32. The preliminary simulations for the current interpretation of the DFN show that the formation response to the injection is dominated by the DFN. At a pumping rate of 20 bpm for 15 minutes, sufficient increase in fluid pressure resulted in failure of some area of the DFN both in tension (opening) and shear (slip). The cases with DFN dilatancy indicate lower injection pressure. The case with higher DFN strength has smaller area of slipping fractures but larger area of open fractures. Decreasing the pumping rate to 10 bpm resulted in lower net fluid pressure but a larger stimulated volume. Increasing fluid viscosity 10 times resulted in much higher fluid pressure and more DFN failure.

1. INTRODUCTION

The U.S. Department of Energy selected a location in south-central Utah near the rural community of Milford to develop and test techniques for creating, sustaining, and monitoring Enhanced Geothermal System (EGS) reservoirs. This field laboratory is the Frontier Observatory for Research in Geothermal Energy (FORGE). A pilot well, 58-32, was drilled into the low permeability granitic rock that will form the EGS reservoir. In 2017 and 2019, injection testing was carried out in three zones of well 58-32 (Xing et al., 2020). From October 2020 to January 2021, the injection well of the injection-production pair, 16A(78)-32 (refer to Figure 1), was drilled, and injection testing including DFIT (Diagnostic Fracture Injection Test) and flowback test was carried out. Within the next two years, a production well of the pair will also be drilled. Both wells of the pair are highly deviated with bottom-hole temperatures near 230°C. After a brief hiatus to analyze reservoir characterization data from well 16A(78)-32, hydraulic fracturing will be carried out near the toe of that well before drilling the second well. Production well 16B(78)-32 will be drilled with a trajectory designed to intersect the microseismic cloud produced during creation of these hydraulic fractures. A key consideration is the geometry of these "near-toe" fractures in the injection well and the need to ensure effective hydraulic communication between the two wells.

Xing et al. (2021) used a fully coupled hydro-mechanical modeling software, *XSite* (Itasca, 2020), to history match

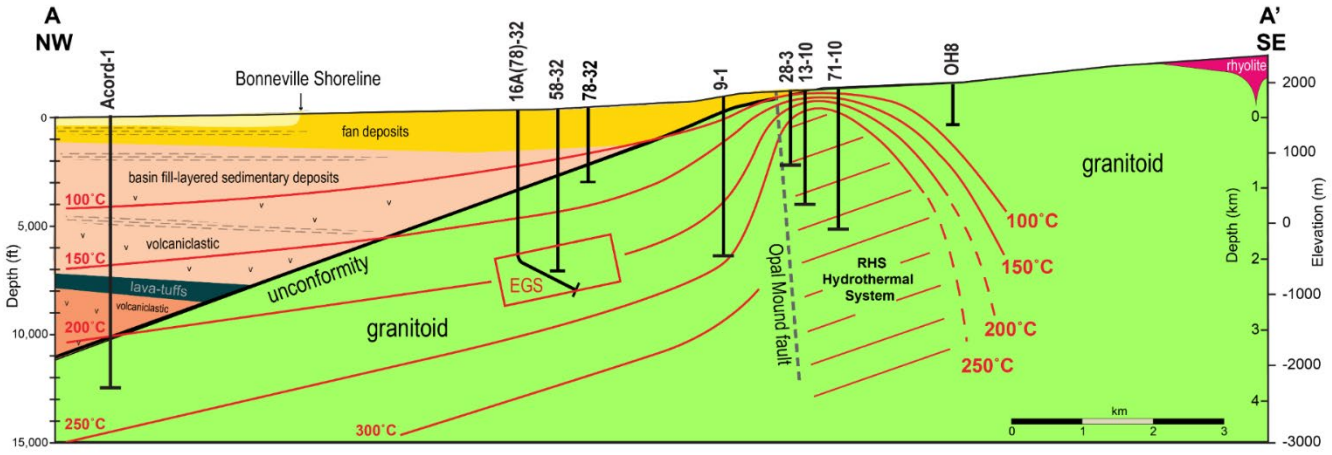

Figure 1. Geological map: northwest-southeast section through the FORGE site (modified from Kirby et al., 2018).

the legacy pressure data from pilot well 58-32 and develop an acceptable representation of the properties and discontinuities of the reservoir and the morphologies of the hydraulic fractures. This modeling was based on the distinct element method with an explicit representation of the discrete fracture network (DFN) (Damjanac et al., 2020). The numerical analyses from the pressure history matching for well 58-32 showed that the specifics of the 3D DFN are key to understanding injection pressure. The location, size, and properties of the natural fractures significantly affect the injection pressure. The numerical investigation enhanced the understanding of the Utah FORGE reservoir response to fluid injection and shed light on what might be called self-shadowing, where one injection cycle impacts the injection performance of a subsequent stage pumped at the exact same physical location.

The numerical model, calibrated by pressure history matching of injections in well 58-32, validates the existing geologic model at that location and constrains the in-situ stresses. With the improved understanding of the Utah FORGE reservoir based on the calibrated numerical model, preliminary designs for the hydraulic fracturing treatments are proposed and analyzed for well 16A(78)-32 in this study. Parametric evaluations include DFN dilatancy, DFN strength, fluid type, and pumping rate. Both slickwater and crosslinked treatment fluids (with a large cooldown pad) are considered.

The paper first describes the basic information of well 16A(78)-32, including drilling and injection activities. Then, pressure history matching of injections in well 58-32 is briefly reviewed. Finally, preliminary simulation of potential stimulation in well 16A(78)-32 is presented and results are discussed.

2. OVERVIEW OF WELL 16A(78)-32

The injection well, 16A(78)-32, is highly deviated and is the first of its kind in granitic rock. Drilling of the well was completed in January 2021. The trajectory of well 16A(78)-32 is shown in Figure 2. The well kicked off (location where directional drilling operations commence) at 5892 ft measured depth (MD) and started to build 5°/100 ft until it reached 65°. The production casing shoe is at 10,787 ft MD, and there is a 200 ft openhole section behind it. Total depth (TD) of the well is 10,987 ft. True vertical depth (TVD) at the toe is 8560 ft and the temperature at the bottomhole is on the order of 446 °F (230 °C). The horizontal offset is 4074 ft.

After drilling to TD and casing, injection testing, including pump-in/shut-in and pump-in/flowback tests, was conducted in the openhole section of well 16A(78)-32. Inferred closure stress gradients from these tests range from 0.71 to 0.75 psi/ft, which is within the range of those inferred from the openhole section of well 58-32.

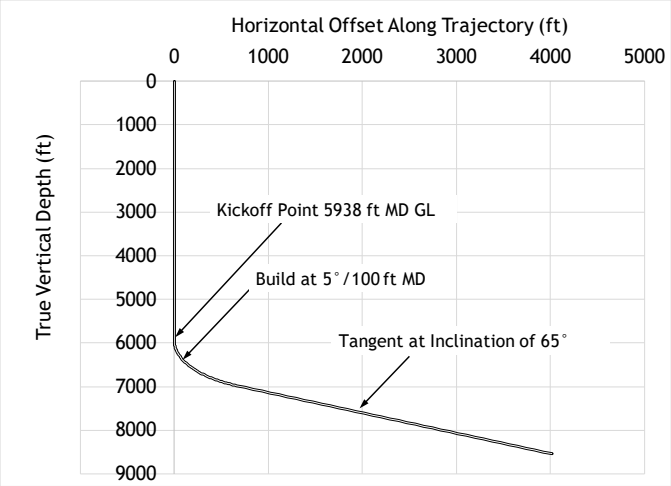

Figure 2. Trajectory of well 16A(78)-32.

3. PRESSURE HISTORY MATCHING OF INJECTION TESTS IN THE PILOT WELL 58-32

Well 58-32 is a pilot well for testing and monitoring at the FORGE site. It was drilled vertically to a depth of 7536 ft in 2017 with a bottomhole temperature of 390 °F (199°C).

In 2017 and 2019, injection testing was carried out in three zones of this well, including one openhole section and two cased and perforated zones. Of particular interest are the increasing pressures observed during the fifth cycle of injection into the upper-cased zone, designated as Zone 2. These pressures exceeded those recorded during the preceding injection cycle (Cycle 4), which resulted in the breakdown of the formation in this zone. Pumping conditions were identical during both cycles. Pressure history matching was conducted for Cycles 4 and 5 of Zone 2 in this well (Xing et al., 2021).

Simulations of the injections in well 58-32 were conducted with *XSite*, which simulates fully coupled hydro-mechanical models with explicit representations of DFN. The 3D DFN contains approximately 2000 natural fractures, based on the natural fractures mapped with resistivity imaging in well 58-32 and nearby representative outcrop data (Finnila et al., 2019). Fracture orientations are somewhat simplified to avoid small angle intersections.

The results of pressure history matching for Cycles 4 and 5 are shown in Figure 3. More details of the pressure history matching can be found in Xing et al. (2021). The model results match the important data trends. The injection pressure generally increases with time in both cycles in the numerical model. Also, the injection pressures during Cycle 5 are consistently greater than those during Cycle 4. The model is thus calibrated with respect to uncertain in-situ reservoir parameters by matching the actual recorded

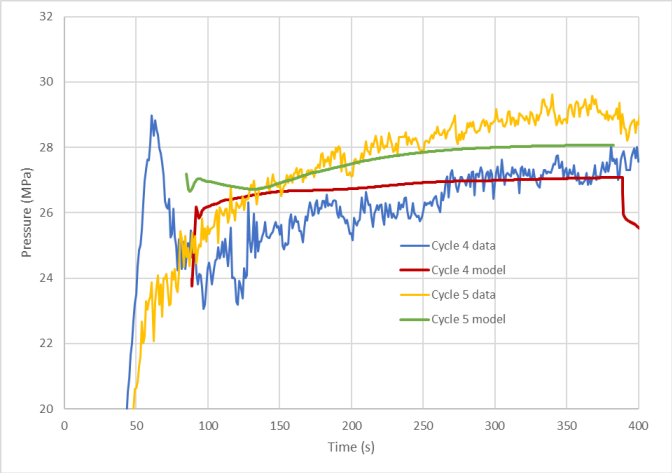

Figure 3. Cycles 4 and 5 of Zone 2 in well 58-32: Pressure (surface pressure) history matching during injection.

pressure histories. The lessons learned from the pressure history matching in well 58-32 include the following:

(i) The formation response to the injection is dominated by the fluid flow and pressure dissipation in the DFN.

(ii) Increasing pressure trends are due to fluid diversion into the DFN as localized leakoff and deformation (including slip and dilation) of the DFN.

(iii) The higher pressure in Cycle 5 is mainly the result of irreversible deformation caused by fluid injection in the previous cycle (Cycle 4).

4. SIMULATION OF HYDRAULIC FRACTURING STIMULATION FOR INJECTION WELL 16A(78)-32

Creating a sustainable fluid pathway between injection and production wells is the key to the success of an EGS. Depending on the geological conditions and the pumping parameters, the stimulation mechanism can be hydraulic fracturing (failure in tension, mode I), hydro-shearing (slipping of pre-existing joints), or a combination of the two. Stimulations in injection well 16A(78)-32 were investigated with the model calibrated by pressure history matching of injections in well 58-32. The effects of different DFN realizations, DFN dilatancy, pumping rate, DFN strength, and fluid viscosity are investigated.

4.1. Description of the model

In this study, the planned stimulation location is the openhole section at the toe of well 16A(78)-32. The model domain is a 300-m-edge cube. The material properties and initial stress conditions used by the numerical model are listed in Table 1 and Table 2.

Table 1 Material Properties used in Numerical Model of well 16A(78)-32

Parameter	Value
Young's modulus	50 GPa (7.25×10^6 psi)
Poisson's ratio	0.25
Fracture toughness	1.75 MPa×$m^{1/2}$ (1600 psi×$in^{1/2}$)
DFN friction angle	37°
DFN cohesion	0
DFN tensile strength	0

Table 2 Initial conditions for well 16A(78)-32 (TVD 8490 ft, 2587.8 m)

Variable	Gradients	Magnitudes
Pore pressure	0.0098 MPa/m (0.433 psi/ft)	25.35 MPa (3676.17 psi)
Minimum horizontal stress	0.017 MPa/m (0.75 psi/ft)	43.99 MPa (6380.2 psi)
Maximum horizontal stress	0.019 MPa/m (0.85 psi/ft)	49.49 MPa (7177.9 psi)
Vertical stress	0.025 MPa/m (1.10 ft/ft)	64.11 MPa (9298.4 psi)

In this study, two different DFN realizations (denoted as DFN1 and DFN2) were investigated. Each set has more than 2000 natural fractures. The DFN model was created

using preliminary information, which might change as a result of detailed study and interpretation of the FMI logs from well 16A(78)-32. Discrete fractures with a radius of 50 m to 150 m are provided in the full model region while fractures with a radius of 10 m to 50 m are present in a smaller 250-m-edge cube in the middle. Fractures with a radius less than 10 m (0.63 m to 10 m), as well as those in the 10 m to 50 m range outside the central 250-m-edge cube, are accounted for with upscaled properties. The DFN close to the injection point is shown in Figure 4.

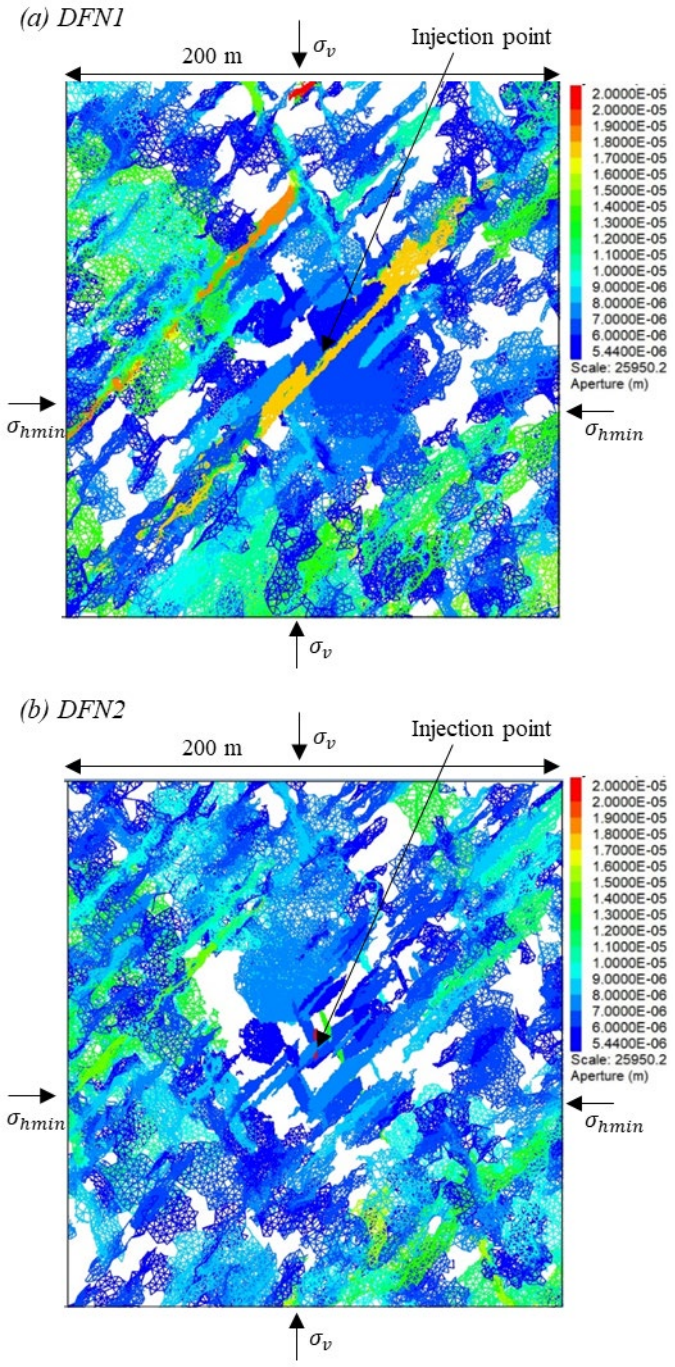

Figure 4. Description of different DFN sets around injection point and their initial apertures.

In the simulations, it was assumed that the DFN fractures are frictional, with a 37° friction angle, zero cohesion, and zero tensile strength. The initial fracture apertures are correlated with fracture sizes. The initial apertures range between 5 and 20 μm (as shown in Figure 4). Since fluid flow is mainly in the DFN, leakoff into matrix is neglected in this model.

4.2. Simulation Results of Well 16A(78)-32

4.2.1 Effect of different DFN realizations

Figure 5 and Figure 6 show the simulation results with two different DFN realizations, DFN1 and DFN2, respectively. For both cases, the pumping rate is 20 bpm and the pumping time is 15 minutes. The results show that the formation response to the injection is dominated by the fluid flow and pressure dissipation in the DFN. The actual DFN for well 16A(78)-32 may be different from the one assumed here and the simulations for the updated DFN will be reported on in the future. These analyses are useful nonetheless for understanding the role of natural fractures in the reservoir stimulation.

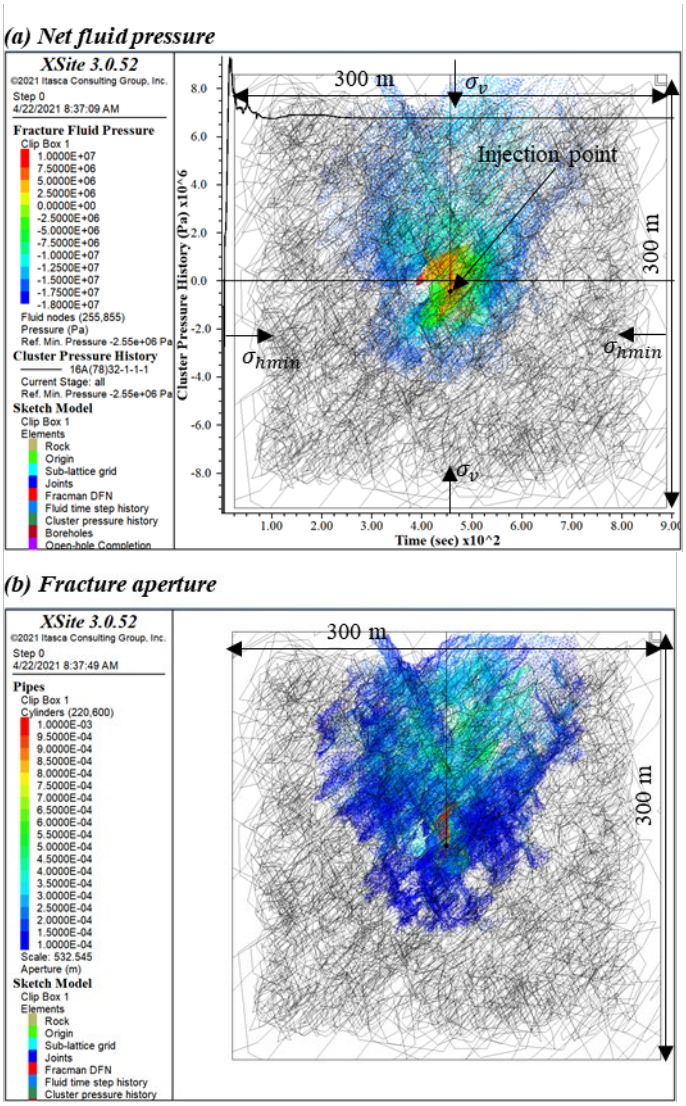

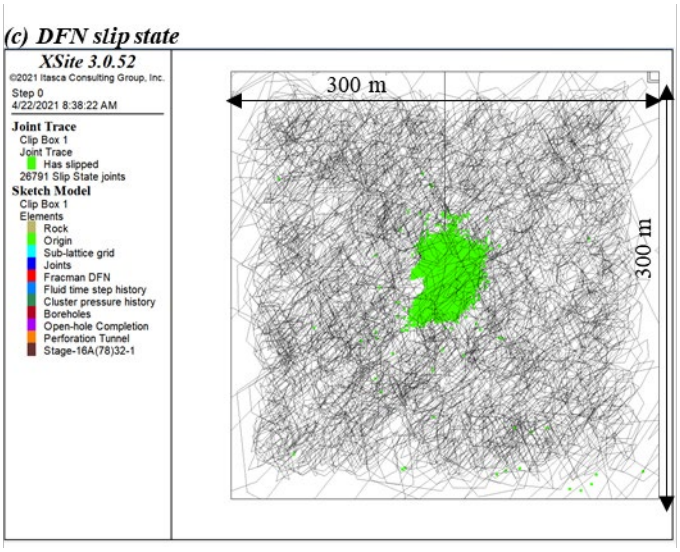

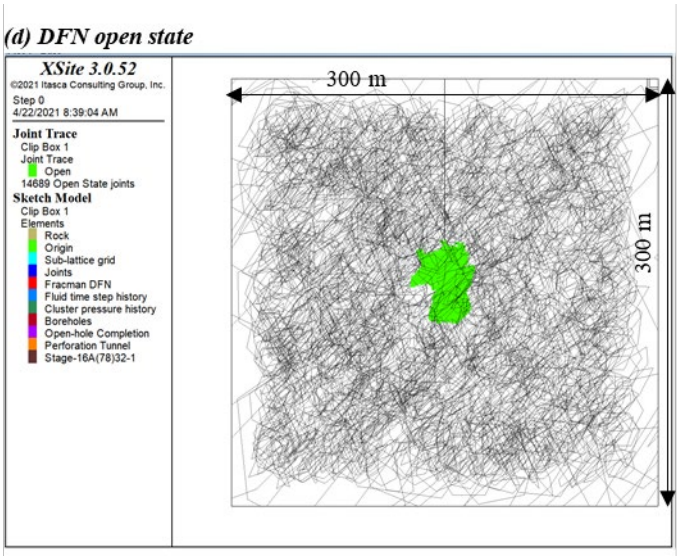

Figure 5. Simulation results of Case 1 with DFN1, 20 bpm for 15 minutes, no dilation of DFN.

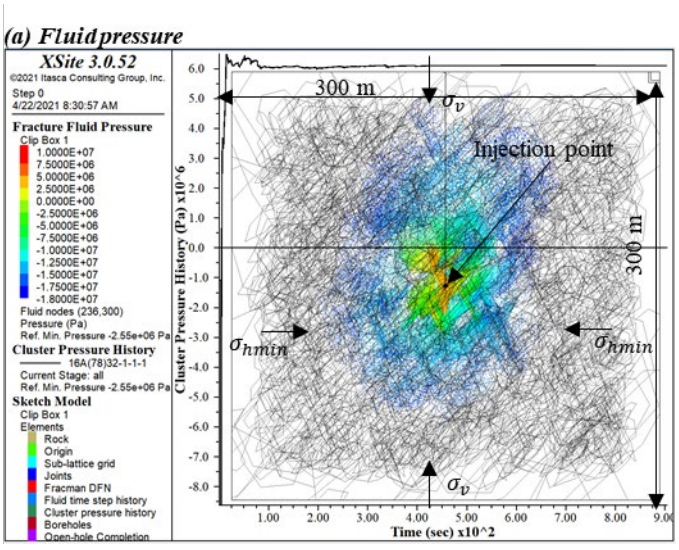

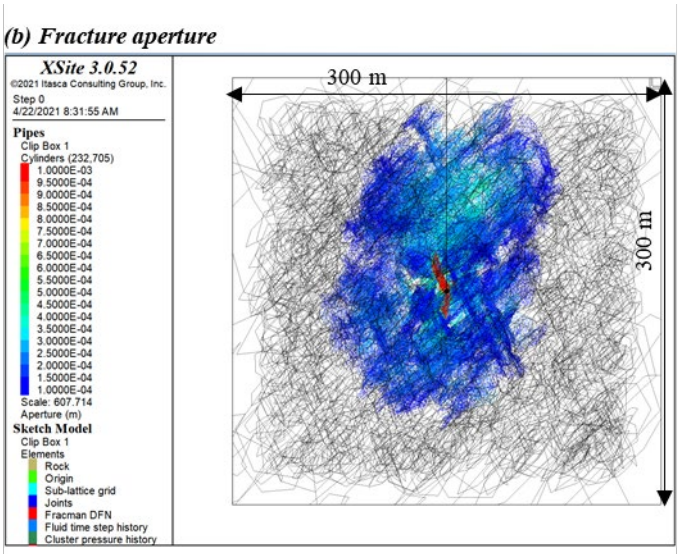

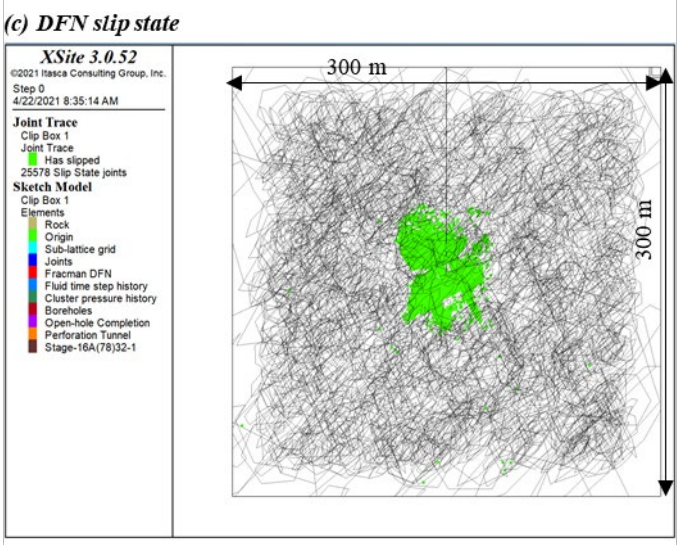

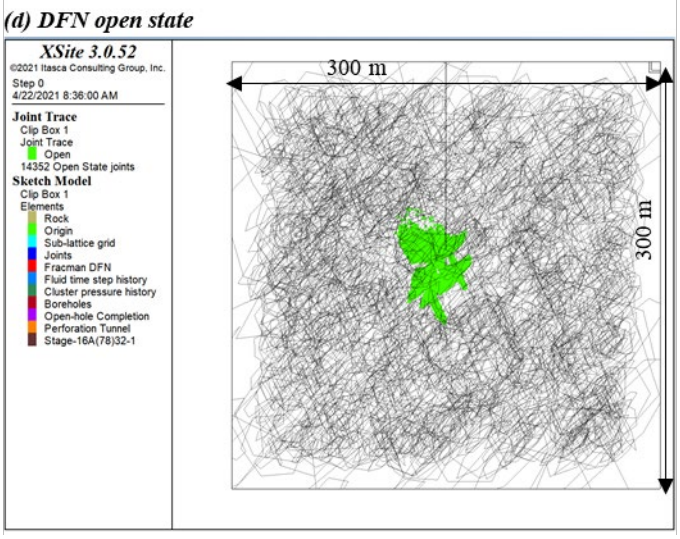

Figure 6. Simulation results of Case 2 with DFN2, 20 bpm for 15 minutes, no dilation of DFN.

Fluid pressure for the case with DFN1 is about 0.7 MPa higher than that of the case with DFN2 because the normal stress acting on the closest-to-cluster natural fracture of DFN1 is larger, which requires higher pressure to reopen the natural fracture. For both cases, about 50%

of the natural fractures that slipped also opened (i.e., have zero effective stress). Another 50% of the affected natural fractures slipped only. Hence, for both cases, 50% of the natural fractures failed in a mixed mode including shear and tension. This is an important observation.

4.2.2 Effect of DFN dilatancy

According to the pressure history matching for well 58-32, DFN dilatancy is a crucial factor that affects the stimulation. Figure 7 and Figure 8 show the simulation results of the cases (DFN1 and DFN2) with 2° dilation angle. As expected, the fluid pressures of the cases with the 2° dilation angle are lower than the cases without dilatancy — for both DFN1 and DFN2. Especially for DFN1, the treatment pressure with 2° dilation is about 2.7 MPa lower than for the case without DFN dilatancy (refer to Figure 5). Due to dilation, the "permeability" of the pressurized fractures increases, which results in a decrease of fluid pressure. For DFN1, a preferential pathway is formed along the large natural fracture close to the cluster.

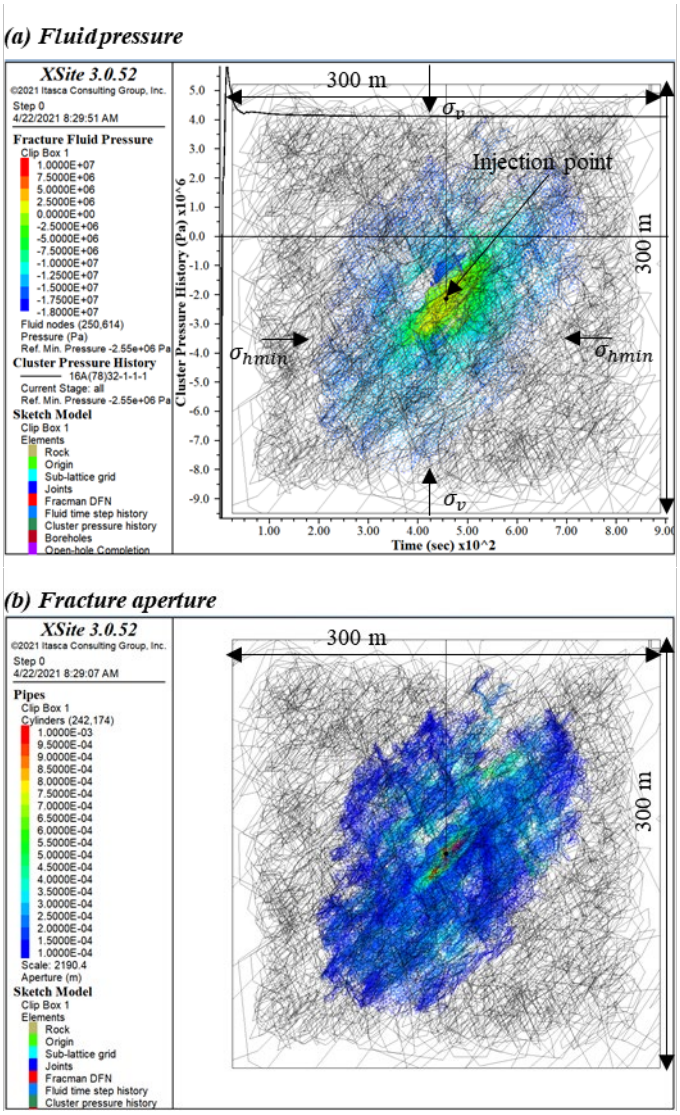

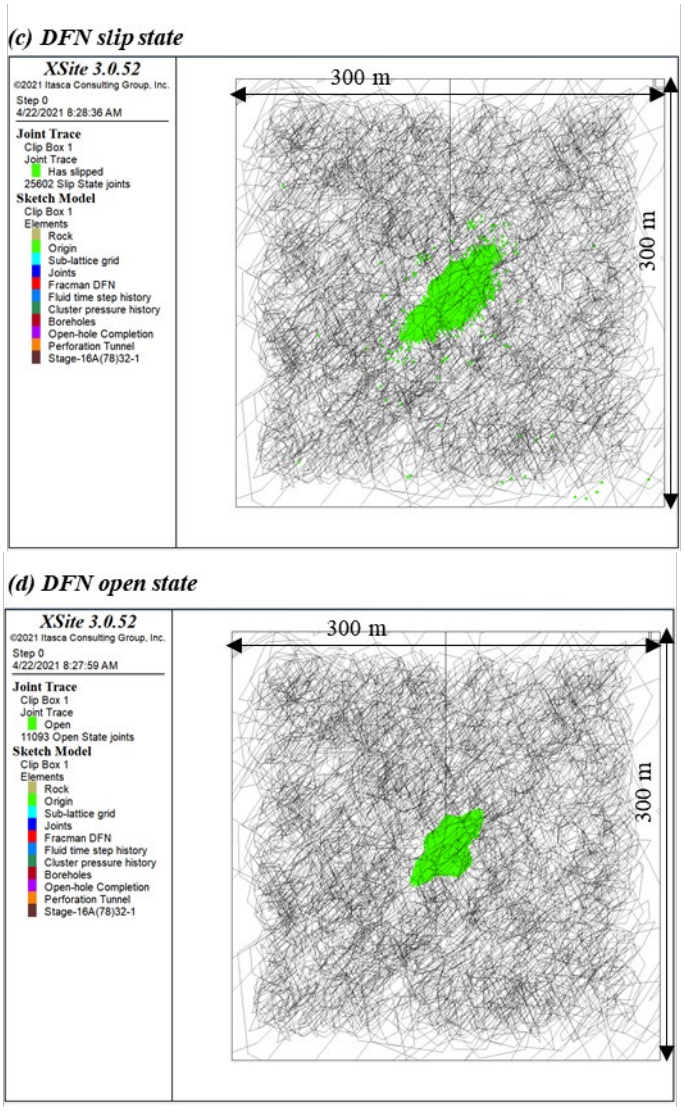

Figure 7. Simulation results of Case 3 with DFN1, 20 bpm for 15 minutes, 2° dilation of DFN.

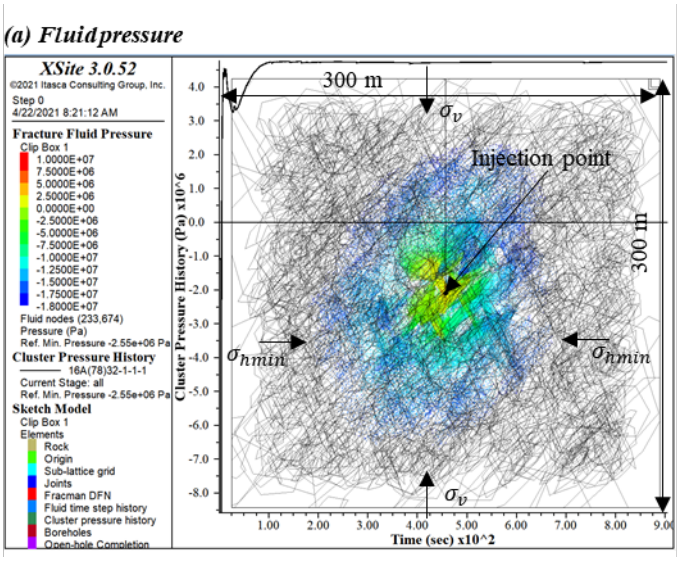

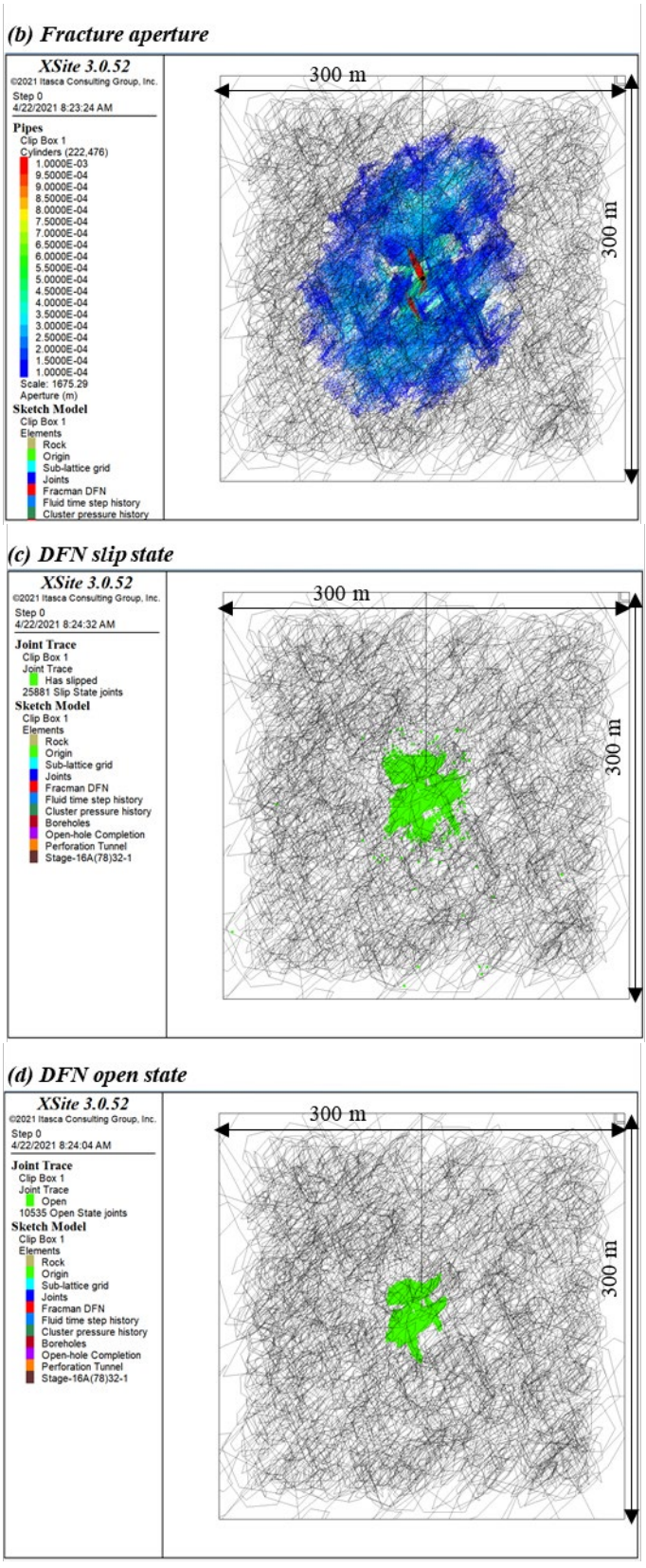

Figure 8. Simulation results of Case 4 with DFN2, 20 bpm for 15 minutes, 2° dilation of DFN.

In both cases (with and without DFN dilatancy) the area of slipping DFN fractures is approximately the same. However, the area of the DFN fractures that opens during injection is smaller for the case with dilating fractures because of greater permeability and, consequently, smaller pressures.

4.2.3 Effect of pumping rate

Pumping rate could affect the hydraulic fracture and natural fracture interaction. Figure 9 shows the results for a case with DFN1 and a lower pumping rate — 10 bpm. To be comparable to the case with a 20 bpm pumping rate (refer to Figure 5), a longer pumping time, 30 minutes, is considered.

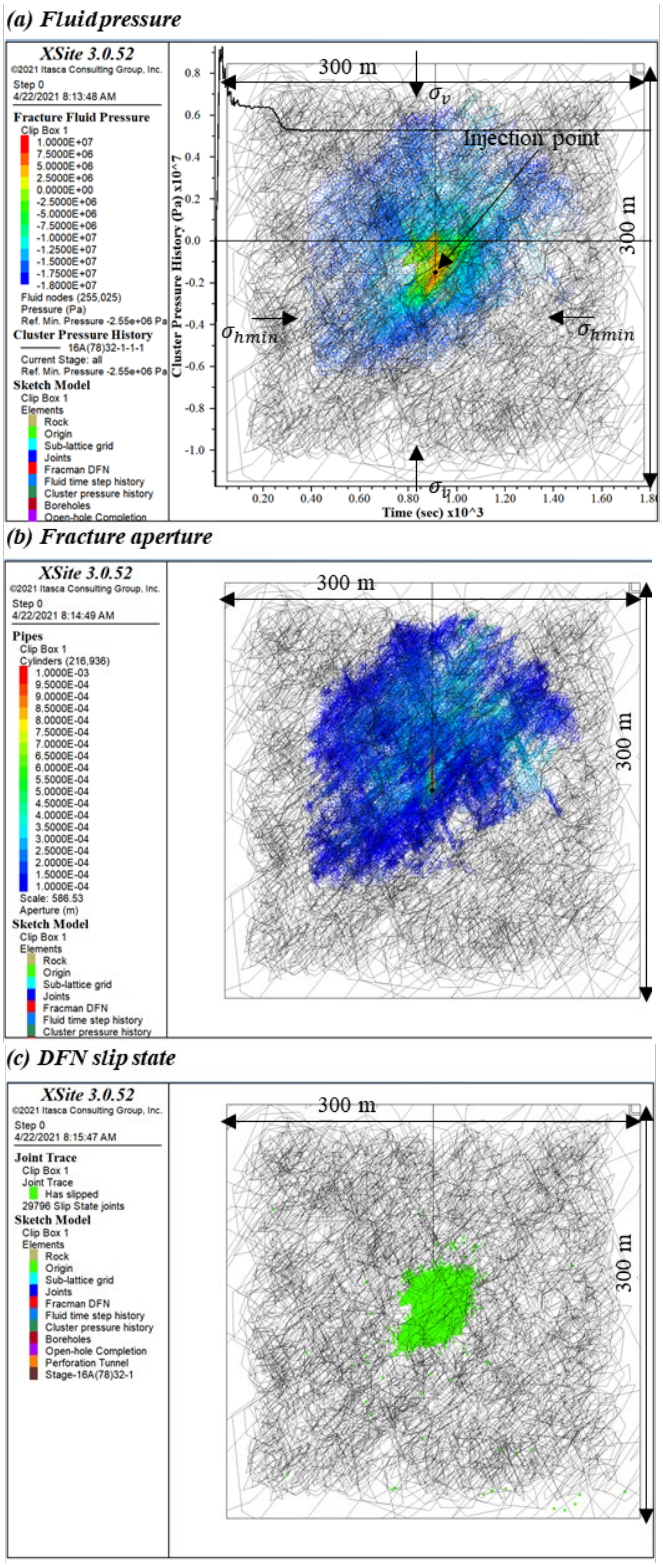

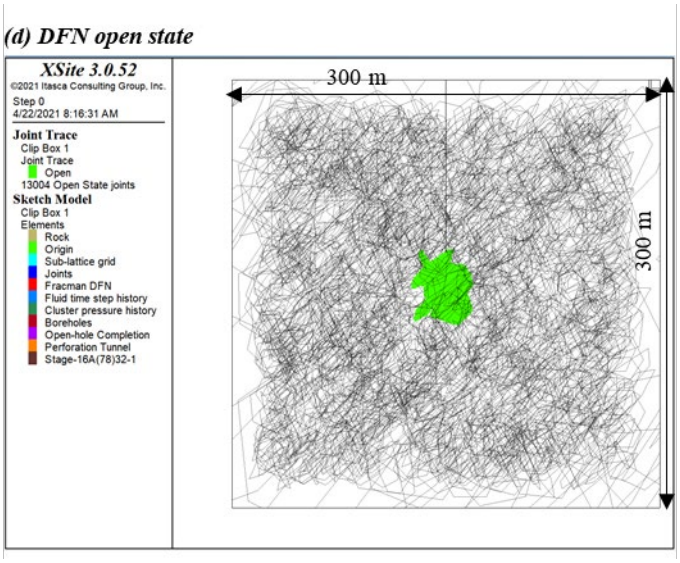

Figure 9. Simulation results of Case 5 with DFN1, 10 bpm for 30 minutes, no dilation of DFN.

The treatment pressure is about 1.5 MPa lower than the case with a 20 bpm pumping rate. With the lower pumping rate of 10 bpm, the area of DFN failure in tension is slightly smaller but slipping area is larger.

4.2.4 Effect of DFN strength

There are uncertainties of strength of DFN natural fractures. In the base model, DFN is weak with zero cohesion and zero tensile strength. In this case a stronger DFN with a cohesion of 10 MPa and tensile strength of 2 MPa is investigated. Friction angle is fixed as 37°. Simulation results with stronger DFN are shown in Figure 10. The treatment pressure with stronger DFN is slightly lower (0.4 MPa) than the case with weak DFN. The area of the fractures with induced apertures greater than 0.0001 m and pressure change is much smaller than the cases with weak DFN. As expected, the area of slipping DFN fractures is smaller due to high cohesion. However, the area of open DFN fractures is much larger than the cases with weak DFN and is even larger than the area of slipping DFN fractures.

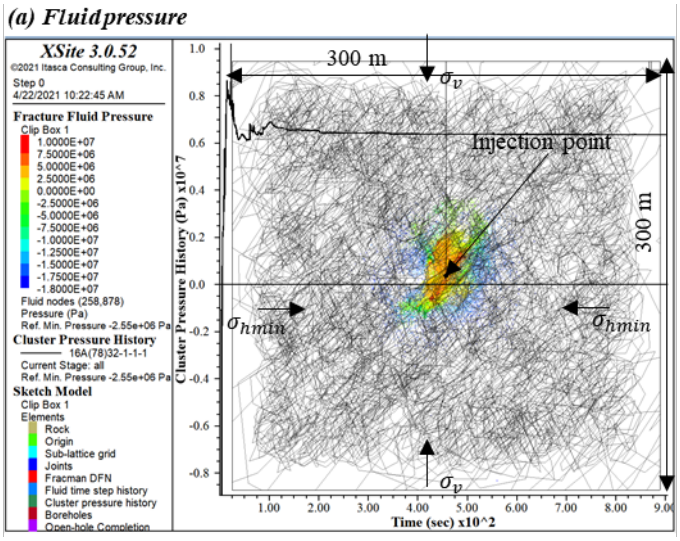

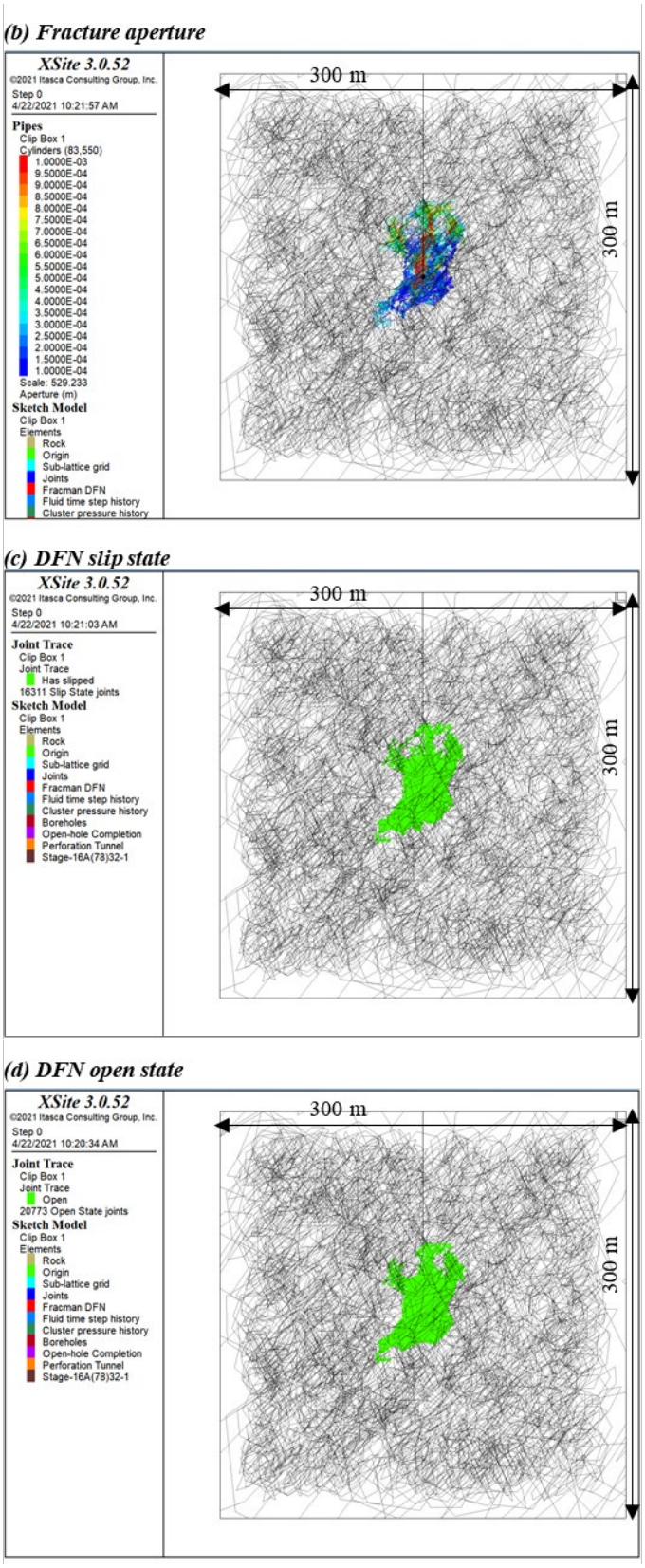

Figure 10. Simulation results of Case 6 with DFN1, 20 bpm for 15 minutes, no dilation of DFN, stronger DFN (cohesion 10 MPa, tensile strength 2 MPa).

4.2.6 Effect fluid viscosity

Fluid viscosity is another important parameter that can be varied during the injection. The viscosity in the base model is 2 cP. Figure 11 shows the results for a case with

a larger fluid viscosity of 20 cP. This case is with DFN1 and pumping at 20 MPa for 6 minutes. The treatment pressure is much higher (about 6.2 MPa) than the case with a 2cP fluid. The areas of aperture greater than 0.0001 m and pressure change are much smaller than for the cases with 2cP fluid viscosity. However, the areas of both open and slipping DFN fractures are much larger than the cases with smaller fluid viscosity.

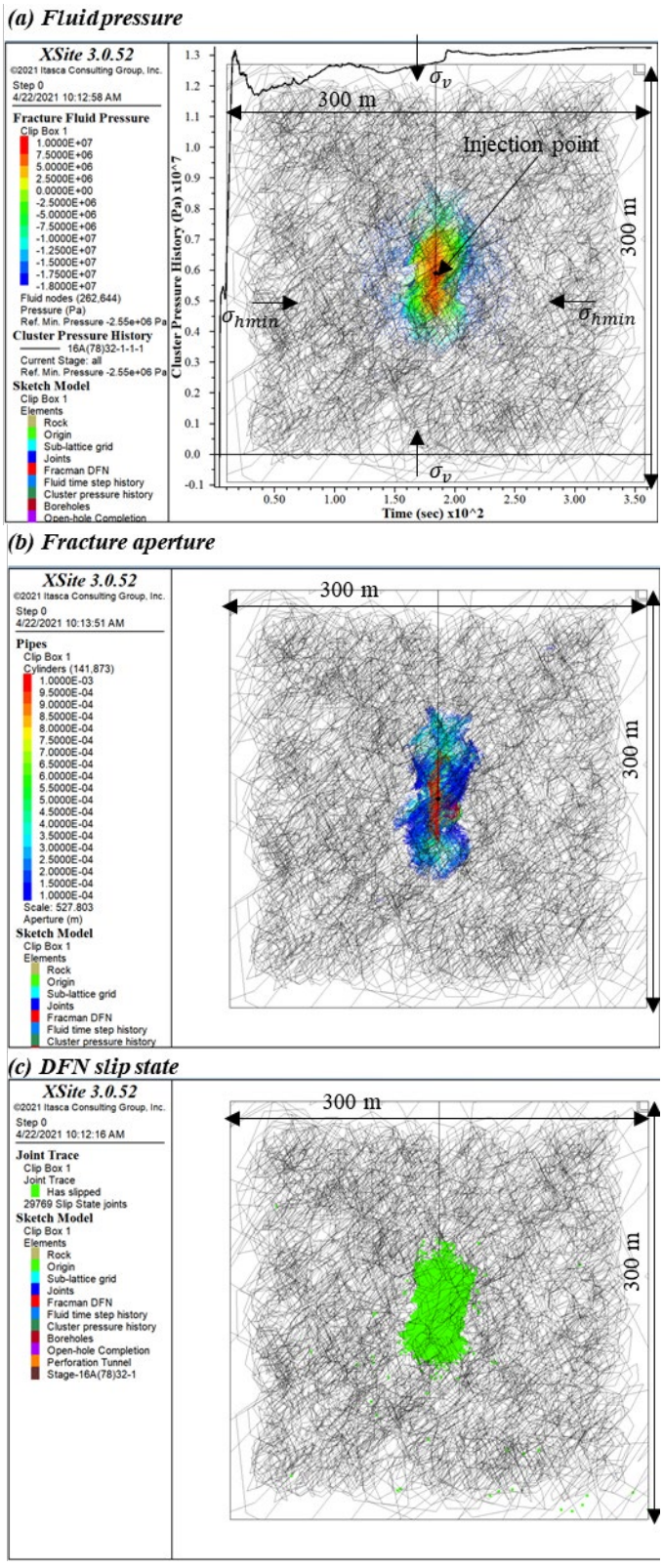

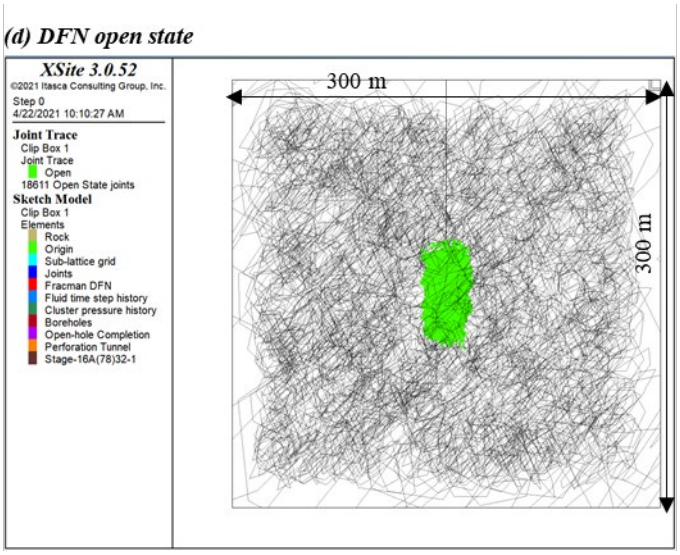

Figure 11. Simulation results of Case 7 with DFN1, 20 bpm for 6 minutes, no dilation of DFN, weak DFN, fluid viscosity 20 cP.

4.3. Summary and Discussion of the Simulations

A series of simulations for well 16A(78)-32 have been conducted. For the natural fracture networks considered, the formation response to injection was dominated by the DFN, especially the large natural fractures closest to the injection point. Of course, this proximity to a large natural fracture will vary with position along the wellbore. For the base model, the pumping rate is 20 bpm, pumping time is 15 minutes, fluid viscosity is 2 cP, and DFN1 realization is considered. In the base model, the resulting net injection pressure is 6.8 MPa, the height above the injection point defined by induced apertures greater than 0.0001 m is 150 m and the height defined by open fractures is 30 m. For 50% of the DFN fractures that failed, the failure mode is a mixture of tension and shear.

As shown in Figure 12, Case 7 with higher viscosity (20 cP) has the largest area of slipping fractures because Case 7 has much larger net pressure. Due to stronger DFN with a high cohesion, Case 6 has the smallest area of slipping fractures. For area of open fractures (refer to Figure 13), Case 6 with stronger DFN is the largest while the cases with weak DFN and dilation is the smallest. Within similar net pressure, slippage of natural fractures tends to impede the opening.

Figure 14 illustrates the stimulated volume with permeability greater than 1e-14 m^2. Case 5 with lower pumping rate has the largest stimulated volume. Case 6 with stronger and initially impermeable DFN has the smallest stimulated volume because pressure change in the far filed is negligible.

Table 3 summarizes the net fluid pressure, fracture height and stimulated volume at the end of injection for all the cases. For the cases with a 2° dilation angle for DFN, the net fluid pressures are lower than those without dilatancy because natural fracture permeability increased due to

aperture increasing during slip. Generally, the cases with DFN dilatancy resulted in a smaller area of DFN failing in tension (DFN1 and DFN2) but approximately the same slipping area compared to those simulations without dilatancy. There are two indices related to the height of the stimulated fractures above the injection point for the stimulation. One is defined by induced fracture apertures that are greater than 1e-4 m and the other is defined the open state of fractures. Case 7 with higher fluid viscosity has the highest pressure and Case 3 with DFN dilation has the smallest pressure. For stimulated volume, Case 5 with lower pumping rate is the largest and Case 6 with stronger DFN is the smallest. For Cases 1 through 5 with weak DFN and smaller viscosity, the fracture heights defined by the aperture threshold are much greater than those defined by fractures open state. For Cases 6 and 7 with stronger DFN or higher fluid viscosity, these two fracture height indices give similar results.

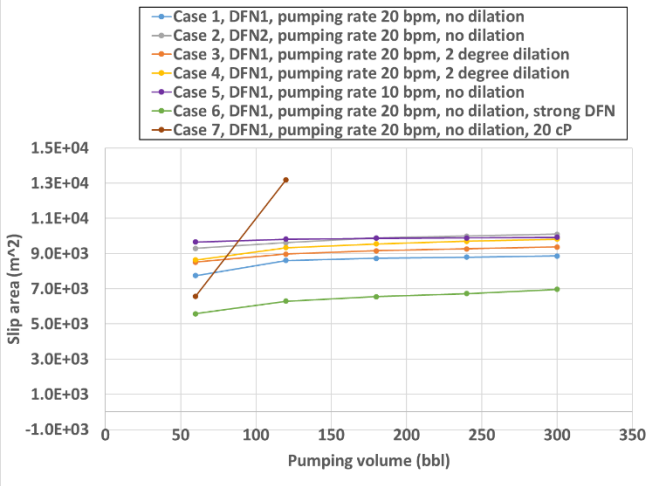

Figure 12. Area of slipping natural fractures vs. pumping volume.

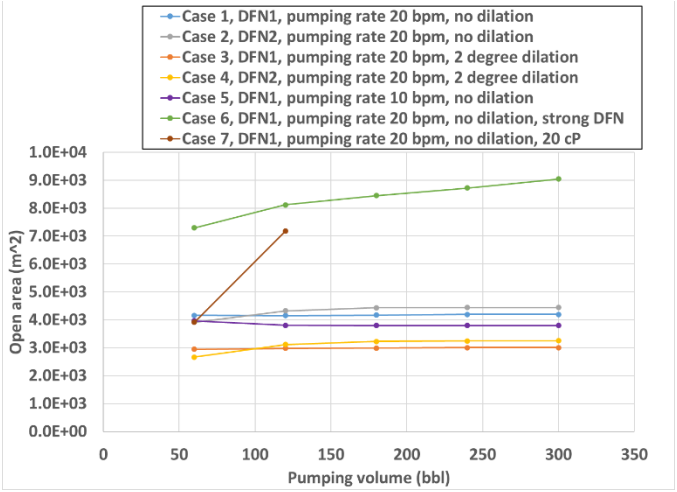

Figure 13. Area of open natural fractures vs. pumping volume.

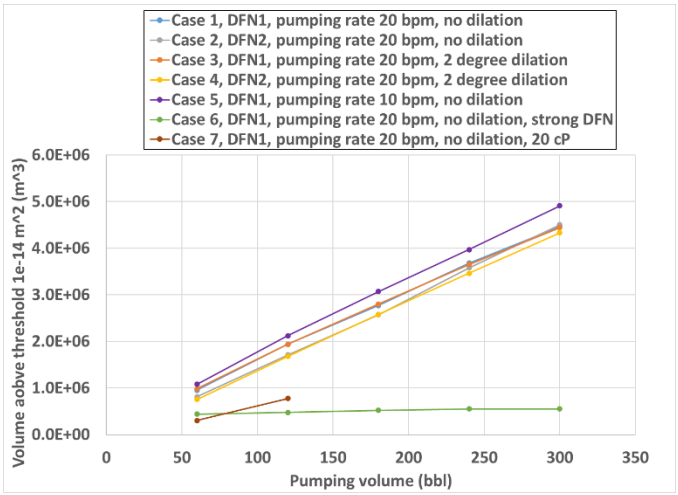

Figure 14. Stimulated volume with permeability greater than 1e-14 m^2 vs. pumping volume.

Table 3. Summary of the simulation results

Case	Net treatment pressure (Pa)	Fracture height upward by aperture threshold 0.0001 m (m)	Fracture height upward by open state (m)	Stimulated volume (m^3)
Case 1: 20 bpm, 300 bbl, DFN1, 2 cP, no dilation, weak DFN	6.8e6	150	30	4.46e6
Case 2: 20 bpm, 300 bbl, DFN2, 2 cP, no dilation, weak DFN	6.1e6	150	40	4.50e6
Case 3: 20 bpm, 300 bbl, DFN1, 2 cP, 2° dilation, weak DFN	4.1e6	100	25	4.44e6
Case 4: 20 bpm, 300 bbl, DFN2, 2 cP, 2° dilation, weak DFN	4.7e6	105	25	4.33e6
Case 5: 10 bpm, 300 bbl, DFN1, 2 cP, no dilation, weak DFN	5.3e6	120	30	4.91e6
Case 6: 20 bpm, 300 bbl, DFN1, 2 cP, no dilation, strong DFN	6.4e6	55	50	5.52e5
Case 7: 20 bpm, 120 bbl, DFN1, 20 cP, no dilation, weak DFN	13.0e6	65	50	7.76e5

Fracture height defined here is the height above the injection point.

5. CONCLUSIONS

Injection well 16A(78)-32 has been drilled at the FORGE site. Hydraulic fracturing will be carried out near the toe to create a sustainable hydraulic communication between the injection and production wells. Preliminary simulations of stimulation for injection well 16A(78)-32 have been conducted. These simulations are considered to be preliminary because the DFN constructed from image logging and deep acoustic log interpretations have not been finalized at the time of writing this paper.

The model has been calibrated by pressure history matching the injection tests in pilot well 58-32. The calibration helps to constrain the material properties and initial stress conditions. The lessons learned from the pressure history matching include: (i) the formation response to the injection is dominated by the fluid flow and pressure dissipation in the DFN; (ii) increasing pressure trends are due to fluid diversion into the DFN as localized leakoff and deformation of the DFN; (iii) previous injection affects the subsequent injection pressure cycles due to the irreversible deformation.

These simulations show us the basic information of the formation response to injection in well 16A(78)-32 for the current interpretation of the DFN. In all the cases, the formation response is dominated by the DFN, which is similar to the phenomenon seen in pressure history matching for 58-32. For the base model, the pumping rate is 20 bpm, the pumping time is 15 minutes, and fluid viscosity is 2 cP. The resulting net treatment pressure is 6.8 MPa, the height of stimulated fractures above the injection point, defined by induced aperture greater than 0.0001 m, is 150 m and the height of stimulated fractures defined by open fractures is 30 m, the volume with permeability greater than 1e-14 m^2 is 4.46e6 m^3.

For the cases with a 2° dilation angle for the natural fractures, the net fluid pressures are lower than those without dilatancy. Decreasing the pumping rate from 20 bpm to 10 bpm resulted in a lower net fluid pressure but a larger stimulated volume. For the case with stronger DFN (10 MPa cohesion), the area of slipping fractures is smaller but the area of open fractures is much larger. Increasing fluid viscosity from 2 cP to 20 cP resulted in a much higher injection pressure (6.2 MPa) and hence larger area of slipping and open fractures.

ACKNOWLEDGMENTS

Funding for this work was provided by the U.S. DOE under grant DE-EE0007080 “Enhanced Geothermal System Concept Testing and Development at the Milford City, Utah FORGE Site.” We thank the many stakeholders who are supporting this project, including Smithfield, Utah School and Institutional Trust Lands Administration, and Beaver County, as well as the Utah Governor’s Office of Energy Development.

REFERENCES

Damjanac, B., C. Detournay, and P. Cundall. 2020. Numerical Simulation of Hydraulically Driven Fractures, in S. Baotang, O. Stephansson, & M. Rinne (Eds.), *Modelling Rock Fracturing Processes (2nd ed.)* pp. 531–561. Springer, Cham. https://doi.org/https://doi.org/10.1007/978-3-030-35525-8

Finnila, A., B. Forbes and R. Podgorney. 2019. Building and Utilizing a Discrete Fracture Network Model of the FORGE Utah Site. In *Proceedings of the 44th Workshop on Geothermal Reservoir Engineering, Stanford University, Stanford, CA, USA, February 2019)* pp. 11-13.

Itasca Consulting Group, Inc. 2020. *XSite* (Version 3.0.48). Minneapolis: Itasca.

Kirby, S.M., T.R. Knudsen, E. Kleber and A. Hiscock. 2018. Geologic setting of the Utah FORGE site, based on new and revised geologic mapping. *Trans. Geotherm. Resour. Counc*, 42, pp.1097-1114.

Xing, P., B. Damjanac, Z. Radakovic-Guzina, A. Finnila, R. Podgorney, J. Moore and J. Mclennan. 2021. Numerical Simulation of Injection Tests at Utah FORGE Site. *In Proceedings of the 46th Workshop on Geothermal Reservoir Engineering, Stanford University, Stanford, CA, USA, February 16-18.*

Xing, P., McLennan, J. and Moore, J. 2020. In-Situ Stress Measurements at the Utah Frontier Observatory for Research in Geothermal Energy (FORGE) Site. *Energies, 13(21)*, p. 5842.

Numerical Investigation of Stimulation from the Injection Well at Utah FORGE Site

Pengju Xing[1], Branko Damjanac[2], Zorica Radakovic-Guzina[2], Aleta Finnila[3], Robert Podgorney[4], Joseph Moore[1], John McLennan[5]

1 Energy & Geoscience Institute, University of Utah, Salt Lake City, UT, USA

2 Itasca Consulting Group, Inc., Minneapolis, MN, USA

3 Golder Associates, Redmond, WA, USA

4 Idaho National Laboratory, Idaho Falls, ID, USA

5 Department of Chemical Engineering, University of Utah, Salt Lake City, UT, USA

Keywords

Utah FORGE, Numerical simulation, Pressure history matching, Hydraulic stimulation

ABSTRACT

A highly deviated injection well, 16A(78)-32, was drilled to a total depth of 10,987 ft at the Frontier Observatory for Research in Geothermal Energy (FORGE) site near Milford, Utah. The lateral tangent was maintained at 65° to the vertical. A series of injection testing was conducted in a 200 ft openhole section at the toe of this well. After a brief hiatus, stimulation by fluid injection will be carried out with three stages near the toe. Numerical modelling should be an essential tool for design and optimization of stimulation strategies that would connect the injection and production wells. These simulations use a lattice-based code, XSite^{TM}, which simulates fully coupled hydro-mechanical processes with explicit representation of a discrete fracture network (DFN). The DFN built from a vertical offset well, 58-32, has recently been updated using the image logs acquired while drilling the injection well 16A(78)-32 and data from another vertical offset well, 56-32. Pressure history matching of the injection testing carried out in well 16A(78)-32 provides the basis for refining the DFN. The simulations of stimulation include different pumping rates (10, 20, 40 bpm), different fluid viscosities (2 cP and 20 cP), and different DFN fracture strengths. For the base model with a pumping rate of 20 bpm for 30 minutes, sufficient increase in fluid pressure resulted in hydraulic fracturing, and failure of some area of the DFN, both in tension (opening) and shear (slip). A higher pumping rate of 40 bpm increases extent of hydraulic fracturing, and areas of open and slipping fractures.

1. Introduction

The U.S. Department of Energy selected a location in south-central Utah near the rural community of Milford to develop and test techniques for creating, sustaining, and monitoring Enhanced Geothermal System (EGS) reservoirs (Moore et al., 2019). This field laboratory is the Frontier Observatory for Research in Geothermal Energy (FORGE). From October 2020 to January 2021, the injection well of the injection-production pair, 16A(78)-32 (refer to Figure 1), was drilled, and injection testing including DFIT (Diagnostic Fracture Injection Test) and flowback test were carried out. Within the next two years, a production well of the pair will also be drilled. Both wells of the pair are highly deviated with bottom-hole temperatures near 230°C. After a brief hiatus to analyze reservoir characterization data from well 16A(78)-32, hydraulic fracturing will be carried out near the toe of that well before drilling the second well. Production well 16B(78)-32 will be drilled with a trajectory designed to intersect the microseismic cloud produced during stimulation. A key consideration is the geometry of these "near-toe" fractures in the injection well and the need to ensure effective hydraulic communication between the two wells.

This modeling is based on the distinct element method with an explicit representation of the discrete fracture network (DFN) (Damjanac et al., 2020). The numerical analyses from the pressure history matching for well 58-32 showed that the specifics of the 3D DFN are key to understanding injection pressure (Xing et al., 2021a). Xing et al. (2021b) conducted the preliminary analysis of the hydraulic fracturing treatments for well 16A(78)-32. Then, the DFN has been updated as a result of a detailed study and interpretation of the FMI logs from well 16A(78)-32 and the offset well 56-32.

In this study, the objective is to investigate the stimulation in well 16A(78)-32 using numerical modeling based on the updated DFN. The paper first provides the basic information of well 16A(78)-32, including drilling and injection activities. Then, pressure history matching of injections in well 16A(78)-32 is shown. Finally, simulation of potential stimulation scenarios based on updated DFN in well 16A(78)-32 is presented, and results are discussed. Parametric evaluations include DFN dilatancy, DFN strength, fluid type, and pumping rate.

2. Overview of Well 16A(78)-32

The injection well, 16A(78)-32, is highly deviated and is the first of its kind in granitic rock. Drilling of the well was completed in January 2021. The trajectory of well 16A(78)-32 is shown in Figure 1. The well kicked off (the location where directional drilling operations commence) at 5892 ft measured depth (MD) and started to build 5°/100 ft until it reached 65°. The production casing shoe is at 10,787 ft MD, and there is a 200 ft openhole section behind it. Total depth (TD) of the well is 10,987 ft. True vertical depth (TVD) at the toe is 8560 ft and the temperature at the bottomhole is on the order of 446 °F (230 °C). The horizontal offset is 4074 ft.

After drilling to TD and casing, injection testing, including pump-in/shut-in and pump-in/flowback tests, was conducted in the openhole section of well 16A(78)-32. Inferred closure stress gradients from these tests range from 0.71 to 0.75 psi/ft, which is within the range of those inferred from the openhole section of well 58-32 (Xing et al., 2021c).

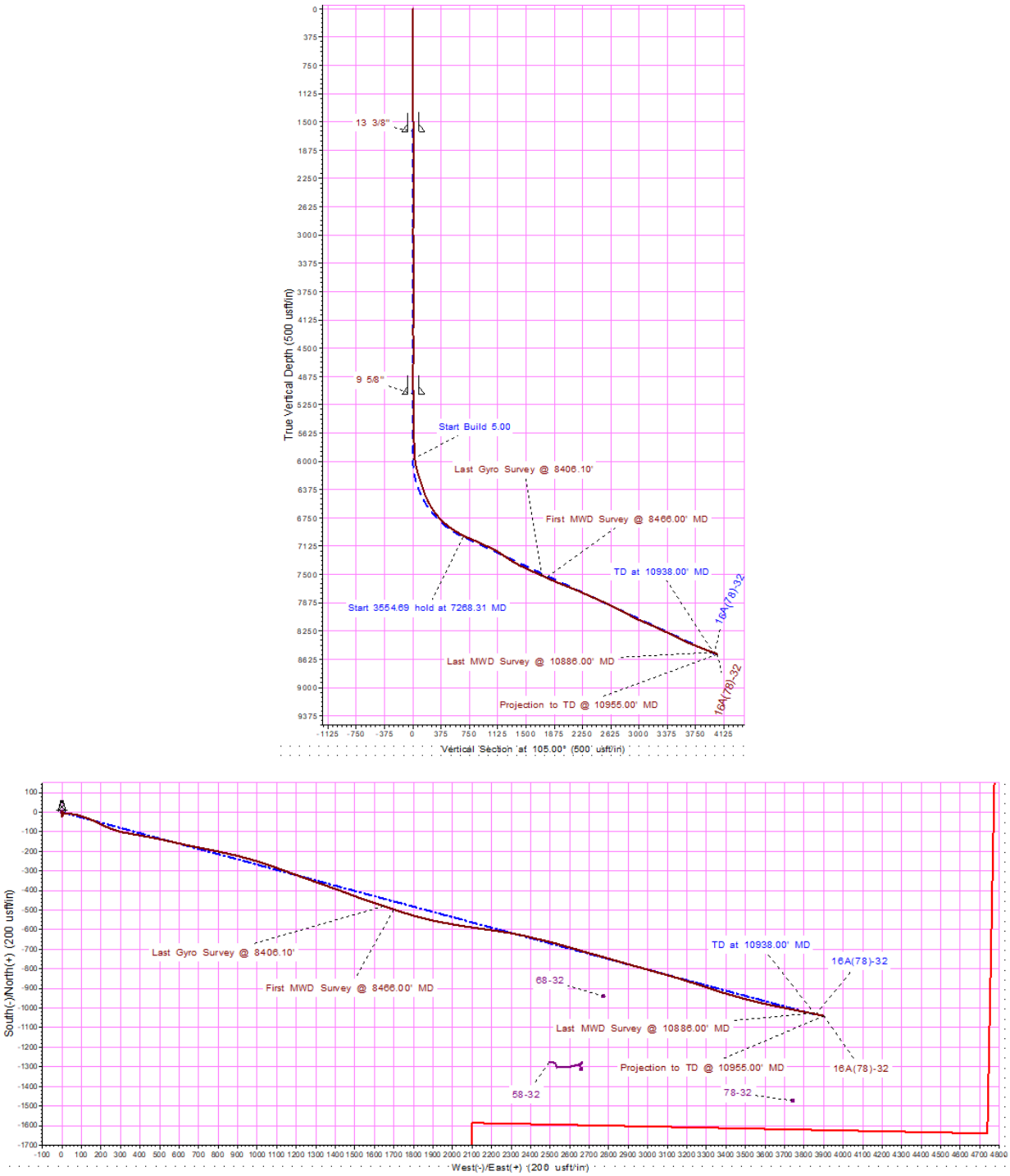

Figure 1. Trajectory of well 16A(78)-32. At the top is the directional profile (approximate elevation view) and at the bottom is the plan view of well trajectory at TD before coring.

2. Pressure History Matching of Injection Tests in Well 16A(78)-32

Pressure history matching of an injection test is often used to calibrate numerical models. There are three injection cycles conducted at the toe of well 16A(78)-32. The details and analyses of these injection tests are documented by Xing et al. (2021c). In this study, pressure history matching is carried out for the DFIT test in well 16A(78)-32. The material properties and initial stress conditions used by the numerical model are listed in Table 1 and Table 2. In this study, an updated DFN is used compared to the DFN used by Xing et al. (2021b). The initial apertures of DFN are shown in Figure 2, ranging from 50 – 200 μm. Discrete stochastic fractures provided in the DFNs have radius values in the 10 to 150 m range and have only four constant orientations.

Table 1. Material Properties used in Numerical Model

Parameter	Value
Young's modulus	55 GPa (8.0×10^6 psi)
Poisson's ratio	0.26
Fracture toughness	3 MPa×m$^{1/2}$ (2740 psi×in$^{1/2}$)
DFN friction angle	37°
DFN cohesion	0
DFN tensile strength	0
Fluid viscosity	2 cP

Table 2. Initial conditions for well 16A(78)-32 (TVD 8490 ft, 2587.8 m)

Variable	Gradients	Magnitudes
Pore pressure	0.0093 MPa/m (0.41 psi/ft)	24.0 MPa (3481 psi)
Minimum horizontal stress	0.0174 MPa/m (0.73 psi/ft)	42.68 MPa (6190 psi)
Maximum horizontal stress	0.0189 MPa/m (0.84 psi/ft)	48.80 MPa (7078 psi)
Vertical stress	0.0243 MPa/m (1.07 ft/ft)	62.80 MPa (9108 psi)

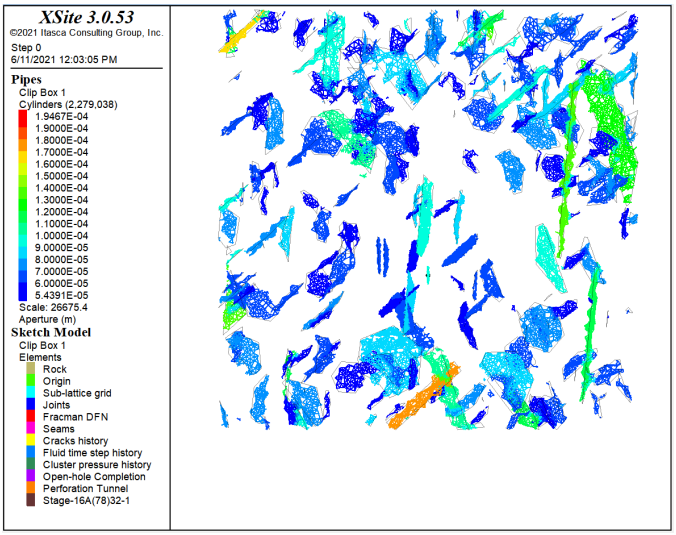

Figure 2. Initial apertures of the DFN.

For the pressure history matching, the model follows the injection procedure of DFIT conducted at the toe of 16A(78)-32. The simulated fluid pressure at the end of simulation (500 seconds after

shut-in) is shown in Figure 3. Fluid penetrated the natural fractures that intersect the openhole section. As shown in Figure 4, the pressure history of the numerical results including both the injection and shut-in periods matches well with the field data.

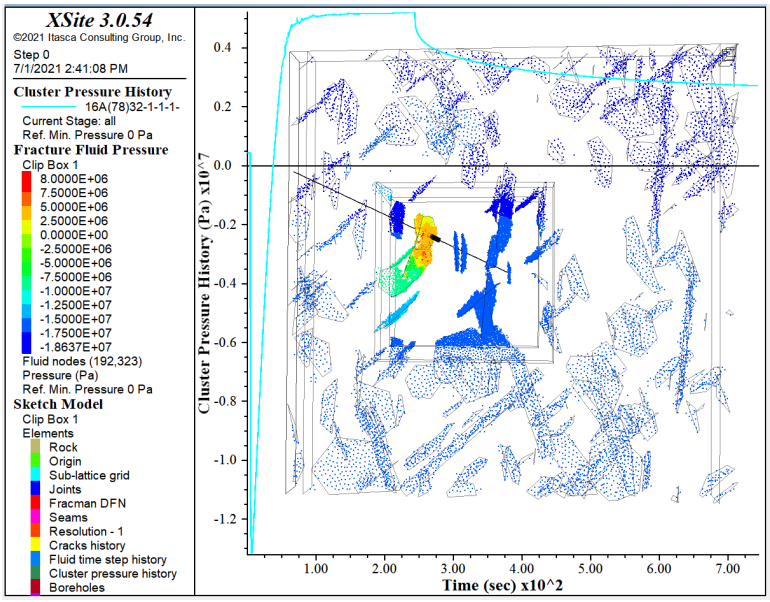

Figure 3. Simulation of the injection test for well 16A(78)-32.

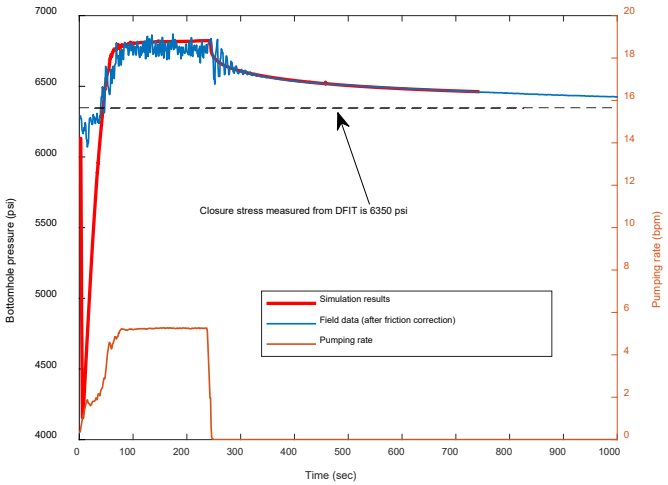

Figure 4. Comparison of the numerical results with the field data for well 16A(78)-32.

3. Simulation of Hydraulic Stimulation for Well 16A(78)-32

Creating a sustainable fluid flow pathway between injection and production wells is the key to the success of an EGS. Depending on the geological conditions and the pumping parameters, the stimulation mechanism can be hydraulic fracturing (failure of intact rock in tension, mode I), opening and slipping (hydro-shearing) of pre-existing joints, or their combination. All mechanisms are investigated. Stimulations in injection well 16A(78)-32 were investigated with the model calibrated by pressure history matching of injections in this well. The effects of DFN dilatancy, pumping rate, DFN strength, and fluid viscosity are investigated.

3.1 Simulation Results of Well 16A(78)-32

3.1.1 Base model

For the base model of simulation of the stimulation, the initial conditions and the material properties are the same as the model used in the pressure history matching. The pumping rate is 20 bpm and the pumping time is 30 minutes. In the base model, DFN is weak with zero cohesion and zero tensile strength. The simulation results of the base model are shown in Figure 5. The height of area with aperture greater than 0.2 mm after stimulation is 235 m above the injection point. The height of slipping fractures above the injection point is 93 m while the height of open fractures is only 73 m. The lateral extent of the stimulated area with aperture greater than 0.2 mm is 130 m. The net fluid pressure is 7.5 MPa.

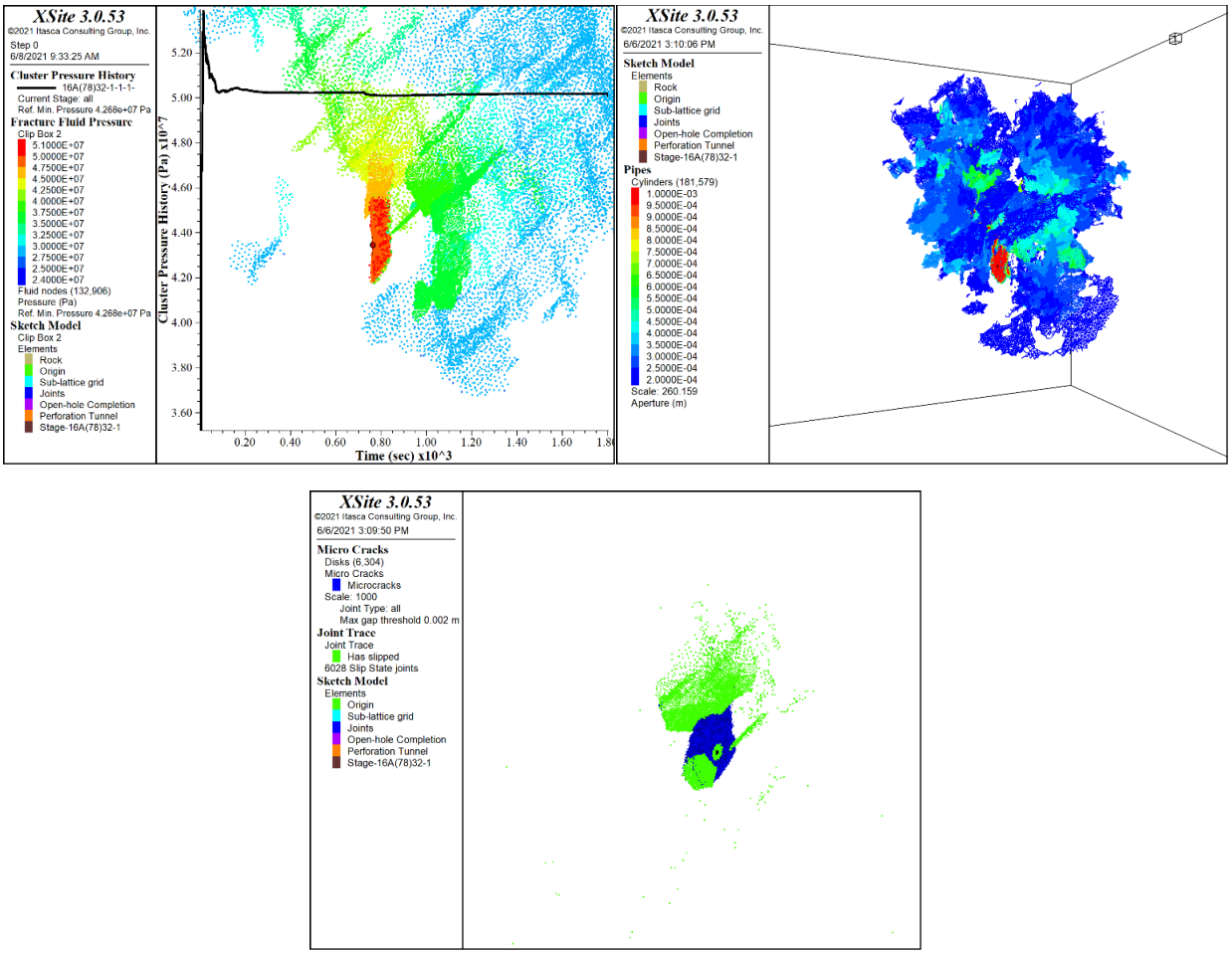

Figure 5. Simulation results of the base model (Case 1): 20 bpm for 30 minutes, no dilation of DFN. Top left: fluid pressure; top right: fracture aperture; bottom: newly created hydraulic fracture (blue) and natural fractures that have slipped (green).

3.1.2 Effect of DFN dilatancy

According to the pressure history matching for well 58-32, DFN dilatancy is a crucial factor that affects the stimulation. Figure 6 shows the simulation results of the case with a 2° dilation angle. As expected, the fluid pressure of the case with the 2° dilation angle is lower than the cases without

dilatancy. The fracture apertures of the case with 2° dilation are larger. Due to dilation, the "permeability" of the slipping fractures increases, which results in a decrease in fluid pressure. The slipping area of DFN is similar to the base model without dilatancy but the open area of DFN is smaller.

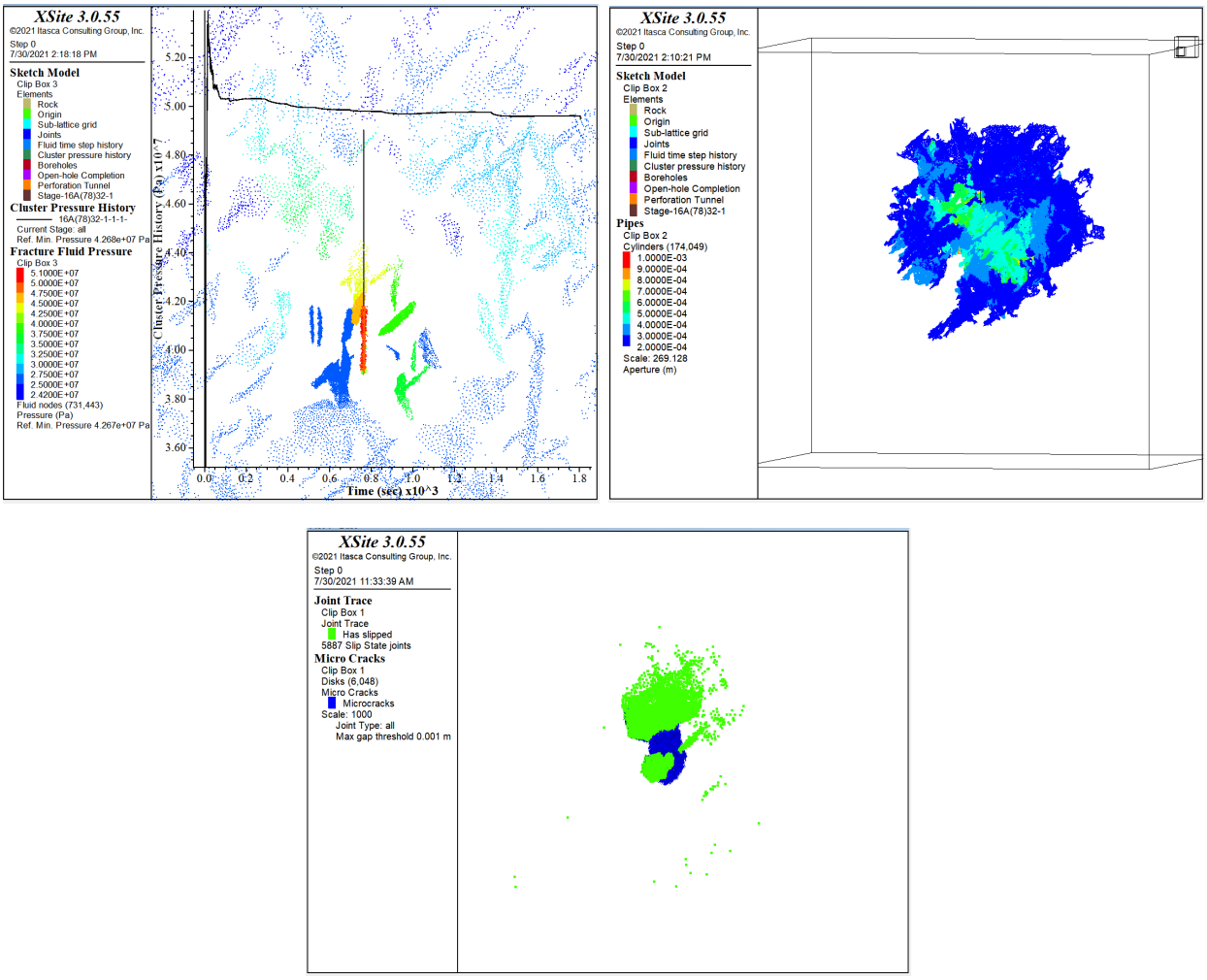

Figure 6. Simulation results of Case 2: 20 bpm for 30 minutes, 2° dilation of DFN. Top left: fluid pressure; top right: fracture aperture; bottom: newly created hydraulic fracture (blue) and natural fractures that have slipped (green). The aperture is larger compared to the no dilatancy case, but there is no preferential pathway.

3.1.3 Effect of pumping rate

Pumping rate could affect the hydraulic fracture and natural fracture interaction. Two cases with pumping rate higher and lower than the base model are investigated. Figure 7 shows the results of a case with a higher pumping rate, 40 bpm. The pumping time is 15 minutes. For the case with the higher rate, the pressure is higher, the fracture aperture is larger, and the slipping and open area of DFN is larger compared to the base case for the same pumped volume.

Figure 8 shows the results for the case with a lower pumping rate — 10 bpm. The pumping time is 60 minutes. As expected, the pressure of the case with the lower pumping rate is smaller. For the same pumping volume, the slipping area and open area of DFN are both smaller than the base

model with the higher pumping rate. This trend is different than the one reported by Xing et al. (2021b) that the slipping area of the case with the lower pumping is larger. The difference is due to different DFN intensity and connectivity.

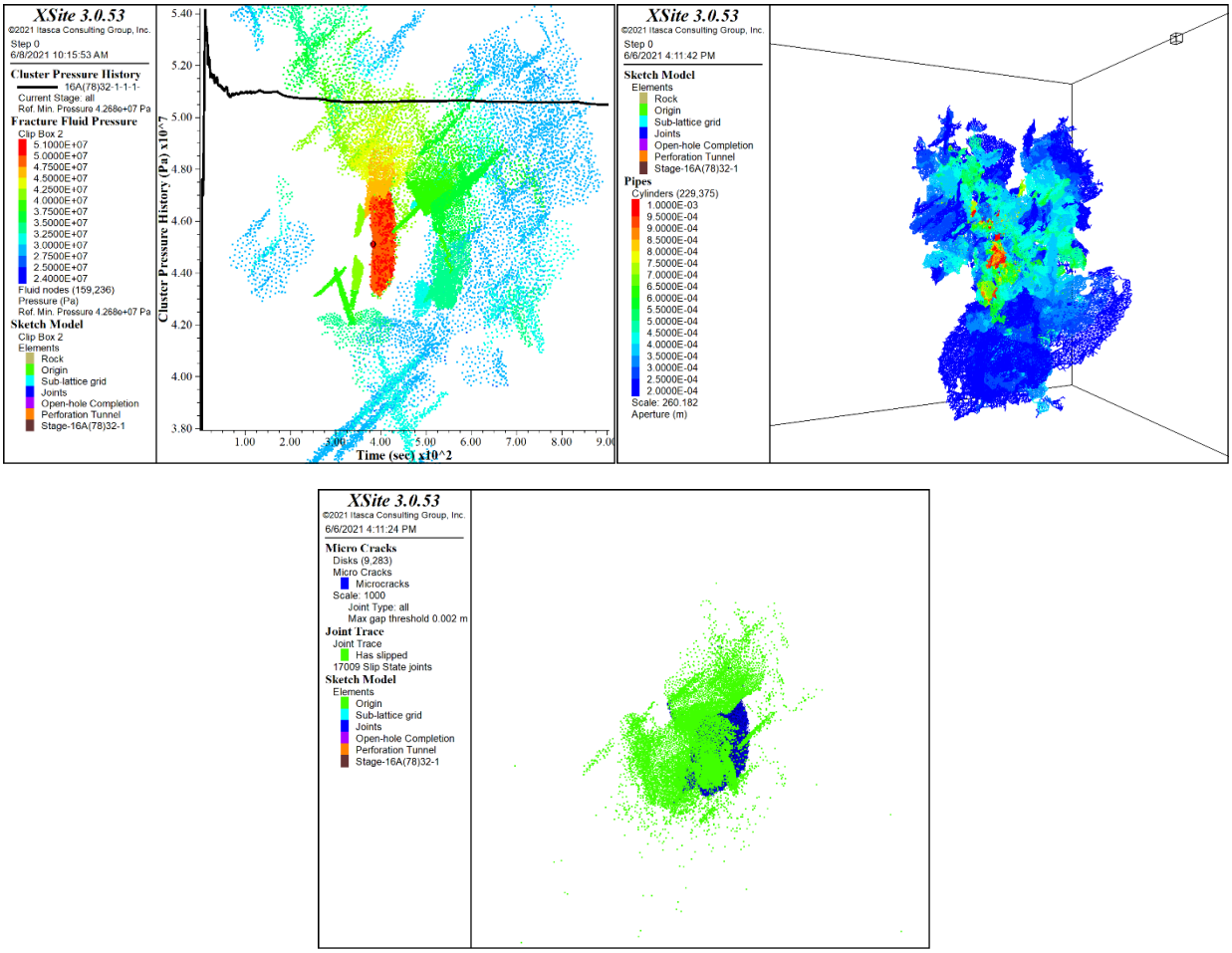

Figure 7. Simulation results of Case 3: 40 bpm for 15 minutes, no dilation of DFN. Top left: fluid pressure; top right: fracture aperture; bottom: newly created hydraulic fracture (blue) and natural fractures that have slipped (green).

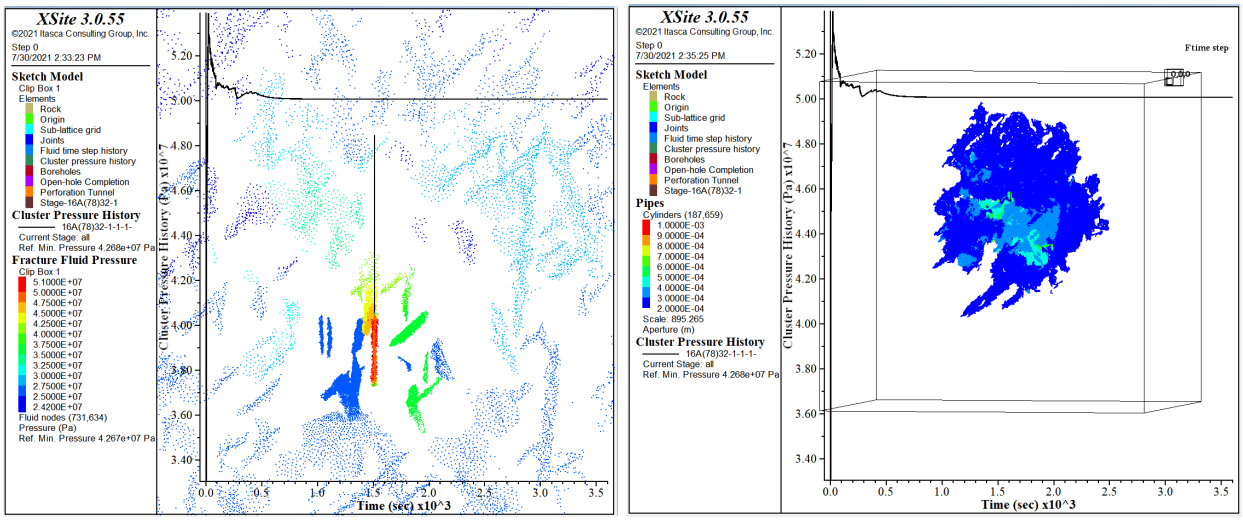

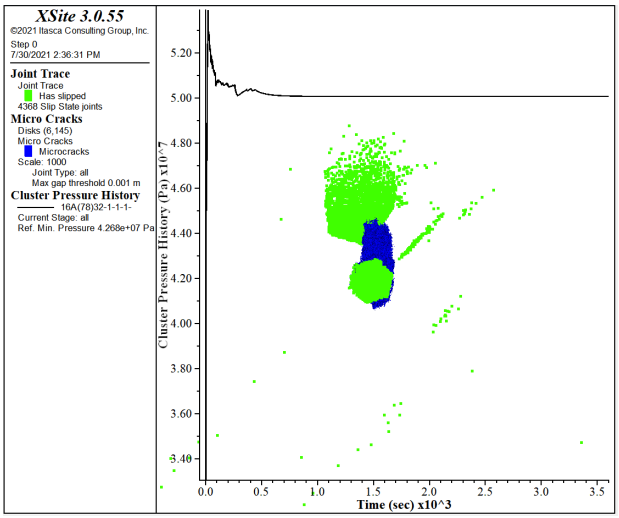

Figure 8. Simulation results of Case 4: 10 bpm for 60 minutes, no dilation of DFN. Top left: fluid pressure; top right: fracture aperture; bottom: newly created hydraulic fracture (blue) and natural fractures that have slipped (green).

3.1.4 Effect of DFN strength

There are uncertainties in the strength of DFN. In the base model, DFN is weak with zero cohesion and zero tensile strength. In this case, a stronger DFN with a cohesion of 10 MPa and tensile strength of 2 MPa is investigated. Friction angle is fixed as 37º. The DFN is also assumed impermeable in-situ. The DFN fractures become permeable only after they fail in tension or shear. The results for stronger DFN are shown in Figure 9.

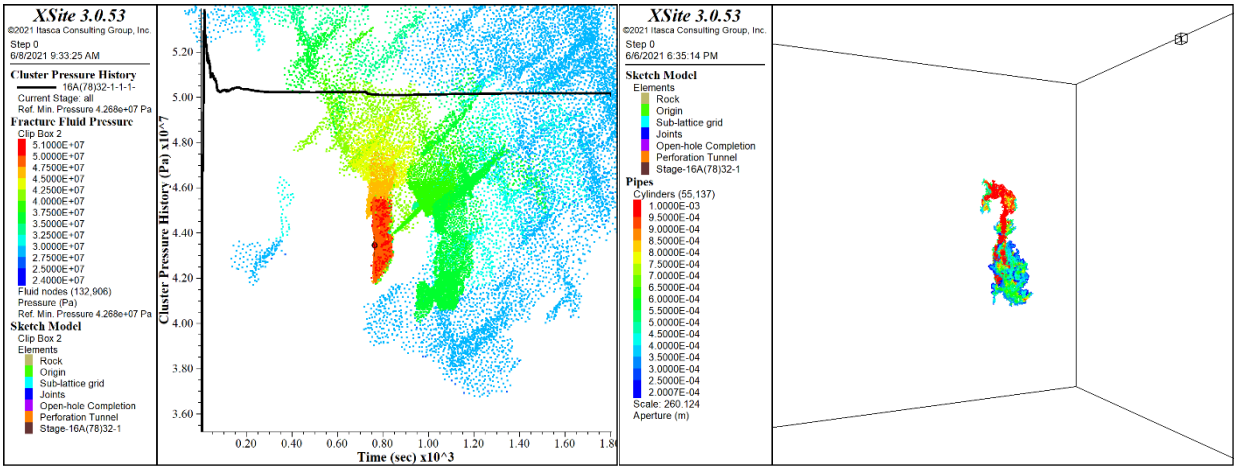

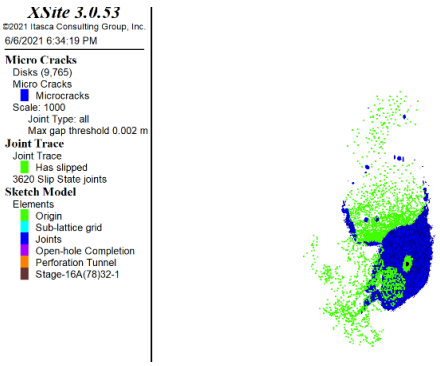

Figure 9. Simulation results of Case 5: 20 bpm for 30 minutes, no dilation of DFN, stronger DFN (cohesion 10 MPa, tensile strength 2 MPa). Top left: fluid pressure; top right: fracture aperture; bottom: newly created hydraulic fracture (blue) and natural fractures that have slipped (green).

The treatment pressure with "stronger" DFN is slightly lower than the case with weak DFN. The area of the fractures with induced apertures greater than 0.2 mm and the area of pressure change is much smaller than the cases with weak DFN. As expected, the area of slipping DFN fractures is smaller due to high cohesion. However, the area of open fractures is much larger than the cases with weak DFN and is even larger than the area of slipping DFN fractures.

3.1.5 Effect fluid viscosity

Fluid viscosity is another important parameter that can be varied during the injection. The viscosity in the base model is 2 cP. Figure 10 shows the results for a case with a larger fluid viscosity of 20 cP. The pumping rate is 20 bpm for 30 minutes. The areas of aperture greater than 0.2 mm and the area of pressure change are much smaller than for the cases with 2cP fluid viscosity because the fluid dissipation is slower for a fluid with higher viscosity (20 cP). However, the areas of both open and slipping fractures are much larger than the cases with smaller fluid viscosity.

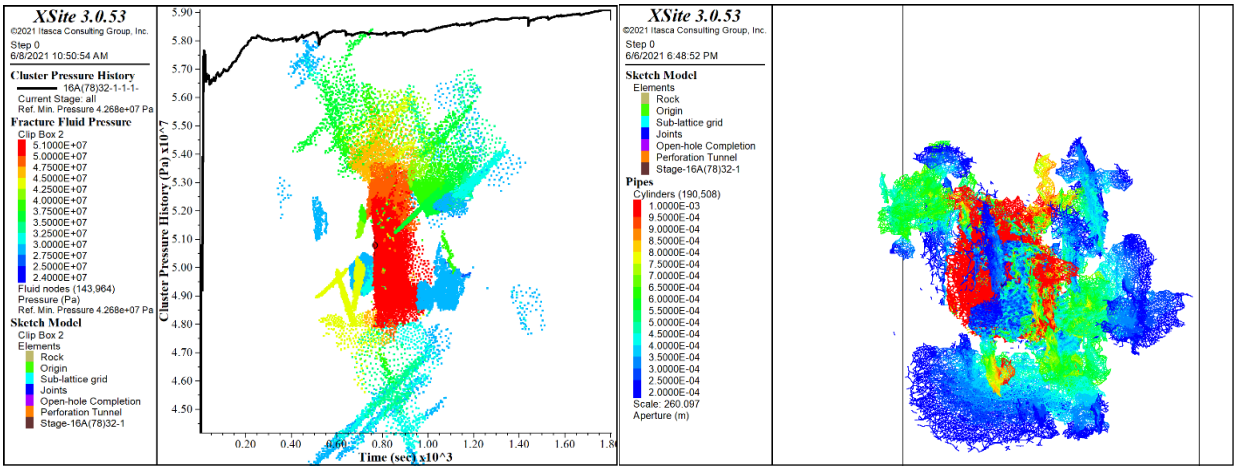

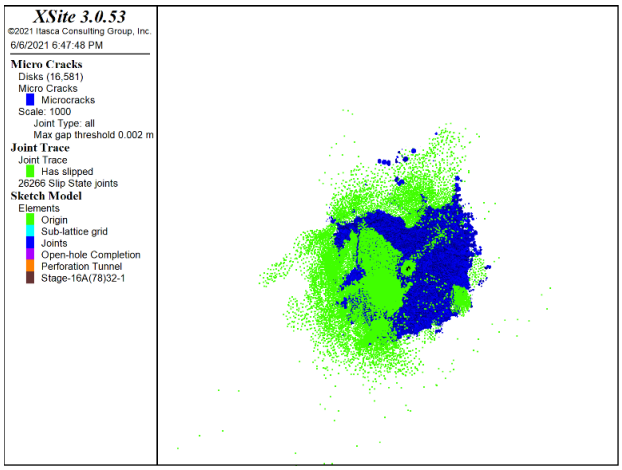

Figure 10. Simulation results of Case 6: 20 bpm for 30 minutes, no dilation of DFN, weak DFN, fluid viscosity 20 cP. Top left: fluid pressure; top right: fracture aperture; bottom: newly created hydraulic fracture (blue) and natural fractures that have slipped (green).

3.2 Summary and Discussion of the Results

A series of simulations for well 16A(78)-32 have been conducted. For the natural fracture networks considered, the formation response to injection was dominated by the DFN. For the base model, the pumping rate is 20 bpm, pumping time is 30 minutes, fluid viscosity is 2 cP. In the base model, the resulting net injection pressure is 7.5 MPa, the height above the injection point defined by induced apertures greater than 0.2 mm is 235 m and the height defined by open fractures is 30 m. The lateral extent of stimulated area with aperture greater than 0.2 mm is 130 m.

Table 1 summarizes fracture height, slipping fracture area, open fracture area, and lateral extent for all the cases. For the cases with a 2° dilation angle for DFN, the net fluid pressures are lower than those without dilatancy because natural fracture permeability increased due to aperture increasing during slip. Generally, the cases with DFN dilatancy resulted in a smaller area of DFN failing in tension but approximately the same slipping area compared to those simulations without dilatancy. Case 2 with weak DFN and dilation has the smallest area of open fractures. For similar net pressure, slippage of natural fractures tends to impede the opening. Case 6 with higher viscosity (20 cP) has the largest area of slipping fractures and largest area of open fractures because it has much larger net pressure. Case 6 with higher fluid viscosity has the highest pressure and Case 3 with DFN dilation has the smallest pressure. Due to stronger DFN with high cohesion, Case 5 has the smallest area of slipping fractures. In this case the network of connected hydraulic fracture and open DFN extends more than 100 m above the injection point.

Table 1. Summary of the simulation results

Case	Height (m) of aperture > 0.2 mm	Area (m^2) of aperture > 0.2 mm	Height (m) of slip	Slip area (m^2)	Height (m) of open fracture	Open fracture area (m^2)	Lateral extent (m)
Case 1: 20 bpm, 600 bbl, 2 cP, no dilation, weak DFN	235	3.18E+05	93	9700	73	5730	130
Case 2: 20 bpm, 600 bbl, 2 cP, 2° dilation, weak DFN	235	3.00E+05	93	9441	73	4123	134
Case 3: 40 bpm, 600 bbl, 2 cP, no dilation, weak DFN	193	2.87E+05	92	19356	73	9134	125
Case 4: 10 bpm, 600 bbl, 2 cP, no dilation, weak DFN	280	3.53E+05	75	4329	50	2529	131
Case 5: 20 bpm, 600 bbl, 2 cP, no dilation, strong DFN	110	1.26E+05	108	3999	108	8844	33
Case 6: 20 bpm, 600 bbl, 20 cP, no dilation, weak DFN	121	1.32E+05	93	30137	82	23897	88

There are three indices related to the height of the stimulated fractures above the injection point for the stimulation. The first one is defined by induced fracture apertures that are greater than 0.2 mm; the second one is defined by the slipping of DFN fractures; and, the third one is defined by the open state of fractures. For Cases 1 through 4 with weak DFN and smaller viscosity, the fracture heights defined by the aperture threshold are much greater than those defined by fractures slipping or open state. For Case 5 with stronger DFN, these three fracture height indices give similar results, and the fracture height defined by fracture open state is much larger than those cases with weak DFN.

4. Conclusions

Injection well 16A(78)-32 has been drilled at the FORGE site. Hydraulic fracturing will be carried out near the toe to create a sustainable hydraulic communication between the injection and production wells. Simulations of stimulation for injection well 16A(78)-32 have been conducted. These simulations are based on the DFN constructed from image logging and deep acoustic log interpretations from this well and the offset wells.

The model has been calibrated by pressure history matching the injection tests in well 16A(78)-32. The calibration helps constraining the material properties and initial stress conditions. The pressure trend during the injection is largely affected by the fluid flow and pressure dissipation in the DFN.

These simulations show forward predictions of the formation response to injection in well 16A(78)-32 for the current interpretation of the DFN. In all the cases, the formation response is dominated by the DFN, and failure is the combination of fracture open and natural fracture slipping. For the base model, the pumping rate is 20 bpm, the pumping time is 30 minutes, and the fluid viscosity is 2 cP. The resulting net treatment pressure is 7.5 MPa, the height of stimulated

fractures above the injection point, defined by induced aperture greater than 0.2 mm, is 235 m, the lateral extent is 130 m, and the height of stimulated fractures defined by open fractures is 73 m.

For the cases with a 2° dilation angle for the natural fractures, the net fluid pressures are lower than those without dilatancy. Increasing the pumping rate from 20 bpm to 40 bpm resulted in a larger area of open and slipping fractures while decreasing the pumping rate from 20 bpm to 10 bpm resulted in a smaller area of open and slipping fractures. For the case with a "stronger" DFN (10 MPa cohesion), the area of slipping fractures is smaller but the area of open fractures is larger. Increasing fluid viscosity from 2 cP to 20 cP resulted in a much higher injection pressure and hence larger area of slipping and open fractures.

Acknowledgement

Funding for this work was provided by the U.S. DOE under grant DE-EE0007080 "Enhanced Geothermal System Concept Testing and Development at the Milford City, Utah FORGE Site." We thank the many stakeholders who are supporting this project, including Smithfield, Utah School and Institutional Trust Lands Administration, and Beaver County, as well as the Utah Governor's Office of Energy Development.

REFERENCES

Damjanac, B., C. Detournay, and P. Cundall. "Numerical Simulation of Hydraulically Driven Fractures", in S. Baotang, O. Stephansson, & M. Rinne (Eds.), *Modelling Rock Fracturing Processes (2nd ed.), (2020),* pp. 531–561. Springer, Cham.

Moore, J., McLennan, J., Allis, R., Pankow, K., Simmons, S., Podgorney, R., Wannamaker, P., Bartley, J., Jones, C., Rickard, W. "The Utah Frontier Observatory for Research in Geothermal Energy (FORGE): An International Laboratory for Enhanced Geothermal System Technology Development." *In Proceedings of the 44thWorkshop on Geothermal Reservoir Engineering, Stanford University, Stanford, CA, USA, 11–13 February (2019).*

Itasca Consulting Group, Inc. 2020. *XSite* (Version 3.0.48). Minneapolis: Itasca.

Xing, P., B. Damjanac, Z. Radakovic-Guzina, A. Finnila, R. Podgorney, J. Moore and J. Mclennan. "Numerical Simulation of Injection Tests at Utah FORGE Site." *In Proceedings of the 46th Workshop on Geothermal Reservoir Engineering, Stanford University, Stanford, CA, USA, February 16-18, (2021a).*

Xing, P., B. Damjanac, Z. Radakovic-Guzina, A. Finnila, R. Podgorney, J. Moore and J. Mclennan. "Numerical Simulation of Hydraulic Fracturing Stimulation of the Enhanced Geothermal System Well at Utah FORGE Site." *In 55TH US ROCK MECHANICS / GEOMECHANICS SYMPOSIUM, online, June 18-25, (2021b).*

Xing, P., Winkler, D., Swearingen, L., McLennan, J. and Moore, J. "In-Situ Stresses and Permeability Measurements from Testings in Injection Well 16A(78)-32 at Utah FORGE Site." *GRC Transactions, Vol. 45, (2021c)*.

Analytical Model for Fluid Flow Distribution in an Enhanced Geothermal Systems (EGS)

Pranay Asai[1], Robert Podgorney[2†], John McLennan[1], Milind Deo[1], Joseph Moore[3]

1. Department of Chemical Engineering, University of Utah

2. Idaho National Laboratory, Idaho Falls, Idaho

3. Energy & Geoscience Institute, University of Utah

[†]Corresponding author

Abstract

Enhanced geothermal system (EGS) is often envisioned to consist of at least two wells spaced sufficiently apart and connected by ~~hydraulic~~ fractures that serve as flow paths. All the flow paths must be utilized efficiently to ensure the system is operated at its highest potential. However, building an efficient and sustainable EGS is a complicated process as the fluid always chooses the path of least resistance, which can lead to uneven flow distribution among the fracture zones.

This study focuses on several critical parameters related to well designs, which can potentially allow for optimized flow distribution. An analytical model is developed based on Kirchhoff's law to calculate the flow distribution in any doublet EGS. Wellbore perforations in the completed wellbores and the fractures are simulated as resistance while the fluid is simulated as a current analog. The model solves the pressure at each node, analogous to voltage, using pipe flow equations and Darcy's law. The model then calculates the flow rate for the next step by solving the set of equations implicitly. This process is continued until convergence is achieved.

Three different doublets EGS designs (parallel, anti-parallel and non-parallel) were simulated using the model, and a detailed sensitivity study was performed. The results for all the cases were compared using the pressure head loss and deviation from ideal flow (equal) distribution in the

fractures. It was observed that the anti-parallel and non-parallel designs performed the best, both leading to better flow distribution and having lower pressure losses.

1. Introduction

Understanding fluid flow distribution in a multi-fractured Enhanced Geothermal System (EGS) is essential for sustainable and efficient heat recovery from the engineered reservoir[1]. The heat from this thermally conductive reservoir[2, 3] can be recovered using an EGS operated in an artificially engineering heat exchange system. A colder fluid is injected into the hydraulically generated fractures in the thermal reservoir, where it acquires heat from the fractured rocks and is pumped back to the surface. A typical EGS reservoir is envisioned to consist of multiple fracture zones to increase the accessible surface area for heat extraction. Depending on the design of the EGS and subsurface conditions, some fractures might receive more fluid than others, leading to uneven drawdown/depletion of heat from the reservoir. One of the fractures near the heel of the well could grow big enough and end up taking all the fluid, also known as short-circuiting. Having a better understanding of flow distribution in a multistage, fractured system would help design efficient EGSs and increase their longevity[4, 5].

The flow in either an injection or production wellbore can be described primarily by the Poiseuille flow[6] equations, while the flow in the fractures can be approximated using Darcy's law[7, 8]. These two sets of equations can be solved iteratively using a node-loop method[9, 10] to determine the fluid distribution in multiple fractures that make up an EGS. This problem is similar to flow distribution in a network of pipes laid around a city block to distribute water to households. Some of the complexity of the problem arises due to the dependence on friction factor, Reynolds' number, and surface roughness in the pipe flow. Due to this, it is necessary to solve the equations iteratively to arrive at a converged solution. This is analogous to current distribution in a circuit consisting of multiple branches and resistors. The maximum current passes through the path of least resistance, leading to uneven current distribution in the system. Solving for current

distribution in a circuit is relatively simple since the resistance of a resistor is not a strong function of the current flowing through it. However, unlike resistors, the friction factor used for predicting turbulent flow in a pipe or fracture is susceptible to the flow rate of the fluid. This requires a sophisticated method to solve the equations which will be discussed in this study.

Cross[11] proposed two efficient methods to solve water flow distribution in a network of pipelines. He proposed a "Method of Balancing Heads" and a "Method of Balancing Flows" that can be applied to a closed flow network. The "Method of Balancing Head" requires an initial guess for flow rates in each pipe, making sure the amount of fluid at every junction is conserved. Using the flow rates in the pipes, the pressure head at each intersection can be calculated. The net head loss should be zero for every closed system of pipes. Consequently, the flow rates in the pipes are changed iteratively until this condition is satisfied. Conversely, in the "Method of Balancing Flows," the initial pressure head is guessed at each junction and then is solved for the flow rates in the pipes. As the total mass of fluid at the junction is conserved, the pressure heads are changed iteratively until the condition is satisfied. Thus, either of these methods can be used to solve for flow distribution in a network of pipes.

In an isolated doublet EGS, consisting of two wells connected by multiple fractures, numerous fluid distributions are possible, assuming that the total mass of fluid is conserved. However, only one of those distributions would also follow the law of conservation of energy, thus giving us a unique solution for a given system. The EGS itself is a dynamic system and adds further complexities to solving for flow distribution. In this study, the thermal and mechanical effects of the reservoir are not considered. The system is assumed to be isothermal, and no stresses on the fractures or the reservoir are considered, which would allow studying a static system with fixed permeabilities for the fractures.

2. Objective of the study

The study aimed to create an analytical model for predicting the flow distribution in a multi-fractured doublet EGS. A doublet system constitutes an injection and a production well interconnected by multiple fractures along their lengths. After the fluid is pumped into the injection well, it passes through the fractures, extracting heat from the reservoir that is eventually produced via the production well[12]. The heat extraction from each fracture (or network of collaborating fractures) is directly proportional to the fluid flowing in that zone[13, 14]. The fractures with the higher flow would locally deplete the thermal reservoir faster and experience localized early thermal breakthrough [15]. The fractures with the higher flow would cool more rapidly, leading to increased conductivity due to thermal contraction. This makes the effect self-catalytic and further increases the flow rate in the cooler fracture(s). Other than the conductivity of the fractures, there are other completion parameters like diameter of the wellbore, number/size of perforations, and orientation of the wellbore, which play a crucial role in determining the flow distribution in a doublet EGS.

The analytical model developed in this study builds on the previous research conducted by Asai et. al.[16]. The model is built on the premise of Kirchhoff's law of current and voltage conservation for a closed system. The previous study shows that in a multi-fractured doublet system with identical fracture conductivities, the first few fractures near the heel would take the most fluid, and the last few fractures near the toe would not get much of the injectate.

The developed model is more robust and can be used for any kind of doublet system. It can incorporate various frictional losses like inside the wellbore, perforations, and pressure losses across the fracture zones. In the model. the EGS is represented as a closed system with pressure at

the junctions being analogous to the voltage, flow rate being analogous to the current, and the frictional resistance is equivalent to the resistance in the circuit. The aim is to solve for the flow rate in each fracture flow path depending on the frictional pressure drop in the system. This study strictly focuses on the distribution of the fluid in the fractures and the factors affecting them. The system is considered to be isothermal to avoid any complexity introduced by thermo-hydraulic coupling. Hence, no heat equations are required to solve the flow distribution in the fractures.

3. Doublet EGS Designs

The doublet EGS system consists of two wells drilled into the subsurface and connected by multiple fractures along their length. Depending on the trajectories of the two wells with respect to each other, they can be further classified into subcategories. In this study, three doublet EGS designs are considered: parallel doublet, anti-parallel doublet, and non-parallel doublet.

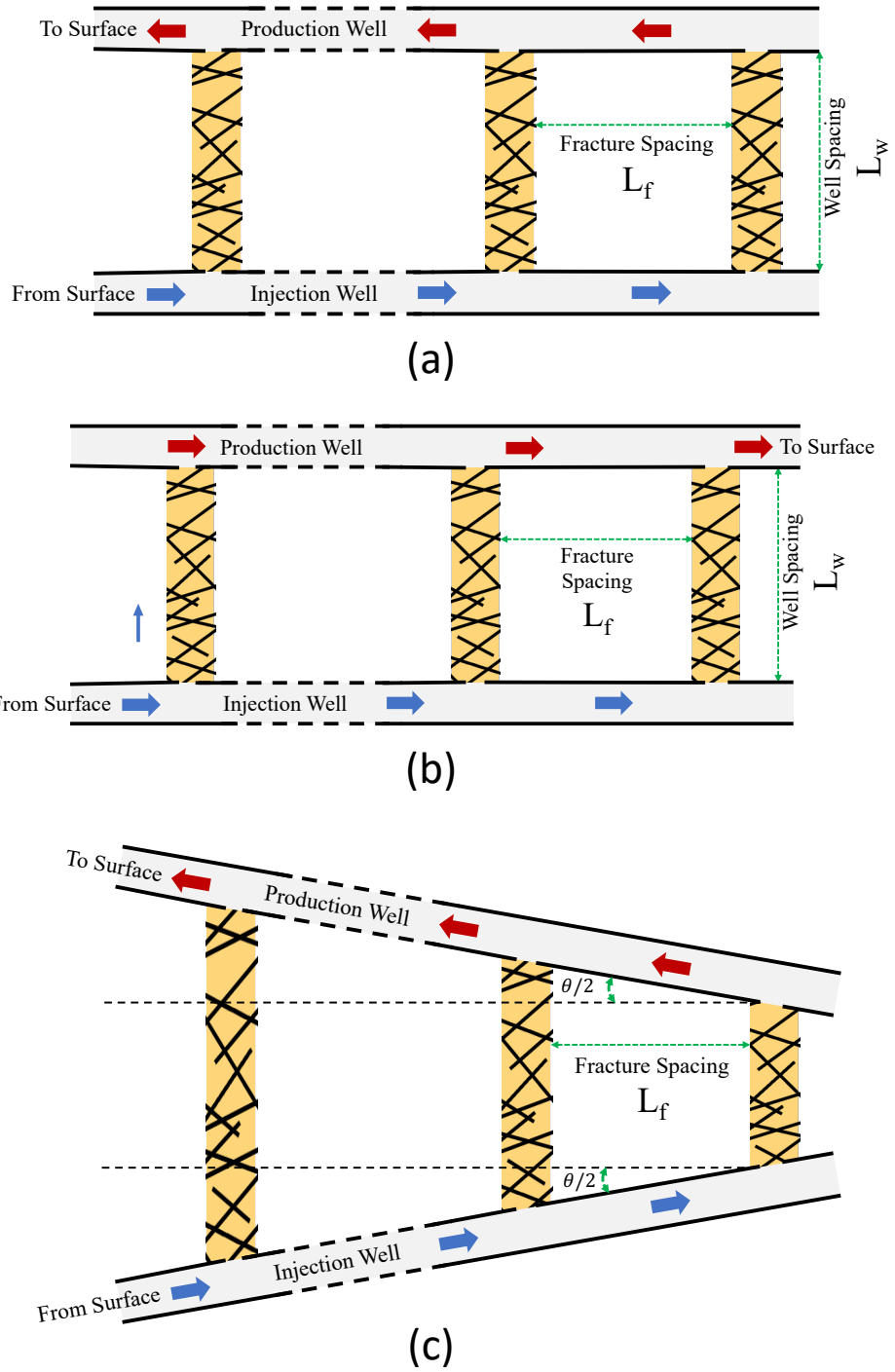

Figure 1: Schematic of different doublet well designs drilled in the xy-plane (elevation view) and passing through multiple fracture zones: (a) Parallel well doublet system, (b) Anti-parallel well doublet system, (c) Non-parallel well doublet system

The parallel doublet system (Figure 1a) has the injection and production wells drilled in the same direction and plane. The wells are connected by multiple (nominally vertical) fracture zones, with constant fracture spacing (fracture spacing "L_f")between them. The distance between the two wells (well spacing, "L_w") is constant throughout the lateral extent of the wells, thus fixing the length of the fracture zones. The anti-parallel doublet system (Figure 1b) is similar to the parallel system in terms of the well and fracture spacing, except the direction of the production well is reversed relative to the injection well (aligned heel to toe). The anti-parallel setup has some advantages and disadvantages, which will be discussed later. The third setup is a non-parallel doublet system (Figure 1c), which has the production well placed at an angle with respect to the injection well. Both the wells are deviated differently by "$\theta/2$" from the horizontal to create a total deviation of "θ" with respect to each other. This angular orientation leads to the variable well spacing between the two wells, causing connecting fracture zones to have different lengths.

Fracture zones are used in this model to represent the connection between the injection and the production well. These are represented as permeable zones with uniform permeability and are defined as cuboidal shapes with length (distance between wells), height, and width (see Figure 2). The surrounding reservoir is assumed to have negligible permeability to ensure no fluid is lost from the system. This is a standard reservoir engineering approximation, where infinite conductivity in a finite aperture fracture (often approximated by pseudo-parallel plate flow) is simplified to finite permeability acting over an artificially wide flow zone.

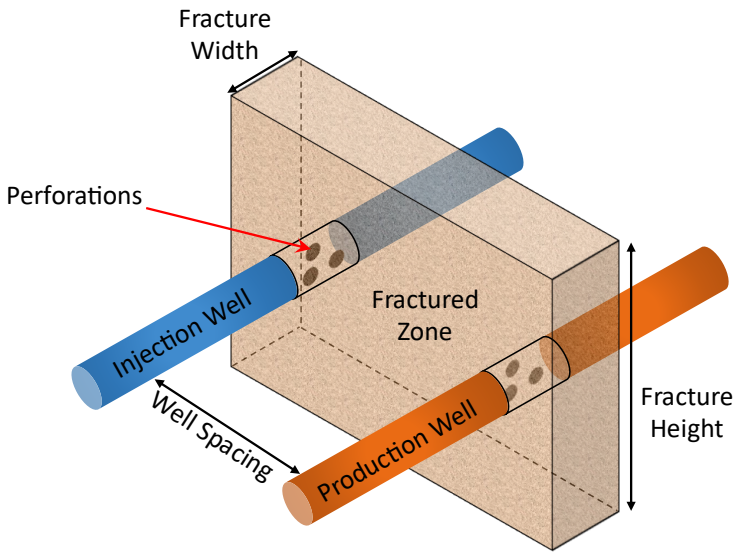

Figure 2: Schematic of wellbores connected to the fracture through perforations.

To perform a comparative study between these three well setups, all the designs were assumed to be drilled in the xy-plane so that gravity effects could be neglected. The number of fractures in all the cases was kept constant. The wells are also assumed to be entirely cased and perforated in single clusters (see Figure 2) at locations intercepting the fractures to allow fluid to move in and out of the fracture zones.

4. Development of the model

The premise of the model is built around Kirchhoff's law of current and voltage[17]. As per Kirchhoff's law, in a closed circuit consisting of multiple pathways, the current flow distribution is based on the resistance present in any given path. The current preferentially flows through the path of least resistance.

The fluid flow in a doublet EGS is analogous to the current flow inside a circuit. The pressure at each node/point is equivalent to the voltage at the nodes. The frictional losses encountered are

analogous to resistance. Since the EGS is also operated under a closed system (assuming no fluid losses), we can apply Kirchhoff's current and voltage conservation law. This allows us to enforce three criteria for the analytical model:

i. The total mass flow rate of fluid entering a node equals the total mass flow rate leaving the node.
ii. The fluid in any branch would flow from a higher potential node to a lower potential node.
iii. The directed sum of potential difference (pressure) in a closed system is zero.

In the doublet EGS system, resistance to the flow would be caused by the friction inside the pipe, pressure drop in the perforations, and flow resistance within the fracture zones themselves. The analogy of Kirchhoff's law dictates that the fluid flowing in a multi-fractured EGS would always choose the path of least resistance.

There would be no pressure drop along the length of the wells in an ideal scenario where there are no frictional losses in the wellbore (e.g., inviscid simplifications). This would lead to an equal pressure difference across each fracture zone in the system in the absence of potential energy considerations. Also, if all the fracture zones are identical (have the same permeability), this would lead to equal distribution of fluid in each fracture. However, such an ideal scenario is impossible. The model developed in this study also allows us to introduce the non-ideality of the EGS, thus creating a realistic model of the EGS. Apart from the flow resistance introduced by pipe, fractures, and perforations, the frictional resistance is also a function of the flow rate itself. As is well known, this requires the system to be solved iteratively to obtain the final flow distribution[9].

4.1 Mathematical representation of the model

The model solves for the fluid flow distribution in the fractures at a steady state. This is done by mathematically representing all the flow resistances, setting the injection pressure and the total flow rate in the system. The equations are solved implicitly to determine the flow distribution. For a doublet EGS consisting of "n" number of fractures, the analytical model is set up as follows:

i. Each point where a fracture intercepts a well is considered a *fracture node (see figure 3)*. Thus, a doublet system consisting of 'n' fractures would have "2n" fracture nodes.

ii. There are two additional nodes to specify the inlet and outlet for an EGS system. These nodes act as a reference to the entire model and are referred to as the *reference nodes*. The number of reference nodes is equal to the number of wells in an EGS.

iii. The connection between a perforated zone and the associated fracture is defined as an intermediate node.

iv. Three resistances are considered in this model. These are the resistance of flow in the pipe ("R_i" for the injection well and "R_o" for the production well), the resistance of flow entering and exiting the fracture ("R_{ip}" for the injection well perforations and "R_{op}" for the production well perforations), and resistance to the flow in a fracture zone ("R_f").

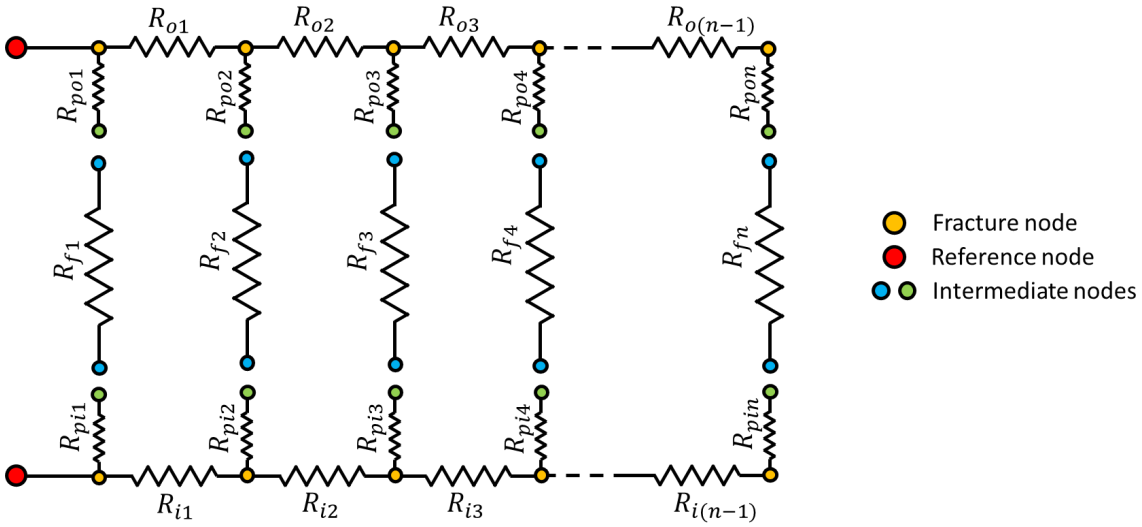

Figure 3: Circuit diagram representing a doublet EGS with n fractures.

Once the model is set up, the frictional pressure drop (resistance) in a branch is calculated using an appropriate formulation, which is chosen depending on the flow rate and type of resistance (perforations, fracture, or pipe). The frictional pressure drop (ΔP_{pipe}) in a section of the pipe is calculated using the Hagan-Poiseuille[6] flow equation (Eq 1), and the friction factor in the pipe section is calculated using Haaland's [18] relationship (Eq 2).

$$\Delta P_{pipe} = f_h \frac{2L_f}{D} \rho \left(\frac{q}{A}\right)^2 \quad \text{Eq 1}$$

$$\frac{1}{f_h} = -1.8 \log\left[\left(\frac{\frac{\varepsilon}{D}}{3.7}\right)^{1.11} + \frac{6.9}{Re}\right] \quad \text{Eq 2}$$

where, "f_h" is Haaland's friction factor, "L_f" is the distance between two fractures, "D" is the diameter of the pipe, "ρ" is the density of the fluid, "q" is the flow rate through the section of the pipe, "A" is the cross-sectional area of the pipe, "Re" is the Reynolds' number, and "ε" is the relative roughness of the pipe. The pressure drop across the fracture zone (ΔP_{frac}) is inferred using Darcy's law (Eq 3).

$$\Delta P_{frac} = q \frac{\mu L_w}{kA} \quad \text{Eq 3}$$

where "q" is the flow rate through the fracture zone, "L_w" is the length of the fracture zone (distance between two wells), "k" is the effective permeability of the fracture zone, "A" is the cross-sectional area of the fractured zone and "μ" is the dynamic viscosity of the fluid. The pressure drop through perforations ($\Delta P_{o_{perf}}$) is calculated using Weddle[19] and Cramer[20] relationships (Eq 4).

$$\Delta P_{o_{perf}} = 0.2369 q_o^2 \frac{\rho_o}{N_p^2 D_{p_o}^4 C_d^2} \quad \text{Eq 4}$$

Equation 4 is represented in oilfield units, where "N_p" is the number of perforations, "D_{p_o}" is the diameter of perforation and "C_d" is the coefficient of discharge. The coefficient of discharge is a function of relative perforation size, the diameter of the pipe, wall thickness, and flow rate and usually lies between 0.6 to 0.9[21]. For this study, a fixed value of 0.75 was chosen for the discharge coefficient[19, 22].

Figure 4 presents a flowchart indicating how the analytical model is solved to get fluid distribution in a multi-fractured EGS. The model is initialized by setting up the reference pressures for the injection well, the total flow in the system, and setting an equal flow distribution in all the fractures (calculated using total flow rate and the number of fractures). The pressure values on all the nodes of the injection well can be calculated by using the initial flow distribution and the Hagen-Poiseuille equation. Next, we solve for the new flow rates based on the pressure drop across all the fractures. These flow rates are then normalized to get a percent distribution to ensure the total flow rate values do not exceed the initially declared one. A conditional block checks if the new distribution matches the old distribution (within the defined tolerance). If the difference between the new and old flow distribution is within the specified tolerance, the new flow distribution is taken as the output; if not, the process loops again with the new flow distribution as the initial condition. The equations in the model are solved implicitly over an iterated loop until convergence is achieved.

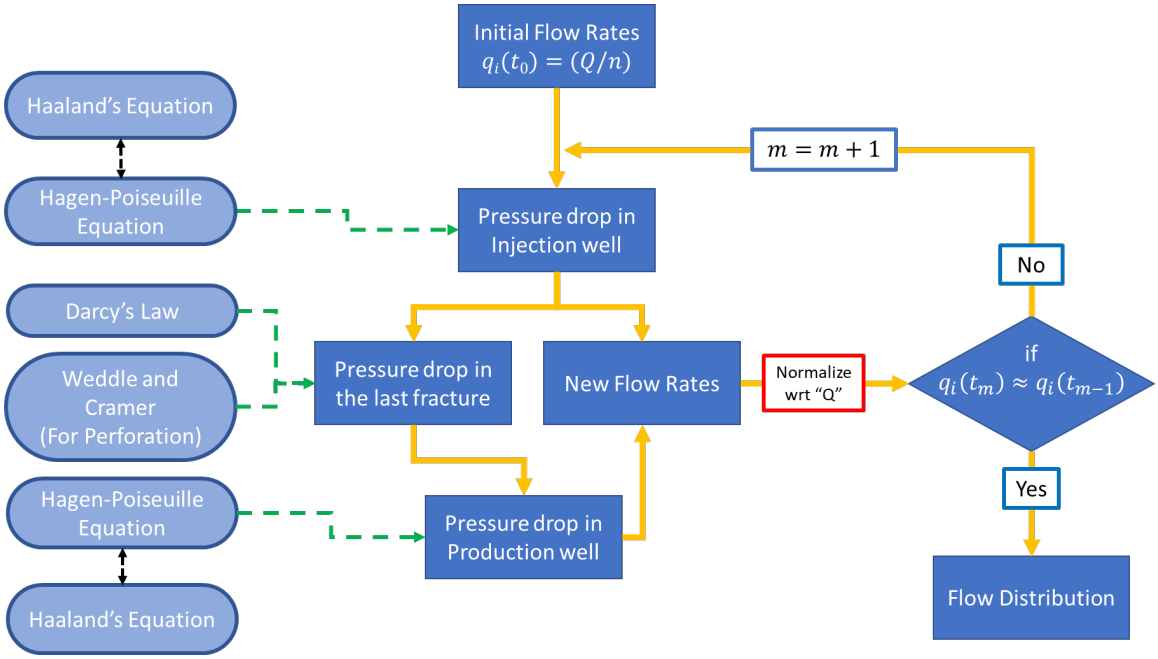

Figure 4: Flowchart represents the workings of the analytical model used to solve fluid flow distribution in a doublet EGS.

The main advantages of the model are that it is robust and could be used for any doublet EGS with different well orientations and trajectories. Furthermore, the methodology is easy to implement and derives a preliminary indication for any well design and configuration performance. It can also be used independently to solve for either the injection or the production well if there is pressure data at each node. This allows the model to be used in combination with computational fluid dynamic codes to get more accurate results.

4.2 Validation of the base model and effect of different parameters

The model for this study is similar to the FORGE EGS site in Milford, Utah[23, 24]. A "parallel" model consists of two wells inclined horizontally (although the wells at Milford are at an angle of 65° to the vertical) and connected by ten fractures. The wells are set 100 m apart vertically, and the fracture spacing is also set to 100 m. The total mass flow rate of water is set

to be 50 kg/s. The depth of the model is assumed to be 2000 m, and the injection pressure is set to be 1.5 times the hydrostatic pressure at that depth. The other properties of the model are shown in Table 1. Also, for this study, the "non-parallel" doublet system was set to have the length of the first fracture as 150 m and the last fracture as 50 m. This design forms multiple trapezoids with two consecutive fractures as the bases and the wellbores (sections) as the remaining two sides. Therefore, the total length of the fractures in the non-parallel case would be equal to the total length in the "parallel" and "anti-parallel" designs. Thus, making these models comparable to each other.

Table 1: Properties for the base case

Parameter	**Value**	
Flow rate	396832 lb/hr	50 kg/s
Diameter of the injection/production casing	6 in	0.1524 m
Injection pressure	4264.11 psi	29.40 MPa
Well spacing	328.08 ft	100 m
Fracture spacing	328.08 ft	100 m
Number of fractures	10	
Permeability	1 Darcy	$1 \times 10^{-12} m^2$
Width of the fracture zone	16.40 ft	5 m
Height of the fracture	328.08 ft	100 m
Number of perforations	10	
Size of perforations	0.375 in	0.009525 m

The parameters are used to validate the analytical model to ensure that the model is functioning correctly. Four different strategies were used to validate the model, as explained below. These validation tests were performed on all the doublet well designs.

5. Results and Discussion

After setting up all the parameters for the doublet well systems, the calculations are initiated with an equal flow distribution in each fracture. After each iteration, the new output values for the flow rates are added and averaged with the previous ones to calculate the next input. This was done to ensure the model does not get stuck between two oscillating values. For each case, the model ran 1000 iterative steps, ensuring convergence. Figure 5 documents the convergence for the anti-parallel well setup consisting of 10 fractures. In this figure, the two lines represent the flow rates in the first fracture (corner-blue color) and the fifth fracture (middle- orange color), at different iterative steps. It can be observed that the value of the flow rate converges to a constant value.

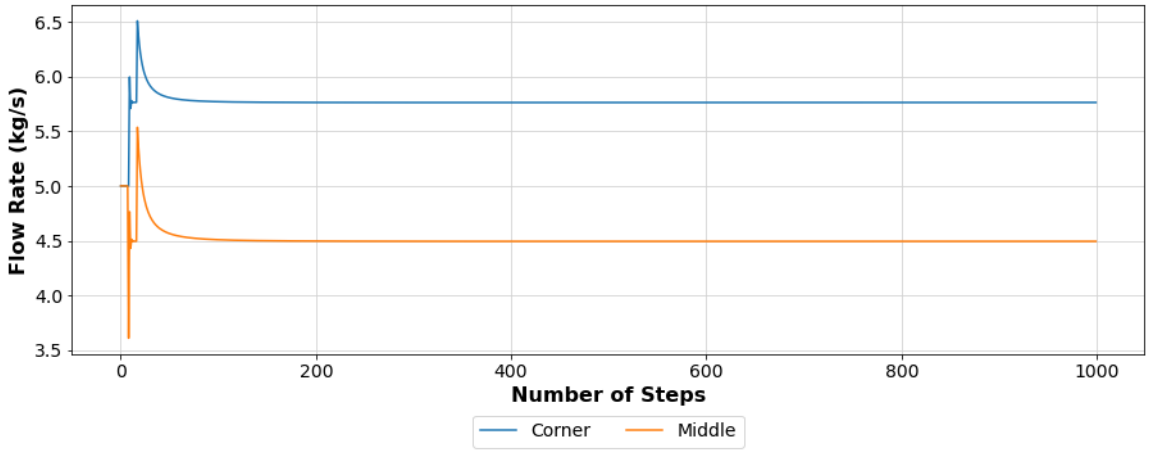

Figure 5: Convergence plot for flow rate values for anti-parallel doublet system.

5.1 Model validation

The analytical model was validated using four test cases. The first test case was frictionless pipe keeping the rest of the parameters at their base values. This creates a scenario with no pressure drop along the horizontal pipe. In this case, the "parallel" and "anti-parallel" doublet designs would have the same pressure drop across the fractures, giving equal flow rates in all fractures. This can

be observed in Figure 6(a). However, for the case of non-parallel wells, even though the pressure drop across each fracture is equal, the lengths of the fractures are different. Hence, the smallest fracture (at the toe) should have the maximum flow rate, and the largest fracture (at the heel) should have the minimum flow rate.

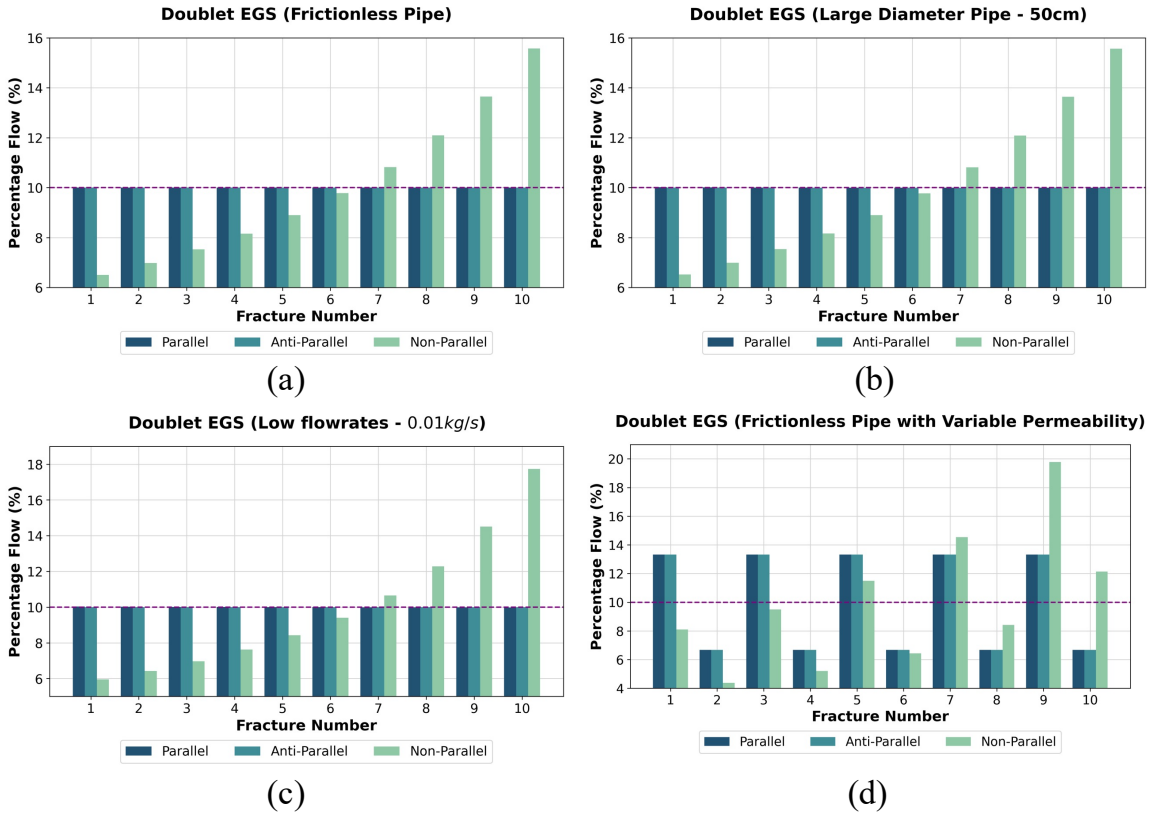

Figure 6: Flow distribution results for model validation using (a) Flow through frictionless wellbores, (b) Flow through 50cm diameter pipe, (c) Extremely small flow rates and (d) Flow through frictionless pipe and variable permeability system.

In the second test case, the internal pipe diameter was set to be 50 cm (not typical for an EGS wellbore). The larger diameter should allow better flow in the wellbore and reduce the overall friction coefficient. This case also leads to negligible pressure drop along the length of the pipe

and hence should give nominally equal flow in each fracture for the parallel and anti-parallel case and increasing flow distribution (when moving from heel to toe) for non-parallel case, see Figure 6(b).

In the third test case, the flow rate was set to a minimal value of 0.01kg/s. The lower flow rate leads to reduced friction. As expected, for this flow rate, it was observed that the wellbore becomes almost frictionless, Figure 6(c). Therefore, the results from this test case match the previous two.

In the fourth case, Figure 6(d), the permeability values for the odd-numbered fractures are reduced to one-half of the base value. Thus, despite having equal pressure drop across all the fractures, the flow rates in the odd-numbered fractures are higher than the even ones for the parallel and anti-parallel design. Reducing the permeability in half almost doubles the flow rates in those fractures. Also, all the odd (and even) numbered fractures have almost equal flow rates. For the case of non-parallel wells, due to different lengths of fractures, the longer fractures would have higher flow resistance and hence would allow less fluid to pass through them. This, combined with lower permeability, would further reduce the flow rate.

These results suggest that the model is robust and capable of evaluating various well designs to predict flow distribution. Also, it should be noted that despite all the four test cases lead to the frictionless flow in the wellbore, the method of eliminating the friction is different in each case.

5.2 Effect of perforation size on flow distribution

Different sensitivity studies were performed on the proposed well designs by varying relevant parameters. The first sensitivity included the effect of the size of the perforations in each zone, keeping the number of perforations constant (Table 2). According to Equation 4, the pressure drop

is inversely proportional to the square of the number of perforations and the fourth power of the size of the perforations, indicating that the size of the perforations affects the pressure drop more than the number of perforations. Hence, only the perforation sizes were varied for this study. Also, the total area of all of the perforations is equal to 10 times the area of each perforation (ten perforations simulated).

Table 2: Sensitivity study for effect of perforations in a doublet EGS

Case	1	2	3 (base)	4	5
Size of Perforation	0.125 in	0.25 in	0.375 in	0.625 in	1 in
Number of Perforations	10	10	10	10	10

The five perforation sizes shown in Table 2 were used for the three well-completion configurations, providing 15 evaluation scenarios in total. In all the doublet designs, the flow distribution was best for the smallest perforation size and worst for the largest ones, as shown in Figure 7 (a, b, c). The black dotted line represents the ideal distribution (equal flow distribution) for all the fractures. For small diameter perforations, limited entry forces the fluid to move down to the subsequent fractures, thus improving flow distribution. However, this restricted flow would lead to substantial frictional losses.

The extent of deviation of the flow distribution from an "ideal" case can be measured by calculating the root mean squared error (RSME). Deviation from the ideal flow distribution, by itself, is not an appropriate measure to compare the performance of different designs. It is also necessary to consider the pressure head losses (frictional losses) inside the system. The difference

between the injection and production pressure is calculated and divided by the density of the fluid (1000 kg/m^3) and the gravitational constant (9.8 m^2/s) to account for the pressure head loss. Using both the parameters together would allow the evaluation of the performance for a given design.

In Figure 7(d), the RMSE for the flow deviation is plotted against the pressure head losses for five different perforation sizes and three well designs. The best design should have the least pressure head loss and the least RMSE. The parallel well has the highest RMSE values compared to the other two well designs. Therefore, the anti-parallel well setup with 0.635- or 1-inch perforation entry diameters stands out as the best option. It should be noted that even though a 0.125-inch perforation diameter gives ideal flow for all three well designs, the pressure head values exceed 900 m, leading to substantial pumping costs.

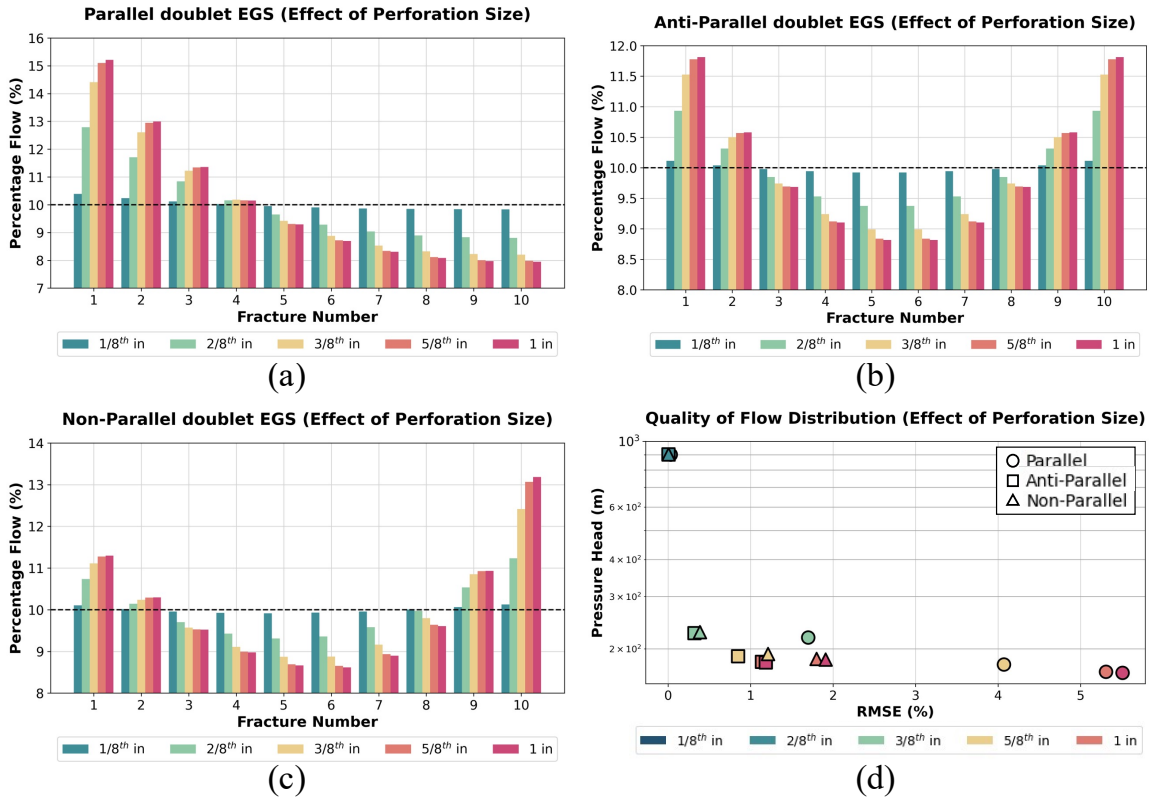

Figure 7: Results for effect of different perforation diameters on (a) Parallel doublet EGS, (b) Anti-parallel doublet EGS, (c) Non-parallel doublet EGS and (d) Quality of flow distribution.

5.3 Effect of fracture permeability on flow distribution

The second sensitivity case focuses on the equivalent permeability of the fracture zones (see Table 3). All evaluation parameters were set to the base case, and the perforation size was set at 3/8th of an inch. The permeabilities in this study were varied by the factor of 10 for three different cases.

Table 3: Sensitivity study for effect of permeability of the fracture zone in a doublet EGS

Case	1	2 (base)	3
Permeability of the fracture zone (m^2)	1×10^{-11}	1×10^{-12}	1×10^{-13}

In general, lower permeability fractures would have a greater resistance to flow, thereby essentially restricting fluid entry. As seen in Figures 8 (a) and 8(b), the lowest permeability value leads to a more uniform flow distribution. With the increase in the permeability value, the flow distribution in a parallel well is skewed towards the heel of the well. Alternatively, for the anti-parallel wells, the middle fractures receive less fluid than the corner ones with an increase in permeability. In a non-parallel design (Figure 8(c)), the first fracture - nearest the heel of the injection well - has the most restriction to the flow since it is the longest fracture. Hence, as the permeability increases, the flow restriction eases out, and the flow distribution improves for the scenario.

Figure 8(d) shows that a decrease in permeability for the fractures would lead to higher pressure head losses, which translates to higher pumping costs. But even at optimal permeability values, the non-parallel and anti-parallel scenarios outperform the parallel well design.

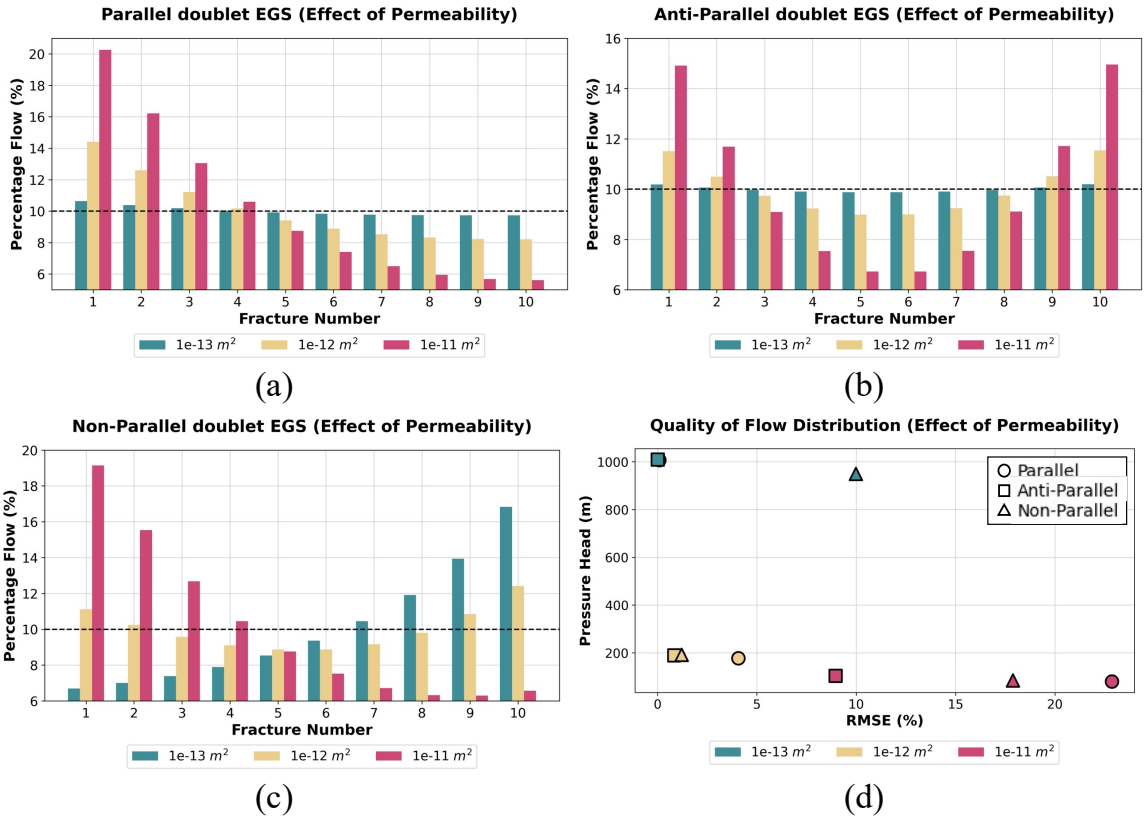

Figure 8: Results for effect of different fracture permeability on (a) Parallel doublet EGS, (b) Anti-parallel doublet EGS, (c) Non-parallel doublet EGS and (d) Quality of flow distribution.

5.4 Effect of Injection Rate

In the third sensitivity case, the flow rate was manipulated to observe the effect on the flow distribution in the doublet system. Three different flow rates were used along with other base parameters, as summarized in Table 4.

Table 4: Sensitivity study for effect of flow rate in a doublet EGS

Case	1	2 (base)	3
Flow Rate	25 kg/s	50 kg/s	75 kg/s

For this sensitivity evaluation, the results show that the flow distribution in the parallel well system, Figure 9(a), deviates further from the ideal and leads to relatively higher pressure head losses as the flow rate increased. In the anti-parallel design, Figure 9(b), the deviation from a uniform flow distribution is not significant, but the pressure head losses increase drastically with an increase in the flow rate. Interestingly in the non-parallel case, Figure 9(c), the increase in flow rate from 25kg/s to 50kg/s increases the pressure head losses but also improves the flow distribution. On further increase in the flow rate, both pressure head losses and RMSE increase. This would indicate that for a given deviation of wells ($\theta/2$ angle), there would be an optimal operating flow rate to ensure a more uniform flow distribution at a minimized or optimized pressure head loss. From Figure 9(d), it can be inferred that, for any given flow rate, the three designs have similar pressure drops; however, the anti-parallel designs outperform in terms of flow distribution.

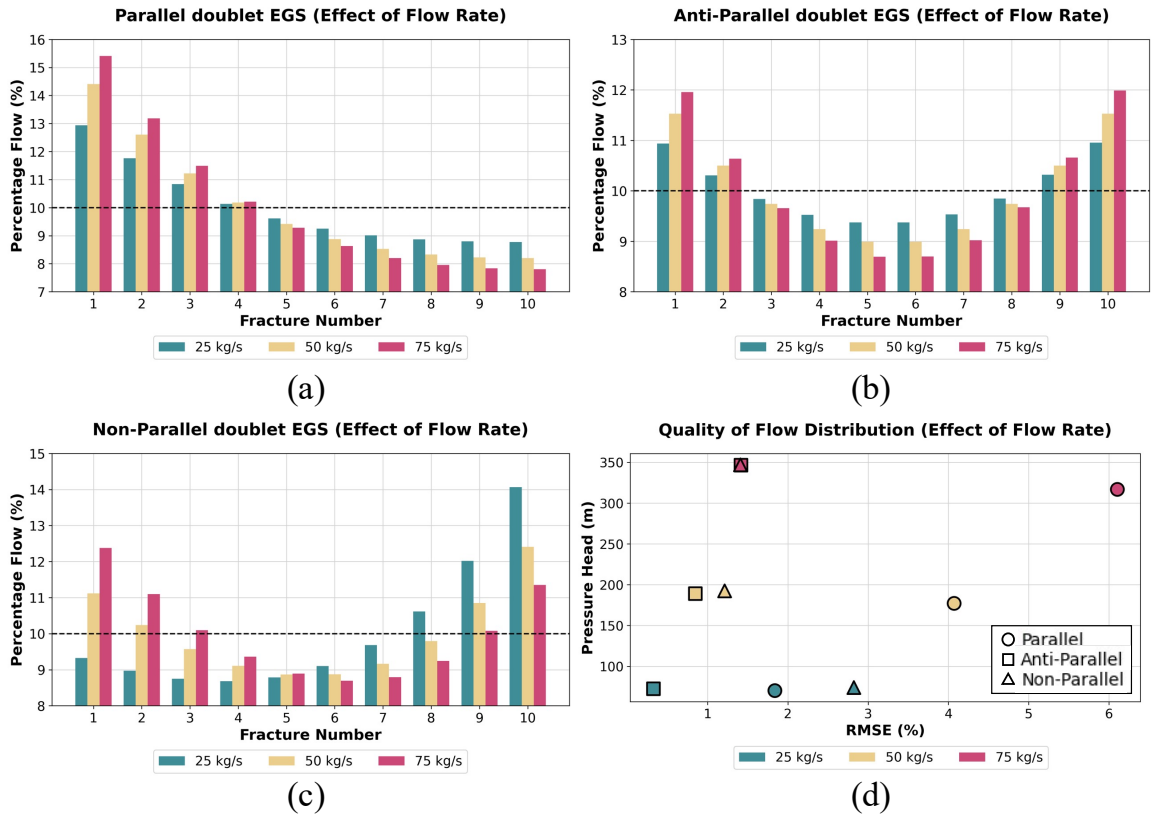

Figure 9: Results for effect of different flow rates on (a) Parallel doublet EGS, (b) Anti-parallel doublet EGS, (c) Non-parallel doublet EGS and (d) Quality of flow distribution.

6. Summary

For a multiple-fractured EGS with identical fracture conductivities, an anti-parallel design leads to a more uniform flow distribution compared to the other two designs. The counter flow in the production and injection well has symmetry about the central fracture (the fracture that is an equal distance from the heel and toe fractures), improving the flow distribution. Another advantage of using an anti-parallel well system is the reversibility in the flow direction. Changing the flow direction in the system would allow even heat extraction from the reservoir, thus increasing the overall efficiency.

The non-parallel design also gives better flow distribution with lower pressure drop. The system performance is optimized when the deviation of the wells is tailored to the reservoir and operational conditions. Any changes to the fracture zone permeability or the flow rate would lead to a skewed flow distribution. However, this sensitivity toward the flow rate could be used as an additional control variable to optimize the flow distribution throughout the lifecycle of the EGS, which is not feasible in the other two designs.

The parallel well EGS performed the poorest of all. The improvement in the flow distribution solely relies on creating a limited entry scenario (i.e., smaller diameter perforations near the heel of the injection well) at the fracture wellbore interface through smaller-diameter perforations, leading to increased pumping costs.

7. Conclusion

An EGS requires high capital investments. Hence it is crucial to have cost- and energy-efficient designs, which would lead to optimal fluid distribution in the system. This could reduce operating expenditures and prolong commercial production. The simplified analytical model created in this study can quickly predict the performance of any well design. The analytical model iteratively solves a system of equations for the flow distribution for a given doublet design, using flow resistance (in pipe, fractures, and perforations). This can narrow down the top well configurations. Later, performance can be assessed using sophisticated THMC (thermo-hydro-mechanical-chemical) simulators (such as Falcon[12, 25, 26]).

The results of our studies indicate that the anti-parallel and non-parallel designs performed the best. In a parallel well design, the improvement in the flow distribution solely depends on creating a limited/restricted entry situation. Whereas, in the anti-parallel well design, the counter-flow

direction of the wellbore facilitates a better flow distribution. In case of non-parallel design, the different length of fractures leads to better flow distribution.

The study can be further extended to be used for triplets or quintuplets well designs. The source code for the analytical model can be accessed at:

https://github.com/pranayasai/FlowDistribution[27]

8. Acknowledgment

The U.S. Department of Energy provided funding for this project, Office of Energy Efficiency & Renewable Energy under grant DE-EE0007080. We are grateful for their support.

This research used Idaho National Laboratory computing resources supported by the Office of Nuclear Energy of the U.S. Department of Energy and the Nuclear Science User Facilities under Contract No. DE-AC07-05ID14517.

9. Nomenclature

Symbol	Description	Units
A	$Cross-sectional\ area\ of\ the\ wellbore$	(m^2)
C_D	$Coefficient\ of\ discharge$	$-$
D	$Diameter\ of\ the\ well$	(m)
D_p	$Diameter\ of\ the\ perforation$	(m)
D_{p_o}	$Diameter\ of\ the\ perforation\ (oil\ field\ units)$	(in)
f_h	$Haaland's\ friction\ factor$	$-$
K	$Permeability\ of\ the\ fracture$	(m^2)

L_f	$Fracture\ spacing$	(m)
L_w	$Length\ of\ the\ fracture$	(m)
n	$Number\ of\ fractures$	$-$
N_p	$Number\ of\ perforations$	$-$
Q	$Total\ mass\ flow\ rate\ in\ the\ system$	(kg/s)
q	$Mass\ flow\ rate\ in\ the\ pipe/fracture$	(kg/s)
q_o	$Total\ mass\ flow\ rate\ in\ the\ system\ (oil\ field\ units)$	(bbl/min)
Re	$Reynolds\ number$	$-$
R_f	$Fracture\ resistance$	$(Pa.s/kg)$
R_{in}	$Resistance\ in\ the\ injection\ well$	$(Pa.s/kg)$
R_{ipn}	$Resistance\ in\ the\ perforation\ of\ the\ injeciton\ well$	$(Pa.s/kg)$
R_{on}	$Resistance\ in\ the\ production\ well$	$(Pa.s/kg)$
R_{opn}	$Resistance\ in\ the\ perforation\ of\ the\ production\ well$	$(Pa.s/kg)$
X_F	$Fracture\ spacing$	(m)
X_L	$Well\ spacing$	(m)
ΔP	$Pressure\ difference$	(Pa)
ΔP_o	$Pressure\ difference\ (oil\ field\ units)$	(psi)
ε	$Roughness\ of\ the\ wellbore$	$-$
μ	$Viscosity$	$(Pa.s)$
ρ	$Density\ of\ the\ fluid$	(kg/m^3)
ρ_o	$Density\ of\ the\ fluid\ (oil\ field\ units)$	(lbm/gal)
θ	$Angle\ of\ deviation\ for\ the\ wells$	$(degrees)$

10. References

[1] A. Bataillé, P. Genthon, M. Rabinowicz, and B. Fritz, "Modeling the coupling between free and forced convection in a vertical permeable slot: Implications for the heat production of an Enhanced Geothermal System," *Geothermics,* vol. 35, no. 5, pp. 654-682, 2006/10/01/ 2006, doi: https://doi.org/10.1016/j.geothermics.2006.11.008.

[2] A. S. Batchelor, "THE CREATION OF HOT DRY ROCK SYSTEMS BY COMBINED EXPLOSIVE AND HYDRAULIC FRACTURING; LA CREATION DE SYSTEMES DE ROCHES SECHES CHAUDES PAR L'ACTION COMBINEE D'EXPLOSIFS ET DE LA FRACTURATION HYDRAULIQUE," 1982.

[3] D. Duchane and D. Brown, "HOT DRY ROCK (HDR) GEOTHERMAL ENERGY RESEARCH AND DEVELOPMENT AT FENTON HILL, NEW MEXICO," 2002.

[4] A. Jelacic *et al.*, "An Evaluation of Enhanced Geothermal Systems Technology," United States, 2008-04-01 2008. [Online]. Available: https://www.osti.gov/biblio/1219317 (accessed on 22 June 2021)

[5] M. Li and N. Lior, "Energy analysis for guiding the design of well systems of deep Enhanced Geothermal Systems," *Energy,* vol. 93, pp. 1173-1188, 2015/12/15/ 2015, doi: https://doi.org/10.1016/j.energy.2015.09.113.

[6] a. S P Sutera and R. Skalak, "The History of Poiseuille's Law," *Annual Review of Fluid Mechanics,* vol. 25, no. 1, pp. 1-20, 1993, doi: 10.1146/annurev.fl.25.010193.000245.

[7] H. Darcy, *Les Fontaines publiques de la ville de Dijon ; Exposition et application des principes ‡ suivre et des formules ‡ employer dans les questions de distribution d'eau*. Paris: V. Dalmont (in French), 1856.

[8] S. Whitaker, "Flow in porous media I: A theoretical derivation of Darcy's law," *Transport in Porous Media,* vol. 1, no. 1, pp. 3-25, 1986/03/01 1986, doi: 10.1007/BF01036523.

[9] D. Brkić, "Iterative Methods for Looped Network Pipeline Calculation," *Water Resources Management,* vol. 25, no. 12, pp. 2951-2987, 2011/09/01 2011, doi: 10.1007/s11269-011-9784-3.

[10] D. Brkić, "An improvement of Hardy Cross method applied on looped spatial natural gas distribution networks," *Applied Energy,* vol. 86, no. 7, pp. 1290-1300, 2009/07/01/ 2009, doi: https://doi.org/10.1016/j.apenergy.2008.10.005.

[11] H. Cross, "Analysis of flow in networks of conduits or conductors," 1936. [Online]. Available: http://hdl.handle.net/2142/4433 (accessed on 22 June 2021).

[12] Y. Xia, M. Plummer, E. Mattson, R. Podgorney, and A. Ghassemi, "Design, modeling, and evaluation of a doublet heat extraction model in enhanced geothermal systems," *Renewable Energy,* vol. 105, pp. 232-247, 2017/05/01/ 2017, doi: https://doi.org/10.1016/j.renene.2016.12.064.

[13] P. Asai, P. Panja, J. McLennan, and J. Moore, "Performance evaluation of enhanced geothermal system (EGS): Surrogate models, sensitivity study and ranking key parameters," *Renewable Energy,* vol. 122, pp. 184-195, 2018/07/01/ 2018, doi: https://doi.org/10.1016/j.renene.2018.01.098.

[14] P. Asai, P. Panja, J. McLennan, and J. Moore, "Efficient workflow for simulation of multifractured enhanced geothermal systems (EGS)," *Renewable Energy,* vol. 131, pp. 763-777, 2019/02/01/ 2019, doi: https://doi.org/10.1016/j.renene.2018.07.074.

[15] T. Li, S. Shiozawa, and M. W. McClure, "Thermal breakthrough calculations to optimize design of a multiple-stage Enhanced Geothermal System," *Geothermics,* vol. 64, pp. 455-465, 2016/11/01/ 2016, doi: https://doi.org/10.1016/j.geothermics.2016.06.015.

[16] P. Asai, P. Panja, R. Velasco, J. McLennan, and J. Moore, "Fluid flow distribution in fractures for a doublet system in Enhanced Geothermal Systems (EGS)," *Geothermics,* vol. 75, pp. 171-179, 2018/09/01/ 2018, doi: https://doi.org/10.1016/j.geothermics.2018.05.005.

[17] P. A. Tipler and G. Mosca, *Physics for scientists and engineers*. New York: W.H. Freeman (in English), 2004.

[18] D. J. Wood, "Discussion: "Simple and Explicit Formulas for the Friction Factor in Turbulent Pipe Flow" (Haaland, S. E., 1983, ASME J. Fluids Eng., 105, pp. 89–90)," *Journal of Fluids Engineering,* vol. 105, no. 2, pp. 242-243, 1983, doi: 10.1115/1.3240975.

[19] P. Weddle, L. Griffin, and C. M. Pearson, "Mining the Bakken II – Pushing the Envelope with Extreme Limited Entry Perforating," in *SPE Hydraulic Fracturing Technology Conference and Exhibition*, 2018, vol. Day 3 Thu, January 25, 2018, D031S008R002, doi: 10.2118/189880-ms. [Online]. Available: https://doi.org/10.2118/189880-MS

[20] D. Cramer, K. Friehauf, G. Roberts, and J. Whittaker, "Integrating DAS, Treatment Pressure Analysis and Video-Based Perforation Imaging to Evaluate Limited Entry Treatment Effectiveness," in *SPE Hydraulic Fracturing Technology Conference and Exhibition*, 2019, vol. Day 3 Thu, February 07, 2019, D031S007R001, doi: 10.2118/194334-ms. [Online]. Available: https://doi.org/10.2118/194334-MS

[21] W. F. SALAS-VALERIO and J. F. STEFFE, "ORIFICE DISCHARGE COEFFICIENTS FOR POWER-LAW FLUIDS," *Journal of Food Process Engineering,* vol. 12, no. 2, pp. 89-98, 1990, doi: https://doi.org/10.1111/j.1745-4530.1990.tb00043.x.

[22] S. Huang, T. Ma, D. Wang, and Z. Lin, "Study on discharge coefficient of perforated orifices as a new kind of flowmeter," *Experimental Thermal and Fluid Science,* vol. 46, pp. 74-83, 2013/04/01/ 2013, doi: https://doi.org/10.1016/j.expthermflusci.2012.11.022.

[23] R. Allis and J. N. Moore, "Geothermal Characteristics of the Roosevelt Hot Springs System and Adjacent FORGE EGS Site, Milford, Utah," 2019, doi: https://doi.org/10.34191/MP-169.

[24] J. Moore *et al.*, "The Utah Frontier Observatory for Research in Geothermal Energy (FORGE): A Laboratory for Characterizing, Creating and Sustaining Enhanced Geothermal Systems" *Proceedings of the 45th Workshop on Geothermal Reservoir Engineering,* 2020. [Online]. Available: https://pangea.stanford.edu/ERE/db/GeoConf/papers/SGW/2020/Moore.pdf (accessed on 22 June 2021).

[25] D. R. Gaston *et al.*, "Physics-based multiscale coupling for full core nuclear reactor simulation," *Annals of Nuclear Energy,* vol. 84, pp. 45-54, 2015/10/01/ 2015, doi: https://doi.org/10.1016/j.anucene.2014.09.060.

[26] A. Wilkins, C. P. Green, and J. Ennis-King, "An open-source multiphysics simulation code for coupled problems in porous media," *Computers & Geosciences,* vol. 154, p. 104820, 2021/09/01/ 2021, doi: https://doi.org/10.1016/j.cageo.2021.104820.

[27] P. Asai and R. Podgorney. "Fluid Flow Distribution in Doublet EGS." https://github.com/pranayasai/FlowDistribution (accessed on 29th July 2021) (accessed.

A Mixed Fracture-Matrix Model for Evaluating Well Orientation and Completion Options for the Utah FORGE Site

Andy Wilkins[a], Lynn Munday[b], Chandrakanth Bolisetti[b], Robert Podgorney[b], Aleta Finnila[c]

[a]CSIRO Australia, [b]Idaho National Laboratory, [c]Golder Associates

Keywords

Discrete fracture network, FORGE, MOOSE

ABSTRACT

Orientation and completion for well pairs that have been subjected to multi-zonal stimulation play a critical role in the long-term performance of an Enhanced Geothermal Reservoir. Here we present the development of a methodology to rapidly and efficiently numerically simulate mixed fracture-matrix flow systems for evaluation of well design and completion options. An example evaluation based on a small fracture network representative of FORGE Well 16(A and B)-78(32) follows a discussion of the theory and model validation.

1. Introduction

Predictive simulations involving fractured porous media requires an accurate representation of the discrete fracture network (DFN) and its role in physical phenomena related to flow and transport. Predictive simulations using computational methods like the finite element method require the geometry to be discretized into elements of a mesh. Ideally, all the DFN's complex geometric features must be captured by the mesh. Creating a 3D mesh containing a 2D or 3D representation of the DFN is difficult. For this reason, we develop a modeling methodology in which the fractured porous media is decomposed into two separate domains – one representing the DFN network and the other containing the surrounding porous matrix – and loosely couple these two domains by exchanging heat energy. This simplifies our workflow by allowing us to produce a mesh of the matrix material completely independent from the mesh of the DFN.

Although the main goal of this loose coupling strategy is to simplify the meshing process, we also expect decreases in computational costs for the following reasons. (1) This simplification in the mesh reduces the number of volumetric elements in the matrix material leading to a smaller computational cost. (2) The computational cost is further reduced by separating the "faster" physics of porous flow in the fracture network from the "slower" diffusion in the matrix, allowing us to use different timestep sizes on each domain. (3) The separation of fast and slow physics also leads to a better conditioned linear system, further reducing the computational overhead. On the other hand, the loose coupling breaks the unconditional stability of a fully-implicit, fully-coupled solve.

In the sections that follow, we provide an overview of the loose coupling methodology as implemented in the MOOSE (Multiphysics Object-Oriented Simulation Environment) framework [Permann et al. (2020)]. We then present an example.

2. Loose Coupling Algorithm

For many years, researchers in various fields have loosely coupled different codes together to achieve goals similar to ours. Conceptually, our methodology is no different than these traditional approaches, but utilizing the MOOSE framework offers many advantages, as outlined below.

The MOOSE framework encapsulates the complexities of writing high performance computational software (e.g. parallel communication, numerical discretization, and nonlinear solvers) allowing a computational scientist to only focus on implementing and solving the differential equations governing the physics of interest. Several sets of differential equations governing different types of physics have been implemented as modules in MOOSE (e.g., diffusion, radiation transport, mechanics). In our work we use the PorousFlow module [Wilkins et al. (2020), Wilkins et al. (2021)] allowing us to capture the physics governing fluid and heat flow in porous media. Our loose coupling methodology is based on the MOOSE MultiApp system [Gaston et al. (2015)], which provides us with the ability to control the execution/time-stepping of multiple computational domains and the data transferred between them. Unlike many previous code-coupling schemes, MOOSE's MultiApp system is well-established and rigorously tested.

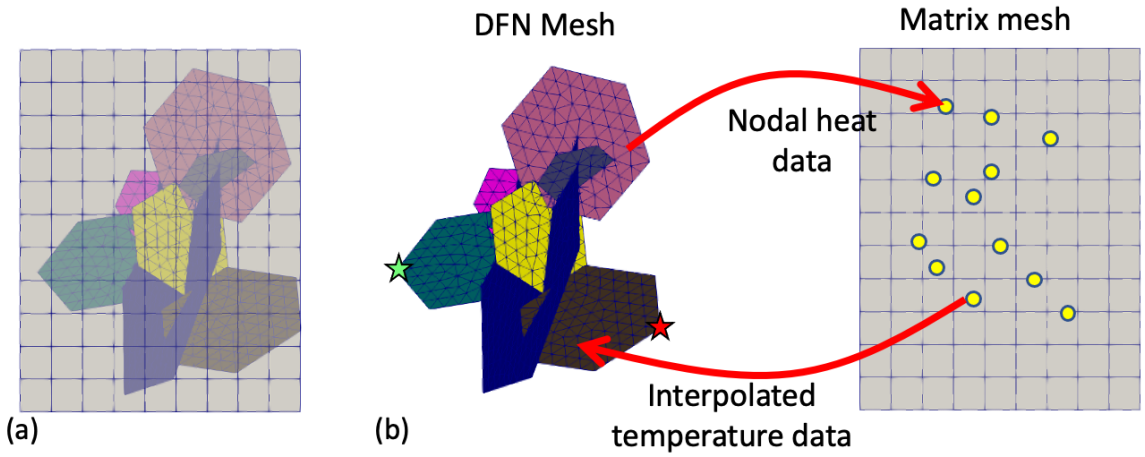

Figure 1: (a) The 2D DFN sits within the volumetric domain of the 3D porous matrix, but the meshes do not conform. (b) illustrates the separate computational domains and the loose coupling. The green and red stars indicate the injection and production points of the example, below.

The starting point of our loose coupling methodology is that the fractures can be considered as lower dimensional entities within the higher-dimensional porous media, such as illustrated in Figure 1~~Figure 1~~(a). (A consequence of our proposed methodology is that fractures do not provide a barrier to flow in their normal direction.) The two computational domains are governed by coupled thermo-hydraulics physics, where the heat equation describes heat conduction and convection, and Darcy's equations describes fully saturated porous flow. The two domains transfer heat information as shown in Figure 1b.

Briefly, the coupling algorithm proceeds as follows.

1. At the start of a timestep, the matrix mesh passes its temperature field, T_m, from the previous timestep to the DFN. The DFN interpolates T_m to every node in the DFN.
2. The DFN simulation then computes a fracture pore pressure and temperature field, T_f. according to the thermo-hydraulic physics along with a heat-transfer rate to the matrix:

$$Q = h(T_f - T) \tag{1}$$

   where h is the heat-transfer coefficient. The heat transfer coefficient is given by

$$h = 2\,\lambda/L \tag{2}$$

   which includes the effect of the matrix element length, L, on the heat transferred to between the matrix and fracture, and the λ is the matrix thermal conductivity in the direction normal to the fracture. This equation is derived assuming close-to steady-state heat flows have been achieved between the fracture and the nearest matrix nodes, so is inappropriate if short-time, small-scale phenomena are of interest. This is quantified below.

3. The matrix simulation applies Q as a point heat source, and using its thermo-hydraulic physics, computes a new matrix pore pressure and temperature field, T_m.
4. This completes the current timestep and the process repeats from step 1.

In this process, the matrix temperature transferred to the fracture is held fixed for each timestep taken in the fracture simulation. The opposite is also true: the heat source from the fracture simulation is held fixed during the matrix simulation timestep. This fixing means that large quantities of heat can be transferred back forth between the matrix and fracture in a single timestep, leading to an unphysical oscillatory behavior in the solution. These issues would not occur in a fully-coupled, conformally meshed DFN-matrix. All of the steps described in the loose coupling algorithm are controlled by the MOOSE MultiApp system.

3. Example DFN Simulation

The above loose coupling methodology is applied to a small DFN representative of FORGE Well 16(A and B)-78(32) [Finnila et al. (2021)], shown in Figure 1. In this analysis, we assume the following:

- the physics is fully-saturated, non-isothermal porous flow with heat conduction and convection;
- the water properties in both the fracture and the porous material are described by the IAPWS (2008, 2014) water equation of state;
- the pore pressure is initially hydrostatic, around 10MPa corresponding to a depth of around 1km;
- the temperature is 200^{o}C;
- injection is into the fracture network only, through the one point shown as a green star in Figure 1, at a rate of 10kg.s^{-1} and temperature of 100^{o}C;
- production is from the fracture network only, through the one point shown as a red star in Figure 1, at a rate of approximately 10kg.s^{-1} (it cannot be exactly 10kg.s^{-1} initially because this causes large pore pressure reductions due to thermal contraction of water and because the aperture increases in response to the injection);

- the fracture aperture dilates elastically in response to enhanced pore pressure;
- only heat energy is transferred between the fracture and the matrix: the matrix heats the cool water injected into the fracture network.

3.1 DFN simulation

The DFN contains 12 individual fractures shown in Figure 1 that range in size from 40-150m, meshed with three-noded triangular elements. The initial fracture aperture is assumed to be a_o=0.1mm for all fracture planes. The fractures are assumed to dilate due to increasing pore pressure by

$$a=a_o+A(P-P_o) \tag{3}$$

where A= 10^{-3} m.MPa^{-1} (a pressure increase of 1MPa dilates the fracture by 1mm) and P_0 is the hydrostatic insitu value of around 10MPa . The permeability of the fracture is proportional to a^2, with insitu permeability of 10^{-11} m^2 when $a=a_0$.

3.2 Matrix Simulation

The matrix computational domain measures 220m x 170m x 220m, and discretized by a structural mesh of eight-noded hexahedral elements. The physics models and material properties used to model the matrix material are more straightforward as they do not contain any information about the DFN or fracture aperture. It is assumed the rock matrix has small porosity of 0.1 and permeability of 10^{-18} m^2. The rock density is 2700kg.m^{-3} with specific heat capacity of 800J.kg^{-1}.K^{-1} and isotropic thermal conductivity of 5W.m^{-1}.K^{-1}.

3.3 DFN-Matrix coupling

Equation (2) for the heat transfer coefficient used to compute the heat rate between the matrix and fracture is only justified if the matrix element sizes are small enough to resolve the physics of interest. The time taken for a pulse of heat to travel through the matrix over half-element distance L is

$$t\sim c\rho\lambda^{-1}L^2 \tag{4}$$

This equation provides an estimate of the element size needed to accurately resolve physical phenomena. The matrix simulations in this example use elements sizes of 20, 10, and 5 m which produce simulation time-scales of 500, 125 and 5 days, respectively. If the simulation time is smaller than these enumerated time-scales, then Equation (2) is inappropriate and the simulation is likely to be inaccurate. To combat this, the matrix mesh should be made finer, or another form for heat transfer coefficient chosen.

3.4 Coupled DFN-Matrix Simulation Results

Figure 2 (a) and (b) show the temperature at the production bore. It is clear that the matrix provides substantial heat-energy to the injectate. However, as time proceeds, the cold injectate cools the surrounding matrix, leading to cooler production temperatures. These figures show how the results depend on the matrix and fracture mesh sizes. Keep in mind the Equation (4), which estimates the time scale at which the results should become accurate (eg, the "20m, 9.2m" case is not expected to be accurate for time-scales less than about 500 days).

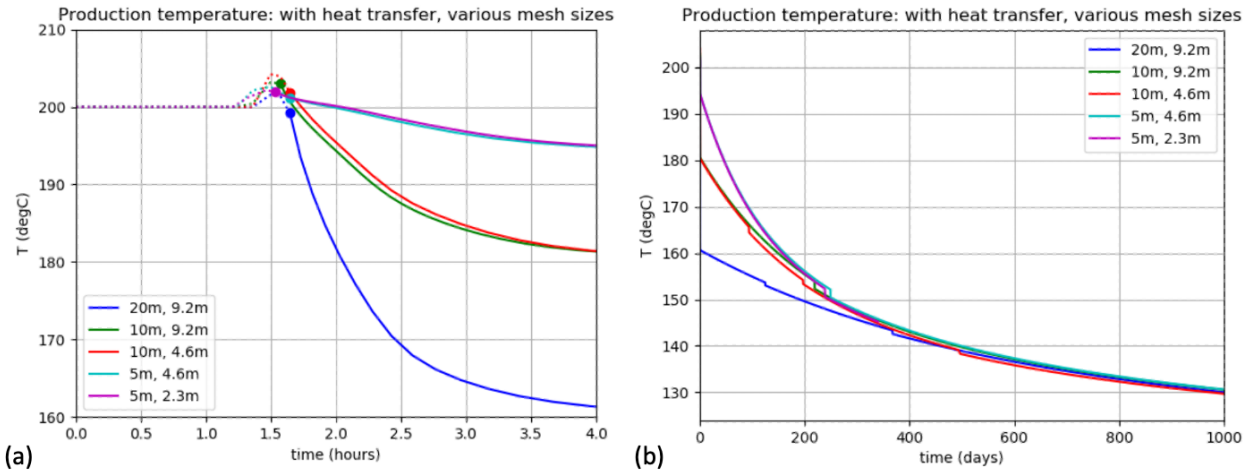

Figure 2: (a) Short term and (b) long term well production temperatures for the loosely coupled DFN-Matrix simulations. The first number in the legend is the mesh element size, while the second is the fracture element size.

Figure 3 shows the evolution of fracture aperture, which dilates from 0.1mm to around 3mm in this simulation.

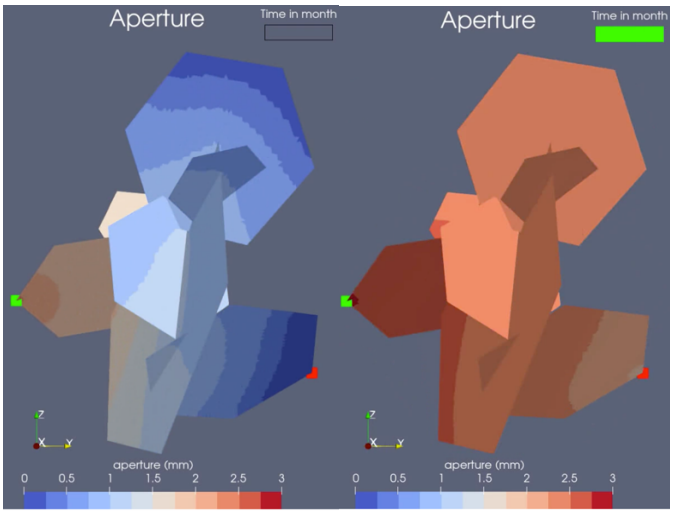

Figure 3: Fracture aperture. (a) a few hours after injection commences. (b) after 1 month of injection.

Figure 4 shows the evolution of the cooled matrix material. By 1000 days, an envelope of 10–20m around the fracture system has cooled by more than 10°C. Some parts of the fracture are not cooled at all by the injectate, most particularly those at the top of the network, where hot, buoyant water tends to reside.

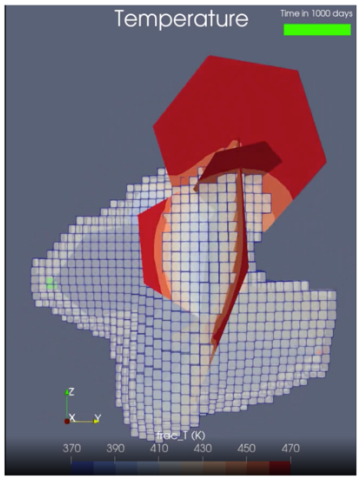

Figure 4: Cooled matrix material after 1000 days. Colors on the fracture system show fracture temperature. The small boxes are matrix elements that have cooled by more than 10°C.

4. Conclusion

In this work we presented a loosely coupled DFN simulation methodology that will greatly improve our workflow used to evaluate the performance of enhanced geothermal reservoirs. This loosely coupled protocol allows us to model the DFN separate from the matrix. This separation of computational domains allows us to mesh each feature separately, simplifying the meshing of DFN's as two-dimensional planes that do not need to be incorporated into the three-dimensional volumetric mesh of the matrix. We expect this framework to provide additional computational savings by simplifying the physics of each computational domain. We applied the loosely coupled simulation protocol to small DFN containing 12 fractures to capture the temperature change across the DFN between an injection and production borehole. Future work will enhance the current set of simulations to include more fractures in the DFN, material properties representative of the FORGE site, and other methods of including fracture aperture changes as the model evolves.

Acknowledgement

Funding for this work was provided by the U.S. DOE under grant DE-EE0007080 "Enhanced Geothermal System Concept Testing and Development at the Milford City, Utah FORGE Site". We thank the many stakeholders who are supporting this project, including Smithfield, Utah School and Institutional Trust Lands Administration, and Beaver County as well as the Utah Governor's Office of Energy Development.

This research made use of the resources of the High Performance Computing Center at Idaho National Laboratory, which is supported by the Office of Nuclear Energy of the U.S. Department of Energy and the Nuclear Science User Facilities under Contract No. DE-AC07-05ID14517.

REFERENCES

Permann, C.J., Gaston, D.R., Andrš, D., Carlsen, R.W., Kong, F., Lindsay, A.D., Miller, J.M., Peterson, J.W., Slaughter, A.E., Stogner, R.H. and Martineau, R.C., 2020. MOOSE: Enabling massively parallel multiphysics simulation. *SoftwareX*, 11, p.100430.

Gaston, D.R., Permann, C.J., Peterson, J.W., Slaughter, A.E., Andrš, D., Wang, Y., Short, M.P., Perez, D.M., Tonks, M.R., Ortensi, J. and Zou, L., 2015. Physics-based multiscale coupling for full core nuclear reactor simulation. *Annals of Nuclear Energy*, 84, pp.45-54.

IAPWS (2008). Release on the IAPWS Formulation 2008 for the Viscosity of Ordinary Water Substance. Technical Report, IAPWS, 2008. URL: www.iapws.org/relguide/visc.pdf

IAPWS (2014). Revised Supplementary Release on Backward Equations for Specific Volume as a Function of Pressure and Temperature v(p,T) for Region 3 of the IAPWS Industrial Formulation 1997 for the Thermodynamic Properties of Water and Steam. Technical Report, IAPWS, 2014. URL: www.iapws.org/relguide/Supp-VPT3-2016.pdf

Wilkins, A., Green, C.P. and Ennis-King, J., 2020. PorousFlow: a multiphysics simulation code for coupled problems in porous media. Journal of Open Source Software, 5(55), p.2176.

Wilkins, A., Green, C.P. and Ennis-King, J., 2021. An open-source multiphysics simulation code for coupled problems in porous media. Computers & Geosciences, 154, p.104820.

Finnila, A., Doe, T., Podgorney, R. Damjanac, B. and Xing, P., 2021. Revisions to the Discrete Fracture Network Model at Utah FORGE Site. *GRC Transactions*, 45